ORIGINS OF THE RESTING-STATE fMRI SIGNAL

EDITED BY: Jean Chen, Garth John Thompson, Shella Keilholz and Peter Herman

PUBLISHED IN: Frontiers in Neuroscience

frontiers Research Topics

frontiers

ISSN 1664-8714
ISBN 978-2-88966-285-2
DOI 10.3389/978-2-88966-285-2

About Frontiers

Frontiers is more than just an open-access publisher of scholarly articles: it is a pioneering approach to the world of academia, radically improving the way scholarly research is managed. The grand vision of Frontiers is a world where all people have an equal opportunity to seek, share and generate knowledge. Frontiers provides immediate and permanent online open access to all its publications, but this alone is not enough to realize our grand goals.

Frontiers Journal Series

The Frontiers Journal Series is a multi-tier and interdisciplinary set of open-access, online journals, promising a paradigm shift from the current review, selection and dissemination processes in academic publishing. All Frontiers journals are driven by researchers for researchers; therefore, they constitute a service to the scholarly community. At the same time, the Frontiers Journal Series operates on a revolutionary invention, the tiered publishing system, initially addressing specific communities of scholars, and gradually climbing up to broader public understanding, thus serving the interests of the lay society, too.

Dedication to Quality

Each Frontiers article is a landmark of the highest quality, thanks to genuinely collaborative interactions between authors and review editors, who include some of the world's best academicians. Research must be certified by peers before entering a stream of knowledge that may eventually reach the public - and shape society; therefore, Frontiers only applies the most rigorous and unbiased reviews.
Frontiers revolutionizes research publishing by freely delivering the most outstanding research, evaluated with no bias from both the academic and social point of view. By applying the most advanced information technologies, Frontiers is catapulting scholarly publishing into a new generation.

What are Frontiers Research Topics?

Frontiers Research Topics are very popular trademarks of the Frontiers Journals Series: they are collections of at least ten articles, all centered on a particular subject. With their unique mix of varied contributions from Original Research to Review Articles, Frontiers Research Topics unify the most influential researchers, the latest key findings and historical advances in a hot research area! Find out more on how to host your own Frontiers Research Topic or contribute to one as an author by contacting the Frontiers Editorial Office: researchtopics@frontiersin.org

ORIGINS OF THE RESTING-STATE fMRI SIGNAL

Topic Editors:
Jean Chen, University of Toronto, Canada
Garth John Thompson, ShanghaiTech University, China
Shella Keilholz, Emory University, United States
Peter Herman, Yale University, United States

Citation: Chen, J., Thompson, G. J., Keilholz, S., Herman, P., eds. (2020). Origins of the Resting-State fMRI Signal. Lausanne: Frontiers Media SA.
doi: 10.3389/978-2-88966-285-2

Table of Contents

frontiers in Neuroscience

EDITORIAL
published: 27 October 2020
doi: 10.3389/fnins.2020.594990

Editorial: Origins of the Resting-State fMRI Signal

J. Jean Chen[1,2]*, *Peter Herman*[3], *Shella Keilholz*[4] *and Garth J. Thompson*[5]

[1] Rotman Research Institute, Baycrest Health Sciences, Toronto, ON, Canada, [2] Department of Medical Biophysics, University of Toronto, Toronto, ON, Canada, [3] Department of Radiology and Biomedical Imaging, Yale University, New Haven, CT, United States, [4] Wallace H. Coulter Department of Biomedical Engineering, Georgia Institute of Technology, Emory University, Atlanta, GA, United States, [5] iHuman Institute, ShanghaiTech University, Shanghai, China

Keywords: resting-state fMRI, fMRI denoising, vascular modulation, head motion, arousal

Editorial on the Research Topic

Origins of the Resting-State fMRI Signal

INTRODUCTION

Resting-state functional magnetic resonance imaging (rs-fMRI) has exponentially increased in adoption in the past decade. It is now a part of nearly every neuroimaging-based large-scale study of the human brain due to ease of use and versatility (Smith et al., 2013; Bookheimer et al., 2019; Zonneveld et al., 2019; Power, 2020). This has also led to the introduction of numerous derivative metrics. rs-fMRI is used in mapping the human-brain connectome and in understanding every aspect of cognitive function. It is also regarded as a promising biomarker for brain diseases ranging from dementia to traumatic brain injury to autism spectrum disorders. However, limitations on the sensitivity and specificity of rs-fMRI (Buckner et al., 2013) are a disadvantage. As we stand on the cusp of widespread adoption of rs-fMRI in clinical research, there is an urgent need to understand what we do not yet know about the origins of the rs-fMRI signal. This is the driving force behind our Research Topic, "Origins of the Resting-state fMRI Signal," in which we strove to provide a comprehensive update on the quest for a better understanding.

NEURONAL ORIGINS

The mechanism behind the rs-fMRI signal is the slight dissociation between the cerebral blood flow and oxygen consumption which gives the physiological basis to blood oxygenation level dependent (BOLD) signal (Kim and Ogawa, 2012). The hemodynamic BOLD signal fluctuations follow the ongoing neuronal activity changes through neurovascular coupling. While this process seems simple and straightforward it has limitations as Lu et al. describes in their mini-review, where they coin the term "neurocentric" model. They bring attention to that the spontaneous neuronal activities can explain only a small percentage of the variation of rs-fMRI fluctuations indicating that more complex neuropil activities together effect the spontaneous fluctuations. In this Research Topic two more original papers show the complex relationship between spontaneous neuronal activity and BOLD fluctuations. Zhang X. et al. describes the relationship between local field potentials (LFP) and simultaneously measured BOLD signal fluctuations in anesthetized rats. This relationship can be non-linear under isoflurane and linear under dexmedetomidine anesthesia, indicating that different brain states have real influence to the origin of rs-fMRI. Zhang Z. et al. demonstrates that the intrinsic functional connectivity depends on the neuronal activity patterns of different brain states. In monkey brains the isoflurane specific burst-suppression activity increased the functional connectivity compared to the stable slow wave activity of the same isoflurane anesthesia.

OPEN ACCESS

Edited and reviewed by:
Vince D. Calhoun,
Georgia State University,
United States

***Correspondence:**
J. Jean Chen
jchen@research.baycrest.org

Specialty section:
This article was submitted to Brain Imaging Methods, a section of the journal Frontiers in Neuroscience

Received: *14 August 2020*
Accepted: *10 September 2020*
Published: *27 October 2020*

Citation:
Chen JJ, Herman P, Keilholz S and Thompson GJ (2020) Editorial: Origins of the Resting-State fMRI Signal. Front. Neurosci. 14:594990. doi: 10.3389/fnins.2020.594990

VASCULAR ORIGINS

While most studies use parameters derived from rs-fMRI as representing neuronal connectivity, it is important to realize that the BOLD rs-fMRI signal is not a direct measure of neuronal activity. Not only is the neuroanally-driven BOLD signal highly sensitive to vascular modulation (Liu, 2013), the frequency range of interest for rs-fMRI (i.e., below 0.1 Hz) is known to contain contributions from signals of non-neuronal origin. These factors have been of increasing interest in recent years (Liu, 2013; Golestani et al., 2016; Chu et al., 2018; Bright et al., 2020; Lewis et al., 2020), and are examined in this Research Topic. Tong et al., who were the first to demonstrate the unique vascular signature of low-frequency rs-fMRI fluctuations, present an update on the origins of these low-frequency vascular oscillations, their correction strategies and more interesting, ways in which they can be used in addressing clinical needs. Furthermore, Whittaker et al. investigate the relationship between systemic blood pressure and the rs-fMRI signal, while demonstrating the potential for the rs-fMRI signal to be used in tracking autoregulation.

COGNITIVE ORIGINS

If the rs-fMRI signal has a neural basis, its properties should be affected by widespread changes in activity linked to arousal. Two papers in this special issue address this question by examining rs-fMRI under different vigilance levels. Yin et al. compare awake humans to anesthetized monkeys and determine that functional flexibility is weakened but that its spatial distribution is somewhat preserved across species and states of consciousness. Liu and Falahpour review existing studies that link changes in vigilance to differences in BOLD signal amplitude and functional connectivity. Both papers indicate that similar time-varying patterns of activity are present in different vigilance states, but that the properties of the activity patterns vary with arousal.

NOISE AND ARTIFACTUAL ORIGINS

As with all biological signals, some shared variance in rs-fMRI comes from noise. Subject motion creates noise, and Maknojia et al. provide a detailed review of its sources, prevention, and removal in post-processing. Physiological signals at a higher sampling rates than rs-fMRI (e.g., respiration and pulse) may alias, so Huotari et al. studied the effect of under-sampling on numerous rs-fMRI metrics. While dynamic rs-fMRI metrics were affected, rs-fMRI metrics calculated over 5 min remained stable. Yuen et al. separated rs-fMRI signals into intrinsic mode functions (IMFs) using variational mode decomposition (VMD). They suggest that some IMFs corresponded to physiological/metabolic processes combined with rs-fMRI networks, while other IMFs corresponded to vasomotor/unknown sources and did not correspond to rs-fMRI networks (Yuen et al.). Moradi et al. applied empirical mode decomposition (EMD) to rs-fMRI and concluded that, vs. regressing the whole-brain "global" signal to remove noise, EMD provided IMFs with more spatially-specific measurements of global effects (Moradi et al.; Yuen et al.). Altogether, these studies suggest that the required sampling rates are dependent upon analysis method, and data-driven decomposition methods like VMD and EMD may provide signal decompositions that enhance noise removal.

PERSPECTIVES ON FUTURE WORK

Despite rs-fMRI's success as a research technique, we see challenges in the two primary application routes: (1) for neuroscience research, for which rs-fMRI has become a mainstay in human studies, but the difficulty of interpreting rs-fMRI metrics has limited application to basic science; (2) for clinical applications, where the lack of sensitivity and specificity has limited the adoption of rs-fMRI in assessing diseases. This Research Topic highlights the strong influence of arousal, vascular changes and noise contributions to rs-fMRI metrics, questioning the general practice of interpreting any rs-fMRI significance as being functional. For the foreseeable future, the community is urged to invest more effort into identifying the neuronal relevance of physiological and vascular oscillations in rs-fMRI, and into standardizing the definition of "resting state."

AUTHOR CONTRIBUTIONS

All authors contributed equally to the writing of this editorial.

REFERENCES

Bookheimer, S. Y., Salat, D. H., Terpstra, M., Barch, D. M., Buckner, R. L., et al. (2019). The lifespan human connectome project in aging: an overview. *Neuroimage* 185, 335–348. doi: 10.1016/j.neuroimage.2018.10.009

Bright, M. G., Whittaker, J. R., Driver, I. D., and Murphy, K. (2020). Vascular physiology drives functional brain networks. *Neuroimage* 217:116907. doi: 10.1016/j.neuroimage.2020.116907

Buckner, R. L., Krienen, F. M., and Yeo, B. T. T. (2013). Opportunities and limitations of intrinsic functional connectivity MRI. *Nat. Neurosci.* 16, 832–837. doi: 10.1038/nn.3423

Chu, P. P. W., Golestani, A. M., Kwinta, J. B., Khatamian, Y. B., and Chen, J. J. (2018). Characterizing the modulation of resting-state fMRI metrics by baseline physiology. *Neuroimage* 173, 72–87. doi: 10.1016/j.neuroimage.2018.02.004

Golestani, A. M., Kwinta, J. B., Strother, S. C., Khatamian, Y. B., and Chen, J. J. (2016). The association between cerebrovascular reactivity and resting-state fMRI functional connectivity in healthy adults: the influence of basal carbon dioxide. *Neuroimage* 132, 301–313. doi: 10.1016/j.neuroimage.2016.02.051

Kim, S.-G., and Ogawa, S. (2012). Biophysical and physiological origins of blood oxygenation level-dependent fMRI signals. *J. Cerebral Blood Flow Metabol.* 32, 1188–1206. doi: 10.1038/jcbfm.2012.23

Lewis, N., Lu, H., Liu, P., Hou, X., Damaraju, E., Iraji, A., et al. (2020). Static and dynamic functional connectivity analysis of cerebrovascular reactivity: an fMRI study. *Brain Behav.* 10:e01516. doi: 10.1002/brb3.1516

Liu, T. T. (2013). Neurovascular factors in resting-state functional MRI. *Neuroimage* 80, 339–348. doi: 10.1016/j.neuroimage.2013.04.071

Power, J. D. (2020). Resting-state fMRI: preclinical foundations. *fMRI* 47–63. doi: 10.1007/978-3-030-41874-8_5

Smith, S. M., Beckmann, C. F., Andersson, J., Auerbach, E. J., Bijsterbosch, J., Douaud, G.,et al. (2013). Resting-state fMRI in the human connectome project. *Neuroimage* 80, 144–168. doi: 10.1016/j.neuroimage.2013.05.039

Zonneveld, H. I., Purim, R. H. R., Bos, D., Vrooman, H. A., Muetel, R., Hofman, A., et al. (2019). Patterns of functional connectivity in an aging population: the rotterdam study. *Neuroimage* 189, 432–444. doi: 10.1016/j.neuroimage.2019.01.041

Conflict of Interest: The authors declare that the research was conducted in the absence of any commercial or financial relationships that could be construed as a potential conflict of interest.

frontiers in Neuroscience

ORIGINAL RESEARCH
published: 28 February 2019
doi: 10.3389/fnins.2019.00174

Brain Map of Intrinsic Functional Flexibility in Anesthetized Monkeys and Awake Humans

*Dazhi Yin[1], Zhao Zhang[2], Zhiwei Wang[1], Kristina Zeljic[1,3], Qian Lv[1], Danchao Cai[1], Yingwei Wang[2] and Zheng Wang[1]**

[1] Institute of Neuroscience, State Key Laboratory of Neuroscience, Key Laboratory of Primate Neurobiology, CAS Center for Excellence in Brain Science and Intelligence Technology, Shanghai Institute for Biological Sciences, Chinese Academy of Sciences, Shanghai, China, [2] Department of Anesthesiology, Huashan Hospital, Fudan University, Shanghai, China, [3] University of Chinese Academy of Sciences, Beijing, China

Emerging neuroimaging studies emphasize the dynamic organization of spontaneous brain activity in both human and non-human primates, even under anesthesia. In a recent study, we were able to characterize the heterogeneous architecture of intrinsic functional flexibility in the awake, resting human brain using time-resolved analysis and a probabilistic model. However, it is unknown whether this organizational principle is preserved in the anesthetized monkey brain, and how anesthesia affects dynamic and static measurements of spontaneous brain activity. To investigate these issues, we collected resting-state functional magnetic resonance imaging (fMRI) datasets from 178 awake humans and 11 anesthetized monkeys (all healthy). Our recently established method, a complexity measurement (i.e., Shannon entropy) of dynamic functional connectivity patterns of each brain region, was used to map the intrinsic functional flexibility across the cerebral cortex. To further explore the potential effects of anesthesia, we performed time series analysis and correlation analysis between dynamic and static measurements within awake human and anesthetized monkey brains, respectively. We observed a heterogeneous profile of intrinsic functional flexibility in the anesthetized monkey brain, which showed some similarities to that of awake humans (r = 0.30, p = 0.007). However, we found that brain activity in anesthetized monkeys generally shifted toward random fluctuations. Moreover, there is a negative correlation between nodal entropy for the distribution of dynamic functional connectivity patterns and static functional connectivity strength in anesthetized monkeys, but not in awake humans. Our findings indicate that the heterogeneous architecture of intrinsic functional flexibility across cortex probably reflects an evolutionarily conserved aspect of functional brain organization, which persists across levels of cognitive processing (states of consciousness). The coupling between nodal entropy for the distribution of dynamic functional connectivity patterns and static functional connectivity strength may serve as a potential signature of anesthesia. This study not only offers fresh insight into the evolution of brain functional architecture, but also advances our understanding of the dynamics of spontaneous brain activity.

Keywords: dynamic brain organization, intrinsic functional flexibility, evolution, monkey, anesthesia, resting-state fMRI

OPEN ACCESS

Edited by:
Shella Keilholz,
Emory University, United States

Reviewed by:
Changsong Zhou,
Hong Kong Baptist University, Hong Kong
Scott Peltier,
University of Michigan, United States

***Correspondence:**
Zheng Wang
zheng.wang@ion.ac.cn

Specialty section:
This article was submitted to Brain Imaging Methods, a section of the journal Frontiers in Neuroscience

Received: *26 October 2018*
Accepted: *14 February 2019*
Published: *28 February 2019*

Citation:
Yin D, Zhang Z, Wang Z, Zeljic K, Lv Q, Cai D, Wang Y and Wang Z (2019) Brain Map of Intrinsic Functional Flexibility in Anesthetized Monkeys and Awake Humans. Front. Neurosci. 13:174. doi: 10.3389/fnins.2019.00174

INTRODUCTION

A fundamental goal of comparative neuroscience is to determine conservation and evolution-driven changes in functional brain organization between species. Functional magnetic resonance imaging (fMRI), a non-invasive technique, has been utilized to identify functionally homologous or unique areas across primate species based on specific experimental tasks (Nakahara et al., 2002; Vanduffel et al., 2002; Wang et al., 2015). This technique has the advantage of providing a direct cross-species comparison using a common physiological measurement, i.e., blood oxygen level-dependent (BOLD) signal. Owing to ease of implementation and the robustness of findings, resting-state fMRI, simply a period of recording of BOLD signal in the absence of any explicit tasks, has become an attractive tool for studying large-scale brain functional organization (Zhang and Raichle, 2010; Power et al., 2014). Resting-state functional connectivity (FC) is typically used to index the interregional coherence in spontaneous low-frequency fluctuations (e.g., 0.01∼0.1 Hz) of BOLD signals (Biswal et al., 1995; Fox and Raichle, 2007). Through this approach, many functional brain networks such as the sensorimotor and default mode networks have been identified in both human and non-human primates (Vincent et al., 2007; Margulies et al., 2009; Hutchison et al., 2011; Hutchison and Everling, 2012; Mantini et al., 2013; Miranda-Dominguez et al., 2014; Neubert et al., 2014). In particular, the patterns of resting-state FC have showed some similarities across species and appear to transcend levels of consciousness, being present under anesthesia, see Raichle (2015) for a review. However, conventional resting-state FC is frequently evaluated in a time-averaged sense, under the potential assumption of stationary functional organization. Moreover, the origins and functional significance of resting-state FC patterns remain to be further understood.

Recently, emerging studies have emphasized the dynamic organization of brain function, suggesting that understanding brain function and dysfunction requires an integrated framework linking brain connectivity and brain dynamics (Deco et al., 2011; Liu and Duyn, 2013; Calhoun et al., 2014; Kopell et al., 2014; Braun et al., 2015; Christoff et al., 2016). Therefore, dynamic FC analysis, e.g., taking into account the temporal fluctuations of FC in different time windows of BOLD signals, has been proposed to characterize spontaneous brain activity (Chang and Glover, 2010; Zalesky et al., 2014; de Pasquale et al., 2015; Karahanoglu and Van De Ville, 2015; Chen et al., 2016). Although a number of challenges in techniques and interpretation remain, time-resolved analysis allows researchers to extract more in-depth information about brain function than static FC analysis (Jia et al., 2014; Keilholz et al., 2017; Liegeois et al., 2017; Preti et al., 2017).

Developing new analytic tools to describe spatiotemporal characteristics of resting-state FC patterns across species and states may provide deeper insight into functional organization of spontaneous brain activity. Based on dynamic FC analysis and clustering method, many discrete, reproducible functional states over the time of scan have been identified in both humans and monkeys (Allen et al., 2014; Barttfeld et al., 2015), see Hutchison et al. (2013a); Calhoun et al. (2014) for reviews. In contrast, our recent work (Yin et al., 2016) focused on quantifying the flexibility of the connectivity pattern for each brain region over time, using a complexity measurement (i.e., Shannon entropy) and probabilistic model. Consistent with task-induced functional reconfigurations (Cole et al., 2013; Braun et al., 2015), we revealed the heterogeneous organization of functional flexibility in the resting human brain. However, it is unknown whether this organizational principle is preserved in the anesthetized monkey brain, and how it corresponds with the human brain during wakeful rest. Although the spatiotemporal dynamics of brain activity have been demonstrated in the anesthetic state (Hutchison et al., 2013b; Barttfeld et al., 2015; Zhang et al., 2018), few studies pay attention to the cross-species correspondence of brain-wide dynamic organizational structure. Moreover, how anesthesia affects dynamic and static measurements of spontaneous brain activity still needs to be clarified.

To investigate these issues, we collected resting-state fMRI datasets from 178 awake humans and 11 anesthetized monkeys (healthy subjects). Our recently established method (Yin et al., 2016), a complexity measurement (i.e., Shannon entropy) of dynamic FC patterns of each brain region, was used to map the intrinsic functional flexibility across the cerebral cortex. Brain regions with high entropy for the distribution of dynamic FC patterns indicate high functional flexibility, and vice versa. For comparison, we conducted another complexity measurement based on distribution of correlation values, which reflects the functional complexity of a system (Zhao et al., 2010; Zamora-Lopez et al., 2016). A temporal variability analysis as a measure of functional flexibility was also carried out (Mueller et al., 2013; Zhang et al., 2016). To further explore the potential effects of anesthesia on the functional organization of spontaneous brain activity, we performed time series analysis and correlation analysis between dynamic and static measurements within awake human and anesthetized monkey brains, respectively. We hypothesized that the heterogeneous organization of intrinsic functional flexibility in the awake human brain persists in the anesthetized monkey brain.

MATERIALS AND METHODS

Participants

All experimental procedures for non-human primate research in this study were approved by the Institutional Animal Care and Use Committee at the Institute of Neuroscience and the Biomedical Research Ethics Committee, Shanghai Institutes for Biological Sciences, Chinese Academy of Sciences, and conformed to National Institutes of Health guidelines for the humane care and use of laboratory animals.

We recruited 11 wild-type monkeys (age 4.68 ± 0.46 years; weight 3.97 ± 1.36 kg; 7 female). In addition, 178 healthy human subjects (age 14.4 ± 3.6 years; 44 female; 35 subjects with eyes closed and 143 subjects with eyes open) were collected from the Autism Brain Imaging Data Exchange (ABIDE)[1]. We

[1]http://fcon_1000.projects.nitrc.org/indi/abide/

screened the human data based on demographic and diagnostic information provided in the ABIDE database (Di Martino et al., 2014). The inclusion criteria in the present study are briefly described as follows: (1) right-handedness, (2) age between 7 and 22 years, (3) a full-scale IQ score greater than 70; and time resolution of fMRI data equal to 2 s (datasets from four sites fit this criterion, including NYU, YALE, TRINITY, and UM).

Monkey Data Acquisition

Magnetic resonance imaging images of monkeys were acquired at the Institute of Neuroscience on a 3T whole-body scanner (Trio; Siemens Healthcare, Erlangen, Germany) running with an enhanced gradient coil insert (AC88; 80 mT/m maximum gradient strength, 800 mT/m/s maximum slew rate). A custom-built 8-channel phased-array transceiver coil was used for animal imaging sessions. Whole-brain resting-state fMRI data were collected using a gradient-echo echo-planar imaging (EPI) sequence (TR = 2000 ms; TE = 29 ms; flip angle = 77°; slices = 32; matrix = 64 × 64; field of view = 96 mm × 96 mm; 1.5 mm × 1.5 mm in plane resolution; slice thickness = 2.5 mm; GRAPPA factor = 2). For each session, 5–10 runs were acquired and each run consisted of 200 functional volumes. A pair of gradient echo images (echo time: 4.22 and 6.68 ms) with the same orientation and resolution as EPI images were acquired to generate a field map for distortion correction of EPI images. High-resolution T1-weighted anatomical images were acquired using a MPRAGE sequence (TR = 2500 ms; TE = 3.12 ms; inversion time = 1100 ms; flip angle = 9°; acquisition voxel size = 0.5 mm × 0.5 mm × 0.5 mm; 144 sagittal slices). Six whole-brain anatomical volumes were acquired and further averaged for better brain segmentation.

For MRI scanning, animals were prepared and maintained in a stable brain state under light anesthesia. The animal preparation procedure was conducted in a manner similar to our previous work (Wang et al., 2013; Lv et al., 2016). Induction of anesthesia was achieved by intramuscular injection with ketamine (10 mg/kg, Gutian Pharma Co., Ltd., China) before MRI scanning sessions, supplemented with atropine sulfate (0.05 mg/kg, Shanghai Harvest Pharma Co., Ltd., China) to decrease bronchial and salivary secretions. After intubation, animals were ventilated with a mixture of isoflurane (2–2.5%, Lunan Pharma Co., Ltd., China) and oxygen via either a standard ventilator (CWE, Inc., Ardmore, PA, United States) outside the scanner room or an MRI-compatible ventilator (CWE Inc., Weston, WI, United States) inside the scanner room. Macaques were maintained with intermittent positive-pressure ventilation to ensure a constant respiration rate (25–35 breaths/min). The concentration of isoflurane was adjusted based on continuously monitored vital signs, including blood oxygenation, electrocardiogram (ECG), rectal temperature (Small Animal Instruments, Inc., Stony Brook, NY, United States), respiration rate and end-tidal CO_2 (Smiths Medical ASD Inc., Dublin, OH, United States). Oxygen saturation was kept over 95% and body temperature was kept constant using a heated water blanket (Gaymar Industries Inc., Orchard Park, NY, United States). Lactated Ringer's solution was given with a maximum rate of 10 ml/kg/h during the anesthesia process (Logothetis et al., 1999). We removed the runs that showed erratic vital signs, image artifacts, as well as burst suppression according to the recordings of MRI-compatible electroencephalograph (Brain Products GmbH, Gilching, Germany) during functional data acquisition. In total, 99 runs were left for the final analyses. We treated each run independently following previous studies (Barttfeld et al., 2015; Lv et al., 2016).

Human Data Acquisition

Human MRI data were acquired from multiple sites with different parameters of pulse sequences (see text footnote 1). In the present study, one of the inclusion criteria was a time resolution of fMRI data equal to 2 s, to match the monkey data. In addition, we kept the same number of time points (i.e., 150 brain volumes) used across different sites.

Preprocessing of Monkey and Human fMRI Data

Functional brain images of monkey and human were preprocessed using the same steps, including slice timing correction, motion correction, coregistration with individual T1-weighted image, normalization to the corresponding standard space, resampling and spatial smoothing, regression of nuisance signals, removal of linear drift, and temporal filtering.

Specifically, the preprocessing of the monkey data were done using the SPM 8.0 toolbox[2] and the FMRIB Software Library toolbox (FSL[3]). The first 10 volumes were discarded. The field map images of each participant were then applied to compensate for the geometric distortion of EPI images caused by magnetic field inhomogeneity using FSL FUGUE. After slice timing correction and motion correction, the corrected images were normalized to standard space of the monkey F99 atlas[4] using an optimum 12-parameter affine transformation and non-linear deformations, and then resampled to 2-mm cubic voxels and spatially smoothed with a 4 mm full-width at half-maximum isotropic Gaussian kernel. Six head motion parameters, ventricle, and white matter signals were removed from the smoothed volumes using linear regression. Linear drift of the volumes was removed and temporal filtering (0.0025–0.05 Hz) (Vincent et al., 2007; Barttfeld et al., 2015; Lv et al., 2016) was performed.

The preprocessing of human data was performed by the Preprocessed Connectomes Project (PCP[5]) using the Data Processing Assistant for Resting-State fMRI (DPARSF) Toolbox (Yan and Zang, 2010). Preprocessing steps included slice timing correction, motion correction, spatial normalization into MNI space, resampled to 3 mm × 3 mm × 3 mm voxels and smoothing with a Gaussian kernel (full-width at half-maximum = 6 mm). Friston-24 parameters of head motion, white matter and ventricle signals were regressed out, followed by linear drift correction and temporal filtering (0.01–0.1 Hz).

[2]http://www.fil.ion.ucl.ac.uk/spm

[3]http://www.fmrib.ox.ac.uk

[4]http://sumsdb.wustl.edu/sums/macaque more.do

[5]http://preprocessed-connectomes-project.org/abide/index.html

For more details, readers may refer to the description in the PCP[6].

Static and Dynamic FC Analysis

For both preprocessed monkey and human datasets, we first divided the brain into different areas. For a direct cross-species comparison, here we adopted a regional map (RM) parcellation (82 cortical regions) for both monkeys and humans (**Table 1**), which is based on a combination of microstructural, functional, and topographic features (Kotter and Wanke, 2005; Bezgin et al., 2012; Reid et al., 2016). This parcellation has the same terminology for the monkey and human brains, but the topographic assignments originate from the monkey cortex. Pearson's correlation coefficients between the mean time courses of any pair of regions over the whole scan were then calculated to represent static FC, resulting in an 82 × 82 connectivity matrix. Finally, Fisher's Z-transformation was applied to the connectivity matrix so that their distributions could better satisfy normality.

To calculate dynamic FC, we applied a commonly used sliding window approach following our previous study (Yin et al., 2016). Briefly, a tapered window was selected and slid 1 TR, resulting in 168 windows for monkeys and 123 windows for humans. For each time window, Pearson's correlation coefficients between the mean time courses of any pair of regions were calculated and then a symmetric 82 × 82 connectivity matrix was generated. Thus, dynamic FC matrices were obtained for each participant.

[6]http://preprocessed-connectomes-project.org/abide/dparsf.html

TABLE 1 | Brain parcellation of regional map.

Label	Abbreviation	Full name
1/2	TCpol	Temporal polar cortex
3/4	Amyg	Amygdala
5/6	PHC	Parahippocampal cortex
7/8	TCi	Inferior temporal cortex
9/10	TCv	Ventral temporal cortex
11/12	HC	Hippocampal cortex
13/14	TCc	Central temporal cortex
15/16	TCs	Superior temporal cortex
17/18	VACv	Anterior visual cortex, ventral part
19/20	V1	Primary visual cortex
21/22	PFCoi	Orbital inferior prefrontal cortex
23/24	V2	Secondary visual cortex
25/26	PFCom	Orbitomedial prefrontal cortex
27/28	Ia	Anterior insula
29/30	Ip	Posterior insula
31/32	CCs	Subgenual cingulate cortex
33/34	PMCvl	Ventrolateral premotor cortex
35/36	CCp	Posterior cingulate cortex
37/38	CCr	Retrosplenial cingulate cortex
39/40	G	Gustatory cortex
41/42	PFCol	Orbitolateral prefrontal cortex
43/44	A2	Secondary auditory cortex
45/46	PFCvl	Ventrolateral prefrontal cortex
47/48	A1	Primary auditory cortex
49/50	VACd	Anterior visual cortex, dorsal part
51/52	S2	Secondary somatosensory cortex
53/54	PFCpol	Prefrontal pole cortex
55/56	S1	Primary somatosensory cortex
57/58	PFCm	Medial prefrontal cortex
59/60	PCm	Medial parietal cortex
61/62	M1	Primary motor cortex
63/64	FEF	Frontal eye field
65/66	CCa	Anterior cingulate cortex
67/68	PFCcl	Centrolateral prefrontal cortex
69/70	PCip	Intraparietal cortex
71/72	PCi	Inferior parietal cortex
73/74	PCs	Superior parietal cortex
75/76	PFCdm	Dorsomedial prefrontal cortex
77/78	PFCdl	Dorsolateral prefrontal cortex
79/80	PMCdl	Dorsolateral premotor cortex
81/82	PMCm	Medial premotor cortex

Odd numbers denote regions in the left hemisphere, and even numbers denote regions in right hemisphere.

Mapping Intrinsic Functional Flexibility of Brain

Based on the dynamic FC matrices of each participant, we computed the normalized probability distribution $P_i\ (j...n)$ for a given brain region i as follows:

$$P_i\ (j) = \frac{n(c_{ij})}{k \times w}, j = 1, 2, \ldots, N, and\ j \neq i$$

where $n(c_{ij})$ denotes how many times the connection between i and j emerged across temporal windows, k is a predefined threshold indicating number of the strongest connections reserved for region i at each time window, and w denotes the number of temporal windows. $P_i(j)$ denotes the probability of occurrence for the connection between regions i and j across all temporal windows. The greater the value of $P_i(j)$, the more frequent the interaction between region i and j across the temporal windows, and vice versa.

Regarding the threshold k, we have justified the choice of k for the human dataset in our previous study (Yin et al., 2016) as follows. Taking into account that brain is organized as a sparse and economical functional network, we first considered a wide range of k from 1 to 10. We then calculated the entropy (see definition below) for all brain regions for each k. Subsequently, two parameters were calculated, including contrast (identifying the value of k most sensitive to differences in entropy across the whole brain) and consistency (identify the value of k where the resulting entropy distribution is most representative of the distributions at other thresholds). We finally summed the two metrics, contrast and consistency, at each threshold k, and the peak value of this total was considered as corresponding to the optimal threshold (a peak value emerges at $k = 3$ for human dataset). Considering that the optimal threshold k may be different for different states or species, we conducted the above analysis for the anesthetized monkeys in this study. We found that the peak value also emerges at $k = 3$, although the maximum value was at $k = 1$ for the anesthetized

monkeys (**Supplementary Figure S1**). We therefore used the same threshold $k = 3$ for both humans and monkeys.

Subsequently, Shannon entropy E_i was applied to the probability distribution of each brain region i:

$$E_i = -\sum_{j=1}^{N} P_i(j) \times \log_2 P_i(j),$$

Here, E_i was used to quantify functional flexibility, which characterizes heterogeneous connectivity between region i and others over time. A higher value of E_i indicates greater functional flexibility, and vice versa. Readers can see our previous study for details regarding methodology (Yin et al., 2016).

Mapping Intrinsic Functional Complexity of Brain

The measure of functional complexity based on the distribution of whole-brain correlation values (for static network) without the need for thresholding has been proposed in earlier work (Zhao et al., 2010; Zamora-Lopez et al., 2016). Inspired by this, we calculated complexity C_i for the distribution of correlation values r_{ij} (for dynamical FC) of a node i. Here, we chose to define complexity as the difference between the observed distribution $p(r_{ij})$ and the uniform distribution, which is most robust to variations in the number of bins compared with alternatives such as entropy (Zamora-Lopez et al., 2016). The formula is as follows:

$$C_i = 1 - \frac{1}{C_m}\sum_{u=1}^{m}\left|p_u(r_{ij}) - \frac{1}{m}\right|,$$

where || means the absolute value, $C_m = 2^*(m\text{-}1)/m$, and m indicates number of bins (here using 50 bins). The C_i reflects functional complexity of a node i.

Mapping Intrinsic Temporal Variability of Brain

A recent study (Zhang et al., 2016) used temporal variability analysis to characterize dynamic functional reconfiguration of each brain region, which can be expressed as follows.

$V_i = 1 - E\left[corrcoef\left(F_{i,j}, F_{i,k}\right)\right], j, k = 1, 2, 3, \ldots w$

where $E[\ ]$ denotes mean value, $F_{i,j}$ indicates FC profile of node i at time window j and w denotes number of temporal windows. This linear measure does not need a threshold for FC values and is indicative of functional flexibility.

Time Series Analysis of Brain Activity

To evaluate fluctuations of brain activity, we performed a time series analysis. For the time series of each brain region, we first calculated the distribution of the BOLD signal values with m bins (here using 30 bins). Then, we used entropy to quantify the randomness of fluctuations of brain activity. The higher the entropy of time series, the more random the fluctuations of brain activity. To further test the statistical significance of the randomness, we finally compared real entropy and entropies of 1000 random time series with the same number of time points and number of bins, and a Z-score was obtained using the following formula.

$$Z = \frac{H_{real} - E[H_{rand}]}{std(H_{rand})},$$

where H_{real} denotes entropy of the observed time series, H_{rand} denotes entropy of the random time series, and $E[]$ indicates mean value. If the Z-score approaches zero (theoretically Z-score ≤ 0), the fluctuations of brain activity tend to be random.

Coupling Between Dynamic and Static Measurements of Spontaneous Brain Activity

To explore the potential effects of anesthesia, we calculated correlations between dynamic measurement (nodal entropy E, complexity C, and temporal variability V) and static measurement (nodal strength, i.e., sum of nodal static FC) within anesthetized monkey and awake human brains, respectively.

Validation Analysis

To validate our results, we considered the effects of different data processing on interspecies comparisons. Following previous studies (Vincent et al., 2007; Barttfeld et al., 2015; Lv et al., 2016), we used temporal filtering (0.0025–0.05 Hz) for monkeys, which is different from that commonly used for humans (0.01–0.1 Hz). To test the effect of different temporal filtering, we first compared the brain map of entropy E, complexity C, and temporal variability V between different temporal filters in monkeys. We then performed interspecies comparisons using the same temporal filtering (i.e., 0.01–0.1 Hz).

In our main analyses, we used a different number of time points for monkey ($n = 190$) and human ($n = 145$) datasets. To test the effect of a different number of time points, we performed the interspecies comparisons using the same number of time points ($n = 145$).

In the human subject sample, there are 35 subjects with eyes closed and 143 subjects with eyes open. To consider the effect of eye status, we first compared the brain map of entropy E, complexity C, and temporal variability V between the two human subgroups with different eye status. We then performed the interspecies comparisons for both anesthetized monkeys versus human subjects with eyes closed and anesthetized monkeys versus human subjects with eyes open.

RESULTS

Static FC Patterns in Anesthetized Monkey and Awake Human Brains

We calculated static, time-averaged FC for both human and monkey datasets. We found that the FC in anesthetized monkeys (mean ± SD = 0.25 ± 0.16) was generally weaker than in awake humans (mean ± SD = 0.44 ± 0.13) (effect size: Cohen's $d = -1.3$). However, FC between anesthetized monkeys and awake humans was significantly correlated ($r = 0.60$, $p < 0.00001$) (**Figure 1**).

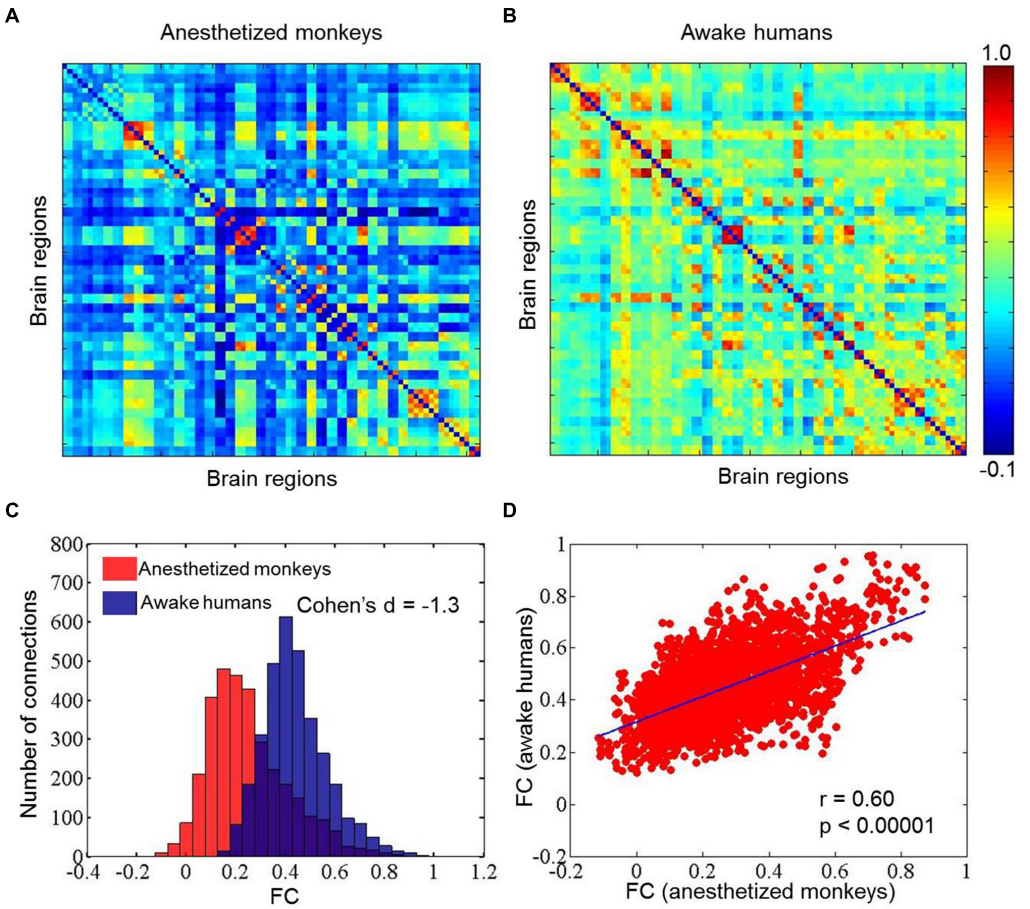

FIGURE 1 | Mean static functional connectivity matrices for anesthetized monkeys **(A)** and awake humans **(B)**; panel **(C)** shows distributions of static functional connectivity for anesthetized monkeys (red) and awake humans (blue); and **(D)** exhibits correlation of static functional connectivity between anesthetized monkeys and awake humans. Color bar denotes Pearson correlation coefficients.

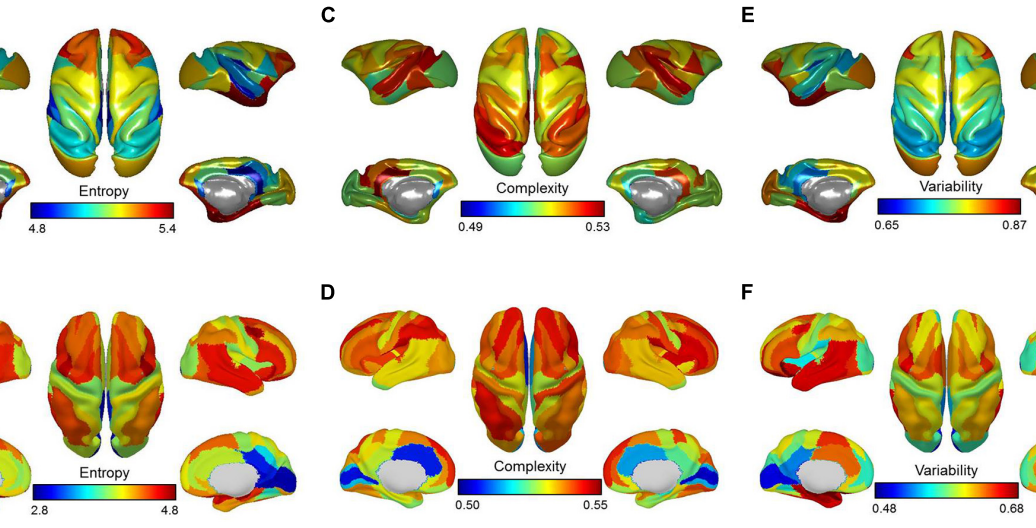

FIGURE 2 | Brain maps of mean entropy for the distribution of dynamic functional connectivity patterns **(A,B)**, complexity for the distribution of correlation values **(C,D)**, and variability for the dynamic functional connectivity patterns **(E,F)** for anesthetized monkeys and awake humans. Color bars denote mean values.

Similarity of Intrinsic Functional Flexibility Between Anesthetized Monkey and Awake Human Brains

For the anesthetized monkeys, we found that the brain regions with higher entropy E mainly involved the lateral prefrontal cortex, anterior insula, and medial temporal lobe. The brain regions that showed lower entropy E included primary sensory areas (e.g., auditory and somatosensory regions) and midline default mode regions (e.g., posterior cingulate cortex/retrosplenial cingulate cortex) (**Figure 2A**).

For the awake humans, we observed that brain regions that showed higher entropy E mainly involved the lateral prefrontal, parietal, and temporal cortex, anterior insula, as well as supplementary motor area. The brain regions that showed lower entropy E included primary sensory areas (e.g., auditory, visual, and somatosensory regions) and midline default mode regions (e.g., posterior cingulate cortex/retrosplenial cingulate cortex) (**Figure 2B**). This result is consistent with our previous study (Yin et al., 2016), despite the use of different brain parcellation and dataset.

Quantitatively, we found a significant correlation of brain-wide entropy E between anesthetized monkeys and awake humans (r = 0.30, p = 0.007) (**Figure 3A**), although averaged entropy E across the whole brain of anesthetized monkeys (mean $\pm$ SD = 5.18 $\pm$ 0.18) was higher than that of awake humans (mean $\pm$ SD = 4.27 $\pm$ 0.41) (effect size: Cohen's d = 2.9) (**Figure 3B**). These findings indicate that the heterogeneous flexibility across brain regions is preserved in anesthetized monkeys. However, there are some inconsistencies. For example, the primary visual cortex showed relatively higher entropy E in the anesthetized monkeys, and relatively lower entropy E in the awake humans. In contrast, the inferior parietal cortex exhibited relatively lower entropy E in the anesthetized monkeys, but higher in the awake humans. By comparing brain regions with top 30% and bottom 30% entropy E values in anesthetized monkeys and awake humans, we found that overlapping regions with higher entropy E between species included the left dorsolateral prefrontal cortex, left frontal eye field, left orbitolateral prefrontal cortex, bilateral anterior insula, bilateral orbital inferior prefrontal cortex, bilateral hippocampus, and bilateral parahippocampal cortex (**Figure 4A**); and that overlapping regions with lower entropy E between species included the bilateral posterior cingulate cortex, bilateral retrosplenial cingulate cortex, left primary auditory cortex, left secondary auditory cortex, right anterior visual area, bilateral secondary somatosensory cortex, bilateral medial parietal cortex, and right posterior insula (**Figure 4B**).

Comparison of Functional Complexity Measurement With Our Method

We found that overall complexity C was higher in awake humans compared with anesthetized monkeys, and the correlation of brain-wide complexity C between anesthetized monkeys and awake humans was similar with that obtained using our method (**Figures 2C,D**, **3C,D**). However, few of the well-known flexible cognitive control regions such as lateral prefrontal cortex, anterior insula, and hippocampal cortex showed higher complexity C in anesthetized monkeys (**Figure 4C**). Instead, we observed unimodal regions such as secondary somatosensory cortex, auditory cortex, and visual cortex showed higher complexity C (**Figure 4D**). It is possible that this complexity measurement C based on the distribution of correlation values is not suitable for quantifying the heterogeneous functional flexibility of the brain, although it can better assess the functional complexity of the system at different states. For instance, we found the hippocampal cortex exhibited narrower distribution of correlation values (lower complexity) than that of secondary somatosensory cortex in both anesthetized monkeys and awake humans, whereas the time-varying strongest connections of hippocampal cortex was more uniform (higher flexibility) across the whole brain than that of secondary somatosensory cortex (**Figure 5**).

Additionally, we found right inferior parietal cortex showed higher complexity C and primary visual cortex showed lower complexity C in both anesthetized monkeys and awake humans (**Figures 4C,D**). However, we observed that the strongest connections of primary visual cortex were local and stereotyped in awake humans while distributed and variable across brain in anesthetized monkeys. Moreover, we found inferior parietal cortex more frequently connected with local brain regions in parietal, temporal, and visual cortices in monkeys while more frequently connected with broad brain regions in parietal, temporal, and frontal cortices in humans (**Figure 6**).

Comparison of Time Variability Measurement With Our Method

We found the results obtained by temporal variability measurement V were highly consistent with that using our method, but not complexity measurement C based on distribution of correlation values (**Figures 2E,F**, **3E,F**, **4E,F**). This suggests that information of spatial connectivity patterns is more important than distribution of correlation values for describing functional flexibility, even with k (= 3) strongest connections at each time window.

Time Series Analysis of Brain Activity

We found the entropy H of time series to be globally higher in anesthetized monkeys compared with awake humans. In particular, we observed that the primary visual cortex showed the highest entropy H in anesthetized monkeys. However, entropy H of time series for all brain regions were remarkably lower than that of random time series in both anesthetized monkeys and awake humans (**Figure 7**). This result suggests that brain activity in anesthetized monkeys generally shifts toward the random fluctuations, but still differs from random fluctuations. In addition, the effect of anesthesia on fluctuations of brain activity is probably non-uniform across brain.

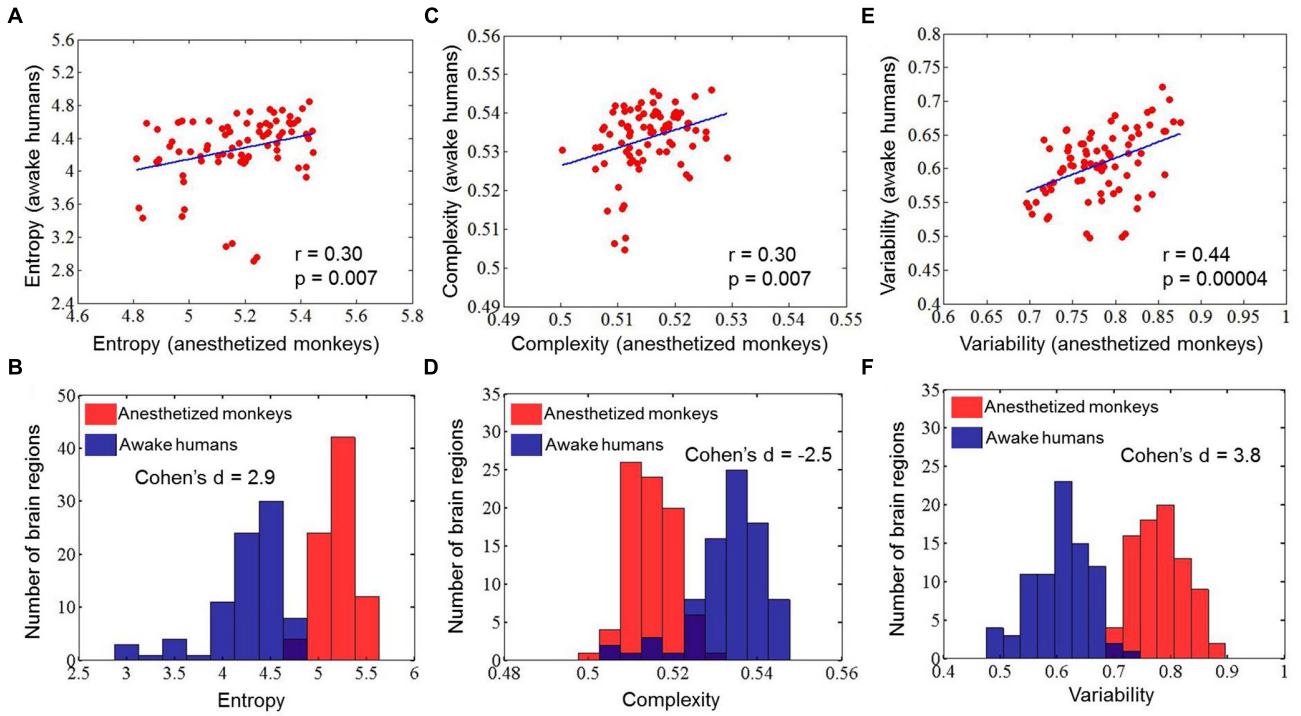

FIGURE 3 | Correlations of mean entropy for the distribution of dynamic functional connectivity patterns **(A)**, complexity for the distribution of correlation values **(C)**, and variability for the dynamic functional connectivity patterns **(E)** between anesthetized monkeys and awake humans. The distribution of mean entropy **(B)**, complexity **(D)**, and variability **(F)** is also shown for anesthetized monkeys and awake humans.

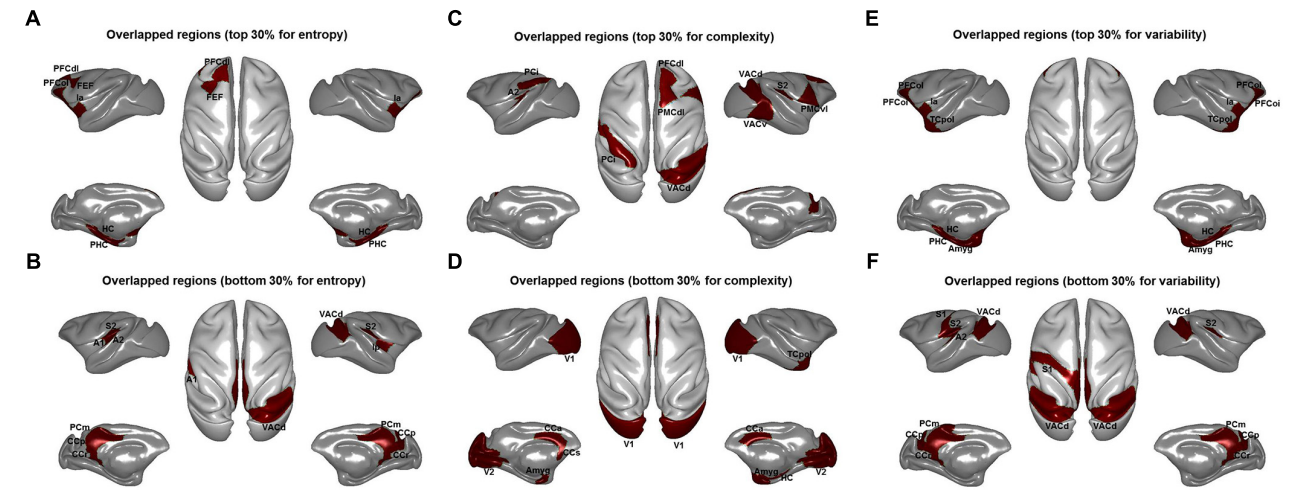

FIGURE 4 | Overlapped brain regions for top 30% entropy values for the distribution of dynamic functional connectivity patterns **(A)**, complexity values for the distribution of correlation values **(C)**, and variability values for the dynamic functional connectivity patterns **(E)** and bottom 30% entropy values for the distribution of dynamic functional connectivity patterns **(B)**, complexity values for the distribution of correlation values **(D)**, and variability values for the dynamic functional connectivity patterns **(F)** between anesthetized monkeys and awake humans. PFCdl, dorsolateral prefrontal cortex; FEF, frontal eye field; PFCol, orbitolateral prefrontal cortex; Ia, anterior insula; HC, hippocampus; PHC, parahippocampal cortex; CCr, retrosplenial cingulate cortex; A1, primary auditory cortex; A2, secondary auditory cortex; VACd, anterior visual area; S2, secondary somatosensory cortex; PCm, medial parietal cortex; Ip, posterior insula; PMCvl, ventrolateral premotor cortex; PCi, inferior parietal cortex; PMCdl, dorsolateral premotor cortex; VACv, anterior visual cortex (ventral part); Amyg, amygdala; V1, primary visual cortex; V2, secondary visual cortex; CCs, subgenual cingulate cortex; TCpol, temporal polar cortex; and S1, primary somatosensory cortex.

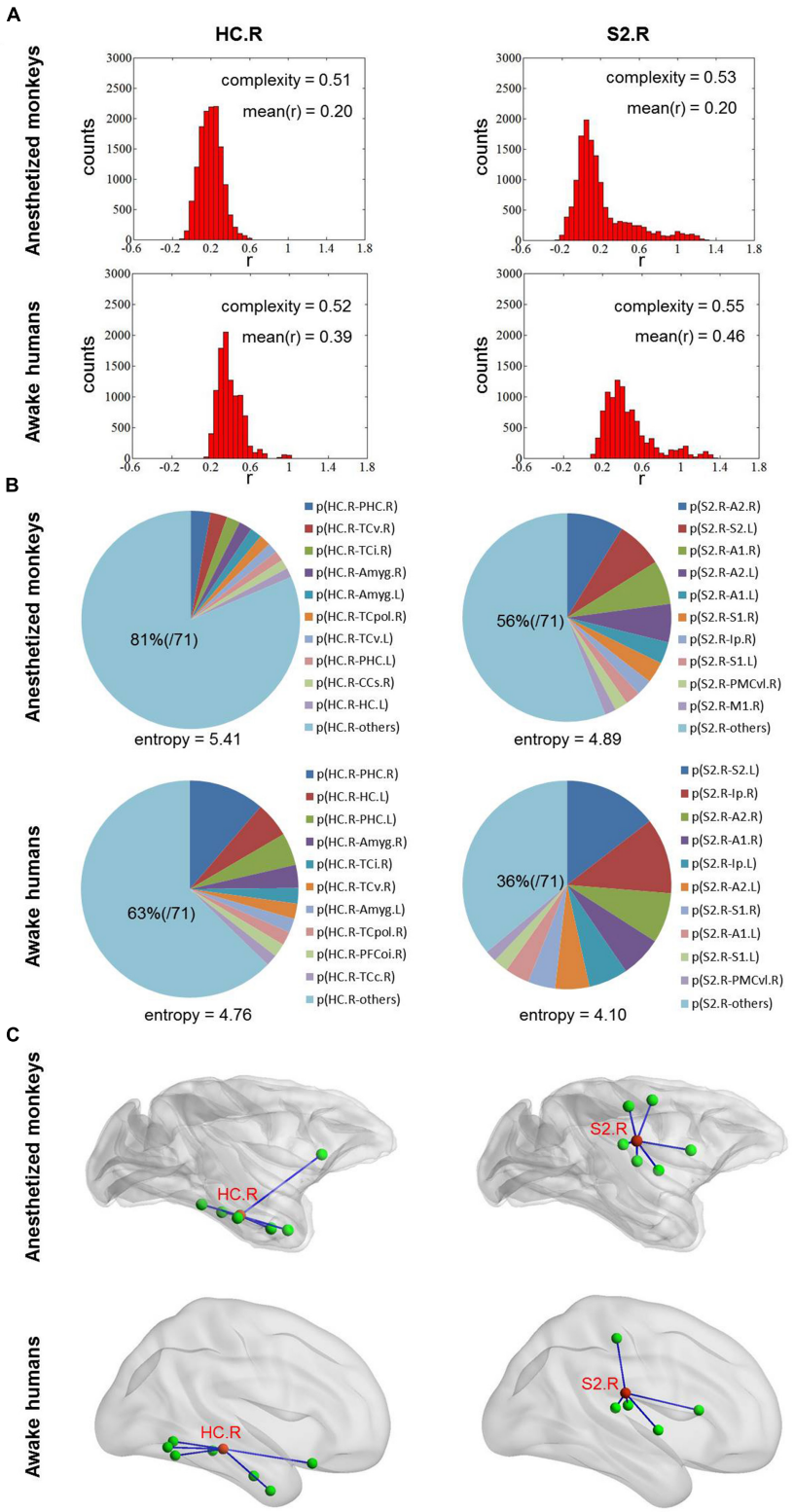

FIGURE 5 | (A) Shows the distribution of correlation values for right HC and S2 in both anesthetized monkeys and awake humans. The distribution of correlation values of right HC is narrower (lower complexity) than that of right S2 in both monkeys and humans. **(B)** Shows the probability distribution of strongest connectivity with right HC and S2 in monkeys and humans. The distribution of strongest connectivity with right HC is more uniform (higher flexibility) across brain than that of right S2 in both monkeys and humans. The most frequent connections with right HC and S2 are rendered in **C**. The patterns of most frequent connections are similar between species for both right HC and S2. HC, hippocampal cortex and S2, secondary somatosensory cortex.

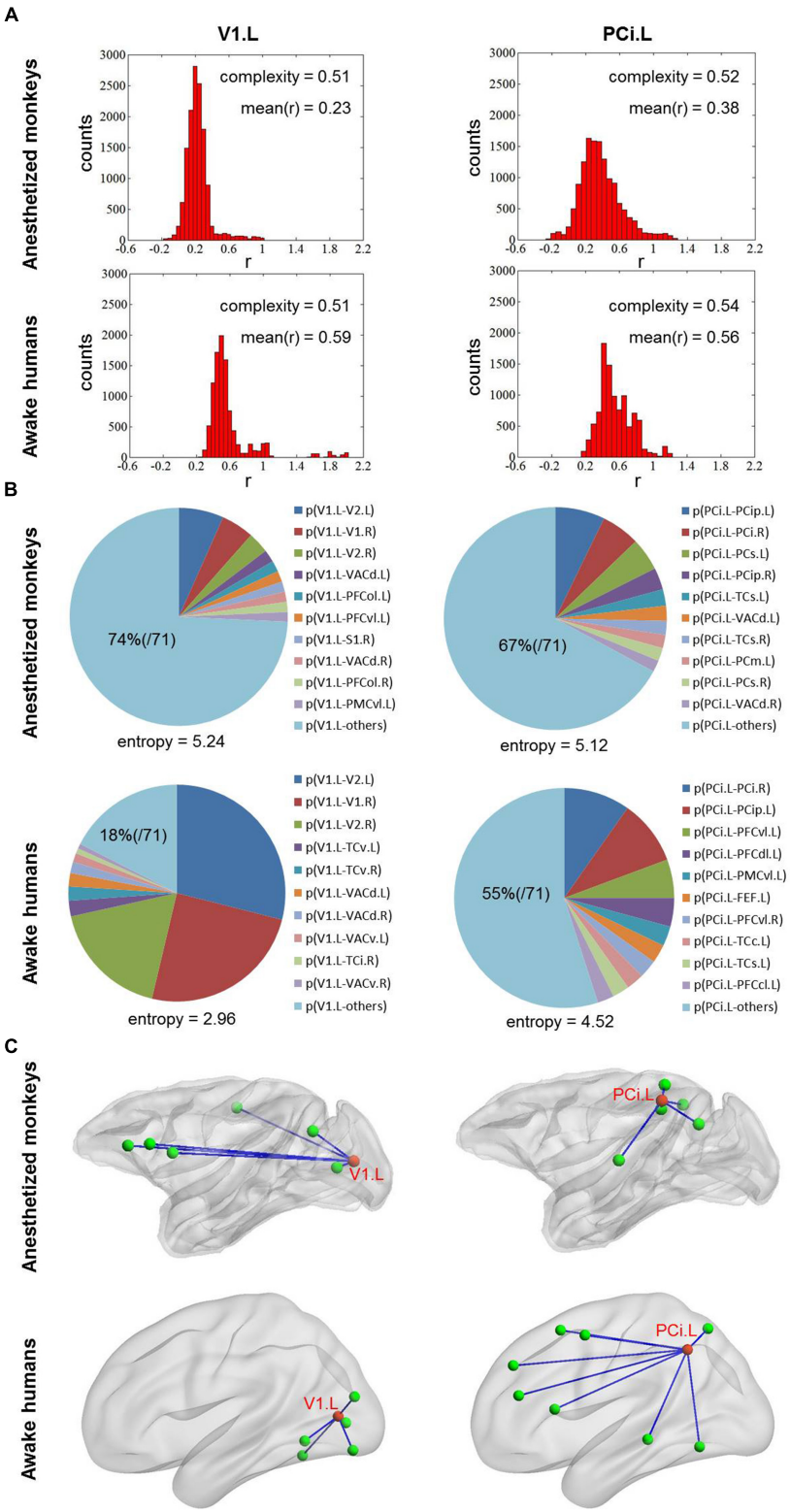

FIGURE 6 | (A) Shows the distribution of correlation values for left V1 and PCi in both anesthetized monkeys and awake humans. The distribution of correlation values of left V1 is narrower (lower complexity) than that of left PCi in both monkeys and humans. **(B)** Shows probability distribution of strongest connectivity with left V1 and PCi in monkeys and humans. The distribution of strongest connectivity with left PCi is more uniform (higher flexibility) across brain than that of left V1 in humans, which the opposite is seen in monkeys. The most frequent connections with left V1 and PCi are rendered in **C**. The patterns of most frequent connections are different between species for both left V1 and PCi. V1, primary visual cortex and PCi, inferior parietal cortex.

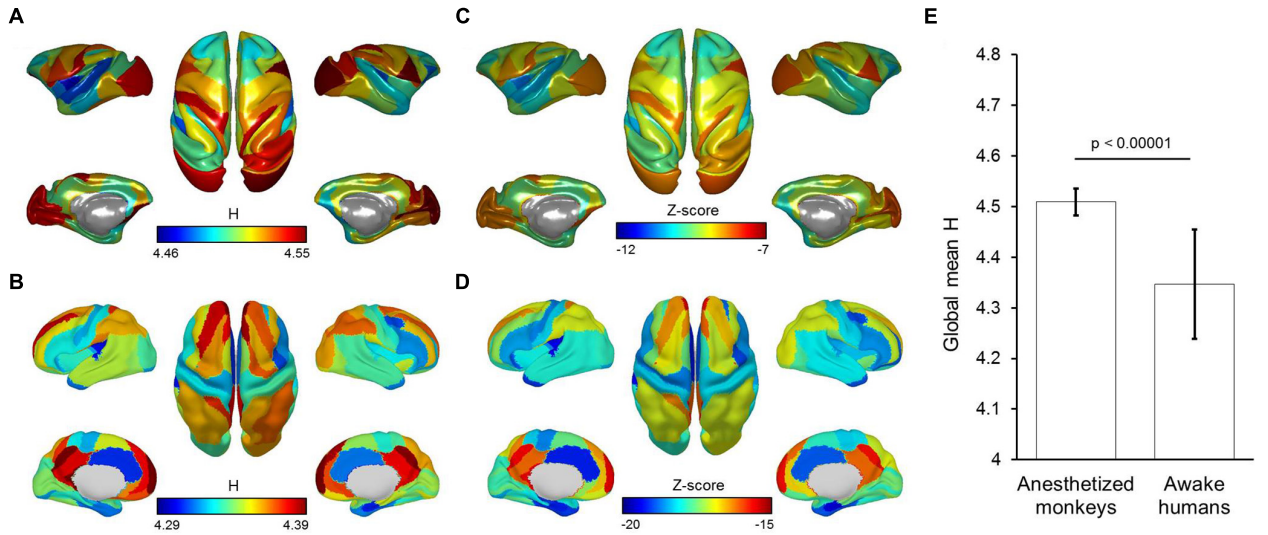

FIGURE 7 | Brain map of mean entropy of time series for anesthetized monkeys **(A)** and awake humans **(B)**. Brain map of mean *Z*-scores for entropy of time series are also shown for monkeys **(C)** and humans **(D)**. **(E)** Shows global mean entropy of time series for monkeys and humans. Color bars denote mean values.

Distinct Relationships Between Dynamic and Static Measurements Within Awake Human and Anesthetized Monkey Brains

To explore the impacts of anesthesia, we calculated correlations between dynamic measurement and static measurement in awake humans and anesthetized monkeys, respectively. We found a negative correlation ($r = -0.47$, $p = 0.00001$) between nodal entropy E and strength in anesthetized monkeys, but not in awake humans ($r = -0.19$, $p = 0.085$). In contrast, we found a positive correlation ($r = 0.69$, $p < 0.00001$) between nodal complexity C and strength in anesthetized monkeys, but not in awake humans ($r = -0.14$, $p = 0.22$). Consistent with our method, we found a negative correlation ($r = -0.68$, $p < 0.00001$) between nodal temporal variability V and strength in anesthetized monkeys, but not in awake humans ($r = -0.19$, $p = 0.089$) (**Figure 8**).

Validation Analysis

Regarding the effect of temporal filtering, we found significant correlations between two different temporal filters in monkeys for entropy E ($r = 0.97$, $p < 0.00001$), complexity C ($r = 0.73$, $p < 0.00001$), and variability V ($r = 0.96$, $p < 0.00001$) (**Supplementary Figure S2**). Moreover, we consistently observed significant correlations between species for entropy E ($r = 0.26$, $p = 0.02$), complexity C ($r = 0.30$, $p = 0.007$), and variability V ($r = 0.37$, $p = 0.0007$) with the same time filtering (**Supplementary Figure S3**). However, the interspecies correlations based on the same temporal filtering were a little weaker than when using different temporal filtering for entropy E and variability V, but the same for complexity C. This result indicates that different temporal filtering for monkeys and humans may give better correspondence between species.

For the effect of different number of time points, we consistently observed significant correlations between species for entropy E ($r = 0.28$, $p = 0.01$), complexity C ($r = 0.30$, $p = 0.005$), and variability V ($r = 0.44$, $p = 0.00003$) with the same number of time points (**Supplementary Figure S4**). This result suggests that the different number of time points used for monkeys and humans did not significantly affect correlations between species.

For the effect of eye status, we found significant correlations between the two human subgroups for entropy E ($r = 0.96$, $p < 0.00001$), complexity C ($r = 0.75$, $p < 0.00001$), and variability V ($r = 0.91$, $p < 0.00001$) with different eye status (**Supplementary Figure S5**). For the interspecies comparisons, we found the correlations were similar for the two conditions of human subjects with different eye status (**Supplementary Figure S6**). This result suggests that our main findings are not significantly affected by eye status of human subjects during resting-state fMRI scanning. Specifically, we observed that the visual cortex showed lowest entropy E in the human subjects for both closed and open eyes. This further implies that eye status does not change the rank of functional flexibility of visual cortex in the brain. In the anesthetized monkeys, the primary visual cortex showed relatively high entropy E. This is probably because anesthesia causes brain activity in primary visual cortex to shift much more toward random fluctuations.

DISCUSSION

Although resting-state connectivity networks have been used for decades to probe functional brain organization (Deco et al., 2011; Raichle, 2015; Bassett and Sporns, 2017), the origins and functional significance of resting-state connectivity patterns require further understanding. In a recent study, we were able to characterize the heterogeneous architecture of

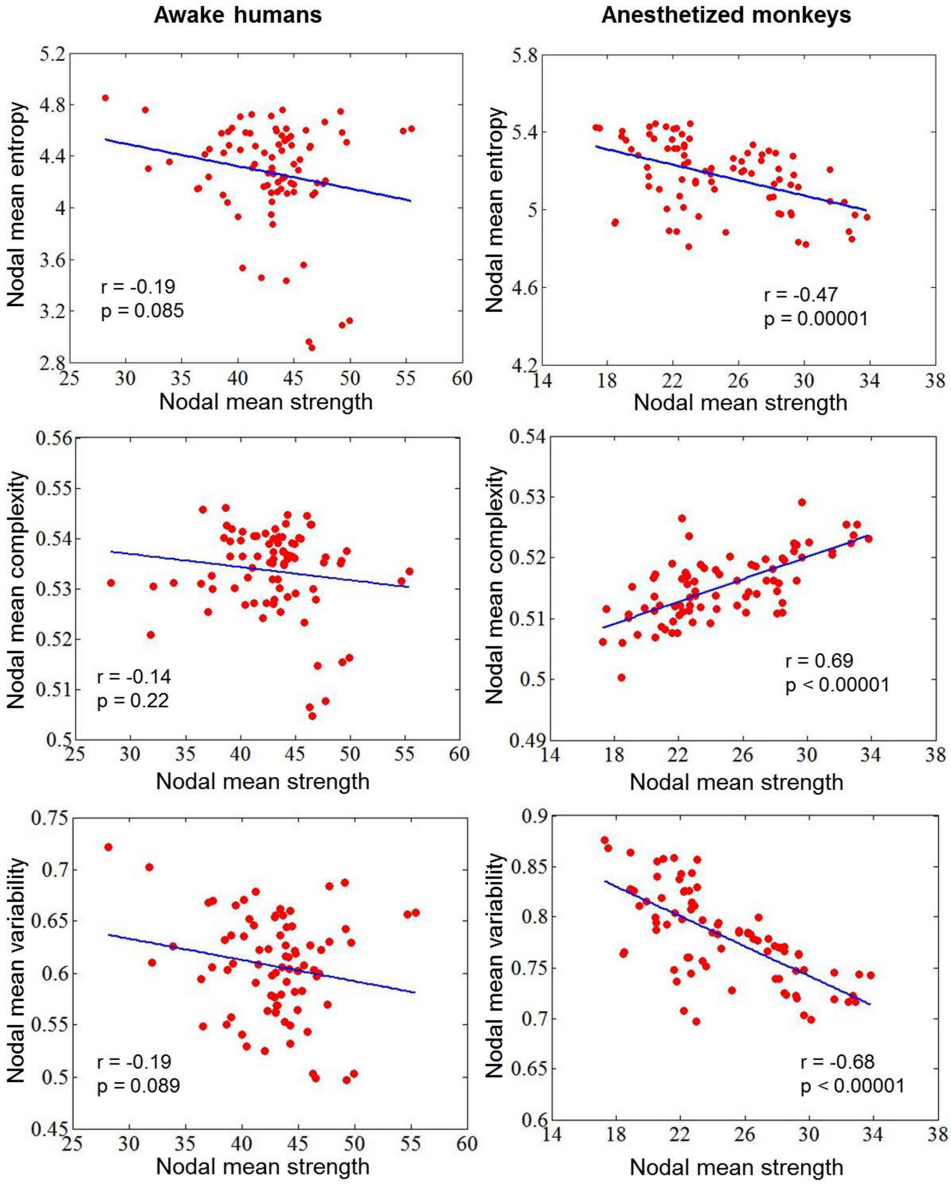

FIGURE 8 | Correlations between dynamic measurement (nodal mean entropy for the distribution of dynamic functional connectivity patterns, complexity for the distribution of correlation values, and variability for the dynamic functional connectivity patterns) and static measurement (nodal mean FC strength) in awake humans and anesthetized monkeys.

intrinsic functional flexibility in the awake, resting human brain using dynamic FC analysis and a probabilistic model (Yin et al., 2016). To further understand functional organization of spontaneous brain activity, in this study, we performed an interspecies comparison of intrinsic functional flexibility between anesthetized monkeys and awake humans.

For reference, we compared conventional, static FC patterns between anesthetized monkeys and awake humans. We found that functional coupling between brain regions in anesthetized monkeys was generally weaker than in awake humans; however, brain-wide connectivity patterns were correlated between species. Previous studies showed that patterns of static FC, such as the default mode network, persist even after loss of consciousness in rodents (Liang et al., 2012; Lu et al., 2012) and primates (Vincent et al., 2007; Hutchison et al., 2011; Hutchison and Everling, 2012). In contrast, other studies suggested a breakdown of both within- and between-network resting-state connectivity in the anesthetized state (Boveroux et al., 2010; Stamatakis et al., 2010) and deep sleep state (Tagliazucchi et al., 2013). These studies raised two hypotheses about the origins of resting-state FC patterns: reflecting a continuous stream of ongoing cognitive process and random fluctuations constrained by a stable anatomical skeleton (Vincent et al., 2007; Honey et al., 2009; Barttfeld et al., 2015; Raichle, 2015). It is possible that

persisting static FC patterns during anesthesia can be attributed to anatomical constraints (Vincent et al., 2007; Deco et al., 2013). On the other hand, consciousness is probably indexed by global integration with strong couplings between long-range brain regions (Alkire et al., 2008).

For our dynamic analysis, we found that the brain regions that showed higher entropy *E* in both anesthetized monkeys and awake humans mainly involved the higher-order association cortex such as the lateral prefrontal cortex, and regions that showed lower entropy *E* included primary sensory areas and midline default mode regions. This result is consistent with the flexible hub theory: the FC patterns of frontoparietal regions shift more than those of other regions across a variety of task states (Cole et al., 2013). A previous study focusing on the temporal dynamics of resting-state functional networks suggested that wakefulness is characterized by the dynamical exploration of a richer repertoire of functional configurations or states (Barttfeld et al., 2015). Moreover, individuals with brain networks showing greater dynamics perform more favorably in behavioral tasks (Jia et al., 2014). Through comparing anesthetized monkeys with awake humans, Hutchison and his colleagues demonstrated that the temporal dynamics of resting-state FC are also an intrinsic property of brain organization and not simply a consequence of conscious or cognitive processing (Hutchison et al., 2013b). Moreover, there is accumulating evidence that many cognitive processes can occur in the absence of awareness (MacDonald et al., 2015). We have demonstrated that brain regions showing higher entropy *E* may represent a more flexible exploration of functional configurations, even under anesthesia. Expanding upon previous studies (Cole et al., 2013; Yin et al., 2016; Zhang et al., 2016), this study reveals that heterogeneous functional flexibility across the cortex is evolutionarily conserved and persists across brain states.

Although there is significant correlation of brain-wide entropy *E* between anesthetized monkeys and awake humans, the whole-brain average entropy *E* is remarkably higher in the anesthetized monkeys. Barttfeld et al. study indicated that anesthesia may lead to a stable brain state that is more similar to the structure, in which time series of brain activity resemble random fluctuations shaped by fixed anatomical connectivity (Barttfeld et al., 2015). Using dynamical systems modeling, a previous study further suggested that low coupling strength between brain regions can coexist with a single stable spontaneous connectivity pattern (Deco et al., 2013). Because it becomes the only available attractor, the sedated brain cannot depart from it and remains confined to a semirandom exploration of the valley surrounding it, thus simultaneously exhibiting interregional correlations along with fixed anatomical connectivity and a memoryless trajectory (Deco et al., 2013; Barttfeld et al., 2015). Consistently, through time series analysis, we found that brain activity in anesthetized monkeys generally shifted toward random fluctuations, but it was still different from random fluctuations. We speculate that the general increase in entropy *E* and decrease in static FC strength in the anesthetized monkey brain is likely attributable to anesthesia-induced random fluctuations of brain activity.

Notably, previous electrophysiological studies have suggested that brain neuronal activity is dominant with slow oscillations under anesthetic states as well as during deep sleep state (Isomura et al., 2006; Alkire et al., 2008; Ni Mhuircheartaigh et al., 2013). A remarkable feature of slow oscillation is the synchrony over large cortical areas (Achermann and Borbely, 1997; Destexhe et al., 1999). Breshears et al. (2010) have demonstrated that stable functional architecture and dynamic neural activity are concurrent during induction of anesthesia. It is possible that the stable functional architecture, i.e., large-scale functional networks frequently observed even in anesthesia (Vincent et al., 2007; Hutchison and Everling, 2012), is result from synchrony induced by slow oscillation. Regarding dynamics of brain activity, a breakdown of long-range temporal correlations was observed in BOLD signals during both anesthesia and deep sleep states, suggesting that the dynamics of time series is close to white noise (Tagliazucchi et al., 2013; Barttfeld et al., 2015). In despite of different temporal scales, the findings that BOLD signal appears to be more random can provide a supplement for understanding anesthesia-induced slow oscillations of electrophysiological activity.

Moreover, previous evidence suggests that the dynamic complexity of the system under anesthetized state is reduced (Barttfeld et al., 2015). Accordingly, we found an overall reduction of functional complexity in anesthetized monkeys based on a complexity measure *C* for distribution of correlation values, but this was not the case for our method and time variability measurement. This suggests that the complexity measure *C* for distribution of correlation values is better to quantify dynamic complexity of system. In contrast, our method and time variability measurement are more suitable for describing functional flexibility, because they enable the capture of information regarding dynamical spatial connectivity patterns of a node, while this is not the case for the complexity measurement based on distribution of correlation values. For instance, the hippocampal cortex exhibited narrower distribution of correlation values (lower complexity) than the secondary somatosensory cortex in both anesthetized monkeys and awake humans, whereas the time-varying strongest connections of hippocampal cortex were more uniform (higher flexibility) than that of secondary somatosensory cortex across the whole brain. Our findings suggest that combining different methods could provide more complete information for in-depth understanding of functional brain organization.

We further found a negative correlation between nodal entropy *E* and strength in anesthetized monkeys, but not in awake humans. Previous simulating and empirical data suggest that brain dynamics may change from a single stable state to multi-stable state, as coupling strength between brain areas increases from the sedated to the conscious condition (Dehaene and Changeux, 2005; Ghosh et al., 2008; Deco et al., 2011, 2013; Hudetz et al., 2015). In agreement, conscious processing is supported by global integration with strong coupling between long-distance brain regions as well as a diversity of cognitive states (Alkire et al., 2008; Dehaene and Changeux, 2011). Loss of consciousness due to anesthesia may lack both strong coupling and a rich repertoire of cognitive states (Barttfeld et al., 2015; Hudetz et al., 2015). A possible explanation is that the negative correlation between nodal entropy *E* and strength (i.e., the

weaker connectivity strength, the higher entropy *E*) is primarily dominated by random fluctuations of brain activity induced by anesthesia. In contrast, the wakeful condition or conscious access with dominance of heterogeneous cognitive states may lead to decoupling between nodal entropy *E* and strength.

Consistently, we observed no correlation between the complexity measurement *C* for distribution of correlation values and static connectivity strength for the awake humans, but there was a positive correlation for the anesthetized monkeys. Zamora-Lopez et al. (2016) reported a reverse U-shaped relationship between functional complexity and coupling strength, with an optimal functional organization at the peak complexity. In other words, the functional complexity increases and then decreases during the increase of coupling strength. We therefore speculate that positive correlation between the complexity measurement *C* and static connectivity strength in anesthetized monkeys is attributed to the anesthesia-induced lower coupling strength (at the left part of reverse U-shape). This result further suggests that the coupling between dynamic and static measures may serve as a potential signature of anesthesia, whereas the direction of correlation is probably dependent on specific metrics.

Although brain-wide correlation exists between species, it should be noted that there were some divergences in intrinsic functional flexibility between the anesthetized monkey and awake human brains. For instance, the primary visual cortex exhibited relatively high entropy *E* in the anesthetized monkeys, although it was low in the awake humans. In contrast, the inferior parietal cortex showed relatively low entropy *E* in the anesthetized monkeys, whereas it was high in the awake humans. A previous human study indicated that anesthesia preferentially modulates higher-order connections, but not low-level sensory connections (Martuzzi et al., 2010). One rodent study also showed that anesthesia profoundly impacted the dynamic resting-state FC of neural circuits subserving higher-order functions but had less effect on sensory systems (Liang et al., 2015). On the other hand, a study by Hudetz et al. (2015) reported that the largest reduction of temporal variance of BOLD signals occurred in the visual cortex and parietal cortex in anesthetized rats. Although conflicting conclusions were drawn in previous studies, the converging evidence suggests a non-uniform impact of anesthesia on brain systems. In anesthetized monkeys, we found brain activity of primary visual cortex and sensorimotor cortex to be much more close to random fluctuations. In addition, the strongest connections of primary visual cortex were local and stereotyped in awake humans, but distributed and variable across the brain in anesthetized monkeys. It is possible the much more random fluctuations may contribute to the difference of functional flexibility observed in primary visual cortex between species.

Regarding inferior parietal cortex, we found it to be more frequently connected with local brain regions in parietal, temporal, and visual cortices in monkeys while more frequently connected with broad brain regions in parietal, temporal, and frontal cortices in humans. From an evolutionary perspective, the inferior parietal cortex in the human brain mainly contains Brodmann areas 39 and 40, but monkeys do not have a comparable area (Kotter and Wanke, 2005; Raichle, 2015). We speculate that the difference of functional flexibility observed in inferior parietal cortex of monkeys and humans is likely attributed to evolution. Although evolution may indeed result in functional reorganization of specific brain regions, it is hard to separate the contributions of evolution and anesthesia in the current study. A further study with awake monkeys and anesthetized humans may help clarify this question.

In addition, there are some limitations to this study. First, our analysis is based on dynamic FC and is affected by the general limits of this technique, such as temporal resolution of fMRI (Hutchison et al., 2013a; Hindriks et al., 2016). Using simultaneous imaging and electrophysiological recording is helpful for interpretation of dynamic FC (Keilholz, 2014). Second, for a direct comparison of brain network between monkeys and humans, we used a regional map template with the same cortical partitions. Previous studies have suggested evolutionary differences in anatomy between monkeys and humans (Kotter and Wanke, 2005; Raichle, 2015). Our findings may be potentially affected by the anatomical differences resulting from primate evolution. Finally, the human data that was collected from multiple centers with different acquisition parameters likely contained non-trivial variability across sites and individuals.

SUMMARY

This study combined dynamical complexity measurements and static connectivity strength measurement to understand functional brain organization in anesthetized monkeys and awake humans. Cross-species comparison suggests that the heterogeneous brain map of intrinsic functional flexibility persists during primate evolution and transcends levels of consciousness, remaining present under anesthesia. Moreover, the coupling between dynamic and static measurements can provide a potential signature of loss of consciousness due to anesthesia. However, each method may capture different biological information and have its own limitation. Specifically, our method and temporal variability approach might be more suitable for describing functional flexibility of a node, whereas there is a potential flaw in characterizing the changes of system complexity induced by anesthesia. In contrast, the complexity measurement based on distribution of correlation values is better for evaluating functional complexity of systems with different states or coupling strength, but is probably not suitable for describing functional flexibility of a node due to failure in capturing information of spatial connectivity patterns. Combining different methods could provide more complete information for in-depth understanding of functional brain organization. This study not only offers fresh insight into evolution of functional brain organization, but also advances our understanding of dynamics of spontaneous brain activity.

DATA AVAILABILITY

The datasets generated for this study are available on request to the corresponding author.

AUTHOR CONTRIBUTIONS

DY, YW, and ZheW designed the research. DY, ZZ, and ZhiW performed the research. DY, ZhiW, QL, and DC analyzed the data. DY, KZ, and ZheW wrote the paper.

FUNDING

This work was supported by the National Key Research and Development Program of China (2017YFC1310400 to DY), Youth Innovation Promotion Association of the Chinese Academy of Sciences (to DY), Strategic Priority Research Program of the Chinese Academy of Sciences (XDB32000000 to ZheW), National Natural Science Foundation of China (81571300 and 31771174 to ZheW, 31600869 and 81527901 to DY), and Natural Science Foundation and Major Basic Research Program of Shanghai (16JC1420100 to ZheW).

ACKNOWLEDGMENTS

We thank Qinying Jiang and Wenwen Yu for their assistance in monkey data collection and also thank Jinqiang Peng for his assistance in data management. DY gratefully acknowledges the support of SA-SIBS Scholarship Program.

SUPPLEMENTARY MATERIAL

The Supplementary Material for this article can be found online at: https://www.frontiersin.org/articles/10.3389/fnins.2019.00174/full#supplementary-material

REFERENCES

Achermann, P., and Borbely, A. A. (1997). Low-frequency (< 1 Hz) oscillations in the human sleep electroencephalogram. *Neuroscience* 81, 213–222. doi: 10.1016/S0306-4522(97)00186-3

Alkire, M. T., Hudetz, A. G., and Tononi, G. (2008). Consciousness and anesthesia. *Science* 322, 876–880. doi: 10.1126/science.1149213

Allen, E. A., Damaraju, E., Plis, S. M., Erhardt, E. B., Eichele, T., and Calhoun, V. D. (2014). Tracking whole-brain connectivity dynamics in the resting state. *Cereb. Cortex* 24, 663–676. doi: 10.1093/cercor/bhs352

Barttfeld, P., Uhrig, L., Sitt, J. D., Sigman, M., Jarraya, B., and Dehaene, S. (2015). Signature of consciousness in the dynamics of resting-state brain activity. *Proc. Natl. Acad. Sci. U.S.A.* 112, 887–892. doi: 10.1073/pnas.1418031112

Bassett, D. S., and Sporns, O. (2017). Network neuroscience. *Nat. Neurosci.* 20, 353–364. doi: 10.1038/nn.4502

Bezgin, G., Vakorin, V. A., van Opstal, A. J., McIntosh, A. R., and Bakker, R. (2012). Hundreds of brain maps in one atlas: registering coordinate-independent primate neuro-anatomical data to a standard brain. *Neuroimage* 62, 67–76. doi: 10.1016/j.neuroimage.2012.04.013

Biswal, B., Yetkin, F. Z., Haughton, V. M., and Hyde, J. S. (1995). Functional connectivity in the motor cortex of resting human brain using echo-planar MRI. *Magn. Reson. Med.* 34, 537–541. doi: 10.1002/mrm.1910340409

Boveroux, P., Vanhaudenhuyse, A., Bruno, M. A., Noirhomme, Q., Lauwick, S., Luxen, A., et al. (2010). Breakdown of within- and between-network resting state functional magnetic resonance imaging connectivity during propofol-induced loss of consciousness. *Anesthesiology* 113, 1038–1053. doi: 10.1097/ALN.0b013e3181f697f5

Braun, U., Schafer, A., Walter, H., Erk, S., Romanczuk-Seiferth, N., Haddad, L., et al. (2015). Dynamic reconfiguration of frontal brain networks during executive cognition in humans. *Proc. Natl. Acad. Sci. U.S.A.* 112, 11678–11683. doi: 10.1073/pnas.1422487112

Breshears, J. D., Roland, J. L., Sharma, M., Gaona, C. M., Freudenburg, Z. V., Tempelhoff, R., et al. (2010). Stable and dynamic cortical electrophysiology of induction and emergence with propofol anesthesia. *Proc. Natl. Acad. Sci. U.S.A.* 107, 21170–21175. doi: 10.1073/pnas.1011949107

Calhoun, V. D., Miller, R., Pearlson, G., and Adali, T. (2014). The chronnectome: time-varying connectivity networks as the next frontier in fMRI data discovery. *Neuron* 84, 262–274. doi: 10.1016/j.neuron.2014.10.015

Chang, C., and Glover, G. H. (2010). Time-frequency dynamics of resting-state brain connectivity measured with fMRI. *Neuroimage* 50, 81–98. doi: 10.1016/j.neuroimage.2009.12.011

Chen, T., Cai, W., Ryali, S., Supekar, K., and Menon, V. (2016). Distinct global brain dynamics and spatiotemporal organization of the salience network. *PLoS Biol.* 14:e1002469. doi: 10.1371/journal.pbio.1002469

Christoff, K., Irving, Z. C., Fox, K. C., Spreng, R. N., and Andrews-Hanna, J. R. (2016). Mind-wandering as spontaneous thought: a dynamic framework. *Nat. Rev. Neurosci.* 17, 718–731. doi: 10.1038/nrn.2016.113

Cole, M. W., Reynolds, J. R., Power, J. D., Repovs, G., Anticevic, A., and Braver, T. S. (2013). Multi-task connectivity reveals flexible hubs for adaptive task control. *Nat. Neurosci.* 16, 1348–1355. doi: 10.1038/nn.3470

de Pasquale, F., Della Penna, S., Sporns, O., Romani, G. L., and Corbetta, M. (2015). A Dynamic core network and global efficiency in the resting human brain. *Cereb. Cortex* 26, 4015–4033. doi: 10.1093/cercor/bhv185

Deco, G., Jirsa, V. K., and McIntosh, A. R. (2011). Emerging concepts for the dynamical organization of resting-state activity in the brain. *Nat. Rev. Neurosci.* 12, 43–56. doi: 10.1038/nrn2961

Deco, G., Jirsa, V. K., and McIntosh, A. R. (2013). Resting brains never rest: computational insights into potential cognitive architectures. *Trends Neurosci.* 36, 268–274. doi: 10.1016/j.tins.2013.03.001

Dehaene, S., and Changeux, J. P. (2005). Ongoing spontaneous activity controls access to consciousness: a neuronal model for inattentional blindness. *PLoS Biol.* 3:e141. doi: 10.1371/journal.pbio.0030141

Dehaene, S., and Changeux, J. P. (2011). Experimental and theoretical approaches to conscious processing. *Neuron* 70, 200–227. doi: 10.1016/j.neuron.2011.03.018

Destexhe, A., Contreras, D., and Steriade, M. (1999). Spatiotemporal analysis of local field potentials and unit discharges in cat cerebral cortex during natural wake and sleep states. *J. Neurosci.* 19, 4595–4608. doi: 10.1523/JNEUROSCI.19-11-04595.1999

Di Martino, A., Yan, C. G., Li, Q., Denio, E., Castellanos, F. X., Alaerts, K., et al. (2014). The autism brain imaging data exchange: towards a large-scale evaluation of the intrinsic brain architecture in autism. *Mol. Psychiatry* 19, 659–667. doi: 10.1038/mp.2013.78

Fox, M. D., and Raichle, M. E. (2007). Spontaneous fluctuations in brain activity observed with functional magnetic resonance imaging. *Nat. Rev. Neurosci.* 8, 700–711. doi: 10.1038/nrn2201

Ghosh, A., Rho, Y., McIntosh, A. R., Kotter, R., and Jirsa, V. K. (2008). Noise during rest enables the exploration of the brain's dynamic repertoire. *PLoS Comput. Biol.* 4:e1000196. doi: 10.1371/journal.pcbi.1000196

Hindriks, R., Adhikari, M. H., Murayama, Y., Ganzetti, M., Mantini, D., Logothetis, N. K., et al. (2016). Can sliding-window correlations reveal dynamic functional connectivity in resting-state fMRI? *Neuroimage* 127, 242–256. doi: 10.1016/j.neuroimage.2015.11.055

Honey, C. J., Sporns, O., Cammoun, L., Gigandet, X., Thiran, J. P., Meuli, R., et al. (2009). Predicting human resting-state functional connectivity from structural connectivity. *Proc. Natl. Acad. Sci. U.S.A.* 106, 2035–2040. doi: 10.1073/pnas.0811168106

Hudetz, A. G., Liu, X., and Pillay, S. (2015). Dynamic repertoire of intrinsic brain states is reduced in propofol-induced

unconsciousness. *Brain Connect.* 5, 10–22. doi: 10.1089/brain.2014.0230

Hutchison, R. M., and Everling, S. (2012). Monkey in the middle: why non-human primates are needed to bridge the gap in resting-state investigations. *Front. Neuroanat.* 6:29. doi: 10.3389/fnana.2012.00029

Hutchison, R. M., Leung, L. S., Mirsattari, S. M., Gati, J. S., Menon, R. S., and Everling, S. (2011). Resting-state networks in the macaque at 7 T. *Neuroimage* 56, 1546–1555. doi: 10.1016/j.neuroimage.2011.02.063

Hutchison, R. M., Womelsdorf, T., Allen, E. A., Bandettini, P. A., Calhoun, V. D., Corbetta, M., et al. (2013a). Dynamic functional connectivity: promise, issues, and interpretations. *Neuroimage* 80, 360–378. doi: 10.1016/j.neuroimage.2013.05.079

Hutchison, R. M., Womelsdorf, T., Gati, J. S., Everling, S., and Menon, R. S. (2013b). Resting-state networks show dynamic functional connectivity in awake humans and anesthetized macaques. *Hum. Brain Mapp.* 34, 2154–2177. doi: 10.1002/hbm.22058

Isomura, Y., Sirota, A., Ozen, S., Montgomery, S., Mizuseki, K., Henze, D. A., et al. (2006). Integration and segregation of activity in entorhinal-hippocampal subregions by neocortical slow oscillations. *Neuron* 52, 871–882. doi: 10.1016/j.neuron.2006.10.023

Jia, H., Hu, X., and Deshpande, G. (2014). Behavioral relevance of the dynamics of the functional brain connectome. *Brain Connect.* 4, 741–759. doi: 10.1089/brain.2014.0300

Karahanoglu, F. I., and Van De Ville, D. (2015). Transient brain activity disentangles fMRI resting-state dynamics in terms of spatially and temporally overlapping networks. *Nat. Commun.* 6:7751. doi: 10.1038/ncomms8751

Keilholz, S., Caballero-Gaudes, C., Bandettini, P., Deco, G., and Calhoun, V. (2017). Time-resolved resting-state functional magnetic resonance imaging analysis: current status, challenges, and new directions. *Brain Connect.* 7, 465–481. doi: 10.1089/brain.2017.0543

Keilholz, S. D. (2014). The neural basis of time-varying resting-state functional connectivity. *Brain Connect.* 4, 769–779. doi: 10.1089/brain.2014.0250

Kopell, N. J., Gritton, H. J., Whittington, M. A., and Kramer, M. A. (2014). Beyond the connectome: the dynome. *Neuron* 83, 1319–1328. doi: 10.1016/j.neuron.2014.08.016

Kotter, R., and Wanke, E. (2005). Mapping brains without coordinates. *Philos. Trans. R. Soc. Lond. B Biol. Sci.* 360, 751–766. doi: 10.1098/rstb.2005.1625

Liang, Z., King, J., and Zhang, N. (2012). Intrinsic organization of the anesthetized brain. *J. Neurosci.* 32, 10183–10191. doi: 10.1523/JNEUROSCI.1020-12.2012

Liang, Z., Liu, X., and Zhang, N. (2015). Dynamic resting state functional connectivity in awake and anesthetized rodents. *Neuroimage* 104, 89–99. doi: 10.1016/j.neuroimage.2014.10.013

Liegeois, R., Laumann, T. O., Snyder, A. Z., Zhou, J., and Yeo, B. T. T. (2017). Interpreting temporal fluctuations in resting-state functional connectivity MRI. *Neuroimage* 163, 437–455. doi: 10.1016/j.neuroimage.2017.09.012

Liu, X., and Duyn, J. H. (2013). Time-varying functional network information extracted from brief instances of spontaneous brain activity. *Proc. Natl. Acad. Sci. U.S.A.* 110, 4392–4397. doi: 10.1073/pnas.1216856110

Logothetis, N. K., Guggenberger, H., Peled, S., and Pauls, J. (1999). Functional imaging of the monkey brain. *Nat. Neurosci.* 2, 555–562. doi: 10.1038/9210

Lu, H., Zou, Q., Gu, H., Raichle, M. E., Stein, E. A., and Yang, Y. (2012). Rat brains also have a default mode network. *Proc. Natl. Acad. Sci. U.S.A.* 109, 3979–3984. doi: 10.1073/pnas.1200506109

Lv, Q., Yang, L., Li, G., Wang, Z., Shen, Z., Yu, W., et al. (2016). Large-scale persistent network reconfiguration induced by ketamine in anesthetized monkeys: relevance to mood disorders. *Biol. Psychiatry* 79, 765–775. doi: 10.1016/j.biopsych.2015.02.028

MacDonald, A. A., Naci, L., MacDonald, P. A., and Owen, A. M. (2015). Anesthesia and neuroimaging: investigating the neural correlates of unconsciousness. *Trends Cogn. Sci.* 19, 100–107. doi: 10.1016/j.tics.2014.12.005

Mantini, D., Corbetta, M., Romani, G. L., Orban, G. A., and Vanduffel, W. (2013). Evolutionarily novel functional networks in the human brain? *J. Neurosci.* 33, 3259–3275. doi: 10.1523/JNEUROSCI.4392-12.2013

Margulies, D. S., Vincent, J. L., Kelly, C., Lohmann, G., Uddin, L. Q., Biswal, B. B., et al. (2009). Precuneus shares intrinsic functional architecture in humans and monkeys. *Proc. Natl. Acad. Sci. U.S.A.* 106, 20069–20074. doi: 10.1073/pnas.0905314106

Martuzzi, R., Ramani, R., Qiu, M., Rajeevan, N., and Constable, R. T. (2010). Functional connectivity and alterations in baseline brain state in humans. *Neuroimage* 49, 823–834. doi: 10.1016/j.neuroimage.2009.07.028

Miranda-Dominguez, O., Mills, B. D., Grayson, D., Woodall, A., Grant, K. A., Kroenke, C. D., et al. (2014). Bridging the gap between the human and macaque connectome: a quantitative comparison of global interspecies structure-function relationships and network topology. *J. Neurosci.* 34, 5552–5563. doi: 10.1523/JNEUROSCI.4229-13.2014

Mueller, S., Wang, D., Fox, M. D., Yeo, B. T., Sepulcre, J., Sabuncu, M. R., et al. (2013). Individual variability in functional connectivity architecture of the human brain. *Neuron* 77, 586–595. doi: 10.1016/j.neuron.2012.12.028

Nakahara, K., Hayashi, T., Konishi, S., and Miyashita, Y. (2002). Functional MRI of macaque monkeys performing a cognitive set-shifting task. *Science* 295, 1532–1536. doi: 10.1126/science.1067653

Neubert, F. X., Mars, R. B., Thomas, A. G., Sallet, J., and Rushworth, M. F. (2014). Comparison of human ventral frontal cortex areas for cognitive control and language with areas in monkey frontal cortex. *Neuron* 81, 700–713. doi: 10.1016/j.neuron.2013.11.012

Ni Mhuircheartaigh, R., Warnaby, C., Rogers, R., Jbabdi, S., and Tracey, I. (2013). Slow-wave activity saturation and thalamocortical isolation during propofol anesthesia in humans. *Sci. Transl. Med.* 5:208ra148. doi: 10.1126/scitranslmed.3006007

Power, J. D., Schlaggar, B. L., and Petersen, S. E. (2014). Studying brain organization via spontaneous fMRI signal. *Neuron* 84, 681–696. doi: 10.1016/j.neuron.2014.09.007

Preti, M. G., Bolton, T. A., and Van De Ville, D. (2017). The dynamic functional connectome: state-of-the-art and perspectives. *Neuroimage* 160, 41–54. doi: 10.1016/j.neuroimage.2016.12.061

Raichle, M. E. (2015). The brain's default mode network. *Annu. Rev. Neurosci.* 38, 433–447. doi: 10.1146/annurev-neuro-071013-014030

Reid, A. T., Lewis, J., Bezgin, G., Khundrakpam, B., Eickhoff, S. B., McIntosh, A. R., et al. (2016). A cross-modal, cross-species comparison of connectivity measures in the primate brain. *Neuroimage* 125, 311–331. doi: 10.1016/j.neuroimage.2015.10.057

Stamatakis, E. A., Adapa, R. M., Absalom, A. R., and Menon, D. K. (2010). Changes in resting neural connectivity during propofol sedation. *PLoS One* 5:e14224. doi: 10.1371/journal.pone.0014224

Tagliazucchi, E., von Wegner, F., Morzelewski, A., Brodbeck, V., Jahnke, K., and Laufs, H. (2013). Breakdown of long-range temporal dependence in default mode and attention networks during deep sleep. *Proc. Natl. Acad. Sci. U.S.A.* 110, 15419–15424. doi: 10.1073/pnas.1312848110

Vanduffel, W., Fize, D., Peuskens, H., Denys, K., Sunaert, S., Todd, J. T., et al. (2002). Extracting 3D from motion: differences in human and monkey intraparietal cortex. *Science* 298, 413–415. doi: 10.1126/science.1073574

Vincent, J. L., Patel, G. H., Fox, M. D., Snyder, A. Z., Baker, J. T., Van Essen, D. C., et al. (2007). Intrinsic functional architecture in the anaesthetized monkey brain. *Nature* 447, 83–86. doi: 10.1038/nature05758

Wang, L., Uhrig, L., Jarraya, B., and Dehaene, S. (2015). Representation of numerical and sequential patterns in macaque and human brains. *Curr. Biol.* 25, 1966–1974. doi: 10.1016/j.cub.2015.06.035

Wang, Z., Chen, L. M., Negyessy, L., Friedman, R. M., Mishra, A., Gore, J. C., et al. (2013). The relationship of anatomical and functional connectivity to resting-state connectivity in primate somatosensory cortex. *Neuron* 78, 1116–1126. doi: 10.1016/j.neuron.2013.04.023

Yan, C. G., and Zang, Y. F. (2010). DPARSF: a MATLAB Toolbox for "Pipeline" Data Analysis of Resting-State fMRI. *Front. Syst. Neurosci.* 4:13. doi: 10.3389/fnsys.2010.00013

Yin, D., Liu, W., Zeljic, K., Wang, Z., Lv, Q., Fan, M., et al. (2016). Dissociable changes of frontal and parietal cortices in inherent functional flexibility across the human life span. *J. Neurosci.* 36, 10060–10074. doi: 10.1523/JNEUROSCI.1476-16.2016

Zalesky, A., Fornito, A., Cocchi, L., Gollo, L. L., and Breakspear, M. (2014). Time-resolved resting-state brain networks. *Proc. Natl. Acad. Sci. U.S.A.* 111, 10341–10346. doi: 10.1073/pnas.1400181111

Zamora-Lopez, G., Chen, Y., Deco, G., Kringelbach, M. L., and Zhou, C. (2016). Functional complexity emerging from anatomical constraints in the brain: the significance of network modularity and rich-clubs. *Sci. Rep.* 6:38424. doi: 10.1038/srep38424

Zhang, D., and Raichle, M. E. (2010). Disease and the brain's dark energy. *Nat. Rev. Neurol.* 6, 15–28. doi: 10.1038/nrneurol.2009.198

Zhang, J., Cheng, W., Liu, Z., Zhang, K., Lei, X., Yao, Y., et al. (2016). Neural, electrophysiological and anatomical basis of brain-network variability and its characteristic changes in mental disorders. *Brain* 139, 2307–2321. doi: 10.1093/brain/aww143

Zhang, J., Huang, Z., Chen, Y., Zhang, J., Ghinda, D., Nikolova, Y., et al. (2018). Breakdown in the temporal and spatial organization of spontaneous brain activity during general anesthesia. *Hum. Brain Mapp.* 39, 2035–2046. doi: 10.1002/hbm.23984

Zhao, M., Zhou, C., Chen, Y., Hu, B., and Wang, B. H. (2010). Complexity versus modularity and heterogeneity in oscillatory networks: combining segregation and integration in neural systems. *Phys. Rev. E Stat. Nonlin. Soft Matter Phys.* 82:046225. doi: 10.1103/PhysRevE.82.046225

Conflict of Interest Statement: The authors declare that the research was conducted in the absence of any commercial or financial relationships that could be construed as a potential conflict of interest.

frontiers in Neuroscience

ORIGINAL RESEARCH
published: 02 April 2019
doi: 10.3389/fnins.2019.00279

Sampling Rate Effects on Resting State fMRI Metrics

Niko Huotari[1,2]*, *Lauri Raitamaa*[1,2], *Heta Helakari*[1,2], *Janne Kananen*[1,2], *Ville Raatikainen*[1,2], *Aleksi Rasila*[1,2], *Timo Tuovinen*[1,2], *Jussi Kantola*[1,2], *Viola Borchardt*[1,2], *Vesa J. Kiviniemi*[1,2] *and Vesa O. Korhonen*[1,2]

[1] Oulu Functional NeuroImaging Group, Research Unit of Medical Imaging, Physics and Technology, University of Oulu, Oulu, Finland, [2] Department of Diagnostic Radiology, Medical Research Center, Oulu University Hospital, Oulu, Finland

Low image sampling rates used in resting state functional magnetic resonance imaging (rs-fMRI) may cause aliasing of the cardiorespiratory pulsations over the very low frequency (VLF) BOLD signal fluctuations which reflects to functional connectivity (FC). In this study, we examine the effect of sampling rate on currently used rs-fMRI FC metrics. Ultra-fast fMRI magnetic resonance encephalography (MREG) data, sampled with TR 0.1 s, was downsampled to different subsampled repetition times (sTR, range 0.3–3 s) for comparisons. Echo planar k-space sampling (TR 2.15 s) and interleaved slice collection schemes were also compared against the 3D single shot trajectory at 2.2 s sTR. The quantified connectivity metrics included stationary spatial, time, and frequency domains, as well as dynamic analyses. Time domain methods included analyses of seed-based functional connectivity, regional homogeneity (ReHo), coefficient of variation, and spatial domain group level probabilistic independent component analysis (ICA). In frequency domain analyses, we examined fractional and amplitude of low frequency fluctuations. Aliasing effects were spatially and spectrally analyzed by comparing VLF (0.01–0.1 Hz), respiratory (0.12–0.35 Hz) and cardiac power (0.9–1.3 Hz) FFT maps at different sTRs. Quasi-periodic pattern (QPP) of VLF events were analyzed for effects on dynamic FC methods. The results in conventional time and spatial domain analyses remained virtually unchanged by the different sampling rates. In frequency domain, the aliasing occurred mainly in higher sTR (1–2 s) where cardiac power aliases over respiratory power. The VLF power maps suffered minimally from increasing sTRs. Interleaved data reconstruction induced lower ReHo compared to 3D sampling ($p < 0.001$). Gradient recalled echo-planar imaging (EPI BOLD) data produced both better and worse metrics. In QPP analyses, the repeatability of the VLF pulse detection becomes linearly reduced with increasing sTR. In conclusion, the conventional resting state metrics (e.g., FC, ICA) were not markedly affected by different TRs (0.1–3 s). However, cardiorespiratory signals showed strongest aliasing in central brain regions in sTR 1–2 s. Pulsatile QPP and other dynamic analyses benefit linearly from short TR scanning.

Keywords: resting state, magnetic resonance encephalography, aliasing, pulsations, quasi-periodic patterns

OPEN ACCESS

Edited by:
Jean Chen,
University of Toronto, Canada

Reviewed by:
Fahmeed Hyder,
Yale University, United States
Stefan Posse,
University of New Mexico, United States

***Correspondence:**
Niko Huotari
niko.huotari@oulu.fi

Specialty section:
This article was submitted to Brain Imaging Methods, a section of the journal Frontiers in Neuroscience

Received: *26 October 2018*
Accepted: *08 March 2019*
Published: *02 April 2019*

Citation:
Huotari N, Raitamaa L, Helakari H, Kananen J, Raatikainen V, Rasila A, Tuovinen T, Kantola J, Borchardt V, Kiviniemi VJ and Korhonen VO (2019) Sampling Rate Effects on Resting State fMRI Metrics. Front. Neurosci. 13:279. doi: 10.3389/fnins.2019.00279

INTRODUCTION

In 1995 Biswal and co-workers discovered functional connectivity (FC) in resting state blood oxygen level dependent (BOLD) signal of motor cortices by their continuous very low frequency fluctuations (VLF $<$ 0.1 Hz) (Biswal et al., 1995). Initially, the VLF phenomena were linked to existing literature on low frequency physiological phenomena like vasomotor waves (Kiviniemi et al., 2000). The current view is that spontaneous neuronal activity avalanches synchronize brain activity in functionally connected areas and become visible in hemodynamic signals after a delay of few seconds (Liu and Duyn, 2013; Palva et al., 2013; Keilholz, 2014; Ma et al., 2016; Liu et al., 2018). The spread of such avalanches can be depicted by novel techniques such as inverse imaging (INI) and magnetic resonance encephalography (MREG), that sample functional magnetic resonance imaging (fMRI) data with short repetition times (TR) (Lin et al., 2012, 2018; Assländer et al., 2013; Rajna et al., 2015).

In addition to neuronal activity that is coupled to hemodynamics, the BOLD signal reflects multiple other signal sources, such as motion, physiological pulsations and technical artifacts. The physiological factors like cardiorespiratory changes modulate the BOLD signal and can mask the neuronally driven VLF activity in resting state BOLD signals (Wise et al., 2004; Birn et al., 2006). As the BOLD signal reflects blood oxygen level, also direct effects of the cardiorespiratory pulses themselves can be detected in fMRI data (Shmueli et al., 2007; Chang and Glover, 2009, 2010).

Previously, the research of cardiorespiratory brain pulsations has not gained as much interest because they have been deemed as noise. However, there is increasing evidence showing that these physiological signals or the "noise" it produces in TR BOLD data with long TR, can be used to measure disease-specific changes in patient groups (Makedonov et al., 2013; Tuovinen et al., 2017). This is strongly supported by the recent discovery of the glymphatic brain tissue clearance mechanism where the cardiovascular pulsations have been shown to drive the glymphatic brain clearance (Iliff et al., 2012; Nedergaard, 2013; Jessen et al., 2015). The short TR in 3D MREG can critically sample the spread of cardiovascular ∼1 Hz and respiratory ∼0.3 Hz pulsations and separate them from VLF ($<$0.1 Hz) quasi-periodic patterns (QPPs) (Kiviniemi et al., 2016).

The extent to which faster physiological pulsations alias over VLF BOLD signal, has been a prevailing uncertainty in BOLD fMRI. Since cardiac frequencies can be faster than 2 Hz, especially in animals and children, the critical sampling rate should be $>$4 Hz according to the Nyquist theorem, i.e., TR $<$ 0.25 s. However, most often the fMRI TRs are $>$0.4 s and therefore the data cannot critically sample faster cardiac signals (Liu, 2016). Consequently, aliasing between cardiac and the VLFs occur and may alter FC metrics. Additionally, the cardiorespiratory rhythms and their pressure modulations and physiological autonomic nervous system mediated counter-regulations, local vasomotor waves induce heart rate variability, which differ between patients and controls (van der Kooy et al., 2006; Thayer et al., 2010) causing yet another confounding factor in measures of FC that may require faster sampling.

Early literature on the sampling rate on FC measures usually utilizes single slice data that suffers from out of plane motion and other registration problems (Purdon and Weisskoff, 1998; Peltier et al., 2003; Kiviniemi et al., 2005). Recent studies on the fMRI sampling rate effects on resting-state FC has shown surprisingly small effects (Golestani et al., 2017; Demetriou et al., 2018). However, that and some other recent studies have usually been limited to $<$4 Hz sampling rates for whole brain coverage (Cordes et al., 2014; Liu, 2016; Golestani et al., 2017; Chen et al., 2019) with different type of signal simulations extending below the critical 4 Hz limit.

However, more and more critically sampled 3D whole brain fMRI data has started to emerge, such as 0.136 sec TR VEPI (Posse et al., 2013), 100 ms MREG (Assländer et al., 2013; Lee et al., 2013; Kiviniemi et al., 2016; Raitamaa et al., 2018), 50 ms GIN (Boyacioglu and Barth, 2013) and currently leading 25 ms 3D whole brain scan INI (Chang et al., 2013b). This critically sampled data shows robust novel phenomena of the human brain physiology, such as propagating cardiorespiratory pulsations that both interact and modulate each other, depending on their anatomical proximity to pulsation sources (Posse et al., 2013; Kiviniemi et al., 2016; Raitamaa et al., 2018). Based on our observations, these novel signal changes cannot be comprehensively simulated due to their complex spatiotemporal pattern that is dynamically changing.

Therefore, in this study we used real critically sampled 0.1 s TR 3D single shot MREG data to explore how different sampling rates affect the results of the most commonly used resting state fMRI analysis tools. The 0.1 s TR MREG signal was downsampled to higher TRs ranging from 0.3 to 3 s. The use of subsampled TR (sTR) removes the confounding factors of imaging different TR values in separate scans and/or individuals, enabling identical physiological status and technological noise structure for comparing different sTRs. The single shot 3D data sampling scheme was further compared with interleaved slice sampling (INT) variant of the MREG data, and, with conventional interleaved gradient recalled echo-planar BOLD imaging (EPI BOLD).

The hypothesis was that the faster sTR produces both spatially more accurate brain maps and more accurate time series without aliasing of physiological pulsations. The quantified connectivity metrics included stationary spatial, time, and frequency domains, as well as dynamic analyses. In addition, the effects of aliasing were evaluated.

MATERIALS AND METHODS

Participants

Ten healthy subjects (8 males, 23.8 ± 2.1 years old) were placed in the MRI scanner and asked to lay still and keep their eyes open and fixated on a cross on the screen while thinking of nothing particular (eyes open, resting state). Ear plugs were used to reduce scanner noise. Cushions were placed beside ears to restrict movement and to further reduce scanner noise. MREG (5 min) and EPI BOLD (5 min) sequences were scanned in said order. Written informed consent was obtained from each subject prior to scanning, in accordance with the Helsinki

declaration. The study protocol was approved by the regional Ethical committee of Northern Ostrobothnia Hospital District in Oulu University Hospital.

Data Acquisition and Preprocessing

Subjects were scanned using Siemens 3T SKYRA scanner with 32-channel head coil. Additional cardiorespiratory data were collected using MRI-compatible multimodal neuroimaging system (Korhonen et al., 2014). MREG is a 3D single shot stack of spirals (SOS) sequence that under-samples k-space to reach a sampling rate of 10 Hz allowing critical imaging of physiological pulsations (Assländer et al., 2013). The SOS gathers k-space in 60 ms with spiral in/out repeating in every other turn continuously in positive z-direction to minimize the air-sinus off-resonance artifact (for more details, c.f. Assländer et al., 2013). The point spread function of the SOS-sequence is 3 mm with minimized off-resonance effects compared to other k-space undersampling strategies like concentric shells and spokes (Zahneisen et al., 2012; Assländer et al., 2013). Scanning parameters (TR=100 ms, TE=36 ms, flip angle=5°, 3D matrix=64^3, FOV=192 mm) enabled scanning of the whole brain in 10 Hz with voxel size of $3 \times 3 \times 3$ mm^3. Conventional EPI BOLD scans were collected from the same subjects (TR = 2,150 ms, TE = 28 ms, flip angle = 15°, voxel size = 3 × 3 × 3 mm, matrix size 64*64, 45 slices = 47 ms in plane readout). In both methods, we used relatively low flip angles to minimize specific absorption rate (SAR), spin history effects, physiological pulsations and radio frequency (RF) artifacts in EEG in comparison to default flip angles (Gonzalez-Castillo et al., 2011; Assländer et al., 2013).

A reference image for MREG was acquired with a multi slice double gradient echo sequence with TR = 593 ms, TE = 2.46/4.92 ms, flip angle = 50°, dwell time = 4.9 us, FOV = 192 mm. The reference and raw data from the MREG sequence were transferred offline to a computing grid and reconstructed using the MATLAB tool provided with the sequence. The tool allows for a choice between several parameters for regularized reconstruction (Hugger et al., 2011); we selected L2-norm with finite difference operator (called "Total Variation" in the tool) and the regularization parameter was reduced to lambda=0.15 from default 0.2 in order to obtain higher signal-to-noise ratio (SNR) images. Conjugate gradient optimization was also performed for 35 iterations for more robust convergence of images, c.f. **Figure 1**. Coil sensitivities were estimated from the reference image with the adaptive method, and dynamic off-resonance correction in k-space was used to minimize respiration and other motion related off-resonance artifacts from the data (Pfeuffer et al., 2002; Zahneisen et al., 2014). Anatomical 3D MPRAGE (TR = 1,900 ms, TE = 2.49 ms, TI = 900 ms, flip angle = 9°, FOV = 240 mm, 0.9 mm cubic voxel) images were used to register both MREG and EPI BOLD data into Montreal Neurological Institute (MNI) space.

Both, EPI BOLD and MREG data were preprocessed with a typical FSL pipeline (Jenkinson et al., 2012). The data were high-pass filtered with cut-off frequency of 0.008 Hz (125 s). T1-relaxation effects were minimized using dummy scans (8 s). Motion correction was performed using FSL MCFLIRT. FSL BET was used for brain extraction (fractional intensity = 0.25, threshold gradient = 0.22, neck and bias-field correction). Images were spatially smoothed with 5 mm FWHM Gaussian kernel using *fslmaths*. Three-dimensional 3DMPRAGE anatomical images were used to register both the EPI BOLD and the MREG data into 4 mm MNI space prior to group ICA using FLIRT (Jenkinson and Smith, 2001; Jenkinson et al., 2002). FILM pre-whitening and data smoothness estimation was produced automatically by FSL MELODIC (Woolrich et al., 2001; Beckmann et al., 2006). FILM implements a robust method of correcting for auto-correlation in fMRI time-series which is (theoretically) independent of TR duration (Woolrich et al., 2001; Smith et al., 2004; Demetriou et al., 2018).

The MREG (TR = 0.1 s) data was downsampled to different sTR settings from TR 0.1 s to 0.3, 0.5, 1.0, 1.5, 1.8, 2.2, and 3.0 s, respectively by taking every n^{th} [n = 3, 5, 10, 15, 18, 22, 30] sample from every voxel timeseries. In addition, an interleaved variant of the MREG data were computed by taking every 1,3,5...21; 2,4,6...22th axial slice (hence the INT sTR = 2.2 s) to emulate the interleaved EPI data gathering for comparing single shot MREG trajectory downsampled at 2.2 s sTR data and conventional gradient recalled EPI (TR = 2.15 s). MATLAB was used for MREG data downsampling and interleaving. Total of 100 datasets were obtained after processing (10 sTR settings for 10 subjects).

As one of the focuses was to assess physiological signal aliasing effects, we retained the physiological pulsations in the data as much as possible. Therefore, cerebrospinal fluid (CSF) and white matter were not regressed out from the datasets like they often are in functional connectivity analyses. Global signal was analyzed but not regressed, as the benefit of its regression is still under debate (Murphy and Fox, 2017). Furthermore, the datasets were not de-spiked, since there is no clear consensus yet what kind of de-spiking is advisable to apply to ultra-short TR fMRI data, especially since most aggressive de-spiking (AFNI *3dDespike - NEW25*) removes some of the physiological pulsations from the data (Raitamaa et al., 2018).

Time and Spatial Domain Analysis (ICA, CV/tSNR, DPARSF)

Group PICA was computed for all 10 sTR settings. For every group ICA run, 70 independent components were calculated using FSL MELODIC in default setting (Kiviniemi et al., 2009). FSL function *fslcc* was used to calculate correlation values between different PICA components calculated for every sTR and 42 resting state network templates defined earlier (Kiviniemi et al., 2009; Abou-Elseoud et al., 2010). Default mode network (DMN) posterior cingulate cortex (PCC), cerebral artery, visual, auditory, motor and ventral attention network components were selected as interesting reference components that were visualized to show the effect of changing sTR (Beckmann et al., 2005; Kiviniemi et al., 2009; Smith et al., 2009).

CV is a standardized measure used in e.g., engineering and physics, which describes the variability of a dataset compared to its mean. CV was used as a metric for the variation of physiological fluctuations in the signal. Recently, the CV of

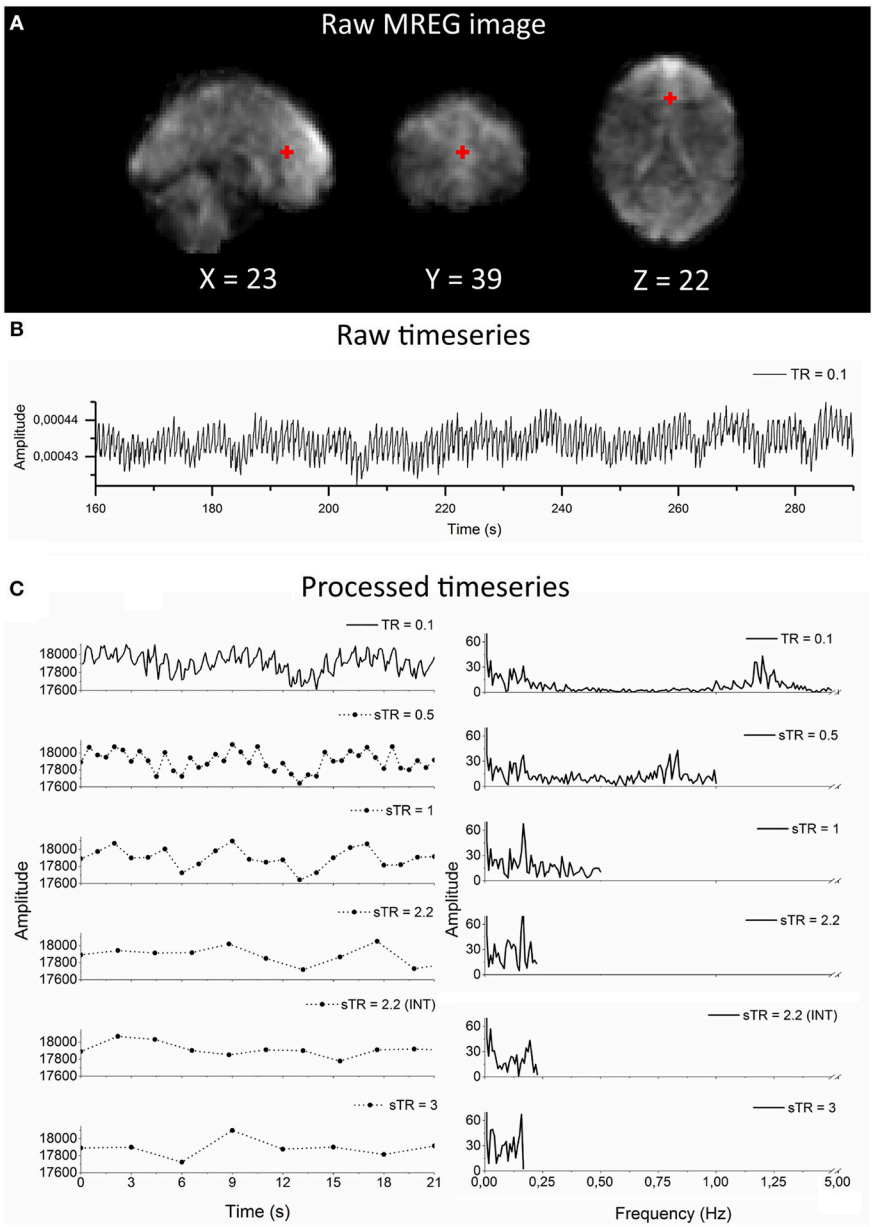

FIGURE 1 | Raw magnetic resonance encephalography (MREG) data with repetition time (TR = 0.1 s) and the subsampling scheme using an example arterial signal ([−2 30 16] mm in Montreal Neurological Institutional (MNI) space). **(A)** Raw spatial MREG image. **(B)** Raw timeseries of the arterial signal. **(C)** Processed and subsampled arterial signal and corresponding frequency amplitude spectra. Please note the aliased cardiac peak in the sTR 1–3 s in the amplitude spectra at ∼0.2 Hz.

BOLD signal (CV_{BOLD}) has been shown to be altered by the disease processes (Makedonov et al., 2016; Tuovinen et al., 2017; Kananen et al., 2018). CV was calculated for each subject and the calculation was carried out for every voxel timeseries:

$$CV = \frac{\sigma}{\mu}$$

where μ is the standard deviation, and σ is the mean of the voxel timeseries. Mean images of the resulting CV maps were computed. For statistical analyses, PCC region of interest (ROI) values were computed for every sTR individually and compared to mean reference (TR = 0.1 s) map. In addition, temporal signal-to-noise ratio (tSNR) values were computed for each sTR using white matter (WM) and gray matter (GM) ROIs. The ROI areas were obtained via FSL atlas tools using a probabilistic threshold value of 50. A mean value from both WM and GM were calculated from each subject.

DPARSF (FC, ReHo, ALFF/fALFF)

For each FSL pre-processed dataset, seed-based functional connectivity (FC), regional homogeneity (ReHo), and amplitude and fractional amplitude of low frequency fluctuations

(ALFF/fALFF) were calculated using Data Processing Assistant for Resting-State fMRI (DPARSF) V4.3_171210 MATLAB software package (Chao-Gan and Yu-Feng, 2010). The processing steps in DPARSF are described for each analysis method separately below. Global signal regression or white matter/CSF signal regressions were not used.

FC calculates seed-based correlation values between mean timeseries of a selected ROI area and the rest of the brain voxel timeseries. Six seed areas (5 mm spherical ROI) were selected for the analyses: DMN PCC (0 −53 26 mm in MNI), cerebral artery (0 32 16 mm in MNI), visual (2 −86 16 mm in MNI), auditory (50 −2 −8 mm in MNI), motor (2 −18 60 mm in MNI) and ventral attention network (-46 18 32 mm in MNI). Mean FC maps for each sTR and ROI were computed to see whether the changing of sTR influence the connectivity. For statistical analyses, correlation coefficient values were calculated between the mean ROIs (TR = 0.1 s) and other sTR settings individually using FSL function fslcc. Additionally, sTR 2.2 s (INT) and sTR 2.2 s were compared to test the effect of interleaving in MREG data.

ReHo measures the degree of regional synchronization of neighboring areas by calculating Kendall's coefficient of concordance (KCC) from the timeseries of every voxel and compares the neighboring voxels (Kendall and Gibbons, 1990; Zang et al., 2004). Cluster size of 27 voxels was used. Spatial smoothing (FWHM: kernel size [4 4 4]) was applied after ReHo calculations. After individual ReHo computations, mean spatial maps were calculated. Furthermore, ReHo KCC values were computed from the mean PCC ROI for all sTR settings.

Frequency Domain Analysis

Fast Fourier transformation (FFT) amplitude spectra from a single subject arterial region ([−2 30 16] mm in MNI) (**Figure 1**) and global image signal, venous (high respiratory power) and arterial (high cardiac power) amplitude spectra were analyzed to observe the impact of sTR in different physiological frequency bands. Additionally, normal distributions curves (bin size 5) of histogram of demeaned global signal in every sTR were computed.

To examine, whether the change in sTR affects the VLF content, ALFF and fALFF were computed. ALFF calculates the sum of spontaneous low frequency activations of a selected frequency band (Zang et al., 2007). FALFF was used to estimate the ratio of amplitude spectrum of VLF in comparison to the whole FFT spectrum (Zou et al., 2008). Frequency band of 0.01–0.1 Hz was selected for the computations.

Furthermore, we studied how the mean FFT power of VLF (0.01–0.1 Hz), respiratory (0.12–0.35 Hz) and cardiac (0.9–1.3 Hz) pulsations occur in different sTR settings. The respiratory and cardiac frequency bands were chosen based on group-level minimum and maximum frequencies observed from the physiological recordings and datasets so that the band is as limited narrow as possible while still encompassing the cardiorespiratory frequencies of each subject. The same frequency bands were used for each subject. Each band was separated by a margin to minimize overlap.

Spectral maps of the frequency bands were calculated for each dataset using AFNI *3dPeriodogram*. The function outputs a power spectrum for each voxel timeseries. The frequency bins corresponding to VLF, respiratory and cardiac bands were collected from the periodogram datasets based on individual physiological monitoring. Furthermore, the collected bins were summed and finally mean of the sums was computed for each sTR. The cardiac bins were not calculated for sTRs > 0.5 s, as the slower sampling rates cannot extract the cardiac frequencies.

The effect of signal aliasing was estimated in two ways: (i) spatially, by correlating the mean cardiac and respiratory FFT power maps to individual respiratory and VLF maps for each sTR setting, respectively, (ii) power spectrally, by calculating the FFT power change in the respiratory and VLF bands in the right medial artery ROI ([46 −2 −8] mm in MNI) with different sTRs. Mean 0.1 s TR MREG datasets were used as baseline maps and compared how much the physiological power starts to overlap per given sTR.

QPP Analysis

All datasets were bandpass filtered to VLF (0.01–0.1 Hz) band using AFNI *3dTproject*. We used a modified pattern finding algorithm to obtain quasi-periodic patterns (QPPs) and evaluated their changes in signal intensities and pulse propagations (Kiviniemi et al., 2016; Raitamaa et al., 2018). Estimation of timing and length of VLF pulse (length: 105–146 time points) for every subject was obtained from the VLF filtered global signal from TR 0.1 s. Length and timing were adjusted to the subsampled datasets. Subject-specific 4D QPP maps were created for every sTR. For the analyses, MATLAB *circshift* was used to ensure that QPP maps were in same phase.

QPP strength (i.e., how closely it resembled the template) of VLF wave for each sTR was quantified by correlation between the average QPP pulse and the VLF pulse at the last iteration of the QPP algorithm (Thompson et al., 2014). The mean correlation coefficients of VLF pulses from the last iteration were extracted from each subject and were compared as a function of sTR.

To measure the repeatability of the detected QPP maps, the spatial correlation of subject-specific average QPP maps of sTR > 0.1 s were compared to TR 0.1 s average QPP map using MATLAB *corrcoef*. For this, each sTR QPP map was interpolated to match the reference TR 0.1 s map.

For group mean images and videos, TR 0.1 s QPP maps were set to length of 150 time points and other sTRs lengths were adjusted accordingly. For every sTR, average group QPP maps were created.

Statistical Tests

Paired sample *t*-tests (MATLAB *ttest*) were used for all statistical testing to compare the reference MREG data (TR = 0.1 s) with sTR results (**Figures 3**, **6**, **7**, **9A**). Furthermore, sTR 2.2 s (INT) and sTR 2.2 s were compared to test the effect of interleaving in MREG data. In QPP repeatability analysis, linear fitting was used as a measure of statistical significance. Statistical significances are indicated as $^{*}p < 0.05$, $^{**}p < 0.01$, and $^{***}p < 0.001$.

RESULTS

As an example of the image quality of MREG 0.1 s TR data, **Figure 1A** illustrates a raw spatial image of one subject in three planes. An example of cardiovascular pulse timeseries (ROI MNI: [-2 30 16] in mm) from the anterior cerebral artery are presented in **Figure 1B**. Respective subsampling scheme is presented in **Figure 1C**, in which six examples of the sTR time series are shown to highlight the effect of changing sTR.

Commonly Used Resting State Metrics (FC, ReHo, CV/tSNR, ICA)

Seed voxel correlation of FC analysis, ReHo and CV produced nearly identical results as a function of sampling rate. Visually, only small differences could be detected in the spatial functional connectivity measures in group level maps as a function of sampling rate in **Figure 2**.

Functional connectivity maps (**Figure 2**) showed nearly identical spatial results, which were also highly comparable to conventional 2.15 s TR EPI BOLD data or with interleaved MREG 2.2 s sTR data. The quantified connectivity measures presented no significant differences excluding INT (sTR = 2.2 s) which had significantly ($p < 0.01$) lower correlation coefficients compared to TR 0.1 s and compared to sTR 2.2 s (**Figure 3A** and **Supplementary Figure 1**). In addition, EPI scans had marginally elevated correlation coefficients compared to the MREG (TR = 0.1 s).

Similarly, ReHo were visually identical at different sampling rates (**Figure 2**). However, with interleaved sampling of 1,3,5...,2,4,6 of axial MREG slices were collected with a final 2.2 s sampling rate, the ReHo values decreased significantly ($p < 0.001$), when compared to both single shot k-space trajectory with TR 0.1 s and sTR 2.2 s (**Figure 3B**). Furthermore, conventional EPI showed significantly ($p < 0.001$) higher and sTR 2.2 lower ($p < 0.05$) values.

CV of the image data were nearly identical with respect to the altering sTR (**Figure 2**). The EPI BOLD data had significantly ($p < 0.05$) lower CVs compared to MREG (TR = 0.1 s), while downsampling or interleaved data gathering had no effect on the CV values. The same effect can be seen from the mean tSNR values from WM and GM ROIs where downsampling did not show any significant change but EPI BOLD values were significantly ($p < 0.001$) higher compared to MREG (**Supplementary Figure 2**).

ICA detected RSNs in all sTR settings, but there was some variability between the results (ICA in **Figure 2**). The conventional EPI BOLD and interleaved data showed similar results as well. In spatial consistency analysis of the 42 RSN template correlations, all sTR settings produced very similar results, except for EPI, which had significantly higher correlation values ($p < 0.01$).

Mean Spectral Metrics

The group mean FFT amplitude spectra of global image signal, respiratory and cardiac signals are presented in **Figure 4**. In global signal spectra, the amplitude peaks were relatively higher in VLF band with increasing sTR. This might occur due to cardiorespiratory aliasing. The respiratory amplitude peaks from sagittal sinus and cardiac amplitude peaks from right middle cerebral artery presents multiple peaks in the spectra due to normal variations in respiratory and cardiac rates. Please notice, these peaks were lost as the sTR was increased >0.5 s. The same effect was observed in the arterial signal on a single subject level (**Figure 1**). EPI BOLD presented the lowest VLF amplitudes in all images.

The global signal distribution curves illustrated the differences in statistical power between sTR values and revealed an exponential decay in histogram counts and widening of the distributions per each sTR. Interestingly the 2.15 EPI BOLD distributions are highly similar in shape with MREG 0.1 s data but >5 times smaller.

BOLD Signal Frequency Amplitude and Power Mapping

ALFF results indicated that the increasing sTR raised the VLF power of the images (**Figure 5**). Conventional EPI data showed lower ALFF values than MREG data, but the interleaving had no effect. FALFF results were most clearly affected by the increasing sTR (**Figure 5**). FALFF showed an increase over the sTR values which is due to the proportional increase of the lowest frequencies due to the reduction of the spectral coverage in higher sTR values.

Group mean FFT amplitude and power encoding maps (**Figure 5**) revealed how the cardiac, respiratory and VLF frequency intensities changed in different sTR settings. The cardiac power started to fade away in sTR >0.3 s and respiratory power above 2.2 s sTR. Furthermore, the cardiac power distributions started to overlap on top of respiratory frequency maps as the sTR is increased >0.5 s indicating aliasing, c.f. **Figures 5–7**. The conventional 2.15 s TR EPI measurement had notably lower power (please notice different scaling for EPI BOLD in **Figure 5**). Interleaved 2.2 s sTR power was also lower compared to 2.2 s sTR single shot trajectory in VLF power images, which agrees with ReHo and mean global signal amplitude spectral changes.

The aliasing was quantified both spatially and in frequency power analyses. This was evaluated by measuring how much different frequency maps start to resemble each other spatially as a function of sTR (**Figure 6**). In critically sampled 0.1 s TR MREG data the cardiac, respiratory and VLF frequencies had a low ∼0.4 mean spatial correlation. For example, the major arteries seen in cardiac frequency maps were lacking from the respiratory maps, while the respiratory band dominated in posterior CSF spaces (**Figure 5**). However, the spatial correlation between cardiac and respiratory power maps became increasingly more similar ($p < 0.001$) and started to increase as a function of the sTR until 1.0 s, after which the similarity plateaus at 0.65 level until sTR 3.0 s (**Figure 6A**). Furthermore, the spatial correlation between cardiac ($p < 0.001$) and respiratory ($p < 0.01$) vs. VLF increased steadily until sTR 1.8 s.

In frequency power analysis of a right medial artery ROI ([46 −2 −8] mm in MNI) near insula, the image signal power from the arterial ROI started to increase significantly ($p < 0.001$) both

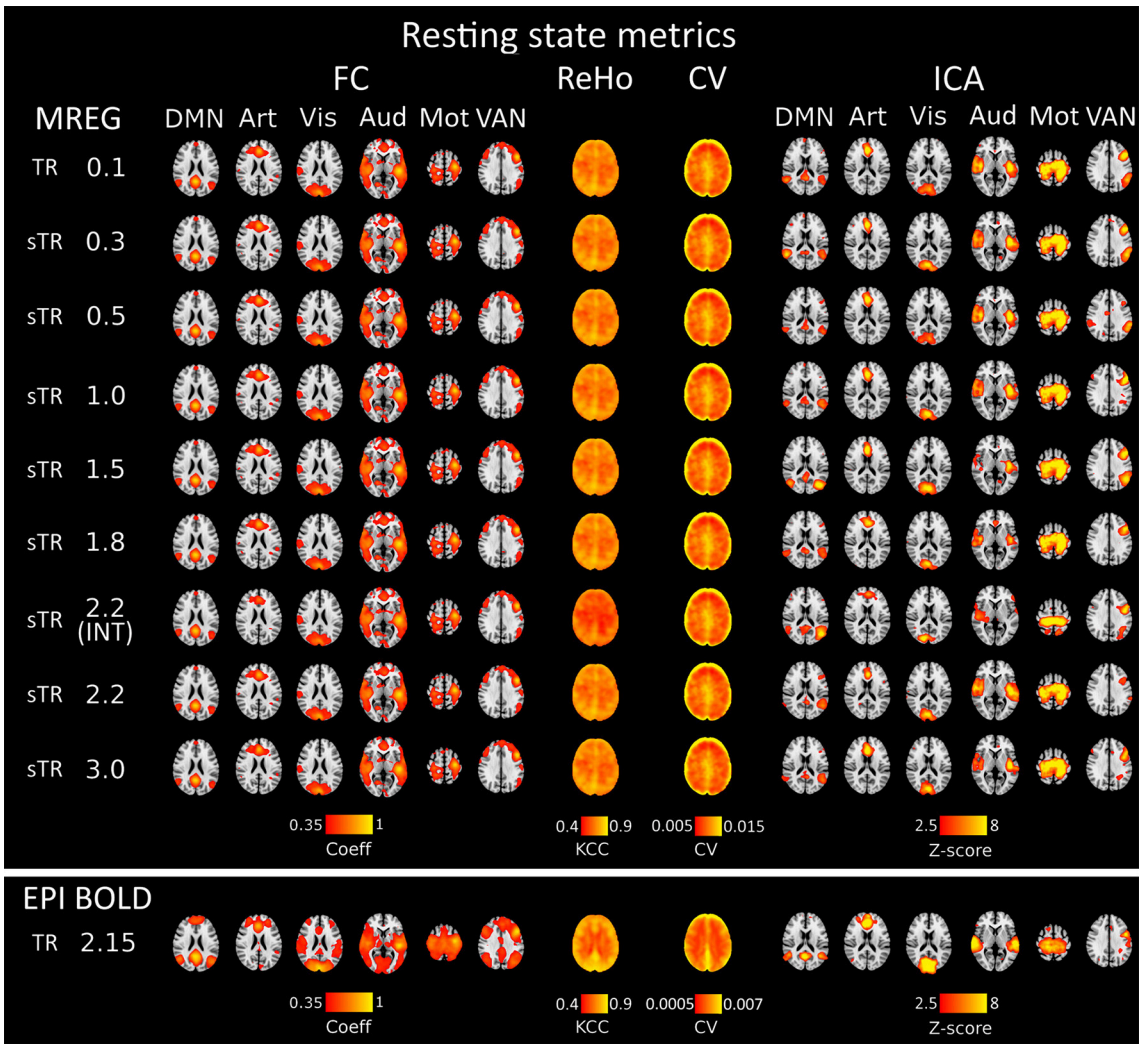

FIGURE 2 | Different group-level resting state metrics with changing subsampled repetition times (sTR) including functional connectivity (FC), regional homogeneity (ReHo), coefficient of variation (CV) and independent component analysis (ICA). FC and ICA analyses comprise default mode network (DMN), artery (Art), visual (Vis), auditory (Aud), motor (Mot) and ventral attention network (VAN). For comparison, echo-planar imaging (EPI) maps below tends to show spatially more widespread FC maps and relatively similar ICA maps depending in the RSN.

in the respiratory and VLF power band in sTR >0.3 s as a sign of aliasing (**Figure 7A**). The results indicate that once the cardiac pulsation is no longer critically sampled, the power starts to become aliased as a "respiratory" and "VLF" power as a function of sTR increase. When correlating the mean respiratory maps to individual VLF maps, the aliasing effect could also be seen in VLF range as the correlation values increased significantly ($p < 0.01$) after 0.1 s TR and almost linearly as the sTR increased. However, the influence of the sTR had a clearly less steep effect by the increasing sTR in the VLF. The conventional 2.15 s BOLD images showed low spatial correlation since the cardiac power is very low to begin with and so the spatial correlation is also low.

QPP Analysis of Spreading BOLD Waves

The power of cardiac pulsation could not be critically detected in sampling rates >0.3 s (**Figures 3–5**) and therefore we did not quantify differences in the detection of cardiac pulse propagation like we did earlier (Raitamaa et al., 2018). Also, the respiratory power suffered from marked aliasing in sTRs above 0.5 s (**Figures 5–7**). Therefore, we quantified the performance of different sTR in detecting VLF (0.01–0.1 Hz) propagating QPP BOLD waves.

Figure 8 illustrates 15 s QPP waves captured with different sTR and how the spatiotemporal illustration of each wave changed as a function of sTR. The lowest sTR 0.1–0.5 s were down-sampled from 150, 50 and 30 to 15 images for illustration of the QPP wave spreading in axial plane. Videos of QPPs in TR of 0.1 s and 0.5, 1.0, 2.2 and 3.0 s are shown in **Supplementary Material**. As expected, much of the dynamics were lost as a function of increasing sTR.

We also quantified the QPP strength within each subject of the QPP VLF waves as a function of sTR (**Figure 9A**). The analysis

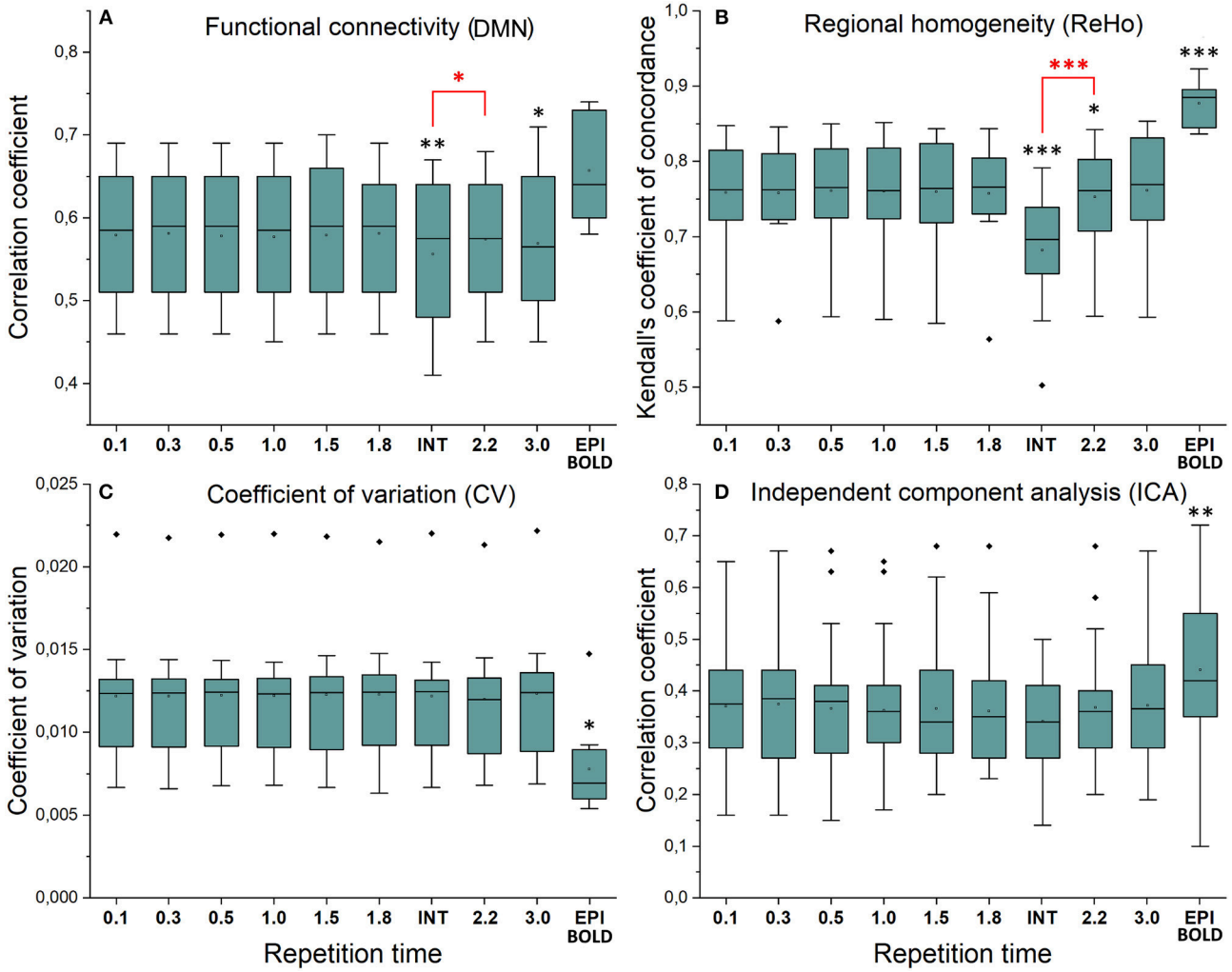

FIGURE 3 | Resting state metrics in different subsampled repetition times (sTR) compared to reference maps (TR = 0.1 s). **(A)** Individual functional connectivity (FC) values from default mode network (DMN), posterior cingulate cortex (PCC ROI) correlated to reference FC map. **(B)** Regional homogeneity (ReHo) Kendall's coefficient of concordance (KCC) values from PCC ROI compared to mean reference map (TR = 0.1 s). **(C)** Coefficient of variation (CV) values from PCC ROI compared to mean reference map. **(D)** Correlation values between group probabilistic independent component analysis (PICA) components in different sTR settings and previously acquired 42 resting state network ICA templates. Significant differences between TR 0.1 and other sTR settings are marked with $^{*}p < 0.05$, $^{**}p < 0.01$, and $^{***}p < 0.001$. Outliers are marked with ♦.

revealed that 0.1 s TR data had highest spatial correlation of the detected VLF waves on average despite the largest number of brain volumes (i.e., 150 vs. 5 volumes between highest and lowest TR). There is a linear trend where the intra-individual detection accuracy of the detected VLF QPP waves gave lower ($0.01 < p < 0.05$) values as a function in sTR > 0.3 s excluding EPI.

When comparing how similar QPP waves were detected between subjects, the 0.1 s MREG data was used as a reference due to highest VLF wave detection accuracy. Each sTR QPP map was interpolated to correspond the 0.1 s MREG time points. On average, the detected QPP waves became linearly less correlated as a function of sTR (**Figure 9B**). Conventional EPI had less robustly detected QPP waves. Interleaved timing of data acquisition showed no effect on the wave detection accuracy nor on repeatability of the detected QPPs.

DISCUSSION

The study analyzed the effect of 3D image sampling rate on most popular fMRI metrics used. The time and spatial resting state fMRI metrics (FC, CV/tSNR, spatial ICA) were not markedly affected by sTR. In frequency domain analysis, the aliasing of the cardiorespiratory power seemed to increase signal power as a function of the sTR (sTR > 0.3 s). Importantly, aliasing effects occur mostly between cardiac and respiratory power. The VLF power increased also significantly as a function of sTR due to aliasing but the power of aliasing was smaller. In dynamic QPP analyses, shorter sTRs seemed to produce more stable results.

Also, to our surprise, the effect of sampling rate on non-dynamic rs-fMRI measures was not as strong as hypothesized. Most of the measures stayed stable within the range of sTR.

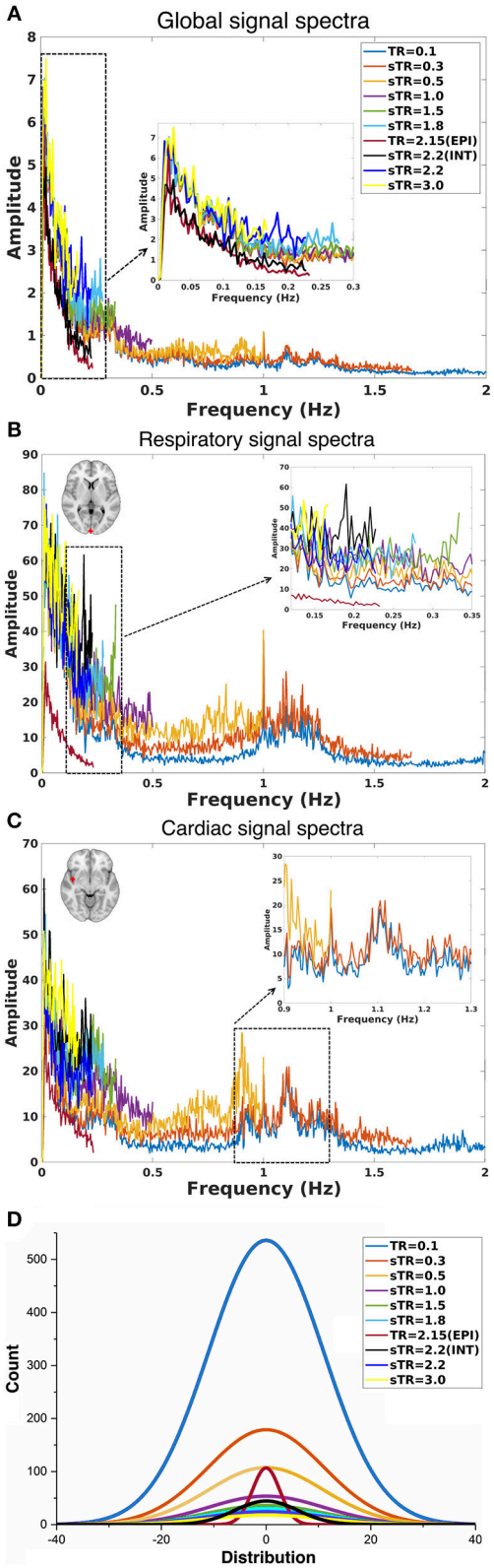

FIGURE 4 | Group-level fast Fourier transform (FFT) amplitude and histogram distribution analyses in different subsampled repetition times (sTRs). **(A)** FFT *(Continued)*

FIGURE 4 | amplitude spectra of global image signal where the 0.1 TR data is cut to 2 Hz from original 5 Hz. **(B)** FFT amplitude spectra of respiratory region of interest (sinus sagittal, ROI, [2 −98 4] mm in Montreal Neurological Institute (MNI) space). **(C)** FFT amplitude spectra of cardiac ROI (right medial artery) [46 −2 −8] mm in MNI. Due to differences in individual cardiorespiratory rates, several frequency peaks can be detected at the group level. **(D)** Mean normal distribution curves from demeaned global signal histograms show lowering and widening of the distributions as a function of sTR.

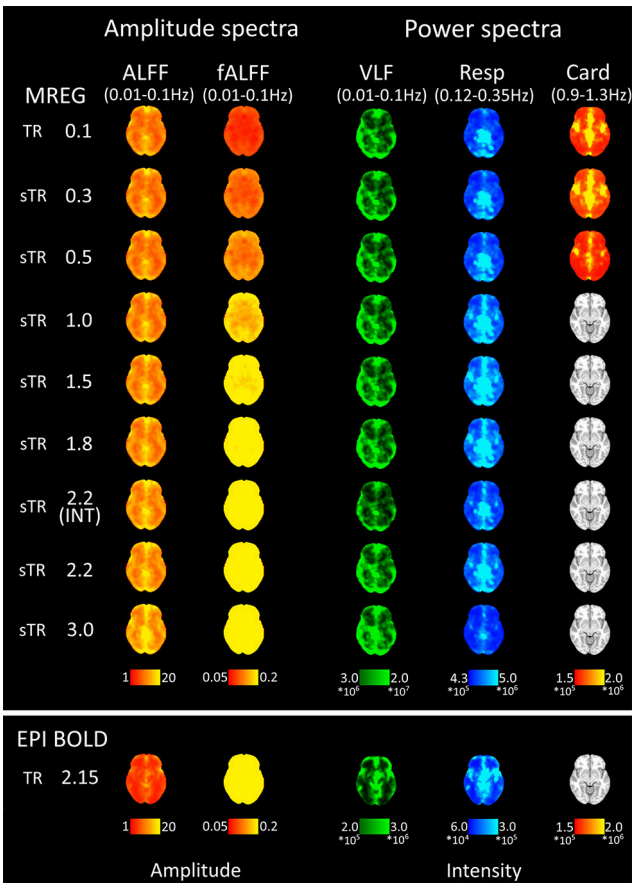

FIGURE 5 | Mean fast Fourier transform (FFT) amplitude (ALFF/fALFF) and power (VLF, Resp, Card) encoding maps for each subsampled repetition times (sTRs). The cardiac power can be detected until 0.3 s and respiratory until 2.2 s sTR. However, the respiratory and cardiac power images started to overlap in sTR > 0.5 s, increasing to sTR 1–2 s. Very low frequency (VLF) power showed a subtle but steady increase with increasing sTR.

Golestani and co-workers found surprisingly minimal effect on sampling rate on ReHo, ALFF and FC results that are in full agreement with our results (Golestani et al., 2017). Several researchers have found that higher sampling rate appears to be beneficial for resting state fMRI measures, especially for ICA/dual regression and our results also agree on this (Smith et al., 2013; Preibisch et al., 2015; Golestani et al., 2017; Demetriou et al., 2018.

Compared to MREG in general, the interleaved EPI BOLD had statistically significantly ($p < 0.001$) increased ReHo

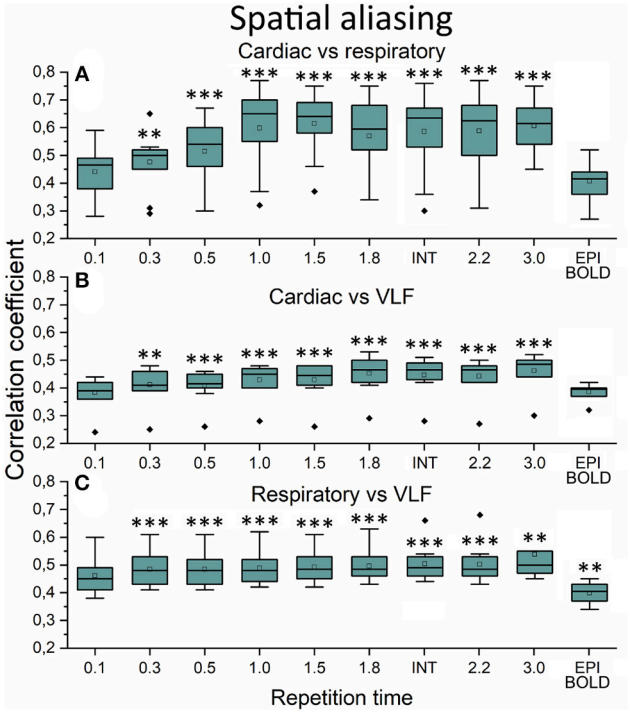

FIGURE 6 | Spatial aliasing measure using spatial correlation values. **(A)** The mean MREG cardiac fast Fourier transform (FFT) power image of repetition time (TR = 0.1 s) correlated to individual respiratory power images as a function of sampled TR (sTR) and echo-planar imaging (EPI) scan. **(B)** Mean cardiac FFT image correlated to individual very low frequency (VLF) images. **(C)** Mean respiratory image correlated to individual VLF images. Significant differences between TR 0.1 s and other sTR settings are marked with $^{**}p < 0.01$ and $^{***}p < 0.001$. Outliers are marked with ♦.

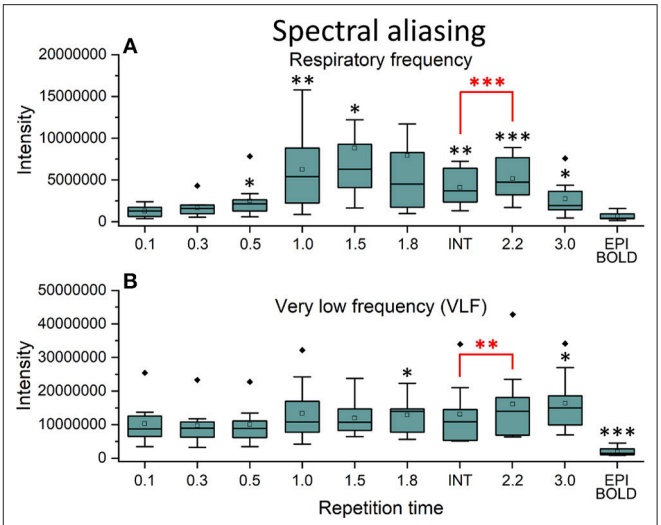

FIGURE 7 | Cardiac aliasing measure using fast Fourier transform (FFT) power intensity values of arterial region of interest (ROI, [46 −2 −8] mm in Montreal Neurological Institute (MNI) space). **(A)** Intensity values of individual respiratory power images. **(B)** Intensity values of individual very low frequency (VLF) power images. Significant differences between repetition time (TR = 0.1 s) and other sampled TR (sTR) settings are marked with $^{*}p < 0.05$, $^{**}p < 0.01$, and $^{***}p < 0.001$. Outliers are marked with ♦.

and tSNR. However, the f/ALFF, global signal amplitude spectrum baseline and signal variance as measured with CV are reduced in EPI compared to MREG. Interleaved MREG variant (INT sTR 2.2 s) also induced significantly ($p < 0.001$) lower ReHo compared to both TR 0.1 and to single shot variant (sTR 2.2 s). The conventional interleaving introduces TR/2 delay and interleaved multislab scanning introduces TR/2xN delay between subsequent scans, where N is the number of slabs. This introduces delays between neighboring voxels in longitudinal z-direction and alters regional similarity and frequency measures due to discontinuous sampling of the propagating cardiorespiratory pulses that traverse the brain repeatedly in addition to VLF pulses (Kiviniemi et al., 2016).

Aliasing in Cortical Connectivity Analysis

The current data illustrates that while the aliasing of cardiorespiratory pulsations is a significant factor in frequency domain, the currently used time and spatial domain analyses tools perform well in detecting robust resting state connectivity. In summary, the stationary spatial and temporal connectivity measures, whether local or long distance, were not significantly affected by changes in sTR. However, interleaved slice acquisition seems to affect some of these measures.

This study confirms the information from reduced data length analytics (Bright and Murphy, 2015) and is consistent with coactivation pattern (CAP) analysis (Liu and Duyn, 2013), where the information on spatial functional connectivity of regions can be depicted even in one single brain volume. However, the CAP analysis for instance, requires individual voxel level thresholding with the time domain signal mean/std.

ICA performs best with large data distributions and therefore conventionally spatial ICA is preferred over temporal ICA, since it offers larger distributions (Calhoun et al., 2001; Kiviniemi et al., 2003; Beckmann et al., 2005). Spatial ICA also uses BOLD signal's temporal variance which induces the non-Gaussian changes in the signal distributions, by which the statistical independence is inferred (Calhoun et al., 2001; Kiviniemi et al., 2003; Beckmann et al., 2005). The clear advantage of the short TR can be seen in **Figure 4**, where 0.1 s TR overall signal distribution histogram has almost 5 times higher and substantially larger distribution compared to other distributions. This is the basis of the statistical power advantage already depicted by several groups for using short TR measurements (Smith et al., 2013; Preibisch et al., 2015; Golestani et al., 2017; Demetriou et al., 2018). Furthermore, in the case of combined spatiotemporal ICA or temporal ICA alone approaches, the 0.1 s data most likely outperforms the slower sTRs simply due to statistically more valid signal histograms (**Figure 4D**).

The physiological pulses themselves modulate the BOLD signal (Birn et al., 2006, 2008; Chang and Glover, 2010; Chang

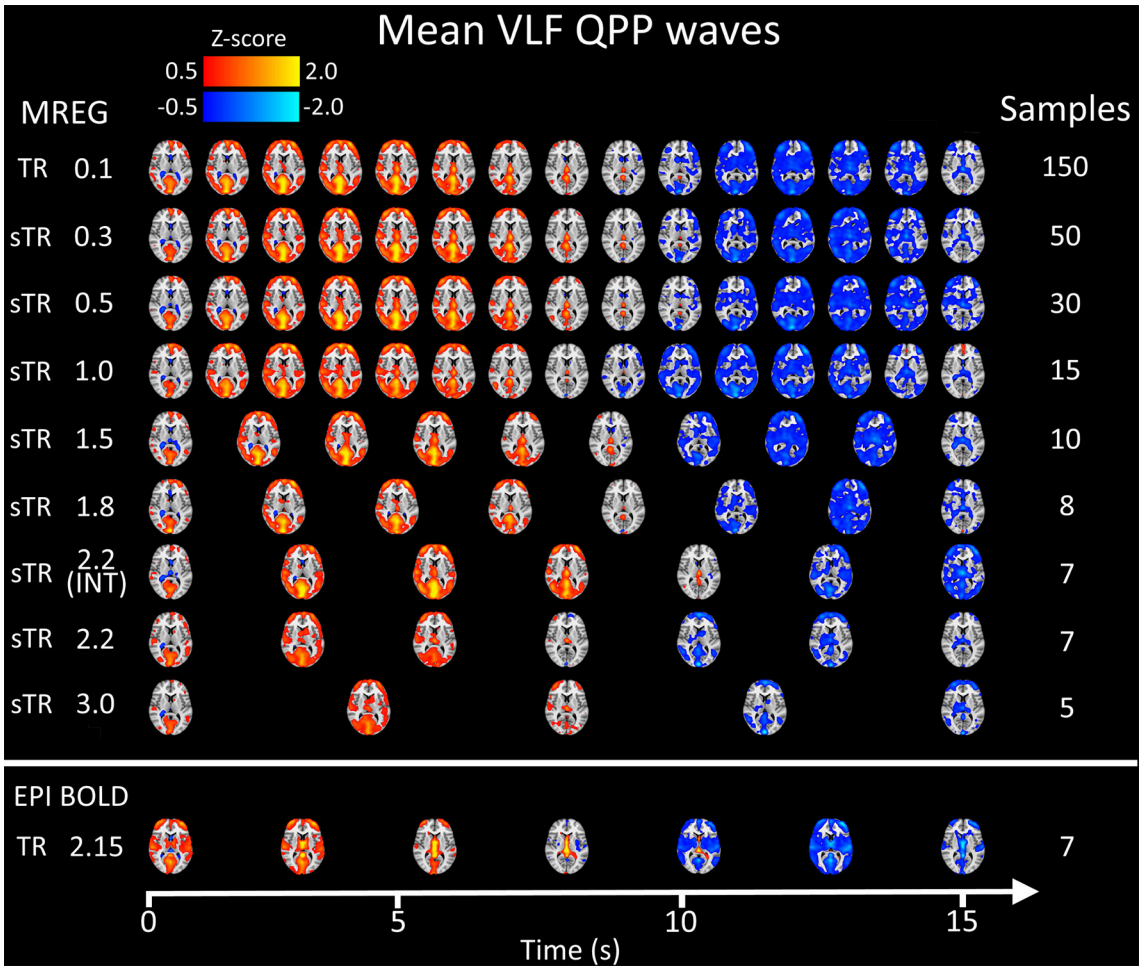

FIGURE 8 | Group mean very low frequency (VLF) waves as a function of subsampled repetition time (sTR). Please notice that the first three rows are downsampled from 150, 50, and 30 to 15 images, respectively to fit the picture.

et al., 2013a). Recently, ultra-fast MREG data was able to illustrate how the cardiac and respiratory pulsations propagate in repeated waves over the whole brain, giving rise to physiologically driven and modulated variance in the data (Kiviniemi et al., 2016; Raitamaa et al., 2018). However, most of the cardiorespiratory power is centered within central areas near CSF ventricles (respiratory) and major arteries and veins (cardiac). The VLF power dominance in the brain cortex seems to enable robust connectivity measurement despite imminent cardiorespiratory aliasing especially in sTRs 1–2 s.

The physiological signal sources need to be separated from the functional signals before any realistic interpretations of the neurovascular task or connectivity data can be drawn. Through the years, source separation tools such as the ICA have been developed to offer robust detection of functionally connected regions or constellations of regions, such as resting state networks (Calhoun et al., 2001; Kiviniemi et al., 2003; Beckmann et al., 2005; Griffanti et al., 2015; Vidaurre et al., 2017). However, in this respect also other measures, such as FC and CV are highly reproducible over a range of sTRs. Therefore, even though there is significant aliasing, especially in areas near medial cerebral artery and sagittal sinus neighborhood, the dominance in VLF induces robust functional connectivity in the cortex.

BOLD signal stability is often measured as tSNR or CV which is the inverse of tSNR. In this study, we calculated both. In terms of signal observations of hemodynamically convolved neuronal activation response, in our sampling scheme the CV or tSNR do not change as we only downsample the MREG data instead of scanning using different TRs. However, compared to EPI BOLD the CV values were significantly higher (**Figures 2**, **3**) and tSNR values significantly lower (**Supplementary Figure 2**) which could be partially caused by higher flip angle and slightly shorter TE in EPI BOLD. In spite of all, both sequences have relatively long TEs, which makes them T2* -weighted.

Recent studies indicate how the CV reflects also physiological pulsation changes, rather than neuronally driven alterations. Furthermore, the CV has recently been shown to have high sensitivity to pathological condition even at individual level (Makedonov et al., 2016; Tuovinen et al., 2017, 2018). Our preliminary experience on disease related BOLD signal noise

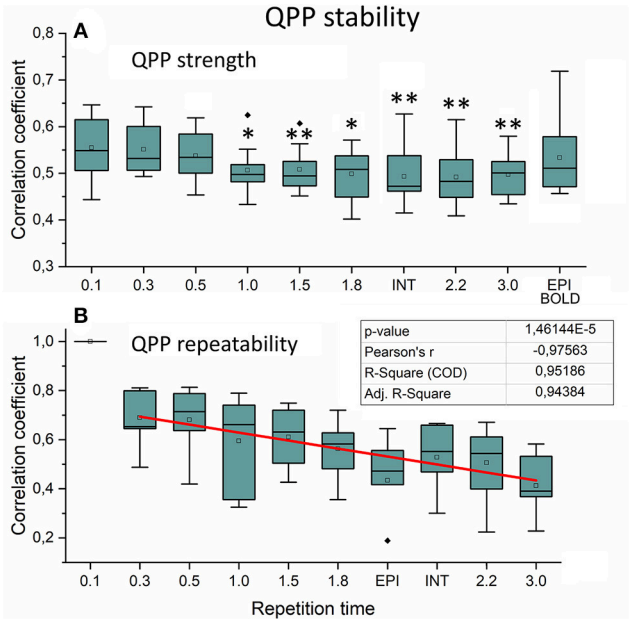

FIGURE 9 | Very low frequency (VLF) quasi-periodic pattern (QPP) stability measurements. **(A)** Intra-individual QPP strength as a function of subsampled repetition time (sTR). Significant differences between repetition time TR 0.1 s and other sTR settings are marked with $*p < 0.05$ and $**p < 0.01$. **(B)** Inter-individual correlation coefficients of QPP wave repeatability as a function of sTR. Correlation coefficients decreased statistically significantly ($p < 0.001$) by decreasing slope of sTR. Outliers are marked with ♦.

metrics suggests that at 1.8 s TR the BOLD signal CV can also be highly sensitive to pathological conditions (Tuovinen et al., 2018). Data from 0.1 s MREG CV measures seem to be at least as sensitive in intractable epileptic patient data (Kananen et al., 2018). This is in line with the CV results that do not alter as a function of TR but can be sensitive to differences in sequence parameters and k-space trajectory and other technical issues, c.f. **Figure 2**.

Aliasing of Physiological Pulsations in Central Areas

The FFT frequency power maps illustrate that the cardiac 1 Hz power is mainly detectable in sTR < 0.3 s. In the most critically sampled data, the 1 Hz cardiovascular signal pulses most prominently in the paravascular space in areas near major cerebral arteries and somewhat in the major venous sinuses. From the periarterial areas the cardiovascular pulses are convected into the CSF ventricles, centerline parasagittal CSF spaces, c.f. **Figure 5**. The respiratory power is nearly absent from the periarterial spaces and dominates more on the posterior and cortical perivenous structures and is relatively stronger in the posterior central CSF spaces. The VLF power tends to align mostly along the cortical gray matter without strong overlap with the midline parasagittal area.

Above 0.3 s sTR, the cardiac power became mostly aliased over respiratory power in central brain bordering CSF spaces. Thus, all critical analysis of respiratory power changes needs to be performed with data < 0.5 s TR. The most prominent aliasing occurred in sTRs between 1 and 2 s, where the respiration is still sampled critically but the cardiac is aliased over it; they become strongly mixed into sTR 1–2 s signal. This type of cardiorespiratory aliasing however seems to affect the measuring of FC on cortical structures minimally (**Figures 2**–**3**), since the connectivity occurs dominantly in VLF frequencies (<0.1 Hz) that dominate in the cortex to begin with. Also, the effects of aliasing as a function of sTR on the VLF FFT power are less severe around sTR 1–2 s but increase further in sTRs >2.0 s (**Figures 2**, **5**, **6**).

The power of FFT amplitude spectra increased in VLF range as a function of sTR, which is a sign of cardiorespiratory aliasing (Kiviniemi et al., 2005; De Luca et al., 2006). The effect was highest in sTR 3.0 s. This reduces sensitivity to changes in physiological pulsations and furthermore does no longer have the capability to differentiate neither cardiorespiratory nor even different VLF fluctuation peaks as different sources. Furthermore, physiological pulsations seen in 0.1 s TR could not be detected on a group level global or individual voxel signal above 0.3 s sampling rate. Also, VLF power peak features became undetectable with vanishing power of the increased sTR.

Importantly, the $f^{-\alpha}$ FFT amplitude spectrum curve became affected by the highest sTRs (**Figure 4**). This has an inevitable effect on measures of signal stationary metrics like Hurst exponent (H) (Bullmore et al., 2001; Wink et al., 2008), fractal dimension (Df) (Kiviniemi et al., 2005; Kiviniemi, 2008) since the power spectral intensity $f(I) = f^{-\alpha}$, where $Df = (3\text{-}\alpha)/2$ and $Df = 2\text{-}H$. The f/ALFF as well as $f^{-\alpha}$ metrics may then also be sensitive to physiological pulsations. In other words, results based on comparing patients with controls may suffer from cardiorespiratory differences between groups. To avoid these factors, physiological signals should be measured and FFT power spectral analyses should be performed on as short TR data as possible. This is our recommendation for future studies.

Dynamic Connectivity and Effect of TR

The recent discoveries of dynamic functional connectivity analytics of fMRI data show that there are marked changes over time (Hutchinson et al., 2012). Wavelet analyses and time windowed approaches have suggested that the connectivity of regions varies markedly over time (Chang and Glover, 2010; Kiviniemi et al., 2011; Smith et al., 2012; Liu and Duyn, 2013). Targeted averaging algorithms can detect quasi-periodic very low frequency BOLD signal pulses that travel over the RSN and connectivity gradient patterns (Majeed et al., 2011; Pan et al., 2013; Keilholz, 2014; Thompson et al., 2014).

In this study we evaluated the VLF QPP maps to quantify effects of sTR on dynamic BOLD connectivity metrics. First, the FFT analysis indicated that the faster cardiorespiratory pulsations could not be even evaluated as a function of sTR: the cardiac power is not visible above 0.5 s sTR and furthermore the cardiac power aliases over respiratory power. Secondly, the VLF pulse analysis indicated that compared to the most critically sampled 0.1 s TR data, both the QPP strength (i.e.,

spatial similarity of waves) and inter-individual repeatability of the QPPs become linearly reduced with increasing sTR. In other words, the QPP analysis significantly lost its accuracy as a function of sTR. Taken together, the analysis of dynamic and physiological pulsations benefits when performed on data with TRs < 0.3 s.

As with most of the dynamic connectivity metrics, the problem has been the reducing statistical power of the analysis when shorter and shorter connectivity epochs have been attempted to be analyzed. Reducing dynamic analysis window length reduces also the number of samples and degrees of freedom for statistical inferences. Our results support the use of short TR in the evaluation of dynamic connectivity metrics as (a) for mathematical procedures, short TR gives more time points per analyzed time window, (b) it enables critical sampling and differentiation of physiological pulsations, (c) it avoids aliasing of the physiological signal over the targeted phenomena, (d) enables mapping of modulations of the pulsations, and e) it offers markedly more accurate signal distributions for statistical inferences, c.f. **Figure 4D**.

LIMITATIONS AND STRENGTHS OF THE STUDY

The results may not be directly comparable due to multiple technical differences between interleaved EPI vs. MREG. However, despite the technical differences, the results in stationary connectivity are highly similar in a wide range of frequencies and RSNs. This study aimed to minimize confounding factors like intra-subject status changes (cardiorespiratory status, vigilance, mood, etc.) as well as technical factors (SNR, sequence parameters, sampling trajectory, scanner model, field strength) issues by using data from the same subjects scanned once with fast TR that was downsampled to higher sTRs. This enables the direct comparison of the effects of sampling rate only. EPI data was scanned for comparing the results to a more conventional technique.

However, the interleaved vs. single shot k-space sampling technique is not the only difference when comparing MREG and EPI data. As mentioned accurately by Golestani and co-workers, comparisons of long vs. short TR measurements need to be taken with a grain of physics, i.e., the EPI vs. MREG also have several other technical differences. In order to be fast, TR is very short in MREG which sensitizes the signal more to T1 inflow and steady state precession effects compared to conventional EPI BOLD (Liu, 2016). On the other hand, TE is relatively long in MREG which makes it T2* -weighted as is EPI BOLD. The low flip angles 5° vs. 15° in MREG and EPI BOLD, respectively, reduces the sensitivity to physiological pulsations on both methods as well (Gonzalez-Castillo et al., 2011). Furthermore, the system noise changes linearly or even quadratically with the TR due to imperfections as the sequence is repeatedly run. All these effects need to be considered while discerning the differences between EPI vs. MREG results and again the direct comparison between them is rather difficult.

According to (Glover, 2012), the spiral readout has reduced sensitivity to motion, shortened readout times, improved signal recovery in most frontal and parietal brain regions, and exhibited blurring artifacts instead of ghosts or geometric distortion. MREG combines Spiral-in/out trajectory which further has diminished susceptibility-induced signal dropout and increased BOLD signal. The EPI readout trajectory is subject to ghosts from off-resonance and gradient imperfections and is intrinsically sensitive to cardiac-induced pulsatile motion from substantial first- and higher order moments of the gradient waveform near the k-space origin (Glover, 2012). So, the artifact and BOLD sensitivity profiles are also different between EPI and MREG. In summary, looking at the similarity of the resting state connectivity measures with different techniques, it seems that human brain connectivity is quite a stable phenomenon that can be measured robustly with technically quite different scanning approaches.

Earlier, the use of two different sampling rates scanned at subsequent scanning sessions have been used to exclude aliasing as a source of very low frequency fluctuations as a source of resting state functional connectivity (Beckmann et al., 2005; Kiviniemi et al., 2005). Theoretically, the previous data that used different scan sessions and so the physiological pulses were not identical between the TRs and therefore not directly comparable. However, in studies with different sampling rate in different scan, also there the results seem to be highly similar to our data (Smith et al., 2013; Golestani et al., 2017).

While attempting to quantify aliasing and dynamic metrics, we used the original 0.1 s TR MREG data as a reference. This may in theory involve a bias since the original MREG data can also detect modulations of cardiorespiratory pulse amplitudes and timing variations, as seen in **Figure 1**. The slower sTRs have no way of depicting these modulations and therefore a comparison of spatial connectivity and signal stability may be somewhat biased toward undermining the accuracy of the fast data, since it is also sensitivity to modulation effects.

CONCLUSION

The overall the effect of sampling rate on most commonly used stationary rs-fMRI metrics is minimal. The dominance of the VLF power in gray matter overpowers aliasing effects and enables highly reproducible stationary connectivity results. The aliasing is most dominant between cardiac and respiratory pulsations in central structures near or within CSF spaces. Different technical imaging approaches (e.g., interleaved EPI vs. SOS MREG) yield differential connectivity metrics stemming from multiple spin acquisition differences. Despite these differences, the results from different techniques give fairly good spatial agreement of human brain connectivity. Interleaved scanning of slices seems to introduce inaccuracies in some analyses due to discontinuous sampling

of physiological signals. The analysis of dynamic connectivity and frequency based physiological pulsation benefits most from faster scanning.

DATA AVAILABILITY

The datasets generated for this study are available on request to the corresponding author.

AUTHOR CONTRIBUTIONS

VKi and VKo: designed the study; NH, VKi, VKo, and VR: collected the data; NH, LR, VKi, VKo: analyzed the data; NH, VKi, VKo, JaK, LR, HH, VB, TT, AR and JuK: wrote the manuscript.

FUNDING

This work was supported by Jane and Aatos Erkko Foundation grant (VKi), Academy of Finland and Aivosäätiö TERVA grant 314497 (VKi), Academy of Finland Grants 123772 & 275342 (VKi), The SalWe Research Program for Mind and Body (Tekes—the Finnish Funding Agency for Technology and Innovation, Grant No. 1104/10) (VKi), Finnish Medical Foundation (VKi, TT), Finnish Neurological Foundation, KEVO grants from Oulu University Hospital (VKi), Epilepsy Research Foundation (JaK), Finnish Cultural Foundation, North Ostrobothnia Regional Fund (JaK), Orion Research Foundation sr (JaK, TT), Tauno Tönning Foundation (JaK) and Health and Biosciences Doctoral programme -grant (HH).

ACKNOWLEDGMENTS

Thanks to all study subjects for participation and thanks to CSC (Tieteen Tietotekniikan Keskus) for supporting the analysis tools.

SUPPLEMENTARY MATERIAL

The Supplementary Material for this article can be found online at: https://www.frontiersin.org/articles/10.3389/fnins.2019.00279/full#supplementary-material

Video 1 | Mean very low frequency quasi-periodic patterns (VLF QPPs) for repetition time (TR = 0.1 s).

Video 2 | Mean very low frequency quasi-periodic patterns (VLF QPPs) for subsampled repetition time (sTR=0.3 s).

Video 3 | Mean very low frequency quasi-periodic patterns (VLF QPPs) for subsampled repetition time (sTR = 0.5 s).

Video 4 | Mean very low frequency quasi-periodic patterns (VLF QPPs) for subsampled repetition time (sTR=1.0 s).

Video 5 | Mean very low frequency quasi-periodic patterns (VLF QPPs) for subsampled repetition time (sTR=1.5 s).

Video 6 | Mean very low frequency quasi-periodic patterns (VLF QPPs) for subsampled repetition time (sTR=1.8 s).

Video 7 | Mean very low frequency quasi-periodic patterns (VLF QPPs) for subsampled repetition time (sTR=2.2 s).

Video 8 | Mean very low frequency quasi-periodic patterns (VLF QPPs) for subsampled repetition time (sTR=3.0 s).

Video 9 | Mean very low frequency quasi-periodic patterns (VLF QPPs) for conventional echo-planar imaging (EPI) acquisition with repetition time (TR=2.15 s).

Video 10 | Mean very low frequency quasi-periodic patterns (VLF QPPs) for interleaved variant with subsampled repetition time (sTR=2.2 s).

REFERENCES

Abou-Elseoud, A., Starck, T., Remes, J., Nikkinen, J., Tervonen, O., and Kiviniemi, V. (2010). The effect of model order selection in group PICA. *Hum. Brain Mapp.* 31, 1207–1216. doi: 10.1002/hbm.20929

Assländer, J., Zahneisen, B., Hugger, T., Reisert, M., Lee, H. L., LeVan, P., et al. (2013). Single shot whole brain imaging using spherical stack of spirals trajectories. *Neuroimage* 73, 59–70. doi: 10.1016/j.neuroimage.2013.01.065

Beckmann, C. F., DeLuca, M., Devlin, J. T., and Smith, S. M. (2005). Investigations into resting-state connectivity using independent component analysis. *Philos. Trans. R. Soc. Lond. B Biol. Sci.* 360, 1001–1013. doi: 10.1098/rstb.2005.1634

Beckmann, C. F., Jenkinson, M., Woolrich, M. W., Behrens, T. E., Flitney, D. E., Devlin, J. T., et al. (2006). Applying FSL to the FIAC data: model-based and model-free analysis of voice and sentence repetition priming. *Hum. Brain Mapp.* 27, 380–391. doi: 10.1002/hbm.20246

Birn, R. M., Diamond, J. B., Smith, M. A., and Bandettini, P. A. (2006). Separating respiratory-variation-related fluctuations from neuronal-activity-related fluctuations in fMRI. *Neuroimage* 31, 1536–1548. doi: 10.1016/j.neuroimage.2006.02.048

Birn, R. M., Smith, M. A., Jones, T. B., and Bandettini, P. A. (2008). The respiration response function: the temporal dynamics of fMRI signal fluctuations related to changes in respiration. *Neuroimage* 40, 644–654. doi: 10.1016/j.neuroimage.2007.11.059

Biswal, B., Yetkin, F. Z., Haughton, V. M., and Hyde, J. S. (1995). Functional connectivity in the motor cortex of resting human brain using echo-planar MRI. *Magn. Reson. Med.* 34, 537–541. doi: 10.1002/mrm.1910340409

Boyacioglu, R., and Barth, M. (2013). Generalized iNverse imaging (GIN): ultrafast fMRI with physiological noise correction. *Magn. Reson. Med.* 70, 962–971. doi: 10.1002/mrm.24528

Bright, M. G., and Murphy, K. (2015). Is fMRI "noise" really noise? resting state nuisance regressors remove variance with network structure. *Neuroimage* 114, 158–169. doi: 10.1016/j.neuroimage.2015.03.070

Bullmore, E., Long, C., Suckling, J., Fadili, J., Calvert, G., Zelaya, F., et al. (2001). Colored noise and computational inference in neurophysiological (fMRI) time series analysis: resampling methods in time and wavelet domains. *Hum. Brain Mapp.* 12, 61–78. doi: 10.1002/1097-0193(200102)12:2<61::AID-HBM1004>3.0.CO;2-W

Calhoun, V. D., Adali, T., Pearlson, G. D., and Pekar, J. J. (2001). A method for making group inferences from functional MRI data using independent component analysis. *Hum. Brain Mapp.* 14, 140–151. doi: 10.1002/hbm.1048

Chang, C., and Glover, G. H. (2009). Relationship between respiration, end-tidal CO2, and BOLD signals in resting-state fMRI. *Neuroimage* 47, 1381–1393. doi: 10.1016/j.neuroimage.2009.04.048

Chang, C., and Glover, G. H. (2010). Time–frequency dynamics of resting-state brain connectivity measured with fMRI. *Neuroimage* 50, 81–98. doi: 10.1016/j.neuroimage.2009.12.011

Chang, C., Metzger, C. D., Glover, G. H., Duyn, J. H., Heinze, H. J., and Walter, M. (2013a). Association between heart rate variability and

fluctuations in resting-state functional connectivity. *Neuroimage* 68, 93–104. doi: 10.1016/j.neuroimage.2012.11.038

Chang, W. T., Nummenmaa, A., Witzel, T., Ahveninen, J., Huang, S., Tsai, K. W., et al. (2013b). Whole-head rapid fMRI acquisition using echo-shifted magnetic resonance inverse imaging. *Neuroimage* 78, 325–338. doi: 10.1016/j.neuroimage.2013.03.040

Chao-Gan, Y., and Yu-Feng, Z. (2010). DPARSF: a MATLAB toolbox for" pipeline" data analysis of resting-state fMRI. *Front. Syst. Neurosci.* 4:13. doi: 10.3389/fnsys.2010.00013

Chen, J. E., Polimeni, J. R., Bollmann, S., and Glover, G. H. (2019). *On the analysis of rapidly sampled fMRI data*. *Neuroimage*. 188, 807–820. doi: 10.1016/j.neuroimage.2019.02.008

Cordes, D., Nandy, R. R., Schafer, S., and Wager, T. D. (2014). Characterization and reduction of cardiac-and respiratory-induced noise as a function of the sampling rate (TR) in fMRI. *Neuroimage* 89, 314–330. doi: 10.1016/j.neuroimage.2013.12.013

De Luca, M., Beckmann, C. F., De Stefano, N., Matthews, P. M., and Smith, S. M. (2006). fMRI resting state networks define distinct modes of long-distance interactions in the human brain. *Neuroimage* 29, 1359–1367. doi: 10.1016/j.neuroimage.2005.08.035

Demetriou, L., Kowalczyk, O. S., Tyson, G., Bello, T., Newbould, R. D., and Wall, M. B. (2018). A comprehensive evaluation of increasing temporal resolution with multiband-accelerated protocols and effects on statistical outcome measures in fMRI. *Neuroimage* 176, 404–416. doi: 10.1016/j.neuroimage.2018.05.011

Glover, G. H. (2012). Spiral imaging in fMRI. *Neuroimage* 62, 706–712. doi: 10.1016/j.neuroimage.2011.10.039

Golestani, A. M., Kwinta, J. B., Khatamian, Y. B., and Chen, J. J. (2017). The effect of low-frequency physiological correction on the reproducibility and specificity of resting-state fMRI metrics: functional connectivity, ALFF, and ReHo. *Front. Neurosci.* 11:546. doi: 10.3389/fnins.2017.00546

Gonzalez-Castillo, J., Roopchansingh, V., Bandettini, P. A., and Bodurka, J. (2011). Physiological noise effects on the flip angle selection in BOLD fMRI. *Neuroimage* 54, 2764–2778. doi: 10.1016/j.neuroimage.2010.11.020

Griffanti, L., Dipasquale, O., Laganà, M. M., Nemni, R., Clerici, M., Smith, S. M., et al. (2015). Effective artifact removal in resting state fMRI data improves detection of DMN functional connectivity alteration in Alzheimer's disease. *Front. Hum. Neurosci.* 9:449. doi: 10.3389/fnhum.2015.00449

Hugger, T., Zahneisen, B., LeVan, P., Lee, K. J., Lee, H. L., Zaitsev, M., et al. (2011). Fast undersampled functional magnetic resonance imaging using nonlinear regularized parallel image reconstruction. *PLoS ONE* 6:e28822. doi: 10.1371/journal.pone.0028822

Hutchinson, J. B., Uncapher, M. R., Weiner, K. S., Bressler, D. W., Silver, M. A., Preston, A. R., et al. (2012). Functional heterogeneity in posterior parietal cortex across attention and episodic memory retrieval. *Cereb. Cortex* 24, 49–66. doi: 10.1093/cercor/bhs278

Iliff, J. J., Wang, M., Liao, Y., Plogg, B. A., Peng, W., Gundersen, G. A., et al. (2012). A paravascular pathway facilitates CSF flow through the brain parenchyma and the clearance of interstitial solutes, including amyloid β. *Sci. Transl. Med.* 4:147ra111. doi: 10.1126/scitranslmed.3003748

Jenkinson, M., Bannister, P., Brady, M., and Smith, S. (2002). Improved optimization for the robust and accurate linear registration and motion correction of brain images. *Neuroimage* 17, 825–841. doi: 10.1006/nimg.2002.1132

Jenkinson, M., Beckmann, C. F., Behrens, T. E., Woolrich, M. W., and Smith, S. M. (2012). Fsl. *Neuroimage* 62, 782–790. doi: 10.1016/j.neuroimage.2011.09.015

Jenkinson, M., and Smith, S. (2001). A global optimisation method for robust affine registration of brain images. *Med. Image Anal.* 5, 143–156. doi: 10.1016/S1361-8415(01)00036-6

Jessen, N. A., Munk, A. S., Lundgaard, I., and Nedergaard, M. (2015). The glymphatic system: a beginner's guide. *Neurochem. Res.* 40, 2583–2599. doi: 10.1007/s11064-015-1581-6

Kananen, J., Tuovinen, T., Ansakorpi, H., Rytky, S., Helakari, H., Huotari, N., et al. (2018). Altered physiological brain variation in drug-resistant epilepsy. *Brain Behav.* 8:e01090. doi: 10.1002/brb3.1090

Keilholz, S. D. (2014). The neural basis of time-varying resting-state functional connectivity. *Brain Connect.* 4, 769–779. doi: 10.1089/brain.2014.0250

Kendall, M., and Gibbons, J. (1990). *Correlation Methods*. Oxford: Oxford University Press.

Kiviniemi, V. (2008). Endogenous brain fluctuations and diagnostic imaging. *Hum. Brain Mapp.* 29, 810–817. doi: 10.1002/hbm.20582

Kiviniemi, V., Jauhiainen, J., Tervonen, O., Pääkkö, E., Oikarinen, J., Vainionpää, V., et al. (2000). Slow vasomotor fluctuation in fMRI of anesthetized child brain. *Magn. Reson. Med.* 44, 373–378. doi: 10.1002/1522-2594(200009)44:3<373::AID-MRM5>3.0.CO;2-P

Kiviniemi, V., Kantola, J. H., Jauhiainen, J., Hyvärinen, A., and Tervonen, O. (2003). Independent component analysis of nondeterministic fMRI signal sources. *Neuroimage* 19, 253–260. doi: 10.1016/S1053-8119(03)00097-1

Kiviniemi, V., Ruohonen, J., and Tervonen, O. (2005). Separation of physiological very low frequency fluctuation from aliasing by switched sampling interval fMRI scans. *Magn. Reson. Imaging* 23, 41–46. doi: 10.1016/j.mri.2004.09.005

Kiviniemi, V., Starck, T., Remes, J., Long, X., Nikkinen, J., Haapea, M., et al. (2009). Functional segmentation of the brain cortex using high model order group PICA. *Hum. Brain Mapp.* 30, 3865–3886. doi: 10.1002/hbm.20813

Kiviniemi, V., Vire, T., Remes, J., Elseoud, A. A., Starck, T., Tervonen, O., et al. (2011). A sliding time-window ICA reveals spatial variability of the default mode network in time. *Brain Connect.* 1, 339–347. doi: 10.1089/brain.2011.0036

Kiviniemi, V., Wang, X., Korhonen, V., Keinänen, T., Tuovinen, T., Autio, J., et al. (2016). Ultra-fast magnetic resonance encephalography of physiological brain activity–Glymphatic pulsation mechanisms? *J. Cereb. Blood Flow Metab.* 36, 1033–1045. doi: 10.1177/0271678X15622047

Korhonen, V., Hiltunen, T., Myllylä, T., Wang, X., Kantola, J., Nikkinen, J., et al. (2014). Synchronous multiscale neuroimaging environment for critically sampled physiological analysis of brain function: hepta-scan concept. *Brain Connect.* 4, 677–689. doi: 10.1089/brain.2014.0258

Lee, H. L., Zahneisen, B., Hugger, T., LeVan, P., and Hennig, J. (2013). Tracking dynamic resting-state networks at higher frequencies using MR-encephalography. *Neuroimage* 65, 216–222. doi: 10.1016/j.neuroimage.2012.10.015

Lin, F. H., Polimeni, J. R., Lin, J. L., Tsai, K. W., Chu, Y. H., Wu, P. Y., et al. (2018). Relative latency and temporal variability of hemodynamic responses at the human primary visual cortex. *Neuroimage* 164, 194–201. doi: 10.1016/j.neuroimage.2017.01.041

Lin, F. H., Tsai, K. W., Chu, Y. H., Witzel, T., Nummenmaa, A., Raij, T., et al. (2012). Ultrafast inverse imaging techniques for fMRI. *Neuroimage* 62, 699–705. doi: 10.1016/j.neuroimage.2012.01.072

Liu, T. T. (2016). Noise contributions to the fMRI signal: an overview. *Neuroimage* 143, 141–151. doi: 10.1016/j.neuroimage.2016.09.008

Liu, X., De Zwart, J. A., Schölvinck, M. L., Chang, C., Ye, F. Q., Leopold, D. A., et al. (2018). Subcortical evidence for a contribution of arousal to fMRI studies of brain activity. *Nat. Commun.* 9:395. doi: 10.1038/s41467-017-02815-3

Liu, X., and Duyn, J. H. (2013). Time-varying functional network information extracted from brief instances of spontaneous brain activity. *Proc. Natl. Acad. Sci. U.S.A.* 110, 4392–4397. doi: 10.1073/pnas.1216856110

Ma, Y., Shaik, M. A., Kozberg, M. G., Kim, S. H., Portes, J. P., Timerman, D., et al. (2016). Resting-state hemodynamics are spatiotemporally coupled to synchronized and symmetric neural activity in excitatory neurons. *Proc. Natl. Acad. Sci. U.S.A.* 113, E8463–E8471. doi: 10.1073/pnas.1525369113

Majeed, W., Magnuson, M., Hasenkamp, W., Schwarb, H., Schumacher, E. H., Barsalou, L., et al. (2011). Spatiotemporal dynamics of low frequency BOLD fluctuations in rats and humans. *Neuroimage* 54, 1140–1150. doi: 10.1016/j.neuroimage.2010.08.030

Makedonov, I., Black, S. E., and MacIntosh, B. J. (2013). BOLD fMRI in the white matter as a marker of aging and small vessel disease. *PLoS ONE* 8:e67652. doi: 10.1371/journal.pone.0067652

Makedonov, I., Chen, J. J., Masellis, M., MacIntosh, B. J., and Initiative, A. D. N. (2016). Physiological fluctuations in white matter are increased in Alzheimer's disease and correlate with neuroimaging and cognitive biomarkers. *Neurobiol. Aging* 37, 12–18. doi: 10.1016/j.neurobiolaging.2015.09.010

Murphy, K., and Fox, M. D. (2017). Towards a consensus regarding global signal regression for resting state functional connectivity MRI. *Neuroimage* 154, 169–173. doi: 10.1016/j.neuroimage.2016.11.052

Nedergaard, M. (2013). Garbage truck of the brain. *Science* 340, 1529–1530. doi: 10.1126/science.1240514

Palva, J. M., Zhigalov, A., Hirvonen, J., Korhonen, O., Linkenkaer-Hansen, K., and Palva, S. (2013). Neuronal long-range temporal correlations and avalanche dynamics are correlated with behavioral scaling laws. *Proc. Natl. Acad. Sci. U.S.A.* 110, 3585–3590. doi: 10.1073/pnas.1216855110

Pan, W. J., Thompson, G. J., Magnuson, M. E., Jaeger, D., and Keilholz, S. (2013). Infraslow LFP correlates to resting-state fMRI BOLD signals. *Neuroimage* 74, 288–297. doi: 10.1016/j.neuroimage.2013.02.035

Peltier, S. J., Polk, T. A., and Noll, D. C. (2003). Detecting low-frequency functional connectivity in fMRI using a self-organizing map (SOM) algorithm. *Hum. Brain Mapp.* 20, 220–226. doi: 10.1002/hbm.10144

Pfeuffer, J., Van de Moortele, P. F., Ugurbil, K., Hu, X., and Glover, G. H. (2002). Correction of physiologically induced global off-resonance effects in dynamic echo-planar and spiral functional imaging. *Magn. Reson. Med.* 47, 344–353. doi: 10.1002/mrm.10065

Posse, S., Ackley, E., Mutihac, R., Zhang, T., Hummatov, R., Akhtari, M., et al. (2013). High-speed real-time resting-state FMRI using multi-slab echo-volumar imaging. *Front. Hum. Neurosci.* 7:479. doi: 10.3389/fnhum.2013.00479

Preibisch, C., Castrillón G J, G., Bührer, M., and Riedl, V. (2015). Evaluation of multiband EPI acquisitions for resting state fMRI. *PLoS ONE* 10:e0136961. doi: 10.1371/journal.pone.0136961

Purdon, P. L., and Weisskoff, R. M. (1998). Effect of temporal autocorrelation due to physiological noise and stimulus paradigm on voxel-level false-positive rates in fMRI. *Hum. Brain Mapp.* 6, 239–249. doi: 10.1002/(SICI)1097-0193(1998)6:4<239::AID-HBM4>3.0.CO;2-4

Raitamaa, L., Korhonen, V., Huotari, N., Raatikainen, V., Hautaniemi, T., Kananen, J., et al. (2018). Breath hold effect on cardiovascular brain pulsations–A multimodal magnetic resonance encephalography study. *J. Cereb. Blood Flow Metab.* 11:271678X18798441. doi: 10.1177/0271678X18798441

Rajna, Z., Kananen, J., Keskinarkaus, A., Seppänen, T., and Kiviniemi, V. (2015). Detection of short-term activity avalanches in human brain default mode network with ultrafast MR encephalography. *Front. Hum. Neurosci.* 9:448. doi: 10.3389/fnhum.2015.00448

Shmueli, K., van Gelderen, P., de Zwart, J. A., Horovitz, S. G., Fukunaga, M., Jansma, J. M., et al. (2007). Low-frequency fluctuations in the cardiac rate as a source of variance in the resting-state fMRI BOLD signal. *Neuroimage* 38, 306–320. doi: 10.1016/j.neuroimage.2007.07.037

Smith, S. M., Beckmann, C. F., Andersson, J., Auerbach, E. J., Bijsterbosch, J., Douaud, G., et al. (2013). Resting-state fMRI in the human connectome project. *Neuroimage* 80, 144–168. doi: 10.1016/j.neuroimage.2013.05.039

Smith, S. M., Fox, P. T., Miller, K. L., Glahn, D. C., Fox, P. M., Mackay, C. E., et al. (2009). Correspondence of the brain's functional architecture during activation and rest. *Proc. Natl. Acad. Sci. U.S.A.* 106, 13040–13045. doi: 10.1073/pnas.0905267106

Smith, S. M., Jenkinson, M., Woolrich, M. W., Beckmann, C. F., Behrens, T. E., Johansen-Berg, H., et al. (2004). Advances in functional and structural MR image analysis and implementation as FSL. *Neuroimage* 23, S208–S219. doi: 10.1016/j.neuroimage.2004.07.051

Smith, S. M., Miller, K. L., Moeller, S., Xu, J., Auerbach, E. J., Woolrich, M. W., et al. (2012). Temporally-independent functional modes of spontaneous brain activity. *Proc. Natl. Acad. Sci. U.S.A.* 109, 3131–3136. doi: 10.1073/pnas.1121329109

Thayer, J. F., Yamamoto, S. S., and Brosschot, J. F. (2010). The relationship of autonomic imbalance, heart rate variability and cardiovascular disease risk factors. *Int. J. Cardiol.* 141, 122–131. doi: 10.1016/j.ijcard.2009.09.543

Thompson, G. J., Pan, W. J., Magnuson, M. E., Jaeger, D., and Keilholz, S. D. (2014). Quasi-periodic patterns (QPP): large-scale dynamics in resting state fMRI that correlate with local infraslow electrical activity. *Neuroimage* 84, 1018–1031. doi: 10.1016/j.neuroimage.2013.09.029

Tuovinen, T., Kananen, J., Rytty, R., Moilanen, V., Elseoud, A. A., Remes, A. M., et al. (2018). Altered BOLD signal variation in Alzheimer's disease and frontotemporal dementia. *BioRxiv [preprint]* 455683, 1–47. doi: 10.1101/455683

Tuovinen, T., Rytty, R., Moilanen, V., Abou Elseoud, A., Veijola, J., Remes, A. M., et al. (2017). The effect of gray matter ICA and coefficient of variation mapping of BOLD data on the detection of functional connectivity changes in Alzheimer's disease and bvFTD. *Front. Hum. Neurosci.* 10:680. doi: 10.3389/fnhum.2016.00680

van der Kooy, K. G., van Hout, H. P., van Marwijk, H. W., de Haan, M., Stehouwer, C. D., and Beekman, A. T. (2006). Differences in heart rate variability between depressed and non-depressed elderly. *Int. J. Geriatr. Psychiatry* 21, 147–150. doi: 10.1002/gps.1439

Vidaurre, D., Smith, S. M., and Woolrich, M. W. (2017). Brain network dynamics are hierarchically organized in time. *Proc. Natl. Acad. Sci. U.S.A.* 114, 12827–12832. doi: 10.1073/pnas.1705120114

Wink, A. M., Bullmore, E., Barnes, A., Bernard, F., and Suckling, J. (2008). Monofractal and multifractal dynamics of low frequency endogenous brain oscillations in functional MRI. *Hum. Brain Mapp.* 29, 791–801. doi: 10.1002/hbm.20593

Wise, R. G., Ide, K., Poulin, M. J., and Tracey, I. (2004). Resting fluctuations in arterial carbon dioxide induce significant low frequency variations in BOLD signal. *Neuroimage* 21, 1652–1664. doi: 10.1016/j.neuroimage.2003.11.025

Woolrich, M. W., Ripley, B. D., Brady, M., and Smith, S. M. (2001). Temporal autocorrelation in univariate linear modeling of FMRI data. *Neuroimage* 14, 1370–1386. doi: 10.1006/nimg.2001.0931

Zahneisen, B., Assländer, J., LeVan, P., Hugger, T., Reisert, M., Ernst, T., et al. (2014). Quantification and correction of respiration induced dynamic field map changes in fMRI using 3D single shot techniques. *Magn. Reson. Med.* 71, 1093–1102. doi: 10.1002/mrm.24771

Zahneisen, B., Hugger, T., Lee, K. J., LeVan, P., Reisert, M., Lee, H. L., et al. (2012). Single shot concentric shells trajectories for ultra fast fMRI. *Magn. Reson. Med.* 68, 484–494. doi: 10.1002/mrm.23256

Zang, Y., Jiang, T., Lu, Y., He, Y., and Tian, L. (2004). Regional homogeneity approach to fMRI data analysis. *Neuroimage* 22, 394–400. doi: 10.1016/j.neuroimage.2003.12.030

Zang, Y. F., He, Y., Zhu, C. Z., Cao, Q. J., Sui, M. Q., Liang, M., et al. (2007). Altered baseline brain activity in children with ADHD revealed by resting-state functional MRI. *Brain Dev.* 29, 83–91. doi: 10.1016/j.braindev.2006.07.002

Zou, Q. H., Zhu, C. Z., Yang, Y., Zuo, X. N., Long, X. Y., Cao, Q. J., et al. (2008). An improved approach to detection of amplitude of low-frequency fluctuation (ALFF) for resting-state fMRI: fractional ALFF. *J. Neurosci. Methods* 172, 137–141. doi: 10.1016/j.jneumeth.2008.04.012

Conflict of Interest Statement: The authors declare that the research was conducted in the absence of any commercial or financial relationships that could be construed as a potential conflict of interest.

frontiers in Neuroscience

ORIGINAL RESEARCH
published: 11 April 2019
doi: 10.3389/fnins.2019.00296

Isoflurane-Induced Burst Suppression Increases Intrinsic Functional Connectivity of the Monkey Brain

Zhao Zhang[1†], Dan-Chao Cai[2†], Zhiwei Wang[2], Kristina Zeljic[2,3], Zheng Wang[2,3,4] and Yingwei Wang[1*]*

[1] Department of Anesthesiology, Huashan Hospital, Fudan University, Shanghai, China, [2] Institute of Neuroscience, State Key Laboratory of Neuroscience, Key Laboratory of Primate Neurobiology, CAS Center for Excellence in Brain Science and Intelligence Technology, Shanghai Institutes for Biological Sciences, Chinese Academy of Sciences, Shanghai, China, [3] University of Chinese Academy of Sciences, Beijing, China, [4] Kunming Institute of Zoology, Chinese Academy of Sciences, Kunming, China

OPEN ACCESS

Edited by:
Peter Herman,
Yale University, United States

Reviewed by:
Kai-Hsiang Chuang,
The University of Queensland, Australia
Elzbieta Olejarczyk,
Institute of Biocybernetics and Biomedical Engineering (PAN), Poland

***Correspondence:**
Zheng Wang
zheng.wang@ion.ac.cn
Yingwei Wang
wangyw@perioperative-science.com

[†] These authors have contributed equally to this work

Specialty section:
This article was submitted to Brain Imaging Methods, a section of the journal Frontiers in Neuroscience

Received: 02 November 2018
Accepted: 13 March 2019
Published: 11 April 2019

Citation:
Zhang Z, Cai D-C, Wang Z, Zeljic K, Wang Z and Wang Y (2019) Isoflurane-Induced Burst Suppression Increases Intrinsic Functional Connectivity of the Monkey Brain. Front. Neurosci. 13:296. doi: 10.3389/fnins.2019.00296

Animal functional magnetic resonance imaging (fMRI) has provided key insights into the physiological mechanisms underlying healthy and diseased brain states. In non-human primates, resting-state fMRI studies are commonly conducted under isoflurane anesthesia, where anesthetic concentration is used to roughly infer anesthesia depth. However, within the recommended isoflurane concentration range (1.00–1.50%), the brain state can switch from moderate anesthesia characterized by stable slow wave (SW) electroencephalogram (EEG) signals to deep anesthesia characterized by burst suppression (BS), which is electrophysiologically distinct from the resting state. To confirm the occurrence rate of BS activity in common setting of animal fMRI study, we conducted simultaneous resting-state EEG and fMRI experiments on 16 monkeys anesthetized using 0.80–1.30% isoflurane, and detected BS activity in two of them. Datasets either featured with BS or SW activity from these two monkeys were analyzed to investigate the intrinsic functional connectivity (FC) patterns during BS. In datasets with BS activity, we observed robust coupling between the BS pattern (the binary alternation between burst and suppression activity in EEG signal) and filtered BOLD signals in most brain areas, which was associated with a non-specific enhancement in whole brain connectivity. After eliminating the BS coupling effect by regressing out the BS pattern, we detected an overall increase in FC with a few decreased connectivity compared to datasets with SW activity. These affected connections were preferentially distributed within orbitofrontal cortex, between orbitofrontal and prefrontal/cingulate/occipital cortex, and between temporal and parietal cortex. Persistence of the default mode network and recovery of thalamocortical connections were also detected under deep anesthesia with BS activity. Taken together,

the observed spatially specific alterations in BS activity induced by isoflurane not only highlight the necessity of EEG monitoring and careful data preprocessing in fMRI studies on anesthetized animals, but also advance our understanding of the underlying multi-phased mechanisms of anesthesia.

Keywords: burst suppression, simultaneous EEG-MRI, functional connectivity, default mode network, thalamocortical connectivity, nonhuman primate

INTRODUCTION

Functional magnetic resonance imaging (fMRI) has become a commonly used noninvasive technique for brain activity research in both animals and humans. Resting-state fMRI (rs-fMRI) measures functional connectivity (FC) between different brain regions in the non-stimulus state and is a valuable technique for exploring complex brain networks in different brain states or disease models (Greicius, 2008; Van Den Heuvel and Hulshoff Pol, 2010). Anesthesia is an effective method to prevent head motion and physiological stress when collecting blood oxygenation level dependent (BOLD) fMRI signals, particularly in animal studies. On the other hand, it is also a critical confounding factor because anesthetic selection and dosage can affect or even inverse the intrinsic BOLD fluctuations readout (Hutchison and Everling, 2012; Grandjean et al., 2014; Lv et al., 2016; Paasonen et al., 2017, 2018; Wu et al., 2017; Bukhari et al., 2018). For instance, isoflurane, the most prevalent inhaled anesthetic for monkey fMRI study, has a significant, concentration-dependent influence on FC networks (Vincent et al., 2007; Nallasamy and Tsao, 2011; Grandjean et al., 2014; Hutchison et al., 2014; Bukhari et al., 2018). A limited range of isoflurane concentration (1.00–1.50%) is therefore recommended to obtain stable FC in anesthetized nonhuman primate resting-state experiments (Hutchison et al., 2014).

However, monkey fMRI studies with simultaneously recorded electroencephalogram (EEG) signals have revealed that relatively deep anesthesia characterized by burst suppression (BS) occasionally occurs at the recommended dosage of isoflurane (end-tidal concentration 1.25–1.50%) (Vincent et al., 2007). BS is a stereotypic electrical activity pattern in the brain that presents as continuous alternation between two states, high-voltage waves (burst) and isoelectric epoch (suppression), and is fundamentally different from the slow wave (SW) activity most commonly observed in the resting state (Steriade et al., 1994). Electrophysiological studies have demonstrated wide synchronization and hyper-excitation across the whole brain during BS activity (Steriade et al., 1994). A robust coupling effect between BS pattern (the binary alternation between burst and suppression activity in EEG signal) and BOLD fluctuations has been revealed in sevoflurane-anesthetized humans (Golkowski et al., 2017). Enhanced BOLD connectivity in the somatosensory network has also been reported in rats during isoflurane-induced BS activity (Liu et al., 2011). Further investigation of the same network showed that connectivity became less spatially specific as anesthesia depth increased to BS status, evidencing functional reorganization of the brain (Liu et al., 2013). These findings indicate multiphasic progression from light to deep anesthesia, suggesting a non-linear relationship between brain activity strength and anesthesia depth (Amzica, 2015).

Here, we aim to explore the signature of the whole-brain functional network connectivity during the isoflurane-induced BS activity in adult macaque monkeys. We are also concerned with the influence of preprocessing strategy on the spatially non-specific increase in FC reported by Liu et al. (2013). We are particularly interested in alterations of the default mode network (DMN) and thalamocortical connections, both of which are sensitive to anesthesia (Alkire et al., 1999; Fiset et al., 1999; Vogt and Laureys, 2005). Despite observed decreases in both DMN (Greicius et al., 2008; Huang et al., 2014) and thalamocortical connectivity (White and Alkire, 2003; Huang et al., 2014) under anesthesia compared to the awake state in humans, it is unknown whether or not these two networks are present during the EEG-defined BS activity in nonhuman primates.

MATERIALS AND METHODS

Participants

All experimental procedures for nonhuman primate research in this study were approved by the Institutional Animal Care and Use Committee at the Institute of Neuroscience and the Biomedical Research Ethics Committee, Shanghai Institutes for Biological Sciences, Chinese Academy of Sciences, and conformed to National Institutes of Health guidelines for the humane care and use of laboratory animals.

The data included in this work were selected from a series of simultaneous resting-state EEG and fMRI experiments of 16 monkeys (*Macaca fascicularis*, six males, 10 females, and ages 4–5) anesthetized using a recommended concentration range of isoflurane. After careful scrutiny of the EEG traces, BS activity was detected in two monkeys (monkey O and monkey T) at 0.8–1.3% isoflurane during four separated experiments, out of which three experiments were performed on monkey O with a minimum separation of one and half month. The occurrence of BS was more frequent in monkey O than monkey T (**Table 1**). Further analysis on FC was based on all the data from monkey O and monkey T, including 20 runs with stable BS activity (BS group) and 8 runs with stable slow wave activity (SW group) from monkey O, 7 and

3 runs, respectively, from monkey T. Each run lasted 7 min with an inter-run interval of approximately 1 min within each experiment.

Animal Preparation

The animal preparation procedure was conducted in a similar manner to our previous work (Wang et al., 2013; Lv et al., 2016).

TABLE 1 | Physiological information of all datasets from monkey O and monkey T.

Monkey ID	Session	Run	Group	Concentration of ISO (%)	BSR(%)	Heart Rate (bpm)	$EtCO_2$ (mmHg)	Temperature (°C)
O	1	1	BS	1.2	10.9	141	28	36.6
O	1	2	BS	1.2	7.7	140	28	36.6
O	1	3	BS	1.2	12.8	136	29	36.8
O	1	4	BS	1.2	11.9	135	29	36.8
O	1	5	BS	1.2	2.6	135	29	36.9
O	1	6	BS	1.2	3.8	142	29	37
O	1	8	BS	1.2	1.2	135	28	37.1
O	1	9	BS	1.2	1.6	131	28	37.2
O	2	10	BS	1.3	38.9	131	26	37.1
O	2	11	BS	1.3	23.3	134	27	37
O	2	12	BS	1.3	32.1	136	27	37
O	2	13	BS	1.3	18	139	27	37
O	2	14	BS	1.3	27.9	140	27	37
O	2	15	BS	1.3	36.7	140	27	37
O	2	16	BS	1.3	26.3	142	28	37.1
O	2	17	BS	1.3	18.4	139	28	37
O	2	18	BS	1.1	14.1	140	28	37
O	2	19	BS	1.1	11.1	142	28	37
O	2	20	BS	1.1	16.5	140	28	37
O	3	27	BS	0.8	1.5	147	27	37.7
BS					15.87	138.25	27.8	36.995
O	3	7	SW	1.2	0	157	29	37
O	3	21	SW	0.8	0	147	26	37.3
O	3	22	SW	0.8	0	148	27	37.4
O	3	23	SW	0.8	0	149	27	37.5
O	3	24	SW	0.8	0	148	27	37.5
O	3	25	SW	0.8	0	149	27	37.7
O	3	26	SW	0.8	0	146	27	37.7
O	3	28	SW	0.8	0	147	27	37.8
SW						148.875	27.125	37.4875
P-value						<0.000	0.064	< 0.000
T	4	31	BS	1.2	1.72	148	27	37.0
T	4	32	BS	1.2	0.56	156	27	37.1
T	4	33	BS	1.2	2.92	157	27	37.0
T	4	34	BS	1.2	1.68	160	27	36.8
T	4	35	BS	1.2	3.10	160	27	36.4
T	4	36	BS	1.2	0.86	159	26	36.3
T	4	38	BS	1.2	1.90	159	27	36.6
BS					1.82	157	26.857	36.743
T	4	29	SW	1.2	0	146	26	36.6
T	4	30	SW	1.2	0	148	26	36.8
T	4	37	SW	1.2	0	159	27	36.3
SW						151	26.333	36.567
P-value						0.125	0.120	0.421

Induction of anesthesia was achieved by intramuscular injection with ketamine (10 mg/kg, Gutian Pharma Co., Ltd., China) before data collection. After intubation, each monkey was ventilated with a mixture of isoflurane (2–2.5%, Lunan Pharma Co., Ltd., China) and pure oxygen via either a standard ventilator (CWE, Inc., Ardmore, PA, United States) in the preparation room or an MRI-compatible ventilator (CWE Inc., Weston, WI, United States) inside the scanner room. The monkey was maintained with intermittent positive-pressure ventilation to ensure a constant respiration rate (25–35 breaths/min). Vital signs including blood oxygenation, electrocardiogram (ECG), rectal temperature (Small Animal Instruments, Inc., Stony Brook, New York), respiration rate and end-tidal CO_2 (Smiths Medical ASD Inc., Dublin, Ohio) were continuously monitored. Oxygen saturation was kept at over 95% and body temperature was kept constant using a heated water blanket (Gaymar Industries Inc., Orchard Park, New York). Lactated Ringer's solution was given with a maximum rate of 10 ml/kg/hour during the anesthesia process (Logothetis et al., 1999).

To ensure adequate EEG data quality, we prepared the animal scalp by shaving and thorough cleaning with abrasive gel and alcohol swabs. A custom EEG cap made of stretchable material was fitted over the scalp and then fastened by a chinstrap. An ECG electrode was attached close to the heart to facilitate off-line removal of cardio-ballistic artifacts. To increase the signal-to-noise ratio, we injected conductive gel and ensured a low impedance (<5 kilo-ohms) at each electrode. The electrode filling holes were subsequently covered with medical tape to prevent the gel from drying out during recording. After setting up the EEG cap, the monkey was restrained within a water blanket in a sphinx-like position with the head protruding and facing forward. The animal's head was secured using a custom-built MRI-compatible stereotaxic frame after local anesthetic (5% lidocaine cream) was applied around the ears to block peripheral nerve stimulation.

The isoflurane concentration was initially set to 1.2–1.3% within the recommended range in rs-fMRI research on isoflurane-anesthetized monkeys (Vincent et al., 2007; Hutchison et al., 2014), and adjusted by 0.05% increase or decrease to keep the continuously monitored physiological parameters within normal ranges (oxygen saturation: >95%; heart rate: 85–160 beats/min; temperature: 36–38°C; respiration rate: 22–35 breaths/min; end-tidal CO_2: 24–30 mmHg) throughout the experiment. Datasets were collected at least 15 min after the adjustment of isoflurane level. Details of isoflurane concentration, BS ratio and physiological parameters for all included datasets were listed in **Table 1**.

Simultaneous EEG-MRI Data Acquisition

MRI images were acquired at the Institute of Neuroscience on a 3T whole-body scanner (Trio; Siemens Healthcare, Erlangen, Germany) running with an enhanced gradient coil insert (AC88; 80 mT/m maximum gradient strength, 800 mT/m/s maximum slew rate) and a custom-built bird-cage volume coil with 8-channel array receiver. Whole-brain resting-state fMRI data were collected using a gradient echo planar sequence (TR = 2000 ms; TE = 29 ms; flip angle = 77°; slices = 32; matrix = 64 × 64; field of view = 96 mm × 96 mm; 1.5 mm × 1.5 mm in plane resolution; slice thickness = 2.5 mm; GRAPPA factor = 2). For each session, 5–10 runs were acquired and each run consisted of 200 functional volumes. A pair of gradient echo images (echo time: 4.22 and 6.68 ms) with the same orientation and resolution as EPI images were acquired to generate a field map for distortion correction of EPI images. High-resolution T1-weighted anatomical images were acquired using a MPRAGE sequence (TR = 2500 ms; TE = 3.12 ms; inversion time = 1100 ms; flip angle = 9°; acquisition voxel size = 0.5 mm × 0.5 mm × 0.5 mm; 144 sagittal slices). Six whole-brain anatomical volumes were acquired and further averaged for better brain segmentation and 3D cortical reconstruction.

Simultaneous EEG scalp recordings were acquired with BrainVision Recorder software using a BrainAmp MR amplifier and a 28-channel EEG cap customized for macaques (Brain Products GmbH, Gilching, Germany) with sintered Ag/AgCl ring electrodes. EEG signals from 21 active channels were sampled at 5000 Hz with a resolution of 0.5 μV per bit and measuring range of ±16 mV. The sampling clocks of the MR and EEG systems were synchronized using the SyncBox (Brain Products GmbH, Gilching, Germany), thus providing the time of fMRI volume acquisition for later gradient artifact removal in EEG signals.

Data Analysis

MRI Data Preprocessing

Preprocessing of functional MRI images was conducted using the SPM8 toolbox[1] and the FMRIB Software Library toolbox (FSL[2]). The first 10 volumes were discarded before preprocessing. The field map images of each session were applied to compensate for the geometric distortion of EPI images caused by magnetic field inhomogeneity using FSL FUGUE. After slice timing correction and motion correction, the corrected images were normalized to standard space of the monkey F99 atlas[3] using an optimum 12-parameter affine transformation and nonlinear deformations, and then resampled to 1.5 mm cubic voxels and spatially smoothed with a 3 mm full-width at half-maximum (FWHM) isotropic Gaussian kernel. Linear drift of the volumes was removed, followed by regression of nuisance covariates (six head motion parameters, white matter and ventricle signals) and temporal filtering (0.01–0.1 Hz). To eliminate the BS coupling effect, we conducted another regression using BS pattern as an additional regressor.

EEG-MRI Coupling Analysis

We first assessed the coupling effect of BS pattern on filtered BOLD fluctuations. For each dataset with BS activity in EEG signal, the suppression episodes were automatically defined by thresholding the normalized amplitude summed across all available EEG channels. All labels of suppression onset or offset were visually inspected by an experienced anesthesiologist. The BS pattern was defined as a binary signal with zero indicating suppression epochs and one indicating non-suppression epochs.

[1] http://www.fil.ion.ucl.ac.uk/spm

[2] http://www.fmrib.ox.ac.uk

[3] http://sumsdb.wustl.edu/sums/macaquemore.do

The time course of the binary BS pattern was then convoluted with the canonical hemodynamic response function (HRF) implemented in SPM8 as a regressor of interest. The significance of BS coupling effect on each voxel was evaluated via one-sample *t*-test. To account for the effect of repeated measure from the same subject, binary variables indicating whether the datasets were collected from a specific animal were included as covariates in the SPM model. Family-wise error (FWE) correction was applied to account for multiple comparisons with voxel-wise $P < 0.001$.

Whole-Brain Functional Connectivity Analysis

For the whole-brain FC analysis, we first parcellated the monkey brain into 82 cortical areas based on the Regional Map template (Kotter and Wanke, 2005; Bezgin et al., 2012) and 12 subcortical areas based on the INIA19 (Rohlfing et al., 2012) (see **Supplementary Table S1** for a complete list of anatomical labels). Pearson's correlation coefficients between the mean time courses of any pair of regions were calculated to represent their FC, resulting in a 94 × 94 connectivity network matrix for each dataset. Statistical significance of group differences were evaluated using linear regression analysis with binary variables of individuals as covariates in the GRETNA toolbox[4]. The edge-wise threshold of the significance level was set at $P = 0.001$, and cluster-level correction of $P < 0.05$ was applied to adjust the multiple comparison using the network-based statistic (Zalesky et al., 2010). Effect sizes measured via *Hedges' g* values were calculated to evaluate the extent of group difference. In addition, we assessed the normalized distribution of disrupted edges within and between lobes. The bias caused by the unbalanced number of brain regions within different lobes was adjusted using the standardized residuals (*Z* scores), defined as the raw residuals (the difference between the observed edge count and expected edge count) divided by the square root of the expected edge count (Sheskin, 2003). The significance of the *Z* scores was estimated via non-parametric permutation (5,000 times). Specifically, the disrupted edges were randomly assigned across the whole brain network and the standardized residuals were re-calculated to generate the null distribution. The percentage of the assignments with a larger or equal *Z* score was defined as the *P* value. Bonferroni correction was applied for the correction of multiple comparisons.

Seed-Based Functional Connectivity Analysis

As the functional connections within the DMN and thalamocortical network are of particular interest during the anesthesia process, we further conducted seed-based functional network analysis. Bilateral posterior cingulate cortex (PCC) and bilateral thalamus defined in Regional Map parcellation were selected as seed regions, respectively. The averaged time course of fMRI signals within the seed region was then treated as a regressor of interest in the generalized regression model in the SPM toolbox. The connectivity strength between each voxel and the seed region was estimated via the beta coefficient in the regression model and statistically tested in each group using a one-sample *t*-test with covariates indicating individual animals. The group difference in voxel-wise connectivity was tested using a one-way repeated measure ANOVA. FWE correction was applied to account for multiple comparisons with voxel-wise $P < 0.001$.

[4]https://www.nitrc.org/projects/gretna

RESULTS

Brain-Wide BOLD Fluctuations Are Coupled With BS Activity

Figure 1 shows robust coupling between the BS pattern in EEG signals (**Figure 1A**) and the spontaneous fluctuations in BOLD signals after temporal filtering (**Figure 1B**, *Z* scored) in one typical dataset. Group analysis results indicated that the BOLD fluctuations of most neocortex were positively correlated with the EEG BS pattern (**Figure 1C**, voxel-wise $P < 0.001$, FWE correction), including the prefrontal cortex, temporal cortex, parietal cortex, somatosensory cortex, PCC, primary motor and premotor cortex, visural cortex, as well as thalamus.

Altered Whole-Brain Functional Connectivity During BS Activity Compared to SW Activity

Results of whole-brain comparison based on datasets with or without removal of BS coupling effect were presented in **Figure 2** and **Supplementary Figure S3**, respectively. Group-averaged connectivity networks from datasets with BS activity and stable SW activity are presented in **Figure 2A**. Group difference in each connection is represented using effect size (Hedges' *g* value, bottom-left triangle in **Figure 2B**). A total of 371 functional connections showed significant differences between BS and SW groups (cluster-level corrected $P < 0.00$, NBS correction with edge-wise $P < 0.001$, top-right triangle in **Figure 2B**), including 317 increased and 54 decreased connections in BS group. As presented in **Figure 2C**, the BS group showed a substantial increase in cortical connectivity, accompanied by significant decrease mainly in connections between parietal and temporal/prefrontal cortex (PFC), and between insula and occipital/parietal cortex. The normalized distribution of altered connections across different brain lobes is summarized in **Figure 2D** (bottom-left triangle). The number of disrupted edges between certain lobes is significantly larger than the random distribution ($P < 0.05$, Bonferroni correction). The majority of within-lobe connections are concentrated in the orbitofrontal cortex (OFC). The majority of across-lobe connections are concentrated between OFC and prefrontal/cingulate/occipital cortex, and between parietal and temporal cortex.

Increased Connectivity in Default Mode Network During BS Activity

The DMN was defined as the voxel-wise FC with bilateral PCC. The statistical results of the connectivity strength in BS and SW groups are presented in **Figures 3A,B**, respectively (voxel-wise $P < 0.001$, FWE correction). The BOLD activity in PCC was positively correlated with bilateral

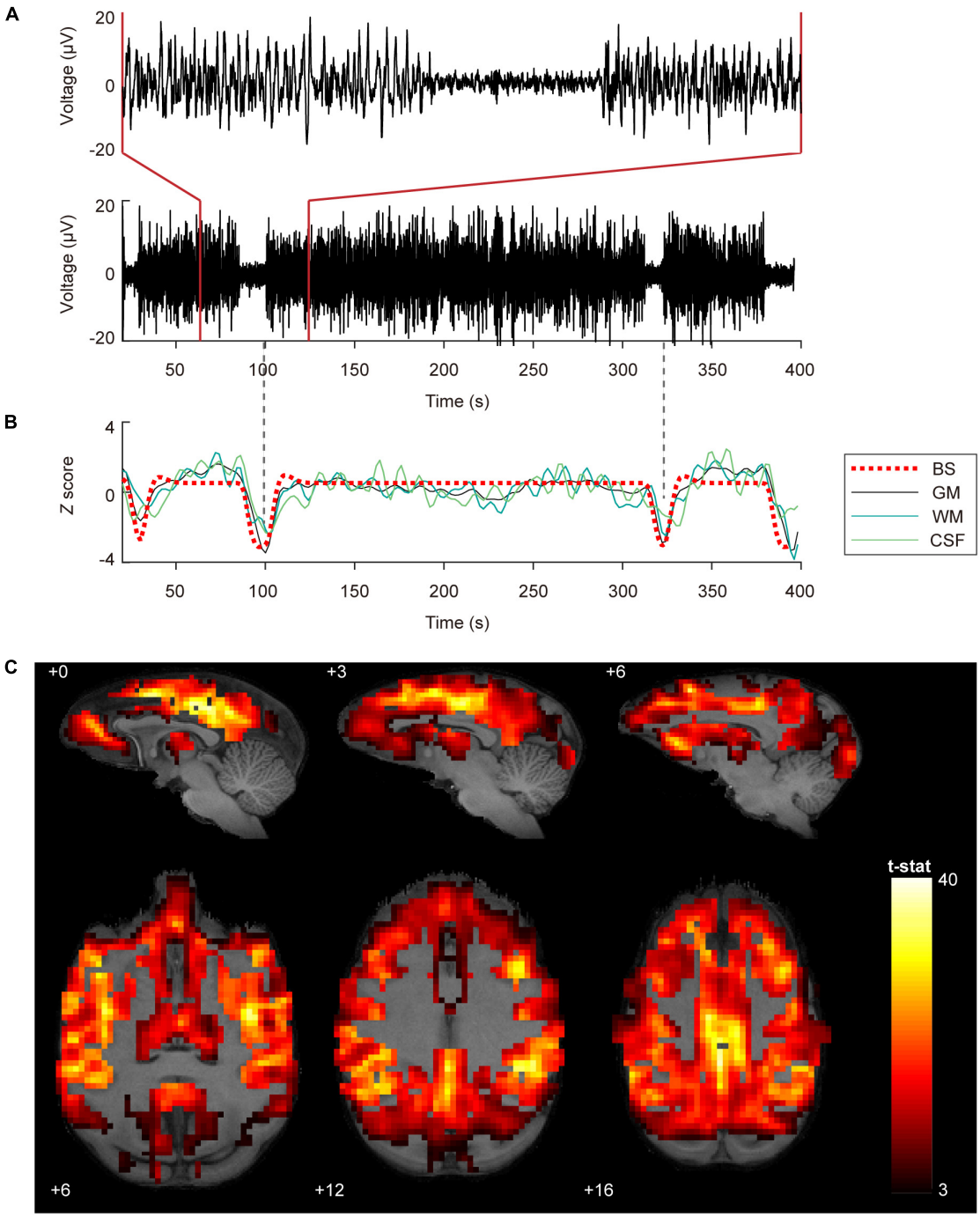

FIGURE 1 | Coupling between BOLD fluctuations and burst suppression patterns in EEG signals. **(A)** EEG signals with burst suppression pattern simultaneously recorded during fMRI scanning from the central frontal electrode. The bottom and top panel show 380 and 60 s EEG, respectively. The time onset corresponds to the acquisition of the first MRI volume. **(B)** Burst suppression pattern with HRF convolution and averaged BOLD signals in gray matter (GM), white matter (WM), and cerebrospinal fluid (CSF). The dashed vertical lines in gray are aligned to the trough of the GM signal. **(C)** Group statistics ($n = 27$) shown as voxel-wise t-values of a generalized linear model modeling burst suppression pattern as a regressor of interest were displayed in bspmview (voxel-wise $P < 0.001$, FWE correction).

parietal cortex, medial and centrolateral prefrontal cortex, superior and ventral temporal cortex, primary motor and dorsolateral premotor cortex, anterior cingulate cortex and visual areas, and anticorrelated with secondary somatosensory and inferior parietal cortex during SW activity (**Figure 3B**). In comparison, there is an overall increase in DMN connectivity during BS activity (**Figure 3A**), particularly in the superior temporal cortex, prefrontal cortex, secondary somatosensory

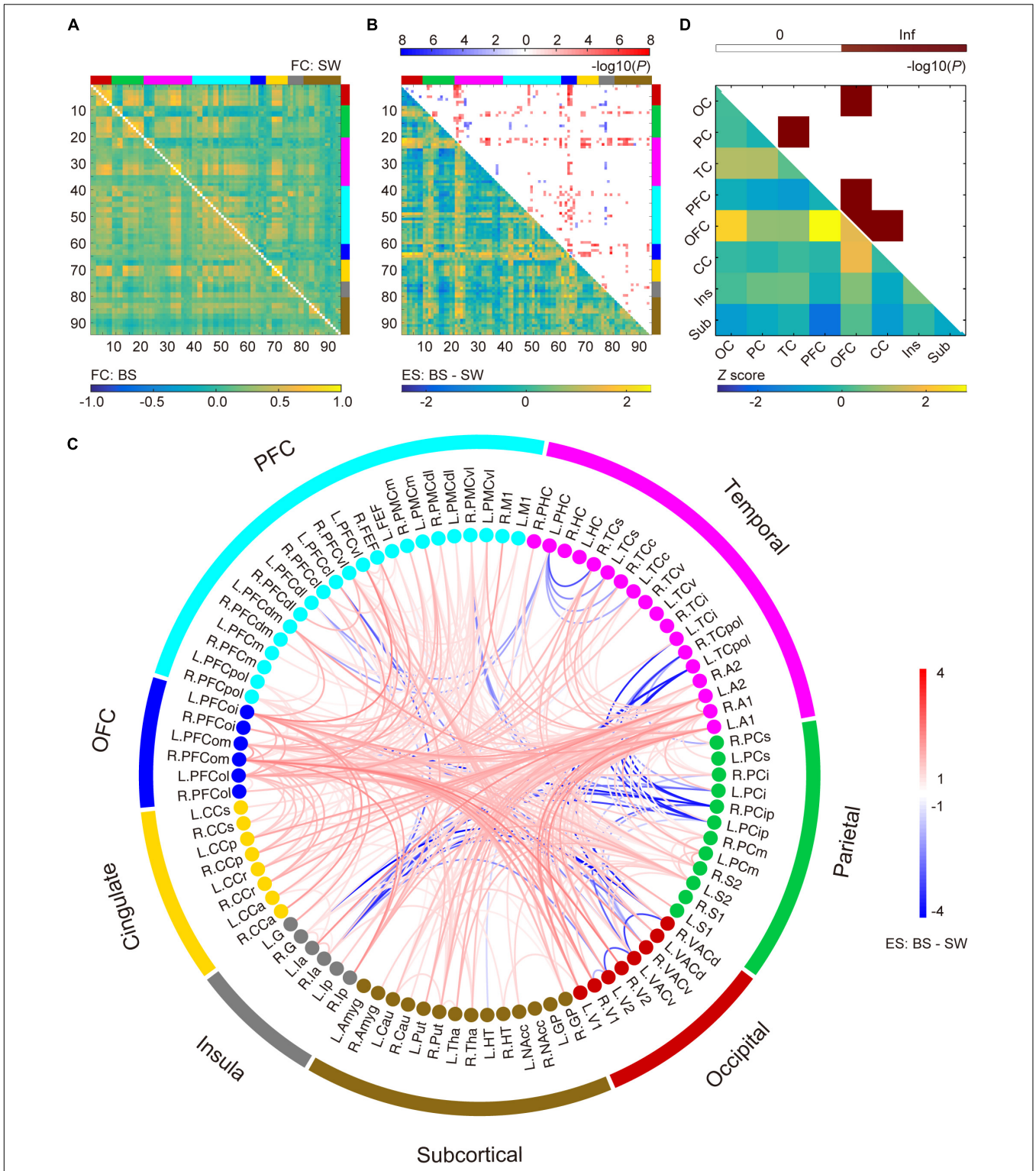

FIGURE 2 | Altered functional connections during burst suppression activity compared to stable slow wave activity after the coupling effect with burst suppression pattern was corrected via regression. **(A)** Averaged functional connectivity (FC) matrices during burst suppression (BS, bottom-left) and slow wave (SW, top-right) activity. Covariates were regressed out before temporal filtering. **(B)** Effect sizes (ES, Hedges' *g* value) of BS versus SW (bottom-left) and corresponding *P* values (top-right, $P < 0.05$, NBS correction with edge-wise $P < 0.001$). Brain nodes are organized according to the regions/lobes as listed in **Supplementary Table S1**. **(C)** Altered functional connections represented with node information. See **Supplementary Table S1** for details of brain area abbreviations. **(D)** Normalized spatial distribution of disrupted connections across the brain (bottom-left) and the corresponding significance (top-right, $P < 0.05$, Bonferroni correction).

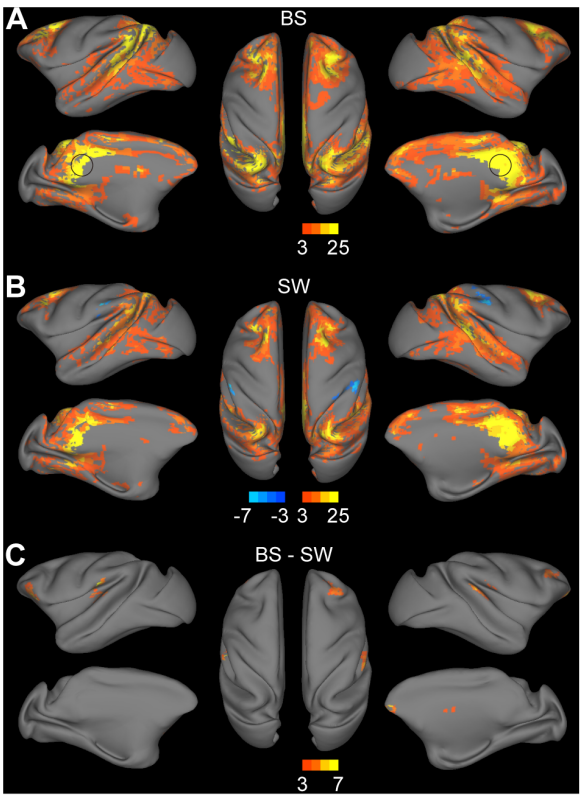

FIGURE 3 | Altered functional connections across anesthesia levels in default mode network. **(A,B)** Voxel-wise connectivity with bilateral posterior cingulate cortex (indicated in black circle) in burst suppression (BS) and slow wave (SW) states. Volume metrics were mapped to cortical surface in CARET5. **(C)** Altered functional connections during BS activity compared to SW activity. All results were corrected for multiple comparisons at a significance level of $P < 0.05$ via FWE with voxel-wise $P < 0.001$.

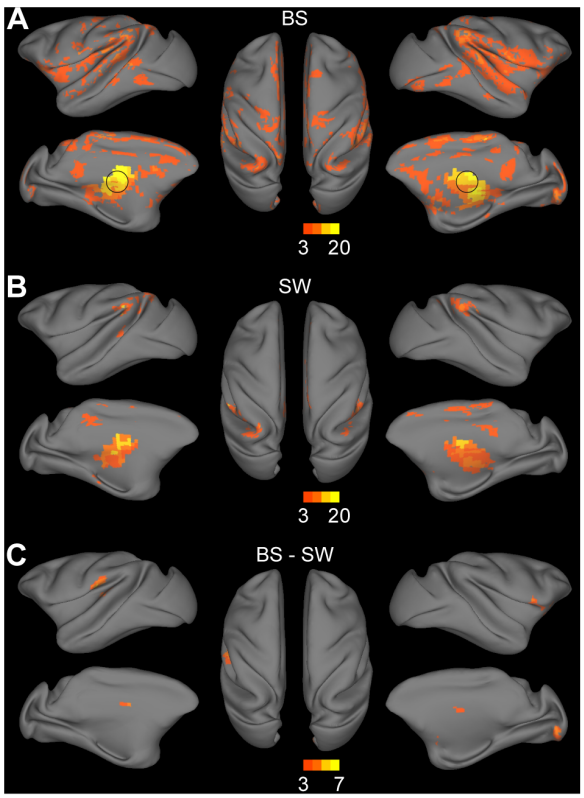

FIGURE 4 | Altered functional connections across anesthesia levels in thalamocortical network. **(A,B)** Voxel-wise connectivity with bilateral thalamus (indicated in black circle) in burst suppression (BS) and slow wave (SW) states. Volume metrics were mapped to cortical surface in CARET5. **(C)** Altered functional connections during BS activity compared to SW activity. All results were corrected for multiple comparisons at a significance level of $P < 0.05$ via FWE with voxel-wise $P < 0.001$.

cortex and auditory cortex (**Figure 3C**, voxel-wise $P < 0.001$, FWE correction).

Increased Thalamocortical Connections During BS Activity

Thalamocortical connections were assessed by seed-based functional analysis with the bilateral thalamus as the seed region. Significant connections with the thalamus were observed in the bilateral striatum, medial prefrontal cortex, inferior parietal cortex, superior temporal cortex, auditory cortex, somatosensory cortex, posterior insula, visual cortex, anterior and posterior cingulate cortex during BS activity (**Figure 4A**, voxel-wise $P < 0.001$, FWE correction). Few thalamocortical connections to striatum, inferior parietal cortex, superior temporal cortex, retrosplenial and posterior cingulate cortex, somatosensory cortex and anterior visual area were observed during SW activity (**Figure 4B**, voxel-wise $P < 0.001$, FWE correction). The group comparison results further confirmed the overall increase during BS activity particularly in bilateral putamen, globus pallidus, right visual area, and left secondary somatosensory cortex (**Figure 4B**, voxel-wise $P < 0.001$, FWE correction).

DISCUSSION

Robust BS Coupling Effect in the Raw BOLD Fluctuations

In the current study, we show dramatic fluctuations in BOLD signal co-occurring with EEG BS activity in the isoflurane-anesthetized monkey brain. The coupling between simultaneously recorded BOLD and EEG signals can be explained by the highly synchronized excitability of the entire cerebral cortex during BS activity. Convergent research has shown that BS is associated with a hyper-excited cortical state, where bursts can be evoked by sub-threshold stimulus or occur spontaneously (Steriade et al., 1994; Hartikainen et al., 1995; Hudetz and Imas, 2007; Kroeger and Amzica, 2007; Ferron et al., 2009). Electrophysiological studies indicate that neurons in almost the entire cerebral cortex exhibit a similar "on-off" pattern during this state, featuring stereotyped alteration between depolarizing events and electrical silence of the neuronal membrane (Steriade et al., 1994). The hyper-excited burst activity was positively correlated with the cerebral blood flow (CBF) fluctuations, which is the base of BOLD fluctuations, as indicated in a recent

isoflurane-anesthetized rat research (Liu et al., 2011). Therefore, the BS coupling effect on BOLD fluctuations is supported by the physiological basis that synchronization of spontaneous high-voltage burst activity across a large population of neurons can result in the synchronization of hemodynamic fluctuations across different brain regions.

Separating Specific and Non-specific Functional Connectivity During BS Activity

Although several lines of evidence suggest a coherent neural activity basis of resting-state FC, whether there is a specific FC signature that underlies the BS anesthesia depth remains unclear. As previously mentioned, neural activity that changes between two electrical phases with enormous disparity can lead to radical changes in BOLD fluctuations at a large time scale, which in turn results in an overwhelming increase in the correlation coefficients between whole-brain BOLD signals during BS activity (**Supplementary Figure S3**). This non-specific coupling effect of BS pattern is superimposed on the potential specific functional changes associated with anesthesia depth or consciousness loss (**Figure 2**), and obscures the latter effect.

In removing regular nuisance effect, we demonstrated that regression of WM and CSF signals before temporal filtering is more effective (**Supplementary Figure S1**). This is consistent with the previous findings in human rs-fMRI studies that nuisance-related variability such as head motion and cardiac artifacts can be better controlled when covariate regression is applied before temporal filtering rather than after filtering in the preprocessing procedure (Hallquist et al., 2013). Further evaluation of the BS coupling effect on preprocessed images indicated that BS related global effect as indicated in **Figure 1C** cannot be fully eliminated by using either preprocessing procedure (**Supplementary Figure S2**). Therefore, we added the HRF convoluted BS pattern as an additional regressor in the linear regression model to eliminate the global coupling effect in fMRI datasets with BS activity.

Overall Increase in Functional Connectivity During BS Activity

An overall increase in functional connections during BS activity was observed compared to SW state in both whole-brain analysis (**Figure 2**) and seed-based analysis (**Figures 3**, **4**). As non-specific increase in the correlation matrix due to BS pattern was well controlled in preprocessing, the remaining alterations across different anesthesia levels may largely reflect specific changes in a subgroup of networks or brain areas. Interestingly, most of the connectivity alterations took place within OFC, and between OFC and other cortical areas. The role of the OFC in BS activity or anesthesia progress merits further investigation. Reduced connectivity strength was observed in a subset of connections between insula and occipital-parietal cortex, suggesting the segregation of the limbic system from the neocortex along with the deepening of anesthesia level. Few alterations were observed within subcortical areas, although a significant increase from subcortical to temporal cortex, parietal cortex, OFC and PFC was detected, which was also verified in the seed-based analysis in thalamus.

Preservation of DMN During BS Activity

The DMN is the most robust intrinsic network of the resting-state brain, which is associated with intrinsic processes such as mind wandering and self-reference (Buckner et al., 2008; Vanhaudenhuyse et al., 2011). Studies of alterations in DMN activity corresponding with different sleep stages indicate a potential correlation between the DMN and consciousness in humans (Raichle et al., 2001). Disconnection between the prefrontal cortex and the PCC has been observed during deep sleep (Horovitz et al., 2009; Samann et al., 2011). Subjects in sedation also exhibit a significant decrease in the default mode activity (Greicius et al., 2008; Martuzzi et al., 2010). Taken together, these findings suggest that the DMN may disappear at a certain stage during loss of consciousness. Nevertheless, preservation of the DMN connectivity under deep anesthesia was recently reported in both anesthetized monkeys and humans (Vincent et al., 2007; Boveroux et al., 2010; Hutchison and Everling, 2012). Our results displayed similar DMN patterns during both BS and SW activity as previous monkey studies (Vincent et al., 2007; Teichert et al., 2010). The robust findings of DMN under deep anesthesia indicate that the DMN may not be tightly associated with consciousness level (Buckner et al., 2008).

Recovery of Thalamocortical Connectivity and the Role of Thalamus During BS Activity

Numerous studies have indicated the influence of anesthesia depth on thalamocortical connections. The presence of thalamocortical connectivity has been reported during light anesthesia where subjects just reached unconsciousness (Martuzzi et al., 2010; Mhuircheartaigh et al., 2010). Recent reports show diminished but detectable thalamocortical connectivity in anesthetized subjects associated with unconsciousness (White and Alkire, 2003; Boveroux et al., 2010; Liang et al., 2012). In the current study, few connections with striatum, cingulate cortex, primary sensory areas, inferior parietal cortex, and superior temporal cortex were observed during SW activity. In contrast, a substantial increase of connections to striatum, somatosensory, and visual cortex were detected during BS activity.

The thalamus is believed to be a crucial region for the synchronized burst activity of neocortex during the BS episodes of EEG (Brown et al., 2010). The first study of the neuronal mechanisms of BS (Steriade et al., 1994) confirmed a close correspondence between neocortical and thalamic activities through intracellular and multisite extracellular simultaneous recordings from cortex, thalamus, and upper brainstem. Despite the overwhelming predominance of cortical electrical silence during EEG suppression epochs, there were still rhythmic oscillations discharged to the cortex from a part of the thalamus. This thalamocortical oscillation was able to facilitate neuron firing or subthreshold depolarizing potentials as well as the revival of EEG activity. However, other studies

indicated that cortical hyper-excitability during BS activity is favored by diminished cortical inhibition rather than thalamus induced excitation (Ferron et al., 2009). In our results, high synchronization between thalamic activity and BS pattern (**Figure 1C**) was revealed. Additionally, after the removal of BS coupling effect, there were significant connections from thalamus to primary sensory networks, which were weaker during SW activity. These enhanced thalamocortical connections might underlie the phenomenon that facilitated global burst activity could be induced by various kinds of subthreshold sensory stimuli under deep anesthesia with BS activity (Kroeger and Amzica, 2007). As for the role of thalamus in BS activity, further studies are desiderated.

Anesthetic Sensitivity and the Importance of Simultaneous EEG Monitoring

For monitoring and defining anesthesia level, most fMRI studies generally employ two kinds of anesthesia depth monitoring indexes. One is behavioral endpoint, such as "loss of responsiveness" for human or "immobility" for animals. The other is end-tidal concentration or minimum alveolar concentration (MAC) for volatile anesthetics, both of which represent the anesthetic concentration level in subjects for inhibiting noxious stimulus (Eger et al., 1965). However, these indexes may not reflect the actual brain state (Antognini and Carstens, 2002; Ryu et al., 2018). The improved comprehension of EEG signals under anesthesia makes it a promising method suitable for more accurate control of anesthesia level (Freye and Levy, 2005; Purdon et al., 2013, 2015; Marchant et al., 2014).

Based on *post-hoc* analysis of the coherence of rs-fMRI correlation at various anesthesia levels, a limited range of isoflurane concentration (1.00–1.50%) is recommended to obtain stable FC (Hutchison et al., 2014). However, as mentioned previously, monkey fMRI studies with simultaneous EEG monitoring have recorded BS activity at 1.25–1.5% isoflurane (Vincent et al., 2007). In current work, we recorded BS activity in two out of 16 monkeys even at 0.8–1.3% isoflurane. The occurrence of BS activity at a commonly used concentration of isoflurane in fMRI studies suggests individual variance in anesthetic sensitivity at the brain level. Anesthetic sensitivity can be affected by both pharmacokinetic and pharmacodynamics factors and varies across different subjects (Chemali et al., 2015). Even in the same subject, there are many other confounding factors, including physiological status on the experiment day, and sleep quality before the experiment. The etiology and mechanism of anesthetic sensitivity in the brain merits further investigation.

Although BS activity induced by an isoflurane level as low as 0.8% rarely happens, it makes a strong argument for the potential occurrence of BS activity when delivering a widely-used range of concentrations in the field. Simultaneous EEG is necessary to monitor the actual brain state in regular rs-fMRI studies on anesthetized animals. More importantly, BS activity-induced changes in FC is robust. In current work, the occurrence of BS activity was spontaneous, resulting in inconsistent burst suppression ratio (BSR, range 0.56–38.9%). BSR is a commonly used parameter to describe the intensity of BS activity with larger BSR indicating higher probability of BS occurrence and deeper anesthesia level. In current study, robust increase of FC was observed across BS runs with different BSR. Greater enhancement was observed under a stable BS state with frequent and long-lasting suppression episodes than those with occasional occurrence of BS event. Further studies with deliberately controlled BSR are needed to investigate the relationship between BSR and BS effect on FC.

LIMITATIONS

There are several limitations worth noting in this research. First, in consideration of the difficulty in controlling the occurrence of BS event and the individual variation in anesthetics sensitivity, present finding of the notably weak thalamocortical connectivity during SW activity could be affected by the relative small sample size. Second, another preliminary analysis on the current datasets suggested that the global synchronization strength during BS activity is potentially associated with BSR, which is not deliberately controlled in current study. Future studies with more subjects and precise control of BSR are needed to probe the biological underpinnings of the BOLD fluctuations at this specific anesthesia level. Third, to explore the influence of preprocessing procedures, we compared two conventional strategies used in monkey fMRI data analysis (**Supplementary Figure S1**). Other widely debated preprocessing steps such as global signal regression were not included. However, Scholvinck et al. (2010) showed that the often discarded global component of resting-state BOLD fluctuations is tightly coupled with underlying neural activity and may affect connectivity analysis. Fourth, there is a great chance that the global BS coupling effect is not fully excluded by regressing out the HRF convoluted BS pattern, although regression is the most commonly used approach to deal with nuisance variables with global influence. Lastly, pure oxygen was used in current experiments, which is considered as a probable confounding factor leading to more widespread connectivity in rs-fMRI studies (Nasrallah et al., 2015). However, we expect that the potential effect of hyperoxia is comparable in both BS and SW runs, as should impose very limited influence on the group difference in FC. Current results on specific alterations in FC during BS activity compared to SW activity should be interpreted with caution. However, the trend of overall increase in intrinsic FC during BS activity is robust and worth attention from researchers in the field.

CONCLUSION

In summary, we present evidence showing a dramatic increase in inter-regional connectivity in fMRI network under deep anesthesia with BS activity. The enhanced connectivity can be explained by the coupling effect of BS pattern on whole-brain BOLD signals. This non-specific coupling effect can be well controlled by covariates regression conducted before temporal filtering with the HRF convoluted BS pattern as an additional regressor. After the coupling effect was separated from the connectivity matrix, we detected an overall increase

in the functional connections under deep anesthesia with BS activity comparing to a lighter level with SW activity, including connections in DMN and thalamocortical networks. The orbitofrontal lobe are the most affected brain areas during BS activity. The non-linear changes in FC from light to deep anesthesia levels highlight the importance of future investigation on the physiological basis underlying BS activity. This is essential to clarify the mechanisms of anesthesia and coma states with BS events.

AUTHOR CONTRIBUTIONS

ZZ, ZheW, and YW designed research. ZZ, D-CC, and ZhiW performed research. D-CC and ZhiW analyzed the data. ZZ, D-CC, KZ, and ZheW wrote the manuscript.

FUNDING

This work was supported by the National Key R&D Program of China (No. 2016YFC1201802 to YW, No. 2017YFC1310400 to ZheW), the Strategic Priority Research Program of Chinese Academy of Sciences (No. XDB32000000), grants from National Natural Science Foundation (81671058 and 81730031 to YW, 81571300 and 31771174 to ZheW), Shanghai Municipal Science and Technology Major Project (No. 2018SHZDZX05) and Natural Science Foundation and Major Basic Research Program of Shanghai (No. 16JC1420100).

ACKNOWLEDGMENTS

We thank Hu Zhang and Qinying Jiang for their assistance in monkey data collection.

SUPPLEMENTARY MATERIAL

The Supplementary Material for this article can be found online at: https://www.frontiersin.org/articles/10.3389/fnins.2019.00296/full#supplementary-material

REFERENCES

Alkire, M. T., Pomfrett, C. J., Haier, R. J., Gianzero, M. V., Chan, C. M., Jacobsen, B. P., et al. (1999). Functional brain imaging during anesthesia in humans: effects of halothane on global and regional cerebral glucose metabolism. *Anesthesiology* 90, 701–709. doi: 10.1097/00000542-199903000-00011

Amzica, F. (2015). What does burst suppression really mean? *Epilepsy Behav.* 49, 234–237. doi: 10.1016/j.yebeh.2015.06.012

Antognini, J. F., and Carstens, E. (2002). In vivo characterization of clinical anaesthesia and its components. *Br. J. Anaesth.* 89, 156–166. doi: 10.1093/bja/aef156

Bezgin, G., Vakorin, V. A., Van Opstal, A. J., Mcintosh, A. R., and Bakker, R. (2012). Hundreds of brain maps in one atlas: registering coordinate-independent primate neuro-anatomical data to a standard brain. *Neuroimage* 62, 67–76. doi: 10.1016/j.neuroimage.2012.04.013

Boveroux, P., Vanhaudenhuyse, A., Bruno, M. A., Noirhomme, Q., Lauwick, S., Luxen, A., et al. (2010). Breakdown of within- and between-network resting state functional magnetic resonance imaging connectivity during propofol-induced loss of consciousness. *Anesthesiology* 113, 1038–1053. doi: 10.1097/ALN.0b013e3181f697f5

Brown, E. N., Lydic, R., and Schiff, N. D. (2010). General anesthesia, sleep, and coma. *N. Engl. J. Med.* 363, 2638–2650. doi: 10.1056/NEJMra0808281

Buckner, R. L., Andrews-Hanna, J. R., and Schacter, D. L. (2008). The brain's default network: anatomy, function, and relevance to disease. *Ann. N. Y. Acad. Sci.* 1124, 1–38. doi: 10.1196/annals.1440.011

Bukhari, Q., Schroeter, A., and Rudin, M. (2018). Increasing isoflurane dose reduces homotopic correlation and functional segregation of brain networks in mice as revealed by resting-state fMRI. *Sci. Rep.* 8:10591. doi: 10.1038/s41598-018-28766-3

Chemali, J. J., Kenny, J. D., Olutola, O., Taylor, N. E., Kimchi, E. Y., Purdon, P. L., et al. (2015). Ageing delays emergence from general anaesthesia in rats by increasing anaesthetic sensitivity in the brain. *Br. J. Anaesth.* 115(Suppl. 1), i58–i65. doi: 10.1093/bja/aev112

Eger, E. I. II, Saidman, L. J., and Brandstater, B. (1965). Minimum alveolar anesthetic concentration: a standard of anesthetic potency. *Anesthesiology* 26, 756–763. doi: 10.1097/00000542-196511000-00010

Ferron, J. F., Kroeger, D., Chever, O., and Amzica, F. (2009). Cortical inhibition during burst suppression induced with isoflurane anesthesia. *J. Neurosci.* 29, 9850–9860. doi: 10.1523/JNEUROSCI.5176-08.2009

Fiset, P., Paus, T., Daloze, T., Plourde, G., Meuret, P., Bonhomme, V., et al. (1999). Brain mechanisms of propofol-induced loss of consciousness in humans: a positron emission tomographic study. *J. Neurosci.* 19, 5506–5513. doi: 10.1523/JNEUROSCI.19-13-05506.1999

Freye, E., and Levy, J. V. (2005). Cerebral monitoring in the operating room and the intensive care unit: an introductory for the clinician and a guide for the novice wanting to open a window to the brain. Part I: the electroencephalogram. *J. Clin. Monit. Comput.* 19, 1–76. doi: 10.1007/s10877-005-0712-z

Golkowski, D., Ranft, A., Kiel, T., Riedl, V., Kohl, P., Rohrer, G., et al. (2017). Coherence of BOLD signal and electrical activity in the human brain during deep sevoflurane anesthesia. *Brain Behav.* 7:e00679. doi: 10.1002/brb3.679

Grandjean, J., Schroeter, A., Batata, I., and Rudin, M. (2014). Optimization of anesthesia protocol for resting-state fMRI in mice based on differential effects of anesthetics on functional connectivity patterns. *Neuroimage* 102(Pt 2), 838–847. doi: 10.1016/j.neuroimage.2014.08.043

Greicius, M. (2008). Resting-state functional connectivity in neuropsychiatric disorders. *Curr. Opin. Neurol.* 21, 424–430. doi: 10.1097/WCO.0b013e328306f2c5

Greicius, M. D., Kiviniemi, V., Tervonen, O., Vainionpaa, V., Alahuhta, S., Reiss, A. L., et al. (2008). Persistent default-mode network connectivity during light sedation. *Hum. Brain Mapp.* 29, 839–847. doi: 10.1002/hbm.20537

Hallquist, M. N., Hwang, K., and Luna, B. (2013). The nuisance of nuisance regression: Spectral misspecification in a common approach to resting-state fMRI preprocessing reintroduces noise and obscures functional connectivity. *Neuroimage* 82C, 208–225. doi: 10.1016/j.neuroimage.2013.05.116

Hartikainen, K. M., Rorarius, M., Perakyla, J. J., Laippala, P. J., and Jantti, V. (1995). Cortical reactivity during isoflurane burst-suppression anesthesia. *Anesth. Analg.* 81, 1223–1228.

Horovitz, S. G., Braun, A. R., Carr, W. S., Picchioni, D., Balkin, T. J., Fukunaga, M., et al. (2009). Decoupling of the brain's default mode network during deep sleep. *Proc. Natl. Acad. Sci. U.S.A.* 106, 11376–11381. doi: 10.1073/pnas.0901435106

Huang, Z., Wang, Z., Zhang, J., Dai, R., Wu, J., Li, Y., et al. (2014). Altered temporal variance and neural synchronization of spontaneous brain activity in anesthesia. *Hum. Brain Mapp.* 35, 5368–5378. doi: 10.1002/hbm.22556

Hudetz, A. G., and Imas, O. A. (2007). Burst activation of the cerebral cortex by flash stimuli during isoflurane anesthesia in rats. *Anesthesiology* 107, 983–991. doi: 10.1097/01.anes.0000291471.80659.55

Hutchison, R. M., and Everling, S. (2012). Monkey in the middle: why non-human primates are needed to bridge the gap in resting-state investigations. *Front. Neuroanat.* 6:29. doi: 10.3389/fnana.2012.00029

Hutchison, R. M., Hutchison, M., Manning, K. Y., Menon, R. S., and Everling, S. (2014). Isoflurane induces dose-dependent alterations in the cortical connectivity profiles and dynamic properties of the brain's functional architecture. *Hum. Brain Mapp.* 35, 5754–5775. doi: 10.1002/hbm.22583

Kotter, R., and Wanke, E. (2005). Mapping brains without coordinates. *Philos. Trans. R. Soc. Lond. B Biol. Sci.* 360, 751–766. doi: 10.1098/rstb.2005.1625

Kroeger, D., and Amzica, F. (2007). Hypersensitivity of the anesthesia-induced comatose brain. *J. Neurosci.* 27, 10597–10607. doi: 10.1523/JNEUROSCI.3440-07.2007

Liang, Z., King, J., and Zhang, N. (2012). Intrinsic organization of the anesthetized brain. *J. Neurosci.* 32, 10183–10191. doi: 10.1523/JNEUROSCI.1020-12.2012

Liu, X., Zhu, X. H., Zhang, Y., and Chen, W. (2011). Neural origin of spontaneous hemodynamic fluctuations in rats under burst-suppression anesthesia condition. *Cereb. Cortex* 21, 374–384. doi: 10.1093/cercor/bhq105

Liu, X., Zhu, X. H., Zhang, Y., and Chen, W. (2013). The change of functional connectivity specificity in rats under various anesthesia levels and its neural origin. *Brain Topogr.* 26, 363–377. doi: 10.1007/s10548-012-0267-5

Logothetis, N. K., Guggenberger, H., Peled, S., and Pauls, J. (1999). Functional imaging of the monkey brain. *Nat. Neurosci.* 2, 555–562. doi: 10.1038/9210

Lv, Q., Yang, L., Li, G., Wang, Z., Shen, Z., Yu, W., et al. (2016). Large-scale persistent network reconfiguration induced by ketamine in anesthetized monkeys: relevance to mood disorders. *Biol. Psychiatry* 79, 765–775. doi: 10.1016/j.biopsych.2015.02.028

Marchant, N., Sanders, R., Sleigh, J., Vanhaudenhuyse, A., Bruno, M. A., Brichant, J. F., et al. (2014). How electroencephalography serves the anesthesiologist. *Clin. EEG Neurosci.* 45, 22–32. doi: 10.1177/1550059413509801

Martuzzi, R., Ramani, R., Qiu, M., Rajeevan, N., and Constable, R. T. (2010). Functional connectivity and alterations in baseline brain state in humans. *Neuroimage* 49, 823–834. doi: 10.1016/j.neuroimage.2009.07.028

Mhuircheartaigh, R. N., Rosenorn-Lanng, D., Wise, R., Jbabdi, S., Rogers, R., and Tracey, I. (2010). Cortical and subcortical connectivity changes during decreasing levels of consciousness in humans: a functional magnetic resonance imaging study using propofol. *J. Neurosci.* 30, 9095–9102. doi: 10.1523/JNEUROSCI.5516-09.2010

Nallasamy, N., and Tsao, D. Y. (2011). Functional connectivity in the brain: effects of anesthesia. *Neuroscientist* 17, 94–106. doi: 10.1177/1073858410374126

Nasrallah, F. A., Yeow, L. Y., Biswal, B., and Chuang, K. H. (2015). Dependence of BOLD signal fluctuation on arterial blood CO2 and O2: implication for resting-state functional connectivity. *Neuroimage* 117, 29–39. doi: 10.1016/j.neuroimage.2015.05.035

Paasonen, J., Salo, R. A., Huttunen, J. K., and Grohn, O. (2017). Resting-state functional MRI as a tool for evaluating brain hemodynamic responsiveness to external stimuli in rats. *Magn. Reson. Med.* 78, 1136–1146. doi: 10.1002/mrm.26496

Paasonen, J., Stenroos, P., Salo, R. A., Kiviniemi, V., and Grohn, O. (2018). Functional connectivity under six anesthesia protocols and the awake condition in rat brain. *Neuroimage* 172, 9–20. doi: 10.1016/j.neuroimage.2018.01.014

Purdon, P. L., Pierce, E. T., Mukamel, E. A., Prerau, M. J., Walsh, J. L., Wong, K. F., et al. (2013). Electroencephalogram signatures of loss and recovery of consciousness from propofol. *Proc. Natl. Acad. Sci. U.S.A.* 110, E1142–E1151. doi: 10.1073/pnas.1221180110

Purdon, P. L., Sampson, A., Pavone, K. J., and Brown, E. N. (2015). Clinical Electroencephalography for anesthesiologists: Part I: background and basic signatures. *Anesthesiology* 123, 937–960. doi: 10.1097/ALN.0000000000000841

Raichle, M. E., Macleod, A. M., Snyder, A. Z., Powers, W. J., Gusnard, D. A., and Shulman, G. L. (2001). A default mode of brain function. *Proc. Natl. Acad. Sci. U.S.A.* 98, 676–682. doi: 10.1073/pnas.98.2.676

Rohlfing, T., Kroenke, C. D., Sullivan, E. V., Dubach, M. F., Bowden, D. M., Grant, K. A., et al. (2012). The INIA19 template and neuromaps atlas for primate brain image parcellation and spatial normalization. *Front. Neuroinform.* 6:27. doi: 10.3389/fninf.2012.00027

Ryu, K. H., Song, K., Lim, T. Y., Choi, W. J., Kim, Y. H., and Kim, H. S. (2018). Does equi-minimum alveolar concentration value ensure equivalent analgesic or hypnotic potency: a comparison between desflurane and sevoflurane. *Anesthesiology* 128, 1092–1098. doi: 10.1097/ALN.0000000000002158

Samann, P. G., Wehrle, R., Hoehn, D., Spoormaker, V. I., Peters, H., Tully, C., et al. (2011). Development of the brain's default mode network from wakefulness to slow wave sleep. *Cereb. Cortex* 21, 2082–2093. doi: 10.1093/cercor/bhq295

Scholvinck, M. L., Maier, A., Ye, F. Q., Duyn, J. H., and Leopold, D. A. (2010). Neural basis of global resting-state fMRI activity. *Proc. Natl. Acad. Sci. U.S.A.* 107, 10238–10243. doi: 10.1073/pnas.0913110107

Sheskin, D. J. (2003). *Handbook of Parametric and Nonparametric Statistical Procedures*, 3rd Edn. Boca Raton, FL: CRC Press. doi: 10.1201/9781420036268

Steriade, M., Amzica, F., and Contreras, D. (1994). Cortical and thalamic cellular correlates of electroencephalographic burst-suppression. *Electroencephalogr. Clin. Neurophysiol.* 90, 1–16. doi: 10.1016/0013-4694(94)90108-2

Teichert, T., Grinband, J., Hirsch, J., and Ferrera, V. P. (2010). Effects of heartbeat and respiration on macaque fMRI: implications for functional connectivity. *Neuropsychologia* 48, 1886–1894. doi: 10.1016/j.neuropsychologia.2009.11.026

Van Den Heuvel, M. P., and Hulshoff Pol, H. E. (2010). Exploring the brain network: a review on resting-state fMRI functional connectivity. *Eur. Neuropsychopharmacol.* 20, 519–534. doi: 10.1016/j.euroneuro.2010.03.008

Vanhaudenhuyse, A., Demertzi, A., Schabus, M., Noirhomme, Q., Bredart, S., Boly, M., et al. (2011). Two distinct neuronal networks mediate the awareness of environment and of self. *J. Cogn. Neurosci.* 23, 570–578. doi: 10.1162/jocn.2010.21488

Vincent, J. L., Patel, G. H., Fox, M. D., Snyder, A. Z., Baker, J. T., Van Essen, D. C., et al. (2007). Intrinsic functional architecture in the anaesthetized monkey brain. *Nature* 447, 83–86. doi: 10.1038/nature05758

Vogt, B. A., and Laureys, S. (2005). Posterior cingulate, precuneal and retrosplenial cortices: cytology and components of the neural network correlates of consciousness. *Prog. Brain Res.* 150, 205–217. doi: 10.1016/S0079-6123(05)50015-3

Wang, Z., Chen, L. M., Negyessy, L., Friedman, R. M., Mishra, A., Gore, J. C., et al. (2013). The relationship of anatomical and functional connectivity to resting-state connectivity in primate somatosensory cortex. *Neuron* 78, 1116–1126. doi: 10.1016/j.neuron.2013.04.023

White, N. S., and Alkire, M. T. (2003). Impaired thalamocortical connectivity in humans during general-anesthetic-induced unconsciousness. *Neuroimage* 19, 402–411. doi: 10.1016/S1053-8119(03)00103-4

Wu, T., Grandjean, J., Bosshard, S. C., Rudin, M., Reutens, D., and Jiang, T. (2017). Altered regional connectivity reflecting effects of different anaesthesia protocols in the mouse brain. *Neuroimage* 149, 190–199. doi: 10.1016/j.neuroimage.2017.01.074

Zalesky, A., Fornito, A., and Bullmore, E. T. (2010). Network-based statistic: identifying differences in brain networks. *Neuroimage* 53, 1197–1207. doi: 10.1016/j.neuroimage.2010.06.041

Conflict of Interest Statement: The authors declare that the research was conducted in the absence of any commercial or financial relationships that could be construed as a potential conflict of interest.

frontiers in Neuroscience

ORIGINAL RESEARCH
published: 07 May 2019
doi: 10.3389/fnins.2019.00433

Cerebral Autoregulation Evidenced by Synchronized Low Frequency Oscillations in Blood Pressure and Resting-State fMRI

Joseph R. Whittaker[1], Ian D. Driver[2], Marcello Venzi[1], Molly G. Bright[3] and Kevin Murphy[1]*

[1] Cardiff University Brain Research Imaging Centre (CUBRIC), School of Physics and Astronomy, Cardiff University, Cardiff, United Kingdom, [2] CUBRIC, School of Psychology, Cardiff University, Cardiff, United Kingdom, [3] Department of Physical Therapy and Human Movement Sciences, Feinberg School of Medicine, Northwestern University, Chicago, IL, United States

Resting-state functional magnetic resonance imaging (rs-fMRI) is a widely used technique for mapping the brain's functional architecture, so delineating the main sources of variance comprising the signal is crucial. Low frequency oscillations (LFO) that are not of neural origin, but which are driven by mechanisms related to cerebral autoregulation (CA), are present in the blood-oxygenation-level-dependent (BOLD) signal within the rs-fMRI frequency band. In this study we use a MR compatible device (Caretaker, Biopac) to obtain a non-invasive estimate of beat-to-beat mean arterial pressure (MAP) fluctuations concurrently with rs-fMRI at 3T. Healthy adult subjects (n = 9; 5 male) completed two 20-min rs-fMRI scans. MAP fluctuations were decomposed into different frequency scales using a discrete wavelet transform, and oscillations at approximately 0.1 Hz show a high degree of spatially structured correlations with matched frequency fMRI fluctuations. On average across subjects, MAP fluctuations at this scale of the wavelet decomposition explain ∼2.2% of matched frequency fMRI signal variance. Additionally, a simultaneous multi-slice multi-echo acquisition was used to collect 10-min rs-fMRI at three echo times at 7T in a separate group of healthy adults (n = 5; 5 male). Multiple echo times were used to estimate the R_2* decay at every time point, and MAP was shown to strongly correlate with this signal, which suggests a purely BOLD (i.e., blood flow related) origin. This study demonstrates that there is a significant component of the BOLD signal that has a systemic physiological origin, and highlights the fact that not all localized BOLD signal changes necessarily reflect blood flow supporting local neural activity. Instead, these data show that a proportion of BOLD signal fluctuations in rs-fMRI are due to localized control of blood flow that is independent of local neural activity, most likely reflecting more general systemic autoregulatory processes. Thus, fMRI is a promising tool for studying flow changes associated with cerebral autoregulation with high spatial resolution.

Keywords: cerebral autoregulation, resting-state fMRI, blood pressure, cerebral physiology, LFO, BOLD, CBF

OPEN ACCESS

Edited by:
Jean Chen,
University of Toronto, Canada

Reviewed by:
Changwei Wesley Wu,
Taipei Medical University, Taiwan
Thomas T. Liu,
University of California, San Diego, United States

****Correspondence:***
Joseph R. Whittaker
whittakerj3@cardiff.ac.uk

Specialty section:
This article was submitted to Brain Imaging Methods, a section of the journal Frontiers in Neuroscience

Received: *31 October 2018*
Accepted: *15 April 2019*
Published: *07 May 2019*

Citation:
Whittaker JR, Driver ID, Venzi M, Bright MG and Murphy K (2019) Cerebral Autoregulation Evidenced by Synchronized Low Frequency Oscillations in Blood Pressure and Resting-State fMRI. Front. Neurosci. 13:433. doi: 10.3389/fnins.2019.00433

INTRODUCTION

Functional connectivity in the brain can be assessed with blood-oxygenation-level-dependent (BOLD) functional magnetic resonance imaging (fMRI). The source of BOLD contrast is the difference in magnetic susceptibility between oxy- and deoxyhemoglobin, which has an effect on apparent transverse relaxation (R_2*), and thus imparts sensitivity to blood oxygenation in the MR signal (Buxton, 2013). Neurovascular coupling (NVC) allows brain activity to be mapped using BOLD fMRI, because localized increases in cerebral blood flow (CBF), which are proportionally larger than changes in oxygen metabolism, cause increases in local venous blood oxygenation. An implicit assumption that predicates BOLD fMRI as a tool for mapping neural activity in the brain is that NVC related changes in CBF are the predominant source of signal variance. There are, however, other mechanisms besides NVC that regulate CBF, such as arterial blood gas concentration, particularly carbon dioxide (CO_2), which is a potent vasodilator with a strong effect on CBF (Battisti-Charbonney et al., 2011). Furthermore, systemic control of the brain's blood supply is governed by numerous homeostatic mechanisms that are broadly defined as cerebral autoregulation (CA) (Willie et al., 2014), the theoretical process that modulates cerebrovascular resistance to ensure CBF is kept at a sufficient level in the face of transient changes in systemic haemodynamics (e.g., blood pressure and cardiac output).

Understanding non-neuronal sources of variance in CBF fluctuations is especially important with regard to resting state fMRI (rs-fMRI) paradigms for two reasons. Firstly, unlike traditional task based paradigms for which the timing and duration of evoked BOLD signal changes is known a priori, the timing of spontaneous neural fluctuations can't be assumed, meaning non-neuronal effects can't be mitigated as they are in task based designs by averaging over trials. Secondly, the low frequency range (∼0.01–0.1 Hz) over which functional connectivity is observed overlaps with the spectrum at which other systemic physiological effects occur (Murphy et al., 2013). Spontaneous fluctuations in breathing cause cerebrovascular reactivity (CVR) to CO_2 to manifest as low frequency (<0.05 Hz) oscillations in the BOLD signal (Wise et al., 2004), and endogenous fluctuations (<0.1 Hz) in vascular tone have been reported in various different vascular beds across multiple species (Nilsson and Aalkjaer, 2003). Recently, low frequency oscillations (LFO) of a systemic origin have been observed by correlating fMRI signals with functional near-infrared spectroscopy (fNIRS) measures of peripheral haemodynamics (Tong and Frederick, 2010; Tong et al., 2012). Intriguingly, these systemic LFOs appear to propagate throughout the brain with spatially structured temporal delays (Erdogan et al., 2016).

Arterial blood pressure (ABP) is dynamic over multiple time scales, including at a beat-to-beat level, and so is likely to contribute significantly to fluctuations in CBF. Transcranial Doppler ultrasound (TCD) studies have consistently demonstrated how ABP fluctuations modulate cerebral blood flow velocity (CBFV) in large intracranial arteries (Aaslid et al., 1989; Zhang et al., 1998), and that they account for a considerable proportion of the total variance, approximately 60% of the total predictive power of CBFV fluctuations in right middle cerebral artery (MCA) (Mitsis et al., 2004). Evidence for how blood pressure dynamics affect fMRI fluctuations is scarce, mostly limited to animal studies on the relationship between transient changes and evoked neural responses (Wang et al., 2006; Qiao et al., 2007; Uchida et al., 2017). Similar to fMRI, ABP time series have a 1/f power spectrum, but also show distinct oscillations (∼0.1 Hz in humans) known as Mayer waves (Mayer, 1876), which are independent of respiration and tightly coupled to efferent sympathetic nervous activity (SNA) (Julien, 2006). Oscillations at this frequency have also been observed in cerebral haemodynamics measured with fNIRS (Obrig et al., 2000; Yucel et al., 2016) and intraoperative multispectral optical intrinsic signal imaging (Rayshubskiy et al., 2014). However, the origins of such signals are unclear, and separating the effects of ABP fluctuations from vasomotion (which is usually regarded as distinct) on cerebral haemodynamics is an open challenge.

Nevertheless, the TCD literature provides compelling reason to believe that ABP fluctuations should contribute to the BOLD fMRI signal. Measurement of the coupling between fluctuations in ABP and CBFV in intracranial arteries has found widespread use as a clinically useful means of assessing CA (Zhang et al., 1998; Panerai et al., 2002; Panerai, 2008), and nonlinear modeling estimates that ABP accounts for 60% of the predictive power of CBFV fluctuations in the MCA (Mitsis et al., 2004). Although TCD has been widely used to assess both CVR and CA in research and clinical practice (Willie et al., 2011), more recently fMRI has emerged as a powerful tool for mapping CVR across the brain (Pillai and Mikulis, 2015), and the feasibility of obtaining BOLD fMRI based measures of CVR from spontaneous CO_2 fluctuations has also been demonstrated (Golestani et al., 2016). So far, these advances in measuring cerebrovascular function with fMRI have not yet extended into the domain of CA. However, the TCD literature proves that blood pressure related spontaneous CBFV fluctuations provide an effective means of characterizing CA, which is promising for the development of an equivalent whole-brain fMRI method.

In this study we explore the relationship between systemic fluctuations in blood pressure and the resting-state fMRI signal. We measure beat-to-beat blood pressure fluctuations concurrently with single-echo fMRI at 3T and multi-echo fMRI at 7T, and show that widespread patterns of correlations exist in low frequency BOLD signals, which we posit are due to fluctuations in CBF associated with CA.

MATERIALS AND METHODS

Experimental Protocol

Magnetic Resonance Imaging Acquisition

The study consisted of two separate experiments conducted on two different scanners. Nine healthy volunteers (age 22–37 years) were recruited for a 3T session to collect single-echo fMRI data (3T) and five additional healthy volunteers (age 30–41 years) were recruited for a 7T session to collect multi-echo fMRI data (7T-ME). All participants gave written informed consent, and the School of Psychology Cardiff University Ethics Committee

approved the study in accordance with the guidelines stated in the Cardiff University Research Framework (version 4.0, 2010).

The 7T scan protocol was added to enable us to address the origin of MAP correlated fMRI signal changes. Primarily this was achieved by using a multi-echo acquisition, which allows us to separate the pure BOLD component from the fMRI signal. Furthermore, the session consisted of two scans with differing acquisition parameters (see section "Multi-Echo Fit" below for theoretical details).

3T

Two twenty-minute rs-fMRI runs were acquired on a 3T GE HDx scanner (GE Healthcare, Milwaukee, WI, United States) with an eight-channel receive head-coil using a gradient-echo EPI readout with a single echo time (TR = 2000 ms; TE = 35 ms; flip angle (α) = 90°; FOV = 224 mm; 3.5 mm^2 in-plane resolution; 33 slices (3.5 + 0.5 mm gap), SENSE (GE ASSET) acceleration factor = 2). Whole-brain T_1-weighted anatomical images were acquired using an FSPGR sequence (FOV = 256 mm, TR = 7900 ms, TE = 3 ms, 172 contiguous sagittal slices, 1 mm^3 isotropic).

7T-ME

Two ten-minute eyes-closed rs-fMRI runs were acquired on a 7T Siemens MAGNETOM scanner (Siemens Healthcare GmbH, Erlangen, Germany) equipped with a single-channel transmit/32-channel receive head coil (Nova Medical, Wilmington, MA, United States). The CMRR SMS-EPI sequence (R015) (Moeller et al., 2010) was used to acquire multi-echo multiband EPI data with three echoes using the following parameters: Scan 1 – [TR = 1000 ms; $TE_{1/2/3}$ = 8.14/21.47/34.8 ms; flip angle (α) = 35°; FOV = 220 mm; 2.4 mm^2 in-plane resolution; 36 slices (2.5 mm thick); multiband factor = 4; GRAPPA acceleration factor = 2] and Scan 2 – [TR = 500 ms; $TE_{1/2/3}$ = 8.14/21.47/34.8 ms; flip angle (α) = 90°; FOV = 220 mm; 2.4 mm^2 in-plane resolution; six slices (2.5 mm thick); multiband factor = 1; GRAPPA acceleration factor = 2]. Whole brain T_1-weighted anatomical images were acquired using an MPRAGE sequence (FOV = 220 mm, TR = 2200 ms, TE = 3 ms, TI = 1050 ms, 224 contiguous sagittal slices, 0.7 mm^3 isotropic).

Physiological Monitoring

Concurrent physiological traces were recorded for all runs and sampled at 500 Hz (CED, Cambridge, United Kingdom). This included using photoplethysmography (PPG) to measure pulse waveforms for deriving cardiac information, a pneumatic respiratory belt for timing and relative respiration volume measures, capnography for measuring expired partial pressure of end-tidal carbon dioxide ($P_{ET}CO_2$). The CareTaker system (Biopac) was used to measure beat-to-beat blood pressure with a cuff attached to the first digit of the hand (thumb). The system uses the cuff to pneumatically sensor the arterial pressure wave, and estimates beat-to-beat systolic and diastolic blood pressure via analysis of the timing between different components of the pulse waveform (Baruch et al., 2011), and has been validated against gold standard arterial line measurements (Baruch et al., 2014).

Data Analysis

Preprocessing

Data were preprocessed and registered to a standard space using a pipeline created with AFNI, FSL, and in-house code. Preprocessing of 3T and 7T-ME data consisted of the same following steps: (1) De-spiking; (2) Motion correction by registering all volumes to the first one. For 7T-ME scans steps 1–2 were performed separately for each echo time dataset, then a nonlinear fit was performed to create S_0 and R_2* datasets (see section "Multi-Echo Fit" below). Subsequent steps were performed separately for S_0 and R_2* datasets. (3) Nuisance regression with pre-whitening (Bright et al., 2017) to remove cardiac and respiratory related noise (Glover et al., 2000; Birn et al., 2008; Chang et al., 2009), end-tidal CO_2 fluctuations (convolved with HRF), and six estimated motion parameters; (4) Slice time correction; (5) Non-linear registration to 2 mm MNI space; (6) De-trending and motion censoring in a single step, with the top 5% of volumes most severely corrupted by motion (according to framewise displacement) being censored. Censored time points were replaced with interpolated values calculated from neighboring (non-censored) time points (NTRP option in 3dTproject) in order to keep to the data temporally consistent for subsequent wavelet decomposition. A discrete wavelet transform was then performed on the preprocessed data (see section "Maximum Overlap Discrete Wavelet Transform" below). Note that physiological noise correction was performed on unfiltered data.

For each subject gray matter (GM) masks were created from segmented T_1 images, with GM voxels defined as those with a partial volume estimate greater than 66%. GM masks were used in subsequent parts of the analysis, and GM mask averaged time series were calculated for 3T and 7T-ME data for estimating the global lag with blood pressure (see section "Blood Pressure Correlation" below).

Multi-Echo Fit

Assuming a mono-exponential decay, the signal across multiple echo times can be described according to Eq. 1.

$$S(TE) = S_0 e^{-R_2^* TE} \quad (1)$$

Where S_0 is spin density weighted signal intensity at zero echo time and R_2* is the apparent transverse relaxation rate (inverse of relaxation time T_2*). S_0 is modulated by changes in apparent T_1 (e.g., due to inflow) and bulk motion and related spin history effects, whereas R_2* reflects magnetic field homogeneity and thus, due to blood oxygenation induced changes in microscopic susceptibility, the source of the BOLD effect (Buxton, 2013). NVC related functional responses in gradient-echo fMRI are considered to be driven almost entirely by R_2* changes, which has motivated the use of multi-echo acquisitions for separating neuronal from non-neuronal signal components (Posse, 2012; Kundu et al., 2017), based on the rationale that non-neuronal components (i.e., not flow related) are mostly restricted to changes in S_0. It should be noted that inflow effects on S_0 are driven by changes in flow velocity through an imaging slice, and so may partially reflect changes in CBF, however, this effect is

generally considered to be small in multi-slice acquisitions with standard TRs (Gao and Liu, 2012).

However, as discussed above, there are non-neuronal contributors to flow, whose activity in principle should manifest primarily in the form of R_2* changes. Ignoring the effects of macroscopic field inhomogeneity, more generally R_2* changes are driven by CBF dynamics (via the changes in blood oxygenation they produce), whether they are neuronally driven or not. The motivation for collecting 7T-ME data as part of this study is that it allows us to determine to what extent MAP-fMRI correlations are driven by changes in R_2* and S_0, and thus whether or not they are related to changes in CBF. Moreover, as S_0 is determined by the steady-state longitudinal magnetization it is intrinsically dependent on acquisition parameters like TR and flip angle. Thus, any significant S_0 fluctuations are likely to be modulated between 7T-ME scans 1 and 2, whereas R_2* fluctuations will not.

For each voxel and TR, 7T-ME data were fit to the mono-exponential signal model with a nonlinear least-squares approach using the Levenberg-Marquardt algorithm (Galassi, 2009), creating S_0 and R_2* datasets. In multi-echo fMRI studies numerous physical limitations restrict the number of echo times that can be achieved to a small number, in this case three, which presents a challenge for accurate estimation of relaxation rates (Gowland and Bowtell, 2007), and sample-by-sample parameter estimates are considered to be noisy (Kundu et al., 2012). Compared with previous studies, here we benefit from the higher SNR afforded by 7T to improve sample-by-sample parameter estimates, and we performed simulations to better understand the precision with which R_2* and S_0 can be measured using our nonlinear fit approach (details included in **Supplementary Material**). These simulations demonstrate that across the expected range of R_2* values, our choice of echo times allows us to estimate both R_2* and S_0 parameters without bias.

Maximum Overlap Discrete Wavelet Transform

Wavelet transforms provide a way of decomposing the total variance within a time series into different frequency scales [see Bullmore et al. (2004) for an fMRI focused review]. They are conceptually similar to Fourier transforms, but because wavelets are compactly supported (i.e., transient, not extending infinitely like sine waves), they provide sensitivity to non-stationary features within the scales of the decomposition. Thus, wavelet coefficients (WC) provide a "time-frequency" representation of data, including both temporal and spectral information, analogous to moving-window Fourier transforms. This makes the discrete wavelet transform useful for analyzing real-world physiological data, which are expected to be non-stationary, and the multi-resolution analysis allows signal energy to be decomposed into distinct frequency bands. Given that fluctuations in MAP are expected to show more power in certain frequency bands, likely reflecting different underlying mechanisms, in this study we used a wavelet transform to identify the frequency scale of interest for the relationship between MAP and fMRI signals.

For each voxel time series the maximum overlap discrete wavelet transform (MODWT) was used to decompose the signal into six scales (Witcher, 2015). The MODWT used a fourth-order Daubechies wavelet filter as has been used previously for fMRI applications (Bullmore et al., 2001; Patel and Bullmore, 2016). The central frequency (f_c) and band between lowest (f_{low}) and highest (f_{high}) frequencies contained within each scale (j) depends on the sampling rate (TR), and is given by Eqs 2 and 3.

$$f_{\text{low}} - f_{\text{high}} = \frac{1}{2^{(j+1)}TR} - \frac{1}{2^{j}TR} \tag{2}$$

$$f_{\text{c}} = \frac{f_{\text{low}} + f_{\text{high}}}{2} \tag{3}$$

In summary, each fMRI time series consisting of N volumes was decomposed into six frequency scales, each composed of N WCs. For reference the scale frequency bands for the TRs used in this study are given in **Table 1** and the frequency response of the filters at each scale are shown in **Supplementary Figure 1**.

Blood Pressure Correlation

Beat-to-beat systolic (SBP) and diastolic (DBP) blood pressure time series were processed in-house with a robust outlier removal procedure and resampled to the relevant TR. Mean arterial pressure (MAP) was estimated according to Eq. 4 (Brzezinski, 1990).

$$MAP = \frac{2}{3}(DBP) + \frac{1}{3}(SBP) \tag{4}$$

MAP time series were decomposed with a MODWT into the same six frequency scales as the fMRI data. **Figure 1** shows a MAP time series and its WCs for a representative subject. For each run the cross-correlation between the average gray matter signal and temporally displaced MAP signals was calculated. The raw cross-correlation functions were then fit to a set of Legendre polynomial functions of increasing order (until $R^2 > 0.95$, or up to a maximum order of 10) to obtain a smooth function from which the lag between MAP and fMRI fluctuations was obtained. Voxelwise correlations between MAP and scale matched fMRI WCs for all frequency scales were calculated with the globally optimized lag. Additionally, although more susceptible to noise, we calculated a voxelwise lag using the same procedure and then calculated corresponding correlations between MAP and scale matched fMRI WCs.

It should be noted that in contrast with the discrete wavelet transform (DWT), which is orthogonal (like the discrete Fourier

TABLE 1 | Table showing the frequency range (Hz) for each scale of the MODWT.

Scale	TR (s)		
	2	1	0.5
1	0.125–0.250	0.250–0.500	0.500–1.000
2	0.063–0.125	0.125–0.250	0.250–0.500
3	0.031–0.063	0.063–0.125	0.125–0.250
4	0.016–0.031	0.031–0.063	0.063–0.125
5	0.008–0.016	0.016–0.031	0.031–0.063
6	0.004–0.008	0.008–0.016	0.016–0.031

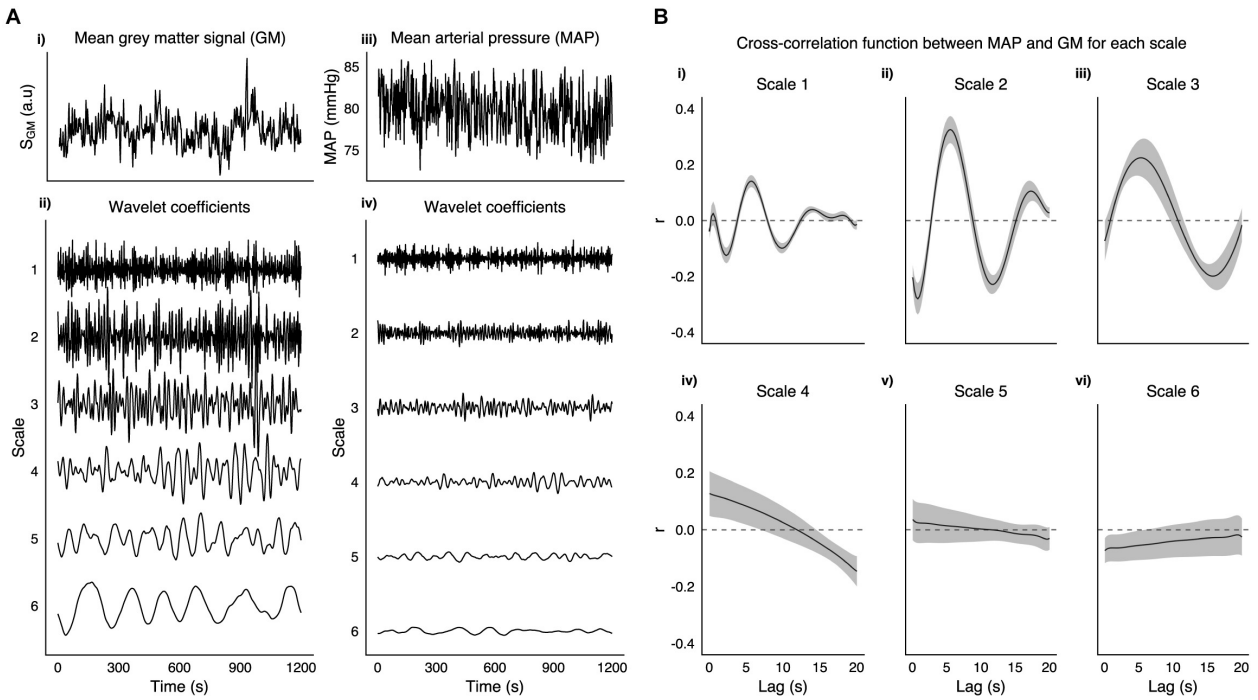

FIGURE 1 | A (i) Shows the mean gray matter signal from 3TSE data in a representative subject along with corresponding mean arterial pressure trace (iii). Wavelet coefficients at 6 scales are shown for both GM (ii) and MAP (iv). **(B)** Group mean cross-correlation function between MAP and GM for each scale (i–vi), with shaded area representing SEM.

transform), the MODWT is an oversampled transform in which there is some redundancy (i.e., coefficients are not completely independent). This means that the effective degrees of freedom are reduced, which impacts on statistical parameters. Additionally, the practice of filtering time series and allowing temporal shifts changes the null distribution of Pearson's correlations (Bright et al., 2017). To address these potential confounds on statistical inference we performed a permutation analysis to determine the correct null hypothesis. The approach, which has been used previously (Bright et al., 2017), estimates the null distribution with phase-randomized versions of the MAP time series. For each subject 1000 phase-randomized MAP traces were correlated with fMRI to get a voxel-wise estimate of the correlation null distribution from which p-values were calculated.

Group Level Analysis

For each frequency scale, subject level MAP - fMRI WC correlation maps were entered into an independent two-tailed t-test, from which group-level correlation and Z-score maps were derived. The mean GM correlation and Z-score values were calculated as a means of identifying the scale with the strongest MAP vs. fMRI coupling. Subsequent analyses of 7T-ME data are restricted to the scale with the matched frequency. Test–retest repeatability was assessed using spatial correlation between Scan 1 and Scan 2 for 3T. For 7T-ME data, Scan 2 parameters were chosen differently from Scan 1 from a theoretical perspective to maximize any potential inflow effect in the S_0 signal (Gao and Liu, 2012). For the different sources of image contrast, R_2* and S_0, to assess their relative contributions to MAP – fMRI correlations, the absolute value of average GM vs. MAP correlations were entered into a two way repeated measures ANOVA.

Note, that although a wavelet transform was used to decompose MAP and fMRI signals into different frequency scales, we also looked at the effect of MAP on unfiltered data by regressing unfiltered optimal lag MAP traces onto voxel-wise unfiltered fMRI data (see **Supplementary Figure 4**).

RESULTS

3T

Global Lag

Figure 1A, shows an example taken from a representative subject of GM and MAP traces, and their respective WCs at the six frequency scales listed in **Table 1**. **Figure 1B** shows the group mean cross-correlation functions between MAP and GM WC time series for each scale of the MODWT. Scales 1–3 all show clear maxima with a similar degree of lag (5.75, 5.50, and 5.25 s for scales 1–3, respectively).

MAP vs. fMRI Correlation

Voxelwise group average correlations (at optimal lag) are shown for scale 2 WCs only in **Figure 2C**, along with corresponding Z-scores in **Figure 2D**. **Figure 2A** shows the mean correlation values and Z-scores within the voxelwise group maps for all scales (at optimal lag), and it can be seen the scale 2 has

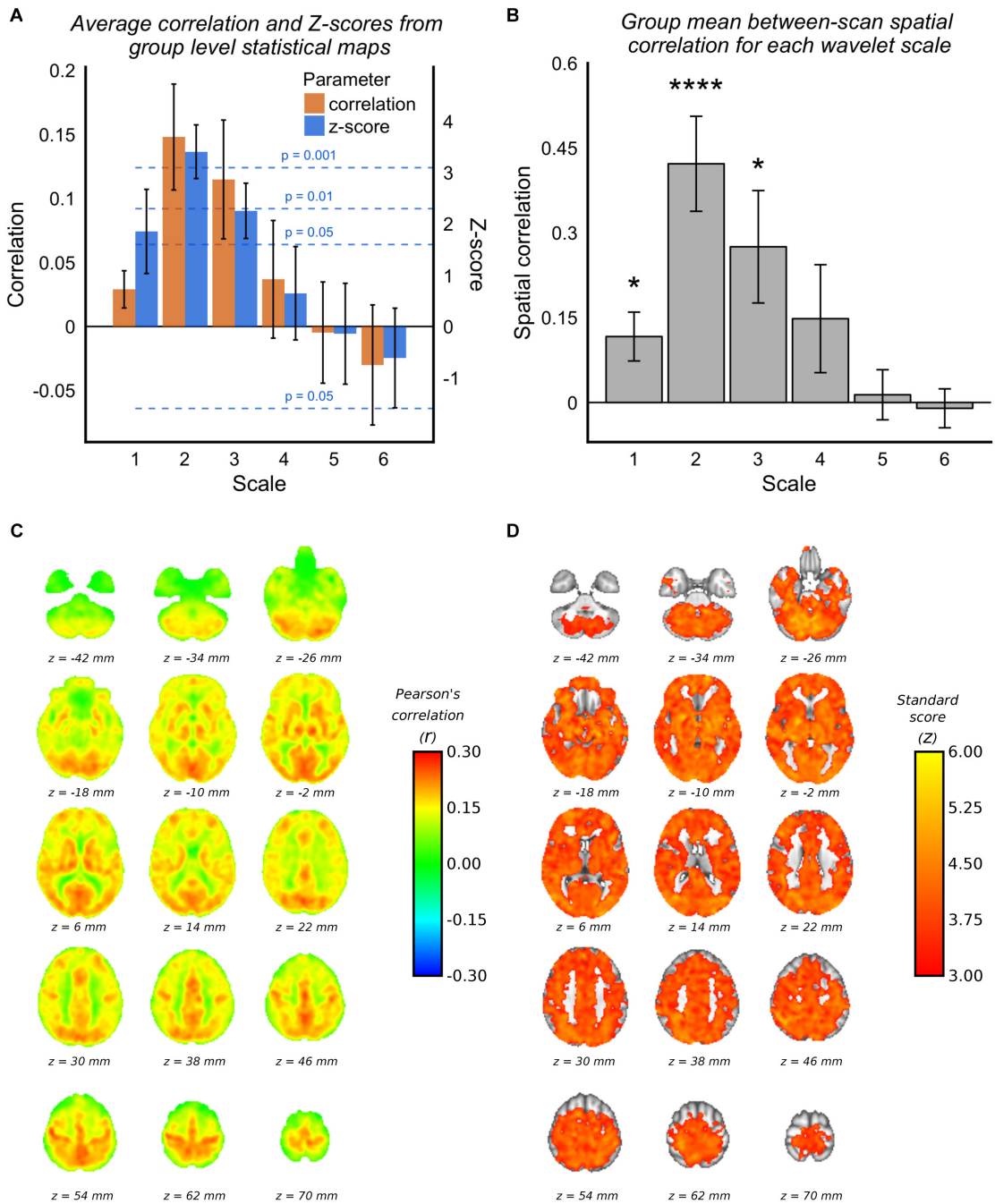

FIGURE 2 | 3TSE data. **(A)** Mean correlations and *Z*-scores (across voxels) from group mean statistical parameter maps for each scale. Dotted lines indicated the *p*-value for give *z*-score vales. **(B)** Spatial correlation scans 1 and 2 MAP-fMRI correlation maps for each scale (*$p < 0.05$, **$p < 0.01$, ***$p < 0.001$, and ****$p < 0.0001$). **(C)** Group mean MAP – fMRI correlation map for scale 2 WC and corresponding *Z*-scores. **(D)** Correlations are those at the optimal lag values as shown in **Figure 1**.

the highest mean correlation value and highest mean *Z*-score value. It can be seen by the standard deviation error bars that the majority of voxels at scale 2 have a *Z*-score >3.1 ($p = 0.001$). **Figure 2B** demonstrates that the spatial correlation between scans (i.e., within subject agreement) is also highest for scale 2 compared with the other scales. As documented in **Table 1**, the frequency band for scale 2 for 3TSE data (TR = 2s) is 0.063–0.125 Hz, which corresponds to a central frequency () of ∼0.1 Hz.

As stated in Section "Maximum Overlap Discrete Wavelet Transform", permutation tests based on phase-randomized MAP time series were used to estimate the correlation null distribution

for each subject on a voxel-wise basis. **Supplementary Figure 3A** shows the correlation null distributions estimated for each subject, and the mean GM correlation value. For each subject the null distribution is non-zero, as expected due to the effect of temporal shifting, but in every case the true mean GM correlation with MAP is more than three standard deviations removed from the null correlation. **Supplementary Figure 2** shows subject level correlation maps along with associated threshold permutation test *p*-values.

For reference, **Supplementary Figure 4** shows the estimated effect size of unfiltered MAP fluctuations on fMRI data. The average GM effect size across subjects (±SD) is 0.01% BOLD/mm Hg (±0.006). Across subjects the average absolute maximum deviation in MAP is ∼12 mm Hg, which suggests fairly modest total BOLD signal changes on the order of ∼0.12% are expected, but given the heterogeneity evident in **Supplementary Figure 4**, it is clear that in some regions this may be as large as ∼0.5%.

Voxelwise Lag

Figure 3A shows group level MAP – fMRI correlations as a function of lag with respect to MAP. It shows how a spatially structured pattern of fMRI signal changes evolves over time in response to MAP fluctuations. **Figures 3B,C** shows the maximum correlation and the lag at which it is seen, respectively. The lag time in cortical gray matter appears relatively uniformly distributed at ∼5 s, in good agreement with the GM signal global lags shown in **Figure 1**. Interestingly, there is a correlation pattern that emerges earlier (∼2–4 s), which appears in deep white matter structures and in the areas bordering the lateral ventricles. **Figure 3B** shows that there are widespread correlations with MAP, albeit with different lags, extending across the whole brain.

7T

The 7T-ME data allows us to tease apart the different sources of contrast underlying the MAP – fMRI correlations. **Figure 4A** shows group level voxelwise MAP – R_2* and MAP – S_0 correlations for Scan 1 and Scan 2. R_2* – MAP correlations show a similar pattern to 3T fMRI – MAP correlations, with well defined gray/white matter contrast and matching areas of high magnitude correlations (e.g., in occipital cortex). Note that negative R_2* – MAP correlations are equivalent to positive MAP – fMRI (3T) correlations, as a decrease in R_2* corresponds to a lengthening of T_2* and a positive increase in BOLD signal. **Figure 4B** shows the spatial correlations between R_2* – MAP and S_0 – MAP correlation maps, and 3T BOLD – MAP correlation maps. Compared with S_0 – MAP correlations, R_2* – MAP correlation maps are more spatially similar to 3T BOLD – MAP correlation maps, with a Pearson's correlation of −0.68 vs. 0.33 of S_0 – MAP, which amounts to ∼4 times as much variance explained. Note that the negative correlation in **Figure 4Bi** is due to the inverse relationship between R_2* and the BOLD signal (a BOLD signal increase results from less dephasing, i.e., a decrease in relaxation rate).

Figure 4C shows the group mean GM absolute correlation values for R_2* and S_0 scans 1 and 2. A two-way repeated measures ANOVA revealed a significant effect of contrast (R_2* > S_0), but no effect of scan. Following the rationale outlined in Section "Multi-Echo Fit," this would suggest that the MAP correlated fMRI signal has a BOLD origin related to changes in CBF. Furthermore, there appears to be minimal non-BOLD contribution, as scan number did not significantly modulate the MAP-S_0 correlation values.

DISCUSSION

Blood Pressure Correlation

To our knowledge, this study is first to demonstrate that MAP LFOs are positively correlated with fMRI LFOs within the frequency band between 0.063 and 0.125 Hz. These correlations appear highly spatially structured, with strong gray/white matter contrast, and are repeatable between subjects with a spatial correlation of ∼0.42. Results from the 7T-ME data suggest that fluctuations in MAP lead to gray matter signal fluctuations in BOLD fMRI that are primarily related to CBF, given that they are related to changes in R_2* and relatively independent of acquisition parameters. This is consistent with a large TCD literature that shows beat-to-beat fluctuations in blood pressure result in measurable changes in CBFV in large intracranial arteries (Aaslid et al., 1989; Diehl et al., 1991; Blaber et al., 1997; Kuo et al., 1998; Zhang et al., 1998), lagged by ∼2 s, with MAP preceding cerebral blood flow velocity (CBFV). As BOLD fMRI is sensitive to deoxygenated blood volume compartments (i.e., capillary and venous) that are downstream of large intracranial arteries that are insonated with TCD, one might assume an extended delay that would allow changes to propagate along the vasculature tree. Given the obvious logic of this, the fact that the true results show that fMRI precedes MAP by ∼5.5 s most likely reflects differences in how MAP is measured in this study compared with previous reports. Continuous non-invasive MAP measurement ismost often done with the Finapres system. However, as this is not MRI compatible we instead used the Caretaker system, from which beat-to-beat blood pressure is estimated from an analysis of the pulse wave in the periphery. Although the Caretaker is validated against invasive arterial line measurement (Baruch et al., 2014), and shows good agreement, this study does not include any investigation of timing differences. However, as it is based on Pulsewave Decomposition Analysis (PDA) of the peripheral arterial pressure wave, transit time differences must be considered.

Instantaneous blood pressure is an idealized concept, as in reality local changes in pressure take time to propagate along the vascular tree, which depends on stiffness of the different arterial vascular beds (Chen et al., 2009). As such, all blood pressure measurements are temporally shifted surrogates of the true aortic value, by which MAP is usually defined. Beat-to-beat blood pressure is predominantly regulated in response to the activity of baroreceptors, which are located in the aortic arch and carotid sinus. Thus, pressure changes are detected centrally, which leads to systemic changes in the downstream vasculature in response. The self-evident logic of cerebral autoregulation is that cerebral hemodynamics change in response to fluctuations MAP. Thus, although we have observed fMRI

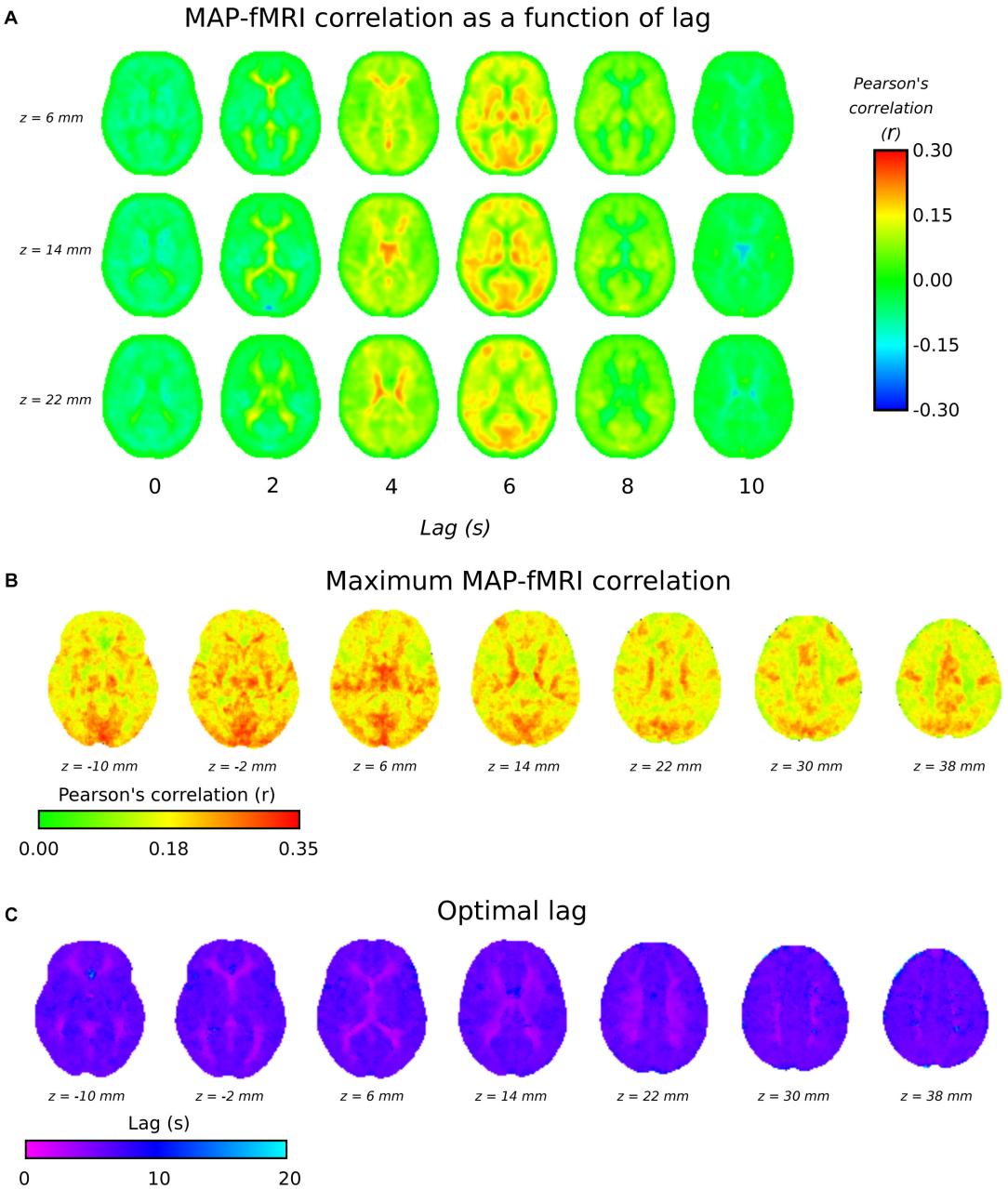

FIGURE 3 | 3TSE data. **(A)** MAP – fMRI as a function of lag with respect to MAP, in 2 s intervals. **(B)** The maximum correlation (i.e., arg max of cross-correlation function) and the associated lag time **(C)**.

signals that precede MAP signals, it seems very unlikely that this is a causative effect. It is more likely that the lag, in which fMRI precedes Caretaker MAP, can be explained by systemic vascular transit time differences. Furthermore, this suggests one should be cautious about interpreting lags between cerebral and peripheral hemodynamics, as they likely depend on the complex interaction of multiple factors, including stiffness of the different arterial vascular beds, and the interplay between autonomic and myogenic activity. Furthermore, the lag time would be expected to account for the fact the flow changes will take time to propagate along the vascular tree. Delayed fMRI responses to hypercapnia challenges are frequently observed on the order of 8–15 s (Blockley et al., 2011; Murphy et al., 2011), although potentially longer in patient groups (Duffin et al., 2015; Donahue et al., 2016), and are presumed to contain both gas bolus transit time and vascular reactivity information. However, untangling the different factors that influence these timing differences could present an interesting new avenue of research. Central (aortic) arterial stiffness is likely to contribute greatly to the measured lag, and so experiments that can separate these general systemic

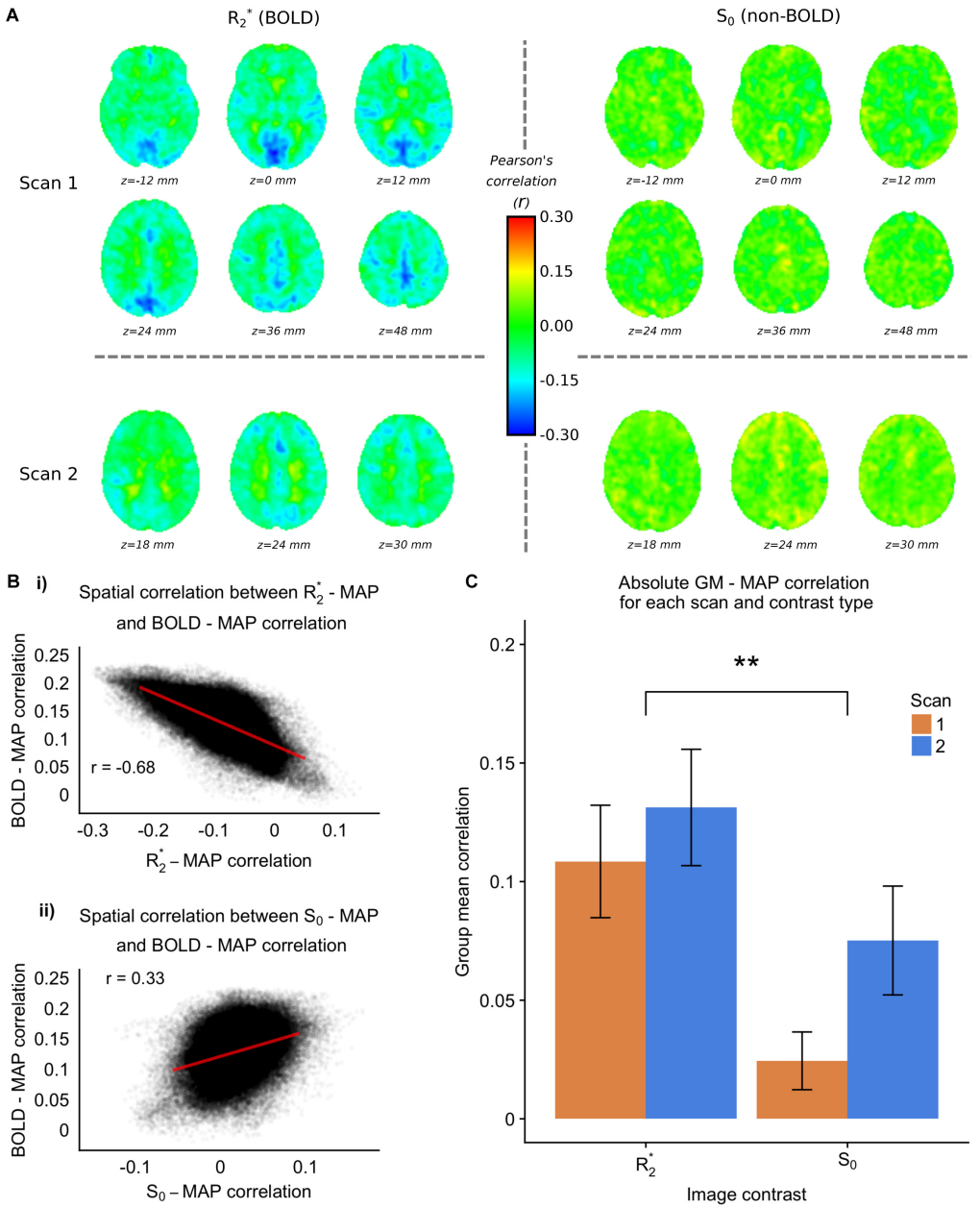

FIGURE 4 | 7TME data. **(A)** group level MAP – fMRI correlation maps for R_2* and S_0 and scans 1 and 2, at the frequency scale corresponding to 0.063 – 0.125 Hz (scales 3 and 4 for scans 1 and 2 respectively). **(B)** (i) Spatial correlation between 7TME MAP – R_2* correlation maps, and 3TSE MAP – fMRI correlation maps. (ii) Spatial correlation between 7TME MAP – S_0 correlation maps, and 3TSE MAP – fMRI correlation maps. **(C)** Bar chart showing group mean GM correlations (absolute value) for R_2*/S_0 and scans 1 and 2 (*$p < 0.05$, **$p < 0.01$).

effects from more specific cerebral vascular ones are desirable, and there are novel MRI methods for quantifying aortic stiffness would allow for this to be done within the same imaging session (Fielden et al., 2008; Grotenhuis et al., 2009; Langham et al., 2011). The voxelwise lag analysis shows that lag times for white matter are shorter than gray matter. Considering the correct directionality of the lag structure, this perhaps make sense, as it suggests that fluctuations in gray matter are followed by fluctuations in white matter, and finally by fluctuations in peripheral MAP measurements. Thus, this is consistent with the fMRI literature showing low frequency fMRI signals of systemic origin that are delayed in white matter, as blood arrival time is extended with respect to gray matter (van Gelderen et al., 2008).

From these data we cannot know the exact origin of these BP correlated fMRI fluctuations. Previous fMRI studies have found signal fluctuations that are correlated with peripheral measures of vascular tone, such as NIRS in fingers/toes (Tong and Frederick, 2010; Tong et al., 2012, 2013) or amplitude of

photoplethysmography (PPG) (van Houdt et al., 2010; Ozbay et al., 2018). These observations support the existence of endogenous systemic LFOs, which propagate throughout the entire cardiovascular system, appearing as synchronized, but out of phase, oscillations at different vascular sites. A common systemic source is one explanation for the MAP correlated fMRI signals we have measured, and a potential candidate for this systemic origin is SNA. The MODWT reveals that MAP coupled fMRI LFOs are strongest in the frequency band centered at ∼0.1 Hz, the frequency of Mayer waves, which are defined in terms of their coherence with SNA (Julien, 2006). SNA regulates blood pressure via modulation of peripheral vascular tone (Fisher and Paton, 2012), but also potentially influences cerebrovascular tone (Brassard et al., 2017), and increases in SNA elicited by post exercise induced ischemia have been shown to decrease compliance in the brain's major arteries (Warnert et al., 2016). Orthostatic challenges such as lower body negative pressure (LBNP), which are associated with increases in SNA, lead to considerable reductions in MCA CBFV (Levine et al., 1994; Serrador et al., 2000; Zhang and Levine, 2007), and reductions in blood volume indicative of vasoconstriction in the brain's largest arteries (Whittaker et al., 2017). Furthermore, studies have shown that ganglion blockade designed to dampen SNA, significantly alter the dynamics between MAP and CBFV (Zhang et al., 2002; Mitsis et al., 2009), suggesting autonomic neural control cerebrovascular tone likely plays a role in beat-to-beat CBF regulation.

Cerebral Autoregulation

The time scale of the BP correlated LFO and its basis predominantly being changes in apparent transverse relaxation is strongly indicative of a CBF related cause. Compared with respiratory challenges for which the CBF response primarily probes CVR, the observed flow response associated with BP is likely to be related to the process of CA. Thus, whereas CVR is a measure of localized vascular integrity, i.e., the ability of arterial vessels to change their resistance, measures of CA relate to the systemic orchestrated vascular mechanisms that regulate CBF (Carrera et al., 2009). The LFO fluctuations we have observed in this study are correlated with BP measured in the periphery, and so are more related to CA than CVR. Impairments in CA associated with adverse cerebrovascular events such as ischaemic stroke and severe head injury have been well studied (Panerai, 2008), and are increasingly thought to play a role in the development of vascular dementia (Toth et al., 2017) and Alzheimer's disease (Claassen and Zhang, 2011; den Abeelen et al., 2014). Despite the widespread clinical implications of pathological CA, its underlying mechanisms are still relatively poorly understood.

TCD is the most widely used modality for measuring CA, which despite having excellent temporal resolution and high suitability for clinical settings, is ultimately of limited value since the measurements are restricted to only the largest intracranial arteries. In contrast, fMRI has whole-brain sensitivity with millimeter resolution and so is a desirable tool for better understanding CA, and has the potential to deliver more predictive clinical measures. For example, CA is critical for keeping stable CBF in the penumbra region following ischemic stroke (Xiong et al., 2017), so a method such as fMRI, which has the spatial resolution to resolve localized alterations, is promising as a more informative prognostic tool. In the TCD literature the transfer function between BP and CBFV is used to characterize CA, primarily through gain and phase shift. It is commonly assumed that a phase shift and low gain constitutes good cerebral autoregulation (i.e., CBFV fluctuations are delayed with respect to BP and are dampened) (van Beek et al., 2008). In this study we observed a lag in MAP with respect to fMRI, i.e., fMRI precedes MAP, which may be related to the phase shifts measured in TCD. Furthermore, although the effect-size of MAP on fMRI measured here appears small (**Supplementary Figure 4**), this may be due to the young healthy subject group. In patient groups with less effective CA both effect-size and lag may be modulated.

Effect on Resting-State fMRI

This study provides the first step in characterizing the relationship between MAP and the fMRI signal, but further work is needed to address the degree to which MAP impacts functional connectivity measures. The estimated effect size on unfiltered data is relatively modest (∼0.01% BOLD/mm Hg), which across subjects on average amounts to total BOLD signal changes on the order of ∼0.1% across all gray matter, although total signal changes as large ∼0.5% are possible, depending on individual subject response variability. The results of the wavelet transformed data show that MAP fluctuations effect fMRI within a particular frequency band, and as in practice resting-state fMRI analyses never use raw unfiltered data, it is likely that the effect of MAP on functional connectivity metrics will depend on a variety of analysis choices, such as filter passband or window length in dynamic connectivity studies. These data also serve as a reminder that not all sources of BOLD contrast are neuronal in origin, and so multi-echo based approaches like ME-ICA (Kundu et al., 2012) are likely to be less effective. An interesting avenue of future research would be look at the effect of different echo combination and de-noising schemes to determine their impact.

CONCLUSION

In this study we have shown that beat-to-beat fluctuations in BP are correlated with fluctuations in the resting-state fMRI that precede them by approximately 5.5 s, and which are strongest at the frequency band centered at ∼0.1 Hz. Using a multi-echo acquisition we were able to isolate the pure BOLD (R_2*) component of the BP correlated fMRI signal and have shown that it is the main source of contrast. This would indicate that it is changes in CBF that mediate this low frequency BP correlated signal, which we hypothesize is related to the process of CA. We propose that resting-state fMRI is a promising new tool for assessment of dynamic CA with high spatial resolution, which

may prove to be a useful biomarker in a range of cerebrovascular and neurological conditions.

ETHICS STATEMENT

The School of Psychology Cardiff University Ethics Committee approved the study in accordance with the guidelines stated in the Cardiff University Research Framework (version 4.0, 2010).

AUTHOR CONTRIBUTIONS

JW and KM conceived of the presented idea. JW, ID, MV, and MB collected the data. JW analyzed the data. All the authors provided critical feedback and helped shape the research, analysis, and manuscript.

FUNDING

This work was supported by the Wellcome Trust [WT200804].

SUPPLEMENTARY MATERIAL

The Supplementary Material for this article can be found online at: https://www.frontiersin.org/articles/10.3389/fnins.2019.00433/full#supplementary-material

REFERENCES

Aaslid, R., Lindegaard, K. F., Sorteberg, W., and Nornes, H. (1989). Cerebral autoregulation dynamics in humans. *Stroke* 20, 45–52. doi: 10.1161/01.str.20.1.45

Baruch, M. C., Kalantari, K., Gerdt, D. W., and Adkins, C. M. (2014). Validation of the pulse decomposition analysis algorithm using central arterial blood pressure. *Biomed. Eng. Online* 13:96. doi: 10.1186/1475-925X-13-96

Baruch, M. C., Warburton, D. E., Bredin, S. S., Cote, A., Gerdt, D. W., and Adkins, C. M. (2011). Pulse decomposition analysis of the digital arterial pulse during hemorrhage simulation. *Nonlinear Biomed. Phys.* 5:1. doi: 10.1186/1753-4631-5-1

Battisti-Charbonney, A., Fisher, J., and Duffin, J. (2011). The cerebrovascular response to carbon dioxide in humans. *J. Physiol.* 589, 3039–3048. doi: 10.1113/jphysiol.2011.206052

Birn, R. M., Smith, M. A., Jones, T. B., and Bandettini, P. A. (2008). The respiration response function: the temporal dynamics of fMRI signal fluctuations related to changes in respiration. *Neuroimage* 40, 644–654. doi: 10.1016/j.neuroimage.2007.11.059

Blaber, A. P., Bondar, R. L., Stein, F., Dunphy, P. T., Moradshahi, P., Kassam, M. S., et al. (1997). Transfer function analysis of cerebral autoregulation dynamics in autonomic failure patients. *Stroke* 28, 1686–1692. doi: 10.1161/01.str.28.9.1686

Blockley, N. P., Driver, I. D., Francis, S. T., Fisher, J. A., and Gowland, P. A. (2011). An improved method for acquiring cerebrovascular reactivity maps. *Magn. Reson. Med.* 65, 1278–1286. doi: 10.1002/mrm.22719

Brassard, P., Tymko, M. M., and Ainslie, P. N. (2017). Sympathetic control of the brain circulation: appreciating the complexities to better understand the controversy. *Auton. Neurosci.* 207, 37–47. doi: 10.1016/j.autneu.2017.05.003

Bright, M. G., Bianciardi, M., de Zwart, J. A., Murphy, K., and Duyn, J. H. (2014). Early anti-correlated BOLD signal changes of physiologic origin. *Neuroimage* 87, 287–296. doi: 10.1016/j.neuroimage.2013.10.055

Bright, M. G., Tench, C. R., and Murphy, K. (2017). Potential pitfalls when denoising resting state fMRI data using nuisance regression. *Neuroimage* 154, 159–168. doi: 10.1016/j.neuroimage.2016.12.027

Brzezinski, W. A. (1990). "Blood pressure," in *Clinical Methods: The History, Physical, and Laboratory Examinations*, eds H. K. Walker and J. W. Hurst (Boston, MA: Butterworths).

Bullmore, E., Fadili, J., Maxim, V., Sendur, L., Whitcher, B., Suckling, J., et al. (2004). Wavelets and functional magnetic resonance imaging of the human brain. *Neuroimage* 23(Suppl. 1), S234–S249.

Bullmore, E., Long, C., Suckling, J., Fadili, J., Calvert, G., Zelaya, F., et al. (2001). Colored noise and computational inference in neurophysiological (fMRI) time series analysis: resampling methods in time and wavelet domains. *Hum. Brain Mapp.* 12, 61–78. doi: 10.1002/1097-0193(200102)12:2<61::aid-hbm1004>3.0.co;2-w

Buxton, R. B. (2013). The physics of functional magnetic resonance imaging (fMRI). *Rep. Prog. Phys.* 76:096601. doi: 10.1088/0034-4885/76/9/096601

Carrera, E., Lee, L. K., Giannopoulos, S., and Marshall, R. S. (2009). Cerebrovascular reactivity and cerebral autoregulation in normal subjects. *J. Neurol. Sci.* 285, 191–194. doi: 10.1016/j.jns.2009.06.041

Chang, C., Cunningham, J. P., and Glover, G. H. (2009). Influence of heart rate on the BOLD signal: the cardiac response function. *Neuroimage* 44, 857–869. doi: 10.1016/j.neuroimage.2008.09.029

Chen, Y., Wen, C., Tao, G., Bi, M., and Li, G., (2009). Continuous and noninvasive blood pressure measurement: a novel modeling methodology of the relationship between blood pressure and pulse wave velocity. *Ann. Biomed. Eng.* 37, 2222–2233. doi: 10.1007/s10439-009-9759-1

Claassen, J. A., and Zhang, R. (2011). Cerebral autoregulation in Alzheimer's disease. *J. Cereb. Blood Flow Metab.* 31, 1572–1577. doi: 10.1038/jcbfm.2011.69

den Abeelen, A. S., Lagro, J., van Beek, A. H., and Claassen, J. A. (2014). Impaired cerebral autoregulation and vasomotor reactivity in sporadic Alzheimer's disease. *Curr. Alzheimer Res.* 11, 11–17. doi: 10.2174/1567205010666131119234845

Diehl, R. R., Diehl, B., Sitzer, M., and Hennerici, M. (1991). Spontaneous oscillations in cerebral blood flow velocity in normal humans and in patients with carotid artery disease. *Neurosci. Lett.* 127, 5–8. doi: 10.1016/0304-3940(91)90880-3

Donahue, M. J., Strother, M. K., Lindsey, K. P., Hocke, L. M., Tong, Y., and Frederick, B. D. (2016). Time delay processing of hypercapnic fMRI allows quantitative parameterization of cerebrovascular reactivity and blood flow delays. *J. Cereb. Blood Flow Metab.* 36, 1767–1779. doi: 10.1177/0271678x15608643

Duffin, J., Sobczyk, O., Crawley, A. P., Poublanc, J., Mikulis, D. J., and Fisher, J. A. (2015). The dynamics of cerebrovascular reactivity shown with transfer function analysis. *Neuroimage* 114, 207–216. doi: 10.1016/j.neuroimage.2015.04.029

Erdogan, S. B., Tong, Y., Hocke, L. M., Lindsey, K. P., and de, B. F. B. (2016). Correcting for blood arrival time in global mean regression enhances functional connectivity analysis of resting state fMRI-BOLD Signals. *Front. Hum. Neurosci.* 10:311. doi: 10.3389/fnhum.2016.00311

Fielden, S. W., Fornwalt, B. K., Jerosch-Herold, M., Eisner, R. L., Stillman, A. E., and Oshinski, J. N. (2008). A new method for the determination of aortic pulse wave velocity using cross-correlation on 2D PCMR velocity data. *J. Magn. Reson. Imaging* 27, 1382–1387. doi: 10.1002/jmri.21387

Fisher, J. P., and Paton, J. F. (2012). The sympathetic nervous system and blood pressure in humans: implications for hypertension. *J. Hum. Hypertens.* 26, 463–475. doi: 10.1038/jhh.2011.66

Galassi, M. (2009). *GNU Scientific Library Reference Manual*, 3rd Edn. Massachusetts, MA: Network Theory Ltd.

Gao, J. H., and Liu, H. L. (2012). Inflow effects on functional MRI. *Neuroimage* 62, 1035–1039. doi: 10.1016/j.neuroimage.2011.09.088

Glover, G. H., Li, T. Q., and Ress, D. (2000). Image-based method for retrospective correction of physiological motion effects in fMRI: RETROICOR. *Magn. Reson. Med.* 44, 162–167. doi: 10.1002/1522-2594(200007)44:1<162::aid-mrm23>3.3.co;2-5

Golestani, A. M., Wei, L. L., and Chen, J. J. (2016). Quantitative mapping of cerebrovascular reactivity using resting-state BOLD fMRI: validation in healthy adults. *Neuroimage* 138, 147–163. doi: 10.1016/j.neuroimage.2016.05.025

Gowland, P. A., and Bowtell, R. (2007). Theoretical optimization of multi-echo fMRI data acquisition. *Phys. Med. Biol.* 52, 1801–1813. doi: 10.1088/0031-9155/52/7/003

Grotenhuis, H. B., Westenberg, J. J., Steendijk, P., van der Geest, R. J., Ottenkamp, J., Bax, J. J., et al. (2009). Validation and reproducibility of aortic pulse wave velocity as assessed with velocity-encoded MRI. *J. Magn. Reson. Imaging* 30, 521–526. doi: 10.1002/jmri.21886

Julien, C. (2006). The enigma of mayer waves: facts and models. *Cardiovasc. Res.* 70, 12–21. doi: 10.1016/j.cardiores.2005.11.008

Kundu, P., Inati, S. J., Evans, J. W., Luh, W. M., and Bandettini, P. A. (2012). Differentiating BOLD and non-BOLD signals in fMRI time series using multi-echo EPI. *Neuroimage* 60, 1759–1770. doi: 10.1016/j.neuroimage.2011.12.028

Kundu, P., Voon, V., Balchandani, P., Lombardo, M. V., Poser, B. A., and Bandettini, P. A. (2017). Multi-echo fMRI: a review of applications in fMRI denoising and analysis of BOLD signals. *Neuroimage* 154, 59–80. doi: 10.1016/j.neuroimage.2017.03.033

Kuo, T. B., Chern, C. M., Sheng, W. Y., Wong, W. J., and Hu, H. H. (1998). Frequency domain analysis of cerebral blood flow velocity and its correlation with arterial blood pressure. *J. Cereb. Blood Flow Metab.* 18, 311–318. doi: 10.1097/00004647-199803000-00010

Langham, M. C., Li, C., Magland, J. F., and Wehrli, F. W. (2011). Nontriggered MRI quantification of aortic pulse-wave velocity. *Magn. Reson. Med.* 65, 750–755. doi: 10.1002/mrm.22651

Levine, B. D., Giller, C. A., Lane, L. D., Buckey, J. C., and Blomqvist, C. G. (1994). Cerebral versus systemic hemodynamics during graded orthostatic stress in humans. *Circulation* 90, 298–306. doi: 10.1161/01.cir.90.1.298

Mayer, S. (1876). Studien zur physiologie des herzens und der blutgefässe. *Sitz Kaiser Akad Wiss* 74, 281–307.

Mitsis, G. D., Poulin, M. J., Robbins, P. A., and Marmarelis, V. Z. (2004). Nonlinear modeling of the dynamic effects of arterial pressure and CO2 variations on cerebral blood flow in healthy humans. *IEEE Trans. Biomed. Eng.* 51, 1932–1943. doi: 10.1109/tbme.2004.834272

Mitsis, G. D., Zhang, R., Levine, B. D., Tzanalaridou, E., Katritsis, D. G., and Marmarelis, V. Z. (2009). Autonomic neural control of cerebral hemodynamics. *IEEE Eng. Med. Biol. Mag.* 28, 54–62. doi: 10.1109/MEMB.2009.934908

Moeller, S., Yacoub, E., Olman, C. A., Auerbach, E., Strupp, J., Harel, N., et al. (2010). Multiband multislice GE-EPI at 7 tesla, with 16-fold acceleration using partial parallel imaging with application to high spatial and temporal whole-brain fMRI. *Magn. Reson. Med.* 63, 1144–1153. doi: 10.1002/mrm.22361

Murphy, K., Birn, R. M., and Bandettini, P. A. (2013). Resting-state fMRI confounds and cleanup. *Neuroimage* 80, 349–359. doi: 10.1016/j.neuroimage.2013.04.001

Murphy, K., Harris, A. D., and Wise, R. G. (2011). Robustly measuring vascular reactivity differences with breath-hold: normalising stimulus-evoked and resting state BOLD fMRI data. *Neuroimage* 54, 369–379. doi: 10.1016/j.neuroimage.2010.07.059

Nilsson, H., and Aalkjaer, C. (2003). Vasomotion: mechanisms and physiological importance. *Mol. Interv.* 3, 79–89, 51.

Obrig, H., Neufang, M., Wenzel, R., Kohl, M., Steinbrink, J., Einhaupl, K., et al. (2000). Spontaneous low frequency oscillations of cerebral hemodynamics and metabolism in human adults. *Neuroimage* 12, 623–639. doi: 10.1006/nimg.2000.0657

Ozbay, P. S., Chang, C., Picchioni, D., Mandelkow, H., Moehlman, T. M., Chappel-Farley, M. G., et al. (2018). Contribution of systemic vascular effects to fMRI activity in white matter. *Neuroimage* 176, 541–549. doi: 10.1016/j.neuroimage.2018.04.045

Panerai, R. B. (2008). Cerebral autoregulation: from models to clinical applications. *Cardiovasc. Eng.* 8, 42–59. doi: 10.1007/s10558-007-9044-6

Panerai, R. B., Hudson, V., Fan, L., Mahony, P., Yeoman, P. M., Hope, T., et al. (2002). Assessment of dynamic cerebral autoregulation based on spontaneous fluctuations in arterial blood pressure and intracranial pressure. *Physiol. Meas.* 23, 59–72. doi: 10.1088/0967-3334/23/1/306

Patel, A. X., and Bullmore, E. T. (2016). A wavelet-based estimator of the degrees of freedom in denoised fMRI time series for probabilistic testing of functional connectivity and brain graphs. *Neuroimage* 142, 14–26. doi: 10.1016/j.neuroimage.2015.04.052

Pillai, J. J., and Mikulis, D. J. (2015). Cerebrovascular reactivity mapping: an evolving standard for clinical functional imaging. *AJNR Am. J. Neuroradiol.* 36, 7–13. doi: 10.3174/ajnr.A3941

Posse, S. (2012). Multi-echo acquisition. *Neuroimage* 62, 665–671. doi: 10.1016/j.neuroimage.2011.10.057

Qiao, M., Rushforth, D., Wang, R., Shaw, R. A., Tomanek, B., Dunn, J. F., et al. (2007). Blood-oxygen-level-dependent magnetic resonance signal and cerebral oxygenation responses to brain activation are enhanced by concurrent transient hypertension in rats. *J. Cereb. Blood Flow Metab.* 27, 1280–1289. doi: 10.1038/sj.jcbfm.9600436

Rayshubskiy, A., Wojtasiewicz, T. J., Mikell, C. B., Bouchard, M. B., Timerman, D., Youngerman, B. E., et al. (2014). Direct, intraoperative observation of ∼0.1 Hz hemodynamic oscillations in awake human cortex: implications for fMRI. *Neuroimage* 87, 323–331. doi: 10.1016/j.neuroimage.2013.10.044

Serrador, J. M., Picot, P. A., Rutt, B. K., Shoemaker, J. K., and Bondar, R. L. (2000). MRI measures of middle cerebral artery diameter in conscious humans during simulated orthostasis. *Stroke* 31, 1672–1678. doi: 10.1161/01.str.31.7.1672

Tong, Y., and Frederick, B. D. (2010). Time lag dependent multimodal processing of concurrent fMRI and near-infrared spectroscopy (NIRS) data suggests a global circulatory origin for low-frequency oscillation signals in human brain. *Neuroimage* 53, 553–564. doi: 10.1016/j.neuroimage.2010.06.049

Tong, Y., Hocke, L. M., Licata, S. C., and Frederick, B. (2012). Low-frequency oscillations measured in the periphery with near-infrared spectroscopy are strongly correlated with blood oxygen level-dependent functional magnetic resonance imaging signals. *J. Biomed. Opt.* 17:106004. doi: 10.1117/1.JBO.17.10.106004

Tong, Y., Hocke, L. M., Nickerson, L. D., Licata, S. C., Lindsey, K. P., and Frederick, B. (2013). Evaluating the effects of systemic low frequency oscillations measured in the periphery on the independent component analysis results of resting state networks. *Neuroimage* 76, 202–215. doi: 10.1016/j.neuroimage.2013.03.019

Toth, P., Tarantini, S., Csiszar, A., and Ungvari, Z. (2017). Functional vascular contributions to cognitive impairment and dementia: mechanisms and consequences of cerebral autoregulatory dysfunction, endothelial impairment, and neurovascular uncoupling in aging. *Am. J. Physiol. Heart Circ. Physiol.* 312, H1–H20. doi: 10.1152/ajpheart.00581.2016

Uchida, S., Bois, S., Guillemot, J. P., Leblond, H., and Piche, M. (2017). Systemic blood pressure alters cortical blood flow and neurovascular coupling during nociceptive processing in the primary somatosensory cortex of the rat. *Neuroscience* 343, 250–259. doi: 10.1016/j.neuroscience.2016.12.014

van Beek, A. H., Claassen, J. A., Rikkert, M. G., and Jansen, R. W. (2008). Cerebral autoregulation: an overview of current concepts and methodology with special focus on the elderly. *J. Cereb. Blood Flow Metab.* 28, 1071–1085. doi: 10.1038/jcbfm.2008.13

van Gelderen, P., de Zwart, J. A., and Duyn, J. H. (2008). Pittfalls of MRI measurement of white matter perfusion based on arterial spin labeling. *Magn. Reson. Med.* 59, 788–795. doi: 10.1002/mrm.21515

van Houdt, P. J., Ossenblok, P. P., Boon, P. A., Leijten, F. S., Velis, D. N., Stam, C. J., et al. (2010). Correction for pulse height variability reduces physiological noise in functional MRI when studying spontaneous brain activity. *Hum. Brain Mapp.* 31, 311–325. doi: 10.1002/hbm.20866

Wang, R., Foniok, T., Wamsteeker, J. I., Qiao, M., Tomanek, B., Vivanco, R. A., et al. (2006). Transient blood pressure changes affect the functional magnetic resonance imaging detection of cerebral activation. *Neuroimage* 31, 1–11. doi: 10.1016/j.neuroimage.2005.12.004

Warnert, E. A., Hart, E. C., Hall, J. E., Murphy, K., and Wise, R. G. (2016). The major cerebral arteries proximal to the circle of willis contribute to cerebrovascular resistance in humans. *J. Cereb. Blood Flow Metab.* 36, 1384–1395. doi: 10.1177/0271678X15617952

Whittaker, J. R., Bright, M. G., Driver, I. D., Babic, A., Khot, S., and Murphy, K. (2017). Changes in arterial cerebral blood volume during lower body negative pressure measured with MRI. *Neuroimage* 187, 166–175. doi: 10.1016/j.neuroimage.2017.06.041

Willie, C. K., Colino, F. L., Bailey, D. M., Tzeng, Y. C., Binsted, G., Jones, L. W., et al. (2011). Utility of transcranial doppler ultrasound for the integrative

assessment of cerebrovascular function. *J. Neurosci. Methods* 196, 221–237. doi: 10.1016/j.jneumeth.2011.01.011

Willie, C. K., Tzeng, Y. C., Fisher, J. A., and Ainslie, P. N. (2014). Integrative regulation of human brain blood flow. *J. Physiol.* 592, 841–859. doi: 10.1113/jphysiol.2013.268953

Wise, R. G., Ide, K., Poulin, M. J., and Tracey, I. (2004). Resting fluctuations in arterial carbon dioxide induce significant low frequency variations in BOLD signal. *Neuroimage* 21, 1652–1664. doi: 10.1016/j.neuroimage.2003.11.025

Witcher, B. (2015). *waveslim: Basic Wavelet Routines for One-, Two- and Three-Dimensional Signal Processing. R Package Version 1.7.5.1*.

Xiong, L., Liu, X., Shang, T., Smielewski, P., Donnelly, J., Guo, Z. N., et al. (2017). Impaired cerebral autoregulation: measurement and application to stroke. *J. Neurol. Neurosurg. Psychiatry* 88, 520–531.

Yucel, M. A., Selb, J., Aasted, C. M., Lin, P. Y., Borsook, D., Becerra, L., et al. (2016). Mayer waves reduce the accuracy of estimated hemodynamic response functions in functional near-infrared spectroscopy. *Biomed. Opt. Express* 7, 3078–3088. doi: 10.1364/BOE.7.003078

Zhang, R., and Levine, B. D. (2007). Autonomic ganglionic blockade does not prevent reduction in cerebral blood flow velocity during orthostasis in humans. *Stroke* 38, 1238–1244. doi: 10.1161/01.str.0000260095.94175.d0

Zhang, R., Zuckerman, J. H., Giller, C. A., and Levine, B. D. (1998). Transfer function analysis of dynamic cerebral autoregulation in humans. *Am. J. Physiol.* 274, H233–H241.

Zhang, R., Zuckerman, J. H., Iwasaki, K., Wilson, T. E., Crandall, C. G., and Levine, B. D. (2002). Autonomic neural control of dynamic cerebral autoregulation in humans. *Circulation* 106, 1814–1820. doi: 10.1161/01.cir.0000031798.07790.fe

Conflict of Interest Statement: The authors declare that the research was conducted in the absence of any commercial or financial relationships that could be construed as a potential conflict of interest.

frontiers in Neuroscience

CORRECTION
published: 24 June 2020
doi: 10.3389/fnins.2020.00544

Corrigendum: Cerebral Autoregulation Evidenced by Synchronized Low Frequency Oscillations in Blood Pressure and Resting-State fMRI

Joseph R. Whittaker[1]*, *Ian D. Driver*[2], *Marcello Venzi*[1], *Molly G. Bright*[3] and *Kevin Murphy*[1]

[1] Cardiff University Brain Research Imaging Centre (CUBRIC), School of Physics and Astronomy, Cardiff University, Cardiff, United Kingdom, [2] CUBRIC, School of Psychology, Cardiff University, Cardiff, United Kingdom, [3] Department of Physical Therapy and Human Movement Sciences, Feinberg School of Medicine, Northwestern University, Chicago, IL, United States

Keywords: cerebral autoregulation, resting-state fMRI, blood pressure, cerebral physiology, LFO, BOLD, CBF

A Corrigendum on

Cerebral Autoregulation Evidenced by Synchronized Low Frequency Oscillations in Blood Pressure and Resting-State fMRI

by Whittaker, J. R., Driver, I. D., Venzi, M., Bright, M. G., and Murphy, K. (2019). Front. Neurosci. 13:433. doi: 10.3389/fnins.2019.00433

In the original article, there was an error. The article describes the lag structure between mean arterial pressure (MAP) and the fMRI signal, both globally and at a voxelwise level. A sign error contained within in-house analysis code led the authors to misattribute the directionality of this lag. In the article it is implied that MAP precedes fMRI by approximately 5.5 s, whereas in fact the fMRI signal precedes the MAP signal. There is no explicit error in the original text as it only states that there is a lag in fMRI "with respect to MAP," which in itself is unfortunately not completely unambiguous, as the precise lag/lead terminology used in the literature is not standardized. However, the authors were still laboring under a misapprehension, and thus as a result a section of the Discussion section is misleading. This error does not alter the primary scientific conclusion of this article, which is that low frequency fluctuations in fMRI are associated with matched frequency fluctuations in MAP. However, the Discussion section includes a body of text which considers the relevance of this lag and posits some speculative physiological interpretations. As these discussion points are based on the aforementioned erroneous lag direction, they are no longer relevant to the reported results. Furthermore, there is an erroneous sentence in the Conclusion that states "fluctuations in the resting-state fMRI signal that are *delayed* by approximately 5.5 s," as this use of the word delay implies MAP precedes fMRI. Finally, we correct the erroneous sentence in the Conclusion. The corrected paragraphs appear below.

The Discussion section, subsection Blood Pressure Correlations, paragraphs 1 and 2:

"To our knowledge, this study is first to demonstrate that MAP LFOs are positively correlated with fMRI LFOs within the frequency band between 0.063 and 0.125 Hz. These correlations appear highly spatially structured, with strong gray/white matter contrast, and are repeatable between subjects with a spatial correlation of ∼0.42. Results from the 7T-ME data suggest that fluctuations in MAP lead to gray matter signal fluctuations in BOLD fMRI that are primarily related to CBF, given that they are related to changes in R_2^* and relatively independent of acquisition parameters. This is consistent with a large TCD literature that shows beat-to-beat fluctuations in blood pressure

OPEN ACCESS

Edited by:
Jean Chen,
University of Toronto, Canada

Reviewed by:
Thomas T. Liu,
University of California, San Diego, United States
Changwei Wesley Wu,
Taipei Medical University, Taiwan

***Correspondence:**
Joseph R. Whittaker
whittakerj3@cardiff.ac.uk

Specialty section:
This article was submitted to Brain Imaging Methods, a section of the journal Frontiers in Neuroscience

Received: *24 February 2020*
Accepted: *04 May 2020*
Published: *24 June 2020*

Citation:
Whittaker JR, Driver ID, Venzi M, Bright MG and Murphy K (2020) Corrigendum: Cerebral Autoregulation Evidenced by Synchronized Low Frequency Oscillations in Blood Pressure and Resting-State fMRI. Front. Neurosci. 14:544. doi: 10.3389/fnins.2020.00544

result in measurable changes in CBFV in large intracranial arteries (Aaslid et al., 1989; Diehl et al., 1991; Blaber et al., 1997; Kuo et al., 1998; Zhang et al., 1998), lagged by ∼2 s, with MAP preceding cerebral blood flow velocity (CBFV). As BOLD fMRI is sensitive to deoxygenated blood volume compartments (i.e., capillary and venous) that are downstream of large intracranial arteries that are insonated with TCD, one might assume an extended delay that would allow changes to propagate along the vasculature tree. Given the obvious logic of this, the fact that the true results show that fMRI precedes MAP by ∼5.5 s most likely reflects differences in how MAP is measured in this study compared with previous reports. Continuous non-invasive MAP measurement is most often done with the Finapres system. However, as this is not MRI compatible we instead used the Caretaker system, from which beat-to-beat blood pressure is estimated from an analysis of the pulse wave in the periphery. Although the Caretaker is validated against invasive arterial line measurement (Baruch et al., 2014), and shows good agreement, this study does not include any investigation of timing differences. However, as it is based on Pulsewave Decomposition Analysis (PDA) of the peripheral arterial pressure wave, transit time differences must be considered.

Instantaneous blood pressure is an idealized concept, as in reality local changes in pressure take time to propagate along the vascular tree, which depends on stiffness of the different arterial vascular beds (Chen et al., 2009). As such, all blood pressure measurements are temporally shifted surrogates of the true aortic value, by which MAP is usually defined. Beat-to-beat blood pressure is predominantly regulated in response to the activity of baroreceptors, which are located in the aortic arch and carotid sinus. Thus, pressure changes are detected centrally, which leads to systemic changes in the downstream vasculature in response. The self-evident logic of cerebral autoregulation is that cerebral hemodynamics change in response to fluctuations MAP. Thus, although we have observed fMRI signals that precede MAP signals, it seems very unlikely that this is a causative effect. It is more likely that the lag, in which fMRI precedes Caretaker MAP, can be explained by systemic vascular transit time differences. Furthermore, this suggests one should be cautious about interpreting lags between cerebral and peripheral hemodynamics, as they likely depend on the complex interaction of multiple factors, including stiffness of the different arterial vascular beds, and the interplay between autonomic and myogenic activity. Furthermore, the lag time would be expected to account for the fact the flow changes will take time to propagate along the vascular tree. Delayed fMRI responses to hypercapnia challenges are frequently observed on the order of 8–15 s (Blockley et al., 2011; Murphy et al., 2011), although potentially longer in patient groups (Duffin et al., 2015; Donahue et al., 2016), and are presumed to contain both gas bolus transit time and vascular reactivity information. However, untangling the different factors that influence these timing differences could present an interesting new avenue of research. Central (aortic) arterial stiffness is likely to contribute greatly to the measured lag, and so experiments that can separate these general systemic effects from more specific cerebral vascular ones are desirable, and there are novel MRI methods for quantifying aortic stiffness would allow for this to be done within the same imaging session (Fielden et al., 2008; Grotenhuis et al., 2009; Langham et al., 2011). The voxelwise lag analysis shows that lag times for white matter are shorter than gray matter. Considering the correct directionality of the lag structure, this perhaps make sense, as it suggests that fluctuations in gray matter are followed by fluctuations in white matter, and finally by fluctuations in peripheral MAP measurements. Thus, this is consistent with the fMRI literature showing low frequency fMRI signals of systemic origin that are delayed in white matter, as blood arrival time is extended with respect to gray matter (van Gelderen et al., 2008)."

The Discussion section, subsection Cerebral Autoregulation, paragraph 2:

"TCD is the most widely used modality for measuring CA, which despite having excellent temporal resolution and high suitability for clinical settings, is ultimately of limited value since the measurements are restricted to only the largest intracranial arteries. In contrast, fMRI has whole-brain sensitivity with millimeter resolution and so is a desirable tool for better understanding CA, and has the potential to deliver more predictive clinical measures. For example, CA is critical for keeping stable CBF in the penumbra region following ischemic stroke (Xiong et al., 2017), so a method such as fMRI, which has the spatial resolution to resolve localized alterations, is promising as a more informative prognostic tool. In the TCD literature the transfer function between BP and CBFV is used to characterize CA, primarily through gain and phase shift. It is commonly assumed that a phase shift and low gain constitutes good cerebral autoregulation (i.e., CBFV fluctuations are delayed with respect to BP and are dampened) (van Beek et al., 2008). In this study we observed a lag in MAP with respect to fMRI, i.e., fMRI precedes MAP, which may be related to the phase shifts measured in TCD. Furthermore, although the effect-size of MAP on fMRI measured here appears small (Supplementary Figure 4), this may be due to the young healthy subject group. In patient groups with less effective CA both effect-size and lag may be modulated."

The Conclusion:

"In this study we have shown that beat-to-beat fluctuations in BP are correlated with fluctuations in the resting-state fMRI that precede them by approximately 5.5 s, and which are strongest at the frequency band centered at ∼0.1 Hz. Using a multi-echo acquisition we were able to isolate the pure BOLD (R_2^*) component of the BP correlated fMRI signal and have shown that it is the main source of contrast. This would indicate that it is changes in CBF that mediate this low frequency BP correlated signal, which we hypothesize is related to the process of CA. We propose that resting-state fMRI is a promising new tool for assessment of dynamic CA with high spatial resolution, which may prove to be a useful biomarker in a range of cerebrovascular and neurological conditions."

The authors apologize for this error and state that this does not change the scientific conclusions of the article in any way. The original article has been updated.

REFERENCES

Aaslid, R., Lindegaard, K. F., Sorteberg, W., and Nornes, H. (1989). Cerebral autoregulation dynamics in humans. *Stroke* 20, 45–52. doi: 10.1161/01.str.20.1.45

Baruch, M. C., Kalantari, K., Gerdt, D. W., and Adkins, C. M. (2014). Validation of the pulse decomposition analysis algorithm using central arterial blood pressure. *Biomed. Eng. Online* 13:96. doi: 10.1186/1475-925X-13-96

Blaber, A. P., Bondar, R. L., Stein, F., Dunphy, P. T., Moradshahi, P., Kassam, M. S., et al. (1997). Transfer function analysis of cerebral autoregulation dynamics in autonomic failure patients. *Stroke* 28, 1686–1692. doi: 10.1161/01.str.28.9.1686

Blockley, N. P., Driver, I. D., Francis, S. T., Fisher, J. A., and Gowland, P. A. (2011). An improved method for acquiring cerebrovascular reactivity maps. *Magn. Reson. Med.* 65, 1278–1286. doi: 10.1002/mrm.22719

Chen, Y., Wen, C., Tao, G., Bi, M., and Li, G., (2009). Continuous and noninvasive blood pressure measurement: a novel modeling methodology of the relationship between blood pressure and pulse wave velocity. *Ann. Biomed. Eng.* 37, 2222–2233. doi: 10.1007/s10439-009-9759-1

Diehl, R. R., Diehl, B., Sitzer, M., and Hennerici, M. (1991). Spontaneous oscillations in cerebral blood flow velocity in normal humans and in patients with carotid artery disease. *Neurosci. Lett.* 127, 5–8. doi: 10.1016/0304-3940(91)90880-3

Donahue, M. J., Strother, M. K., Lindsey, K. P., Hocke, L. M., Tong, Y., and Frederick, B. D. (2016). Time delay processing of hypercapnic fMRI allows quantitative parameterization of cerebrovascular reactivity and blood flow delays. *J. Cereb. Blood Flow Metab.* 36, 1767–1779. doi: 10.1177/0271678x15608643

Duffin, J., Sobczyk, O., Crawley, A. P., Poublanc, J., Mikulis, D. J., and Fisher, J. A. (2015). The dynamics of cerebrovascular reactivity shown with transfer function analysis. *Neuroimage* 114, 207–216. doi: 10.1016/j.neuroimage.2015.04.029

Fielden, S. W., Fornwalt, B. K., Jerosch-Herold, M., Eisner, R. L., Stillman, A. E., and Oshinski, J. N. (2008). A new method for the determination of aortic pulse wave velocity using cross-correlation on 2D PCMR velocity data. *J. Magn. Reson. Imaging* 27, 1382–1387. doi: 10.1002/jmri.21387

Grotenhuis, H. B., Westenberg, J. J., Steendijk, P., van der Geest, R. J., Ottenkamp, J., Bax, J. J., et al. (2009). Validation and reproducibility of aortic pulse wave velocity as assessed with velocity-encoded MRI. *J. Magn. Reson. Imaging* 30, 521–526. doi: 10.1002/jmri.21886

Kuo, T. B., Chern, C. M., Sheng, W. Y., Wong, W. J., and Hu, H. H. (1998). Frequency domain analysis of cerebral blood flow velocity and its correlation with arterial blood pressure. *J. Cereb. Blood Flow Metab.* 18, 311–318. doi: 10.1097/00004647-199803000-00010

Langham, M. C., Li, C., Magland, J. F., and Wehrli, F.W. (2011). Nontriggered MRI quantification of aortic pulse-wave velocity. *Magn. Reson. Med.* 65, 750–755. doi: 10.1002/mrm.22651

Murphy, K., Harris, A. D., and Wise, R. G. (2011). Robustly measuring vascular reactivity differences with breath-hold: normalising stimulus-evoked and resting state BOLD fMRI data. *Neuroimage* 54, 369–379. doi: 10.1016/j.neuroimage.2010.07.059

van Beek, A. H., Claassen, J. A., Rikkert, M. G., and Jansen, R. W. (2008). Cerebral autoregulation: an overview of current concepts and methodology with special focus on the elderly. *J. Cereb. Blood Flow Metab.* 28, 1071–1085. doi: 10.1038/jcbfm.2008.13

van Gelderen, P., de Zwart, J. A., and Duyn, J. H. (2008). Pittfalls of MRI measurement of white matter perfusion based on arterial spin labeling. *Magn. Reson. Med.* 59, 788–795. doi: 10.1002/mrm.21515

Whittaker, J. R., Driver, I. D., Venzi, M., Bright, M. G., and Murphy, K. (2019). Cerebral autoregulation evidenced by synchronized low frequency oscillations in blood pressure and resting-state fMRI. *Front. Neurosci.* 13:433. doi: 10.3389/fnins.2019.00433

Xiong, L., Liu, X., Shang, T., Smielewski, P., Donnelly, J., Guo, Z. N., et al. (2017). Impaired cerebral autoregulation: measurement and application to stroke. *J. Neurol. Neurosurg. Psychiatry* 88, 520–531.

Zhang, R., Zuckerman, J. H., Giller, C. A., and Levine, B. D. (1998). Transfer function analysis of dynamic cerebral autoregulation in humans. *Am. J. Physiol.* 274, H233–H241.

frontiers in Neuroscience

ORIGINAL RESEARCH
published: 23 July 2019
doi: 10.3389/fnins.2019.00736

Spatiotemporal Empirical Mode Decomposition of Resting-State fMRI Signals: Application to Global Signal Regression

Narges Moradi[1,2,3]*, *Mehdy Dousty*[4,5] *and Roberto C. Sotero*[1,2,3]

[1] *Biomedical Engineering Graduate Program, University of Calgary, Calgary, AB, Canada,* [2] *Hotchkiss Brain Institute, University of Calgary, Calgary, AB, Canada,* [3] *Computational Neurophysics Lab, Department of Radiology, University of Calgary, Calgary, AB, Canada,* [4] *Institute of Biomaterials and Biomedical Engineering, University of Toronto, Toronto, ON, Canada,* [5] *KITE, Toronto Rehab, University Health Network, Toronto, ON, Canada*

Resting-state functional connectivity MRI (rs-fcMRI) is a common method for mapping functional brain networks. However, estimation of these networks is affected by the presence of a common global systemic noise, or global signal (GS). Previous studies have shown that the common preprocessing steps of removing the GS may create spurious correlations between brain regions. In this paper, we decompose fMRI signals into 5 spatial and 3 temporal intrinsic mode functions (SIMF and TIMF, respectively) by means of the empirical mode decomposition (EMD), which is an adaptive data-driven method widely used to analyze non-linear and non-stationary phenomena. For each SIMF, functional connectivity matrices were computed by means of Pearson correlation between TIMFs of different brain areas. Thus, instead of a single connectivity matrix, we obtained $5 \times 3 = 15$ functional connectivity matrices. Given the high correlation and global efficiency values of the connectivity matrices related to the low spatial maps (SIMF3, SIMF4, and SIMF5), our results suggest that these maps can be considered as spatial global signal masks. Thus, by summing up the first two SIMFs extracted from the fMRI signals, we have automatically excluded the GS which is now voxel-specific. We compared the performance of our method with the conventional GS regression and to the results when the GS was not removed. While the correlation pattern identified by the other methods suffers from a low level of precision in identifying the correct brain network connectivity, our approach demonstrated expected connectivity patterns for the default mode network and task-positive network.

Keywords: resting-state functional connectivity MRI, global Signal, fMRI, empirical mode decomposition, spatial intrinsic mode function, temporal intrinsic mode function, low-pass filtering

OPEN ACCESS

Edited by:
Garth John Thompson, ShanghaiTech University, China

Reviewed by:
Ehsan Shokri Kojori, National Institutes of Health (NIH), United States
Elmar W. Lang, University of Regensburg, Germany

***Correspondence:**
Narges Moradi
narges.moradi1@ucalgary.ca

Specialty section:
This article was submitted to Brain Imaging Methods, a section of the journal Frontiers in Neuroscience

Received: *30 January 2019*
Accepted: *02 July 2019*
Published: *23 July 2019*

Citation:
Moradi N, Dousty M and Sotero RC (2019) Spatiotemporal Empirical Mode Decomposition of Resting-State fMRI Signals: Application to Global Signal Regression. Front. Neurosci. 13:736. doi: 10.3389/fnins.2019.00736

1. INTRODUCTION

Resting-state functional connectivity MRI (rs-fcMRI) has considerable potential for mapping functional brain networks (Biswal et al., 1995; Kandel et al., 2000; De Luca et al., 2006; Fox et al., 2006; Shmuel and Leopold, 2008; Friston, 2011). This mapping, which reveals the brain's functional architecture and operational principles (Kandel et al., 2000; Friston, 2011), can be used for early detection of brain connectivity pathologies in neuropsychiatric patients (Erdoğan et al., 2016).

However, the presence of broadly shared synchronous fluctuations, termed as the global signal (GS) in Blood Oxygen Level Dependent (BOLD) responses, is a significant problem for fcMRI analysis. Its presence is problematic as it is of unknown origin (Damoiseaux et al., 2006; Fox et al., 2009; Erdoğan et al., 2016). Therefore, effective removal of GS has become an important step in data preprocessing and must be done prior to fcMRI analysis. GS is generally defined as the average of the BOLD signals over the whole brain (Zarahn et al., 1997; Fox et al., 2009; Liu et al., 2017) and can be computed from the raw images or after some preprocessing steps (Liu et al., 2017). The average-based GS is typically called conventional GS (or static GS (SGS) Erdoğan et al., 2016).

Application of SGS regression (SGSR) was at first just limited to task-related fMRI imaging (Zarahn et al., 1997; Macey et al., 2004). More recently, SGSR usage has received more attention in the analysis of resting-state fMRI than in task-related fMRI studies (Liu et al., 2017). Some studies suggest that application of SGSR improves the functional specificity of resting-state correlation maps and helps to remove non-neuronal sources of global variance like respiration and movement (Fox and Raichle, 2007; Fox et al., 2009; Liu et al., 2017). However, other studies found that these improvements are limited to systems that would exhibit only positive correlations with the specific selected seeds (Fox et al., 2009; Weissenbacher et al., 2009). On the other hand, many studies have shown that the common preprocessing steps of removing GS via a general linear model can create correlations between regions that may never have existed (Murphy et al., 2009; Anderson et al., 2010; Saad et al., 2012; Murphy and Fox, 2017), which results in spurious fcMRI values. Moreover, it has been shown that SGSR do not consider the brain's spatial heterogeneities and biases correlations in different regions of the brain (Saad et al., 2012). Accordingly, the extracted correlation maps are known to present artifacts and do not reflect underlying neurological properties (Murphy et al., 2009; Anderson et al., 2010; Saad et al., 2012; Murphy and Fox, 2017). Therefore, regressing out GS is under debate as its removal by applying current approaches may introduce artifacts into the fMRI data or cause the loss of important neuronal components (Murphy et al., 2009; Anderson et al., 2010; Saad et al., 2012; Murphy and Fox, 2017). These concerns about the GSR methods and the need for accurate brain functional connectivity maps motivate the need to develop new methods for dealing with GS. Moreover, it has been shown that GS has a variety of sources with different spatial distributions which are voxel-specific. Accordingly, it is desirable to use a new method that works selectively and is able to identify and remove the spatially specific GS for each voxel or region (Saad et al., 2012; Tong and Frederick, 2014; Chang et al., 2016; Power et al., 2017; Turchi et al., 2018), and also produce known connectivity patterns in networks such as the default mode network and task-positive network (Fox et al., 2009; Erdoğan et al., 2016), thus avoiding the creation of spurious correlations.

In addition to GS, in fMRI studies, BOLD signal is low-pass filtered (<0.1 Hz) during the preprocessing procedure to be sure that the effects of the high frequency physiological noises are removed from the data (Boubela et al., 2013; Brooks et al., 2013; Liu et al., 2017). This is because, physiological noises which are mainly cardiac and respiratory, are spatially widespread and have cycles located prominently at the frequency range of 0.1–2.5 Hz. It is indicated that, among different noise-removal methods (such as band-pass filtering and Independent component analysis), EMD based methods facilitate the noise removal from fMRI data. In EMD-based methods, IMFs with specific frequency bands are identified and removed from fMRI data to enhance the functional sensitivity of the data (Typically the first and second IMFs which have the highest frequency bands among all IMFs are considered as a noise) (Lin et al., 2016). However, removing the whole high-frequency data from fMRI time series is controversial, as smoothing the signals via low-pass filtering decreases the signal to noise ratio by smoothing the peaks and amplifying the noise (Brooks et al., 2013). In fact, it has been shown that filtering high frequency modes may also remove the signal of interest that contains similar frequencies. The main reason is that the TR time for sampling fMRI data is too low to distinguish the high frequency components and causes signal's frequencies being aliased that can not be separated by temporal filtering (Brooks et al., 2013). Furthermore, even using very high sampling rate (TR $<$ 0.4 s) to detect the high frequency modes may cause losing information of neuronal activation in high frequencies by filtering high frequency modes (Tagliazucchi et al., 2011, 2012; Boubela et al., 2013). Accordingly, in resting-state studies, we cannot do the band-pass filtering through previous methods as the brain dynamics in all frequency bands needs to be investigated. Therefore, we need a method that can remove the physiological noises more specifically from BOLD signal.

There are several signal processing methods, such as Fourier transform (Gallagher et al., 2008), Wavelet transform (Yves, 1993), spatial and temporal Blind source separation (Comon and Jutten, 2010), and the EMD (Huang et al., 1998). However, all of the mentioned method except EMD require predefined basis function or some prior knowledge to decompose the signal. Considering the fact that real-world signals including fMRI signals are non-linear and non-stationary data and do not perfectly obey our assumption, EMD method would be the best method to apply, as it does not need any basis functions and parameters that need to be adjusted such as wavelet type in wavelet transform or informed separation ideas in Blind source separation method (Liutkus et al., 2013; Riffi et al., 2014; He et al., 2017). EMD is a computationally efficient method that can adaptively decompose any non-linear and non-stationary signals into Intrinsic mode functions (IMF) and obtain meaningful frequencies estimation (Huang et al., 1998; Mandic et al., 2008; Riffi et al., 2014; He et al., 2017).

In this paper, we define an adaptive global signal regression (AGSR) by performing a spatiotemporal decomposition of the fMRI time series through EMD-based methods. The GS which is computed using this method is voxel-specific and depends on brain regions' heterogeneity.

Additionally, we show that by applying AGSR, we do not need the traditional low-pass filtering methods as the proposed method exhibits the potential to adaptively remove the physiological noises from high temporal frequency modes of fMRI time series, that are shared in whole brain regions.

Therefore, AGSR method, besides removing the GS, helps to eliminate the high frequency physiological noises without needing to perform the low-pass filtering step separately.

In AGSR method, We do not use the Multidimensional EMD approach as it requires great runtime and cannot decompose a multidimensional signal into multidimensional components (Wu et al., 2009; Riffi et al., 2014; He et al., 2017). Consequently, in this paper, two EMD-based methods are used sequentially to decompose the fMRI signals adaptatively and voxel-specifically. We acquired the Spatial and Temporal Intrinsic Mode Functions (SIMF and TIMF, respectively) of fMRI data by applying FATEMD (Riffi et al., 2014) and ICEEMDAN (Colominas et al., 2014) methods, respectively (Huang et al., 1998; Mandic et al., 2008). It has been shown that applying EMD-based methods on fMRI data separate inherent brain oscillations and fundamental modes embedded in BOLD signal. Each of these oscillations occupies a unique frequency band and can be used to investigate the frequency characteristics in resting-state brain networks (McGonigle et al., 2010; Zheng et al., 2010; Niazy et al., 2011; Song et al., 2014, 2015; Qian et al., 2015; Lin et al., 2016; Cordes et al., 2018).

To explore the frequency characteristics of the brain networks, first, we obtain the average functional connectivity matrices for different TIMFs of each SIMFs over all subjects. Functional connectivity was computed using pearsons' coefficient between the peak voxels of each brain regions included in the AAL 116 atlas (Tzourio-Mazoyer et al., 2002).

We then compute the efficiency (Fair et al., 2007; Rubinov and Sporns, 2009; Cohen and D'Esposito, 2016) of the brain network of different spatiotemporal IMFs, which is used as a measure of integration. Integration values are used to identify the GS, since GS is defined as a synchronous fluctuation which is shared among all brain regions that makes it being highly integrated in the whole brain. Given the high values of efficiency in the low spatial maps (SIMF3, SIMF4, and SIMF5), our results suggest that these maps can be considered as spatial global signal masks. The performance of the proposed method is compared with the SGSR method, and also with the results when GS is not removed. This is done by investigating the functional connections within an extracted peak voxel of the known network's regions and the selected seed region. While the correlation pattern identified by the other methods suffers from a low level of precision, our method demonstrates a high level of accuracy due to its data-driven adaptive nature.

2. METHODS

2.1. fMRI Data Acquisition

The resting-state fMRI preprocessed data-set of 21 subjects from the NIH Human Connectome Project (HCP) (https://db.humanconnectome.org) (Essen et al., 2013) is used in this research. Each subject was involved in 4 runs of 15 min each using a 3 T Siemens, while their eyes were open and had a relaxed fixation on a projected bright cross-hair on a dark background. The data were acquired with 2.0 mm isotropic voxels for 72 slices, TR = 0.72 s, TE = 33.1 ms, 1,200 frames per run, 0.58 ms Echo spacing, and 2,290 Hz/Px Bandwidth (Moeller et al., 2010). Therefore, the fMRI data were acquired with a spatial resolution of 2 × 2 × 2 mm and a temporal resolution of 0.72 s, using multibands accelerated echo-planar imaging to generate a high quality and the most robust fMRI data (Moeller et al., 2010). The fMRI data were preprocessed to remove spatial artifacts produced by head motion, B0 distortions, and gradient non-linearities (Jovicich et al., 2006). As comparison of fMRI images across subjects and studies is possible when the images have been transformed from the subject's native volume space to the MNI space (Evans et al., 1993; Ashburner and Friston, 1999), fMRI images were wrapped and aligned into the MNI space with FSL's FLIRT 12 DOF affine and then a FNIRT non-linear registration (Jenkinson and Smith, 2001; Jenkinson et al., 2002; Jahanshad et al., 2013). In this study, the MNI-152-2 mm atlas (Mazziotta et al., 1995, 2001a,b) was utilized for fMRI data registration.

2.2. Estimation of the Temporal IMFs (TIMFs)

EMD is an adaptive data-driven signal processing method, which does not need any prior functional basis such as the wavelet transform (Mandic et al., 2008). The basic functions are derived adaptively from the data by the EMD sifting procedure. The EMD method developed and established by Huang et al. (1998) decomposes non-linear and non-stationary time series into their fundamental oscillatory components, called Intrinsic Mode Functions (IMFs). There are two criteria defining an IMF during the sifting process: 1) the number of extrema and zero crossings must be either equal or differ at most by one, and, 2) at any instant in time, the mean value of the envelope defined by the local maximum and the envelope of the local minimum is zero. The EMD algorithm for estimating the IMFs of the time series $x(t)$ is:

1. $r_0(t) = x(t)$, $j = 1$.
2. For extracting the j-th IMF:
   (a) $h_0(t) = r_j(t), k = 1$,
   (b) Locate local maximum and minimum of $h_{k-1}(t)$,
   (c) Identify the average envelope using cubic spline interpolation to define upper and lower envelope of $h_{k-1}(t)$,
   (d) Calculate the mean value $m_{k-1}(t)$,
   (e) Put $h_k(t) = h_{k-1}(t) - m_{k-1}(t)$,
   (f) Check the stopping criteria. The stopping criteria determines the number of sifting steps to decompose an IMF Huang et al. (1998). If stopping criteria is satisfied then $h_j(t) = h_k(t)$ otherwise, go to (a) to extract next IMF with $k = k + 1$.
3. $r_j(t) = r_{j-1}(t) - h_j(t)$.
4. If at least two extrema were in the $r_j(t)$, the next IMF is extracted otherwise the EMD algorithm is finished and $r_j(t)$ is the residue of $x(t)$. Accordingly, $x(t)$ is defined as:

$$x(t) = \sum_{j=1}^{n} h_j(t) + r_n(t), \tag{1}$$

where $h_j(t)$ is the j-th IMF, n is the number of IMFs, and $r_n(t)$ is the residue of the signal. Thus, the EMD method adaptively decomposes a time series into a set of IMFs and a residue

where the first IMF (IMF1) corresponds to the fastest oscillatory mode and the last IMF (IMFn) to the slowest one, the sum of these components yields the original signal (Huang et al., 1998; Hassan and John, 2005). However, frequent occurrences of the mode-mixing phenomenon in analyzing real signals using EMD algorithm is problematic. To address this problem and improve the spectral separation of modes, the ensemble empirical mode decomposition (EEMD) method was proposed (Wu and Huang, 2009). This method extracts modes by performing the decomposition over an ensemble of noisy copies of the original signal combined with white Gaussian noises, and taking the average of all IMFs in the ensemble (Colominas et al., 2014).

The EEMD method solves the mode mixing problem, but certain issues remain. First, the number of IMFs extracted from each of the noisy signal copies is different, and this creates a problem when averaging the IMFs. The second problem is a reconstruction error in the EEMD method (Wu and Huang, 2009; Colominas et al., 2014). To fix this error the complementary EEMD (CEEMD) was proposed (Yeh et al., 2010). In the CEEMD algorithm, pairs of positive and negative white noise processes are added to the original signal to make two sets of ensemble IMFs. Accordingly, the CEEMD effectively eliminates residual noise in the IMFs which alleviate the reconstruction problem. Nonetheless, the problem of the different number of modes when averaging still persists. To overcome this problem, the CEEMD with adaptive noise (CEEMDAN) was developed (Torres et al., 2011; Colominas et al., 2014). In this approach, the first mode is computed exactly as in EEMD. Then, for the next modes, IMFs are computed by estimating the local means of the residual signal plus different modes extracted from the white noise realizations. CEEMDAN decomposition can create some spurious modes with high-frequency and low-amplitude due to overlapping in the scales. Additionally, some residual noise is still present in the modes. As a consequence, the new optimization algorithm, Improved Complete Ensemble Empirical Mode Decomposition with Adaptive Noise (ICEEMDAN), was proposed (Colominas et al., 2014).

During the sifting process using ICEEMDAN method the local mean of realizations is estimated, instead of using the average of modes from the first step. This change in the algorithm reduces the amount of noise present in the final computed modes. To deal with the issue of creation of spurious modes in the final results, ICEEMDAN method proceeds differently than the EEMD and CEEMDAN methods. In ICEEMDAN, white noise is not added directly; instead EMD modes of white noise are added to the original signal and to the IMFs during the sifting process (Wu and Huang, 2009; Colominas et al., 2014). Furthermore, in this method as in CEEMDAN, a constant coefficient is added to the noise that makes the desired signal to noise ratio between the added noise and the residue to which the noise is added. This coefficient is computed based on the standard deviation of the residue at each step of the sifting process. Therefore, the IMFs computed with ICEEMDAN have less noise and more physical content than IMFs obtained with other methods (Colominas et al., 2014) (More detailed description of ICEEMDAN method can be found at Colominas et al., 2014). The high accuracy rate, reduction in the amount of noise contained in the modes, and the alleviation of mode mixing phenomenon qualify this method to effectively decompose biological signals. In this paper the ICEEMDAN method with 300 ensembles and a level of noise of 0.2 (Wu and Huang, 2009) is used to extract the Temporal Intrinsic Mode Functions (TIMFs) from the fMRI data.

2.3. Estimation of the Spatial IMFs (SIMFs)

A fast, time efficient, and effective method is essential for processing real images that have a large size. Previous EMD-based methods were limited to small size images as the extrema detection, interpolation at each iteration, and the large number of iterations make their processing time consuming and complicated (Bhuiyan et al., 2008; Riffi et al., 2013, 2014; He et al., 2017). Therefore, those methods were just applicable to reduced size images, which resulted in losing some information during their process. Fast and Adaptive Tridimensional (3D) EMD, abbreviated as FATEMD, is a recent extension of the EMD method to three dimensions (Riffi et al., 2014). The FATEMD method is able to estimate volume components called tridimensional Intrinsic Mode Functions (3D-IMFs) quickly and accurately by limiting the number of iterations per 3D-IMF to one, and changing the process of computing upper and lower envelopes, which reduce the computation time for each iteration (Bhuiyan et al., 2008; Riffi et al., 2014; He et al., 2017). In the FATEMD method, the steps of extracting 3D-IMFs are almost the same as the previous EMD based methods, except for the number of iterations and the estimations of the maximum and minimum envelopes. The steps for decomposing a volume $V(m, n, p)$ with dimensions m, n, and p using the FATEMD approach are as follows (Bhuiyan et al., 2008; Riffi et al., 2014):

1. Set $i = 1$ and $R_i(m, n, p) = V(m, n, p)$.
2. Determine the local maximum and minimum values by browsing $R_i(m, n, p)$ using a 3D window (cube) with a size of $3 \times 3 \times 3$ which results in an optimum extrema maps ($\mathrm{Map}_{\max}(m, n, p)$ and $\mathrm{Map}_{\min}(m, n, p)$). These local maximum (or minimum) values are strictly higher (or lower) than all of their neighborhoods contained in the cube.
3. Calculate the size of the Max and the Min filters which will be used in making extrema envelopes and their smoothness. The maximum and minimum filters are made by computing the nearest Euclidean distances between the maximum ($d_{\text{adj. max}}$) (minimum ($d_{\text{adj. min}}$)) points. The cubic window width (w_{en}) then is determined by using one of the following four formulae for both maximum and minimum filters. Here, we used the 4-th formula as outlined below, although using the other formulas will result in approximately the same decomposition result:

$$\begin{aligned} w_{\text{en}} &= \min\left\{\min\{d_{\text{adj. max}}\}, \min\{d_{\text{adj. min}}\}\right\}, \\ w_{\text{en}} &= \min\left\{\max\{d_{\text{adj. max}}\}, \max\{d_{\text{adj. min}}\}\right\}, \\ w_{\text{en}} &= \max\left\{\min\{d_{\text{adj. max}}\}, \min\{d_{\text{adj. min}}\}\right\}, \\ w_{\text{en}} &= \max\left\{\max\{d_{\text{adj. max}}\}, \max\{d_{\text{adj. min}}\}\right\}. \end{aligned} \quad (2)$$

4. Create the envelopes of maxima and minima ($\mathrm{Env}_{\max}(m, n, p)$ and $\mathrm{Env}_{\min}(m, n, p)$) of size ($w_{\text{en}}$).

5. Use the mean filter to compute the smoothed envelopes: $\mathrm{Env}_{\max -s}(m,n,p)$ and $\mathrm{Env}_{\min -s}(m,n,p)$.
6. Calculate the mean filter by averaging the smoothed upper and lower envelopes ($\mathrm{Env}_A(m,n,p)$).
7. Calculate the *i-th* 3D-IMF: $\mathrm{IMF}_i(m,n,p) = \mathrm{R}_i(m,n,p) - \mathrm{Env}_A(m,n,p)$.
8. Calculate $\mathrm{R}_{i+1}(m,n,p) = \mathrm{R}_i(m,n,p) - \mathrm{IMF}_i(m,n,p)$.
9. If $\mathrm{R}_{i+1}(m,n,p)$ contains more than two extrema then
   Go to the step 2 and set $i = i + 1$,
   Else
   The FATEMD decomposition is completed.

Therefore, FATEMD is an adaptive approach as all of the processes for computing filters and making the maximum, minimum, and the mean envelops are data driven. FATEMD decomposes a volume into a set of 3D-IMFs (Riffi et al., 2014). In general, a volume V can be reconstructed from the summation of the K 3D-IMFs and the residue as follows:

$$V(m,n,p) = \sum_{i=1}^{\mathrm{K}} \mathrm{IMF}_i(m,n,p) + \mathrm{R}_{K+1}(m,n,p). \quad (3)$$

K is the number of IMFs, and $R(m,n,p)$ is the residue of the signal.

In this paper, we apply the FATEMD method at each time instant to decompose the resting-state fMRI data into tridimensional IMFs called Spatial Intrinsic Mode Functions (SIMF). **Figure 1** shows the spatial decomposition results of a sample resting-state fMRI image. The ICEEMDAN method is then utilized to decompose each SIMF into its corresponding TIMFs.

2.4. Spatiotemporal Pattern Analysis of the fMRI Data

To define an adaptive and voxel-specific GS, the spectral information of fMRI data is investigated by constructing the functional connectivity matrices using extracted TIMFs and SIMFs data. To fulfill this aim, first, the SIMFs of the fMRI data at each TR time are computed by applying the FATEMD method, then, all spatial components are merged together in time to construct the time series of each SIMF. Second, the peak voxel at each region, that is, the voxel of maximal activation, is selected by computing the Root Mean Square (RMS) for each voxel's signal over all time. It has been shown that peak voxel provides the best effect of any voxel in the ROI (Sharot et al., 2005). Additionally, the peak voxel activity correlates better with evoked scalp electrical potentials than approaches that average activity across the ROI. This means that the peak voxel represents the ROI's activity better than other choices (Arthurs and J Boniface, 2003). The peak voxel in each region is determined using previously published Talairach coordinates (after conversion to MNI coordinates and using AAL 116 atlas) (Fox et al., 2005). After determining the peak voxels of each region, the ICEEMDAN method is applied to its time series to compute the TIMFs. Thus, the TIMFs of all regions for each SIMF are computed.

We then compare the predefined distinct frequency bands presented in fMRI studies (slow5 [0.01–0.027 Hz], slow4 [0.027–0.073 Hz], slow3 [0.073–0.198 Hz], slow2 [0.198–0.25 Hz], and slow1 [0.5–0.75 Hz]) (Penttonen and Buzsáki, 2003; Zhan et al., 2014), to the frequency content of the extracted TIMFs. In all subjects, TIMFs consistently corresponded to the same frequency bands. As seen in the **Figure 2**, the frequency range comprised in TIMF1 to TIMF3 is approximately the same as the frequency range of the sum of slow1 to slow3. The frequency range of TIMF4 is the same as slow4, and the frequency range of the sum of TIMF5 to TIMF9 has the same frequency range as the slow5 frequency band. Accordingly, we label the summation of TIMF1 to TIMF3 as TIMF1, TIMF4 as TIMF2, and the summation of TIMF5 to TIMF9 as TIMF3. **Figure 3** represents the pipeline used in computing SIMFs and TIMFs for each resting-state fMRI data. Accordingly, the functional connectivity matrices are constructed by computing the average of correlation coefficients between all possible pairs of TIMFs correspond to different Spatial domains for all brain regions comprised in the AAL 116 atlas over all 21 subjects. Consequently, instead of the classical functional connectivity matrix, the decomposition presented here produces $5 \times 3 = 15$ connectivity matrices (each with size 116×116), 3 temporal domains and 5 spatial domains, encompassing the rich spatiotemporal dynamics of brain activity.

2.5. Topological Properties of the Brain Network

The GS is a synchronous fluctuation shared among all brain regions. Consequently, the GS component in the brain connectivity matrix should present a high integration value, where integration is the topological property of a network that describes how information from distributed brain regions is combined (Fair et al., 2007; Rubinov and Sporns, 2009; Cohen and D'Esposito, 2016). To compute the integration of the brain network at different spatiotemporal scales we use the global efficiency measure (Fair et al., 2007; Rubinov and Sporns, 2009). The global efficiency is computed as the average inverse shortest path length between all the node pairs of the network that is normalized by the maximal number of network's links. Therefore, the weighted global efficiency is computed via the following equation:

$$E^{\mathrm{w}} = \frac{1}{\mathrm{N}(\mathrm{N}-1)} \sum_{j=1}^{\mathrm{N}} \sum_{i=1, i\neq j}^{\mathrm{N}} (d_{ij}{}^{\mathrm{w}})^{-1}, \quad (4)$$

where N is the number of nodes in the network and d_{ij} is the minimum path length between nodes i and j (Fair et al., 2007; Rubinov and Sporns, 2009). The shortest path length is computed by counting the smallest number of edges needed to get from node i to node j which is inversely related to node weight. The information needed to estimate the weight of all pairs of brain regions are provided by functional connectivity matrices (Rubinov and Sporns, 2009; Cohen and D'Esposito, 2016), strong association between regions has a large weight which leads to a shorter length. When two nodes are disconnected the length of

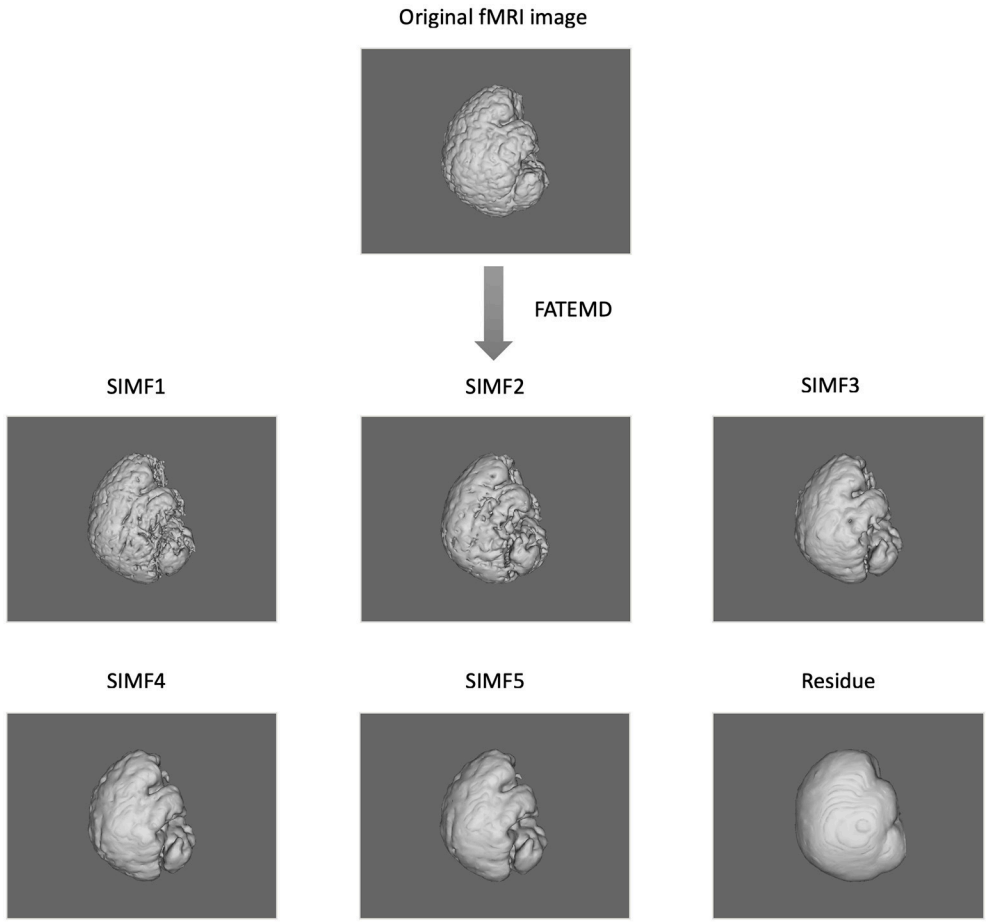

FIGURE 1 | Spatial decomposition of a sample fMRI image using FATEMD method. The original fMRI image at one TR time is decomposed into 5 SIMFs (SIMF1 to SIMF5) and a residue.

that path would be infinite and correspondingly, the efficiency would be zero (Fair et al., 2007; Rubinov and Sporns, 2009).

3. RESULTS

3.1. Defining Adaptive Global Signal (AGS)

We computed the functional connectivity matrices between all pairs of brain regions for different spatiotemporal domains extracted from fMRI data for each subject. **Figure 4** shows the average connectivity matrices computed by Pearson's coefficient over the 21 subjects. As seen in the figures, SIMF1 and SIMF2 in all TIMFs showed low connectivity whereas SIMF3 to SIMF5 in all TIMFs showed high connectivity. Besides, they indicate that the magnitude of the correlation does not significantly depend on the TIMFs. Thus, based on the connectivity strength for different spatiotemporal domains, the summation of the SIMF1 to SIMF2 and the SIMF3 to SIMF5 including all TIMFs, were considered as two separate signals. We also averaged the six connectivity matrices resulting from the summation of TIMF1 to TIMF3 with SIMF1 and SIMF2 (**Figure 4**) and labeled it as AGSR (**Figure 5A**), and the nine connectivity matrices resulting when combining TIMF1 to TIMF3 with SIMF3 to SIMF5, which we labeled as AGS (**Figure 5B**).

We also computed the global efficiency (**Figure 6A**) for different spatial and temporal IMFs using Equation (4) and also based on functional connectivity results. **Figure 6A** shows that there are high values of efficiency in the low frequencies of spatial domains, SIMF3, SIMF4, and SIMF5, which indicate active shared connections between all the nodes in the brain, suggesting the existence of GS in the low-frequency spatial domains, called Adaptive Global Signal(AGS). Furthermore, SIMF3 to SIMF5 with high temporal frequency mode (TIMF1) which is included in the AGS can be considered as an adaptive filter to reduce the effects of the highly integrated physiological noises in high frequency modes instead of applying low-pass filtering (Shmueli et al., 2007; Boubela et al., 2013; Liu et al., 2017).

As seen in **Figure 6B** and **Table 1**, the high values of integration of AGS (summation of SIMF3 to SIMF5 including all TIMFs) confirm that they can be considered as a GS which has to be removed from the fMRI data to have more accurate brain connectivity results. In the last results' section (represented in **Figures 8**, **9**) we show that, including low frequency spatial

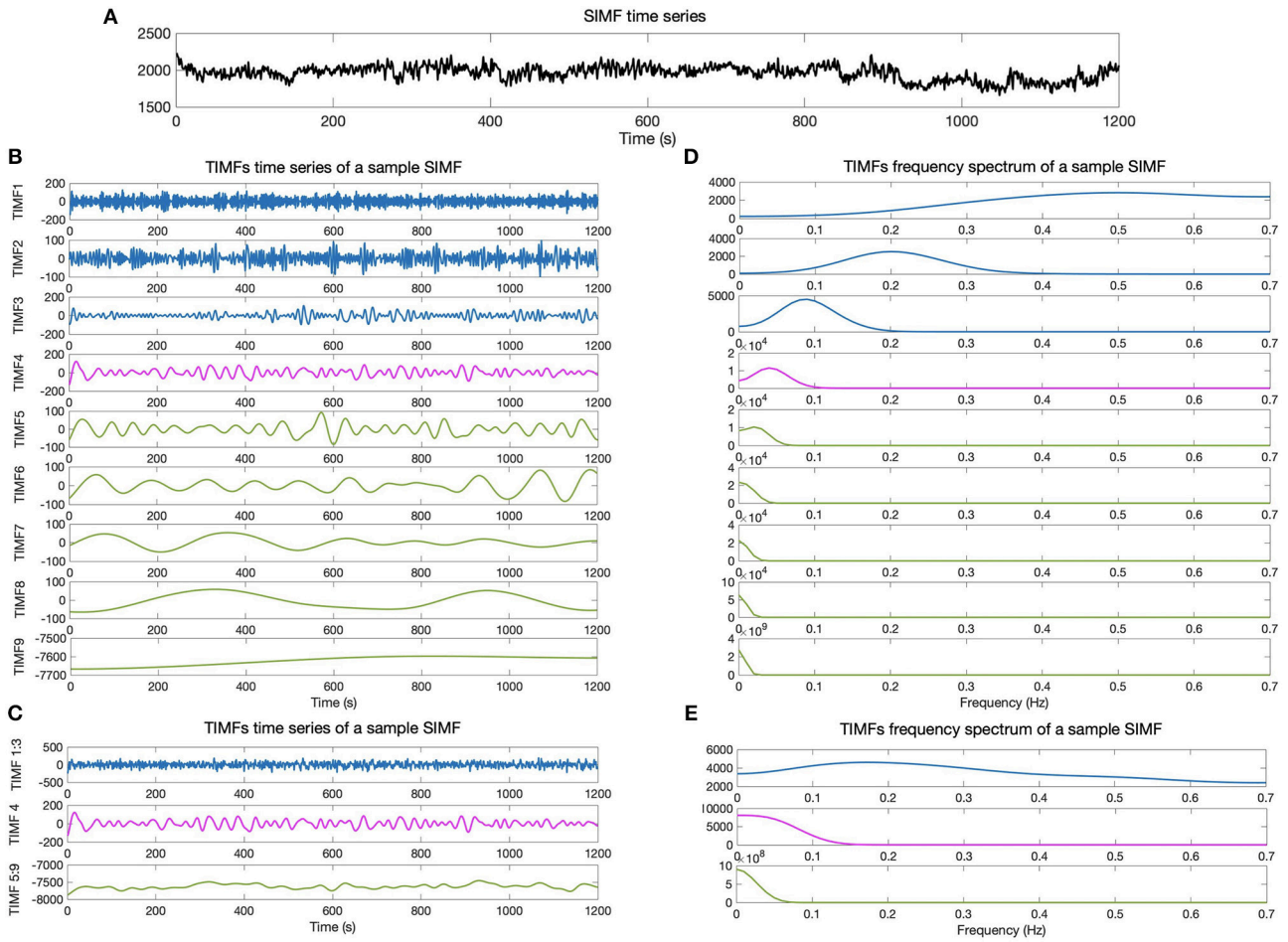

FIGURE 2 | Temporal IMFs and their corresponding frequency spectrum of the sample SIMF time series. **(A)** Sample of SIMF time series before temporal decomposition **(B)** 9 decomposed TIMFs of a sample SIMF by applying the ICEEMDAN method with 300 ensembles and a level of noise of 0.2. **(C)** The 9 decomposed TIMFs are divided into three different frequency bands. According to slow1 to slow3 and slow5 frequency bands defined in the literature, TIMFs1 to 3 and 5 to 9 are combined, respectively. **(D)** Represents the frequency spectrum of the 9 TIMFs. **(E)** The frequency spectrum of TIMFs in part **(C)** that correspond to frequency bands used in the literature for slow1 to slow5 Penttonen and Buzsáki (2003), Zhan et al. (2014). TIMF, Temporal Intrinsic Mode Function; ICEEMDAN, Improved Complete Ensemble Empirical Mode Decomposition with Adaptive Noise.

domains may cause spurious connectivity results between brain regions.

3.2. Regressing Out the AGS and SGS From fMRI Data

According to the definition of AGS, for each brain voxel signal, there is a corresponding AGS while the SGS is common for the whole brain voxels. The AGS for each voxel is computed by summing up the SIMF3, SIMF4, and SIMF5 with all TIMFs while the SGS is computed by taking the average of all brain voxels' time series. It should be noted that in computing AGS, the residues of spatiotemporal decomposition of the fMRI data are added to the last TIMF and SIMF. The three time courses in **Figures 7A–C** correspond to the AGS, the fMRI sample time course [the peak voxel's time course in Medial Prefrontal cortex (MPF) ROI], and the conventional or Static GS (SGS), respectively. **Figures 7D,E** show resting-state fluctuations of the sample fMRI time series from MPF ROI after regressing out (subtracting) the AGS and the SGS. It also has to be mentioned that to be consistent with the previous fMRI studies, data are conventionally low-pass filtered except when the AGSR method is applied.

3.3. Connectivity Map of Task-Positive and Task-Negative Networks

The default mode network or Task Negative Network (TNN) is a state of brain activation whereby the individual is not attending to any external cues in the environment but certain brain regions are still activated and they are less active during task performance rather than during the resting-state. It has been shown that (Fox et al., 2005) the default mode network responses are significantly activated in three of the seeded regions: the Posterior Cingulate Cortex (PCC), Medial Prefrontal cortex (MPF), and Lateral Parietal cortex (LP). The efficacy of our approach is examined by computing the connectivity map. In computing functional

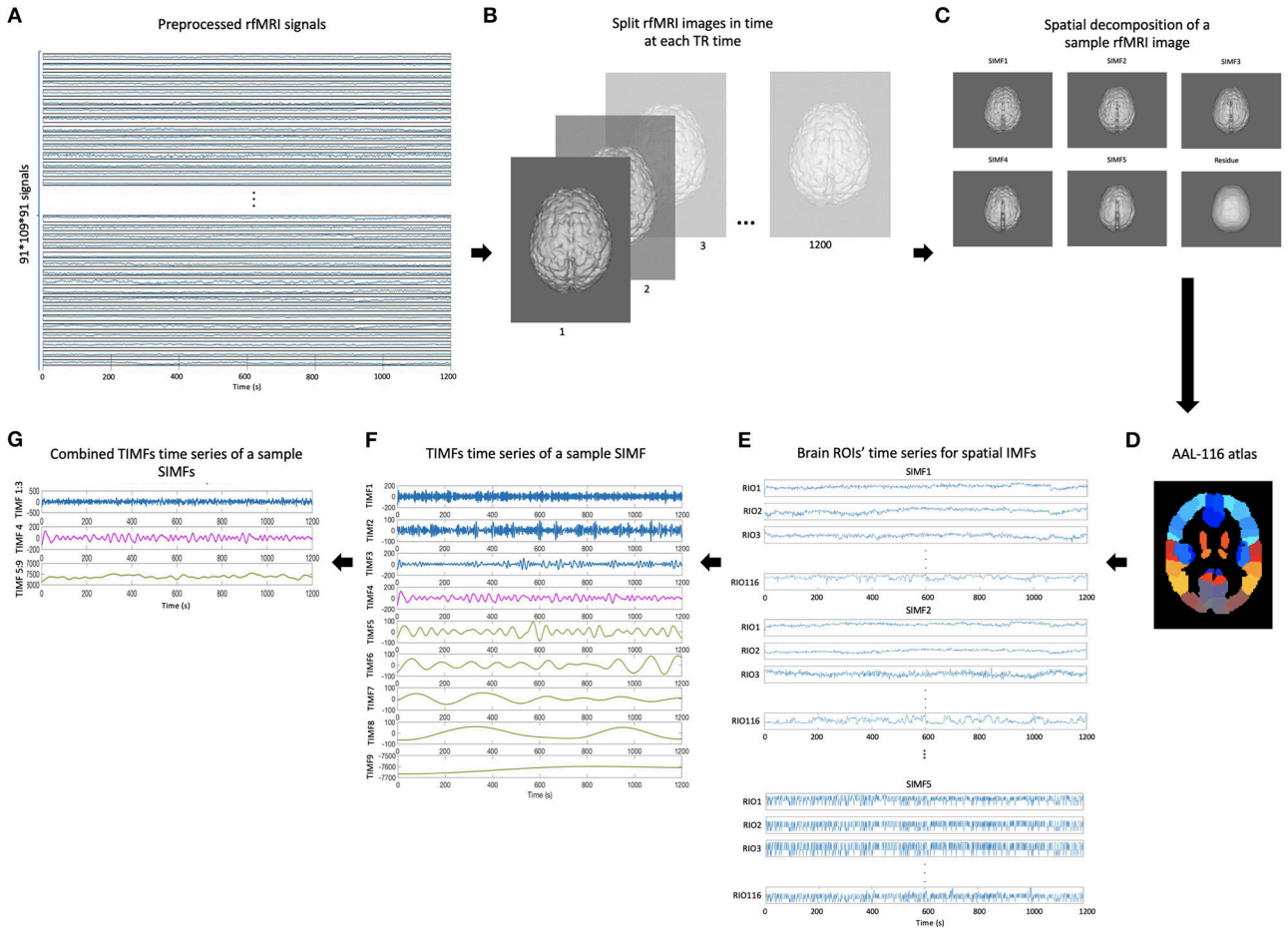

FIGURE 3 | Pipeline for computing spatial and temporal IMFs (SIMF and TIMF) of the fMRI data. **(A)** A sample of fMRI data. **(B)** Splitting each fMRI data in time at each TR time. **(C)** SIMFs at each TR time which are computed by applying FATEMD approach. **(D)** Shows the AAL 116 atlas used after merging SIMFs in time to select the peak voxel of each region. **(E)** Time series of all brain ROIs for each SIMF. **(F)** The TIMFs' time series of a sample SIMF for one ROI computed by using ICEEMDAN approach. **(G)** Summation of time series of the TIMFs in **(F)** based on frequency bands of slow1 to slow5 defined in the literature. The summation of the TIMF1 to TIMF3, TIMF4, and the combination of TIMF5 to TIMF9 are labeled as TIMF1, TIMF2, and TIMF3 in the rest of the paper, respectively. rfMRI, resting-state fMRI; TIMF, Temporal Intrinsic Mode Function; SIMF, Spatial Intrinsic Mode Function; ICEEMDAN, Improved Complete Ensemble Empirical Mode Decomposition with Adaptive Noise; FATEMD, Fast and Adaptive Empirical Mode Decomposition; ROI, Region of Interest.

connectivity maps, we computed Pearson's correlation which is popular in fMRI studies and also allows our findings to be comparable with other papers to test the validity of the proposed method. We computed the average connectivity between the time course of the PCC region as a seed region and the main regions of the Task Positive Network (TPN) which are the Middle Temporal (MT), right Frontal Eye Field (FEF), left Intraparietal Sulcus (IPS), Supplementary Motor Area (SMA), Inferior Parietal Lobule (IPL), Visual regions, and the left Auditory region and the TNN ROIs which are MPF, PCC, and left LP which includes the Angular Gyrus, Hippocampus, and Cerebellar tonsils ROIs (Fox et al., 2009; Erdoğan et al., 2016).

Considering the AGS definition, the combination of the SIMF1 and SIMF2 was used to compute the functional connectivity between PCC and TNN and TPN including visual ROIs by using Pearson's correlation coefficient (r), $P \leq 0.01$. **Figure 8** is functional connectivity brain map for different brain layers along the Z axis which show the mean connectivity over all subjects between brain regions and the PCC ROI as a seed region when the AGSR, NR, and the SGSR are performed.

Figure 9 shows expected average connectivity between the PCC ROI and different regions of the TPN and the TNN (positive correlation between the PCC and the TNN and negative correlation between the PCC and TPN) applying the new approach of GSR in resting-state fMRI data.

While the NR and SGSR (conventional GSR which is based on averaging) are unable to identify the expected connectivity in some regions for TPN and TNN ROIs, the AGSR approach obtains expected functional connectivity for all regions in TNN and TPN which confirms the effectiveness of the proposed method for GSR (**Figure 9**). As AGSR is an adaptive and voxel-specific method, we have a unique local signal for each voxel which by being removed from fMRI data augments the precision of the rsfc-MRI results.

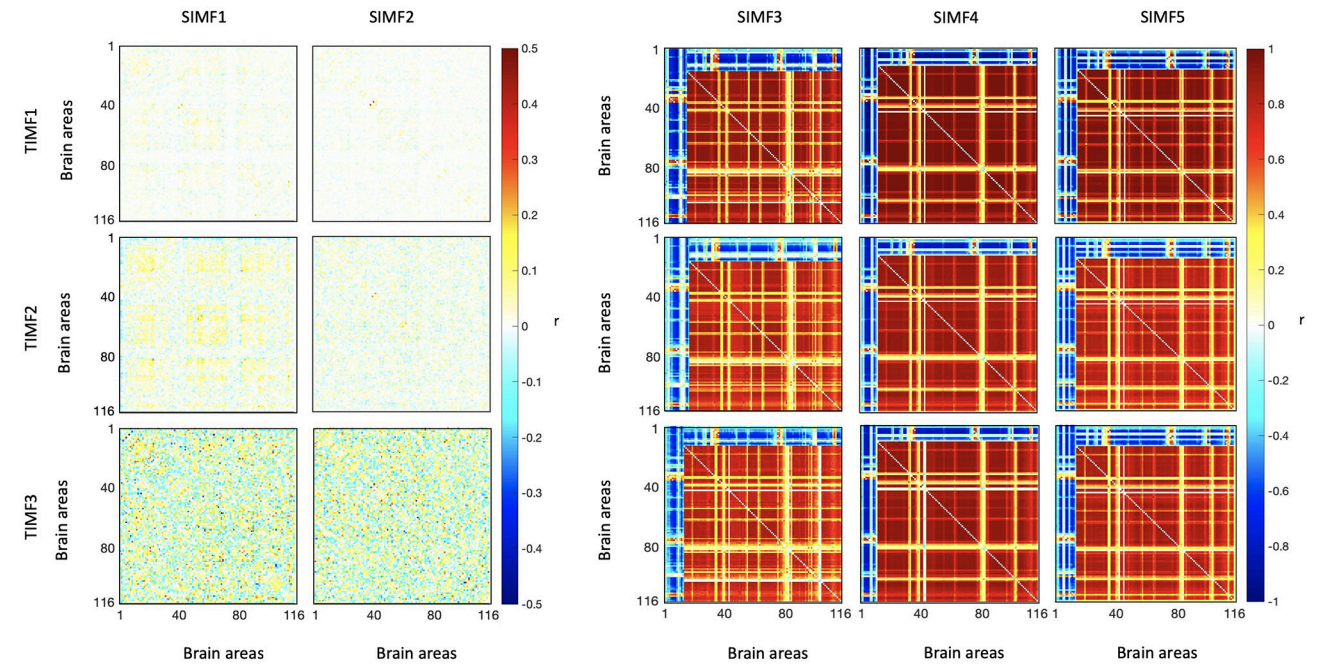

FIGURE 4 | Functional connectivity matrices of the whole brain regions using AAL 116 atlas for different spatial and temporal IMFs. Pearson's correlation coefficient (*r*) with $P \leq 0.01$ is computed between all the brain regions' spatiotemporal domains extracted from fMRI data. Spatial domains are extracted by applying FATEMD method on fMRI signal. The three temporal domains including TIMF1, TIMF2, and TIMF3 are computed by applying ICEEMDAN on each SIMF. SIMF, Spatial Intrinsic Mode Function; TIMF, Temporal Intrinsic Mode Function; ICEEMDAN, Improved Complete Ensemble Empirical Mode Decomposition with Adaptive Noise; FATEMD, Fast and Adaptive Empirical Mode Decomposition.

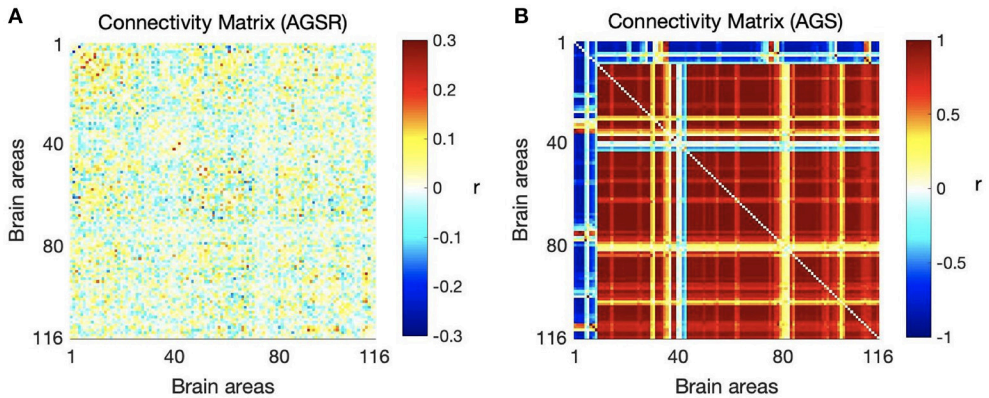

FIGURE 5 | Average functional connectivity matrices of the whole brain regions using AAL 116 atlas over all subjects. **(A)** Average connectivity matrix of fMRI data applying AGSR which means the connectivity matrix of combination of SIMF1 and SIMF2 including all TIMFs of the fMRI data, **(B)** connectivity matrix of the AGS which is the combination of SIMF3 to SIMF5 including all TIMFs. AGSR, Adaptive Global Signal regression; AGS, Adaptive Global Signal; SIMF, Spatial Intrinsic Mode Function; TIMF, Temporal Intrinsic Mode Function.

4. DISCUSSION

In contrast to previous works (Zarahn et al., 1997; Fox et al., 2009; Liu et al., 2017), the present study provides a new method for GSR, called AGSR, that works voxel-specifically and adaptively. It is believed that fMRI data are a superposition of the GS and network-specific fluctuations. However, the main reason for the controversy over the use of GSR in fMRI studies is that the average-based GS is a mixture of signals from multiple brain regions without considering the possibility of spatial heterogeneity in the GS (Fox et al., 2009; Murphy et al., 2009; Weissenbacher et al., 2009; Saad et al., 2012; Murphy and Fox, 2017). It has been shown that regressing out average-based GS results in negative correlations that do not have a biological basis and are artifacts in the voxels' time series which lead to distortion in the connectivity results or activation measures (Fox et al.,

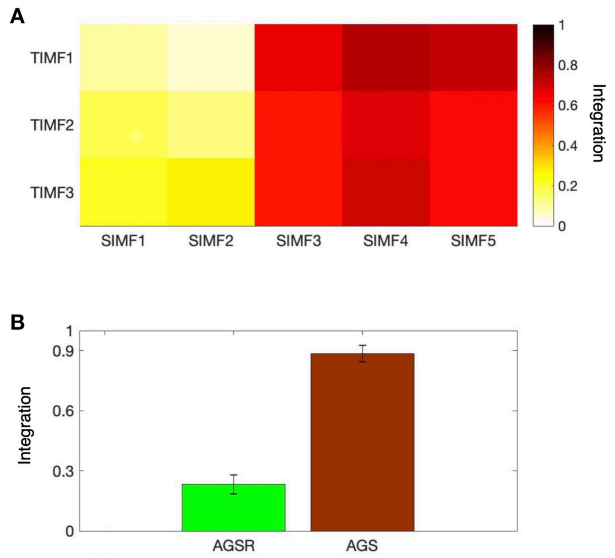

FIGURE 6 | Integration of the brain network at different spatiotemporal scales. **(A)** Average efficiency of the whole brain network for different spatial and temporal IMFs defined in functional connectivity. **(B)** Comparing the magnitude of average efficiency of the brain network over all subjects when the AGS is removed from the fMRI time series (the sum of SIMF3 to SIMF5 in all TIMFS are removed and the sum of SIMF1 to SIMF2 including all TIMFs of the fMRI signal are considered to compute the connectivity), and the average efficiency of the AGS (summing up SIMF3 to SIMF5 in all TIMFs). High efficiency values in the SIMF3 to SIMF5 which represent the AGS in the fMRI data are seen in the figures. GS, Global Signal; AGS, Adaptive GS.

TABLE 1 | Integration of AGSR and AGS. The average efficiency of the brain network over all subjects, when the AGSR are performed, and the average efficiency of the AGS. AGS, Adaptive Global Signal; AGSR, AGS Regression.

Network measure	Label	Interpretation	Value
Efficiency	AGSR	The brain network's average efficiency when AGSR is performed	0.2325±0.0480
Efficiency	AGS	The brain network's average efficiency of the AGS	0.8850±0.0417

2009; Murphy et al., 2009; Murphy and Fox, 2017). In this paper, we showed that the AGSR method works voxel-specifically and can compute the neuronal correlations of the brain's networks more accurately. This is because using the FATEMD method in computing AGS maximizes the spatial contributions to the GS. In other words, decomposing fMRI data in space using the FATEMD approach, which is done by considering features of each voxel's neighbors, makes the computed AGS sensitive to brain regions' heterogeneity.

When assessing the efficiency for different spatiotemporal domains of the fMRI data, no large differences in different temporal IMFs at the same spatial IMF were obtained. Thus, we concluded that the variability of efficiency is just related to the spatial frequency domains. The high values of the efficiency in the low spatial frequencies demonstrated the existence of the GS. On the other hand, high spatial frequencies, SIMF1 and SIMF2, represented the most network-specific data. Accordingly, the low spatial frequencies, SIMF3 to SIMF5 including all TIMFs, were considered as the AGS.

Additionally, it has been shown that motion, cardiac, and respiratory noise components which have high frequency cycles and are spatially coherent, cause spatially widespread fluctuations in the BOLD signals that contribute to the global signal (Shmueli et al., 2007; Liu et al., 2017). Conventionally, filtering the high frequency components of the fMRI data to remove above mentioned physiological noises and the GSR are done separately as two preprocessing steps in fMRI studies (He and Liu, 2012; Caballero-Gaudes and Reynolds, 2017; Liu et al., 2017), however, common low-pass filtering methods through removing high frequency components cause missing a considerable amount of information on resting-state brain functional network (Tagliazucchi et al., 2011, 2012; Boubela et al., 2013; Turchi et al., 2018). In our proposed method, in addition to GSR, physiological noise components that are common across voxels and are mainly included in the high frequency modes are also removed from the data by removing the SIMF3 to SIMF5 of TIMF1 through AGSR. Thus, our proposed method, through AGSR, filters the highly connected part of high frequency modes adaptively without applying low-pass filter separately. It can help to provide more informative data by involving high frequency modes in the data.

We examined the efficacy of our method by computing the seed-based functional connectivity for the TPN and TNN regions. Our results in agreement with previous studies (Chang and Glover, 2009; Fox et al., 2009; Chai et al., 2012), show that the negative correlations are intrinsic to the brain and do not appear just as a result of the GSR. We found that the AGSR method identifies the connectivity between the TPN and TNN regions according with the expected results of prior studies (Fox et al., 2005, 2009). We compared the connectivity results of the AGSR with the SGSR and when there is NR in the fMRI data. Despite the connectivity results of the SGSR method and when there is NR, applying our proposed method resulted in an enhancement to the detection of network-specific fluctuations of the brain. Furthermore, although the strength of the correlations is related to cognitive function, in auditory regions, lower activity seen in the result of applying AGSR appears to be related to the better removal of the acoustic noise heard by subjects during fMRI. This shows that the acoustic noise of the fMRI device which is almost constant in all TR times and interferes with auditory system activity can be removed better through AGSR (Ravicz et al., 2000; Moelker and Pattynama, 2003). Thus, it is inferred from the results that AGSR method is able to remove physiological and remained systemic noises after preprocessing more correctly and without introducing artifactual correlations as confirmed by correlations between PCC and the reference regions.

In conclusion, AGS is a unique local signal for each voxel's BOLD signal. In the AGSR method, the first and second spatial IMFs of each fMRI data, decomposed by FATEMD method, are simply summed up to have a band-pass filtered fMRI data without GS. AGSR is a reliable method that works voxel-specifically for all subjects which leads to provide information about brain function with more accuracy. There are some

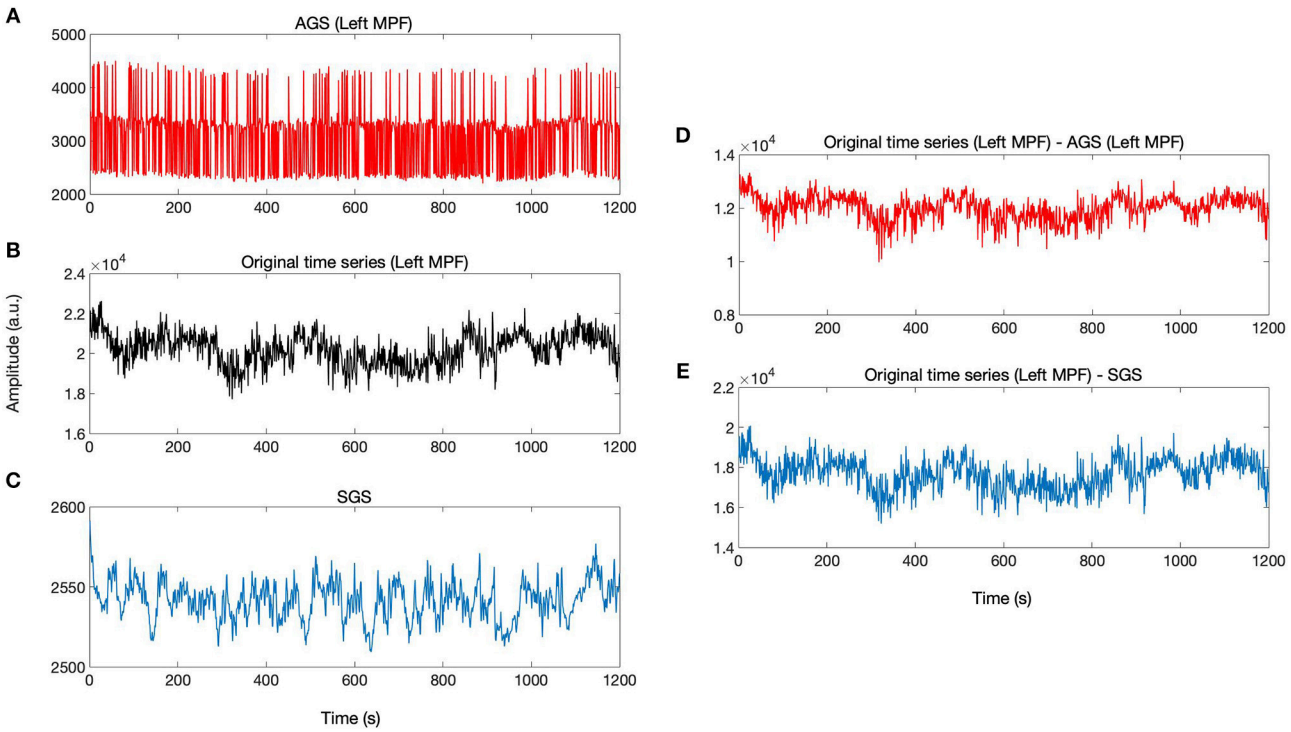

FIGURE 7 | AGSR and SGSR of a sample fMRI data. **(A)** The voxel-specific AGS of Medial Prefrontal (MPF) cortex region and **(B)** the original fMRI time series of the peak voxel in MPF cortex region. **(C)** The SGS which is common for all region's voxels. **(D,E)** Show the time series with the SGSR and AGSR, respectively. These time series are computed by subtracting the AGS and SGS from the original time series. MPF, Medial Prefrontal cortex; AGS, Adaptive Global Signal; SGS, Static(conventional) Global Signal; AGSR, AGS Regression; SGSR, SGS Regression.

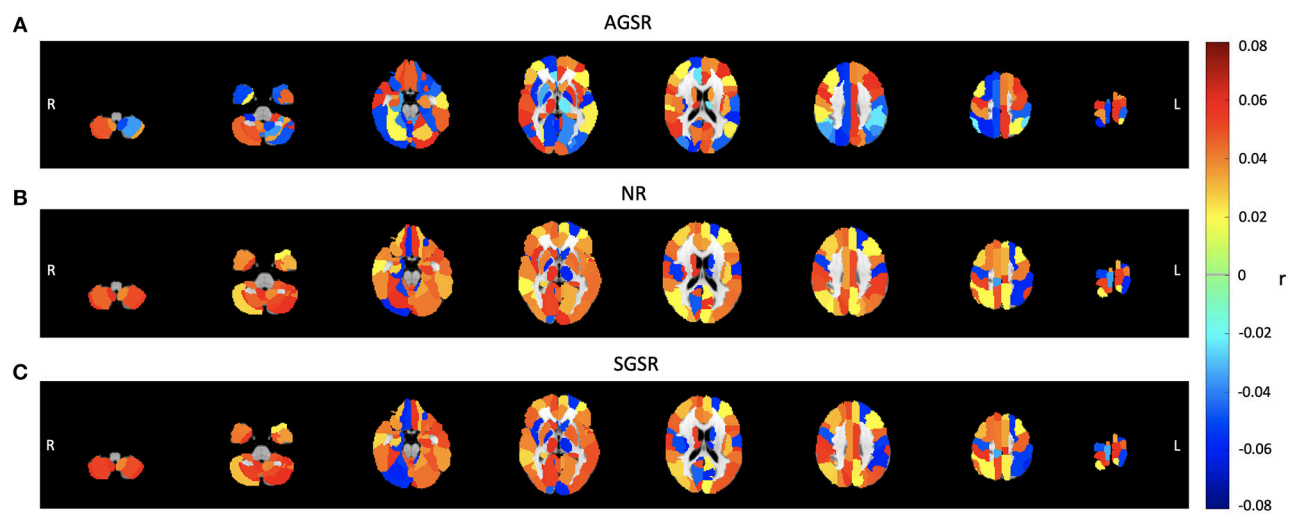

FIGURE 8 | Comparing the average functional connectivity between the PCC ROI as a seed region and the brain ROIs using the AAL 116 atlas for fMRI data of all subjects. The average functional connectivity applying **(A)** AGSR, **(B)** NR, and **(C)** SGSR. Slices shown in the maps are at Z = 09, 15, 25, 35, 45, 55, 65, 75, respectively. AGSR, Adaptive Global Signal Regression; NR, No Regression; SGSR, Static (conventional) Global signal regression.

limitations to the methods used in this study that should be noted. Although the FATEMD and ICEEMDAN are optimized approaches for finding the best IMF sets, they still need more improvement in the sifting procedure to yield better decomposition performance. For instance, finding the optimum values of added white noise and the ensemble number to overcome the mode mixing problem and speed up the calculation in ICEEMDAN approach are two drawbacks of this approach.

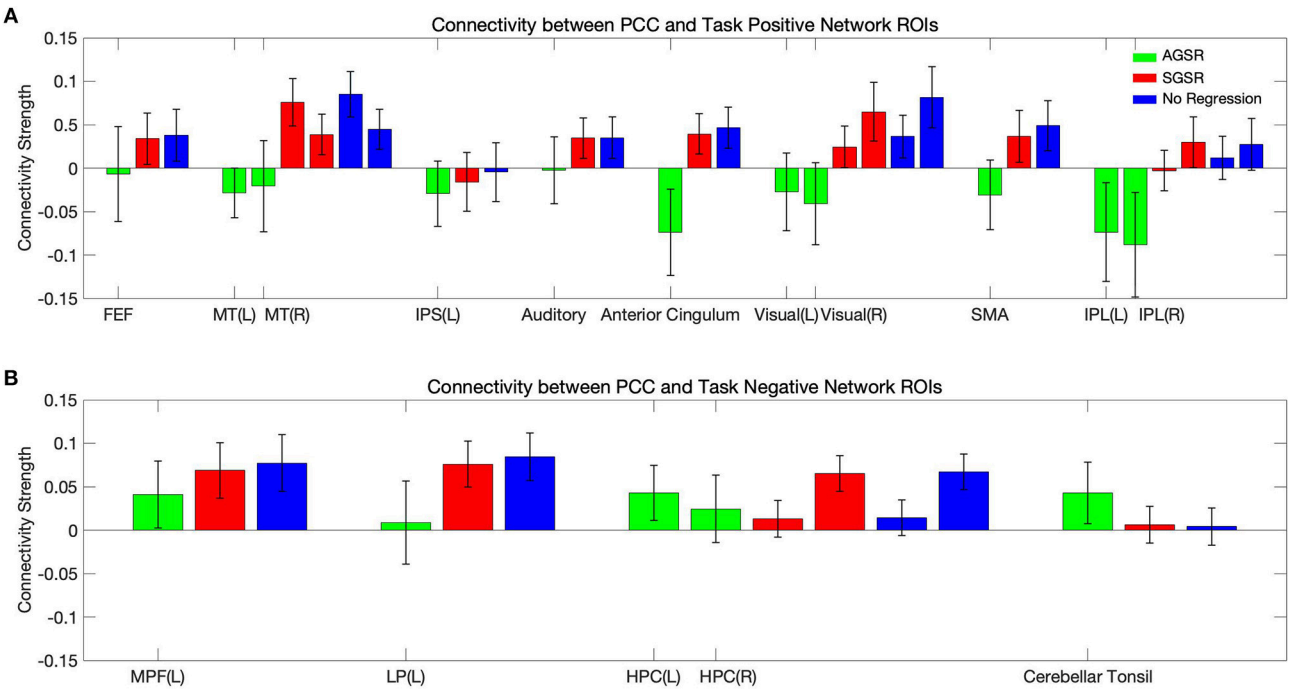

FIGURE 9 | The average connectivity map between the PCC as a seed region and **(A)** the TPN and **(B)** TNN ROIs for fMRI data of all subjects. Connectivity results of applying AGSR and SGSR are shown in green and red, respectively, and the blue ones are the results of computing connectivity without applying any GSR (NR). Connectivity map is made by computing Pearson's correlation coefficient (r) with $P \leq 0.01$ between the PCC region as a seed region and the main regions of the TPN and TNN. PCC, Posterior Cingulate Cortex; MPF, Medial Prefrontal cortex; LP, Lateral Parietal cortex; MT, Middle Temporal; FEF, Frontal Eye Field; IPS, Intraparietal Sulcus; SMA, Supplementary Motor Area; IPL, Inferior Parietal Lobule; ROI, Region Of Interest; NR, No Regression; AGS, Adaptive Global Signal Regression; SGS, Static (conventional) Global Signal Regression.

We computed the GS for each region of the AAL 116 atlas specifically, however, as this method has a "voxel-specific" nature, it can be applied to all voxels of the brain. Computing voxel-specific GS just needs more memory and computer power, such as a larger computer cluster but no additional changes to the underlying algorithm are needed. It is more feasible to compute the AGSR for all the voxels when we are interested in some specific regions of the brain and not the whole brain.

Therefore, the proposed method in this paper provides the opportunity to characterize the whole brain function and reflect the intrinsic property of the spatiotemporal nature of the fMRI data through removing the voxel-specific GS and not removing the whole high frequency modes. Future studies can be devoted to the application of our proposed method to the other image processing areas.

AUTHOR CONTRIBUTIONS

NM and RS designed the research. NM analyzed the data, interpreted the results and wrote the main manuscript. MD assisted with analysis and interpretation of data. RS supervised the development of the work, helped in data interpretation and manuscript evaluation.

ACKNOWLEDGMENTS

We are grateful to Doug Phillips for generous assistance in computational work on Compute Canada cluster and Jordan Chad for proofreading the manuscript. This work was partially supported by grant RGPIN-2015-05966 from Natural Sciences and Engineering Research Council of Canada. Data were provided [in part] by the Human Connectome Project, WU-Minn Consortium (Principal Investigators: David Van Essen and Kamil Ugurbil; 1U54MH091657) funded by the 16 NIH Institutes and Centers that support the NIH Blueprint for Neuroscience Research; and by the McDonnell Center for Systems Neuroscience at Washington University. The computational work was enabled by support provided of WestGrid (www.westgrid.ca) through Compute Canada (www.computecanada.ca).

REFERENCES

Anderson, J. S., Druzgal, T. J., Lopez Larson, M., Jeong, E. K., Desai, K., and Yurgelun-Todd, D. (2010). Network anticorrelations, global regression, and phase-shifted soft tissue correction. *Hum. Brain Mapp.* 32, 919–934. doi: 10.1002/hbm.21079

Arthurs, O., and J Boniface, S. (2003). What aspect of the fmri bold signal best reflects the underlying electrophysiology in human somatosensory

cortex? *Clin. Neurophysiol.* 114, 1203–1209. doi: 10.1016/S1388-2457(03)00080-4

Ashburner, J., and Friston, K. J. (1999). Nonlinear spatial normalization using basis functions. *Hum. Brain Mapp.* 7, 254–266. doi: 10.1002/(SICI)1097-0193(1999)7:4<254::AID-HBM4>3.0.CO;2-G

Bhuiyan, S. M. A., Adhami, R. R., and Khan, J. F. (2008). Fast and adaptive bidimensional empirical mode decomposition using order-statistics filter based envelope estimation. *EURASIP J. Adv. Signal Process.* 2008:728356. doi: 10.1155/2008/728356

Biswal, B., Zerrin Yetkin, F., Haughton, V. M., and Hyde, J. S. (1995). Functional connectivity in the motor cortex of resting human brain using echo-planar MRI. *Magn. Resonan. Med.* 34, 537–541. doi: 10.1002/mrm.1910340409

Boubela, R., Kalcher, K., Huf, W., Kronnerwetter, C., Filzmoser, P., and Moser, E. (2013). Beyond noise: using temporal ica to extract meaningful information from high-frequency fMRI signal fluctuations during rest. *Front. Hum. Neurosci.* 7:168. doi: 10.3389/fnhum.2013.00168

Brooks, J., Faull, O., Pattinson, K., and Jenkinson, M. (2013). Physiological noise in brainstem fMRI. *Front. Hum. Neurosci.* 7:623. doi: 10.3389/fnhum.2013.00623

Caballero-Gaudes, C., and Reynolds, R. C. (2017). Methods for cleaning the bold fMRI signal. *NeuroImage* 154, 128–149. doi: 10.1016/j.neuroimage.2016.12.018

Chai, X. J., Castañón, A. N., Ongür, D., and Whitfield-Gabrieli, S. (2012). Anticorrelations in resting state networks without global signal regression. *NeuroImage* 59, 1420–1428. doi: 10.1016/j.neuroimage.2011.08.048

Chang, C., and Glover, G. H. (2009). Effects of model-based physiological noise correction on default mode network anti-correlations and correlations. *NeuroImage* 47, 1448–1459. doi: 10.1016/j.neuroimage.2009.05.012

Chang, C., Leopold, D., Schölvinck, M., Mandelkow, H., Picchioni, D., Liu, X., et al. (2016). Tracking brain arousal fluctuations with fmri. *Proc. Natl. Acad. Sci. U.S.A.* 113, 4518–4523. doi: 10.1073/pnas.1520613113

Cohen, J. R., and D'Esposito, M. (2016). The segregation and integration of distinct brain networks and their relationship to cognition. *J. Neurosci.* 36, 1283–2094. doi: 10.1523/JNEUROSCI.2965-15.2016

Colominas, M., Schlotthauer, G., and Torres, M. E. (2014). Improved complete ensemble EMD: a suitable tool for biomedical signal processing. *Biomed. Signal Process. Control* 14, 19–29. doi: 10.1016/j.bspc.2014.06.009

Comon, P., and Jutten, C. (2010). *Handbook of Blind Source Separation, Independent Component Analysis and Applications, 1st Edn*. Boston, MA: Academic Press; Elsevier.

Cordes, D., Zhuang, X., Kaleem, M., Sreenivasan, K., Yang, Z., Mishra, V., et al. (2018). Advances in functional magnetic resonance imaging data analysis methods using empirical mode decomposition to investigate temporal changes in early parkinson's disease. *Alzheimer's Dementia Transl. Res. Clin. Intervent.* 4, 372–386. doi: 10.1016/j.trci.2018.04.009

Damoiseaux, J. S., Rombouts, S. A. R. B., Barkhof, F., Scheltens, P., Stam, C. J., Smith, S. M., et al. (2006). Consistent resting-state networks across healthy subjects. *Proc. Natl. Acad. Sci. U.S.A.* 103, 13848–13853. doi: 10.1073/pnas.0601417103

De Luca, M., Beckmann, C., De Stefano, N., Matthews, P., and Smith, S. (2006). fMRI resting state networks define distinct modes of long-distance interactions in the human brain. *NeuroImage* 29, 1359–1367. doi: 10.1016/j.neuroimage.2005.08.035

Erdoğan, S. B., Tong, Y., Hocke, L. M., Lindsey, K. P., and DeB Frederick, B. (2016). Correcting for blood arrival time in global mean regression enhances functional connectivity analysis of resting state fMRI-BOLD signals. *Front. Hum. Neurosci.* 10:311. doi: 10.3389/fnhum.2016.00311

Essen, D. C. V., Smith, S. M., Barch, D. M., Behrens, T. E., Yacoub, E., and Ugurbil, K. (2013). The WU-Minn human connectome project: an overview. *NeuroImage* 80, 62–79. doi: 10.1016/j.neuroimage.2013.05.041

Evans, A. C., Collins, D. L., Mills, S. R., Brown, E. D., Kelly, R. L., and Peters, T. M. (1993). "3D statistical neuroanatomical models from 305 mri volumes," in *1993 IEEE Conference Record Nuclear Science Symposium and Medical Imaging Conference, Vol. 3*, 1813–1817.

Fair, D. A., Dosenbach, N. U. F., Church, J. A., Cohen, A. L., Brahmbhatt, S., Miezin, F. M., et al. (2007). Development of distinct control networks through segregation and integration. *Proc. Natl. Acad. Sci. U.S.A.* 104, 13507–13512. doi: 10.1073/pnas.0705843104

Fox, M., Snyder, A., Zacks, J., and Raichle, M. (2006). Coherent spontaneous activity accounts for trial-to-trial variability in human evoked brain responses. *Nat. Neurosci.* 9, 23–25. doi: 10.1038/nn1616

Fox, M. D., and Raichle, M. E. (2007). Spontaneous fluctuations in brain activity observed with functional magnetic resonance imaging. *Nat. Rev. Neurosci.* 8, 700–711. doi: 10.1038/nrn2201

Fox, M. D., Snyder, A. Z., Vincent, J. L., Corbetta, M., Van Essen, D. C., and Raichle, M. E. (2005). The human brain is intrinsically organized into dynamic, anticorrelated functional networks. *Proc. Natl. Acad. Sci. U.S.A.* 102, 9673–9678. doi: 10.1073/pnas.0504136102

Fox, M. D., Zhang, D., Snyder, A. Z., and Raichle, M. E. (2009). The global signal and observed anticorrelated resting state brain networks. *J. Neurophysiol.* 101, 3270–3283. doi: 10.1152/jn.90777.2008

Friston, K. J. (2011). Functional and effective connectivity: a review. *Brain Connect.* 1, 13–36. doi: 10.1089/brain.2011.0008

Gallagher, T. A., Nemeth, A. J., and Hacein-Bey, L. (2008). An introduction to the fourier transform: relationship to MRI. *Am. J. Roentgenol.* 5, 1396–1405. doi: 10.2214/AJR.07.2874

Hassan, H., and John, W. P. (2005). Empirical mode decomposition (EMD) of potential field data: airborne gravity data as an example. *Can. Soc. Explor. Geophys.* 24, 704–706. doi: 10.1190/1.2144422

He, H., and Liu, T. T. (2012). A geometric view of global signal confounds in resting-state functional MRI. *NeuroImage* 59, 2339–2348. doi: 10.1016/j.neuroimage.2011.09.018

He, Z., Li, J., Liu, L., and Shen, Y. (2017). Three-dimensional empirical mode decomposition (TEMD): a fast approach motivated by separable filters. *Signal Process.* 131, 307–319. doi: 10.1016/j.sigpro.2016.08.024

Huang, N., Shen, Z., Long, S., Wu, M., Shih, H., Zheng, Q., et al. (1998). The empirical mode decomposition and the hilbert spectrum for nonlinear and non-stationary time series analysis. *Proc. R. Soc. Lond. A* 454, 903–995. doi: 10.1098/rspa.1998.0193

Jahanshad, N., Kochunov, P. V., Sprooten, E., Mandl, R. C., Nichols, T. E., Almasy, L., et al. (2013). Multi-site genetic analysis of diffusion images and voxelwise heritability analysis: a pilot project of the ENIGMA–DTI working group. *NeuroImage* 81, 455–469. doi: 10.1016/j.neuroimage.2013.04.061

Jenkinson, M., Bannister, P., Brady, M., and Smith, S. (2002). Improved optimization for the robust and accurate linear registration and motion correction of brain images. *NeuroImage* 17, 825–841. doi: 10.1006/nimg.2002.1132

Jenkinson, M., and Smith, S. (2001). A global optimisation method for robust affine registration of brain images. *Med. Image Anal.* 5, 143–156. doi: 10.1016/S1361-8415(01)00036-6

Jovicich, J., Czanner, S., Greve, D., Haley, E., van der Kouwe, A., Gollub, R., et al. (2006). Reliability in multi-site structural MRI studies: effects of gradient non-linearity correction on phantom and human data. *NeuroImage* 30, 436–443. doi: 10.1016/j.neuroimage.2005.09.046

Kandel, E. R., Schwartz, J. H., and Jessell, T. M. (2000). *Principles of Neural Science, Vol. 4, 4th Edn.* McGraw-Hill Medical.

Lin, S.-H. N., Lin, G.-H., Tsai, P.-J., Hsu, A.-L., Lo, M.-T., Yang, A. C., Lin, C.-P., et al. (2016). Sensitivity enhancement of task-evoked fMRI using ensemble empirical mode decomposition. *J. Neurosci. Methods* 258, 56–66. doi: 10.1016/j.jneumeth.2015.10.009

Liu, T. T., Nalci, A., and Falahpour, M. (2017). The global signal in fMRI: nuisance or information? *NeuroImage* 150, 213–229. doi: 10.1016/j.neuroimage.2017.02.036

Liutkus, A., Durrieu, J.-L., Daudet, L., and Richard, G. (2013). "An overview of informed audio source separation," in *Proceedings of the 14th International Workshop Image Analysis Multimedia Interaction Service* (Paris), 1–4.

Macey, P., Macey, K., Kumar, R., and Harper, R. (2004). A method for removal of global effects from fMRI time series. *NeuroImage* 22, 360–366. doi: 10.1016/j.neuroimage.2003.12.042

Mandic, D., Golz, M., Kuh, A., Obradovic, D., and Tanaka, T. (2008). *Signal Processing Techniques for Knowledge Extraction and Information Fusion, 1st Edn*. New York, NY: Springer Publishing Company, Incorporated.

Mazziotta, J. C., Toga, A., Evans, A., Fox, P., Lancaster, J. N., Zilles, K., et al. (2001a). A probabilistic atlas and reference system for the human brain: international consortium for brain mapping (ICBM). *Philos. Trans. R. Soc. Lond. Ser. B Biol. Sci.* 1412, 1293–1322. doi: 10.1098/rstb.2001.0915

Mazziotta, J. C., Toga, A., Evans, A., Fox, P., Lancaster, J. N., Zilles, K., et al. (2001b). Four-dimensional probabilistic atlas of the human brain: international consortium for brain mapping (ICBM). *J. Am. Med. Inform. Assoc.* 8, 401–430. doi: 10.1136/jamia.2001.0080401

Mazziotta, J. C., Toga, A. W., Evans, A., Fox, P., and Lancaster, J. (1995). A probabilistic atlas of the human brain: theory and rationale for its development: the international consortium for brain mapping (ICBM). *NeuroImage* 2, 89–101.

McGonigle, J. E., Mirmehdi, M., and Malizia, A. L. (2010). "Empirical mode decomposition in data-driven fMRI analysis," in *Proceedings of the IEEE Workshop on Brain Decoding: Pattern Recognition Challenges in Neuroimaging* (Istanbul), 25–28. doi: 10.1109/WBD.2010.14

Moelker, A., and Pattynama, P. M. (2003). Acoustic noise concerns in functional magnetic resonance imaging. *Hum. Brain Mapp.* 20, 123–141. doi: 10.1002/hbm.10134

Moeller, S., Yacoub, E., Olman, C. A., Auerbach, E., Strupp, J., Harel, N., et al. (2010). Multiband multislice GE-EPI at 7 tesla, with 16-fold acceleration using partial parallel imaging with application to high spatial and temporal whole-brain fMRI. *Magn. Reson. Med.* 63, 1144–1153. doi: 10.1002/mrm.22361

Murphy, K., Birn, R. M., Handwerker, D. A., Jones, T. B., and Bandettini, P. A. (2009). The impact of global signal regression on resting state correlations: are anti-correlated networks introduced? *NeuroImage* 44, 893–905. doi: 10.1016/j.neuroimage.2008.09.036

Murphy, K., and Fox, M. D. (2017). Towards a consensus regarding global signal regression for resting state functional connectivity MRI. *NeuroImage* 154, 169–173. doi: 10.1016/j.neuroimage.2016.11.052

Niazy, R. K., Xie, J., Miller, K., Beckmann, C. F., and Smith, S. M. (2011). Spectral characteristics of resting state networks. *Prog. Brain Res.* 193, 259–276. doi: 10.1016/B978-0-444-53839-0.00017-X

Penttonen, M., and Buzsáki, G. (2003). Natural logarithmic relationship between brain oscillators. *Thalamus Relat. Syst.* 2, 145–152. doi: 10.1017/S1472928803000074

Power, J. D., Plitt, M., Laumann, T. O., and Martin, A. (2017). Sources and implications of whole-brain fMRI signals in humans. *NeuroImage* 146, 609–625. doi: 10.1016/j.neuroimage.2016.09.038

Qian, L., Zhang, Y., Zheng, L., Shang, Y., Gao, J.-H., and Liu, Y. (2015). Frequency dependent topological patterns of resting-state brain networks. *PLoS ONE* 10:e124681. doi: 10.1371/journal.pone.0124681

Ravicz, M. E., Melcher, J. R., and Kiang, N. Y.-S. (2000). Acoustic noise during functional magnetic resonance imaging. *J. Acoust. Soc. Am.* 108, 1683–1696. doi: 10.1121/1.1310190

Riffi, J., Adnane, M. M., Abbad, A., and Tairi, H. (2014). 3D extension of the fast and adaptive bidimensional empirical mode decomposition. *Multidim. Syst. Signal Process.* 26, 823–834. doi: 10.1007/s11045-014-0283-6

Riffi, J., Mahraz, A. M., and Tairi, H. (2013). Medical image registration based on fast and adaptive bidimensional empirical mode decomposition. *IET Image Process.* 7, 567–574. doi: 10.1049/iet-ipr.2012.0034

Rubinov, M., and Sporns, O. (2009). Complex network measures of brain connectivity: uses and interpretations. *NeuroImage* 52, 1059–1069. doi: 10.1016/j.neuroimage.2009.10.003

Saad, Z. S., Gotts, S. J., Murphy, K., Chen, G., Jo, H. J., Martin, A., et al. (2012). Trouble at rest: how correlation patterns and group differences become distorted after global signal regression. *Brain Connect.* 2, 25–32. doi: 10.1089/brain.2012.0080

Sharot, T., Delgado, M. R., and Phelps, E. A. (2005). How emotion enhances the feeling of remembering. *Nat. Neurosci.* 7, 1376–1380. doi: 10.1038/nn1353

Shmuel, A., and Leopold, D. A. (2008). Neuronal correlates of spontaneous fluctuations in fMRI signals in monkey visual cortex: implications for functional connectivity at rest. *Hum. Brain Mapp.* 29, 751–761. doi: 10.1002/hbm.20580

Shmueli, K., van Gelderen, P., de Zwart, J. A., Horovitz, S. G., Fukunaga, M., Jansma, J. M., et al. (2007). Low-frequency fluctuations in the cardiac rate as a source of variance in the resting-state fMRI bold signal. *NeuroImage* 38, 306–320. doi: 10.1016/j.neuroimage.2007.07.037

Song, X., Hu, X., Zhou, S., Xu, Y., Zhang, Y., Yuan, Y., et al. (2015). Association of specific frequency bands of functional MRI signal oscillations with motor syptoms and depression in Parkinson's disease. *Sci. Rep.* 5:16376. doi: 10.1038/srep16376

Song, X., Zhang, Y., and Liu, Y. (2014). Frequency specificity of regional homogeneity in the resting-state human brain. *PLoS ONE* 9:e86818. doi: 10.1371/journal.pone.0086818

Tagliazucchi, E., Balenzuela, P., Fraiman, D., and Chialvo, D. (2012). Criticality in large-scale brain fMRI dynamics unveiled by a novel point process analysis. *Front. Physiol.* 3:15. doi: 10.3389/fphys.2012.00015

Tagliazucchi, E., Balenzuela, P., Fraiman, D., Montoya, P., and Chialvo, D. R. (2011). Spontaneous bold event triggered averages for estimating functional connectivity at resting state. *Neurosci. Lett.* 488, 158–163. doi: 10.1016/j.neulet.2010.11.020

Tong, Y., and Frederick, B. (2014). Studying the spatial distribution of physiological effects on bold signals using ultrafast fMRI. *Front. Hum. Neurosci.* 8:196. doi: 10.3389/fnhum.2014.00196

Torres, M. E., Colominas, M. A., Schlotthauer, G., and Flandrin, P. (2011). "A complete ensemble empirical mode decomposition with adaptive noise," in *Proceedings of the 36th IEEE International Conference on Acoustics, Speech and Signal Process, ICASSP 2011* (Prague), 4144–4147. doi: 10.1109/ICASSP.2011.5947265

Turchi, J., Chang, C., Ye, F. Q., Russ, B. E., Yu, D. K., Cortes, C. R., et al. (2018). The basal forebrain regulates global resting-state fMRI fluctuations. *Neuron* 97, 940–952.e4. doi: 10.1016/j.neuron.2018.01.032

Tzourio-Mazoyer, N., Landeau, B., Papathanassiou, D., Crivello, F., Etard, O., Delcroix, N., et al. (2002). Automated anatomical labeling of activations in SPM using a macroscopic anatomical parcellation of the MNI MRI single-subject brain. *NeuroImage* 15, 273–289. doi: 10.1006/nimg.2001.0978

Weissenbacher, A., Kasess, C., Gerstl, F., Lanzenberger, R., Moser, E., and Windischberger, C. (2009). Correlations and anticorrelations in resting-state functional connectivity MRI: a quantitative comparison of preprocessing strategies. *NeuroImage* 47, 1408–1416. doi: 10.1016/j.neuroimage.2009.05.005

Wu, Z., Huang, N., Chen, X. (2009). The multi-dimensional ensemble empirical mode decomposition method. *Adv. Adapt. Data Anal.* 1, 339–372. doi: 10.1142/S1793536909000187

Wu, Z., and Huang, N. E. (2009). Ensemble empirical mode decomposition: a noise-assisted data analysis method. *Adv. Adapt. Data Anal.* 1, 1–41. doi: 10.1142/S1793536909000047

Yeh, J. R., Shieh, J. S., and Huang, N. E. (2010). Complementary ensemble empirical mode decomposition: a novel noise enhanced data analysis method. *Adv. Adapt. Data Anal.* 2, 135–156. doi: 10.1142/S1793536910000422

Yves, M. (1993). Wavelets-algorithms and applications. *Wavelets-Algorith. Appl. Soc. Indus. Appl. Math. Transl.* 36, 526–528.

Zarahn, E., Aguirre, G., and D'Esposito, M. (1997). Empirical analyses of bold fMRI statistics. I. spatially unsmoothed data collected under null-hypothesis conditions. *NeuroImage* 5, 179–197. doi: 10.1006/nimg.1997.0263

Zhan, Z., Xu, L., Zuo, T., Xie, D., Zhang, J., Yao, L., et al. (2014). The contribution of different frequency bands of fMRI data to the correlation with EEG alpha rhythm. *Brain Res.* 1543, 235–243. doi: 10.1016/j.brainres.2013.11.016

Zheng, T., Cai, M., and Jiang, T. (2010). A novel approach to activation detection in fmri based on empirical mode decomposition. *J. Integr. Neurosci.* 9, 407–427. doi: 10.1142/S021963521000255X

Conflict of Interest Statement: The authors declare that the research was conducted in the absence of any commercial or financial relationships that could be construed as a potential conflict of interest.

frontiers in Neuroscience

REVIEW
published: 13 August 2019
doi: 10.3389/fnins.2019.00825

Resting State fMRI: Going Through the Motions

Sanam Maknojia[1], Nathan W. Churchill[2], Tom A. Schweizer[2,3,4] and S. J. Graham[1,5]**

[1] Physical Sciences Platform, Sunnybrook Research Institute, Sunnybrook Health Sciences Centre, Toronto, ON, Canada, [2] Keenan Research Centre for Biomedical Science, St. Michael's Hospital, Toronto, ON, Canada, [3] Division of Neurosurgery, Faculty of Medicine, University of Toronto, Toronto, ON, Canada, [4] Institute of Biomaterials and Biomedical Engineering, Faculty of Medicine, University of Toronto, Toronto, ON, Canada, [5] Department of Medical Biophysics, Faculty of Medicine, University of Toronto, Toronto, ON, Canada

Resting state functional magnetic resonance imaging (rs-fMRI) has become an indispensable tool in neuroscience research. Despite this, rs-fMRI signals are easily contaminated by artifacts arising from movement of the head during data collection. The artifacts can be problematic even for motions on the millimeter scale, with complex spatiotemporal properties that can lead to substantial errors in functional connectivity estimates. Effective correction methods must be employed, therefore, to distinguish true functional networks from motion-related noise. Research over the last three decades has produced numerous correction methods, many of which must be applied in combination to achieve satisfactory data quality. Subject instruction, training, and mild restraints are helpful at the outset, but usually insufficient. Improvements come from applying multiple motion correction algorithms retrospectively after rs-fMRI data are collected, although residual artifacts can still remain in cases of elevated motion, which are especially prevalent in patient populations. Although not commonly adopted at present, "real-time" correction methods are emerging that can be combined with retrospective methods and that promise better correction and increased rs-fMRI signal sensitivity. While the search for the ideal motion correction protocol continues, rs-fMRI research will benefit from good disclosure practices, such as: (1) reporting motion-related quality control metrics to provide better comparison between studies; and (2) including motion covariates in group-level analyses to limit the extent of motion-related confounds when studying group differences.

Keywords: resting state fMRI, noise, motion artifacts, motion compensation, image processing

OPEN ACCESS

Edited by:
Shella Keilholz,
Emory University, United States

Reviewed by:
Veena A. Nair,
University of Wisconsin-Madison, United States
Jodie Reanna Gawryluk,
University of Victoria, Canada

****Correspondence:***
Sanam Maknojia
sanam.kadiwal@gmail.com
S. J. Graham
sgraham@sri.utoronto.ca

Specialty section:
This article was submitted to Brain Imaging Methods, a section of the journal Frontiers in Neuroscience

Received: *27 March 2019*
Accepted: *23 July 2019*
Published: *13 August 2019*

Citation:
Maknojia S, Churchill NW, Schweizer TA and Graham SJ (2019) Resting State fMRI: Going Through the Motions. Front. Neurosci. 13:825. doi: 10.3389/fnins.2019.00825

INTRODUCTION

Since the first report of temporal correlations between spontaneous blood oxygenation level-dependent (BOLD) signals in the bilateral motor cortices (Biswal et al., 1995), "resting-state" functional magnetic resonance imaging (rs-fMRI) has become an important tool to probe functionally connected networks throughout the brain (Smith et al., 2013b). The rs-fMRI method continues to advance the scientific understanding of brain development, aging, and disease (Woods et al., 1998; Fair et al., 2008; Supekar et al., 2009; Bettus et al., 2010; Qin et al., 2012; Lin et al., 2018), among other application areas, and affords a number of advantages over the original task-based fMRI approach for recording brain activity. For example, multiple resting-state networks

can be revealed from a single rs-fMRI study without the need to administer one or more prescribed behavioral tasks, typically by measuring BOLD signal correlations relative to a "seed" region of interest, or by using multivariate component models to identify networks based on statistical criteria. The absence of the task(s) also removes the need for fMRI-compatible devices to present sensory stimuli and record behavioral responses, along with the device-related software and computer control. Thus, the relatively straightforward acquisition of the data, coupled with the wealth of information that is obtained, have spurred adoption of the rs-fMRI method for research purposes. This is especially the case for clinical neuroimaging research involving patient populations, in which the workflow of the fMRI experiment must be efficient and task performance may not be possible or is confounded by impairments related to the brain disease under study.

Although rs-fMRI is an effective tool for studying the brain function of healthy and patient populations, the measured BOLD signal fluctuations are caused not only by neuronal activity, but also by multiple other confounding factors. These include physiological effects (e.g., respiration and cardiac pulsatility) and various imperfections in MRI system hardware (e.g., heating of the imaging gradients during experiments). Of all the confounding factors, however, the effects of head motion are especially complex and troublesome. The small amplitude of BOLD signals – typically a few percent or less – ensures that millimeter-scale head motions may be problematic even after various correction algorithms are applied to fMRI data. In the case of task-based fMRI, head motion can be temporally correlated with task performance and under many circumstances, the resulting "motion artifacts" cannot be distinguished from brain activity. The interpretation of the fMRI data becomes compromised as a result (Johnstone et al., 2006). Although prescribed behavioral tasks are not a part of rs-fMRI, head motion still is problematic and may even be exacerbated when imaging individuals while they are at rest (Engelhardt et al., 2017; Huijbers et al., 2017). Numerous effects of head motion have been reported in the rs-fMRI literature. For example, sub-millimeter motions have been shown to distort functional connectivity estimates from approaches that include seed correlation analyses, graph theoretic network modularity, dual regression independent component analysis (ICA), and power spectrum methods (Power et al., 2012; Satterthwaite et al., 2012; van Dijk et al., 2012). Depending on the amplitude and spatio-temporal characteristics of the head motion, estimates of functional connectivity can be increased, decreased, or even driven to zero (Power et al., 2014). Characteristic "distance" and "orientation" dependencies of the errors have been reported in correlation-based estimates, with decreased long-distance connectivity and increased local connectivity (Power et al., 2012; van Dijk et al., 2012); and increased lateral connectivity at the expense of connectivity in the inferior–superior and anterior–posterior directions (Power et al., 2012). The effects are especially problematic in between-group studies of brain development and of neurological diseases, as the groups may differ significantly in their levels of head motion (Seto et al., 2001; Mowinckel et al., 2012; Satterthwaite et al., 2012; Haller et al., 2014). In these cases, it may be very difficult to decouple hypothesized effects (Courchesne and Pierce, 2005; Andrews-Hanna et al., 2007), from motion-related differences with the greatest effects of motion often observed in groups with the greatest brain impairment (Wylie et al., 2014).

Given these reports and the need to generate data with improved quality in the long term, this focused review discusses how head motion affects rs-fMRI data, and summarizes the existing and emerging strategies for motion correction. The pertinent characteristics of human head motion are first discussed, followed by the physical principles that cause head motion to introduce signal confounds in rs-fMRI data. The second half of the review discusses the strengths and weaknesses of various retrospective motion correction strategies, and the potential benefit that "real-time" correction techniques can provide in the future.

This focused review is not exhaustive in terms of the references that are included. Interested readers are encouraged to seek out other discourses that provide more in-depth discussion of topics that are covered here (e.g., Power et al., 2015; Esteban et al., 2019). In addition, for balance and brevity, the review focuses on the main concepts behind various motion correction strategies without explicitly mentioning and defining all their acronyms. The acronyms are available in the references that are cited.

HEAD MOTION: CHARACTERISTICS

As a reasonable starting point, the head may be considered as a rigid body that can move in space. Three dimensional (3D) rigid body motion is usually parameterized by six degrees of freedom (DOF), for example described in Cartesian coordinates as translations in *x*- (left/right), *y*- (anterior/posterior), and *z*-axes (inferior/superior), and rotations about the *x*-axis (pitch), *y*-axis (yaw), and *z*-axis (roll). Each of the six parameters will vary as a function of time as the head moves dynamically during an rs-fMRI experiment (a time series data collection of images of the brain volume, acquired with BOLD signal contrast). In reality, the brain is not perfectly rigid, given the biomechanical properties of its constituent tissues and the pulsatile flow of blood within it (Dagli et al., 1999). Nevertheless, given the dynamics of the motions involved and the millimeter spatial resolution that is presently available on most MRI systems operating at 1.5 and 3.0 T, the rigid body approximation is very reasonable. The rapid imaging protocols that are used in rs-fMRI [typically echo planar imaging (EPI) or spiral k-space readouts] also ensure that motion is effectively "frozen" during the time needed to encode the spatial information for each image slice (∼50 ms or less) in a typical two-dimensional (2D) multi-slice imaging protocol. Although each slice samples the head motion at a slightly different point in time, this issue is usually dealt with effectively by temporal interpolation of slices to a single time point (Parker et al., 2017).

Although head motion often varies considerably from subject to subject, multiple studies have revealed that certain general characteristics are common. In healthy individuals, for example,

translations in the inferior/superior direction together with a "nodding" rotational motion are often evident, possibly with superposition of more rapid oscillatory motion from the respiratory cycle (Seto et al., 2001). This pattern of motion arises because a pivot point occurs at the back of the head or the base of the neck while the subject lies supine in the magnet bore, with relatively constrained motion in the other directions. This common pattern has implications for the extent of motion in different brain regions: anterior frontal and orbitofrontal areas are likely to be more affected than posterior areas such as the primary visual cortex. Furthermore, this motion is not well represented by fluctuations in just one DOF in Cartesian coordinates – instead, coupled translation and rotation signals are observed that may be difficult to resolve unambiguously.

Another characteristic feature of head motion is that the temporal patterns of movement and associated artifacts do not display band-limited frequency content. As such, frequency filtering commonly applied in rs-fMRI to isolate the frequency range of interest (∼0.01–0.1 Hz) may be ineffective for motion correction, and can even smear motion contamination across the entire dataset if not applied carefully (Carp, 2013). Low-frequency, autocorrelated trends are readily apparent in rs-fMRI data due to motion, and work initially focused on developing methods other than frequency filters to remove these artifacts while retaining the true fMRI signal content (Woods et al., 1998; Lund et al., 2006). More recent work has focused on the need for specialized methods to account for transient motions (Satterthwaite et al., 2013), for example due to involuntary twitches or tics, which also occur at non-trivial levels.

There is also evidence that head motion can differ across various populations of subjects. Task-based fMRI studies show that patient populations, older adults, and pediatric subjects exhibit larger motions compared to young healthy adults (Seto et al., 2001; Yuan et al., 2009; Haller et al., 2014; Graham et al., 2016; Huijbers et al., 2017). For example, patients with stroke, Alzheimer's Disease, bipolar disorder and schizophrenia move more compared to age-matched healthy subjects (Seto et al., 2001; Haller et al., 2014; Huijbers et al., 2017). Similarly, young children and older adults show larger motions when compared to young adults (Seto et al., 2001; Yuan et al., 2009). Elderly subjects show more random head motions whereas young adults move more slowly and rhythmically (Graham et al., 2016). Sex-related differences have also been observed, with girls showing less tendency to move than boys during three of four language tasks in a task-based fMRI study (Yuan et al., 2009). Finally, less engaging task paradigms and rs-fMRI protocols may also lead to levels of head motion that are higher than those observed in task-related fMRI measurements (Huijbers et al., 2017) although more research would be useful in this area. As the amount of rs-fMRI data increases and becomes more freely accessible throughout the human brain mapping community, the opportunity should be taken to evaluate the head motion characteristics in studies with large sample size and different subject populations, as this may help to inform motion correction and data analysis methods in the future.

HEAD MOTION ARTIFACTS

The consequences of head motion on rs-fMRI data can be very complex. Rather than producing a single type of image artifact, multiple types are possible with very different physical mechanisms. A list of the possibilities is given below. This list is not exhaustive, and some of the possibilities are more commonly appreciated than others.

Partial Volume Effects

Functional MRI data are almost always acquired within the static coordinate frame of the MRI system, assuming that each voxel represents the signal content of the same brain structure for the entire duration of the time series data collection. However, head motion causes the proportion of various brain tissue types in a voxel to fluctuate over this duration, each with slightly different MRI signal contrast properties (Stanisz et al., 2005). This is commonly referred to as the "partial volume effect" (Hajnal et al., 1994) and is most problematic for voxels in the vicinity of tissue boundaries where large signal differences occur [e.g., between gray matter (GM) and white matter (WM), and especially between GM and cerebrospinal fluid (CSF)]. The partial volume artifact characteristically appears as spurious correlated signal fluctuations that rim the surface of the brain, or that occur along the interhemispheric fissure. It is increasingly realized that as fMRI protocols are developed with greater spatial resolution, for example using ultra-high field systems at 7 T or beyond, the reduction of voxel size will cause the partial volume effect to increase (Zaitsev et al., 2017) and thus better correction strategies will be needed (see section "Correction Strategies" below).

Spin History Effects

As mentioned above, head motion tends to have major components that involve "nodding" and displacements in the inferior–superior direction (Seto et al., 2001). As fMRI protocols commonly adopt 2D multi-slice imaging with an axial or oblique-axial slice prescription, brain tissue will inevitably move through each slice, producing an artifact that is usually referred to as the "spin history effect." In an rs-fMRI experiment, the baseline signal intensity is a function of multiple MR acquisition parameters and MR tissue properties, but the quantities relevant to spin history are the flip angle (θ) of radiofrequency excitation, the repetition time (TR) determining the temporal resolution of the rs-fMRI time series, and the longitudinal relaxation time (T1) at a particular voxel location. At the start of any time series data acquisition, it takes several TR intervals to establish the steady-state baseline signal intensity, which is achieved from a balance of how far the tissue magnetization or "spins" are flipped toward the transverse plane, and the time allotted for T1 recovery before the next θ pulse is applied. Ideally, the θ value should be constant through the slice, but in reality there is significant spatial non-uniformity. Thus, through-plane motion disturbs the steady state magnetization of the imaged slice by introducing spins with different excitation history. The steady state will also be disturbed if tissues with different T1 values move in and out of the slice – which is particularly observable for voxels that include blood vessels.

Spin history effects have been modeled empirically (Friston et al., 1996; Muresan et al., 2002) and in phantom experiments to establish the dependency on MR acquisition parameters and tissue properties (Yancey et al., 2011). The characteristic behavior is that a discrete through-plane displacement causes a signal transient that may be similar in amplitude to the rs-fMRI signal and requires several TR intervals to attenuate. In cases of slow, smooth motion, spin-history artifacts may be quite difficult to distinguish from the true BOLD fluctuations in rs-fMRI data.

Dynamic Geometric Distortions

Although EPI and spiral k-space readouts provide good temporal resolution for rs-fMRI experiments, both are very sensitive to spatial non-uniformity in the static magnetic field (Jezzard and Clare, 1999; Glover, 2012). Automatic "shimming" procedures are available on all clinical MRI systems and provide some benefit, but the differences in magnetic susceptibility at interfaces between brain tissues, bone, and air are sufficiently large that regions of geometric distortion and signal loss remain – typically in inferior frontal and inferior lateral temporal areas (Ojemann et al., 1997). It is well appreciated that a constant correction for these effects may be needed at each point in the rs-fMRI the time series data collection, but dynamic corrections may be needed as well (Zaitsev et al., 2017). Lung ventilation effects during the respiratory cycle cause magnetic field fluctuations in inferior brain regions at 3 T and above (Raj et al., 2001; Van de Moortele et al., 2002). Furthermore, head motion causes the susceptibility-induced field non-uniformities to fluctuate in a manner such that the boundary conditions at each tissue interface satisfy Maxwell's Equations. The end result is dynamic geometric distortions that are observable in the EPI phase-encoding direction (Wu et al., 1997; Jezzard and Clare, 1999; Andersson et al., 2001). The effects are non-linear with respect to motion estimates and vary depending on the position and orientation of the tissue interfaces relative to the main magnetic field, the amount of head motion, and the magnetic field strength.

Coil Sensitivity

Multi-channel receiver coils are now an established part of fMRI protocols, providing higher signal-to-noise ratio (SNR) than previously achievable and enabling higher temporal resolution through various parallel imaging reconstruction approaches (Pruessmann, 2006). Channel count continues to increase, with 64-channel coils currently available from at least one major MRI system vendor. The higher the channel count, the smaller each individual element becomes. The associated area of sensitivity of each element also becomes more localized, with steeper spatial sensitivity gradients. This implies that at some point, multi-channel receiver coils will become appreciably sensitive to head motion, if the translation or rotation of brain tissue becomes sufficiently large in relation to the sensitivity gradients of the individual coil elements. Two recent reports have indicated that this problem may be relevant for rs-fMRI at 3 T in a 16-channel coil geometry, for a conventional EPI k-space readout (Faraji-Dana et al., 2016a) as well as for parallel imaging reconstruction, with worse artifacts occurring as the acceleration factor was increased (Faraji-Dana et al., 2016b). In both cases, it was possible to suppress these artifacts by tracking and correcting for the relative motion between the head and the receiver coil, at each point during the fMRI-time series data collection.

CORRECTION STRATEGIES

Given the complexity of the problem, it is not surprising that a multifaceted approach is needed in the quest to achieve full and robust motion correction in rs-fMRI data. A brief summary of the available correction strategies is given below. The choices range from simple commonsense approaches, to more sophisticated retrospective corrections as well as "real-time" corrections.

Head Restraints and Behavioral Intervention

At the outset, it would seem straightforward simply to restrain individuals so that no head motion occurs during rs-fMRI. The problem would thus be solved at the source, without introducing artifacts into the data. Unfortunately, it is often very difficult to achieve this goal in practice. Mild head restraint is an essential part of all fMRI procedures: padding between the head and the coil is commonly adopted (with other options available such as the use of vacuum pillows, and thermoplastic facial masks fixed to the MRI table), whereas bite bars and even more restrictive clamping systems are used less frequently (Bettinardi et al., 1991; Green et al., 1994; Righini et al., 1996; Schültke et al., 2013). Although restraints decrease the extent of head motion in cooperative subjects, in many cases the milder forms of restraint are ineffective at eliminating some component of motion at the sub-millimeter and millimeter level, such as nodding. However, the stronger restraints have the potential to increase claustrophobia, can become uncomfortable and tiresome especially for lengthy fMRI sessions, and in some cases can exacerbate motion as subjects try to alleviate associated pain or pressure (Zeffiro, 1996). Brain activity is also likely to be altered as a result, especially in very young or very old healthy individuals. Furthermore, clinical contraindications make strong restraints unacceptable for certain patient populations (Zeffiro, 1996; Schültke et al., 2013).

Subjects are also commonly instructed to "try to lie still and not move" as part of setup and positioning prior to rs-fMRI experiments. For these instructions to have the intended effect, subjects must appreciate the small level of motion that can be tolerated and also must remain vigilant at keeping still. As mentioned above, pediatric and patient populations may not be able to fulfill these requirements, with reduced rs-fMRI data quality as a consequence. For example, children are more prone to head motion when tasks are less engaging, making motion correction strategies important for rs-fMRI acquisitions (Yuan et al., 2009; Engelhardt et al., 2017). Pre-training using "mock scanning" or "fMRI simulator" sessions may help to reduce the need for sedation when imaging children and may provide more runs with usable MRI data (Epstein et al., 2007; De Bie et al., 2010; Barnea-Goraly et al., 2014), but significant benefit of this approach is not consistently demonstrated (Thieba et al., 2018; Li et al., 2019). Training tools and interventions

such as watching a movie and/or motion feedback training (visual or verbal) have shown promise in children, young adults and stroke patients (Vanderwal et al., 2015; Graham et al., 2016; Greene et al., 2018). In the case of the movie paradigm, however, functional connectivity measures are contaminated by brain activity associated with watching the movie and cannot be considered truly "resting-state." Collectively, these methods require additional set-up, lengthen the duration of the imaging session, and are not widely adopted yet, at least partly for these reasons. Another alternative is to monitor head motion and adjust the length of the time series data acquisition so that enough data of sufficient quality are collected (Dosenbach et al., 2017). Although useful, this approach is rather open-ended and may be inefficient for patients with moderate-to-excessive motion.

Imaging Protocol

The rapid 2D multi-slice imaging methods commonly used in rs-fMRI not only provide adequate temporal resolution to sample BOLD responses, but also afford some protection against motion artifacts. In addition to the "snap-shot" imaging capability provided by the raster scan k-space readouts used in EPI, the spiral k-space readout intrinsically compensates for motion in the plane of each image slice (Glover and Lai, 1998). Researchers have also continued to develop imaging methods with even better motion compensation (Lee et al., 2010; Krämer et al., 2012; Graedel et al., 2017; Kecskemeti et al., 2018). The increasingly popular alternative involves simultaneous multi-slice acquisitions together with parallel imaging reconstruction to provide increased temporal resolution, better snap-shot imaging capability, and robustness to static and dynamic geometric distortion (Feinberg et al., 2010; Setsompop et al., 2012; Zahneisen et al., 2014b). However, this approach introduces a different set of noise characteristics which may have implications for rs-fMRI analysis (Golestani et al., 2018). Dual- and multi-echo imaging methods have also been receiving attention recently because the acquisition of two or more images of each slice at different echo time (TE) values helps to isolate BOLD signals from noise. This can be achieved by regressing low TE value data (with minimal BOLD weighting plus noise) from higher TE value data (with more optimal BOLD weighting plus noise) (Buur et al., 2009; Bright and Murphy, 2013), or by a more complex multivariate denoising approach relying on signal decay properties (Kundu et al., 2013). Dual- and multi-echo approaches must be applied judiciously, however, so that the spatiotemporal resolution of 2D multi-slice rs-fMRI is not compromised.

Retrospective Motion Correction

Over the years, many strategies have been developed that help to suppress the effects of head motion after fMRI data have been collected. These "retrospective" methods are an essential part of processing rs-fMRI signals and are easily implemented as part of freeware analysis packages developed and applied by the functional neuroimaging research community (e.g., Esteban et al., 2019).

Rigid-Body Registration

Volumetric rigid-body registration primarily corrects for partial volume effects and is typically viewed as an essential step of rs-fMRI analysis. Head motion parameters are estimated iteratively with six DOF by optimizing a cost function that quantifies the similarity between each image in the time series and a reference image (Friston et al., 1995; Cox, 1996; Jenkinson et al., 2002; Oakes et al., 2005). The reference image should be chosen carefully (such as the average image over the time series), as the error in motion parameter estimates increases with the extent that each image must be re-aligned. Although very useful, volumetric rigid-body registration does have some limitations. Most implementations do not correct for motion that occurs during multi-slice acquisition of the entire brain volume, so slice-to-volume as well as slice-to-slice registration approaches have been developed (Kim et al., 1999, 2008; Yeo et al., 2008; Beall and Lowe, 2014; Chen et al., 2015; Ferrante and Paragios, 2017). The accuracy of motion estimates also depends on the signal quality in the image slices, which are acquired at low spatial resolution and at relatively low SNR, with BOLD-related signal variations that can bias motion estimates toward neural activations depending on the choice of the cost function (Freire and Mangin, 2001). The latter effect can be mitigated in principle by simultaneously optimizing the registration while estimating fMRI signals, although the approach has only been tested for task-based fMRI thus far (Orchard et al., 2003). Furthermore, the registration process inherently requires resampling and interpolation so that all motion-corrected images utilize a common Cartesian coordinate system. This can further reduce spatial resolution and bias activation estimates (Grootoonk et al., 2000; Yuan et al., 2016). Lastly, volumetric registration algorithms work well for small head movements, but become less accurate or fail completely for larger motion (Oakes et al., 2005; Morgan et al., 2007). In particular, large motions can invalidate the assumption of rigid-body motion as a consequence of the geometric distortions introduced by dynamic magnetic field inhomogeneity (Elliott et al., 2004). In such cases, complex affine or non-linear transformation models are beneficial, as well as use of dynamic maps of the magnetic field (Hutton et al., 2002; Roopchansingh et al., 2003; Sutton et al., 2004; Visser et al., 2012; Ooi et al., 2013b), although these methods are more computationally intensive and have not been widely adopted yet.

Linear Regression

Various linear regression strategies are also commonly adopted to address the residual motion-related signal variance that can arise from imperfect volumetric rigid-body registration. For example, the six time-dependent motion parameter estimates that are output from the registration are easily applied in multiple linear regression to remove these "nuisance" effects from the rs-fMRI data. The approach has been extended further to 12 parameters (including temporal derivatives; Power et al., 2012), 24 parameters (squares of the motion parameters and temporal derivatives; Friston et al., 1996; Satterthwaite et al., 2013; Yan et al., 2013) and even 36

parameters (squares of the motion parameters, and both first and second temporal derivatives; Power et al., 2014). Specialized regression procedures have also been proposed for group comparisons (Satterthwaite et al., 2012; Yan et al., 2013). The use of higher-order regressors has demonstrated greater reduction in motion-related variance (Lund et al., 2005) and has been suggested for high-motion subjects (Satterthwaite et al., 2013; Yan et al., 2013; Yuan et al., 2016), for which low-order regression (6 or 12 parameters) has been found less effective (Power et al., 2012; Satterthwaite et al., 2013). However, concerns associated with overfitting and removal of BOLD signals arise in cases where head motion is minimal and large numbers of nuisance regressors are used. Direct evidence of this effect has been shown in task-based fMRI (Johnstone et al., 2006; Ollinger et al., 2009) whereas more investigations remain to be undertaken in rs-fMRI. Moreover, motion parameter estimates are often highly coupled and fitting with better statistical power is achieved when a method such as principal component analysis (PCA) is used to reduce the dimensionality of the nuisance regressors (Woods et al., 1998).

When considering regression approaches, it should also be recognized that fMRI signal changes from movements can have a latency of several seconds (due to spin history effects, for example) (Power et al., 2014). Simple motion parameter regression cannot completely remove such deviations and thus more sophisticated methods are of interest, such as the use of more nuisance regressors as indicated above. Another approach considers that BOLD signals arise predominantly from GM, and thus additional effects from motion and non-neural sources can be removed by using spatially averaged time series signals of WM and CSF (WM-CSF) as nuisance regressors, and possibly the related derivatives (Weissenbacher et al., 2009). To address the dimensionality concerns raised above, a regressor from WM-CSF PCA space can be used (Behzadi et al., 2007; Muschelli et al., 2014). Different WM regressors can also be obtained for each GM voxel, accounting for spatial variations in WM noise that may not be apparent in the average regressor (Jo et al., 2010). Both the latter methods have been shown to perform better than regression of the average WM-CSF time series. Irrespective of how the WM-CSF regressors are derived, however, they should be implemented with "erosion" of the corresponding spatial masks to avoid contamination from adjacent GM voxels – otherwise the rs-fMRI signal can be attenuated (Jo et al., 2010). Furthermore, when applying WM regressors, it should be recognized that they may represent signal of functional origin (Ding et al., 2013; Peer et al., 2017). More research on this topic will be important in clarifying the noise or information characteristics of WM signals.

An additional nuisance regressor of potential interest is obtained by spatially averaging the rs-fMRI time series data over the whole brain. This "global signal" is usually correlated with the first PC of the whole brain time series (Carbonell et al., 2011). The value of global signal regression (GSR) is currently in dispute (Murphy and Fox, 2017; Xu et al., 2018). Originally, GSR was performed assuming that any source that modulates the global brain signal is non-neural (Desjardins et al., 2001), but more recent studies have shown that the global signal does contain measurable neural contributions (Schölvinck et al., 2010; Wong et al., 2016) and even distinguishes healthy subjects from schizophrenia patients (Hahamy et al., 2014). Nevertheless, many studies have demonstrated the usefulness of GSR for mitigating motion-related noise, although with residual artifacts that depend on the distance between functional connections (Yan et al., 2013; Power et al., 2014; Ciric et al., 2017). Other studies report that GSR introduces false anticorrelations (Murphy et al., 2009; Weissenbacher et al., 2009). This discrepancy in the literature may relate to the level of non-neural noise that has a global effect on the rs-fMRI signal, and suggests that it may be useful to quantify the global noise level to determine whether GSR should be adopted (Chen et al., 2012).

Scrubbing

Involuntary head motion can produce substantial transients in the rs-fMRI signal. The transients can be identified by establishing a threshold for outlier signals, for example based on relative signal difference followed by corrections such as "spike" regression (Lemieux et al., 2007), or scrubbing/censoring (ignoring) the erroneous data (Power et al., 2012). Both methods are effective at removing transient motion artifacts (Satterthwaite et al., 2013; Power et al., 2014; Ciric et al., 2017; Parkes et al., 2018), with some notable caveats in the latter case. Temporal interpolation or spectral decomposition of un-scrubbed data can be used when outliers occur at multiple adjacent time points, but this must be done carefully to avoid residual artifacts and subtle motion bias (Power et al., 2014). Moreover, rs-fMRI analysis can be complicated by the variation in temporal DOF across subjects or groups of subjects with considerable differences in head motion (Parkes et al., 2018). Data sets with a greater number of scrubbed spikes will have systematically reduced temporal autocorrelation. "Trimming" each dataset to equal length provides a simple solution, although the reliability of functional connectivity estimates may be reduced (Birn et al., 2013; Power et al., 2014). Subjects with high levels of motion may need to be excluded if many points in the rs-fMRI time series are scrubbed.

Data-Driven Methods

Various multivariate methods are useful to determine what components, or "features," exist in the rs-fMRI data without imposing a mathematical model *a priori* for the signal and noise properties. Such data-driven methods are advantageous because they place less burden on the operator to identify all types of motion artifacts and implement specific correction methods – potentially allowing results to be replicated more easily across studies. However, data-driven methods do require some form of *post hoc* feature selection of the components (and the number of components used) to identify the signals of interest and remove structured noise. For example, mutually orthogonal features are identified by PCA, which has been used to remove motion-related signal fluctuations

at the edge of the brain for improved temporal SNR compared to use of motion parameter regression (Patriat et al., 2015). In addition, ICA (Thomas et al., 2002) is popular to identify features based on statistical independence rather than orthogonality. Manual identification of noise-related ICs requires detailed knowledge of the spatiotemporal properties of the rs-fMRI signal (see Griffanti et al., 2017 for guidance) and is laborious and operator-dependent, but multiple automatic methods have been developed that are robust and objective (Tohka et al., 2008). These include methods specifically focused on removing physiological noise associated with cardiac pulsatility and respiration (Beall and Lowe, 2007; Perlbarg et al., 2007), and more general artifact removal methods with different processes for feature selection (Bhaganagarapu et al., 2013; Salimi-Khorshidi et al., 2014; Pruim et al., 2015b). Work has also been done to compare the effectiveness of these methods, as well as in relation to other de-noising approaches such as spike regression and scrubbing (Pruim et al., 2015a; Parkes et al., 2018). Additional comparisons of this type will be necessary to establish whether one or more methods are particularly advantageous across different populations of test subjects in rs-fMRI studies.

Other Methods and Considerations

Briefly, it is important to make three additional comments about retrospective correction of motion artifacts in rs-fMRI data. First, comparative work on volumetric versus surface-based fMRI analysis shows that the latter provides superior inter-subject alignment and better preservation of functional regions upon smoothing (Anticevic et al., 2008; Tucholka et al., 2012; Smith et al., 2013a). Even so, retrospective motion correction is usually performed as a preliminary step in the volumetric domain prior to the projection of de-noised fMRI data onto the brain surface. Second, artifact reduction is an intensive field of MRI research and new correction methods are continuously being developed, some of which may have significant merit without aligning to the categories listed above. One example is a method called "wavelet despike" that has been developed to identify dynamic events occurring across various frequencies, for the removal of sudden spikes from head motion as well as slower spin-history related artifacts (Patel et al., 2014). This method is particularly useful for subjects with elevated head motion and is capable of reducing or even removing distance-dependent connectivity artifacts without the need for scrubbing (Patel et al., 2014). Third, it is evident that because no gold-standard protocol exists to correct artifacts in rs-fMRI data, the data analyst is confronted with choosing from very many rs-fMRI artifact correction methods, many of which have multiple parameter settings. Multiple correction methods must be selected to suppress artifacts most successfully, and the various methods are likely to interact with one another, sometimes in an order-dependent fashion. This state of affairs has led to multiple studies that compare various correction methods and/or their interaction effects, using various metrics to indicate the quality of the rs-fMRI results (Churchill et al., 2012a,b; Carp, 2013; Hallquist et al., 2013; Satterthwaite et al., 2013; Power et al., 2014; Pruim et al., 2015a; Shirer et al., 2015; Ciric et al., 2017; Vytvarová et al., 2017; Gargouri et al., 2018; Parkes et al., 2018). Such work will continue to be necessary as MRI systems, imaging protocols, and methods of analysis improve over time.

Real-Time Motion Correction

Although patient setup procedures, use of rapid imaging acquisitions, and retrospective de-noising approaches are commonly adopted in rs-fMRI experiments, another class of correction methods described as "real-time," "adaptive," or "prospective" show considerable promise and may become essential tools in the long term. Here, the term "real-time" is adopted for these methods, which depart from typical rs-fMRI protocols that produce reconstructed images in a Cartesian coordinate system that is static with respect to the MRI system. Instead, images acquired with real-time motion correction are reconstructed in a moving coordinate system that is fixed to the head. In principle, images viewed in the moving coordinate system will appear to be static, provided that rigid body motion is a good approximation. (In reality, effects that violate this assumption will also have to be corrected either in real-time or retrospectively, as indicated below). Real-time motion correction requires (a) a method to track head motion, usually relative to an initial head position and orientation; and (b) incorporation of the tracking data to update MRI spatial encoding synchronously with the moving coordinate system. The latter requirement necessitates software modifications to the underlying image acquisition method (e.g., EPI). Depending on how rapidly and accurately the update occurs, real-time approaches have the potential to account for both partial volume effects and spin-history effects in very convenient fashion. In cases where the real-time update is relatively slow, prospective correction can be added to account for the lag between motion measurement and acquisition of the next multi-slice image dataset – using a Kalman filter, for example (White et al., 2010). Various real-time motion correction methods exist, categorized below based on the choice of motion tracking strategy.

Navigator Echoes

Magnetic resonance signals that are acquired and spatially encoded specifically for position tracking are known as "navigator echoes" and were among the first methods of real-time motion correction developed for fMRI (Lee et al., 1996, 1998). The main advantage of such methods is that position tracking is achieved without requiring custom ancillary hardware or fiducial markers (see below). Navigator echoes have progressed from tracking motion in 1D (Ehman and Felmlee, 1989) to full 3D capability (Welch et al., 2002; Wastiaux et al., 2006; Tisdall et al., 2012) based on calculations performed in k-space (Lin et al., 2010) or image space (White et al., 2010; Hoinkiss and Porter, 2017). However, the methods have not been widely adopted in fMRI studies to date (Boksman et al., 2005). Possible reasons for this include (a) insufficient position tracking accuracy for fMRI applications, arising from sensitivity to imperfections such as gradient non-linearity and magnetic field inhomogeneity; and (b) potential disruption of the steady state magnetization in brain regions where functional connectivity is of interest.

Image-Based Methods

A more popular method for real-time motion correction involves the use of volumetric image registration to track the change in head position and orientation at each point in the fMRI time series in relation to a reference volume of multi-slice images (Thesen et al., 2000). This approach is now a standard option on some MRI systems, and assumes that multiple effects are negligible: head motion on the timescale of the TR interval (typically ∼2 s); dynamic geometric distortion; and other artifacts that violate the rigid-body assumption, such as interactions between head motion and coil sensitivity. One or more of these assumptions may not always be valid. For improved functionality, a revised version of this method has recently been implemented to take advantage of simultaneous multi-slice fMRI for higher temporal resolution and intra-volume motion correction (Hoinkiss et al., 2018).

Other Position Tracking Devices

Many additional methods have been investigated for real-time motion correction that either adopt novel MRI signal approaches for position tracking, or other MRI-compatible sensor technologies. "Active marker" methods use at least three non-collinear RF micro-coils, each containing an MRI-sensitive material, as fiducials to measure rigid-body head motion with minimal impact on temporal resolution (Erhart et al., 1998; Krueger et al., 2006; Ooi et al., 2009, 2013a). "Passive marker" approaches have also been explored that use small pickup coils for position tracking based on the voltages induced by imaging gradients (Haeberlin et al., 2014; Aranovitch et al., 2018). As for navigator echoes and image-based methods, active and passive MRI marker devices can also suffer from instrumental imperfections that introduce errors in signal localization. Nonetheless, improved image stability has been demonstrated in standard EPI sequences (Ooi et al., 2011) as well as increased statistical significance for fMRI (Muraskin et al., 2013). The most recent and sophisticated work in this area uses an inductively coupled microcoil and a series of other passive marker components: a pickup coil, magnetometer, accelerometer and angular rate sensor. When all the sensor measurements are combined, position tracking with sub-millimeter accuracy is achievable from a single fiducial device (van Niekerk et al., 2019).

Optical sensors are also attractive for their high temporal resolution and spatial accuracy, and intrinsic MRI-compatibility. The original work involved laser interferometry (Eviatar et al., 1999), but was not pursued due to impracticalities in achieving line-of-sight and mirror adjustment. Better results are achieved using one or more optical cameras to track reflective fiducial markers affixed to the head (Zaitsev et al., 2006; Maclaren et al., 2012; Todd et al., 2015). These methods enable a tracking accuracy of ∼5–100 μm with temporal resolution of ∼20–50 ms, exceeding the capabilities of most MRI-based methods (Eschelbach et al., 2018). However, there are also some concerns about the practicality, cost and robustness of these methods at present. Calibration is required to transform optical position tracking data into the spatial coordinates of the MRI system, which may be time-consuming (Maclaren et al., 2018). Calibration errors can create further artifacts (Zahneisen et al., 2014a) that must be corrected retrospectively (Aksoy et al., 2012). The cost of optical tracking systems tends to be high, due to hardware considerations involving the MRI-compatibility of the cameras, and the research and development required to develop motion-correction capabilities with good calibration and real-time integration in MRI systems and imaging protocols. The camera view of markers (typically through openings in the head coil) may be obstructed if motion is substantial, and there is the general concern with all fiducial marker approaches (optical and other) that movement of the skin, for example due to frowning or facial expressions, may not accurately reflect motion of the brain. Each of these problems is being actively investigated and ameliorated (Singh et al., 2015; Benjaminsen et al., 2016; Eschelbach et al., 2017; Frost et al., 2018). Notably, optical motion correction has been shown to improve temporal SNR of both resting state and task-based 3D EPI acquisitions (Todd et al., 2015), with demonstrated benefits for increased significance and sensitivity of connectivity measures (Chu et al., 2018). Based on the promising outcomes of this collective work, optical tracking devices are also available for MRI applications commercially through third-party vendors, and are starting to be offered by MRI system vendors themselves.

One final comment is required about real-time motion correction methods for rs-fMRI. The existing literature in this area predominantly relies on the assumption of rigid-body head motion and, as emphasized earlier, this is likely insufficient for full suppression of motion artifacts. For example, residual geometric distortions will likely be present due to motion-induced dynamic magnetic field inhomogeneities, which can be resolved by real-time shim updates or by distortion corrections from time-dependent field maps (Ooi et al., 2013b; Rotenberg et al., 2013). Corrections for the interaction between head motion and multi-channel coil sensitivity can also be included (Faraji-Dana et al., 2016a,b). More research is needed to establish what combinations of retrospective and real-time corrections are most appropriate for rs-fMRI analyses, with the promise of more robust methodology and improved detection sensitivity in the future.

CONCLUSION

Despite its utility in neuroscience, rs-fMRI is confounded by the effects of head motion during data collection, which may result in complex spatial-temporal patterns of artifact. Diverse and efficacious methods are now available that can be combined to correct for these artifacts. Much progress has been made to improve rs-fMRI data quality, but the existing methods are not yet sufficiently robust to provide full control for motion-related confounds. Real-time correction methods show considerable promise toward reaching this goal in the future. At present, however, the following recommendations represent our view of how to address the potential for confounds in rs-fMRI experiments due to motion artifacts – reasonably, and transparently. Neuroimaging data analysts should:

- report summary statistics of the head motion characteristics for the group(s) under study, including whether group differences in head motion are statistically significant;
- report and justify the methods used in the research to correct for motion artifact;
- include statistical corrections in group level comparisons to ensure that, as much as is reasonably possible, motion artifacts to do not introduce confounds in the interpretation of rs-fMRI results; and
- survey the fMRI literature for ongoing improvements in motion artifact correction methods, and evaluate and incorporate new methods as appropriate to maintain state-of-the-art capabilities.

These practices will help to advance the neuroscientific research that can be conducted using rs-fMRI, as will the continued focus on technical developments to ensure that motion artifacts become less of a problem in rs-fMRI data.

AUTHOR CONTRIBUTIONS

SM and SG were responsible for drafting and editing of the manuscript. NC and TS provided the additional edits for this manuscript.

FUNDING

This work was supported by grants from FedDev Ontario (Grant No. 806468), the Natural Sciences and Engineering Research Council (Grant No. RGPIN-2017-06040), Canada, and the Canadian Institutes of Health Research (Grant No. PJT-162241).

REFERENCES

Aksoy, M., Forman, C., Straka, M., Çukur, T., Hornegger, J., Bammer, R., et al. (2012). Hybrid prospective and retrospective head motion correction to mitigate cross-calibration errors. *Magn. Reson. Med.* 67, 1237–1251. doi: 10.1002/mrm.23101

Andersson, J. L. R., Hutton, C., Ashburner, J., Turner, R., and Friston, K. (2001). Modeling geometric deformations in EPI time series. *Neuroimage* 13, 903–919. doi: 10.1006/nimg.2001.0746

Andrews-Hanna, J. R., Snyder, A. Z., Vincent, J. L., Lustig, C., Head, D., Raichle, M. E. E., et al. (2007). Disruption of large-scale brain systems in advanced aging. *Neuron* 56, 924–935. doi: 10.1016/J.NEURON.2007.10.038

Anticevic, A., Dierker, D. L., Gillespie, S. K., Repovs, G., Csernansky, J. G., Van Essen, D. C., et al. (2008). Comparing surface-based and volume-based analyses of functional neuroimaging data in patients with schizophrenia. *Neuroimage* 41, 835–848. doi: 10.1016/j.neuroimage.2008.02.052

Aranovitch, A., Haeberlin, M., Gross, S., Dietrich, B. E., Wilm, B. J., Brunner, D. O., et al. (2018). Prospective motion correction with NMR markers using only native sequence elements. *Magn. Reson. Med.* 79, 2046–2056. doi: 10.1002/mrm.26877

Barnea-Goraly, N., Weinzimer, S. A., Ruedy, K. J., Mauras, N., Beck, R. W., Marzelli, M. J., et al. (2014). High success rates of sedation-free brain MRI scanning in young children using simple subject preparation protocols with and without a commercial mock scanner-the diabetes research in children network (DirecNet) experience. *Pediatr. Radiol.* 44, 181–186. doi: 10.1007/s00247-013-2798-2797

Beall, E. B., and Lowe, M. J. (2007). Isolating physiologic noise sources with independently determined spatial measures. *Neuroimage* 37, 1286–1300. doi: 10.1016/j.neuroimage.2007.07.004

Beall, E. B., and Lowe, M. J. (2014). SimPACE: generating simulated motion corrupted BOLD data with synthetic-navigated acquisition for the development and evaluation of SLOMOCO: a new, highly effective slicewise motion correction. *Neuroimage* 101, 21–34. doi: 10.1016/J.NEUROIMAGE.2014.06.038

Behzadi, Y., Restom, K., Liau, J., and Liu, T. T. (2007). A component based noise correction method (CompCor) for BOLD and perfusion based fMRI. *Neuroimage* 37, 90–101. doi: 10.1016/j.neuroimage.2007.04.042

Benjaminsen, C., Jensen, R. R., Wighton, P., Tisdall, M. D., Johannesen, H. H., Law, I., et al. (2016). "Real Time MRI motion correction with markerless tracking," in *Proceedings of the International Society for Magnetic Resonance in Medicine*, Singapore, 1860.

Bettinardi, V., Scardaoni, R., Gilardi, M. C., Rizzo, G., Perani, D., Paulesu, E., et al. (1991). Head holder for PET, CT, and MR studies. *J. Comput. Assist. Tomogr.* 15, 886–892. doi: 10.1097/00004728-199109000-199109034

Bettus, G., Bartolomei, F., Confort-Gouny, S., Guedj, E., Chauvel, P., Cozzone, P. J., et al. (2010). Role of resting state functional connectivity MRI in presurgical investigation of mesial temporal lobe epilepsy. *J. Neurol. Neurosurg. Psychiatry* 81, 1147–1154. doi: 10.1136/jnnp.2009.191460

Bhaganagarapu, K., Jackson, G. D., and Abbott, D. F. (2013). An automated method for identifying artifact in independent component analysis of resting-state fMRI. *Front. Hum. Neurosci.* 7:343. doi: 10.3389/fnhum.2013.00343

Birn, R. M., Molloy, E. K., Patriat, R., Parker, T., Meier, T. B., Kirk, G. R., et al. (2013). The effect of scan length on the reliability of resting-state fMRI connectivity estimates. *Neuroimage* 83, 550–558. doi: 10.1016/j.neuroimage.2013.05.099

Biswal, B., Zerrin Yetkin, F., Haughton, V. M., and Hyde, J. S. (1995). Functional connectivity in the motor cortex of resting human brain using echo-planar mri. *Magn. Reson. Med.* 34, 537–541. doi: 10.1002/mrm.1910340409

Boksman, K., Théberge, J., Williamson, P., Drost, D. J., Malla, A., Densmore, M., et al. (2005). A 4.0-T fMRI study of brain connectivity during word fluency in first-episode schizophrenia. *Schizophr. Res.* 75, 247–263. doi: 10.1016/j.schres.2004.09.025

Bright, M. G., and Murphy, K. (2013). Removing motion and physiological artifacts from intrinsic BOLD fluctuations using short echo data. *Neuroimage* 64, 526–537. doi: 10.1016/j.neuroimage.2012.09.043

Buur, P. F., Poser, B. A., and Norris, D. G. (2009). A dual echo approach to removing motion artefacts in fMRI time series. *NMR Biomed.* 22, 551–560. doi: 10.1002/nbm.1371

Carbonell, F., Bellec, P., and Shmuel, A. (2011). Global and system-specific resting-state fMRI fluctuations are uncorrelated: principal component analysis reveals anti-correlated networks. *Brain Connect.* 1, 496–510. doi: 10.1089/brain.2011.0065

Carp, J. (2013). Optimizing the order of operations for movement scrubbing: comment on power et al. *Neuroimage* 76, 436–438. doi: 10.1016/j.neuroimage.2011.12.061

Chen, G., Chen, G., Xie, C., Douglas Ward, B., Li, W., Antuono, P., et al. (2012). A method to determine the necessity for global signal regression in resting-state fMRI studies. *Magn. Reson. Med.* 68, 1828–1835. doi: 10.1002/mrm.24201

Chen, Y.-H., Mittelman, R., Kim, B., Meyer, C., and Hero, A. (2015). Multimodal MRI neuroimaging with motion compensation based on particle filtering. *ArXiv*

Chu, Y.-H., Wu, P.-Y., Zaitsev, M., Hsu, Y.-C., and Lin, F.-H. (2018). "Cortical depth dependent resting state fMRI with motion correction," in *Proceedings of the Joint Annual Meeting ISMRM-ESMRMB*, Paris, 389.

Churchill, N. W., Oder, A., Abdi, H., Tam, F., Lee, W., Thomas, C., et al. (2012a). Optimizing preprocessing and analysis pipelines for single-subject fMRI. I. Standard temporal motion and physiological noise correction methods. *Hum. Brain Mapp.* 33, 609–627. doi: 10.1002/hbm.21238

Churchill, N. W., Yourganov, G., Oder, A., Tam, F., Graham, S. J., and Strother, S. C. (2012b). Optimizing preprocessing and analysis pipelines for single-subject fMRI: 2. Interactions with ICA, PCA, task contrast and inter-subject heterogeneity. *PLoS One* 7:e31147. doi: 10.1371/journal.pone.0031147

Ciric, R., Wolf, D. H., Power, J. D., Roalf, D. R., Baum, G. L., Ruparel, K., et al. (2017). Benchmarking of participant-level confound regression strategies for the control of motion artifact in studies of functional connectivity. *Neuroimage* 154, 174–187. doi: 10.1016/j.neuroimage.2017.03.020

Courchesne, E., and Pierce, K. (2005). Why the frontal cortex in autism might be talking only to itself: local over-connectivity but long-distance disconnection. *Curr. Opin. Neurobiol.* 15, 225–230. doi: 10.1016/j.conb.2005.03.001

Cox, R. W. (1996). AFNI: software for analysis and visualization of functional magnetic resonance neuroimages. *Comput. Biomed. Res.* 29, 162–173. doi: 10.1006/cbmr.1996.0014

Dagli, M. S., Ingeholm, J. E., and Haxby, J. V. (1999). Localization of cardiac-induced signal change in fMRI. *Neuroimage* 9, 407–415. doi: 10.1006/nimg.1998.0424

De Bie, H. M. A., Boersma, M., Wattjes, M. P., Adriaanse, S., Vermeulen, R. J., Oostrom, K. J., et al. (2010). Preparing children with a mock scanner training protocol results in high quality structural and functional MRI scans. *Eur. J. Pediatr.* 169, 1079–1085. doi: 10.1007/s00431-010-1181-z

Desjardins, A. E., Kiehl, K. A., and Liddle, P. F. (2001). Removal of confounding effects of global signal in functional MRI analyses. *Neuroimage* 13, 751–758. doi: 10.1006/NIMG.2000.0719

Ding, Z., Newton, A. T., Xu, R., Anderson, A. W., Morgan, V. L., and Gore, J. C. (2013). Spatio-temporal correlation tensors reveal functional structure in human brain. *PLoS One* 8:e82107. doi: 10.1371/journal.pone.0082107

Dosenbach, N. U. F. F., Koller, J. M., Earl, E. A., Miranda-Dominguez, O., Klein, R. L., Van, A. N., et al. (2017). Real-time motion analytics during brain MRI improve data quality and reduce costs. *Neuroimage* 161, 80–93. doi: 10.1016/j.neuroimage.2017.08.025

Ehman, R. L., and Felmlee, J. P. (1989). Adaptive technique for high-definition MR imaging of moving structures. *Radiology* 173, 255–263. doi: 10.1148/radiology.173.1.2781017

Elliott, M. A., Gualtieri, E. E., Hulvershorn, J., Ragland, J. D., and Gur, R. (2004). The effects of geometric distortion correction on motion realignment in fMRI. *Acad. Radiol.* 11, 1005–1010. doi: 10.1016/j.acra.2004.04.022

Engelhardt, L. E., Roe, M. A., Juranek, J., DeMaster, D., Harden, K. P., Tucker-Drob, E. M., et al. (2017). Children's head motion during fMRI tasks is heritable and stable over time. *Dev. Cogn. Neurosci.* 25, 58–68. doi: 10.1016/j.dcn.2017.01.011

Epstein, J. N., Casey, B. J., Tonev, S. T., Davidson, M., Reiss, A. L., Garrett, A., et al. (2007). Assessment and prevention of head motion during imaging of patients with attention deficit hyperactivity disorder. *Psychiatry Res.* 155, 75–82. doi: 10.1016/j.pscychresns.2006.12.009

Erhart, P., Ladd, M. E., Steiner, P., Heske, N., Dumoulin, C. L., and Debatin, J. F. (1998). Tissue-independent MR tracking of invasive devices with an internal signal source. *Magn. Reson. Med.* 39, 279–284. doi: 10.1002/mrm.1910390215

Eschelbach, M., Aghaeifar, A., Bause, J., Handwerker, J., Anders, J., Engel, E.-M., et al. (2018). Comparison of prospective head motion correction with NMR field probes and an optical tracking system. *Magn. Reson. Med.* 81, 719–729. doi: 10.1002/mrm.27343

Eschelbach, M., Aghaeifar, A., Engel, E.-M., and Scheffler, K. (2017). "Prospective Head Motion Correction Using Multiple Tracking Modalities," in *Proceedings of the ESMRMB Annual Scientific Meeting*, Barcelona.

Esteban, O., Markiewicz, C. J., Blair, R. W., Moodie, C. A., Isik, A. I., Erramuzpe, A., et al. (2019). fMRIPrep: a robust preprocessing pipeline for functional MRI. *Nat. Methods* 16, 111–116. doi: 10.1038/s41592-018-0235-234

Eviatar, H., Schattka, B., Sharp, J. C., Rendell, J., and Alexander, M. E. (1999). "Real time head motion correction for functional MRI," in *Proceedings of the International Society for Magnetic Resonance in Medicine*, Philadelphia, 269.

Fair, D. A., Cohen, A. L., Dosenbach, N. U. F., Church, J. A., Miezin, F. M., Barch, D. M., et al. (2008). The maturing architecture of the brain's default network. *Proc. Natl. Acad. Sci. U.S.A.* 105, 4028–4032. doi: 10.1073/pnas.0800376105

Faraji-Dana, Z., Tam, F., Chen, J. J., and Graham, S. J. (2016a). A robust method for suppressing motion-induced coil sensitivity variations during prospective correction of head motion in fMRI. *Magn. Reson. Imaging* 34, 1206–1219. doi: 10.1016/j.mri.2016.06.005

Faraji-Dana, Z., Tam, F., Chen, J. J., and Graham, S. J. (2016b). Interactions between head motion and coil sensitivity in accelerated fMRI. *J. Neurosci. Methods* 270, 46–60. doi: 10.1016/j.jneumeth.2016.06.005

Feinberg, D. A., Moeller, S., Smith, S. M., Auerbach, E., Ramanna, S., Gunther, M., et al. (2010). Multiplexed echo planar imaging for sub-second whole brain FMRI and fast diffusion imaging. *PLoS One* 5:e15710. doi: 10.1371/journal.pone.0015710

Ferrante, E., and Paragios, N. (2017). Slice-to-volume medical image registration: a survey. *Med. Image Anal.* 39, 101–123. doi: 10.1016/j.media.2017.04.010

Freire, L., and Mangin, J. F. (2001). Motion correction algorithms may create spurious brain activations in the absence of subject motion. *Neuroimage* 14, 709–722. doi: 10.1006/nimg.2001.0869

Friston, K. J., Ashburner, J., Poline, J.-B., Frith, C. D., Heather, J. D., and Frackowiak, R. (1995). Spatial registration and normalization of images. *Hum. Brain Mapp.* 2, 165–189. doi: 10.1002/hbm.460030303

Friston, K. J., Williams, S., Howard, R., Frackowiak, R. S. J., and Turner, R. (1996). Movement-related effects in fMRI time-series. *Magn. Reson. Med.* 35, 346–355. doi: 10.1002/mrm.1910350312

Frost, R., Wighton, P., Karahanoglu, I., Robertson, R. L., Grant, P. E., Fischl, B., et al. (2018). "Markerless real-time motion correction for T1- and T2-weighted neuroanatomical MRI," in *Proceedings of the Joint Annual Meeting ISMRM-ESMRMB*, Paris, 4–7.

Gargouri, F., Kallel, F., Delphine, S., Ben Hamida, A., Lehéricy, S., and Valabregue, R. (2018). The influence of preprocessing steps on graph theory measures derived from resting state fMRI. *Front. Comput. Neurosci.* 12:8. doi: 10.3389/fncom.2018.00008

Glover, G. H. (2012). Spiral imaging in fMRI. *Neuroimage* 62, 706–712. doi: 10.1016/j.neuroimage.2011.10.039

Glover, G. H., and Lai, S. (1998). Self-navigated spiral fMRI: interleaved versus single-shot. *Magn. Reson. Med.* 39, 361–368. doi: 10.1002/mrm.1910390305

Golestani, A. M., Faraji-Dana, Z., Kayvanrad, M., Setsompop, K., Graham, S. J., and Chen, J. J. (2018). Simultaneous multislice resting-state functional magnetic resonance imaging at 3 Tesla: slice-acceleration-related biases in physiological effects. *Brain Connect.* 8, 82–93. doi: 10.1089/brain.2017.0491

Graedel, N. N., McNab, J. A., Chiew, M., and Miller, K. L. (2017). Motion correction for functional MRI with three-dimensional hybrid radial-Cartesian EPI. *Magn. Reson. Med.* 78, 527–540. doi: 10.1002/mrm.26390

Graham, S. J., Ranieri, S., Boe, S., Ween, J. E., Tam, F., and Schweizer, T. A. (2016). fMRI simulator training to suppress head motion. *Neurosci. Biomed. Eng.* 4, 96–103. doi: 10.2174/2213385204666160425155104

Green, M. V., Seidel, J., Stein, S. D., Tedder, T. E., Kempner, K. M., Kertzman, C., et al. (1994). Head movement in normal subjects during simulated PET brain imaging with and without head restraint. *J. Nucl. Med.* 35, 1538–1546.

Greene, D. J., Koller, J. M., Hampton, J. M., Wesevich, V., Van, A. N., Nguyen, A. L., et al. (2018). Behavioral interventions for reducing head motion during MRI scans in children. *Neuroimage* 171, 234–245. doi: 10.1016/j.neuroimage.2018.01.023

Griffanti, L., Douaud, G., Bijsterbosch, J., Evangelisti, S., Alfaro-Almagro, F., Glasser, M. F., et al. (2017). Hand classification of fMRI ICA noise components. *Neuroimage* 154, 188–205. doi: 10.1016/j.neuroimage.2016.12.036

Grootoonk, S., Hutton, C., Ashburner, J., Howseman, A. M., Josephs, O., Rees, G., et al. (2000). Characterization and correction of interpolation effects in the realignment of fMRI time series. *Neuroimage* 11, 49–57. doi: 10.1006/nimg.1999.0515

Haeberlin, M., Aranovitch, A., Kasper, L., Barmet, C., and Pruessmann, K. P. (2014). "Motion Correction of EPI sequences using their intrinsic high-frequency content," in *Proceedings of the International Society for Magnetic Resonance in Medicine*, Montreal, 6008.

Hahamy, A., Calhoun, V., Pearlson, G., Harel, M., Stern, N., Attar, F., et al. (2014). Save the global: global signal connectivity as a tool for studying clinical populations with functional magnetic resonance imaging. *Brain Connect.* 4, 395–403. doi: 10.1089/brain.2014.0244

Hajnal, J. V., Myers, R., Young, I. R., and Bydder, G. M. (1994). Artifacts due to stimulus-correlated motion in functional imaging of the brain. *Magn. Reson. Med.* 31, 283–291. doi: 10.1002/mrm.1910310307

Haller, S., Monsch, A. U., Richiardi, J., Barkhof, F., Kressig, R. W., Radue, E. W., et al. (2014). head motion parameters in fMRI differ between patients with mild cognitive impairment and Alzheimer Disease versus elderly control subjects. *Brain Topogr.* 27, 801–807. doi: 10.1007/s10548-014-0358-356

Hallquist, M. N., Hwang, K., and Luna, B. (2013). The nuisance of nuisance regression: spectral misspecification in a common approach to resting-state fMRI preprocessing reintroduces noise and obscures functional connectivity. *Neuroimage* 82, 208–225. doi: 10.1016/j.neuroimage.2013.05.116

Hoinkiss, D. C., Erhard, P., Günther, M., Breutigam, N., von Samson-Himmelstjerna, F., and Porter, D. A. (2018). "Prospective Motion Correction in Multiband fMRI Using Multislice-to-Volume Image Registration," in *Proceedings of the 2018 Joint Annual Meeting of the International Society for Magnetic Resonance in Medicine and the European Society of Magnetic Resonance in Medicine and Biology*, Paris, 3–5. doi: 10.1002/mrm.26951.5

Hoinkiss, D. C., and Porter, D. A. (2017). Prospective motion correction in 2D multishot MRI using EPI navigators and multislice-to-volume image registration. *Magn. Reson. Med.* 78, 2127–2135. doi: 10.1002/mrm.26951

Huijbers, W., Van Dijk, K. R. A., Boenniger, M. M., Stirnberg, R., and Breteler, M. M. B. (2017). Less head motion during MRI under task than resting-state conditions. *Neuroimage* 147, 111–120. doi: 10.1016/j.neuroimage.2016.12.002

Hutton, C., Bork, A., Josephs, O., Deichmann, R., Ashburner, J., and Turner, R. (2002). Image distortion correction in fMRI: a quantitative evaluation. *Neuroimage* 16, 217–240. doi: 10.1006/nimg.2001.1054

Jenkinson, M., Bannister, P., Brady, M., and Smith, S. (2002). Improved optimization for the robust and accurate linear registration and motion correction of brain images. *Neuroimage* 17, 825–841. doi: 10.1016/S1053-8119(02)91132-91138

Jezzard, P., and Clare, S. (1999). Sources of distortion in functional MRI data. *Hum. Brain Mapp.* 8, 80–85. doi: 10.1002/(sici)1097-0193(1999)8:2/3<80::aid-hbm2>3.0.co;2-c

Jo, H. J., Saad, Z. S., Simmons, W. K., Milbury, L. A., and Cox, R. W. (2010). Mapping sources of correlation in resting state FMRI, with artifact detection and removal. *Neuroimage* 52, 571–582. doi: 10.1016/j.neuroimage.2010.04.246

Johnstone, T., Ores Walsh, K. S., Greischar, L. L., Alexander, A. L., Fox, A. S., Davidson, R. J., et al. (2006). Motion correction and the use of motion covariates in multiple-subject fMRI analysis. *Hum. Brain Mapp.* 27, 779–788. doi: 10.1002/hbm.20219

Kecskemeti, S., Samsonov, A., Velikina, J., Field, A. S., Turski, P., Rowley, H., et al. (2018). Robust motion correction strategy for structural MRI in unsedated children demonstrated with three-dimensional radial MPnRAGE. *Radiology* 289, 509–516. doi: 10.1148/radiol.2018180180

Kim, B., Boes, J. L., Bland, P. H., Chenevert, T. L., and Meyer, C. R. (1999). Motion correction in fMRI via registration of individual slices into an anatomical volume. *Magn. Reson. Med.* 41, 964–972. doi: 10.1002/(sici)1522-2594(199905)41:5<964::aid-mrm16>3.3.co;2-4

Kim, B., Yeo, D. T. B., and Bhagalia, R. (2008). Comprehensive mathematical simulation of functional magnetic resonance imaging time series including motion-related image distortion and spin saturation effect. *Magn. Reson. Imaging* 26, 147–159. doi: 10.1016/j.mri.2007.05.007

Krämer, M., Jochimsen, T. H., and Reichenbach, J. R. (2012). Functional magnetic resonance imaging using PROPELLER-EPI. *Magn. Reson. Med.* 68, 140–151. doi: 10.1002/mrm.23220

Krueger, S., Schaeffter, T., Weiss, S., Nehrke, K., Rozijn, T., and Boernert, P. (2006). "Prospective Intra-Image Compensation for Non-Periodic Rigid Body Motion Using Active Markers," in *Proceedings of the International Society for Magnetic Resonance in Medicine*, Seattle, 3196.

Kundu, P., Brenowitz, N. D., Voon, V., Worbe, Y., Vértes, P. E., Inati, S. J., et al. (2013). Integrated strategy for improving functional connectivity mapping using multiecho fMRI. *Proc. Natl. Acad. Sci. U.S.A.* 110, 16187–16192. doi: 10.1073/pnas.1301725110

Lee, C. C., Grimm, R. C., Manduca, A., Felmlee, J. P., Ehman, R. L., Riederer, S. J., et al. (1998). A prospective approach to correct for inter-image head rotation in FMRI. *Magn. Reson. Med.* 39, 234–243. doi: 10.1002/mrm.1910390210

Lee, C. C., Jack, C. R., Grimm, R. C., Rossman, P. J., Felmlee, J. P., Ehman, R. L., et al. (1996). Real-time adaptive motion correction in functional MRI. *Magn. Reson. Med.* 36, 436–444. doi: 10.1002/mrm.1910360316

Lee, G. R., Griswold, M. A., and Tkach, J. A. (2010). Rapid 3D radial multi-echo functional magnetic resonance imaging. *Neuroimage* 52, 1428–1443. doi: 10.1016/j.neuroimage.2010.05.004

Lemieux, L., Salek-Haddadi, A., Lund, T. E., Laufs, H., and Carmichael, D. (2007). Modelling large motion events in fMRI studies of patients with epilepsy. *Magn. Reson. Imaging* 25, 894–901. doi: 10.1016/j.mri.2007.03.009

Li, J., Li, Q., Dai, X., Li, J., and Zhang, X. (2019). Does pre-scanning training improve the image quality of children receiving magnetic resonance imaging?: a meta-analysis of current studies. *Medicine* 98:e14323. doi: 10.1097/MD.0000000000014323

Lin, Q., Rosenberg, M. D., Yoo, K., Hsu, T. W., O'Connell, T. P., and Chun, M. M. (2018). Resting-State functional connectivity predicts cognitive impairment related to Alzheimer's Disease. *Front. Aging Neurosci.* 10:94. doi: 10.3389/fnagi.2018.00094

Lin, W., Huang, F., Bornert, P., Li, Y., and Reykowski, A. (2010). Motion correction using an enhanced floating navigator and GRAPPA operations. *Magn. Reson. Med.* 63, 339–348. doi: 10.1002/mrm.22200

Lund, T. E., Madsen, K. H., Sidaros, K., Luo, W.-L., and Nichols, T. E. (2006). Non-white noise in fMRI: does modelling have an impact? *Neuroimage* 29, 54–66. doi: 10.1016/j.neuroimage.2005.07.005

Lund, T. E., Nbrgaard, M. D., Rostrup, E., Rowe, J. B., and Paulson, O. B. (2005). Motion or activity: their role in intra-and inter-subject variation in fMRI. *Neuroimage* 26, 960–964. doi: 10.1016/j.neuroimage.2005.02.021

Maclaren, J., Aksoy, M., Ooi, M. B., Zahneisen, B., and Bammer, R. (2018). Prospective motion correction using coil-mounted cameras: cross-calibration considerations. *Magn. Reson. Med.* 79, 1911–1921. doi: 10.1002/mrm.26838

Maclaren, J., Armstrong, B. S. R., Barrows, R. T., Danishad, K. A., Ernst, T., Foster, C. L., et al. (2012). Measurement and correction of microscopic head motion during magnetic resonance imaging of the brain. *PLoS One* 7:e48088. doi: 10.1371/journal.pone.0048088

Morgan, V. L., Dawant, B. M., Li, Y., and Pickens, D. R. (2007). Comparison of fMRI statistical software packages and strategies for analysis of images containing random and stimulus-correlated motion. *Comput. Med. Imaging Graph.* 31, 436–446. doi: 10.1016/j.compmedimag.2007.04.002

Mowinckel, A. M., Espeseth, T., and Westlye, L. T. (2012). Network-specific effects of age and in-scanner subject motion: a resting-state fMRI study of 238 healthy adults. *Neuroimage* 63, 1364–1373. doi: 10.1016/j.neuroimage.2012.08.004

Muraskin, J., Ooi, M. B., Goldman, R. I., Krueger, S., Thomas, W. J., Sajda, P., et al. (2013). Prospective active marker motion correction improves statistical power in BOLD fMRI. *Neuroimage* 68, 154–161. doi: 10.1016/j.neuroimage.2012.11.052

Muresan, L., Renken, R., Roerdink, J. B., and Duifhuis, H. (2002). "Position-history and spin-history artifacts in fMRI time series," in *Proceedings of the SPIE Medical Imaging 2002: Physiology and Function from Multidimensional Images International Society for Optics and Photonics*, San Diego, CA, 444. doi: 10.1117/12.463613

Murphy, K., Birn, R. M., Handwerker, D. A., Jones, T. B., and Bandettini, P. A. (2009). The impact of global signal regression on resting state correlations: are anti-correlated networks introduced? *Neuroimage* 44, 893–905. doi: 10.1016/j.neuroimage.2008.09.036

Murphy, K., and Fox, M. D. (2017). Towards a consensus regarding global signal regression for resting state functional connectivity MRI. *Neuroimage* 154, 169–173. doi: 10.1016/j.neuroimage.2016.11.052

Muschelli, J., Nebel, M. B., Caffo, B. S., Barber, A. D., Pekar, J. J., and Mostofsky, S. H. (2014). Reduction of motion-related artifacts in resting state fMRI using aCompCor. *Neuroimage* 96, 22–35. doi: 10.1016/j.neuroimage.2014.03.028

Oakes, T. R., Johnstone, T., Ores Walsh, K. S., Greischar, L. L., Alexander, A. L., Fox, A. S., et al. (2005). Comparison of fMRI motion correction software tools. *Neuroimage* 28, 529–543. doi: 10.1016/j.neuroimage.2005.05.058

Ojemann, J. G., Akbudak, E., Snyder, A. Z., McKinstry, R. C., Raichle, M. E., and Conturo, T. E. (1997). Anatomic localization and quantitative analysis of gradient refocused Echo-Planar fMRI susceptibility artifacts. *Neuroimage* 6, 156–167. doi: 10.1006/nimg.1997.0289

Ollinger, J. M., Oakes, T. R., Alexander, A. L., Haeberli, F., Dalton, K. M., and Davidson, R. J. (2009). The secret life of motion covariates. *Neuroimage* 47:S122. doi: 10.1016/S1053-8119(09)71160-71167

Ooi, M. B., Aksoy, M., MacLaren, J., Watkins, R. D., and Bammer, R. (2013a). Prospective motion correction using inductively coupled wireless RF coils. *Magn. Reson. Med.* 70, 639–647. doi: 10.1002/mrm.24845

Ooi, M. B., Muraskin, J., Zou, X., Thomas, W. J., Krueger, S., Aksoy, M., et al. (2013b). Combined prospective and retrospective correction to reduce motion-induced image misalignment and geometric distortions in EPI. *Magn. Reson. Med.* 69, 803–811. doi: 10.1002/mrm.24285

Ooi, M. B., Krueger, S., Muraskin, J., Thomas, W. J., and Brown, T. R. (2011). Echo-planar imaging with prospective slice-by-slice motion correction using active markers. *Magn. Reson. Med.* 66, 73–81. doi: 10.1002/mrm.22780

Ooi, M. B., Krueger, S., Thomas, W. J., Swaminathan, S. V., and Brown, T. R. (2009). Prospective real-time correction for arbitrary head motion using active markers. *Magn. Reson. Med.* 62, 943–954. doi: 10.1002/mrm.22082

Orchard, J., Greif, C., Golub, G. H., Bjornson, B., and Atkins, M. S. (2003). Simultaneous registration and activation detection for fMRI. *IEEE Trans. Med. Imaging* 22, 1427–1435. doi: 10.1109/TMI.2003.819294

Parker, D., Liu, X., and Razlighi, Q. R. (2017). Optimal slice timing correction and its interaction with fMRI parameters and artifacts. *Med. Image Anal.* 35, 434–445. doi: 10.1016/j.media.2016.08.006

Parkes, L., Fulcher, B., Yücel, M., and Fornito, A. (2018). An evaluation of the efficacy, reliability, and sensitivity of motion correction strategies for resting-state functional MRI. *Neuroimage* 171, 415–436. doi: 10.1016/j.neuroimage.2017.12.073

Patel, A. X., Kundu, P., Rubinov, M., Jones, P. S., Vértes, P. E., Ersche, K. D., et al. (2014). A wavelet method for modeling and despiking motion artifacts from resting-state fMRI time series. *Neuroimage* 95, 287–304. doi: 10.1016/j.neuroimage.2014.03.012

Patriat, R., Molloy, E. K., and Birn, R. M. (2015). Using edge voxel information to improve motion regression for rs-fMRI connectivity studies. *Brain Connect.* 5, 582–595. doi: 10.1089/brain.2014.0321

Peer, M., Nitzan, M., Bick, A. S., Levin, N., and Arzy, S. (2017). Evidence for functional networks within the human brain's white matter. *J. Neurosci.* 37, 6394–6407. doi: 10.1523/JNEUROSCI.3872-16.2017

Perlbarg, V., Bellec, P., Anton, J. L., Pélégrini-Issac, M., Doyon, J., and Benali, H. (2007). CORSICA: correction of structured noise in fMRI by automatic identification of ICA components. *Magn. Reson. Imaging* 25, 35–46. doi: 10.1016/j.mri.2006.09.042

Power, J. D., Barnes, K. A., Snyder, A. Z., Schlaggar, B. L., and Petersen, S. E. (2012). Spurious but systematic correlations in functional connectivity MRI networks arise from subject motion. *Neuroimage* 59, 2142–2154. doi: 10.1016/j.neuroimage.2011.10.018

Power, J. D., Mitra, A., Laumann, T. O., Snyder, A. Z., Schlaggar, B. L., and Petersen, S. E. (2014). Methods to detect, characterize, and remove motion artifact in resting state fMRI. *Neuroimage* 84, 320–341. doi: 10.1016/j.neuroimage.2013.08.048

Power, J. D., Schlaggar, B. L., and Petersen, S. E. (2015). Recent progress and outstanding issues in motion correction in resting state fMRI. *Neuroimage* 105, 536–551. doi: 10.1016/j.neuroimage.2014.10.044

Pruessmann, K. P. (2006). Encoding and reconstruction in parallel MRI. *NMR Biomed.* 19, 288–299. doi: 10.1002/nbm.1042

Pruim, R. H. R., Mennes, M., Buitelaar, J. K., and Beckmann, C. F. (2015a). Evaluation of ICA-AROMA and alternative strategies for motion artifact removal in resting state fMRI. *Neuroimage* 112, 278–287. doi: 10.1016/j.neuroimage.2015.02.063

Pruim, R. H. R., Mennes, M., van Rooij, D., Llera, A., Buitelaar, J. K., and Beckmann, C. F. (2015b). ICA-AROMA: a robust ICA-based strategy for removing motion artifacts from fMRI data. *Neuroimage* 112, 267–277. doi: 10.1016/j.neuroimage.2015.02.064

Qin, L., Wang, Z., Sun, Y., Wan, J., Su, S., Zhou, Y., et al. (2012). A preliminary study of alterations in default network connectivity in post-traumatic stress disorder patients following recent trauma. *Brain Res.* 1484, 50–56. doi: 10.1016/j.brainres.2012.09.029

Raj, D., Anderson, A. W., and Gore, J. C. (2001). Respiratory effects in human functional magnetic resonance imaging due to bulk susceptibility changes. *Phys. Med. Biol.* 46, 3331–3340. doi: 10.1088/0031-9155/46/12/318

Righini, A., de Divitiis, O., Prinster, A., Spagnoli, D., Appollonio, I., Bello, L., et al. (1996). Functional MRI: primary motor cortex localization in patients with brain tumors. *J. Comput. Assist. Tomogr.* 20, 702–708. doi: 10.1097/00004728-199609000-00003

Roopchansingh, V., Cox, R. W., Jesmanowicz, A., Ward, B. D., and Hyde, J. S. (2003). Single-shot magnetic field mapping embedded in echo-planar time-course imaging. *Magn. Reson. Med.* 50, 839–843. doi: 10.1002/mrm.10587

Rotenberg, D., Chiew, M., Ranieri, S., Tam, F., Chopra, R., and Graham, S. J. (2013). Real-time correction by optical tracking with integrated geometric distortion correction for reducing motion artifacts in functional MRI. *Magn. Reson. Med.* 69, 734–748. doi: 10.1002/mrm.24309

Salimi-Khorshidi, G., Douaud, G., Beckmann, C. F., Glasser, M. F., Griffanti, L., and Smith, S. M. (2014). Automatic denoising of functional MRI data: combining independent component analysis and hierarchical fusion of classifiers. *Neuroimage* 90, 449–468. doi: 10.1016/j.neuroimage.2013.11.046

Satterthwaite, T. D., Elliott, M. A., Gerraty, R. T., Ruparel, K., Loughead, J., Calkins, M. E., et al. (2013). An improved framework for confound regression and filtering for control of motion artifact in the preprocessing of resting-state functional connectivity data. *Neuroimage* 64, 240–256. doi: 10.1016/j.neuroimage.2012.08.052

Satterthwaite, T. D., Wolf, D. H., Loughead, J., Ruparel, K., Elliott, M. A., Hakonarson, H., et al. (2012). Impact of in-scanner head motion on multiple measures of functional connectivity: relevance for studies of neurodevelopment in youth. *Neuroimage* 60, 623–632. doi: 10.1016/j.neuroimage.2011.12.063

Schölvinck, M. L., Maier, A., Ye, F. Q., Duyn, J. H., and Leopold, D. A. (2010). Neural basis of global resting-state fMRI activity. *Proc. Natl. Acad. Sci. U.S.A.* 107, 10238–10243. doi: 10.1073/pnas.0913110107

Schültke, E., Nanko, N., Pinsker, M., Katzev, M., Sebastian, A., Feige, B., et al. (2013). Improving MRT image quality in patients with movement disorders. *Acta Neurochir. Suppl.* 117, 13–17. doi: 10.1007/978-3-7091-1482-7_3

Seto, E., Sela, G., McIlroy, W. E., Black, S. E., Staines, W. R., Bronskill, M. J., et al. (2001). Quantifying head motion associated with motor tasks used in fMRI. *Neuroimage* 14, 284–297. doi: 10.1006/nimg.2001.0829

Setsompop, K., Gagoski, B. A., Polimeni, J. R., Witzel, T., Wedeen, V. J., and Wald, L. L. (2012). Blipped-controlled aliasing in parallel imaging for simultaneous multislice echo planar imaging with reduced g-factor penalty. *Magn. Reson. Med.* 67, 1210–1224. doi: 10.1002/mrm.23097

Shirer, W. R., Jiang, H., Price, C. M., Ng, B., and Greicius, M. D. (2015). Optimization of rs-fMRI Pre-processing for enhanced signal-noise separation, test-retest reliability, and group discrimination. *Neuroimage* 117, 67–79. doi: 10.1016/j.neuroimage.2015.05.015

Singh, A., Zahneisen, B., Keating, B., Herbst, M., Chang, L., Zaitsev, M., et al. (2015). Optical tracking with two markers for robust prospective motion correction for brain imaging. *Magn. Reson. Mater. Phys. Biol. Med.* 28, 523–534. doi: 10.1007/s10334-015-0493-4

Smith, S. M., Beckmann, C. F., Andersson, J., Auerbach, E. J., Bijsterbosch, J., Douaud, G., et al. (2013a). Resting-state fMRI in the human connectome project. *Neuroimage* 80, 144–168. doi: 10.1016/j.neuroimage.2013.05.039

Smith, S. M., Vidaurre, D., Beckmann, C. F., Glasser, M. F., Jenkinson, M., Miller, K. L., et al. (2013b). Functional connectomics from resting-state fMRI. *Trends Cogn. Sci.* 17, 666–682. doi: 10.1016/j.tics.2013.09.016

Stanisz, G. J., Odrobina, E. E., Pun, J., Escaravage, M., Graham, S. J., Bronskill, M. J., et al. (2005). T1, T2 relaxation and magnetization transfer in tissue at 3T. *Magn. Reson. Med.* 54, 507–512. doi: 10.1002/mrm.20605

Supekar, K., Musen, M., and Menon, V. (2009). Development of large-scale functional brain networks in children. *PLoS Biol.* 7:e1000157. doi: 10.1371/journal.pbio.1000157

Sutton, B. P., Noll, D. C., and Fessler, J. A. (2004). Dynamic field map estimation using a spiral-in/spiral-out acquisition. *Magn. Reson. Med.* 51, 1194–1204. doi: 10.1002/mrm.20079

Thesen, S., Heid, O., Mueller, E., and Schad, L. R. (2000). Prospective acquisition correction for head motion with image-based tracking for real-time fMRI. *Magn. Reson. Med.* 44, 457–465. doi: 10.1002/1522-2594(200009)44:3<457::aid-mrm17>3.3.co;2-i

Thieba, C., Frayne, A., Walton, M., Mah, A., Benischek, A., Dewey, D., et al. (2018). Factors associated with successful MRI scanning in unsedated young children. *Front. Pediatr.* 6:146. doi: 10.3389/fped.2018.00146

Thomas, C. G., Marshman, R. A., and Menon, R. S. (2002). Noise reduction in BOLD-Based fMRI using component analysis. *Neuroimage* 17, 1521–1537. doi: 10.1006/nimg.2002.1200

Tisdall, M. D., Hess, A. T., Reuter, M., Meintjes, E. M., Fischl, B., and Van Der Kouwe, A. J. W. (2012). Volumetric navigators for prospective motion correction and selective reacquisition in neuroanatomical MRI. *Magn. Reson. Med.* 68, 389–399. doi: 10.1002/mrm.23228

Todd, N., Josephs, O., Callaghan, M. F., Lutti, A., and Weiskopf, N. (2015). Prospective motion correction of 3D echo-planar imaging data for functional MRI using optical tracking. *Neuroimage* 113, 1–12. doi: 10.1016/j.neuroimage.2015.03.013

Tohka, J., Foerde, K., Aron, A. R., Tom, S. M., Toga, A. W., and Poldrack, R. A. (2008). Automatic independent component labeling for artifact removal in fMRI. *Neuroimage* 39, 1227–1245. doi: 10.1016/j.neuroimage.2007.10.013

Tucholka, A., Fritsch, V., Poline, J.-B., and Thirion, B. (2012). An empirical comparison of surface-based and volume-based group studies in neuroimaging. *Neuroimage* 63, 1443–1453. doi: 10.1016/j.neuroimage.2012.06.019

Van de Moortele, P.-F., Pfeuffer, J., Glover, G. H., Ugurbil, K., and Hu, X. (2002). Respiration-induced B0 fluctuations and their spatial distribution in the human brain at 7 Tesla. *Magn. Reson. Med.* 47, 888–895. doi: 10.1002/mrm.10145

van Dijk, K. R. A., Sabuncu, M. R., and Buckner, R. L. (2012). The influence of head motion on intrinsic functional connectivity MRI. *Neuroimage* 59, 431–438. doi: 10.1016/j.neuroimage.2011.07.044

van Niekerk, A., Meintjes, E., and van der Kouwe, A. (2019). A wireless radio frequency triggered acquisition device (WRAD) for self-synchronised measurements of the rate of change of the MRI gradient vector field for motion tracking. *IEEE Trans. Med. Imaging* 38, 1610–1621. doi: 10.1109/TMI.2019.2891774

Vanderwal, T., Kelly, C., Eilbott, J., Mayes, L. C., and Castellanos, F. X. (2015). Inscapes: a movie paradigm to improve compliance in functional magnetic resonance imaging. *Neuroimage* 122, 222–232. doi: 10.1016/j.neuroimage.2015.07.069

Visser, E., Poser, B. A., Barth, M., and Zwiers, M. P. (2012). Reference-free unwarping of EPI data using dynamic off-resonance correction with multiecho acquisition (DOCMA). *Magn. Reson. Med.* 68, 1247–1254. doi: 10.1002/mrm.24119

Vytvarová, E., Fousek, J., Bartoň, M., Mareček, R., Gajdoš, M., Lamoš, M., et al. (2017). "The impact of diverse preprocessing pipelines on brain functional connectivity," in *Proceedings of the 25th European Signal Processing Conference, EUSIPCO*, Kos, doi: 10.23919/EUSIPCO.2017.8081690

Wastiaux, L., Dale, A., and van der Kouwe, A. (2006). "Real-time Motion Correction in 3D EPI using Cloverleaf Navigators," in *Proceedings 14th Scientific Meeting, International Society for Magnetic Resonance in Medicine*, Paris, 746.

Weissenbacher, A., Kasess, C., Gerstl, F., Lanzenberger, R., Moser, E., and Windischberger, C. (2009). Correlations and anticorrelations in resting-state functional connectivity MRI: a quantitative comparison of preprocessing strategies. *Neuroimage* 47, 1408–1416. doi: 10.1016/j.neuroimage.2009.05.005

Welch, E. B., Manduca, A., Grimm, R. C., Ward, H. A., and Jack, C. R. (2002). Spherical navigator echoes for full 3D rigid body motion measurement in MRI. *Magn. Reson. Med.* 47, 32–41. doi: 10.1002/mrm.10012

White, N., Roddey, C., Shankaranarayanan, A., Han, E., Rettmann, D., Santos, J., et al. (2010). PROMO: real-time prospective motion correction in MRI using image-based tracking. *Magn. Reson. Med.* 63, 91–105. doi: 10.1002/mrm.22176

Wong, C. W., DeYoung, P. N., and Liu, T. T. (2016). Differences in the resting-state fMRI global signal amplitude between the eyes open and eyes closed states are related to changes in EEG vigilance. *Neuroimage* 124, 24–31. doi: 10.1016/j.neuroimage.2015.08.053

Woods, R. P., Grafton, S. T., Holmes, C. J., Cherry, S. R., and Mazziotta, J. C. (1998). Automated image registration: I. General methods and intrasubject, intramodality validation. *J. Comput. Assist. Tomogr.* 22, 139–152. doi: 10.1097/00004728-199801000-00027

Wu, D. H., Lewin, J. S., and Duerk, J. L. (1997). Inadequacy of motion correction algorithms in functional MRI: role of susceptibility-induced artifacts. *J. Magn. Reson. Imaging* 7, 365–370. doi: 10.1002/jmri.1880070219

Wylie, G. R., Genova, H., DeLuca, J., Chiaravalloti, N., and Sumowski, J. F. (2014). Functional magnetic resonance imaging movers and shakers: does subject-movement cause sampling bias? *Hum. Brain Mapp.* 35, 1–13. doi: 10.1002/hbm.22150

Xu, H., Su, J., Qin, J., Li, M., Zeng, L. L., Hu, D., et al. (2018). Impact of global signal regression on characterizing dynamic functional connectivity and brain states. *Neuroimage* 173, 127–145. doi: 10.1016/j.neuroimage.2018.02.036

Yan, C.-G., Cheung, B., Kelly, C., Colcombe, S., Craddock, R. C., Di Martino, A., et al. (2013). A comprehensive assessment of regional variation in the impact of head micromovements on functional connectomics. *Neuroimage* 76, 183–201. doi: 10.1016/j.neuroimage.2013.03.004

Yancey, S. E., Rotenberg, D. J., Tam, F., Chiew, M., Ranieri, S., Biswas, L., et al. (2011). Spin-history artifact during functional MRI: potential for adaptive correction. *Med. Phys.* 38, 4634–4646. doi: 10.1118/1.3583814

Yeo, D. T. B., Fessler, J. A., and Kim, B. (2008). Concurrent correction of geometric distortion and motion using the map-slice-to-volume method in echo-planar imaging. *Magn. Reson. Imaging* 26, 703–714. doi: 10.1016/j.mri.2007.11.001

Yuan, L., He, H., Zhang, H., and Zhong, J. (2016). Evaluating the influence of spatial resampling for motion correction in resting-state functional MRI. *Front. Neurosci.* 10:591. doi: 10.3389/fnins.2016.00591

Yuan, W., Altaye, M., Ret, J., Schmithorst, V., Byars, A. W., Plante, E., et al. (2009). Quantification of head motion in children during various fMRI language tasks. *Hum. Brain Mapp.* 30, 1481–1489. doi: 10.1002/hbm.20616

Zahneisen, B., Keating, B., and Ernst, T. (2014a). Propagation of calibration errors in prospective motion correction using external tracking. *Magn. Reson. Med.* 72, 381–388. doi: 10.1002/mrm.24943

Zahneisen, B., Poser, B. A., Ernst, T., and Stenger, A. V. (2014b). Simultaneous Multi-Slice fMRI using spiral trajectories. *Neuroimage* 92, 8–18. doi: 10.1016/j.neuroimage.2014.01.056

Zaitsev, M., Akin, B., LeVan, P., and Knowles, B. R. (2017). Prospective motion correction in functional MRI. *Neuroimage* 154, 33–42. doi: 10.1016/j.neuroimage.2016.11.014

Zaitsev, M., Dold, C., Sakas, G., Hennig, J., and Speck, O. (2006). Magnetic resonance imaging of freely moving objects: prospective real-time motion correction using an external optical motion tracking system. *Neuroimage* 31, 1038–1050. doi: 10.1016/j.neuroimage.2006.01.039

Zeffiro, T. (1996). Clinical functional image analysis: artifact detection and reduction. *Neuroimage* 4, S95–S100. doi: 10.1006/NIMG.1996.0059

Conflict of Interest Statement: The authors declare that the research was conducted in the absence of any commercial or financial relationships that could be construed as a potential conflict of interest.

frontiers in Neuroscience

REVIEW
published: 14 August 2019
doi: 10.3389/fnins.2019.00787

Low Frequency Systemic Hemodynamic "Noise" in Resting State BOLD fMRI: Characteristics, Causes, Implications, Mitigation Strategies, and Applications

*Yunjie Tong[1], Lia M. Hocke[2,3] and Blaise B. Frederick[2,3]**

[1] Weldon School of Biomedical Engineering, Purdue University, West Lafayette, IN, United States, [2] McLean Imaging Center, McLean Hospital, Belmont, MA, United States, [3] Department of Psychiatry, Harvard Medical School, Boston, MA, United States

Advances in functional magnetic resonance imaging (fMRI) acquisition have improved signal to noise to the point where the physiology of the subject is the dominant noise source in resting state fMRI data (rsfMRI). Among these systemic, non-neuronal physiological signals, respiration and to some degree cardiac fluctuations can be removed through modeling, or in the case of newer, faster acquisitions such as simultaneous multislice acquisition, simple spectral filtering. However, significant low frequency physiological oscillation (~0.01–0.15 Hz) remains in the signal. This is problematic, as it is the precise frequency band occupied by the neuronally modulated hemodynamic responses used to study brain connectivity, precluding its removal by spectral filtering. The source of this signal, and its method of production and propagation in the body, have not been conclusively determined. Here, we summarize the defining characteristics of the systemic low frequency noise signal, and review some current theories about the signal source and the evidence supporting them. The strength and distribution of the systemic LFO signal make characterizing and removing it essential for accurate quantification, especially for resting state connectivity, when no stimulation can be compared with the signal. Widespread correlated non-neuronal signals obscure and distort the more localized patterns of neuronal correlations between interacting brain regions; they may even cause apparent connectivity between regions with no neuronal interaction. Here, we discuss a simple method we have developed to parse the global, moving, blood-borne signal from the stationary, neuronal connectivity signals, substantially reducing the negative correlations that result from global signal regression. Finally, we will discuss some of the uses to which the moving systemic low frequency oscillation can be put if we consider it a "signal" carrying information, rather than simply "noise" complicating the interpretation of resting state connectivity. Properly utilizing this signal may offer insights into subtle hemodynamic alterations that can be used as early indicators of circulatory dysfunction in a number of neuropsychiatric conditions, such as prodromal stroke, moyamoya, and Alzheimer's disease.

Keywords: low frequency oscillation, noise modeling, denoising, vascular mapping, cerebrovascular reactivity, physiological noise, physiological noise modeling

OPEN ACCESS

Edited by:
Jean Chen,
University of Toronto, Canada

Reviewed by:
Thomas T. Liu,
University of California, San Diego, United States
Muhammad E. H. Chowdhury,
Qatar University, Qatar

***Correspondence:**
Blaise B. Frederick
bbfrederick@mclean.harvard.edu

Specialty section:
This article was submitted to Brain Imaging Methods, a section of the journal Frontiers in Neuroscience

Received: *29 November 2018*
Accepted: *15 July 2019*
Published: *14 August 2019*

Citation:
Tong Y, Hocke LM and Frederick BB (2019) Low Frequency Systemic Hemodynamic "Noise" in Resting State BOLD fMRI: Characteristics, Causes, Implications, Mitigation Strategies, and Applications. Front. Neurosci. 13:787. doi: 10.3389/fnins.2019.00787

INTRODUCTION

Resting state functional magnetic resonance imaging (rsfMRI) seeks to elucidate neuronal connectivity throughout the brain by examining of fMRI signal correlations between regions during scans when the brain is not performing any specific task (it is "at rest"). However, the BOLD signal does not measure neuronal activation directly. It is a composite measurement of hemodynamic properties of blood flow, volume, and oxygenation changes in response to neuronal activity (Buxton et al., 1998) (i.e., neurovascular coupling). In short, increased neuronal firing leads to an increase in regional blood flow, which brings an oversupply of oxygenated blood (Fox and Raichle, 1986). The increase in blood flow and oxygenation leads to an elevation of the BOLD signal. As a result, the observable BOLD signal (blood-related) is much slower (∼s) than neuronal firing (∼ms) (Logothetis et al., 2001) and cannot reflect fast changes of the field potential of neuronal firings. In mathematical terms, the BOLD signal is the result of the convolution of the fast neuronal signals with the slow hemodynamic functions. Therefore, the frequencies of "neuronal" BOLD signals are generally below 0.15 Hz (Josephs and Henson, 1999).

However, neuronal activations are not the only contributors to BOLD signals in the low frequency band. Advances in fMRI acquisition techniques and hardware have improved signal to noise to the point where the physiology of the subject being studied is the dominant noise source in rsfMRI data. In addition to neuronal BOLD, there are systemic, non-neuronal fluctuations in brain hemodynamics due to heartbeat, respiration, and so-called "low frequency oscillations" (LFOs). These signals are unavoidable, and taken together can account for 20–70% of the BOLD signal variance (see **Figure 1**), depending on acquisition, and locations of the voxels (Liu, 2017). Numerous processing strategies have been devised to mitigate them. Recent improvements in hardware and pulse sequences (specifically simultaneous multislice acquisition protocols) have pushed the temporal resolution of fMRI high enough that respiration, and to some degree cardiac fluctuations (see **Figure 1**) can be removed through simple spectral filtering, or through more advanced modeling methods when these signals are aliased (Glover et al., 2000; Birn et al., 2006, 2008; Behzadi et al., 2007; Chang et al., 2009, 2013). These methods are well described elsewhere and are not the focus of this manuscript. However, significant signal power remains in the "low frequency oscillation band," a loosely defined region from ∼0.01–0.15 Hz. Non-neuronal signal in this frequency band accounts for at least 30% of the signal variance in gray matter (Frederick et al., 2012a). This is problematic as it is the precise frequency band occupied by the neuronally modulated hemodynamic responses used to study brain connectivity, precluding its removal by filtering.

The strength and distribution of the systemic LFO signal make characterizing and removing it essential for accurate quantification of neuronal connectivity. Moreover, these signals might not be "noise" after all. Understanding their origins and characteristics will help to develop novel methods to assess brain physiology which could greatly compliment the functional findings.

CHARACTERISTICS OF LOW FREQUENCY OSCILLATIONS

LFOs in BOLD fMRI have been found and studied extensively, but as noted above, there are numerous potential explanations for this signal, and even some variation in what in particular should be considered a "low frequency oscillation." For the remainder of this paper, we will apply two criteria to our discussions of LFOs; the frequency band of the signal, and whether the signal is stationary, or moves with the blood.

Frequency Content

The first criterion is simply a definition. LFOs are signals that occur in the brain (and in some cases throughout the body) that have frequencies between ∼0.009 and 0.2 Hz. The exact endpoints of this band are extremely variable in the literature. Biswal's original paper on resting state connectivity used 0.01–0.1 Hz (Biswal et al., 1995), but later papers expanded this range; for the purpose of this discussion, we will use the range of 0.01–0.15. 0.15 Hz has a particular significance as the top of the range, as this is the highest expected frequency in neuronally generated hemodynamic signals (based on the shape of the canonical hemodynamic response function) (Josephs and Henson, 1999), so this defines the frequency range where spectral filtering cannot be used to remove non-neuronal signal. The frequency content of a typical BOLD signal is shown in **Figure 1**.

Dynamic Versus Stationary Noise Signals

The second defining characteristic of LFOs is less commonly considered. Our research into low frequency physiological noise in fMRI has established that a significant fraction of the low frequency variance in fMRI data can be modeled quite effectively as a single low frequency signal with varying delay times across the brain. Moreover, the pattern of relative delay times in different regions of the brain is consistent with the delays that would be expected if the signal were moving through the brain with blood as it flowed through the vasculature. We refer to this dynamic signal as "systemic low frequency oscillations" (sLFOs) (Tong et al., 2015). The realization that a significant fraction of the low frequency "noise" in fMRI appears to be moving has important implications for how to identify, remove, or even utilize this signal (Tong and Frederick, 2010, 2012, 2014b; Tong et al., 2011b,c, 2013, 2014, 2017, 2018; Frederick et al., 2012b).

Temporal Pattern – sLFOs Propagate on a Hemodynamic Timescale

Our research on sLFOs strongly suggest that the underlying oscillations propagate on hemodynamic, physiological, rather than on neuronal, timescales, taking several seconds to fully transit the brain rather than milliseconds. Circulatory measurements of the traversal of a Tc99 tracer through the brain vasculature (from the carotid, to the internal brain arteries, through the parenchyma, to the superior sagittal sinus) showed that the transit time of blood from the anterior and middle cerebral arteries to the superior sagittal sinus takes ∼6.7 s in healthy middle-aged controls (Crandell et al., 1973), timing

consistent with results found by other imaging methods. For example, using echo contrast-enhanced ultrasound, delays of 7.5 ± 1.8 s from the carotids to the jugulars were found in 64 healthy subjects (Schreiber et al., 2002). Similar, but smaller delays (4.9–6.4 s) were found in other ultrasound studies (Schreiber et al., 2005). Direct evidence can also be found in digital subtraction angiography (DSA), where an x-ray contrast bolus was injected directly into the ICA and followed as it passed through the brain (Monti et al., 2015; Jann et al., 2016).

Spatial Pattern – sLFOs Travel Along the Vasculature

The patterns of the delays of the sLFO signal clearly suggest that this signal is related to blood flow, evolving in a pattern that reflects the vasculature – the sLFO signal appears first in the center of the brain, propagates out through the parenchyma, and ends up in the superior sagittal sinus, with a range of delays of ∼6.5 s (Tong and Frederick, 2010), a pattern we have seen consistently in many subsequent studies over several years (Tong et al., 2011a,b,c, 2013, 2014, 2015; Frederick et al., 2012a; Tong and Frederick, 2012, 2014a). In our most recent studies we have directly confirmed the association between the sLFO delay pattern and blood flow, first by performing sLFO analysis and time resolved dynamic susceptibility imaging in the same scan session (Tong et al., 2017), and more recently by following the sLFO signal all the way from the internal carotid arteries through the draining veins (Tong et al., 2018).

Origin – sLFOs Seem to Originate Outside the Brain

The sLFO BOLD signal identified from the carotids preceded the signal found in any voxel of the brain. Indeed, the same sLFO signal can be found throughout the body (measured in the periphery using NIRS) (Frederick and Tong, 2010; Tong and Frederick, 2010; Li et al., 2018). The delays in the periphery are symmetric across the midline of the body, and the arrival time of the sLFO signal found in the fingers and toes precede the arrival in many brain voxels (Tong et al., 2012). While it is possible that some process in the brain is the ultimate source of this moving signal, there is no evidence whatsoever in the fMRI data that this is the case – to the contrary the implication is that the signal does *not* originate in the brain.

Summary

From the growing body of evidence from our group and others we can summarize that the sLFO BOLD signal: (1) is a spontaneous physiological oscillation, (2) travels with the blood, and (3) has an extracerebral origin. Given the large amount of LFO signal variance that is clearly attributable to the moving component (at least 30% of the low frequency signal variance in gray matter, Frederick et al., 2012a), we believe this constitutes the majority of the physiological LFO signal power. In addition, these qualities provide the key to isolating the signal from the neuronal signals of interest.

In contrast, there may also be non-neuronal LFOs which do not propagate. However, because of the difficulty in separating these signals from putative neuronal signals, they are far harder to characterize. Certain mechanisms (detailed below) such as the Mayer wave, are thought to be synchronous throughout the body, and therefore stationary. Isolating the contribution of stationary LFOs to the resting state signal would require as yet undeveloped processing strategies, which is why we will discuss these possible sources, however we will focus primarily on the dynamic portion of the signal during the remainder of the paper.

POTENTIAL CAUSES OF THE LOW FREQUENCY OSCILLATION

The source of LFO signal, and its mechanism of production and propagation in the body, have not been conclusively determined – LFOs have been variously attributed to alterations in sympathetic nervous system tone, partial pressure of carbon dioxide ($paCO_2$) fluctuations modulated by respiration, blood pressure regulation, low frequency neuronal "waves," and even gastric motility. It may in fact be a combination of multiple, independent signals with distinct sources. We will review these current theories about the signal source and the evidence supporting them. This section is summarized in **Table 1**.

Variations in Heart Rate and Respiratory Volumes

One major potential source of LFOs comes from variations of the heart rate and respiration. For example respiration volume per time (RVT) (Birn et al., 2006) and respiration variation (convolved with the respiratory response function, Birn et al., 2008; Chang et al., 2009) are two methods to model fluctuations from CO_2 concentration. In specific, the former model describes the depth of the respiration, whereas the latter reflects the variation in respiration. Previously, these methods have been shown to explain additive variation in data with longer TRs between 9 and 11% (Birn et al., 2006, 2008; Chang et al., 2009) in the voxels affected. From the same group a model taking the variation in heart rate into account was developed (Chang et al., 2009), explaining 3% more variance in the affected voxels. The underlying mechanism of this change is still not well understood, but was proposed to relate to neuronal activity linked with changes in levels of arousal (Chang et al., 2009). These models typically incorporate a delay of several seconds to best match the modeled noise waveforms with the fMRI data, suggesting that these signals are in the moving category (although the standard implementations of these methods do not account for regional delays within the brain).

Carbon Dioxide

Carbon dioxide changes are closely related to the previous topic, and they partially share the same mechanism, namely induced changes in cerebral blood flow and volume due to CO_2 induced vasodilation. However, here we discuss the direct effects of $paCO_2$ by comparing BOLD fMRI to measured fluctuations in the partial pressure of end-tidal carbon dioxide, especially in the lower range of the LF band, namely 0–0.05 Hz (Wise et al., 2004; Sassaroli et al., 2012), rather than the indirect estimation of this effect from the respiratory and/or cardiac waveforms.

TABLE 1 | Summary of the common explanations for low frequency physiological noise.

Source	Description	Properties	Cerebral origin?	Causes sLFO?
Mayer wave	Mayer waves are spontaneous LFOs at around 0.1 Hz.	Highly synchronous within the brain – it seems unlikely that it would appear to move.	Yes?	Not likely
Vasomotion	Vasomotion is a spontaneous oscillation (0.01∼0.3 Hz) in the vascular tone, which is independent of respiration, pulsation and neuronal activity.	The induced vascular variations could propagate with the blood, resulting in a mix of stationary and moving signal.	Unclear	Possible
CO_2	Carbon dioxide is a potent vassal dilator. It can travel with the blood and induce changes in cerebral blood flow and volume.	Clearly a moving signal – the CO_2 travels in the blood.	No	Possible
Variations in heart rate and respiratory volumes	The variations of the heart rate and respiration, including the depth of the respiration, are in the low frequency range.	Depth of respiration and heart rate variation can alter blood volume (through CO_2 and pressure changes), and the effects should move with the blood.	No	Possible
Gastric oscillations	The electrogastrogram signal (i.e., synchronized gut motions at ∼0.05 Hz) significant correlates with BOLD fMRI data with time delays.	May be controlled neuronally, but the effects seem to originate in the gut and move with blood.	Mostly no	Possible
Aliased signals of cardiac and respiration	Aliased signals of cardiac and respiration due to long TR are in the low frequency range.	These signals are in the right frequency range and can travel with blood, but are not highly correlated with the sLFO signal when tested by fMRI data with very short TR or fNIRS.	No	Not likely

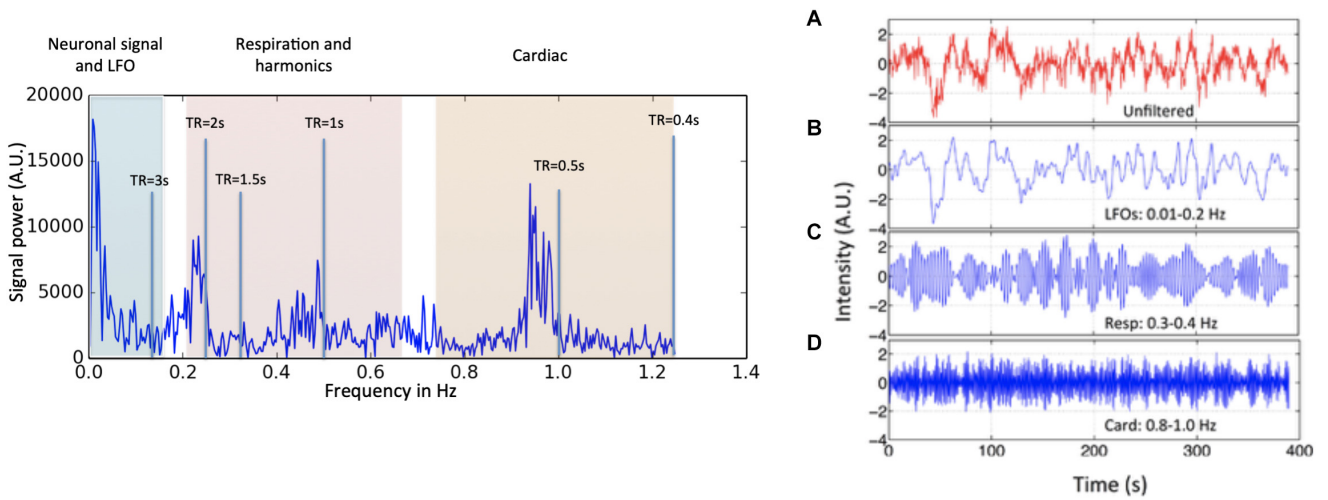

FIGURE 1 | Power spectrum (left) and time domain data (right) presented in different spectral bands, from a voxel in a resting state data (TR = 0.4 s) of one participant. Three distinct spectral ranges corresponding to different physiological processes were marked. The spectral area captured by various TR values is also depicted on the power spectrum. The right hand panel shows a BOLD timecourse from a resting state fMRI scan (TR = 0.4 s) without filtration (**A**, in red) and its band-passed versions in panel **(B)** 0.01–0.2 Hz; **(C)** 0.3–0.4 Hz; and **(D)** 0.8–1.0 Hz (in blue) (Figure adapted from Tong and Frederick, 2014a).

Wise et al. (2004) found that $paCO_2$ levels measured with end tidal CO_2 in the 0–0.05 Hz band were significantly correlated with both increased middle cerebral artery blood velocity and increased BOLD fMRI signal in gray and white matter. This is attributed to the vasodilatory effect of CO_2 – increased CO_2 leads to increased arterial diameter and blood volume. As a consequence, this signal can be clearly placed in the group of sLFOs that move with the blood. Wise found up to 28% of the low frequency signal variance in the BOLD signal was attributable to the $paCO_2$. This is likely the lower limit, because while the peak

correlation delays between the BOLD and $paCO_2$ timecourses were between 3 and 13 s, only a single delay of 6.3 s was used for all voxels, which would reduce the apparent correlation.

Mayer Waves

Mayer waves are spontaneous LFOs at around 0.1 Hz (Julien, 2006) and are associated with variations in mean arterial pressure, and have been associated with a sympathetic autoregulation mechanism (Tsuji et al., 2000), in particular below 0.1 Hz (Obrig et al., 2000; van Beek et al., 2008; Sassaroli et al., 2012). These studies connected mean arterial blood pressure to cerebral intravascular oxygenation when monitoring cerebral circulation and blood flow with NIRS. However, a characteristic of Mayer waves is their largely synchronous nature within the brain (Sassaroli et al., 2012), differing from the sLFOs, which have differing delays across the brain (Tong and Frederick, 2010; Tong et al., 2011b). We would therefore classify Mayer waves as stationary LFO signals.

Vasomotion From Oscillations in the Vascular Tone

Vasomotion is a spontaneous oscillation (0.01∼0.3 Hz) in the vascular tone, which is independent of respiration, pulsation and neuronal activity (Hundley et al., 1988; Mayhew et al., 1996; Rivadulla et al., 2011). These oscillations of the lumen diameter modify blood flow in a corresponding fashion resulting in periodic oscillations in the blood flow (Aalkjær et al., 2011). Another LF signal is attributed to vasomotion, referring to the oscillations in the vascular tone, thought to be generated movement within the vessel walls (Zhang et al., 1998; Aalkjær et al., 2011; Sassaroli et al., 2012; Müller and Österreich, 2014). These changes are highly localized and have been linked to oscillatory intracellular calcium (Aalkjær et al., 2011). This would give the signals a local, stationary nature, however the vascular variations induced would then propagate with the blood, resulting in a mix of stationary and moving signal.

Aliased Signals of Cardiac and Respiration

Because fMRI is usually not sampled fast enough to resolve cardiac or respiratory waveforms, some fraction of the energy in these signals will be aliased to the low frequency band. In order to determine the significance of this component of the signal, we evaluated sLFOs in a dataset with high temporal resolution in which the respiration and cardiac waveforms are fully sampled (Hocke et al., 2016). We found that even with fully sampled data, in which the respiration and cardiac bands can be isolated with spectral filters, the purely non-neuronal sLFOs (as determined by time-delayed correlation with a peripheral NIRS signal) still account for over 13% of the total BOLD signal variance across all frequency bands.

Gastric Oscillations

A somewhat more recent theory for the cause of sLFOs is proposed by Rebollo et al. (2018) who found significant correlations between electrogastrogram signals (which measure synchronized gut motions at ∼0.05 Hz) and BOLD fMRI data. Unfortunately, the technique used was unable to determine directionality. However, the authors found delays between the earliest (somatosensory cortices) and the latest (dorsal precuneous and extrastriate body area) nodes of the proposed "gastric network" were about 3.3 s. These later regions lie in close proximity to the superior sagittal and transverse sinuses, respectively, vessels at the end of the vascular path through the brain. While Rebollo's analysis could not ascertain directionality – this observation is consistent with a hemodynamic perturbation generated in the stomach which then propagated through the cerebral vasculature, which suggests that gastric signals likely contribute to the "moving signal" category.

This finding is in good agreement with previous work by Yacin et al. (2011) which showed a strong relationship between gastric activity and systemic LFOs in the periphery. Yacin was able to reconstruct the gastric slow wave signal from a fingertip photoplethysmogram, using a deep learning approach. The reconstructed signal correlated with the measured electrogastrogram slow wave with $R >= 0.9$, clearly establishing that the gastric signal contributed a significant portion of the sLFO variance observable in the periphery.

IMPLICATIONS FOR RESTING STATE ANALYSIS

As mentioned previously, BOLD fMRI infers neuronal activation indirectly through neurovascular coupling. As a result, the neuronal activation will appear in the low frequency range (∼0.01–0.15 Hz) of BOLD signal in both resting state and task fMRI studies. This frequency range significantly overlaps with that of sLFO. Therefore, the presence of sLFO in the BOLD signal will confound the results of fMRI analyses, especially in resting state studies, as the neuronal firing is also spontaneous and of unknown timecourse (like sLFO), unlike task activation which can be modeled.

Pure Physiological sLFOs in Resting State Networks

In the following, we describe a previously published study demonstrating the confounding effect of sLFO to the resting state network analysis in both simulation as well as using concurrent fMRI/fNIRS data (Tong et al., 2013). The signals measured by NIRS (concentration changes in oxyhemoglobin and deoxy-hemoglobin: Δ[HbO] and Δ[Hb]) are, like BOLD fMRI signal, blood-related measures. High consistency between these NIRS and fMRI signals has been demonstrated in concurrent studies (Strangman et al., 2002; Sassaroli et al., 2006; Cui et al., 2011). In this particular concurrent study, Δ[HbO] and Δ[Hb] were measured in the periphery (i.e., on finger and toes) using NIRS, instead of the brain. We found that the LFO band component of Δ[HbO] in the periphery was highly correlated with the sLFOs of the BOLD signal in the brain, with a time delay. Most importantly, since the data was recorded in the periphery, the sLFOs measured here represented "pure" physiological

fluctuations that were clearly not contaminated by the neuronal LFO as they would be in the brain.

We used this pure signal to assess the physiological influence of sLFOs on each resting state network. In detail, each subject's connectivity networks were identified from rsfMRI data using ICA (Melodic and FSL), from which, the signature BOLD signals of each network were extracted. To assess the sLFO signal's influence, we correlated each network's signature BOLD signal with the subject's own concurrent peripheral data (i.e., Δ[HbO] of the fingertip). The networks with high correlations are the ones being significantly influenced by the sLFOs. The results showed that in addition to clearly vascular components, such as the superior sagittal sinus, several sensory networks (i.e., visual, auditory, etc.) are strongly affected by the sLFOs (**Figure 2**).

The Dynamic Nature of sLFOs in Resting State Networks

With this in mind, we sought to determine if the dynamic nature of the sLFO signal in BOLD could, on its own, lead to artifactual connectivity in "*Can apparent network patterns be generated by the moving physiological sLFO signal alone?*" (Tong et al., 2015). First, we performed a simple test on simulated data, which consisted of a sinusoidal wave with gradually increased time delay along the traveling direction (**Figure 3a**, the direction of the arrows), representing the traveling sLFO BOLD signal in the brain, additive noise, and a constant offset (see **Figure 3**). We then applied a standard resting state analysis methodology, namely ICA. The result showed that multiple "networks" along the traveling direction were identified, even though the only difference between the time series of these networks is the time delay (see **Figure 3c**). This simulation demonstrated that methods like ICA are prone to being confounded by time delayed versions of identical signals in different voxels.

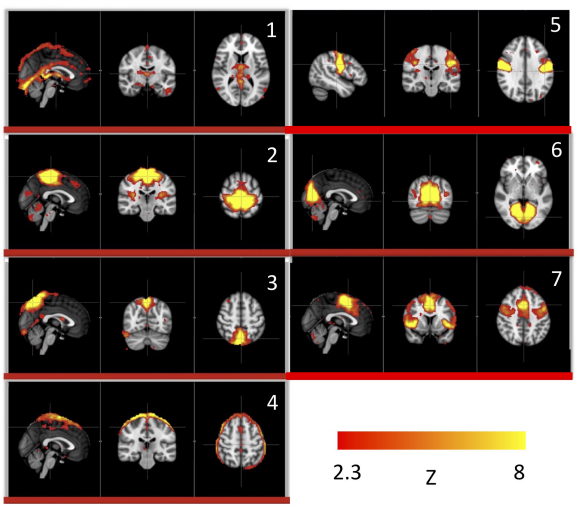

FIGURE 2 | Independent components (1–7) from a group analysis of 10 subjects' resting state data that have high, significant positive correlations with simultaneously recorded peripheral NIRS data (Figure adapted from Tong et al., 2015).

We then performed this test on data much closer to real rsfMRI data. Initially, we calculated the delay between every brain voxel and the peripheral NIRS signal using the subjects' real sLFO BOLD data as described above (Tong et al., 2013). Then, a sinusoidal signal, adjusted with these delays (the real delays of the subjects resting state data) replaced the real BOLD signal at each voxel (i.e., the voxel-specific time delay was decided by the delay value of that voxel). After that, we applied ICA on these simulated fMRI data with identical time series at each voxel differing only by the time delay. As a result, several "resting state networks" (RSNs) were identified (see **Figure 4**), some of which closely matched standard networks described in the literature. Finally, we applied seed analysis on the same simulated data and were able to identify "RSNs" as well (it is known that seed analysis is sensitive to time delays). This study demonstrated that physiological noise signals, depending only on vascular time delays can generate network patterns similar to well-known RSNs through common analytical procedures.

While clearly worrisome, these results should not be interpreted as suggesting that RSNs are nothing but a vascular artifact. There is extensive evidence for the existence of neuronal RSNs, from both animal and human studies, with a range of imaging technologies (Martinez-Montes et al., 2004; Hillman et al., 2007; Brookes et al., 2011; Ma et al., 2016). Moreover, while we have shown that up to 30% of the low frequency gray matter variance (13% of the total variance across *all* frequency bands, Hocke et al., 2016) is due to non-neuronal sLFOs (Frederick et al., 2012a), this means, necessarily, that 70% of the variance *is not* due to sLFOs, and likely represents neuronal signal. However, it is clear that there are both vascular and neuronal "connectivity" networks, with significant spatial overlap.

In order to support the metabolic demands of neurons, vascular networks are formed according to various factors, such as neuron density and metabolic demand. Areas of the brain which routinely coactivate likely develop similar vascular supplies, at similar times. This could lead to overlapping of both networks. It is also possible that, despite being a map of sLFO arrival time, the delay map may nevertheless contain some neuronal information. We hypothesize that elevated neuronal activation within a network will increase the blood flow locally, minimizing the time delays within the network. These subtle differences could be identified by ICA. Nevertheless, we demonstrated that sLFO signals will confound the quantification of some RSNs, in both the spatial and temporal domains, unless some steps are taken to disentangle these signals.

MITIGATION STRATEGIES

As discussed, these widespread, correlated, non-neuronal sLFOs obscure and distort the more localized patterns of neuronal correlations between interacting brain regions, and may even cause apparent connectivity between regions with no neuronal interaction – numerous vascular "networks" are commonly seen in data driven connectivity analyses. Standard mitigation methods such as global signal regression (GSR) have serious drawbacks, and may in fact induce artifactual negative

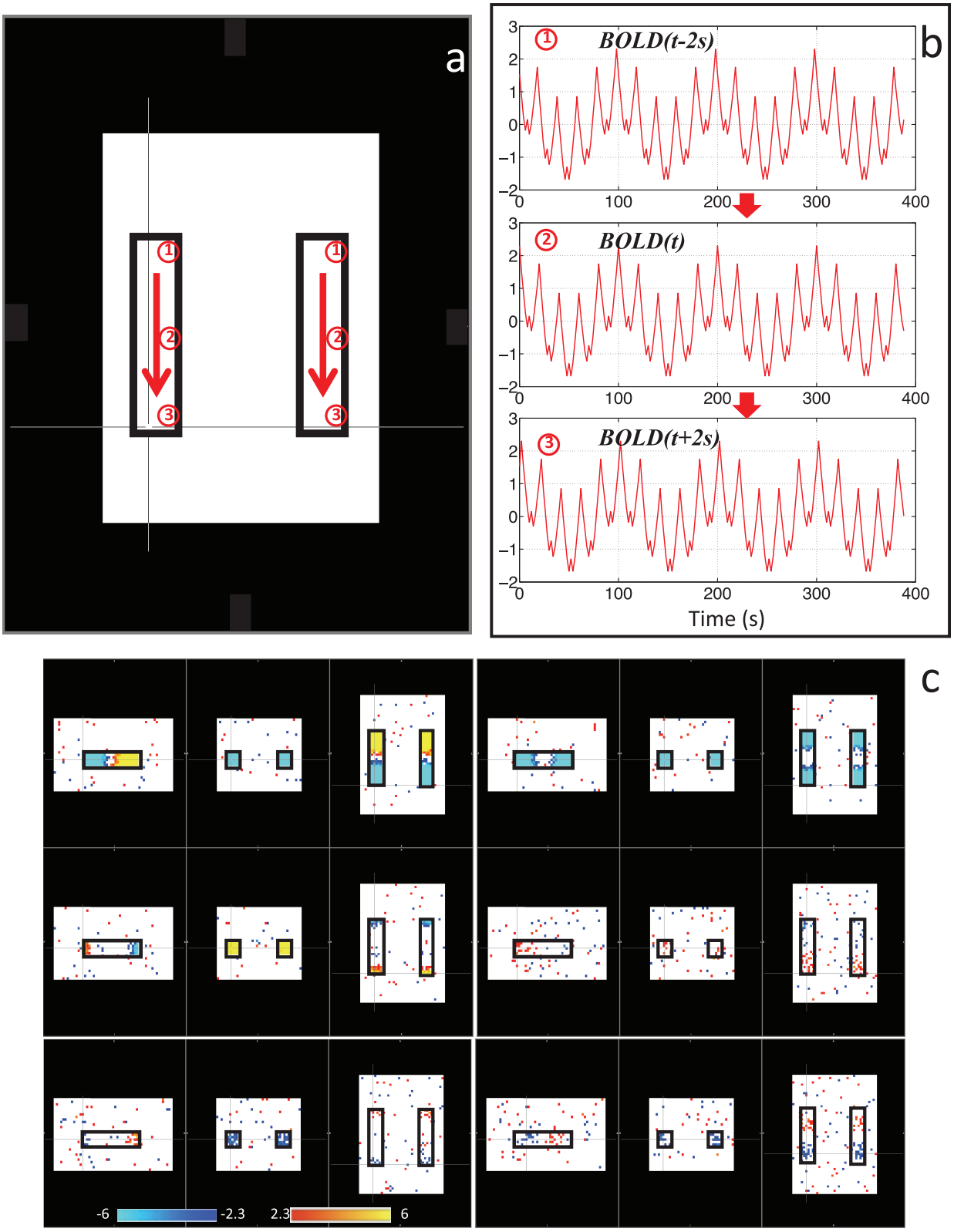

FIGURE 3 | Synthetic data consisting of progressively delayed sum of sinusoids was placed inside two identical blocks **(a)**. The red arrows indicate the direction of the moving wave (increasing time delay). The examples of moving waves at the circles (1–3) are shown in panel **(b)**. Six independent components resulting from ICA are shown in panel **(c)** with the corresponding color bars (Figure adapted from Tong et al., 2015).

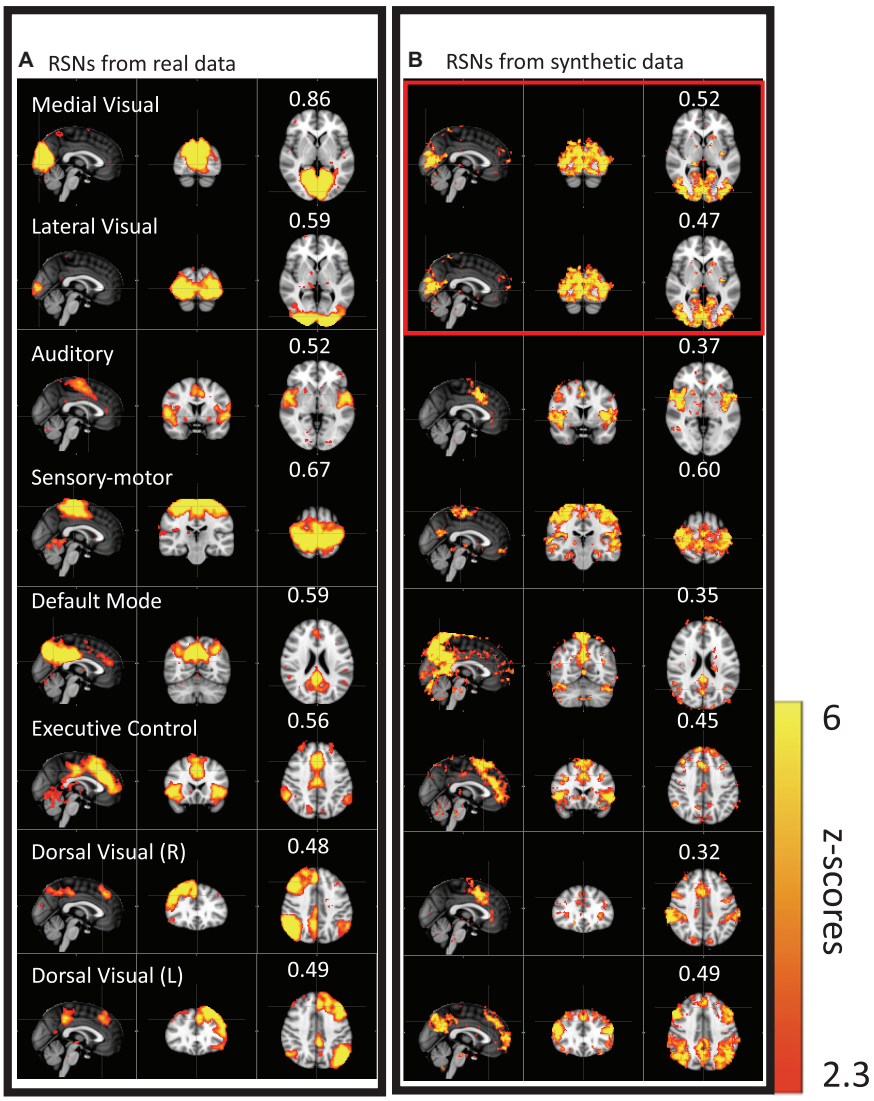

FIGURE 4 | Results from group ICA on 11 subjects' real BOLD data were shown in panel **(A)**. Results from group ICA on 11 subjects' synthetic data were shown in panel **(B)**. The value in each result showed the spatial correlation coefficient calculated between that component and the corresponding RSN from the template (Beckmann et al., 2005). The two components in the red block are the same (Figure adapted from Tong et al., 2015).

correlations between brain regions. Newer methods such as CompCor (Behzadi et al., 2007) avoid some of these problems, but may not fully remove the sLFO signal. By examining the structure of temporal cross-correlations with non-zero time delays throughout the brain (or by making simultaneous, independent measurements in the periphery), it is possible to parse the global, moving, blood-borne signal from the stationary, neuronal connectivity signals. In the following we describe a simple method to remove this signal, leaving the neuronal connectivity intact, while substantially reducing the negative (potentially spurious) correlations that result from global signal regression.

We have conducted continuous research on isolating, characterizing, and separating the neuronal LFO and sLFO in the resting state BOLD fMRI during the past 8 years (Tong and Frederick, 2010, 2012, 2014a,b; Tong et al., 2011a,b,c, 2012, 2013, 2014, 2015, 2016, 2017, 2018; Frederick et al., 2012a; Erdogan et al., 2016; Hocke et al., 2016). The methods developed utilized the key differences between these two oscillations, part of which are discussed in "Characteristics of LFOs": (1) neuronal LFO is regional, while sLFO is global; (2) the neuronal LFO signal does not "propagate" in space, while sLFO does (sLFOs are dynamic), traversing the brain on the time scale of seconds; (3) while neuronal LFO should be found largely in the capillary bed (it is known to biased toward veins), sLFO BOLD is also detected near/in the large blood vessels, especially veins as well as capillaries; (4) neuronal LFO originates in the brain, while sLFO has extracerebral origins and propagates into and through the brain with the blood. These differences do allow us to effectively parse the sLFO and neuronal components of the low

frequency BOLD signal, and examine them separately using a technique we call Regressor Interpolation at Progressive Time Delays (RIPTiDe) which is described in more detail below.

Regressor Interpolation at Progressive Time Delays (RIPTiDe)

The RIPTiDe procedure has been described in detail previously (Frederick et al., 2012a). Initially, we developed a method to determine relative blood arrival times in the voxels of a resting state fMRI (rsfMRI) dataset by using simultaneous NIRS to estimate the non-neuronal, systemic signal. We use a cross-correlation procedure to determine the delay time between this peripheral signal and the timecourse of each voxel in the fMRI dataset. Determination of the precise arrival time of blood-borne signal at every brain voxel also allows correct determination of the fraction of that voxel's signal that is accounted for by the moving blood signal, which depends on the voxel's relative cerebral blood volume (rCBV) and the oxygenation of blood in the voxel (Tong et al., 2018). We have used this NIRS based method to remove non-neuronal signal from BOLD data (Frederick et al., 2012a), as a probe to study physiological signal partitioning in brain (Tong and Frederick, 2012, 2014a; Tong et al., 2012, 2013), and to measure cerebrovascular reserve (Tong et al., 2011a).

Our previous time-delay image analysis work focused closely on two physiological inputs – endogenous hemodynamic fluctuations in normal controls measured directly and concurrently with scanning using NIRS, and exogenous hemodynamic fluctuations (caused by a carbogen gas challenge) extracted *post hoc* from BOLD imaging data collected in symptomatic IC stenosis patients undergoing CVR experiments (Donahue et al., 2016). However, we have determined that in many cases, the signal can be extracted from the fMRI data itself, either from a region rich in venous blood (such as in the superior sagittal sinus) (Tong et al., 2016), or more simply from the global mean average of the data (Erdogan et al., 2016).

Using the global mean data has a number of advantages relative to other methods, the most obvious being that it requires nothing other than the fMRI data itself – no external recordings – and processing is extremely simple, as there is no need to define anatomic regions *a priori*. Moreover, we showed in our recent study (Tong et al., 2018) that the global mean signal is highly correlated with the BOLD signal extracted from the SSS (i.e., maximum cross-correlation values are 0.81 ± 0.1), which indicates that essential components of global mean overlap with those of large veins (with little neuronal contamination). The drawback is that the global mean signal is essentially a temporally "blurred" version of the physiological regressor, because it contains contributions from voxels over a range of delay values. Moreover, each voxel contains fluctuations caused by local neuronal activity (which in this case are considered noise). To overcome these drawbacks, we have developed bootstrap sharpening method to recover the source signal, which is diagrammed in **Figure 5**. We have released an open source software package, "rapidtide"[1], to perform this fitting procedure and isolate and remove the sLFO signal from resting state (or task) fMRI data.

One of the most widespread methods of preprocessing rsfMRI to remove low frequency physiological noise is GSR. In this procedure, the mean signal of all voxels over time is regressed out of all of the BOLD time series prior to resting state analysis. While this does remove a significant amount of physiological signal, it has a serious drawback – the creation of spurious, negative correlations between brain regions (Carbonell et al., 2011). This is an unavoidable consequence of simple regression. The global mean signal is a summation of many copies of the sLFO signal with a range of delays reflecting the blood arrival time throughout the brain. Because the sLFO signal is low frequency (below 0.1–0.15 Hz), when copies of the signal over the range of delays found in the brain are summed, the signal strongly resembles the driving sLFO signal. However, this signal is not properly aligned in time in the vast majority of the voxels of the brain – it is shifted forward or backward relative to each voxels' signal, but the correlation with each voxel is generally high. Regressing out a delayed version of the driving signal at the wrong time delay unavoidably results in a lower amplitude, inverted version of the global signal being added to the voxel at the correct time delay. This will necessarily create artifactual negative correlations in GSR processed data, as shown by Erdogan in both real and simulated data (see **Figure 6**, reproduced from Erdogan et al., 2016). In a detailed comparison of static global signal regresson (sGSR) with the dynamic global signal regression (dGSR) performed by rapidtide, we found that by regressing the sLFO signal out of each voxel at the proper time delays, the efficacy of noise removal was improved. More importantly, we demonstrated that by removing the sLFO dynamically, negative correlations, which were present in the results of sGSR processing, were substantially attenuated (Erdogan et al., 2016). We would argue that many of these negative correlations are potentially spurious, being generated by the removal process itself, but this has yet to be confirmed. Aso et al. (2017) have found that an analogous noise removal procedure yield similar improvements in task based analyses, and also showed significant increases in reproducibility of analyses over time.

We also compared sLFOs derived from peripheral NIRS Δ[HbO] with other LFO models (Hocke et al., 2016), namely the model-based methods for respiration and cardiac listed above in "Potential causes of the low frequency oscillation." With high temporal resolution (TR of 400 ms), we found only small contributions (1–5%) of explained variance by the models considering respiration and cardiac variation. We also found that sLFO explained significantly more variance (up to 16%) when aliased respiration or cardiac signals do not play a critical role when fully sampled and filtered. In addition, sLFO was also substantially different from the variation models with very little temporal and spatial overlap (Hocke et al., 2016), even though NIRS Δ[HbO] is closely related to modulations in CO_2 concentration. This study showed that sLFO is not an artificial signal created by suboptimal acquisition parameters, but a real and pervasive physiological signal accounting for a substantial amount of the variance in the BOLD LFO, and which is not accounted of by previous methods. It should be noted that

[1] https://github.com/bbfrederick/rapidtide

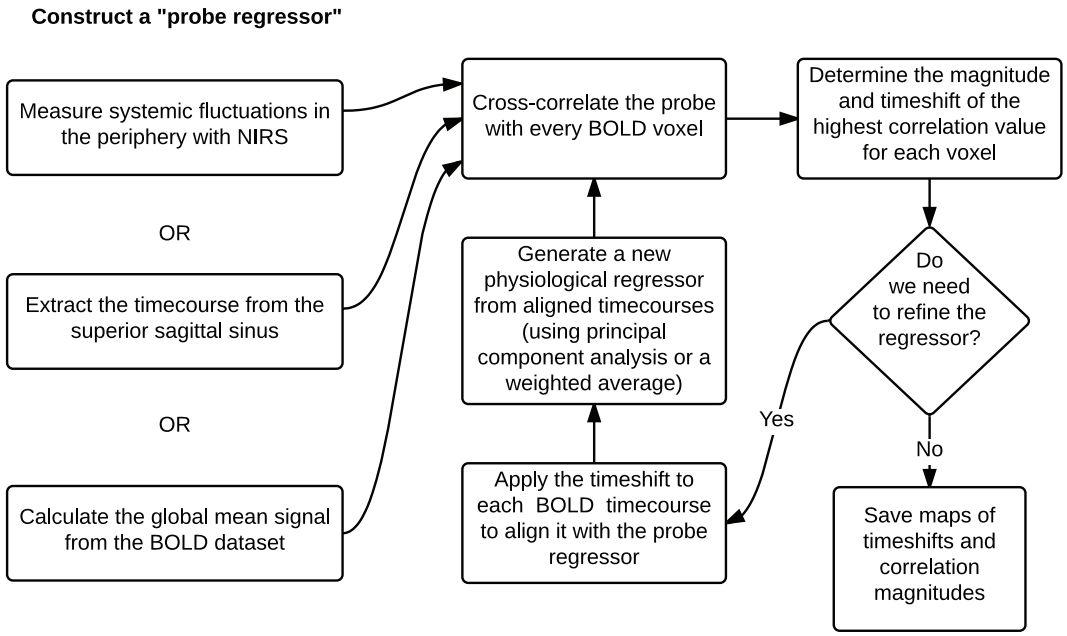

FIGURE 5 | A schematic representation of the RIPTiDe regressor refinement procedure (Figure reproduced from Erdogan et al., 2016).

this procedure cannot remove stationary non-neuronal signal. However, this type of noise, should it exist, could be removed using ICA techniques, which are well suited to detecting (and removing) spatial patterns of synchronized signals.

Significance Determination

Because RIPTiDe analysis relies on the cross-correlation of low pass filtered signals, there is some concern that the correlations derived by the method may be spurious. Until recently, determination of the statistical significance of RIPTiDe metrics has been problematic. As the method is based on the cross-correlation of time series, it is tempting to use standard formulae, which determine significance based on number of degrees of freedom and the correlation coefficient. However, this greatly overestimates the statistical significance of the data obtained through our procedure, for two reasons. The first is that both our test regressor and the fMRI data are bandpass filtered to select the LFO component prior to correlation, which effectively reduces the degrees of freedom in the correlation. One method proposed to correct for this, specifically for the case of fMRI data, is to apply a correction factor to the degrees of freedom based on the portion of the spectrum retained by the filtering procedure (Davey et al., 2013). While this improves the estimation of significance in filtered correlations, to be strictly correct, both the exact transfer function of the filter function and the spectrum of the data being filtered must be known *a priori* and included in the calculation of the correction factor. In practice, the power spectra of fMRI data in general and the systemic low frequency oscillation signal in particular are not white (see section "Limitations" for further discussion on this topic), even over the limited frequency band of the sLFO, and vary in space. This second condition makes this procedure cumbersome.

The second, and more difficult aspect of the analysis to address, is that the peak correlation value within a range is selected to determine the "optimal" time lag, which necessarily serves to inflate the correlation value, and bias it toward more positive values. Proper application of correction for multiple comparisons requires accounting for the smoothness of the correlation function, which in turn is determined by the factors listed above. There are analytical methods for doing this (Olden and Neff, 2001), however they too are somewhat intractable for fMRI data.

While analytical calculation of the significance is difficult, there are two straightforward numerical methods to achieve this goal. The first, and simplest, method is to perform mismatched correlations. In this case the voxel timecourses are correlated with an sLFO signal from a different subject (or from the same subject at an extremely large time delay of several minutes). In this case any correlations between the timecourses are known to be spurious; a distribution of spurious correlations can be calculated to find various significance thresholds. We have employed this method in many of our analyses where the data permits (most recently here, Yao et al., 2019).

However, in cases where datasets are small, or time delayed sLFO signals are not available, there is a more general method which is also quite straightforward – we can estimate the distribution of null correlations using a Monte Carlo approach (Hocke et al., 2016). The probe regressor is permuted by randomizing the time indices, preserving the distribution of intensity values but destroying any temporal correlations, and the RIPTiDe procedure (filtering, cross-correlation, and peak finding) is performed on this timecourse with the unpermuted regressor. The procedure is repeated a sufficient number of times that the null distribution of correlation coefficients can be

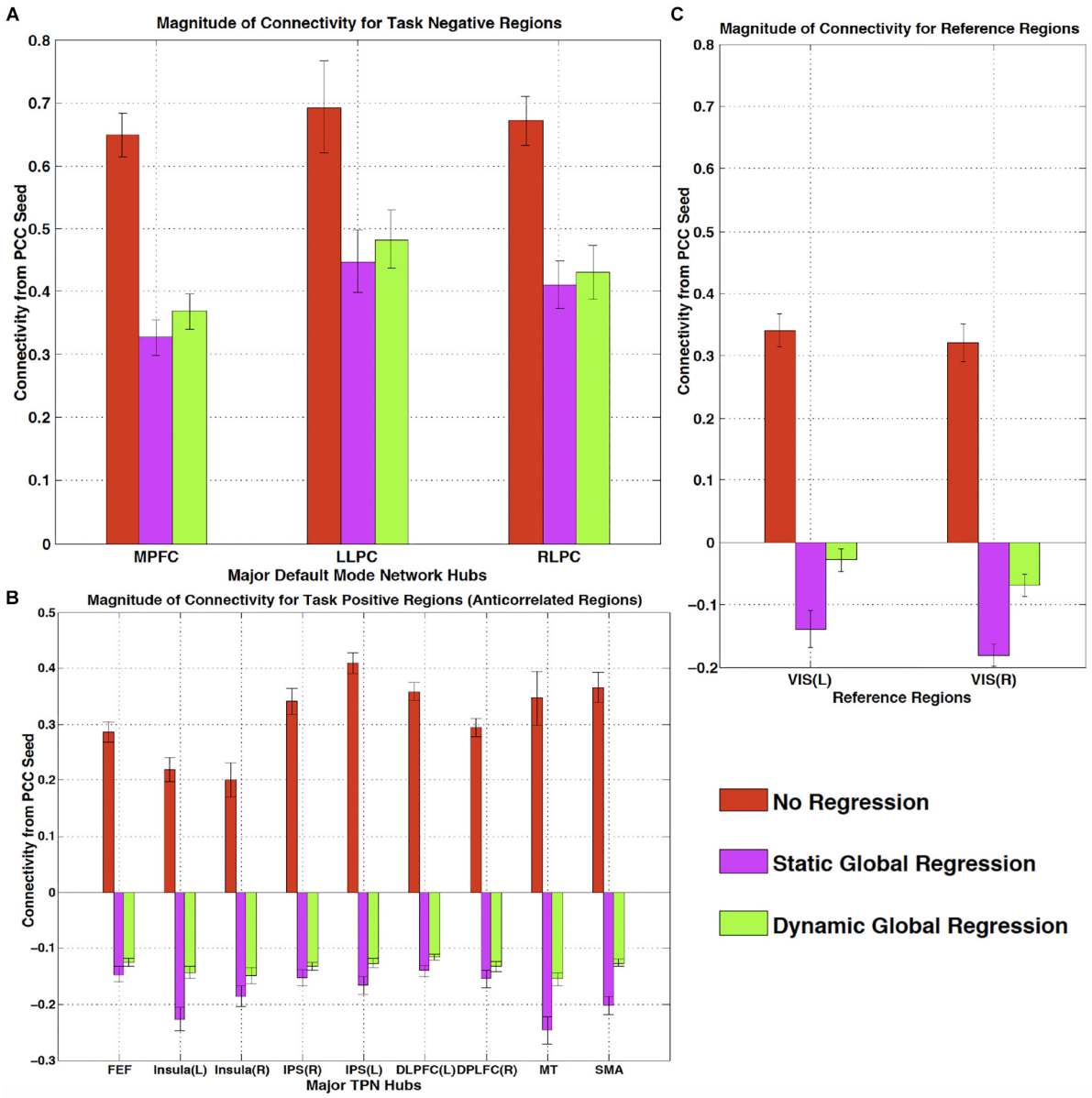

FIGURE 6 | The effect of static and dynamic global signal regression on group level connectivity strengths from a posterior cingulate cortex (PCC) seed to ROIs in panel **(A)** major default mode network (DMN) ROIs (task negative regions), **(B)** Task positive network (TPN) ROIs, **(C)** and reference regions thought not to be involved in either network. L, left hemisphere; R, right hemisphere; VIS, visual cortex ROI. Both static and dynamic global signal regression remove spurious connectivity within the DMN (panel **A**), while preserving the expected anticorrelations with regions of the task positive network (panel **B**). Spurious positive correlations with unrelated reference regions were eliminated with both types of regression; however this came at the cost of large, significant spurious anticorrelations using static GSR, but not with dGSR (panel **C**) (Figure reproduced from Erdogan et al., 2016).

estimated, so the *p*-Values of different correlation coefficients can be directly determined. This procedure is rapid – our analysis software estimates this distribution from 10000 iterations at the beginning of each refinement cycle for each subject's data in under 25 s. By default, the results presented by rapidtide are thresholded to the $p < 0.05\%$ level. This is probably too stringent in general, as there will be many voxels with true, lower correlation due to low rCBV. In practice for high quality data though, this is not too much of a problem.

It is important to note that for autocorrelated data, such as fMRI, one should only permute samples within exchangeability blocks to maintain the autocorrelation – time index shuffling is not generally correct. A better (but significantly slower) procedure is to randomize the phase of the Fourier transform of the data, which preserves the autocorrelation structure (Handwerker et al., 2012). However, in the case of RIPTiDe processing, both the regressor and shuffled data are filtered to the LFO band *after* shuffling, and the effect of this filter dominates

the autocorrelation properties of the inputs to the correlation, so time shuffling performs well. This was verified in the HCP data, where we estimated the $p < 0.05$ correlation level both by the shuffling procedure described, and with the mismatched correlation method. The results were in close agreement, with an average spurious correlation threshold of 0.2.

APPLICATIONS OF THE sLFO SIGNAL

Up to now we have discussed the moving sLFO as a noise signal contaminating rsfMRI. But whether the moving signal is noise or signal is simply a matter of perspective. If we reframe the moving, blood-borne variance as a "signal" carrying information, rather than simply a nuisance complicating the interpretation of resting state connectivity, we can use it as a sensitive measure of hemodynamic function. The relative arrival time and strength of this signal as it propagates through the cerebral vasculature carries information regarding the distribution and timing of blood flow in the brain. We propose that the moving hemodynamic signal is a unique contrast mechanism in its own right, which provides information not currently available to other techniques. It may offer insights into subtle hemodynamic alterations that can be used as early indicators of circulatory dysfunction in a number of neuropsychiatric conditions, such as prodromal stroke, moyamoya, and Alzheimer's disease. Characterization of the sLFO signal throughout the brain allows for continuous monitoring of blood arrival time delay without a dedicated acquisition, with high sensitivity, and over a wide range of delay times, without any externally administered contrast.

Cerebrovascular Reactivity (CVR) Mapping

The moving sLFO signal can be used to determine cerebrovascular reactivity (CVR) to CO_2 changes both for clinical evaluation and to calibrate the BOLD response. CVR is typically measured using a hypercapnic challenge (either exogenously applied gas or breathhold) (Heyn et al., 2010; Bright and Murphy, 2013; Hare et al., 2013; Donahue et al., 2014). Accounting for the particular dynamics of the sLFO signal can give more accurate estimates of the regional response (Tong et al., 2011a). Golestani et al. (2016a,b) fully exploited the effect of the moving $paCO_2$ sLFO waveform on voxel wise BOLD to perform quantitative CVR mapping throughout the brain using only resting state data. By correcting for time delay and correlating the end-tidal CO_2 (a proxy for $paCO_2$) with the BOLD signal (with additional noise removal and modeling), they were able to determine the local BOLD response per percent change in $paCO_2$ simply from the resting state signal fluctuations.

Quantitative Blood Flow Imaging

In addition to assessing CVR, sLFO signals can be used to track blood throughout the brain to reveal both normal circulation patterns, and circulatory alterations in response to tasks, pharmacological challenges, or pathology. The temporal resolution of delay measured using cross-correlation depends on the length of the input signals, rather than the signal repetition time, so very fine delay distinctions are possible with normal fMRI data. Furthermore, because the delay measurement relies on a pattern of pseudorandom signal fluctuations over the entire timecourse, rather than a single tag, such as that used in arterial spin labeling (ASL), extremely long delay times can be measured. Newer ASL techniques, such as multidelay ASL offer some information on arrival time, but are still limited by the short lifetime of the ASL tag (under 3 s). Velocity-selective ASL does remove the restrictions on tag lifetime, and has been used for delays over 6 s (Qiu et al., 2012), however, the ability to quantify delay over a range of 10 to 100 s of seconds has not been demonstrated, and this does require another scan in addition to the resting state.

Healthy Circulation

We have used RIPTiDe analysis extensively in healthy subjects to quantify typical blood flow patterns, have validated these measurements against gold standard dynamic susceptibility contrast (DSC) imaging data (see **Figure 7**) collected in the same session (Tong et al., 2017), as shown in **Figure 7**, and have followed signal through the head from the inflowing carotid arteries to the exiting jugular veins (Tong et al., 2018) to establish that the sLFO signal does indeed move with the blood.

Because the bootstrap RIPTiDe analysis requires only fMRI data to assess hemodynamic parameters, it can be applied retrospectively to existing data [as in the myconnectome analysis described above (Tong et al., 2017), and a wider analysis of myconnectome, ABCD, and HCP data (Yao et al., 2019)]. We have also applied this technique to the resting state data from the Human Connectome Project (Frederick et al., 2017), and were able to produce very detailed maps of average time delay and correlation strength throughout the brain (shown in **Figure 8**). This can provide a standard comparison dataset for young healthy controls.

It is important to note that the time delay measurement is always relative. Our standard is to set "zero time" at the peak of the histogram of delay values. As a result, there are necessarily always positive and negative delay times – positive delays tend to be in the later parts of the vascular tree – large draining veins, etc., while negative delays correspond to parts of the brain close to the source arteries (so they get blood before most other regions). This is a somewhat arbitrary choice – we could (and have) used an anatomical reference region such as the cerebellum as the delay time origin (Donahue et al., 2016) depending on the application.

We note that we consistently observe higher positive delay values in white matter (by a few seconds) than in the cortex; presumably this is because gray matter circulation is prioritized. This observation has been confirmed with DSC imaging, the gold standard MR technique for perfusion measurement.

Circulatory Pathology

This technique is not limited to studying healthy circulation, however. Compromised circulation due to arterial occlusion from to atherosclerosis, moyamoya disease, or stroke, can lead to extremely long delay times (up to 10 s of seconds) which are not quantifiable using conventional methods such as ASL or CT angiography. We demonstrated that time delay

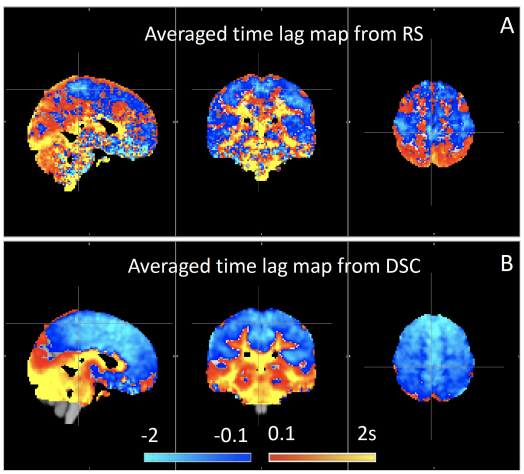

FIGURE 7 | Blood arrival time delay values (in seconds) obtained from rapidtide analysis of **(A)** resting state fMRI data and from **(B)** dynamic susceptibility contrast imaging during the same imaging session in healthy controls ($N = 8$) (Figure adapted from Tong et al., 2017).

imaging with exogenous CO_2 manipulation can reveal and accurately quantitate extremely long delays *in vivo* (Frederick et al., 2013; Donahue et al., 2016). However, the exogenous CO_2 manipulation is not necessary – the hemodynamic delays arising from moyamoya disease can also be quantified using the endogenous sLFO signal from rsfMRI alone as a probe (Christen et al., 2014). Others have used the endogenous sLFO in a number of clinical applications.

Stroke

There have been several studies using global signal correlation delays to investigate hypoperfusion acutely and longterm after strokes. Lv et al. (2013) showed that "significant delay in BOLD signal corresponded to areas of hypoperfusion identified by contrast-based perfusion MRI" in 11 subjects acutely after ischemic stroke. Amemiya et al. (2014) found similar agreement in the results of BOLD delay and contrast perfusion measurements in five patients with chronic hypoperfusion and six with acute stroke. In 2016, Siegel assessed 130 subjects 2 weeks, and 3 and 12 months post-stroke onset (and 30 controls), and showed that increased BOLD lag delay was strongly correlated with decreased blood flow assessed with ASL. Furthermore, they found that removing the delayed hemodynamic signal somewhat normalized functional connectivity measurements (which were distorted by delayed hemodynamics) (Siegel et al., 2016). Khalil et al. (2017) assessed delay changes of sLFO BOLD signals among acute stroke patients in two separate studies. In one study, they found the delay maps were highly correlated with the time-to-peak maps derived from DSC-MRI in ischemic stroke. In another longitudinal study, they found the sizes of the extended-delay regions and the corresponding delay values changed according to the vessel conditions (Khalil et al., 2018). Recently, Nishida et al. (2018) has found the delay maps from patients with the arterial occlusive disease were correlated with the CVR maps from SPECT. These multimodal studies validated the method of BOLD delay and showed its great potential in perfusion assessment of cerebrovascular disease.

Other Conditions

Christen et al. (2014) were able to quantify delayed blood flow in moyamoya disease using a cross-correlation technique. In addition, Yan et al. (2018) have successfully detected perfusion deficits (from BOLD delay) in patients with Alzheimer's disease and mild cognitive impairment.

LIMITATIONS

There are two rather significant factors that can complicate the crosscorrelation method for tracking sLFO's – unfortunate

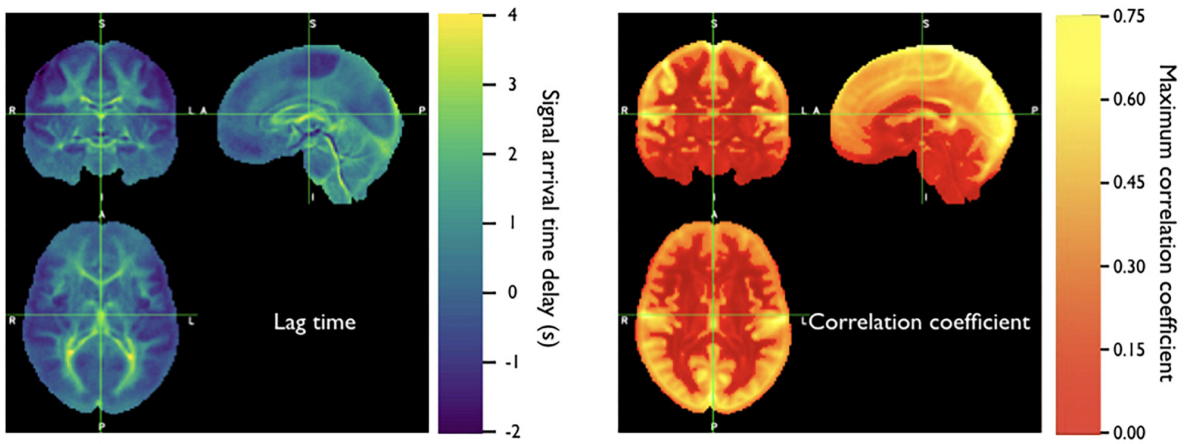

FIGURE 8 | Averaged correlation parameters (lag time of maximum correlation and maximum correlation value) for 487 subjects from the 500 subjects release of the Human Connectome Project data. Each subject had four scans (LR and RL phase encode in two sessions, REST1 and REST2) (Figure adapted from Frederick et al., 2017).

spectral characteristics of the sLFO signal, and initializing the proper regressor to perform the calculation. These factors are discussed below.

Spectral Characteristics

The first problem is the random nature of the sLFO signal itself. Usually this benefits us in that it allows us to find the signal throughout the brain despite whatever local signal variations are present, and to determine its time delay – the cross-correlation of the sLFO with any other random variation (such as neuronal signals) is, in general, low, and the correlation with delayed copies of itself is high and strongly peaked at the appropriate time delay. The spurious correlation threshold can be determined through permutation or comparison of correlations between subjects, as discussed above, so we can decide when correlation is "real."

However, all of this rests on the assumption that that sLFO signal is (1) truly random, or at least not determined by factors that will influence other noise signals found in the brain, and that (2) the signal is sufficiently "white" within the band of interest. While the first condition seems to be satisfied in general, the second frequently is not. The random nature of the signal means that by chance it sometimes has undesirable spectral properties which make it less suitable for our purposes. This leads to two problems – pseudoperiodicity and non-uniform spectra. The first is a special case of the second, but is common enough to be discussed on its own.

Pseudoperiodicity

The first uncontrolled quantity is pseudoperiodicity. From time to time, signal energy in the 0.09–0.15 Hz band will be strongly concentrated in one or more spectral peaks. Whether this is completely random, or due to some pathological or congenital condition that affects circulation is not known – it seems for the most part to be purely by chance, as it is occasionally seen when looking at multiple runs in the same subject, where one run is pseudoperiodic while the rest are not.

The effect of this is to cause the crosscorrelation between the probe signal and voxel timecourses to have more than one strong correlation peak. This means that in the presence of noise, or extreme spectral concentration of the sLFO, the wrong crosscorrelation peak can appear larger, leading to an incorrect delay estimation. This is particularly problematic if the pseudoperiod is shorter than the reciprocal of the search window (for example, if the search window for correlation peaks is between −5 and +5 s, and the sLFO has a strong spectral component at 0.1 Hz or higher, more than one correlation peak will occur within the search window). As the width of the search range increases, the spectral range of potentially confounding spectral peaks covers more of the sLFO frequency band.

Implications of pseudoperiodicity

The extent to which pseudoperiodicity is a problem depends on the application. In the case of noise removal, where the goal is to remove the global sLFO signal, and leave the local or networked neuronal signal variance, it turns out not to be much of a problem at all. If the sLFO signal in given voxel is sufficiently periodic that that the correctly delayed signal is indistinguishable from the signal one or more periods away, then it doesn't matter which signal is removed – the resulting denoised signal is the same.

Mitigation of pseudoperiodicity

While we continue to work on fully resolving this issue, we have a number of ways of dealing with this. First of all, spectral analysis of the sLFO signal allows us to determine if the signal may be problematic. Rapidtide checks the autocorrelation function of the sLFO signal for large sidelobes with periods within the delay search window and issues a warning when these signals are present. Then after delay maps are calculated, they are processed with an iterative despeckling process analogous to phase unwrapping. The delay of each voxel is compared to the median delay of its neighbors. If the voxel delay differs by the period of an identified problematic sidelobe, the delay is constrained to "correct" value and refit. This procedure greatly attenuates, but does not completely solve, the problem of bad sidelobes. A more general solution to the problem of non-uniform spectra will likely improve the correction.

Non-uniform Spectra

As noted before, the pseudoperiodicity is a special case of non-uniformity within the sLFO spectral region. In addition to peaks in the power spectrum, there can be gaps, which are also problematic.

Implications of non-uniform spectra due to spectral gaps

Non-uniform spectra will tend to distort the crosscorrelation between the sLFO and any given voxel signal. In addition to sidelobes which lead to the periodic correlation functions discussed above, gaps in the spectrum, especially in the higher frequency regions, can lead to blurry correlation functions. Our method relies on identifying peaks in the crosscorrelation waveform – the sharpness of these peaks depends on the higher frequency portion of the sLFO power spectrum. If the energy of the sLFO is concentrated in the lower frequency portion of the LFO band, the crosscorrelation peaks become broad, which makes the estimation of the peak location less accurate in the presence of noise. This makes delay maps less accurate, and will tend to lower the correlation values closer to the spurious correlation threshold.

Mitigation of non-uniform spectra

The most straightforward solution to non-uniform spectra is to prewhiten the sLFO and voxel signals (effectively flattening the peaks and troughs of the magnitude spectrum, while preserving phase) prior to performing the correlation; there are numerous variants of this procedure, known as generalized crosscorrelation (Knapp and Carter, 1976; Liang et al., 2015). The methods require some tuning to determine thresholds for magnitude recovery to avoid inflating noise, but are included as options in rapidtide. However, when using the generalize crosscorrelation, the resulting maximum correlation magnitudes are difficult to interpret, as they no longer directly represent the amount of variance explained by the sLFO regressor.

Inhomogeneous Time Delays

Finally, there is the problem of obtaining the sLFO regressor to begin with. In subjects with healthy circulation, the majority of the brain has delays which are relatively tightly clustered over a range of a few seconds; in this case the global mean is a good starting regressor. After multiple refinement passes, the regressor will converge on a stable candidate sLFO signal. However, pathology can lead to significant volumes of brain tissue with a large delay relative to the rest of the brain, but with a small spread of values around that delay. This can result in a global mean regressor which includes one or more "echoes" – strong, delayed copies of the true driving regressor.

Implications of Inhomogenous Delays and Mitigation

Having a regressor with multiple delayed copies of the driving sLFO signal will lead to ambiguous delay values, and will keep the refinement process from converging. While it may be possible to clean the signal using a technique analogous to echo cancelation, it is generally easier to avoid the situation to begin with by starting from a region of homogenous delay values. A number of the cited studies in pathology have used regressors derived from the superior sagittal sinus, which is easy to locate and clearly homogenous. However, its location at the end of the vascular tree means that blood in that region may have traversed multiple distinct paths to get there, which could result in multiple delay components. Our current thinking is to use a cerebellar ROI to derive the starting sLFO regressor, as circulation in that region is undisturbed in a wide range of pathologies (Donahue et al., 2016).

Stationarity

One assumption that has been made throughout these discussions is that the time delay in a region is constant over time, or "stationary." While convenient, this is clearly a simplification. We know that these delays are not, in fact, completely constant over time. There are slight variations in delay time within HCP subjects between runs on the same day, and larger variations between days. There is no reason to suspect that there are not variations within runs as well – the correlation delays presented are averaged over the entire run. Moreover, when we calculate the delay maps from the HCP motor task data, we consistently see a regional, average 0.5 s decrease in the blood arrival time in the motor cortex relative to the values from the resting state scans, consistent with increased blood flow due to neuronal load – this is presumably an average change between the active and non-active periods leading to a shorter average delay time. This is a potential interesting area of research that as of yet, does not seem to have been explored. We have experimented some with a windowed version of RIPITiDe analysis analogous to dynamic connectivity studies, but have not worked out whether there is sufficient SNR to do this routinely.

CONCLUSION

Low frequency oscillations contribute significantly to the rsfMRI signal. The signal is defined by its characteristics rather than by its origins – in specific, a low frequency range of ∼0.01–0.15 Hz. In fact, there are likely many sources of signals in this spectral region. We have discussed a number of theories for the origin of LFOs; it is important to note that these theories do not conflict – power in this frequency band is likely due to some combination of the sources we describe. Because of this, it is more useful to talk about how the low frequency contamination in the fMRI signal behaves, and what can be done about and with it.

Unlike other physiological signals, such as respiration and cardiac contamination, LFOs cannot be separated from neuronal signals through spectral filtering – they must be modeled. We have observed that up to 30% of the low frequency signal power in the gray matter moves through the vasculature, and is carried with the blood into and through the brain. This portion of the signal is therefore amenable to detection, quantitation, and removal using cross-correlation techniques, which perform well at the task of noise removal, without introducing the significant artifacts seen with other methods, such as global signal regression.

Finally, we and others have demonstrated that this moving signal can be used as a probe to quantitate cerebral hemodynamic parameters, over a wide range of conditions, without the use of contrast or specialized imaging techniques, making this an ideal method for inferring hemodynamic information both in new studies and in retrospective analysis of existing datasets. Half of these studies have been in the last 2 years, demonstrating the increasing interest in the broad clinical application of the method. As large-scale public databases such as the Human Connectome Project and the UK Biobank become available, we expect the use of these techniques to continue to expand into new research areas.

AUTHOR CONTRIBUTIONS

All authors listed have made a substantial, direct and intellectual contribution to the work, and approved it for publication.

FUNDING

This research was supported by the National Institute of Neurological Disorders and Stroke, grant R01NS097512, and NIDA, Grant K25 DA031769.

REFERENCES

Aalkjær, C., Boedtkjer, D., and Matchkov, V. (2011). Vasomotion – what is currently thought? *Acta Physiol.* 202, 253–269. doi: 10.1111/j.1748-1716.2011.02320.x

Amemiya, S., Kunimatsu, A., Saito, N., and Ohtomo, K. (2014). Cerebral hemodynamic impairment: assessment with resting-state functional MR imaging. *Radiology* 270, 548–555. doi: 10.1148/radiol.13130982

Aso, T., Jiang, G., Urayama, S. I., and Fukuyama, H. (2017). A Resilient, non-neuronal source of the spatiotemporal lag structure detected by BOLD signal-based blood flow tracking. *Front. Neurosci.* 11:256. doi: 10.3389/fnins.2017.00256

Beckmann, C. F., Deluca, M., Devlin, J. T., and Smith, S. M. (2005). Investigations into resting-state connectivity using independent component analysis. *Philos. Trans. R. Soc. Lond. B Biol. Sci.* 360, 1001–1013. doi: 10.1098/rstb.2005.1634

Behzadi, Y., Restom, K., Liau, J., and Liu, T. T. (2007). A component based noise correction method (CompCor) for BOLD and perfusion based fMRI. *Neuroimage* 37, 90–101. doi: 10.1016/j.neuroimage.2007.04.042

Birn, R. M., Diamond, J. B., Smith, M. A., and Bandettini, P. A. (2006). Separating respiratory-variation-related fluctuations from neuronal-activity-related fluctuations in fMRI. *Neuroimage* 31, 1536–1548. doi: 10.1016/j.neuroimage.2006.02.048

Birn, R. M., Smith, M. A., Jones, T. B., and Bandettini, P. A. (2008). The respiration response function: the temporal dynamics of fMRI signal fluctuations related to changes in respiration. *Neuroimage* 40, 644–654. doi: 10.1016/j.neuroimage.2007.11.059

Biswal, B., Yetkin, F. Z., Haughton, V. M., and Hyde, J. S. (1995). Functional connectivity in the motor cortex of resting human brain using echo-planar MRI. *Magn. Reson. Med.* 34, 537–541. doi: 10.1002/mrm.1910340409

Bright, M. G., and Murphy, K. (2013). Reliable quantification of BOLD fMRI cerebrovascular reactivity despite poor breath-hold performance. *Neuroimage* 83, 559–568. doi: 10.1016/j.neuroimage.2013.07.007

Brookes, M. J., Woolrich, M., Luckhoo, H., Price, D., Hale, J. R., Stephenson, M. C., et al. (2011). Investigating the electrophysiological basis of resting state networks using magnetoencephalography. *Proc. Natl. Acad. Sci. U.S.A.* 108, 16783–16788. doi: 10.1073/pnas.1112685108

Buxton, R. B., Wong, E. C., and Frank, L. R. (1998). Dynamics of blood flow and oxygenation changes during brain activation: the balloon model. *Magn. Reson. Med.* 39, 855–864. doi: 10.1002/mrm.1910390602

Carbonell, F., Bellec, P., and Shmuel, A. (2011). Global and system-specific resting-state fMRI fluctuations are uncorrelated: principal component analysis reveals anti-correlated networks. *Brain Connect.* 1, 496–510. doi: 10.1089/brain.2011.0065

Chang, C., Cunningham, J. P., and Glover, G. H. (2009). Influence of heart rate on the BOLD signal: the cardiac response function. *Neuroimage* 44, 857–869. doi: 10.1016/j.neuroimage.2008.09.029

Chang, C., Metzger, C. D., Glover, G. H., Duyn, J. H., Hans-Jochen, H., and Walter, M. (2013). Association between heart rate variability and fluctuations in resting-state functional connectivity. *Neuroimage* 68, 93–104. doi: 10.1016/j.neuroimage.2012.11.038

Christen, T., Jahanian, H., Ni, W. W., Qiu, D., Moseley, M. E., and Zaharchuk, G. (2014). Noncontrast mapping of arterial delay and functional connectivity using resting-state functional MRI: a study in Moyamoya patients. *J. Magn. Reson. Imaging* 41, 424–430. doi: 10.1002/jmri.24558

Crandell, D., Moinuddin, M., Fields, M., Friedman, B., and Robertson, J. (1973). Cerebral transit time of 99mtechnetium sodium pertechnetate before and after cerebral arteriography. *J. Neurosurg.* 38, 545–547. doi: 10.3171/jns.1973.38.5.0545

Cui, X., Bray, S., Bryant, D. M., Glover, G. H., and Reiss, A. L. (2011). A quantitative comparison of NIRS and fMRI across multiple cognitive tasks. *Neuroimage* 54, 2808–2821. doi: 10.1016/j.neuroimage.2010.10.069

Davey, C. E., Grayden, D. B., Egan, G. F., and Johnston, L. A. (2013). Filtering induces correlation in fMRI resting state data. *NeuroImage* 64, 728–740. doi: 10.1016/j.neuroimage.2012.08.022

Donahue, M. J., Dethrage, L. M., Faraco, C. C., Jordan, L. C., Clemmons, P., Singer, R., et al. (2014). Routine clinical evaluation of cerebrovascular reserve capacity using carbogen in patients with intracranial stenosis. *Stroke* 45, 2335–2341. doi: 10.1161/STROKEAHA.114.005975

Donahue, M. J., Strother, M. K., Lindsey, K. P., Hocke, L. M., Tong, Y., and Frederick, B. D. (2016). Time delay processing of hypercapnic fMRI allows quantitative parameterization of cerebrovascular reactivity and blood flow delays. *J. Cereb. Blood Flow Metab.* 36, 1767–1779. doi: 10.1177/0271678x15608643

Erdogan, S. B., Tong, Y., Hocke, L. M., Lindsey, K. P., and de, B. F. B. (2016). Correcting for blood arrival time in global mean regression enhances functional connectivity analysis of resting state fMRI-BOLD signals. *Front. Hum. Neurosci.* 10:311. doi: 10.3389/fnhum.2016.00311

Fox, P., and Raichle, M. (1986). Focal physiological uncoupling of cerebral blood flow and oxidative metabolism during somatosensory stimulation in human subjects. *Proc. Natl. Acad. Sci. U.S.A.* 83, 1140–1144. doi: 10.1073/pnas.83.4.1140

Frederick, B., Lindsey, K., Erdogan, S., Hocke, L., and Tong, Y. (2017). "Mapping hemodynamic delay times from Human Connectome Project Resting State Data," in *Prceedings of the 23rd Annual Meeting of the Organization for Human Brain Mapping*, Vancouver, BC.

Frederick, B., Nickerson, L. D., and Tong, Y. (2012a). Physiological denoising of BOLD fMRI data using regressor interpolation at progressive time delays (RIPTiDe) processing of concurrent fMRI and near-infrared spectroscopy (NIRS). *Neuroimage* 60, 1913–1923. doi: 10.1016/j.neuroimage.2012.01.140

Frederick, B., Nickerson, L., and Tong, Y. (2012b). "Retrospective identification of global hemodynamic fluctuations from resting state fMRI," in *Proceedings of the 3rd Biennial Resting State Brain Connectivity Conference*, Magdeburg.

Frederick, B., and Tong, Y. (2010). "Physiological noise reduction in BOLD data using simultaneously acquired NIRS data," in *Proceedings of the 16th Annual Meeting of the Organization for Human Brain Mapping*, Barcelona. doi: 10.1016/j.neuroimage.2012.01.140

Frederick, B., Tong, Y., Strother, M., Nickerson, L., Lindsey, K., and Donahue, M. (2013). "Derivation of Flow Information from a Hypocarbia Challenge Study Using Time Delay Correlation Processing," in *Proceedings of the 21st annual meeting of the International Society for Magnetic Resonance In Medicine*, Salt Lake City, UT.

Glover, G. H., Li, T. Q., and Ress, D. (2000). Image-based method for retrospective correction of physiological motion effects in fMRI: RETROICOR. *Magn. Reson. Med.* 44, 162–167. doi: 10.1002/1522-2594(200007)44:1<162::aid-mrm23>3.3.co;2-5

Golestani, A. M., Kwinta, J. B., Strother, S. C., Khatamian, Y. B., and Chen, J. J. (2016a). The association between cerebrovascular reactivity and resting-state fMRI functional connectivity in healthy adults: the influence of basal carbon dioxide. *Neuroimage* 132, 301–313. doi: 10.1016/j.neuroimage.2016.02.051

Golestani, A. M., Wei, L. L., and Chen, J. J. (2016b). Quantitative mapping of cerebrovascular reactivity using resting-state BOLD fMRI: validation in healthy adults. *Neuroimage* 138, 147–163. doi: 10.1016/j.neuroimage.2016.05.025

Handwerker, D. A., Roopchansingh, V., Gonzalez-Castillo, J., and Bandettini, P. A. (2012). Periodic changes in fMRI connectivity. *Neuroimage* 63, 1712–1719. doi: 10.1016/j.neuroimage.2012.06.078

Hare, H. V., Germuska, M., Kelly, M. E., and Bulte, D. P. (2013). Comparison of CO2 in air versus carbogen for the measurement of cerebrovascular reactivity with magnetic resonance imaging. *J. Cereb. Blood Flow Metab.* 33, 1799–1805. doi: 10.1038/jcbfm.2013.131

Heyn, C., Poublanc, J., Crawley, A., Mandell, D., Han, J. S., Tymianski, M., et al. (2010). Quantification of cerebrovascular reactivity by blood oxygen level-dependent MR imaging and correlation with conventional angiography in patients with Moyamoya disease. *Am. J. Neuroradiol.* 31, 862–867. doi: 10.3174/ajnr.A1922

Hillman, E. M. C., Devor, A., Bouchard, M. B., Dunn, A. K., Krauss, G. W., Skoch, J., et al. (2007). Depth-resolved optical imaging and microscopy of vascular compartment dynamics during somatosensory stimulation. *Neuroimage* 35, 89–104. doi: 10.1016/j.neuroimage.2006.11.032

Hocke, L. M., Tong, Y., Lindsey, K. P., and de, B. F. B. (2016). Comparison of peripheral near-infrared spectroscopy low-frequency oscillations to other denoising methods in resting state functional MRI with ultrahigh temporal resolution. *Magn. Reson. Med.* 76, 1697–1707. doi: 10.1002/mrm.26038

Hundley, W. G., Renaldo, G. J., Levasseur, J. E., and Kontos, H. A. (1988). Vasomotion in cerebral microcirculation of awake rabbits. *Am. J. Physiol.* 254(1 Pt 2), H67–H71.

Jann, K., Hauf, M., Kellner Weldon, F., El Koussy, M., Kiefer, C., Federspiel, A., et al. (2016). Implication of cerebral circulation time in intracranial stenosis measured by digital subtraction angiography on cerebral blood flow estimation measured by arterial spin labeling. *Diagn. Interv. Radiol.* 22, 481–488. doi: 10.5152/dir.2016.15204

Josephs, O., and Henson, R. N. A. (1999). Event-related functional magnetic resonance imaging: modelling, inference and optimization. *Philos. Trans. R. Soc. London Ser. B Biol. Sci.* 354, 1215–1228. doi: 10.1098/rstb.1999.0475

Julien, C. (2006). The enigma of Mayer waves: facts and models. *Cardiovasc. Res.* 70, 12–21. doi: 10.1016/j.cardiores.2005.11.008

Khalil, A. A., Ostwaldt, A.-C., Nierhaus, T., Ganeshan, R., Audebert, H. J., Villringer, K., et al. (2017). Relationship between changes in the temporal dynamics of the blood-oxygen-level-dependent signal and hypoperfusion in acute ischemic stroke. *Stroke* 48, 925–931. doi: 10.1161/STROKEAHA.116.015566

Khalil, A. A., Villringer, K., Filleböck, V., Hu, J.-Y., Rocco, A., Fiebach, J. B., et al. (2018). Non-invasive monitoring of longitudinal changes in cerebral hemodynamics in acute ischemic stroke using BOLD signal delay. *J. Cereb. Blood Flow Metab.*doi: 10.1177/0271678X18803951 [Epub ahead of print].

Knapp, C., and Carter, G. (1976). The generalized correlation method for estimation of time delay. *IEEE Trans. Acoust.SpeechSignal Proc.* 24, 320–327. doi: 10.1109/tassp.1976.1162830

Li, Y., Zhang, H., Yu, M., Yu, W., Frederick, B. D., and Tong, Y. (2018). Systemic low-frequency oscillations observed in the periphery of healthy human subjects. *J. Biomed. Opt.* 23, 1–11. doi: 10.1117/1.JBO.23.5.057001

Liang, M., Xi-Hai, L., Wan-Gang, Z., and Dai-Zhi, L. (2015). "The Generalized Cross-Correlation Method for Time Delay Estimation of Infrasound Signal," in *Proceedings of the Fifth International Conference on Instrumentation and Measurement, Computer, Communication and Control (IMCCC)*, (Los Alamitos, CA: IEEE), 1320–1323.

Liu, T. T. (2017). Reprint of 'Noise contributions to the fMRI signal: an overview'. *Neuroimage* 154, 4–14. doi: 10.1016/j.neuroimage.2017.05.031

Logothetis, N. K., Pauls, J., Augath, M., Trinath, T., and Oeltermann, A. (2001). Neurophysiological investigation of the basis of the fMRI signal. *Nature* 412, 150–157. doi: 10.1038/35084005

Lv, Y., Margulies, D. S., Cameron Craddock, R., Long, X., Winter, B., Gierhake, D., et al. (2013). Identifying the perfusion deficit in acute stroke with resting-state functional magnetic resonance imaging. *Ann. Neurol.* 73, 136–140. doi: 10.1002/ana.23763

Ma, Y., Shaik, M. A., Kozberg, M. G., Kim, S. H., Portes, J. P., Timerman, D., et al. (2016). Resting-state hemodynamics are spatiotemporally coupled to synchronized and symmetric neural activity in excitatory neurons. *Proc. Natl. Acad. Sci. U.S.A.* 113, E8463–E8471. doi: 10.1073/pnas.1525369113

Martinez-Montes, E., Valdes-Sosa, P. A., Miwakeichi, F., Goldman, R. I., and Cohen, M. S. (2004). Concurrent EEG/fMRI analysis by multiway Partial Least Squares. *Neuroimage* 22, 1023–1034. doi: 10.1016/j.neuroimage.2004.03.038

Mayhew, J. E. W., Askew, S., Zheng, Y., Porrill, J., Westby, G. W. M., Redgrave, P., et al. (1996). Cerebral vasomotion: a 0.1-Hz oscillation in reflected light imaging of neural activity. *Neuroimage* 4, 183–193. doi: 10.1006/nimg.1996.0069

Monti, L., Donati, D., Menci, E., Cioni, S., Bellini, M., Grazzini, I., et al. (2015). Cerebral circulation time is prolonged and not correlated with EDSS in multiple sclerosis patients: a study using digital subtracted angiography. *PLoS One* 10:e0116681. doi: 10.1371/journal.pone.0116681

Müller, M. W. D., and Österreich, M. (2014). A comparison of dynamic cerebral autoregulation across changes in cerebral blood flow velocity for 200 seconds. *Front. Physiol.* 5:327.

Nishida, S., Aso, T., Takaya, S., Takahashi, Y., Kikuchi, T., Funaki, T., et al. (2018). Resting-state functional magnetic resonance imaging identifies cerebrovascular reactivity impairment in patients with Arterial Occlusive diseases: a pilot study. *Neurosurgery*. doi: 10.1093/neuros/nyy434 [Epub ahead of print].

Obrig, H., Neufang, M., Wenzel, R., Kohl, M., Steinbrink, J., Einhaupl, K., et al. (2000). Spontaneous low frequency oscillations of cerebral hemodynamics and metabolism in human adults. *Neuroimage* 12, 623–639. doi: 10.1006/nimg.2000.0657

Olden, J. D., and Neff, B. D. (2001). Cross-correlation bias in lag analysis of aquatic time series. *Mar. Biol.* 138, 1063–1070. doi: 10.1007/s002270000517

Qiu, D., Straka, M., Zun, Z., Bammer, R., Moseley, M. E., and Zaharchuk, G. (2012). CBF measurements using multidelay pseudocontinuous and velocity-selective arterial spin labeling in patients with long arterial transit delays: comparison with xenon CT CBF. *J. Magn. Reson. Imaging* 36, 110–119. doi: 10.1002/jmri.23613

Rebollo, I., Devauchelle, A.-D., Béranger, B., and Tallon-Baudry, C. (2018). Stomach-brain synchrony reveals a novel, delayed-connectivity resting-state network in humans. *eLife* 7:e33321.

Rivadulla, C., de Labra, C., Grieve, K. L., and Cudeiro, J. (2011). Vasomotion and neurovascular coupling in the visual thalamus in vivo. *PLoS One* 6:e28746. doi: 10.1371/journal.pone.0028746

Sassaroli, A., de, B. F. B., Tong, Y., Renshaw, P. F., and Fantini, S. (2006). Spatially weighted BOLD signal for comparison of functional magnetic resonance imaging and near-infrared imaging of the brain. *Neuroimage* 33, 505–514. doi: 10.1016/j.neuroimage.2006.07.006

Sassaroli, A., Pierro, M., Bergethon, P. R., and Fantini, S. (2012). Low-frequency spontaneous oscillations of cerebral hemodynamics investigated with near-infrared spectroscopy: a review. *IEEE J. Sel. Top. Quantum Electron.* 18, 1478–1492. doi: 10.1109/jstqe.2012.2183581

Schreiber, S. J., Doepp, F., Spruth, E., Kopp, U. A., and Valdueza, J. M. (2005). Ultrasonographic measurement of cerebral blood flow, cerebral circulation time and cerebral blood volume in vascular and Alzheimer's dementia. *J. Neurol.* 252, 1171–1177. doi: 10.1007/s00415-005-0826-8

Schreiber, S. J., Franke, U., Doepp, F., Staccioli, E., Uludag, K., and Valdueza, J. M. (2002). Dopplersonographic measurement of global cerebral circulation time using echo contrast-enhanced ultrasound in normal individuals and patients with arteriovenous malformations. *Ultrasound Med. Biol.* 28, 453–458. doi: 10.1016/s0301-5629(02)00477-5

Siegel, J. S., Snyder, A. Z., Ramsey, L., Shulman, G. L., and Corbetta, M. (2016). The effects of hemodynamic lag on functional connectivity and behavior after stroke. *J. Cereb. Blood Flow Metab.* 36, 2162–2176. doi: 10.1177/0271678x15614846

Strangman, G., Culver, J. P., Thompson, J. H., and Boas, D. A. (2002). A quantitative comparison of simultaneous BOLD fMRI and NIRS recordings during functional brain activation. *Neuroimage* 17, 719–731. doi: 10.1016/s1053-8119(02)91227-9

Tong, Y., Bergethon, P. R., and Frederick, B. D. (2011a). An improved method for mapping cerebrovascular reserve using concurrent fMRI and near-infrared spectroscopy with Regressor Interpolation at Progressive Time Delays (RIPTiDe). *Neuroimage* 56, 2047–2057. doi: 10.1016/j.neuroimage.2011.03.071

Tong, Y., Hocke, L. M., and Frederick, B. (2011b). Isolating the sources of widespread physiological fluctuations in functional near-infrared spectroscopy signals. *J. Biomed. Opt.* 16:106005. doi: 10.1117/1.3638128

Tong, Y., Lindsey, K. P., and de, B. F. B. (2011c). Partitioning of physiological noise signals in the brain with concurrent near-infrared spectroscopy and fMRI. *J. Cereb. Blood Flow Metab.* 31, 2352–2362. doi: 10.1038/jcbfm.2011.100

Tong, Y., and Frederick, B. (2012). Concurrent fNIRS and fMRI processing allows independent visualization of the propagation of pressure waves and bulk blood flow in the cerebral vasculature. *Neuroimage* 61, 1419–1427. doi: 10.1016/j.neuroimage.2012.03.009

Tong, Y., and Frederick, B. D. (2010). Time lag dependent multimodal processing of concurrent fMRI and near-infrared spectroscopy (NIRS) data suggests a global circulatory origin for low-frequency oscillation signals in human brain. *Neuroimage* 53, 553–564. doi: 10.1016/j.neuroimage.2010.06.049

Tong, Y., and Frederick, B. D. (2014a). Studying the Spatial distribution of physiological effects on BOLD signals using ultrafast fMRI. *Front. Hum. Neurosci.* 8:196. doi: 10.3389/fnhum.2014.00196

Tong, Y., and Frederick, B. (2014b). Tracking cerebral blood flow in BOLD fMRI using recursively generated regressors. *Hum. Brain Mapp.* 35, 5471–5485. doi: 10.1002/hbm.22564

Tong, Y., Hocke, L. M., Fan, X., Janes, A. C., and Frederick, B. (2015). Can apparent resting state connectivity arise from systemic fluctuations? *Front. Hum Neurosci.* 9:285. doi: 10.3389/fnhum.2015.00285

Tong, Y., Hocke, L. M., and Frederick, B. (2014). Short repetition time multiband echo-planar imaging with simultaneous pulse recording allows dynamic imaging of the cardiac pulsation signal. *Magn. Reson. Med.* 72, 1268–1276. doi: 10.1002/mrm.25041

Tong, Y., Hocke, L. M., Licata, S. C., and Frederick, B. (2012). Low-frequency oscillations measured in the periphery with near-infrared spectroscopy are strongly correlated with blood oxygen level-dependent functional magnetic resonance imaging signals. *J. Biomed. Opt.* 17:106004. doi: 10.1117/1.JBO.17.10.106004

Tong, Y., Hocke, L. M., Lindsey, K. P., Erdogan, S. B., Vitaliano, G., Caine, C. E., et al. (2016). Systemic low-frequency oscillations in BOLD signal vary with tissue type. *Front. Neurosci.* 10:313. doi: 10.3389/fnins.2016.00313

Tong, Y., Hocke, L. M., Nickerson, L. D., Licata, S. C., Lindsey, K. P., and Frederick, B. (2013). Evaluating the effects of systemic low frequency oscillations measured in the periphery on the independent component analysis results of resting state networks. *Neuroimage* 76, 202–215. doi: 10.1016/j.neuroimage.2013.03.019

Tong, Y., Lindsey, K. P., Hocke, L. M., Vitaliano, G., Mintzopoulos, D., and Frederick, B. D. (2017). Perfusion information extracted from resting state functional magnetic resonance imaging. *J. Cereb. Blood Flow Metab.* 37, 564–576. doi: 10.1177/0271678x16631755

Tong, Y., Yao, J. F., Chen, J. J., and Frederick, B. B. (2018). The resting-state fMRI arterial signal predicts differential blood transit time through the brain. *J. Cereb. Blood Flow Metab.* 39, 1148–1160. doi: 10.1177/0271678X17753329

Tsuji, M., Saul, J. P., du Plessis, A., Eichenwald, E., Sobh, J., Crocker, R., et al. (2000). Cerebral intravascular oxygenation correlates with mean arterial pressure in critically Ill premature infants. *Pediatrics* 106, 625–632. doi: 10.1542/peds.106.4.625

van Beek, A. H., Claassen, J. A., Rikkert, M. G. O., and Jansen, R. W. (2008). Cerebral autoregulation: an overview of current concepts and methodology with special focus on the elderly. *J. Cereb. Blood Flow Metab.* 28, 1071–1085. doi: 10.1038/jcbfm.2008.13

Wise, R. G., Ide, K., Poulin, M. J., and Tracey, I. (2004). Resting fluctuations in arterial carbon dioxide induce significant low frequency variations in BOLD signal. *Neuroimage* 21, 1652–1664. doi: 10.1016/j.neuroimage.2003.11.025

Yacin, S. M., Chakravarthy, V. S., and Manivannan, M. (2011). Reconstruction of gastric slow wave from finger photoplethysmographic signal using radial basis function neural network. *Med. Biol. Eng. Comput.* 49, 1241–1247. doi: 10.1007/s11517-011-0796-1

Yan, S., Qi, Z., An, Y., Zhang, M., Qian, T., and Lu, J. (2018). Detecting perfusion deficit in Alzheimer's disease and mild cognitive impairment patients by resting-state fMRI. *J. Magn. Reson. Imaging*388(Suppl. 1), 505–506.

Yao, J. F., Wang, J. H., Yang, H. C. S., Liang, Z., Cohen-Gadol, A. A., Rayz, V. L., et al. (2019). Cerebral circulation time derived from fMRI signals in large blood vessels. *J. Magn. Reson. Imaging*. doi: 10.1002/jmri.26765

Zhang, R., Zuckerman, J. H., Giller, C. A., and Levine, B. D. (1998). Transfer function analysis of dynamic cerebral autoregulation in humans. *Am. J. Physiol.* 274, H233–H241.

Conflict of Interest Statement: The authors declare that the research was conducted in the absence of any commercial or financial relationships that could be construed as a potential conflict of interest.

frontiers in Neuroscience

ORIGINAL RESEARCH
published: 04 September 2019
doi: 10.3389/fnins.2019.00900

Intrinsic Frequencies of the Resting-State fMRI Signal: The Frequency Dependence of Functional Connectivity and the Effect of Mode Mixing

*Nicole H. Yuen[1], Nathaniel Osachoff[1] and J. Jean Chen[1,2]**

[1] Rotman Research Institute at Baycrest, Toronto, ON, Canada, [2] Department of Medical Biophysics, University of Toronto, Toronto, ON, Canada

The frequency characteristics of the resting-state BOLD fMRI (rs-fMRI) signal are of increasing scientific interest, as we discover more frequency-specific biological interpretations. In this work, we use variational mode decomposition (VMD) to precisely decompose the rs-fMRI time series into its intrinsic mode functions (IMFs) in a data-driven manner. The accuracy of the VMD decomposition of constituent IMFs is verified through simulations, with higher reconstruction accuracy and much-reduced mode mixing relative to previous methods. Furthermore, we examine the relative contribution of the VMD-derived modes (frequencies) to the rs-fMRI signal as well as functional connectivity measurements. Our primary findings are: (1) The rs-fMRI signal within the 0.01–0.25 Hz range can be consistently characterized by four intrinsic frequency clusters, centered at 0.028 Hz (IMF4), 0.080 Hz (IMF3), 0.15 Hz (IMF2) and 0.22 Hz (IMF1); (2) these frequency clusters were highly reproducible, and independent of rs-fMRI data sampling rate; (3) not all frequencies were associated with equivalent network topology, in contrast to previous findings. In fact, while IMF4 is most likely associated with physiological fluctuations due to respiration and pulse, IMF3 is most likely associated with metabolic processes, and IMF2 with vasomotor activity. Both IMF3 and IMF4 could produce the brain-network topology typically observed in fMRI, whereas IMF1 and IMF2 could not. These findings provide initial evidence of feasibility in decomposing the rs-fMRI signal into its intrinsic oscillatory frequencies in a reproducible manner.

Keywords: resting-state fMRI, resting state functional connectivity, intrinsic mode function, frequency dependence characteristics, variational modal decomposition, empirical mode decomposed, physiological origins

OPEN ACCESS

Edited by:
Amir Shmuel,
McGill University, Canada

Reviewed by:
Lirong Yan,
University of Southern California, United States
Patricia Figueiredo,
Instituto Superior Técnico, Portugal

***Correspondence:**
J. Jean Chen
jchen@research.baycrest.org

Specialty section:
This article was submitted to Brain Imaging Methods, a section of the journal Frontiers in Neuroscience

Received: *02 April 2019*
Accepted: *12 August 2019*
Published: *04 September 2019*

Citation:
Yuen NH, Osachoff N and Chen JJ (2019) Intrinsic Frequencies of the Resting-State fMRI Signal: The Frequency Dependence of Functional Connectivity and the Effect of Mode Mixing. Front. Neurosci. 13:900. doi: 10.3389/fnins.2019.00900

INTRODUCTION

The frequency characteristics of the resting-state BOLD fMRI (rs-fMRI) signal are of increasing scientific interest (Salvador et al., 2005; Niazy et al., 2011; Kalcher et al., 2014), as we discover more frequency-specific biological interpretations within the conventional data-acquisition bandwidth of 0–0.25 Hz (Golestani et al., 2015; Hocke et al., 2016). In particular, specific spectral content have

been associated with physiological and vascular processes (Birn et al., 2008; Golestani et al., 2015; Mark et al., 2015; Hocke et al., 2016) and with the resulting brain-network measures (Nikolaou et al., 2016). Thus, spectral analysis of the rs-fMRI signal appears to be a compelling approach to achieving a better appreciation of how much neurally relevant information is conveyed by rs-fMRI. To that end, band-pass filtering has been used in the initial efforts (Kalcher et al., 2014). However, in theory, the rs-fMRI signal does not lend itself to conventional band-pass filtering approaches, as it is not stationary and cannot be defined by a few frequencies in Fourier domain. The band-pass filtering approach is inadequate for studying non-stationary signals, as the frequency content of such signals changes with time, while a filter bank is limited by assumptions regarding frequency, bandwidths and the type of filter design.

Previous studies examining the frequency characteristics of the resting-state BOLD fMRI (rs-fMRI) signal were largely based on the decomposition of the rs-fMRI signal into its intrinsic mode functions (IMFs). Existing studies (Niazy et al., 2011; Song et al., 2014) have used empirical mode decomposition (EMD) (Huang et al., 1998) and later used complementary ensemble empirical mode decomposition (CEEMD) (Wu and Huang, 2009; Yeh et al., 2012; Qian et al., 2015). At the core of EMD and CEEMD is a simple workflow. Signal local minima and maxima are recursively detected, based on which an upper and lower envelope are obtained through interpolation; subsequently, the midline of the resultant envelope is removed and the high-frequency component becomes the IMF. The same process is then performed on the signal composed of the low-frequency midline. Thus, each IMF can be expressed as a combination of a low-frequency amplitude-modulated and a high-frequency frequency-modulated signal Eq. (1),

$$m(t) = A(t)cos(\emptyset(t)) \tag{1}$$

Where $\emptyset(t)$ modulates the carrier frequency. The total bandwidth of this signal is described by Eq. (2),

$$BW_{\mathrm{IMF}} = 2(\Delta f + f_{\mathrm{FM}} + f_{\mathrm{AM}}) \tag{2}$$

where Δf is the total deviation from the instantaneous frequency of the IMF, while f_{FM} represents the maximum rate of the change of the instantaneous frequency, and f_{AM} represent the highest frequency of the envelope modulating the frequency-modulated signal. The IMF frequency estimate could be dominated by either of these, depending on noise conditions.

Previous works using EMD and CEEMD have both found that the rs-fMRI can be approximated by 4 to 5 IMFs covering the entire sampling bandwidth (Niazy et al., 2011; Qian et al., 2015), and that all IMFs can be used to reproduce similar network topologies. A fundamental assumption of EMD and its derivatives is that each IMF occupies a well-defined frequency range (Huang et al., 1998). In theory, the IMF-based representation is insensitive to non-stationarity and non-linearity in the original signal. EMD-type approaches are known to have difficulty separating tones of similar frequencies. Moreover, high levels of non-white noise can interfere with the accurate identification of the instantaneous frequency, and cause the frequency to appear to shift in a non-linear fashion, leading to mode mixing between IMFs (Wu and Huang, 2009) as well as the same mode to be spread across multiple IMFs. In addition, EMD-derived methods have a tendency to attribute wider bandwidths to IMFs occupying higher frequencies. This is likely a result of the recursions, which present the highest degree of uncertainty to the first (highest-frequency) IMFs, and not allowing for backward error correction after subsequent IMFs have been extracted. Indeed, when applied to rs-fMRI data, CEEMD resulted in visible modal widening as frequency increased (Qian et al., 2015).

Our study incorporates the usage of the recently proposed variational mode decomposition (VMD) method (Dragomiretskiy and Zosso, 2014) to decompose the BOLD rs-fMRI time series into its IMFs. Recently, the VMD method has recently found application in the analysis of geological signals (Liu et al., 2016; Xiao et al., 2016) and electrocardiographic data (Lahmiri, 2014; Mert, 2016; Tripathy et al., 2016). The theory of VMD has been described in detail elsewhere (Dragomiretskiy and Zosso, 2014), and will not be repeated here. We will simply point out that unlike its predecessors, VMD is non-recursive, and can reconstruct all modes simultaneously, controlled by a convergence criterion. The variational model assesses the bandwidth of the modes by minimizing the Gaussian-regularized mean-square error between the signal and its representation as a series of Wiener filters, with the modal instantaneous frequency being determined as the center of mass of the power-spectral density function of each IMF. This approach increases the robustness of the model to estimation uncertainties. VMD provides error checking, as the VMD solution is be updated by minimizing the mean-squared residual of all IMFs against the estimate of any given IMF. Lastly, the VMD convergence depends on a series of iterative optimizations, during which the balance between overfitting and signal-estimation accuracy can be adjusted, for instance, based on *a priori* knowledge about the signal.

In this work, we hypothesize that VMD is able to more precisely extract frequency bands from the rs-fMRI signal, reducing the issue of mode mixing and mode spreading demonstrated in the previous work. To verify this hypothesis, we tested the EMD, CEEMD, and VMD techniques through a Monte Carlo simulation. Furthermore, although prior work (using EMD and CEEMD) have suggested that resting-state networks (RSNs) measured through rs-fMRI are frequency independent, we hypothesize that existing results are affected by modal mixing and limited frequency precision as described herein. To address this hypothesis, we re-examine the frequency dependence of functional connectivity of RSNs using VMD.

MATERIALS AND METHODS

VMD Optimization

As documented in the original paper, the VMD technique follows three steps: (1) estimate individual IMFs by computing the Hilbert transform of the original signal f; (2) shift each mode to its base frequency using heterodyne demodulation; (3) estimate the bandwidth of each mode as the H1 Gaussian smoothness of

the demodulated signal. The target for the decomposition should be that

$$\sum_{\mathrm{k}} u_{\mathrm{k}} = f \tag{3}$$

where k is the number of IMFs. If the signal f is smooth, the solution could be obtained through Tikhonov regularized minimization,

$$min_{\mathrm{f}}\left\{ \left|\left|\mathrm{f\text{-}f_0}\right|\right|_2^2 + \alpha \left|\left|\partial_{\mathrm{t}} f\right|\right|_2^2 \right\} \tag{4}$$

where f_0 is the measured signal, f is the original (clean) signal, and α is the regularization parameter. From this, we obtained the Euler-Lagrange equation:

$$f - f_0 = \alpha \partial_{\mathrm{t}}^2 f \tag{5}$$

where (δ_tt is the partial derivative with respect to time and is the frequency in radians.

The minimization target of the VMD algorithm can be summarized by Eq. 6, which describes the inverse of the Gaussian smoothness of the demodulated signal,

$$\min_{u_k, w_k} \left\{ \left|\left| \partial_t \left[\left(\delta(t) + \frac{j}{\pi t} \right) . u_k(t) \right] e^{-jw_k t} \right|\right|_2^2 \right\} \tag{6}$$

where (δ(t) is Dirac's delta function, $||_2^2$ is the Euclidean norm squared,and j (=(v−1. This is solved using the augmented Lagrangian:

$$\mathscr{L}(u_k, w_k, \lambda) = a + b + c \tag{7}$$

where

$$a = \alpha \sum_k \left|\left| \partial_t \left[\left(\delta(t) + \frac{j}{\pi t} \right) . u_k(t) \right] e^{-jw_k t} \right|\right|_2^2 \tag{8}$$

$$b = \left|\left| f - \sum_{\mathrm{k}} u_{\mathrm{k}} \right|\right|_2^2 \tag{9}$$

$$c = \left\langle \lambda, f - \sum_{\mathrm{k}} u_{\mathrm{k}} \right\rangle \tag{10}$$

where (λ is the Langragian multiplier, b is the quadratic penalty term (squared residual) and c is the inner product of and the residual. The solution to the original variational problem is solved as the saddle point of the augmented Lagrangian. Each IMF is updated iteratively (by solving the VMD problem with respect to u and to ω until convergence is reached. In this way, all modes are extracted and optimized concurrently instead of sequentially.

In this study, we explicitly optimized the value of the regularization parameter α to balance the bandwidths of the spectral bands and the reconstruction error between the sum of the bands and the original signal. This parameter was chosen to minimize the overlap between the spectral bands in the Fourier domain while keeping the parameter as low as possible to retain reconstruction fidelity.

Simulated Data

To compare the performance of the VMD method in relation to EMD and CEEMD methods, we performed a Monte Carlo simulation involving a known, "ground-truth" signal. First, we generated a signal composed of equal power contributions from four frequencies (0.03, 0.08, 0.15, and 0.23 Hz). This signal was sampled at 0. 25 Hz to emulate the typical sampling rate of rs-fMRI data (TR = 2 s), and the constituent frequencies were informed in part by those previously reported (Niazy et al., 2011; Qian et al., 2015). We then generated 200 variants of signal-noise mixtures, in which 200 different realizations of white noise time series were added to the signal to achieve a signal-to-noise ratio (SNR) of ∼1.2. This is representative of the lower end of the realistic SNR range in rs-fMRI data, particularly to accommodate the fact that the spectral signature of noise in real rs-fMRI data is imprecise and non-stationary. All three decomposition methods were then applied to extract the original frequencies. To quantify the performances of the different algorithms, we computed the fractional inter-modal overlap (mode mixing) for each, defined as the amount of spectral power in the neighboring IMFs as a fraction of the total spectral power of each "ground-truth" IMF.

MRI Data Acquisition

MRI data were collected from 8 healthy adults (mean age 30 ± 6.7 years) on a 3T Siemens TIM Trio scanner and a 32-channel head coil. Specifically, whole-brain resting-state fMRI (rs-fMRI) data were acquired using single-shot gradient-echo EPI. The conventional-TR scans are later referred as "long-TR" scans: 26 slices, TR = 2 s, flip angle = 70°, FOV = 220 mm × 200 mm, voxel size = 3.4 mm × 3.4 mm × 4.6 mm in 240 frames. To enable assessment of reproducibility of our methods, the rs-fMRI scan was performed twice for each subject (two trials per subject) within the same session. On a subset of seven subjects, we also acquired rs-fMRI data using simultaneous multi-slice (SMS) acceleration on the gradient-echo EPI (Feinberg et al., 2010) (TR = 323 ms, TE = 30 ms, flip angle = 40°, 15 slices, 3.44 mm × 3.44 mm × mm, 2230 time points, acceleration factor = 3, phase encoding shift factor = 2, slices ascending). The brain coverage of these "short-TR" scans was matched to that of the "long-TR" scans, and we only used 1486 frames of the short-TR scans for comparison with the long-TR scan results. This would permit us to assess the dependence of our results to fMRI sampling rate. A 3D T1-weighted anatomical scan was acquired using MPRAGE, with resolution 1 × 1 × 1 mm, repetition time (TR) = 2400 ms, inversion time (TI) = 1000 ms, echo time (TE) = 2.43 ms, flip angle = 8, field of view × 256 × 256 mm (sagittal), matrix size = 256 × 256, 192 slices (ascending order), bandwidth = 180 Hz/pixel, and GRAPPA acceleration factor = 2.

Image Preprocessing

The rs-fMRI data were preprocessed using FSL FEAT version 5.0.8 (Jenkinson et al., 2002). Functional data had the first 10 volumes removed and skull stripped using the Brain Extraction Tool (BET). Data were corrected for motion (reference being

the middle frame of each data set) and slice time then band-pass filtered to be between 0.01 and 0.25 Hz (using fslmaths, which implements a Gaussian filter). The cut-off of 0.25 Hz was chosen to represent the maximum detectable frequency in typical rs-fMRI acquisitions (i.e., TR = 2 s). Similar to prior work of a similar nature (Niazy et al., 2011; Tong et al., 2011), we did not actively correct physiological artifacts. The VMD technique was then used to decompose the preprocessed BOLD signal, and the results were compared to those obtained using the EMD and CEEMD methods.

The T1 anatomical scans were used in defining noise regions of interest (ROIs) for further analysis. Specifically, we used FMRIB Automated Segmentation Tool (FAST) for segmentation of gray matter, white matter, and cerebrospinal fluid ROIs. The FSL-FAST segmentation routine is based on a Hidden Markov Random Field model that is optimized using the expectation-maximization algorithm (Zhang et al., 2001). The ROI masks are then aligned with the fMRI data using anatomical-to-fMRI transformation matrices determined using FSL Flirt (Jenkinson and Smith, 2001; Jenkinson et al., 2002).

Furthermore, we performed cortical-surface reconstruction using FreeSurfer[1]. The procedure includes removal of non-brain tissue using a hybrid watershed/surface deformation procedure (Segonne et al., 2004), automated transformation into the MNI152 standard space, intensity normalization (Sled et al., 1998), tessellation of the gray matter white matter boundary, automated topology correction (Segonne et al., 2007), and surface deformation following intensity gradients to optimally place the gray/white and gray/CSF borders at the location where the greatest shift in intensity defines the transition to the other tissue class (Fischl and Dale, 2000). The subsequent segmentation of the cortex and subcortical gray matter volumetric structures were performed for each subject based on probabilistic models of tissue magnetic resonance parameters and of anatomical locations (Fischl et al., 2004). The resultant cortical models permitted surface inflation (Fischl et al., 1999) and registration to a spherical atlas, whereby individual cortical folding patterns were used to match cortical geometry across subjects (Fischl et al., 1999).

IMF Clustering and Spectral Analysis

VMD was used decompose each voxel in the rs-fMRI data into a specified number of IMFs. For each IMF in each voxel, the frequency associated with the center of mass of the power spectral density function of each IMF was used to define the dominant frequency of said IMF. After this procedure was repeated for each voxel, one challenge remained – as each voxel is associated with a slightly different set of IMF frequencies, it was difficult to identify any generalizable findings regarding frequency content. To overcome this, we identified the existence of whole brain "*IMF frequency clusters*" by plotting the histograms of IMF frequencies including all IMFs of all voxels of each tissue type. In plotting the histogram, each IMF is weighted by its normalized power contribution (normalized by total spectral power at each voxel).

We then modeled the peaks in the histograms as Gaussian functions (Qian et al., 2015) and identified the *widths of the IMF frequency clusters* as including 95% of the areas of the fitted Gaussians. Using these cluster definitions, we classified each IMF from each voxel as belonging to an IMF cluster (named IMF 1–4), each associated with a distinct frequency range. We repeated this for all eight subjects, and assessed the reproducibility of these frequency ranges in gray and white matter using the intra-class correlation coefficient (ICC). For this purpose, each IMF map was further masked to include only white or only gray matter (FSL 5.0.8).

In this work, in order to arrive at the best number of IMFs to use, we compared IMF- frequency clusters resulting from assuming 2 IMFs, 4 IMFs, 5 IMFs and 8 IMFs. Sample IMF histograms are shown in **Appendix Figure A1**. The comparison metrics are precision and reproducibility. The precision metrics include: (1) the group-wise standard deviation of the frequency-cluster locations; (2) the group-wise standard deviation of the frequency-cluster widths. The reproducibility metrics include: (1) the percentage of subjects manifesting a particular frequency cluster; (2) the correlation between frequency-cluster locations estimated from 2 runs of each subject. The results are detailed in the (**Appendix Figure A2**), and indicate the choice of 4 IMFs produced the most precise and reproducible frequency-cluster estimates. Note that there was no direct link between the number of IMFs targeted for at the VMD stage and the number of IMF frequency clusters detected at the clustering stage.

Note that for the short-TR data set, we first low-pass filtered the data at 0.25 Hz in order to emulate the sampling rate of conventional rs-fMRI. The main difference between the data acquired at 0.25 Hz and the filtered short-TR data is that the latter is associated with reduced aliasing in the 0–0.25 Hz range.

Amplitude Analysis

For both long- and short-TR data sets, we also computed the *fractional IMF amplitude*. This is computed at each voxel as the fractional contribution of the spectral power of each IMF (as defined by its associated IMF cluster) to the total spectral power of all IMFs (as defined by the remaining IMF clusters). This parameter was defined to overcome the limitation that the raw spectral powers of IMFs from different subjects and different acquisitions are not directly comparable (Zou et al., 2008), given variability in factors such as scanner tuning and analog-to-digital conversion range. To demonstrate the spatial distribution of the fractional IMF amplitude, we transformed each subject's fractional amplitude map into MNI152 space using FSL flirt (Jenkinson et al., 2002). The reference image for the registration was the middle frame of the original fMRI data, and the resulting transformation matrix was applied to the IMF amplitude and frequency maps. Subsequently, we overlaid the group-mean fractional amplitude map onto a cortical-surface model using FreeSurfer (Fischl et al., 1999).

Functional Connectivity Matrices

As the fMRI data were registered with MNI152 space, we used the automated anatomical labeling (AAL) (Tzourio-Mazoyer et al., 2002)to divide the brain into 116 anatomical regions of interest (ROIs), including both the cortex and the cerebellum. These ROIs are listed in **Table 1**. For each subject, we averaged all

[1]http://surfer.nmr.mgh.harvard.edu

TABLE 1 | List of regions of interest (ROIs) used when computing correlation matrices.

Index	Region of Interest	Index	Region of Interest	Index	Region of Interest
1	Precentral_L	40	ParaHippocampal_R	79	Heschl_L
2	Precentral_R	41	Amygdala_L	80	Heschl_R
3	Frontal_Sup_L	42	Amygdala_R	81	Temporal_Sup_L
4	Frontal_Sup_R	43	Calcarine_L	82	Temporal_Sup_R
5	Frontal_Sup_Orb_L	44	Calcarine_R	83	Temporal_Pole_Sup_L
6	Frontal_Sup_Orb_R	45	Cuneus_L	84	Temporal_Pole_Sup_R
7	Frontal_Mid_L	46	Cuneus_R	85	Temporal_Mid_L
8	Frontal_Mid_R	47	Lingual_L	86	Temporal_Mid_R
9	Frontal_Mid_Orb_L	48	Lingual_R	87	Temporal_Pole_Mid_L
10	Frontal_Mid_Orb_R	49	Occipital_Sup_L	88	Temporal_Pole_Mid_R
11	Frontal_Inf_Oper_L	50	Occipital_Sup_R	89	Temporal_Inf_L
12	Frontal_Inf_Oper_R	51	Occipital_Mid_L	90	Temporal_Inf_R
13	Frontal_Inf_Tri_L	52	Occipital_Mid_R	91	Cerebellum_Crus1_L
14	Frontal_Inf_Tri_R	53	Occipital_Inf_L	92	Cerebellum_Crus1_R
15	Frontal_Inf_Orb_L	54	Occipital_Inf_R	93	Cerebellum_Crus2_L
16	Frontal_Inf_Orb_R	55	Fusiform_L	94	Cerebellum_Crus2_R
17	Rolandic_Oper_L	56	Fusiform_R	95	Cerebellum_3_L
18	Rolandic_Oper_R	57	Postcentral_L	96	Cerebellum_3_R
19	Supp_Motor_Area_L	58	Postcentral_R	97	Cerebellum_4_5_L
20	Supp_Motor_Area_R	59	Parietal_Sup_L	98	Cerebellum_4_5_R
21	Olfactory_L	60	Parietal_Sup_R	99	Cerebellum_6_L
22	Olfactory_R	61	Parietal_Inf_L	100	Cerebellum_6_R
23	Frontal_Sup_Medial_L	62	Parietal_Inf_R	101	Cerebellum_7b_L
24	Frontal_Sup_Medial_R	63	SupraMarginal_L	102	Cerebellum_7b_R
25	Frontal_Med_Orb_L	64	SupraMarginal_R	103	Cerebellum_8_L
26	Frontal_Med_Orb_R	65	Angular_L	104	Cerebellum_8_R
27	Rectus_L	66	Angular_R	105	Cerebellum_9_L
28	Rectus_R	67	Precuneus_L	106	Cerebellum_9_R
29	Insula_L	68	Precuneus_R	107	Cerebellum_10_L
30	Insula_R	69	Paracentral_Lobule_L	108	Cerebellum_10_R
31	Cingulum_Ant_L	70	Paracentral_Lobule_R	109	Vermis_1_2
32	Cingulum_Ant_R	71	Caudate_L	110	Vermis_3
33	Cingulum_Mid_L	72	Caudate_R	111	Vermis_4_5
34	Cingulum_Mid_R	73	Putamen_L	112	Vermis_6
35	Cingulum_Post_L	74	Putamen_R	113	Vermis_7
36	Cingulum_Post_R	75	Pallidum_L	114	Vermis_8
37	Hippocampus_L	76	Pallidum_R	115	Vermis_9
38	Hippocampus_R	77	Thalamus_L	116	Vermis_10
39	ParaHippocampal_L	78	Thalamus_R		

Sup, superior; Mid, middle; Inf, inferior; L, left; R, right.

IMFs within each IMF-cluster frequency range in each ROI. We then generated matrices of Pearson correlation coefficients between the IMF time series of all pairs of ROIs. These were then averaged across subjects to provide an overview of RSN organization.

For comparison with the literature, we created an additional set of correlation matrices using the band-pass filtered data (at 0.01–0.08 Hz) for each subject. This is the frequency range typical of rs-fMRI analyses. Furthermore, to help explain the spectral makeup of this reference correlation matrix, we also generated correlation matrices using signals band-pass filtered into the frequency ranges corresponding to the IMFs. These were also averaged across subjects.

Statistical Comparisons

In this work, comparison between IMF clusters and tissue types is performed using the Student's *t*-test, and linear correlation is used as the similarity index.

RESULTS

The average results of the Monte Carlo simulation are shown in **Figure 1**. While the noiseless signal was successfully reconstructed using all three algorithms (not shown), they performed very differently when noise was introduced. It is evident that IMF1 derived using EMD (**Figure 1B**) contains two

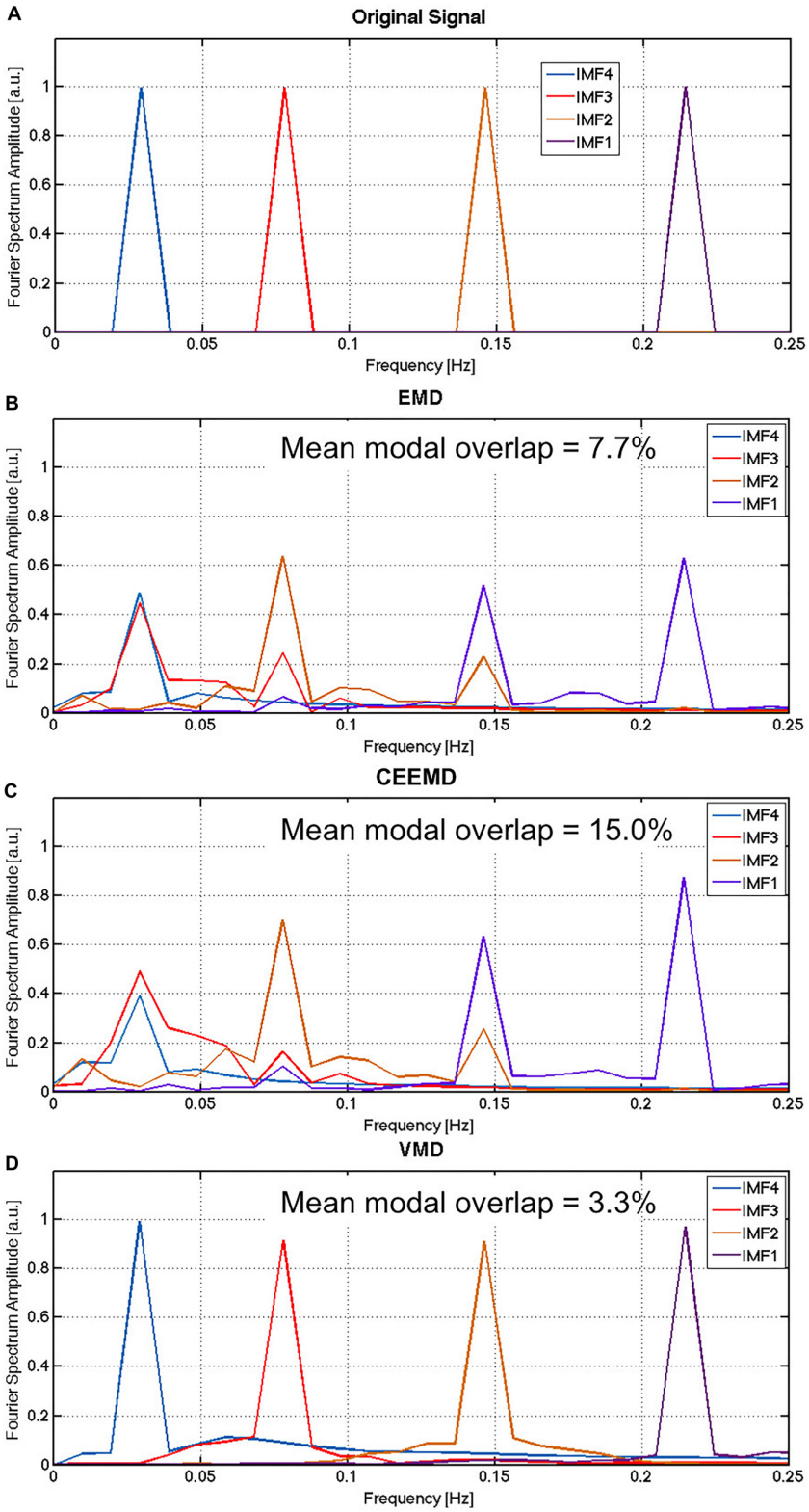

FIGURE 1 | Comparison of performance for EMD, CEEMD and VMD on simulated data: The Fourier spectrum of the original noiseless signal **(A)** is compared to the average spectra obtained by EMD **(B)**, CEEMD **(C)** and VMD **(D)** on the noisy version if the signal, averaged across all iterations of the Monte Carlo simulation. Gaussian noise was simulated in this case, with the SNR of the simulated noisy signals was approximately 1.2, approximated by the total power of the noise over the total power of the signal. In EMD and CEEMD, the 4 IMFs with highest powers are displayed.

distinct modes that would ideally have been attributed to two different IMFs. This is the manifestation of modal spreading, which is also seen in the CEEMD results (**Figure 1C**). Due to the existence of substantial modal spreading, inter-modal mixing (overlapping between IMFs in the frequency domain) is also found. Compared to EMD and CEEMD, VMD was able to identify the 4 IMFs of the original simulated signal with the least mode spreading and mode mixing (**Figure 1D**), with the noise component being split across the 4 IMFs. These simulation results confirm the theory-based hypothesis of increased IMF-estimation precision using VMD.

Intrinsic Frequencies of the rs-fMRI Signal

Sample results from human rs-fMRI data are shown in **Figure 2**. VMD was able to extract IMFs from all data sets with high consistency and the lowest reconstruction error compared to both EMD and CEEMD. Based on results similar to these, IMFs were estimated for all voxels for each rs-fMRI data set. The corresponding IMF frequencies were organized into histograms for gray and white matter. A sample histogram of IMF frequencies is shown in **Figure 3**. Note that not all voxels returned 4 IMFs. Yet, when aggregated, the histograms revealed 4 clusters of IMF frequencies. This was common across all subjects, and across tissue types. Based on these clusters, IMF frequency ranges were identified for each subject in the group. We noted regional variability in the location of IMF clusters, with IMF4 being the most stable across brain regions and IMF2 being the least (**Appendix Figure A3**).

The group-average VMD-decomposed peak frequencies in both gray and white matter are shown in **Figure 4**. Using the IMF-frequency clustering procedure described earlier, we identified 4 robust IMF-cluster frequency ranges. This was the case for all subjects and common to both gray and white matter. The frequency ranges of the 4 VMD IMF-frequency clusters are (mean frequency ± mean width/2):

- VMD IMF1: 0.20–0.24 Hz
- VMD IMF2: 0.13–0.17 Hz
- VMD IMF3: 0.063–0.098 Hz
- VMD IMF4: 0.021–0.036 Hz

These frequencies were evenly distributed across the majority of voxels (both gray and white matter), with no specific spatial features. Thus, we do not show spatial maps of the frequency distributions. Also, these frequencies were highly reproducible based on the long-TR acquisitions (**Figure 4**), with an ICC of 0.99 for both gray and white matter. This was confirmed by the absence of significant difference between IMF peak frequencies across each trial in either tissue type ($p > 0.21$). Henceforth, all IMFs associated with actual rs-fMRI data will be identified by their cluster numbers (i.e., IMF1-4 refer to IMF cluster 1–4).

The IMF frequency clusters obtained from long-TR and short-TR data acquisitions are highly similar, as shown by the frequency groupings identified in **Figures 5A,B** – at a group level, there were no significant differences between the two TRs for any of the IMFs. However, the fractional IMF amplitudes are less consistent across different TRs, as shown in **Figures 5C,D**. In particular, IMF4 (the frequency cluster with the lowest mean frequency) is a consistently greater contributor to total spectral power in short-TR data sets. However, once again, the differences are not statistically significant.

In **Figure 6**, we show the spatial distribution of the fractional contributions of each VMD-derived IMF to the total spectral power of the rs-fMRI signal. The equivalent maps are shown for CEEMD-based IMFs as well. Note that for CEEMD as well, 4 IMF clusters were identified within the range of 0.01–0.25 Hz, confirming previous findings by Qian et al. (2015). However, due to the aforementioned decreasing spectral resolution with increasing IMF frequency exhibited by CEEMD, the frequency ranges of the CEEMD IMF clusters, listed below, are not directly comparable to those of VMD.

- CEEMD IMF1: 0.12–0.23 Hz
- CEEMD IMF2: 0.05–0.12 Hz
- CEEMD IMF3: 0.025–0.05 Hz
- CEEMD IMF4: 0.01–0.025 Hz

For both VMD and CEEMD results, maps of fractional spectral power were averaged across all subjects for each IMF, and overlaid on a cortical surface. IMF4, which is associated with the lowest frequency, is markedly elevated in the occipital lobe, as reflected by VMD results (**Figure 6b**). This is consistent with the CEEMD results (**Figure 6a**). IMF1 and 2, associated with the highest frequencies, were elevated in the temporal lobe and the frontal/limbic cortices, respectively. These are not clearly seen in CEEMD-derived IMFs. It is important to note that the CEEMD-derived IMF frequency ranges were as follows: IMF1: 0.12–0.23 Hz, IMF2: 0.05–0.10 Hz, IMF3: 0.025–0.05 Hz, IMF4: 0.01–0.025 Hz. These 4 IMF groupings were chosen to best match those of the VMD groupings.

Frequency Dependence of Network Organization

In **Figure 7**, we show strong RSN correlation patterns in areas that are part of the motor and control networks (indices 1–20), visual network (indices 43–60) and the medial-temporal network (indices 80–90). These results, based on the conventionally band-pass filtered rs-fMRI signal (to 0.01–0.08 Hz), are consistent with existing literature (Zhang and Li, 2014; Qian et al., 2015).

In **Figure 8**, we compare the RSN topology derived from VMD with those based on the 4 IMFs in comparable frequency ranges obtained using CEEMD. We can see that the highest correlations are found using IMF4, followed by IMF3, while no strong patterns were seen for IMFs 1 and 2. Moreover, IMFs 3 and 4 were associated with correlation matrices that most resemble that of the conventionally band-pass filtered signal (**Figure 7**), but not in IMF 1 and 2. Even in IMFs 3 and 4, the values of the correlations are much lower than those from band-pass filtering. However, the values are comparable to those obtained based on CEEMD. In fact, we note that the highest agreement between VMD and CEEMD results can be seen in IMF 4 (**Figure 8B**, $r = 0.79$), and secondarily in IMF 1 (**Figure 8H**, $r = 0.58$), the lowest and highest frequencies, respectively.

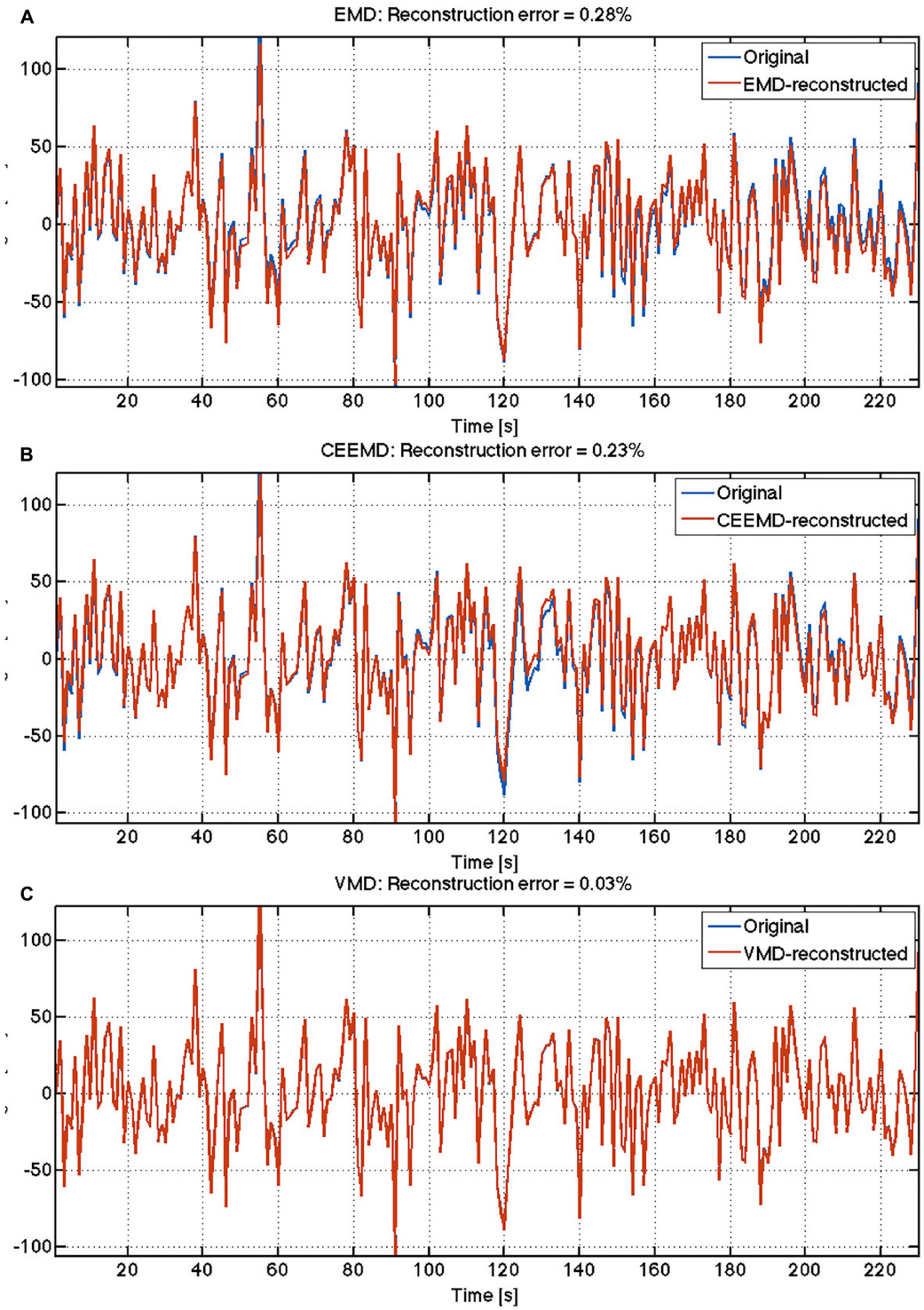

FIGURE 2 | Comparison of reconstruction accuracy of rs-fMRI time series: The reconstruction errors are indicated for each algorithm: **(A)** EMD; **(B)** CEEMD; **(C)** VMD.

In **Figure 9**, we repeat the comparison, substituting CEEMD with band-pass filtered versions of the rs-fMRI data, with each band-pass filter range determined based on VMD derivations of IMF frequency ranges. The conventional RSN topology can be observed across all band-passed frequencies (the top-left, middle and bottom-right areas of the matrix corresponding to

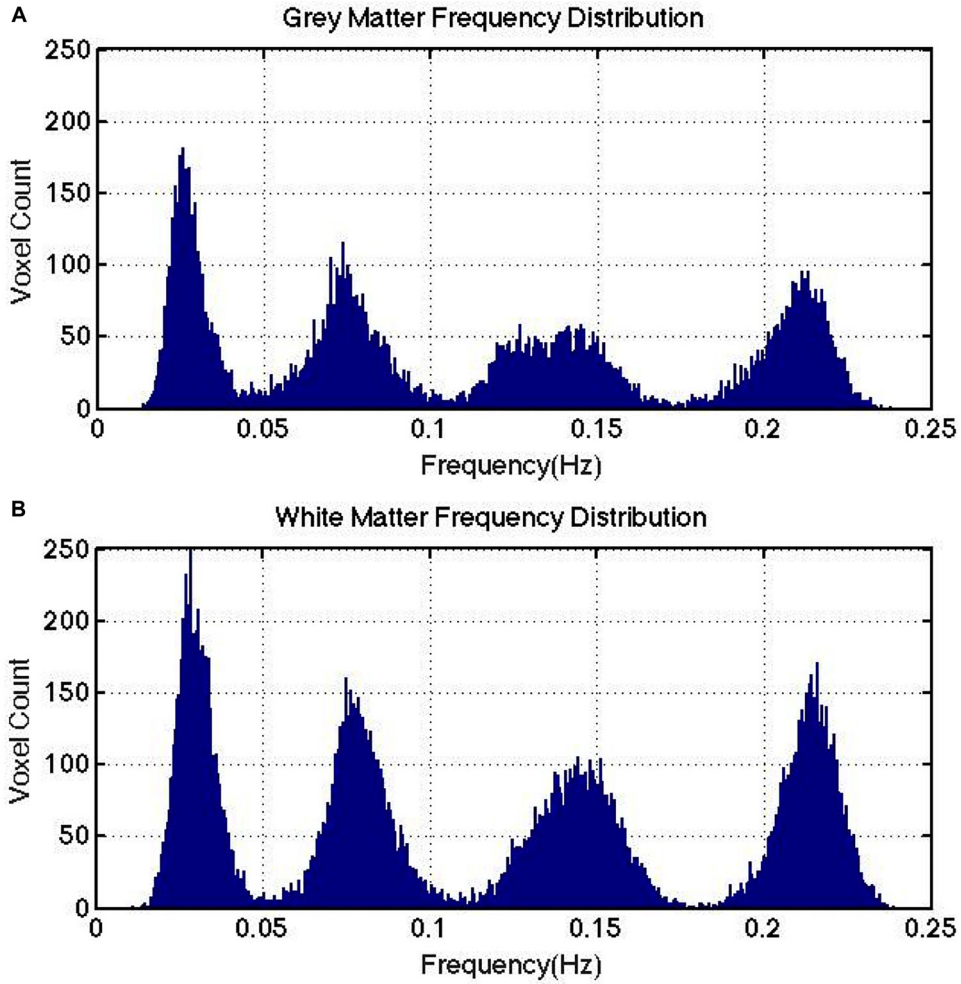

FIGURE 3 | IMF frequency cluster distributions computed for a representative subject. Gray matter **(A)** and white matter **(B)** are shown to exhibit similar frequency clusters. Note that there is no direct link between the number of IMFs targeted for at the VMD stage and the number of IMF frequency clusters detected at the clustering stage.

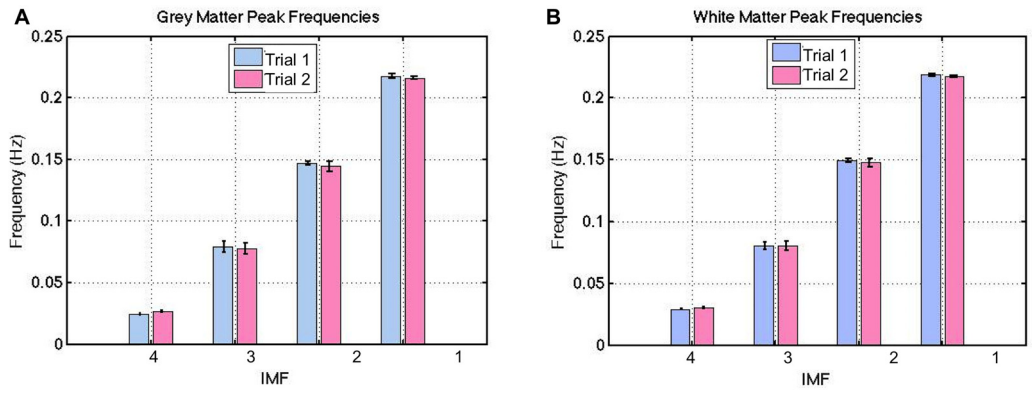

FIGURE 4 | Between-session reproducibility of IMF frequency estimations. These frequencies were highly reproducible, with a ICC of 0.99 for both gray **(A)** and white matter **(B)**. The error bars indicate the standard deviations across all subjects.

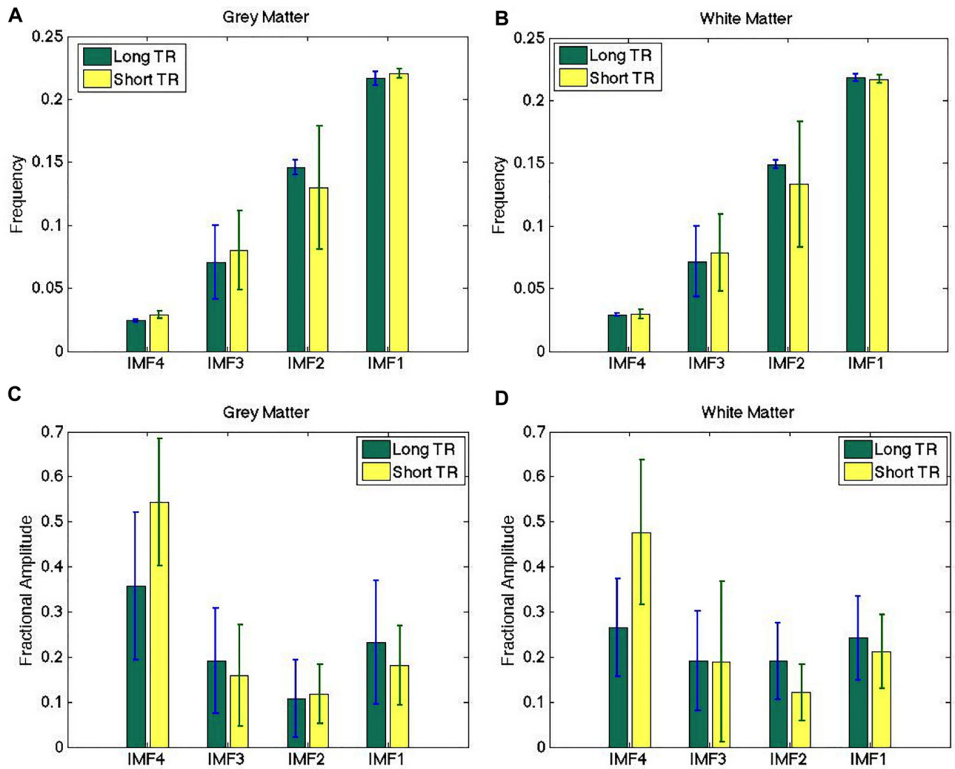

FIGURE 5 | Comparison of IMF frequency **(A,B)** and fractional amplitude estimates **(C,D)** across different sampling rates. The IMF frequency groupings obtained from long-TR and short-TR data acquisitions are highly similar, although the fractional IMF amplitudes are less consistent across different TRs. There are no significant differences between the estimates obtained from the two data sets. The error bars indicate the standard deviations across all subjects.

the sensorimotor, visual and default-mode network, respectively), although it is most prominent at the lowest frequency. While this trend of decreasing correlation with increasing frequency is consistent with findings from VMD, the strengths of the correlations in VMD are markedly lower than those found using band-pass filtering. We also notice that the similarities (**Figures 9B,D,F,H**) are lower than observed between VMD and CEEMD results.

DISCUSSION

In studying the spectral properties of the rs-fMRI signal, there is an increasing desire to use data-driven methods rather than band-pass filtering to decipher frequency content (Niazy et al., 2011; Qian et al., 2015). The main differences between methods based intrinsic-modal decomposition and those based on band-pass filtering are: (1) results and interpretations of band-pass filtering are sensitive to the shape of the band-pass filter; (2) band-pass filtering is sensitive to non-linearity in the signal, such as introduced when the signal is non-stationary. The latter is particularly the case in rs-fMRI, affecting the oscillatory validity of band-pass filtered rs-fMRI signal components.

Our work is novel in the following aspects: (1) instead of relying on the assumption that our data-driven method accurately decomposes the modes of the signal, we test this accuracy using rs-fMRI-informed simulations; (2) we not only compared the findings from short-TR acquisitions with those based on conventional acquisitions (TR = 2 s), but also assessed the reproducibility of these results for both scenarios; (3) instead of defining the rs-fMRI spectral information by broad frequency ranges (up to >1 Hz), we specifically target the frequency range typically used in functional-connectivity analyses (<0.25 Hz).

Our primary findings are: (1) the rs-fMRI signal within the 0.01–0.25 Hz range can be consistently characterized by four intrinsic modal clusters (frequency clusters), centered at 0.028, 0.080, 0.15, and 0.22 Hz, respectively; (2) these frequency clusters were highly reproducible, and independent of rs-fMRI data sampling rate; (3) not all frequencies were associated with equivalent RSN topology, in contrast to previous findings.

Intrinsic Frequencies of the rs-fMRI Signal

In this work, we demonstrate that as expected, compared to the previously used EMD and CEEMD techniques, VMD resulted in less inter-modal mixing as well as minimal modal spreading (**Figure 1**). When applied to rs-fMRI data, we demonstrate high reconstruction accuracy when using VMD-derived IMFs relative to the alternatives (EMD and CEEMD). We also see that VMD is able to decompose fMRI signals in a reproducible

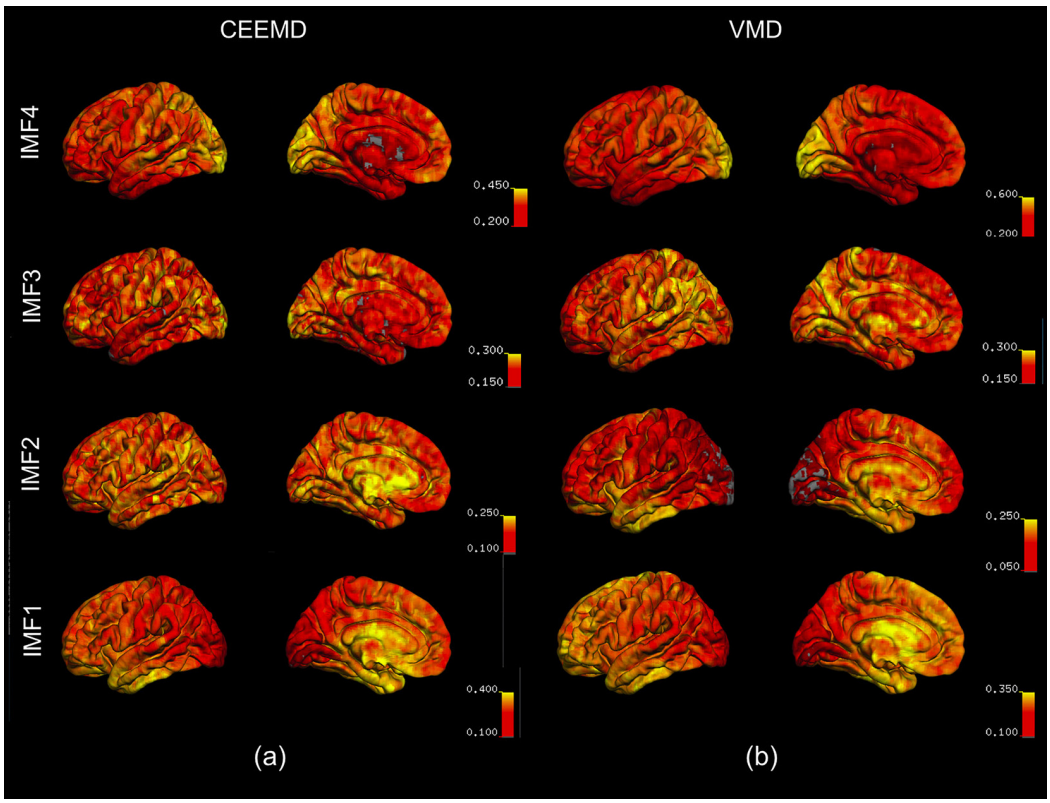

FIGURE 6 | Spatial distribution of the fractional contributions of each IMF to the total spectral power of the rs-fMRI signal. The maps were averaged across all subjects for each IMF, and overlaid on a cortical surface. IMF4, which is associated with the lowest frequency, is markedly elevated in the occipital lobe, as reflected by VMD results **(b)**. This is consistent with the CEEMD results **(a)**. IMF1 and 2, associated with the highest frequencies, are elevated in the temporal lobe and the frontal/limbic cortices, respectively. These are not clearly seen in CEEMD-derived IMFs.

manner, given the small variability associated with each IMF frequency across 8 subjects. Interestingly, we found that both gray and white matter of the healthy brain are characterized by IMF clusters centered at the frequencies of 0.028, 0.080, 0.15, and 0.23 Hz, identifiable in all of our subjects. While all brain voxels exhibited these frequencies, the contribution of each to the total signal power varied spatially (**Figure 6**). In the literature, a similar clustering of IMF frequencies across brain voxels has been observed previously using EMD (Song et al., 2014) and CEEMD (Qian et al., 2015), although the previously reported center frequencies were 0.02, 0.04, 0.08, and 0.17 Hz, respectively. This difference is likely driven by the higher degree of mode spreading in the higher-frequency IMFs that is inherent in CEEMD, as described in the sections "Introduction" and "Results."

When we used short-TR acquisitions (TR on the scale of 300 ms) (Niazy et al., 2011; Kalcher et al., 2014) to reduce respiratory and cardiac aliasing in the frequency range of interest, our findings of these IMF cluster frequencies did not change. Moreover, we acquired two trials of rs-fMRI data per subject, within the same scan session. To our best knowledge, no previous study has examined the reproducibility of intrinsic mode functions derived from rs-fMRI data, nor did any study examine the TR sensitivity of the decompositions. The frequency clusters we identified were highly reproducible across fMRI trials, and insensitive to the TR used (**Figure 5**), strengthening our confidence in the potential biological relevance of our findings.

Possible Interpretations of Intrinsic rs-fMRI Frequencies

Our current data do not permit us to conclusively pinpoint the physiological source(s) of these frequencies, although we may refer to independent evidence of physiological oscillatory signatures.

IMF4, being at the lowest frequency, contributed the most to the overall signal power. This is in general agreement with findings by Kalcher et al. (2014), who nonetheless examined a different set of frequency bands (i.e., < 0.1 Hz, 0.1–0.25 Hz, 0.25–0.75 Hz, and 0.75–1.4 Hz). It has been well established that within the 0.01–0.25 Hz frequency range, low-frequency cardiac-rate variations and respiratory-volume variations are observable near 0.01 Hz and 0.036 Hz in fMRI data, respectively. Therefore, it is probable that IMF4 (range: 0.021–0.031 Hz) is associated with these phenomena. Indeed, the high power contribution of IMF4 to the occipital region (**Figure 6**) is consistent with previous reports on the amplitude of rs-fMRI BOLD signal modulation

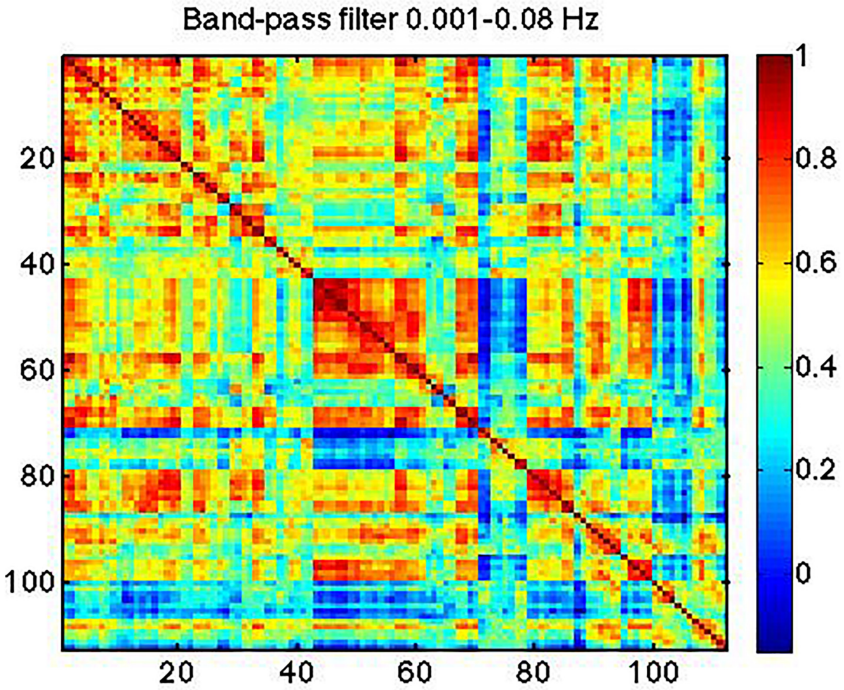

FIGURE 7 | Typical correlation matrix based on the rs-fMRI signal within 0.001–0.08 Hz.

by respiratory variability (Chang and Glover, 2009a; Tong et al., 2011; Golestani et al., 2015). Moreover, the contribution of IMF4 to the overall power is the only fraction that is lower in white matter than in gray matter (**Figures 5C,D**), in agreement with recent findings by Tong et al. (2016), although the difference is not statistically significant. However, the effects of these different physiological variances could not be distinguished from one another, potentially due to oscillatory variations across different tissue locations (Chang and Glover, 2009a; Golestani et al., 2015). Moreover, while we may expect the short-TR data to exhibit lower IMF4 amplitude than long-TR data due to the enhanced ability for physiological nose removal, it is unclear which IMF the physiological signal would be aliased into in the long-TR data. At the maximum sampling frequency of 0.25 Hz, such noise sources could equally alias into IMF3. Indeed, such is the case in the gray matter, albeit the difference between short- and long-TR not statistically significant.

The frequency ranges of IMF3 (0.063–0.098 Hz, peaking at 0.080 Hz) and IMF2 (0.13–0.17 Hz, peaking at 0.15 Hz) have both been associated with low-frequency vascular oscillations (Tong and Frederick, 2014; Hocke et al., 2016; Tong et al., 2016). A major source of these vascular oscillations is vasomotion (Intaglietta, 1990; Rivadulla et al., 2011). Vasomotion has long been observed in the BOLD signal (Kiviniemi et al., 2000; Cordes et al., 2001), and refers to a spontaneous oscillation in the diameter of primarily pre-capillary vessels (Cooper et al., 1966) that propagates through the entire vasculature but does not influence cognitive processes. Vasomotion is associated with oscillations in red blood-cell velocity (Biswal and Hudetz, 1996) and modulates local blood flow (Morita et al., 1994; Biswal and Hudetz, 1996; Aalkjaer et al., 2011). In particular, initially observed in superficial blood vessels at around 0.1 Hz (Mayhew et al., 1996; Meyer et al., 2003; Murphy et al., 2013), vasomotion's main frequency signature has been consistent between the animal (Mayhew et al., 1996; Bernardi, 1997; Haddock et al., 2002; Meyer et al., 2003) and human subcutaneous endothelium (Kvernmo et al., 1999, 1998).

The origins of vasomotion observed in fMRI could be caused by oscillations in both vascular diameter (Intaglietta, 1990; Biswal and Hudetz, 1996) and blood oxygenation (Biswal and Hudetz, 1996; Nikulin et al., 2014). Until recently, there have not been fMRI-based measurements of vasomotion in the human brain. Rayshubskiy et al. (2014) were able to measure sinusoids at (∼0.1 Hz near using intraoperative optical intrinsic-signal imaging and preoperative fMRI near the same pial veins of awake humans. However, an added challenge of *in vivo* isolation of vasomotion is that vasomotion frequency may in fact be dependent on vascular size, increasing with decrease vessel size (Intaglietta, 1990; Harrison and Cai, 2003). This, coupled with the fact that frequencies below 0.1 Hz (clusters IMF3 and IMF4) have typically revealed robust brain-network patterns, suggests that the effects of vasomotion may be embodied in IMF2. In support of the closer neuronal relevance of IMF3, we note that the regions of the highest fractional power distribution by IMF3 are the superior parietal, posterior cingulate and precuneus regions (**Figure 6**), coinciding with regions of high resting neuronal activity determined using positron-emission tomography (Raichle, 2011).

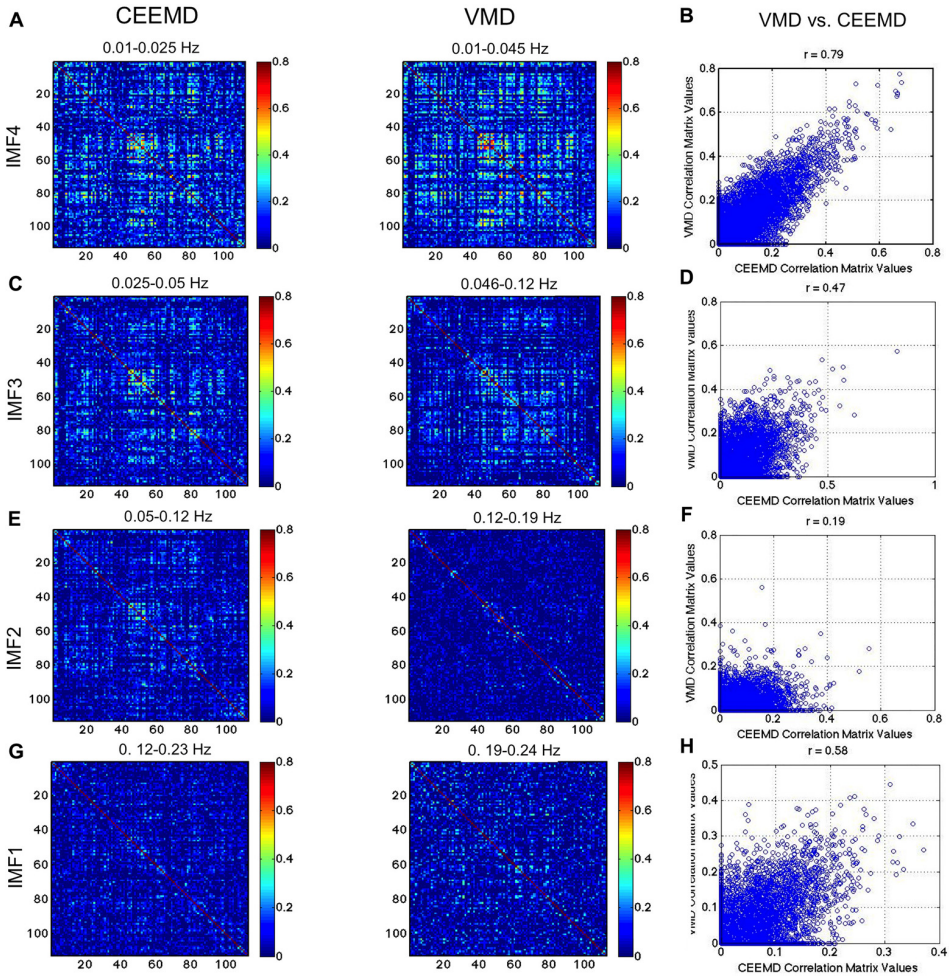

FIGURE 8 | Comparison of VMD with CEEMD RSN-matrix topology. IMFs 4, 3, 2, and 1 are represented in **(A)**, **(B)**, **(C)**, and **(D)**, respectively. The VMD and CEEMD IMFs are in comparable frequency ranges. The highest agreement between VMD and CEEMD results are seen in IMF 4 (r = 0.79), and secondarily in IMF 1 (r = 0.58), the lowest and highest frequencies, respectively. Note that the maximum displayed correlations value has been reduced from 1 to 0.8 for display purposes.

At very high frequencies (IMF1), the fractional spectral power is second only to the contribution of IMF4 (very low frequencies), as shown in **Figure 5**. This frequency band (0.20–0.24 Hz, peaking at 0.21 Hz) has previously been associated with head motion (Razavi et al., 2008). Although motion was corrected in the preprocessing pipeline, the effect of motion cannot be completely removed (Faraji-Dana et al., 2016a,b). In the case of the long-TR data, this frequency may also be associated with aliased cardiac pulsations, although this theory is refuted by the fact that IMF1 is equally strong in short-TR and long-TR data sets. The functional significance of IMF1 will need to be interpreted in the context of network-related features.

Frequency Dependence of Network Organization

We found that the functional connectivity patterns of RSNs are dependent on frequency and that not all IMFs reveal the same connectivity patterns, contrary to previous reports (Niazy et al., 2011; Qian et al., 2015). The connectivity-matrix patterns found in IMF 3 and 4 (**Figure 7**) were most similar to those from the 0.01–0.08 Hz band-passed signal (**Figure 8**), and were not seen in the higher frequency range (IMF 1 and 2). This is expected and is likely to reflect differences in biological significance of high- and low-frequency signals as described earlier.

Our findings echo those of Song et al. (2014), who found cortical RSNs to be best represented in low-frequency oscillations (<0.05 Hz). While both IMF clusters 3 and 4 demonstrated visible RSN connectivity-matrix patterns (**Figures 8A,B**), IMF4 was associated with the highest signal power and highest correlation. The fact that IMF4 is also most likely to contain low-frequency physiological contributions supports previous findings that physiological processes are stable (Birn, 2012) and can equally generate highly robust connectivity-matrix patterns (Chang and Glover, 2009b). This is an important point to consider in

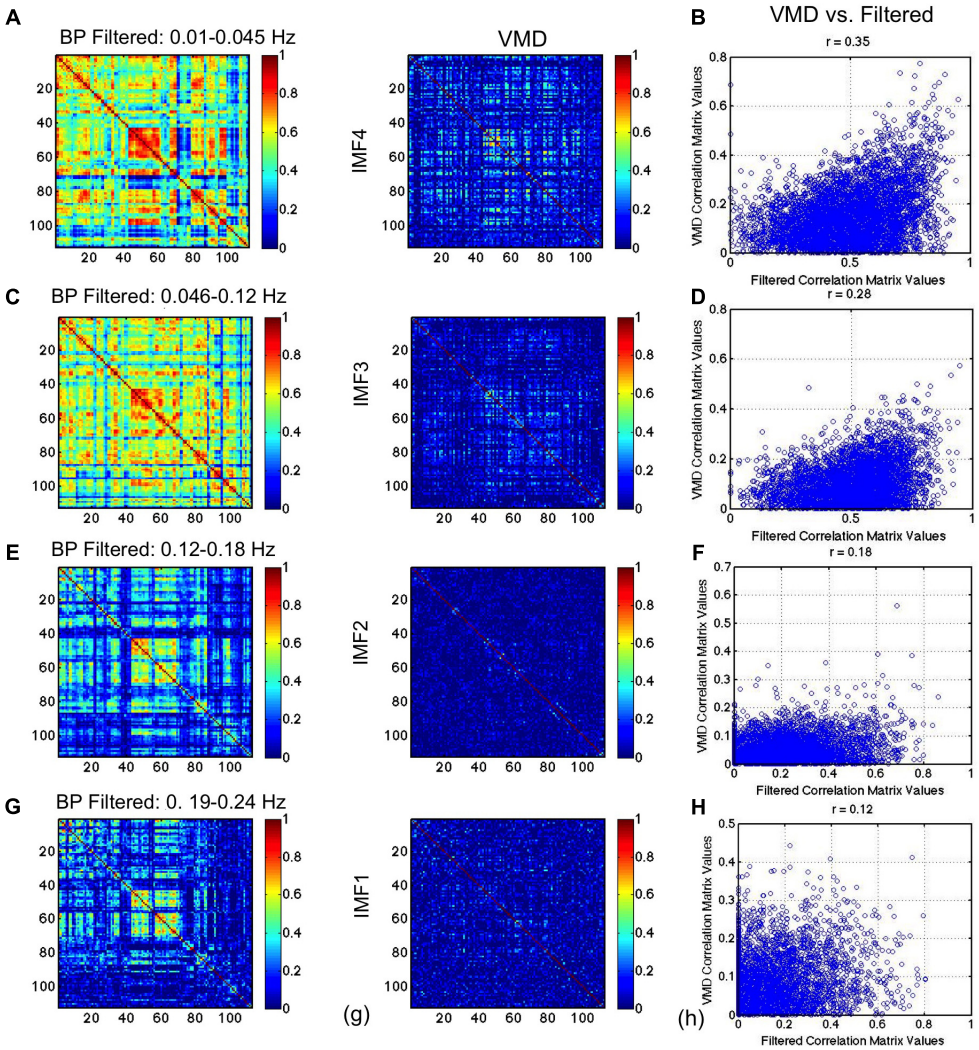

FIGURE 9 | Comparison of VMD RSN-matrix topology with results of band-pass filtering. IMFs 4, 3, 2, and 1 are represented in **(A)**, **(B)**, **(C)**, and **(D)**, respectively. Each band-pass filter range determined based on VMD derivations of IMF frequency ranges. The conventional RSN topology can be observed across all band-passed frequencies, although it is most prominent at the lowest frequency. While this trend of decreasing correlation with increasing frequency is consistent with findings from VMD, the strengths of the correlations in VMD are markedly lower than those found using band-pass filtering.

interpreting the quality of RSN results based on strength and reproducibility alone.

However, our findings contrast previous findings that RSNs are a broadband phenomenon (Niazy et al., 2011; Qian et al., 2015). These previous findings are in line with band-pass filtering results (**Figure 9**), whereby similar connectivity patterns are observed across all frequency bands. Nonetheless, previous work has also demonstrated the frequency dependence of task-fMRI-based brain networks (Baria et al., 2011). Moreover, our results are also corroborated by near-infrared optical connectivity measures in the resting state (Sasai et al., 2011), whereby long-range and local connections were associated with distinct frequencies within the 0.009–0.1 Hz range.

As, we demonstrated significant mode mixing using EMD and CEEMD (**Figure 1**), we argue this effect could have resulted in the similarities between IMFs that were previously reported. The same logic may explain why band-pass filtered maps were similar across frequency bands, as IMFs are difficult to isolate using such filtering methods. Notwithstanding, the similarity of the IMF1 connectivity matrices obtained through VMD and CEEMD (**Figure 8A**) despite their different frequency bands, serves to cross validate previous findings against our findings at low frequencies. Lastly, we are unclear as to the reason the correlations values corresponding to VMD are much lower than those based on band-pass filtering (**Figure 9**).

On average (across the group), the functional connectivity values found with the VMD and CEEMD are lower than found with conventional bandpass filtering. This is to be expected, signal bands produced by BPF always have the same frequency ranges,

but IMFs do not always have the same frequency ranges, and can vary from subject to subject in that regard. This variability can reflect in inter-subject variations in connectivity strength, as exemplified in the **Appendix Figure A4**.

Limitations

In this work, we focused on the use of the empirical model decomposition (EMD) family of methods, and more specifically, on the use of the VMD method to provide estimates of intrinsic modes while avoiding mode mixing. In general, EMD has long been used for investigating the frequency composition of biological signals that are non-stationary. Compared to prevalent techniques such as independent-component analysis (ICA), EMD has the advantage of being able to operate on individual signals instead relying on multiple measurements. Furthermore, the focus on EMD is "intrinsic frequencies" instead of statistical independence, more directly addressing our main focus. Nevertheless, a combination of EMD and ICA may be investigated in our future work.

In adopting VMD, the main thrust of our work is to reduce the spectral overlapping in previous works. Our choice of IMFs is driven by precision and reproducibility, which may be a strength and a limitation, depending on whether the intrinsic modes are expected to be reproducible. Such assumptions have been used broadly in the rs-fMRI field, but requires further dissection. While the motivation for using VMD (and EMD in general) is the non-stationarity of the rs-fMRI signal, the ground-truth testing was done using simulated stationary signals. As it was unclear what alternative noise model would be appropriate for such a simulation (where the ground truth signal vs. noise distributions are unknown in rs-fMRI data), we used white noise. While this may be a limitation, such an approach provided us with a clear way to evaluate the techniques – if a given technique could not faithfully reconstruct a stationary signal, its performance on a non-stationary signal could be no better than presented. Although we have identified the frequency cluster IMF3 as most representative of neutrally relevant BOLD, both by frequency and by spatial contribution, we are not able, in the current study, to provide direct experimental verification. Likewise, we are unable to determine the amount of physiological contributions to IMF4, which is deemed most representative of respiratory and cardiac effects using the current data. In future studies, we will involve physiological monitoring during the rs-fMRI sessions. This will be augmented by the use of simultaneous EEG-fMRI to capture neural fluctuations as well as blood-oxygenation effects, ideally in the presence of stimuli that can modulate baseline cerebral metabolism. Furthermore, the use phase locking is also an effective tool for estimating the sources of the IMFs and their interplay (Pfurtscheller et al., 2017), given sufficient SNR.

Furthermore, while we determined that the cluster IMF2 is most likely associated with low-frequency vascular oscillations (or vasomotion), the central frequency of IMF2 is 0.15 Hz, deviating from the typically reported to be 0.1 Hz in surface vessels. Furthermore, we did not find any observable vascular networks based on specific frequencies in the fMRI signal. While we have evidence to believe the frequency of vasomotion increases with decreasing diameter (Intaglietta, 1990), our ability to isolate smaller blood vessels is limited by the spatial resolution of the fMRI acquisition and by the BOLD effect itself. One possibility for targeting this issue is to repeat these measurements in conjunction with independent monitoring of subcutaneous vasomotion as well as vascular stimuli that can modulate vasomotion amplitude.

Finally, in this study, we do not examine network properties such as the differences between local and long-range connections in our study of RSN frequency dependence. The intention of our current work is to establish the validity of our decomposition procedure, and a comprehensive examination of the frequency dependence of multiple network metrics will be part of our future work.

DATA AVAILABILITY

The datasets generated for this study are available on request to the corresponding author.

ETHICS STATEMENT

This study was approved by the Baycrest Research Ethics Board. All subjects provided informed written consent.

AUTHOR CONTRIBUTIONS

NY contributed to 90% of the analysis and 30% of the writing. NO contributed to 10% of the analysis. JC contributed to 70% of the analysis and writing.

FUNDING

This research was supported by the Natural Sciences and Engineering Council of Canada (NSERC FGPIN# 418443 to JC and NSERC Undergraduate Research Awards to NY and NO), the Canadian Institutes of Health Research (CIHR: FRN# 126164 to JC), and the Sandra Rotman Foundation.

ACKNOWLEDGMENTS

We thank Prof. Stephen Smith (Oxford) for helpful discussions on the manuscript.

SUPPLEMENTARY MATERIAL

The Supplementary Material for this article can be found online at: https://www.frontiersin.org/articles/10.3389/fnins.2019.00900/full#supplementary-material

REFERENCES

Aalkjaer, C., Boedtkjer, D., and Matchkov, V. (2011). Vasomotion - what is currently thought? *Acta Physiol.* 202, 253–269. doi: 10.1111/j.1748-1716.2011.02320.x

Baria, A. T., Baliki, M. N., Parrish, T., and Apkarian, A. V. (2011). Anatomical and functional assemblies of brain bold oscillations. *J. Neurosci.* 31, 7910–7919. doi: 10.1523/JNEUROSCI.1296-11.2011

Bernardi, L. (1997). Reduction of 0.1 Hz microcirculatory fluctuations as evidence of sympathetic dysfunction in insulin-dependent diabetes. *Cardiovasc. Res.* 34, 185–191. doi: 10.1016/s0008-6363(97)00017-5

Birn, R. M. (2012). The role of physiological noise in resting-state functional connectivity. *Neuroimage* 62, 864–870. doi: 10.1016/j.neuroimage.2012.01.016

Birn, R. M., Smith, M. A., Jones, T. B., and Bandettini, P. A. (2008). The respiration response function: the temporal dynamics of fMRI signal fluctuations related to changes in respiration. *Neuroimage* 40, 644–654. doi: 10.1016/j.neuroimage.2007.11.059

Biswal, B. B., and Hudetz, A. G. (1996). Synchronous oscillations in cerebrocortical capillary red blood cell velocity after nitric oxide synthase inhibition. *Microvasc. Res.* 52, 1–12. doi: 10.1006/mvre.1996.0039

Chang, C., and Glover, G. H. (2009a). Effects of model-based physiological noise correction on default mode network anti-correlations and correlations. *Neuroimage* 47, 1448–1459. doi: 10.1016/j.neuroimage.2009.05.012

Chang, C., and Glover, G. H. (2009b). Relationship between respiration, end-tidal CO2, and bold signals in resting-state fMRI. *Neuroimage* 47, 1381–1393. doi: 10.1016/j.neuroimage.2009.04.048

Cooper, R., Crow, H. J., Walter, W. G., and Winter, A. L. (1966). Regional control of cerebral vascular reactivity and oxygen supply in man. *Brain Res.* 3, 174–191. doi: 10.1016/0006-8993(66)90075-8

Cordes, D., Haughton, V. M., Arfanakis, K., Carew, J. D., Turski, P. A., Moritz, C. H., et al. (2001). Frequencies contributing to functional connectivity in the cerebral cortex in "resting-state" data. *AJNR Am. J. Neuroradiol.* 22, 1326–1333.

Dragomiretskiy, K., and Zosso, D. (2014). Variational mode decomposition. *IEEE Trans. Signal Process.* 62, 531–544.

Faraji-Dana, Z., Tam, F., Chen, J. J., and Graham, S. J. (2016a). A robust method for suppressing motion-induced coil sensitivity variations during prospective correction of head motion in fMRI. *Magn. Reson. Imaging* 34, 1206–1219. doi: 10.1016/j.mri.2016.06.005

Faraji-Dana, Z., Tam, F., Chen, J. J., and Graham, S. J. (2016b). Interactions between head motion and coil sensitivity in accelerated fMRI. *J. Neurosci. Methods* 270, 46–60. doi: 10.1016/j.jneumeth.2016.06.005

Feinberg, D. A., Moeller, S., Smith, S. M., Auerbach, E., Ramanna, S., Glasser, M. F., et al. (2010). Multiplexed echo planar imaging for sub-second whole brain fMRI and fast diffusion imaging. *PLoS One* 5:e15710. doi: 10.1371/journal.pone.0015710

Fischl, B., and Dale, A. M. (2000). Measuring the thickness of the human cerebral cortex from magnetic resonance images. *Proc. Natl. Acad. Sci. U.S.A.* 97, 11050–11055. doi: 10.1073/pnas.200033797

Fischl, B., Sereno, M. I., Tootell, R. B., and Dale, A. M. (1999). High-resolution intersubject averaging and a coordinate system for the cortical surface. *Hum. Brain Mapp.* 8, 272–284. doi: 10.1002/(sici)1097-0193(1999)8:4<272::aid-hbm10>3.0.co;2-4

Fischl, B., van der Kouwe, A., Destrieux, C., Halgren, E., Segonne, F., Salat, D. H., et al. (2004). Automatically parcellating the human cerebral cortex. *Cereb. Cortex* 14, 11–22. doi: 10.1093/cercor/bhg087

Golestani, A. M., Chang, C., Kwinta, J. B., Khatamian, Y. B., and Chen, J. J. (2015). Mapping the end-tidal CO2 response function in the resting-state BOLD fMRI signal: spatial specificity, test–retest reliability and effect of fMRI sampling rate. *Neuroimage* 104, 266–277. doi: 10.1016/j.neuroimage.2014.10.031

Haddock, R. E., Hirst, G. D. S., and Hill, C. E. (2002). Voltage independence of vasomotion in isolated irideal arterioles of the rat. *J. Physiol.* 540, 219–229. doi: 10.1113/jphysiol.2001.013698

Harrison, D. G., and Cai, H. (2003). Endothelial control of vasomotion and nitric oxide production. *Cardiol. Clin.* 21, 289–302. doi: 10.1016/s0733-8651(03)00073-0

Hocke, L. M., Tong, Y., Lindsey, K. P., de, B., and Frederick, B. (2016). Comparison of peripheral near-infrared spectroscopy low-frequency oscillations to other denoising methods in resting state functional MRI with ultrahigh temporal resolution. *Magn. Reson. Med.* 76, 1697–1707. doi: 10.1002/mrm.26038

Huang, N. E., Shen, Z., Long, S. R., Wu, M. C., Shih, H. H., Zheng, Q., et al. (1998). The empirical mode decomposition and the hilbert spectrum for nonlinear and non-stationary time series analysis. *Proc. R. Soc. Lond. A Math. Phys. Sci.* 454, 903–905.

Intaglietta, M. (1990). Vasomotion and flowmotion: physiological mechanisms and clinical evidence. *Vasc. Med.* 1, 101–112. doi: 10.1177/1358836x9000100202

Jenkinson, M., Bannister, P., Brady, M., and Smith, S. (2002). Improved optimization for the robust and accurate linear registration and motion correction of brain images. *Neuroimage* 17, 825–841. doi: 10.1006/nimg.2002.1132

Jenkinson, M., and Smith, S. (2001). A global optimisation method for robust affine registration of brain images. *Med. Image Anal.* 5, 143–156. doi: 10.1016/S1361-8415(01)00036-6

Kalcher, K., Boubela, R. N., Huf, W., Bartova, L., Kronnerwetter, C., Derntl, B., et al. (2014). The spectral diversity of resting-state fluctuations in the human brain. *PLoS One* 9:e93375. doi: 10.1371/journal.pone.0093375

Kiviniemi, V., Jauhiainen, J., Tervonen, O., Paakko, E., Oikarinen, J., Vainionpaa, V., et al. (2000). Slow vasomotor fluctuation in fMRI of anesthetized child brain. *Magn. Reson. Med.* 44, 373–378. doi: 10.1002/1522-2594(200009)44:3<373::aid-mrm5>3.3.co;2-g

Kvernmo, H. D., Stefanovska, A., Bracic, M., Kirkeboen, K. A., and Kvernebo, K. (1998). Spectral analysis of the laser doppler perfusion signal in human skin before and after exercise. *Microvasc. Res.* 56, 173–182. doi: 10.1006/mvre.1998.2108

Kvernmo, H. D., Stefanovska, A., Kirkeboen, K. A., and Kvernebo, K. (1999). Oscillations in the human cutaneous blood perfusion signal modified by endothelium-dependent and endothelium-independent vasodilators. *Microvasc. Res.* 57, 298–309. doi: 10.1006/mvre.1998.2139

Lahmiri, S. (2014). Comparative study of ECG signal denoising by wavelet thresholding in empirical and variational mode decomposition domains. *Healthc. Technol. Lett.* 1, 104–109. doi: 10.1049/htl.2014.0073

Liu, W., Cao, S., and Chen, Y. (2016). Applications of variational mode decomposition in seismic time-frequency analysis. *Geophysics* 81, V365–V378.

Mark, C. I., Mazerolle, E. L., and Chen, J. J. (2015). Metabolic and vascular origins of the BOLD effect: implications for imaging pathology and resting-state brain function. *J. Magn. Reson. Imaging* 42, 231–246. doi: 10.1002/jmri.24786

Mayhew, J. E., Askew, S., Zheng, Y., Porrill, J., Westby, G. W., Redgrave, P., et al. (1996). Cerebral vasomotion: a 0.1-Hz fluctuation in reflected light imaging of neural activity. *Neuroimage* 4, 183–193. doi: 10.1006/nimg.1996.0069

Mert, A. (2016). ECG feature extraction based on the bandwidth properties of variational mode decomposition. *Physiol. Meas.* 37, 530–543. doi: 10.1088/0967-3334/37/4/530

Meyer, M. F., Rose, C. J., Hülsmann, J. O., Schatz, H., and Pfohl, M. (2003). Impaired 0.1-Hz vasomotion assessed by laser doppler anemometry as an early index of peripheral sympathetic neuropathy in diabetes. *Microvasc. Res.* 65, 88–95. doi: 10.1016/s0026-2862(02)00015-8

Morita, Y., Hardebo, J. E., and Bouskela, E. (1994). Influence of cerebrovascular parasympathetic nerves on resting cerebral blood flow, spontaneous vasomotion, autoregulation, hypercapnic vasodilation and sympathetic vasoconstriction. *J. Auton. Nerv. Syst.* 49, S9–S14.

Murphy, K., Birn, R. M., and Bandettini, P. A. (2013). Resting-state fMRI confounds and cleanup. *Neuroimage* 80, 349–359. doi: 10.1016/j.neuroimage.2013.04.001

Niazy, R. K., Xie, J., Miller, K., Beckmann, C. F., and Smith, S. M. (2011). Spectral characteristics of resting state networks. *Brain Res.* 193, 259–276. doi: 10.1016/b978-0-444-53839-0.00017-x

Nikolaou, F., Orphanidou, C., Papakyriakou, P., Murphy, K., Wise, R. G., and Mitsis, G. D. (2016). Spontaneous physiological variability modulates dynamic functional connectivity in resting-state functional magnetic resonance imaging. *Philos. Trans. A Math. Phys. Eng. Sci.* 374:20150183. doi: 10.1098/rsta.2015.0183

Nikulin, V. V., Fedele, T., Mehnert, J., Lipp, A., Noack, C., Steinbrink, J., et al. (2014). Monochromatic ultra-slow (˜0.1Hz) oscillations in the human electroencephalogram and their relation to hemodynamics. *Neuroimage* 97, 71–80. doi: 10.1016/j.neuroimage.2014.04.008

Pfurtscheller, G., Schwerdtfeger, A., Brunner, C., Aigner, C., Fink, D., Brito, J., et al. (2017). Distinction between neural and vascular bold oscillations and

intertwined heart rate oscillations at 0.1 Hz in the resting state and during movement. *PLoS One* 12:e0168097. doi: 10.1371/journal.pone.0168097

Qian, L., Zhang, Y., Zheng, L., Shang, Y., Gao, J.-H., and Liu, Y. (2015). Frequency dependent topological patterns of resting-state brain networks. *PLoS One* 10:e0124681. doi: 10.1371/journal.pone.0124681

Raichle, M. E. (2011). The restless brain. *Brain Connect.* 1, 3–12. doi: 10.1089/brain.2011.0019

Rayshubskiy, A., Wojtasiewicz, T. J., Mikell, C. B., Bouchard, M. B., Timerman, D., Youngerman, B. E., et al. (2014). Direct, intraoperative observation of ˜0.1 Hz hemodynamic oscillations in awake human cortex: implications for fMRI. *Neuroimage* 87, 323–331. doi: 10.1016/j.neuroimage.2013.10.044

Razavi, M., Eaton, B., Paradiso, S., Mina, M., Hudetz, A. G., and Bolinger, L. (2008). Source of low-frequency fluctuations in functional MRI signal. *J. Magn. Reson. Imaging* 27, 891–897. doi: 10.1002/jmri.21283

Rivadulla, C., Labra, D. C., Grieve, L. K., and Cudeiro, J. (2011). Vasomotion and neurovascular coupling in the visual thalamus in vivo. *PLoS One* 6:e28746. doi: 10.1371/journal.pone.0028746

Salvador, R., Suckling, J., Schwarzbauer, C., and Bullmore, E. (2005). Undirected graphs of frequency-dependent functional connectivity in whole brain networks. *Philos. Trans. R Soc. Lond. B Biol. Sci.* 360, 937–946. doi: 10.1098/rstb.2005.1645

Sasai, S., Homae, F., Watanabe, H., and Taga, G. (2011). Frequency-specific functional connectivity in the brain during resting state revealed by NIRS. *Neuroimage* 56, 252–257. doi: 10.1016/j.neuroimage.2010.12.075

Segonne, F., Dale, A. M., Busa, E., Glessner, M., Salat, D., Hahn, H. K., et al. (2004). A hybrid approach to the skull stripping problem in MRI. *Neuroimage* 22, 1060–1075. doi: 10.1016/j.neuroimage.2004.03.032

Segonne, F., Pacheco, J., and Fischl, B. (2007). Geometrically accurate topology-correction of cortical surfaces using nonseparating loops. *IEEE Trans. Med. Imaging* 26, 518–529. doi: 10.1109/TMI.2006.887364

Sled, J. G., Zijdenbos, A. P., and Evans, A. C. (1998). A non-parametric method for automatic correction of intensity non-uniformity in MRI data. *IEEE Trans. Med. Imaging* 17, 87–97. doi: 10.1109/42.668698

Song, X., Zhang, Y., and Liu, Y. (2014). Frequency specificity of regional homogeneity in the resting-state human brain. *PLoS One* 9:e86818. doi: 10.1371/journal.pone.0086818

Tong, Y., and Frederick, B. D. (2014). Studying the spatial distribution of physiological effects on bold signals using ultrafast fMRI. *Front. Hum. Neurosci.* 8:196. doi: 10.3389/fnhum.2014.00196

Tong, Y., Hocke, L. M., Lindsey, K. P., Erdo∂an, S. B., Vitaliano, G., Caine, C. E., et al. (2016). Systemic low-frequency oscillations in bold signal vary with tissue type. *Front. Neurosci.* 10:313. doi: 10.3389/fnins.2016.00313

Tong, Y., Lindsey, K. P., and De, B. F. B. (2011). Partitioning of physiological noise signals in the brain with concurrent near-infrared spectroscopy and fMRI. *J. Cereb. Blood Flow Metab.* 31, 2352–2362. doi: 10.1038/jcbfm.2011.100

Tripathy, R. K., Sharma, L. N., and Dandapat, S. (2016). Detection of shockable ventricular arrhythmia using variational mode decomposition. *J. Med. Syst.* 40:79. doi: 10.1007/s10916-016-0441-5

Tzourio-Mazoyer, N., Landeau, B., Papathanassiou, D., Crivello, F., Etard, O., Delcroix, N., et al. (2002). Automated anatomical labeling of activations in SPM using a macroscopic anatomical parcellation of the MNI MRI single-subject brain. *Neuroimage* 15, 273–289. doi: 10.1006/nimg.2001.0978

Wu, Z., and Huang, N. E. (2009). Ensemble empirical mode decomposition: a noise-assisted data analysis method. *Adv. Adapt. Data Anal.* 01, 1–41. doi: 10.1142/s1793536909000047

Xiao, Q., Li, J., Bai, Z., Sun, J., Zhou, N., and Zeng, Z. (2016). A small leak detection method based on VMD adaptive de-noising and ambiguity correlation classification intended for natural gas pipelines. *Sensors* 16:2116. doi: 10.3390/s16122116

Yeh, J.-R., Lin, T.-Y., Chen, Y., Sun, W.-Z., Abbod, M. F., and Shieh, J.-S. (2012). Investigating properties of the cardiovascular system using innovative analysis algorithms based on ensemble empirical mode decomposition. *Comput. Math. Methods Med.* 2012:943431. doi: 10.1155/2012/943431

Zhang, S., and Li, C. (2014). Functional clustering of the human inferior parietal lobule by whole-brain connectivity mapping of resting-state functional magnetic resonance imaging signals. *Brain Connect.* 4, 53–69. doi: 10.1089/brain.2013.0191

Zhang, Y., Brady, M., and Smith, S. (2001). Segmentation of brain MR images through a hidden Markov random field model and the expectation-maximization algorithm. *IEEE Trans. Med. Imaging* 20, 45–57. doi: 10.1109/42.906424

Zou, Q. H., Zhu, C. Z., Yang, Y., Zuo, X. N., Long, X. Y., Cao, Q. J., et al. (2008). An improved approach to detection of amplitude of low-frequency fluctuation (ALFF) for resting-state fMRI: fractional ALFF. *J. Neurosci. Methods* 172, 137–141. doi: 10.1016/j.jneumeth.2008.04.012

Conflict of Interest Statement: The authors declare that the research was conducted in the absence of any commercial or financial relationships that could be construed as a potential conflict of interest.

frontiers in Neuroscience

MINI REVIEW
published: 23 October 2019
doi: 10.3389/fnins.2019.01136

Origins of the Resting-State Functional MRI Signal: Potential Limitations of the "Neurocentric" Model

Hanbing Lu[1], Saul Jaime[2,3] and Yihong Yang[1]*

[1] Neuroimaging Research Branch, National Institute on Drug Abuse (NIDA) Intramural Research Program, National Institutes of Health, Bethesda, MD, United States, [2] Division of Pharmacology & Toxicology, College of Pharmacy, The University of Texas at Austin, Austin, TX, United States, [3] Waggoner Center for Alcohol & Addiction Research, The University of Texas at Austin, Austin, TX, United States

Resting-state functional connectivity (rsFC) is emerging as a research tool for systems and clinical neuroscience. The mechanism underlying resting-state functional MRI (rsfMRI) signal, however, remains incompletely understood. A widely held assumption is that the spontaneous fluctuations in blood oxygenation level-dependent (BOLD) signal reflect ongoing neuronal processes (herein called "neurocentric" model). In support of this model, evidence from human and animal studies collectively reveals that the spatial synchrony of spontaneously occurring electrophysiological signal recapitulates BOLD rsFC networks. Two recent experiments from independent labs designed to specifically examine neuronal origins of rsFC, however, suggest that spontaneously occurring neuronal events, as assessed by multiunit activity or local field potential (LFP), although statistically significant, explain only a small portion (∼10%) of variance in resting-state BOLD fluctuations. These two studies, although each with its own limitations, suggest that the spontaneous fluctuations in rsfMRI, may have complex cellular origins, and the "neurocentric" model may not apply to all brain regions.

Keywords: resting-state MRI, functional connectivity, MUA, LFP, BOLD

OPEN ACCESS

Edited by:
Garth John Thompson, ShanghaiTech University, China

Reviewed by:
Wen-Ju Pan, Emory University, United States
Mauro DiNuzzo, Independent Researcher, Rome, Italy

****Correspondence:***
Hanbing Lu
luha@mail.nih.gov

Specialty section:
This article was submitted to Brain Imaging Methods, a section of the journal Frontiers in Neuroscience

Received: *06 July 2019*
Accepted: *08 October 2019*
Published: *23 October 2019*

Citation:
Lu H, Jaime S and Yang Y (2019) Origins of the Resting-State Functional MRI Signal: Potential Limitations of the "Neurocentric" Model. Front. Neurosci. 13:1136. doi: 10.3389/fnins.2019.01136

INTRODUCTION

Noise exists in all measurements. The significance of spatially coherent "noise" in blood oxygenation level-dependent (BOLD) signal was appreciated in a seminal paper by Biswal et al. (1995), who revealed temporal synchrony in human sensorimotor system. As similar results accumulated for other brain systems (Greicius et al., 2003; Beckmann et al., 2005; Fox et al., 2005; Seeley et al., 2007; Habas et al., 2009; Raichle, 2011), in particular the discovery of the "default mode network (DMN) (Raichle et al., 2001; Greicius et al., 2003)," a concept emerged suggesting that the persistent, correlated spontaneous activity between brain regions [functional connectivity (FC)], initially thought to be noise (i.e., random error) in BOLD measurements, is in fact a meaningful source of information, reflecting a fundamental feature of brain functional organization (Raichle, 2009). Further supporting this view, a recent study defined depression subtypes based on FC patterns; the resulting biotypes predicted individuals' responsiveness to transcranial magnetic stimulation (TMS) therapy, pointing to clinical potentials of resting-state functional connectivity (rsFC) (Greicius, 2008).

A cornerstone assumption in rsFC is that the ongoing, spontaneously occurring synchrony among brain areas reflects the inherent functional organization of the neural network. The definition of "neural network" in the context of resting-state functional MRI (rsfMRI), however, remains vague. Data accumulated over the past decade, more or less, lend support to the hypothesis that synchronized neuronal activity underlies the BOLD FC. Recent animal studies from two independent labs designed to directly test this hypothesis, however, suggest cautious interpretation of the data (see below). As rsFC becomes increasingly used as a research tool for basic and clinical neuroscience, a thorough understanding of its physiological basis and origin becomes essential and critical.

In the spirit of stimulating scientific debate, in this *opinionated* mini-review, we will start with methodological considerations that we deem important in elucidating the physiological basis of BOLD fluctuations, followed by critical review of recent evidence that supports neuronal origin of the rsfMRI signal, herein we will call it "neurocentric" model; we will then present several lines of recent evidence that appear divergent from this concept. Finally, we will bring forward testable hypotheses from a perspective of BOLD signal transduction. Extensive review of this subject can be found elsewhere (Leopold and Maier, 2012; Lu and Stein, 2013). We will focus on progress in the past 5 years.

METHODOLOGICAL CONSIDERATIONS

Brain's electrical signals can be measured at different scales, from intra- and extra-cellular recording, local field potential (LFP) to electroencephalogram and magnetoencephalography (Buzsáki et al., 2012). The LFP signal has been shown to be correlated with BOLD response to a task (e.g., visual stimulation) (Lauritzen, 2001; Logothetis et al., 2001). By extension, LFP is often used to investigate the electrophysiological correlate of the rsfMRI signal (Lu et al., 2007; Mantini et al., 2007; He et al., 2008; Shmuel and Leopold, 2008; de Pasquale et al., 2010; Schölvinck et al., 2010; Pan et al., 2011; Wang et al., 2012; Hutchison et al., 2015; Shi et al., 2019). The underlying assumption is that BOLD fluctuation in the resting-state and the evoked BOLD response to a task manipulation share the same signal transduction mechanism. As will be discussed later in this article, this assumption may require a careful assessment.

On the other hand, BOLD signal results from the mismatch between blood flow and oxygen metabolism (Fox and Raichle, 1986; Kim and Ogawa, 2012), indirectly reflecting neuronal activity. Thus, LFP and BOLD signals are two fundamentally different readouts of brain activity. We have previously argued that (Lu and Stein, 2013), in order for the fMRI signal to be considered as a surrogate of a specific neuronal physiological measure, at a minimum, the following criteria should be met: (i) the temporal fluctuations of the electrical and the BOLD signals should remain correlated, and such correlation should be persistent across brain states; (ii) the spatially correlated patterns from electrical signal should recapitulate that from BOLD signal across brain states; and (iii) each pattern should be unique to each network. To meet the above three criteria, it would appear necessary that both types of signals should be recorded simultaneously on the same subject. Due to substantial technical difficulties and for practical reasons, to the best of our knowledge, most published studies employed experimental designs that partially meet these criteria, and thus should be considered critically.

SPATIALLY CORRELATED PATTERNS OF THE ELECTRICAL SIGNAL RECAPITULATE BOLD RSFC

Perhaps the most intuitive evidence to support the "neurocentric" model is the distinct spatial patterns of the electrical signal, which bear remarkable similarity to BOLD FC (Fukushima et al., 2012; Liu et al., 2015; Hacker et al., 2017; Kucyi et al., 2018; Shi et al., 2019). Data from voltage sensitive dye (VSD) fluorescent imaging appear particularly compelling (Mohajerani et al., 2010). Conventional electrophysiological recording necessitates reference and ground electrodes; and there is more or less "volume conduction effect" (Kajikawa and Schroeder, 2011). Confounds from these technical aspects lead to certain degrees of ambiguity in terms of spatial localization of the electrical signal. This could potentially introduce artifactual inter-regional correlation. VSD imaging measures membrane potential changes, avoiding these confounds entirely.

In a mouse model with a large craniotomy preparation, Mohajerani et al. (2010) simultaneously recorded VSD signals in both hemispheres. Strong oscillations exist in spontaneous ongoing VSD signals, which mirror LFP signal in the low frequency band (3–6 Hz). The oscillations in homotopic cortical regions were correlated; discrete peaks characterized each region. Awake and urethane anesthetized mice showed similar inter-hemispheric synchrony. Furthermore, they found that, in genetically acallosal mice, the interhemispheric synchrony was significantly reduced, a finding similar to rsFC studies in humans (Lowe et al., 1997; Quigley et al., 2003; Johnston et al., 2008). The localized synchrony patterns in homotopic cortical regions recorded using VSD are strikingly similar to rsFC reported in rodent fMRI literature (Lu et al., 2007, 2012; Pawela et al., 2008; Zhao et al., 2008; Hutchison et al., 2010; Liang et al., 2011; Magnuson et al., 2014; Gozzi and Schwarz, 2016), including sensory networks in the forelimb region, whisker cortex, motor cortex etc. Notably, the retrosplenial cortex, a major component of the DMN (Lu et al., 2012), was also depicted in the VSD data.

Spatially correlated patterns between electrophysiological signals recorded in areas of classic FC networks were also observed in humans (He et al., 2008; Hacker et al., 2017; Kucyi et al., 2018). In these studies, patients underwent neurosurgical electrocorticography (ECoG) electrode implantation. Based on clinical needs, each study had a unique cohort of patients with electrodes covering specific brain regions. Taken together, the electrodes covered sensory motor network (SMN), dorsal attention network (DAN), DMN, and frontoparietal control system (FPC). In general, these studies found a higher within network correlation than between network correlation, and there is a spatial correspondence between ECoG and BOLD FC

patterns. Less consistent was which frequency band contributes the most to the within and between network correlations. For example, Hacker et al. (2017) showed that the correspondence appeared to be frequency band-specific: theta (4–8 Hz) band-limited power (BLP) correspondence appeared stronger in the DMN and FPC, while theta (8–12 Hz) BLP correspondence was stronger in the SMN and DAN. They also found that gamma BLP correspondence was commonly observed throughout the brain. Kucyi et al. (2018) reported that correlation patterns in high frequency broadband (70–170 Hz) power were consistent during wakeful rest and sleep; although similar correlation pattern exist in lower-frequency (1–70 Hz) power, but the spatial specificity and temporal consistency were inferior to higher frequency broadband power.

A recent study by Shi et al. (2019) recorded ECoG signal from the primary somatosensory cortex (areas 3b and 1) of anesthetized monkeys, and found that spontaneous fluctuations in low frequency LFP signal was the major contributor to resting-state LFP coherence. Furthermore, they reported that the temporal dynamics in BOLD FC behaved most similarly to the low frequency LFP coherence. These results are generally in line with the conclusions from studies in anesthetized rats (Lu et al., 2007, 2014; Pan et al., 2010; Magnuson et al., 2014). It is not clear whether the use of anesthesia in rats and monkeys played a role in the discrepancy mentioned above.

In summary, evidence from animals and humans collectively suggests a high degree of correspondence in spatial correlation patterns derived from electrophysiological recording and BOLD rsFC, it would appear tempting to conclude that the electrophysiological signal underlies BOLD rsFC. However, making this leap requires correspondence in temporal behavior of these two types of brain readouts, which necessitates simultaneous measurement of both types of signals. Unfortunately, two lines of evidence from simultaneously recorded electrophysiological and hemodynamic signals seem difficult to reconcile with the "neurocentric" model.

LFP–BOLD CORRELATION IS WEAK

We developed a simultaneous fMRI–electrophysiological recording technique (Jaime et al., 2018), and performed chronic repetitive recordings in rat striatum. The electrophysiological recording and BOLD data acquisition were coupled with pharmacological modulation of the well-defined dopaminergic pathway (**Figure 1A**). We found three distinct BOLD rsFC networks using the independent component analysis. These three networks are consistent with well-known three functional domains in rat striatum (Voorn et al., 2004). We thus implanted silicon-based microelectrode array (16 contacts) that covered the dorsolateral to ventral medial striatum (**Figures 1B,C**). With microinjection of alpha-amino-3-hydroxy-5-methyl-4-isoxazole propionic acid (AMPA) receptor agonist into the ventral tegmental area (VTA), we systematically modulated dopamine release and neuronal activity in the striatum, to which VTA dopamine neurons project most densely. As shown in **Figure 1D**, both the amplitude and the frequency of the striatal LFP signal were modulated. VTA AMPA microinjection significantly modulated FC only in the ventral striatum (nucleus accumbens) (**Figures 1E,F**), consistent with known neuroanatomy.

Concurrent LFP and BOLD signal recording allowed us to directly interrogate the temporal relationship of these two types of brain readouts. Perhaps the most unexpected finding is the low correlation between LFP and BOLD signal: although the LFP-BOLD time courses were statistically correlated, the average LFP-BOLD correlation was below 0.1 (**Figure 1G**). The correlation between gamma LFP and the fMRI signal was similar but opposite in sign (Jaime et al., 2017). These data suggest that spontaneous LFP fluctuations explain only a small portion of variance in BOLD fluctuations (Sumiyoshi et al., 2019).

The above observation by Jaime et al. (2017) is corroborated by a recent optical imaging study (Winder et al., 2017). In this study, Winder et al. (2017) applied intrinsic optical imaging to measure hemodynamic signal [total hemoglobin signal, reflecting cerebral blood volume (CBV)] while at the same time recording neuronal activity in the whisker barrel cortex of the awake, head-fixed mice. What made this study especially unique in the context of spontaneous brain activity was that they carefully monitored whisker and body movements. They found that spontaneous CBV changes in the absence of experimenter-delivered sensory input were largely driven by volitional whisker and body movements. During periods of "rest" when there was no experimenter-delivered sensory stimulation, volitional whisker and body movements, CBV signal was only weakly correlated with neural activity assessed with either gamma band LFP or multiunit activity (with an R^2 of about 0.1, **Figure 2**). They performed pharmacological manipulations to block local neural spiking, glutamatergic input and noradrenergic receptors, and found that spontaneous fluctuations in CBV and vessel diameter persisted, indicating that spontaneous CBV fluctuations may have a non-neuronal origin.

The results reported by Winder et al. (2017) are divergent from several recent optical studies (Matsui et al., 2011; Ma et al., 2016; Mateo et al., 2017). For example, Ma et al. (2016) reported that spontaneous CBV fluctuations highly correlated with ongoing neuronal activity as measured with GCaMP optical imaging. The reasons for this discrepancy are unknown, but one might speculate that the differential definition of "resting-state" may have played a role, an issue particularly relevant in studies employing awake animals. Ma et al. (2016) stated in their paper: "Awake mice were imaged head-fixed but positioned on a saucer wheel and were free to run during imaging. The motion of the wheel was monitored throughout imaging using a webcam synchronized with image acquisition. All periods of running were removed, and 'resting-state' epochs were defined as periods of at least 30 s of continuous rest." Over a duration of 30 s or more, a head-fixed awake mouse likely whisks volitionally (Winder et al., 2017). Ma et al. (2016) did not specifically state whether they had taken whisking behavior or fidgeting into account in their definition of the "resting-state."

Whisking is an important, albeit subtle, behavior in rodents. As pointed out by Sofroniew and Svoboda (2015): "rodents use their mechanosensitive whiskers for a diverse range of tactile behaviors such as navigation, object recognition, and social

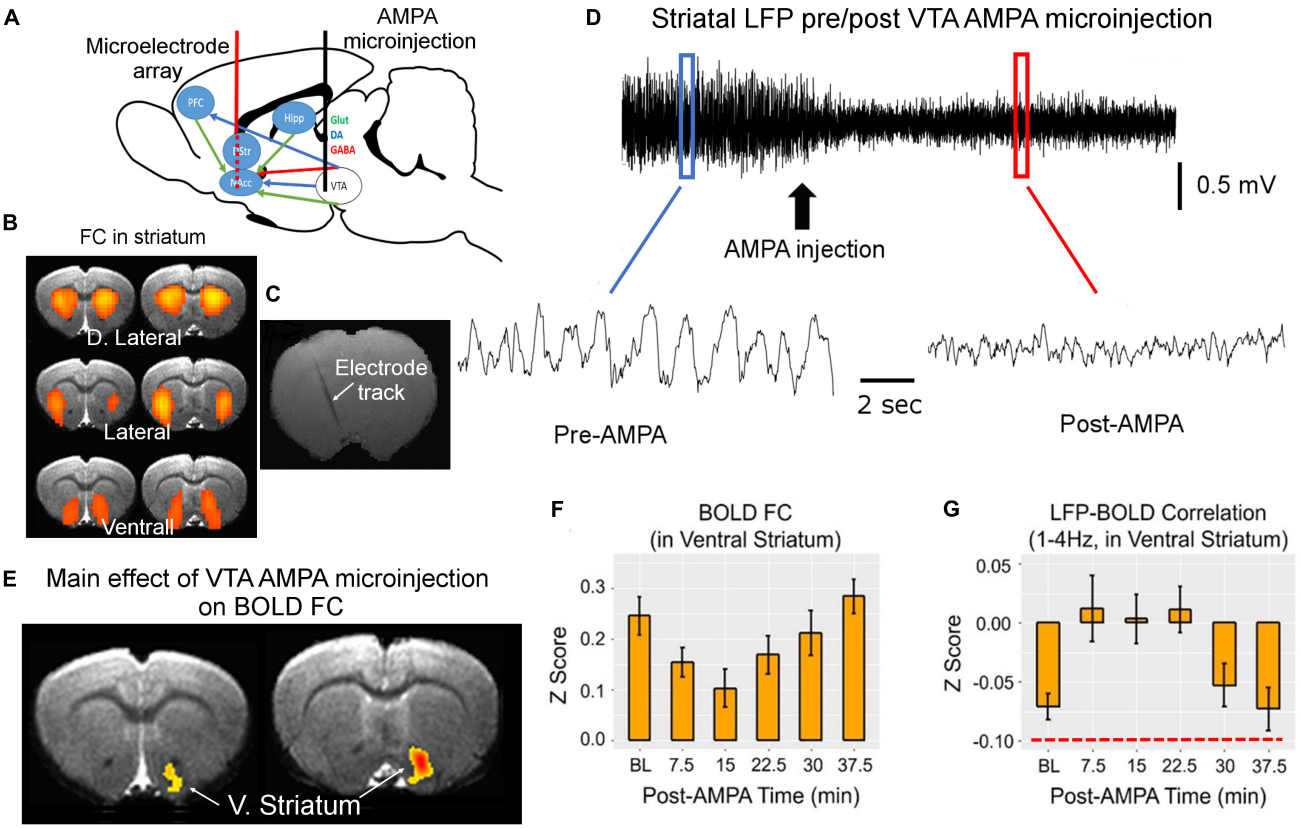

FIGURE 1 | MRI-compatible linear electrode array was implanted into the rat striatum covering the dorsolateral and ventrolateral domains **(A–C)**. These domains were identified based on the three bilateral rsFC network in rat striatum that correspond to the three functional domains of the rat striatum **(B)**. Alpha-amino-3-hydroxy-5-methyl-4-isoxazole propionic acid (AMPA) was injected into the ventral tegmental area (VTA) via a guide cannula to enhance the activity of VTA dopaminergic neurons, which project primarily to the ventral striatum, modulating striatal local field potential (LFP) signal **(D)**. The waveforms before and after AMPA injection were derived from the blue and red boxes, respectively. **(E,F)** The main effect of AMPA on BOLD functional connectivity (FC). **(G)** The effects of VTA AMPA microinjections LFP–BOLD correlation (corr.). Note the low correlation value in LFP–BOLD correlation, indicated by red dashed line in panel **(G)**. All maps are thresholded at $p < 0.05$ after correction for multiple comparisons. DA, dopamine; D. Striatum, dorsal striatum; V. Striatum, ventral striatum (nucleus accumbens); GABA, gamma-aminobutyric acid; Glut, glutamate; Hipp, hippocampus; NAcc, nucleus accumbens core; and PFC, prefrontal cortex (adapted with permission from the authors).

interactions. These animals move their whiskers in a purposive manner to locations of interest." Furthermore, whisking triggers cortical dynamics in many brain regions including S1, S2, M1, M2, PPC, thalamus, etc. (O'Connor et al., 2010; Sofroniew et al., 2015; Helmchen et al., 2018). Thus, the individual moments when a mouse volitionally whisks and fidgets should be treated as individual task events; both GCaMP and CBV recordings during these periods should be excluded for analyzing neuronal correlates of resting-state hemodynamic signal. Winder et al. (2017) showed that auditory, whisker stimulation and some volitional whisking events induced distinct hemodynamic responses – an observation appears compelling. Furthermore, Winder et al. (2017) showed that the high correlation between electrophysiological signal (MUA and LFP) was largely driven by these events, a point that warrants further exploration (see section "Technical Limitations"). Additionally, certain transgenic mouse lines are known to have aberrant firing patterns (Steinmetz et al., 2017); it is unknown whether the mouse line used by Ma et al. (2016) had normal basal cortical activity.

The neurophysiological basis of rsFC has been under debate for more than a decade. The debate has been framed in the context of "neurocentric" model. In support of this view, in the spatial domain, converging evidence from animals and human suggests that the interregional correlation patterns derived from electrophysiological recording recapitulate BOLD rsFC (Hacker et al., 2017; Kucyi et al., 2018).

Experiments designed to specifically test the "neurocentric" model only appeared in recent years (Matsui et al., 2011; Ma et al., 2016; Jaime et al., 2017; Mateo et al., 2017; Winder et al., 2017). The two independent studies (Jaime et al., 2017; Winder et al., 2017) employed concurrent electrophysiological recording and hemodynamic measurement, and found weak LFP–BOLD correlation. In particular, the study by Winder et al. (2017) suggests that hemodynamic signal may reflect a combination of potential sources, including behavior, local neural activity, and putatively non-neural processes, calling for careful definition of the "resting-state." This may be especially relevant in studies using animal models.

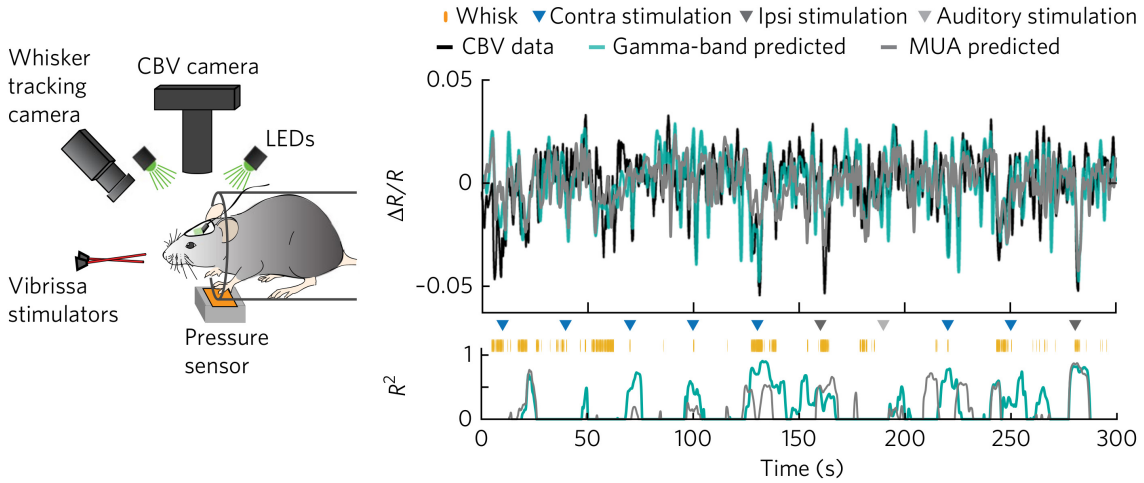

FIGURE 2 | Weak correlation between electrophysiological and hemodynamic signal during periods of "rest." **(Left)** Schematic of the experimental setup for optical imaging of intrinsic signal (the isosbestic point green light measures total hemoglobin signal, reflecting CBV). Animal's behavior and movement were dynamically monitored. **(Right)** Predictions of ongoing CBV for a single trial. **(Top)** Predictions by gamma-band (teal blue, R^2 = 0.29) and MUA-derived (gray, R^2 = 0.20) HRFs. **(Bottom)** Goodness-of-fit (R^2) for 8-s sliding windows. Colored triangles indicate sensory stimuli. Orange tick marks indicate volitional whisking events. Note that R^2 was low during the "rest." Here, the "rest" was defined as the periods absent of experimenter-delivered stimulation, fidgeting, and volitional whisking events (adapted with permission from the authors).

TECHNICAL LIMITATIONS

The weak correlation between ongoing neuronal activity and hemodynamic signals during the resting-state is somewhat unexpected, and is not in line with the "neurocentric" doctrine of rsfMRI. Several technical issues must be critically reviewed when interpreting this finding. Jaime et al. (2017) performed LFP and rsfMRI recordings in the striatum of anesthetized rats. The anesthetic regime, a combination of low dose isoflurane and dexmedetomdine, has been shown to preserve brain networks (Lu et al., 2012; Brynildsen et al., 2016). But LFP signals recorded with this regime are dominated by low frequency (delta) activity. It is unknown how the use of anesthetics affects neurovascular coupling, particularly in the resting-state. Additionally, the longitudinally implanted microelectrode array unavoidably degrades the quality of rsfMRI signal in voxels around the electrodes. Cytoarchitectonically, inhibitory medium spiny neurons represent 95% of neuronal cells in rat striatum, as opposed to in the neocortex where a majority of neurons are excitatory glutamatergic neurons (Kreitzer and Malenka, 2008). Several studies reported differential neurovascular coupling in the striatum than in the neocortex (Shih et al., 2009, 2012). Specifically, Shih et al. documented bilateral CBV decreases associated with enhanced neuronal activity in the caudate–putamen induced by unilateral noxious electrical stimulation, and that the activation of dopamine D_2 receptor played a role in this process (Chen et al., 2005). It is thus possible that finding in the striatum may not be generalizable to other brain regions.

The study by Winder et al. (2017) was performed in the neocortex of awake mice, and thus avoided the confounding effects from anesthesia. Nevertheless, they inserted Teflon-coated tungsten-wire stereotrode into the barrel cortex, which necessitated an invasive cranial window preparation, and in some experiments, a cannula was chronically implanted for pharmacological manipulations. Since an acute cranial window preparation likely causes certain degree of tissue insult, it is unknown whether the tissue insult arising from this procedure might have affected neurovascular coupling in the resting-state, although they were able to record robust hemodynamic response to whisker stimulation. In support of this argument, Hudetz et al. (1998) pointed out that spontaneous fluctuation in cerebral blood flow requires the preservation of the flow control system. The fluctuations are absent in focally ischemic cortical territories when the ischemia is severe.

POTENTIAL ROLES OF ASTROCYTE IN rsfMRI SIGNAL

The potential roles of astrocytes in rsfMRI have been largely ignored. Neurons and associated astrocytes are organized in large-scale synaptic and astrocytic networks. Complex signaling within and between these networks causes fluctuations in cerebral metabolic rate of oxygen ($CMRO_2$) and hemodynamic response (Attwell and Iadecola, 2002). The BOLD signal is vascular in origin, and ultimately relies on vasoactive substance release. Neuronal activity is known to cause the release of many vasoactive agents, including H^+, K^+, adenosine, arachidonic acid metabolites, nitric oxide (NO) etc. (Iadecola and Nedergaard, 2007). On the other hand, astrocytes are strategically positioned

between neuronal and vascular systems: astrocytes forms end-feet on capillaries and arterioles while having contacts with synapses (Mishra, 2017). Importantly, astrocytes are known to express many ion channels, receptors, transporters, and vesicles (Verkhratsky and Nedergaard, 2018). Indeed, astrocytic Ca^{2+} signaling has been shown to play an role in regulating neurovascular coupling (Zonta et al., 2003) and in controlling vessel tone (Rosenegger et al., 2015). Furthermore, several lines of evidence suggest that alterations in parenchymal vascular tone influence astrocytic Ca^{2+} activity and potentially neuronal activity as well, such that the "hemo-neural" hypothesis has been proposed (Moore and Cao, 2008; Kim et al., 2016). Modeling studies suggest that cyclic neuron-astrocyte cross talk could produce slow oscillations in BOLD signal (DiNuzzo et al., 2011; DiNuzzo, 2015). Thus, in addition to the "neurocentral" model, an alternative testable hypothesis could be that the spontaneous BOLD fluctuation is at least partially caused by spontaneous astrocyte activity. Additionally, the role of spontaneous vasomotion in spontaneous BOLD fluctuation may warrant further investigation.

Imaging of astrocytic activity has traditionally relied on fluorescent dyes (Mulligan and MacVicar, 2004; Scemes and Giaume, 2006; Schulz et al., 2012; Otsu et al., 2015). The development of transgenic mouse lines, viral vector targeting strategies and genetically encode Ca^{2+} indicators has made astrocyte-specific recording and manipulation more readily available (Biesecker et al., 2016; Poskanzer and Yuste, 2016; Takata et al., 2018). For example, using transgenic approaches, Takata et al. (2018) generated mice expressing channelrhodopsin specifically in neurons or in astrocytes, and measured BOLD response to astrocyte-specific optogenetic stimulation. They reported that optogenetic activation of astrocytes, in the absence of apparent neuronal modulation, evoked BOLD response. It is thus conceivable that spontaneous activity in astrocyte may cause spontaneous vasodilation and vasoconstriction, leading to variations in BOLD signal that are decoupled from spontaneous neural activity. Future experiments that combine optical readouts of neuronal and astrocytic calcium activities with hemodynamic measurement may shed light on the origins of rsfMRI signal.

AUTHOR CONTRIBUTIONS

All authors listed have made a substantial, direct and intellectual contribution to the work, and approved it for publication.

FUNDING

This work was supported by the NIDA Intramural Research Program, NIH.

REFERENCES

Attwell, D., and Iadecola, C. (2002). The neural basis of functional brain imaging signals. *Trends Neurosci.* 25, 621–625. doi: 10.1016/s0166-2236(02)02264-6

Beckmann, C., DeLuca, M., Devlin, J., and Smith, S. (2005). Investigations into resting-state connectivity using independent component analysis. *Philos. Trans. R. Soc. Lond. B Biol. Sci.* 360, 1001–1013. doi: 10.1098/rstb.2005.1634

Biesecker, K. R., Srienc, A. I., Shimoda, A. M., Agarwal, A., Bergles, D. E., Kofuji, P., et al. (2016). Glial cell calcium signaling mediates capillary regulation of blood flow in the retina. *J. Neurosci.* 36, 9435–9445. doi: 10.1523/JNEUROSCI.1782-16.2016

Biswal, B., Yetkin, F. Z., Haughton, V. M., and Hyde, J. S. (1995). Functional connectivity in the motor cortex of resting human brain using echo-planar MRI. *Magn. Reson. Med.* 34, 537–541. doi: 10.1002/mrm.1910340409

Brynildsen, J. K., Hsu, L. M., Ross, T. J., Stein, E. A., Yang, Y., and Lu, H. (2016). Physiological characterization of a robust survival rodent fMRI method. *Magn. Reson. Imaging* 35, 54–60. doi: 10.1016/j.mri.2016.08.010

Buzsáki, G. F., Anastassiou, C. A., and Koch, C. (2012). The origin of extracellular fields and currents–EEG, ECoG, LFP and spikes. *Nat. Rev. Neurosci.* 13, 407–420. doi: 10.1038/nrn3241

Chen, Y. C., Choi, J. K., Andersen, S. L., Rosen, B. R., and Jenkins, B. G. (2005). Mapping dopamine D2/D3 receptor function using pharmacological magnetic resonance imaging. *Psychopharmacology* 180, 705–715. doi: 10.1007/s00213-004-2034-0

de Pasquale, F., Della Penna, S., Snyder, A. Z., Lewis, C., Mantini, D., Marzetti, L., et al. (2010). Temporal dynamics of spontaneous MEG activity in brain networks. *Proc. Natl. Acad. Sci. U.S.A.* 107, 6040–6045. doi: 10.1073/pnas.0913863107

DiNuzzo, M. (2015). Isn't functional neuroimaging all about Ca2+ signaling in astrocytes? *J. Neurophysiol.* 114, 1353–1356. doi: 10.1152/jn.00826.2014

DiNuzzo, M., Gili, T., Maraviglia, B., and Giove, F. (2011). Modeling the contribution of neuron-astrocyte cross talk to slow blood oxygenation level-dependent signal oscillations. *J. Neurophysiol.* 106, 3010–3018. doi: 10.1152/jn.00416.2011

Fox, M., Snyder, A., Vincent, J., Corbetta, M., Van Essen, D., and Raichle, M. (2005). The human brain is intrinsically organized into dynamic, anticorrelated functional networks. *Proc. Natl. Acad. Sci. U.S.A.* 102, 9673–9678. doi: 10.1073/pnas.0504136102

Fox, P. T., and Raichle, M. E. (1986). Focal physiological uncoupling of cerebral blood flow and oxidative metabolism during somatosensory stimulation in human subjects. *Proc. Natl. Acad. Sci. U.S.A.* 83, 1140–1144. doi: 10.1073/pnas.83.4.1140

Fukushima, M., Saunders, R. C., Leopold, D. A., Mishkin, M., and Averbeck, B. B. (2012). Spontaneous high-gamma band activity reflects functional organization of auditory cortex in the awake macaque. *Neuron* 74, 899–910. doi: 10.1016/j.neuron.2012.04.014

Gozzi, A., and Schwarz, A. J. (2016). Large-scale functional connectivity networks in the rodent brain. *Neuroimage* 127, 496–509. doi: 10.1016/j.neuroimage.2015.12.017

Greicius, M. (2008). Resting-state functional connectivity in neuropsychiatric disorders. *Curr. Opin. Neurol* 21, 424–430. doi: 10.1097/WCO.0b013e328306f2c5

Greicius, M., Krasnow, B., Reiss, A., and Menon, V. (2003). Functional connectivity in the resting brain: a network analysis of the default mode hypothesis. *Proc. Natl. Acad. Sci. U.S.A.* 100, 253–258. doi: 10.1073/pnas.0135058100

Habas, C., Kamdar, N., Nguyen, D., Prater, K., Beckmann, C. F., Menon, V., et al. (2009). Distinct cerebellar contributions to intrinsic connectivity networks. *J. Neurosci.* 29, 8586–8594. doi: 10.1523/jneurosci.1868-09.2009

Hacker, C. D., Snyder, A. Z., Pahwa, M., Corbetta, M., and Leuthardt, E. C. (2017). Frequency-specific electrophysiologic correlates of resting state fMRI networks. *Neuroimage* 149, 446–457. doi: 10.1016/j.neuroimage.2017.01.054

He, B. J., Snyder, A. Z., Zempel, J. M., Smyth, M. D., and Raichle, M. E. (2008). Electrophysiological correlates of the brain's intrinsic large-scale functional architecture. *Proc. Natl. Acad. Sci. U.S.A.* 105, 16039–16044. doi: 10.1073/pnas.0807010105

Helmchen, F., Gilad, A., and Chen, J. L. (2018). Neocortical dynamics during whisker-based sensory discrimination in head-restrained mice. *Neuroscience* 368, 57–69. doi: 10.1016/j.neuroscience.2017.09.003

Hudetz, A. G., Biswal, B. B., Shen, H., Lauer, K. K., and Kampine, J. P. (1998). Spontaneous fluctuations in cerebral oxygen supply. An introduction. *Adv. Exp. Med. Biol.* 454, 551–559. doi: 10.1007/978-1-4615-4863-8_66

Hutchison, R. M., Hashemi, N., Gati, J. S., Menon, R. S., and Everling, S. (2015). Electrophysiological signatures of spontaneous BOLD fluctuations in macaque prefrontal cortex. *Neuroimage* 113, 257–267. doi: 10.1016/j.neuroimage.2015.03.062

Hutchison, R. M., Mirsattari, S. M., Jones, C. K., Gati, J. S., and Leung, L. S. (2010). Functional networks in the anesthetized rat brain revealed by independent component analysis of resting-state FMRI. *J. Neurophysiol.* 103, 3398–3406. doi: 10.1152/jn.00141.2010

Iadecola, C., and Nedergaard, M. (2007). Glial regulation of the cerebral microvasculature. *Nat. Neurosci.* 10, 1369–1376. doi: 10.1038/nn2003

Jaime, S., Cavazos, J. E., Yang, Y., and Lu, H. (2018). Longitudinal observations using simultaneous fMRI, multiple channel electrophysiology recording, and chemical microiontophoresis in the rat brain. *J. Neurosci. Methods* 306, 68–76. doi: 10.1016/j.jneumeth.2018.05.010

Jaime, S., Gu, H., Sadacca, B. F., Stein, E. A., Cavazos, J. E., Yang, Y., et al. (2017). Delta rhythm orchestrates the neural activity underlying the resting state BOLD signal via phase-amplitude coupling. *Cereb. Cortex* 29, 119–133. doi: 10.1093/cercor/bhx310

Johnston, J. M., Vaishnavi, S. N., Smyth, M. D., Zhang, D., He, B. J., Zempel, J. M., et al. (2008). Loss of resting interhemispheric functional connectivity after complete section of the corpus callosum. *J. Neurosci.* 28, 6453–6458. doi: 10.1523/JNEUROSCI.0573-08.2008

Kajikawa, Y., and Schroeder, C. E. (2011). How local is the local field potential? *Neuron* 72, 847–858. doi: 10.1016/j.neuron.2011.09.029

Kim, K. J., Ramiro Diaz, J. J., Iddings, A., and Filosa, J. A. (2016). Vasculo-neuronal coupling: retrograde vascular communication to brain neurons. *J. Neurosci.* 36, 12624–12639. doi: 10.1523/jneurosci.1300-16.2016

Kim, S. G., and Ogawa, S. (2012). Biophysical and physiological origins of blood oxygenation level-dependent fMRI signals. *J. Cereb. Blood Flow Metab.* 32, 1188–1206. doi: 10.1038/jcbfm.2012.23

Kreitzer, A. C., and Malenka, R. C. (2008). Striatal plasticity and basal ganglia circuit function. *Neuron* 60, 543–554. doi: 10.1016/j.neuron.2008.11.005

Kucyi, A., Schrouff, J., Bickel, S., Foster, B. L., Shine, J. M., and Parvizi, J. (2018). Intracranial electrophysiology reveals reproducible intrinsic functional connectivity within human brain networks. *J. Neurosci.* 38, 4230–4242. doi: 10.1523/JNEUROSCI.0217-18.2018

Lauritzen, M. (2001). Relationship of spikes, synaptic activity, and local changes of cerebral blood flow. *J. Cereb. Blood Flow Metab.* 21, 1367–1383. doi: 10.1097/00004647-200112000-00001

Leopold, D. A., and Maier, A. (2012). Ongoing physiological processes in the cerebral cortex. *Neuroimage* 62, 2190–2200. doi: 10.1016/j.neuroimage.2011.10.059

Liang, Z., King, J., and Zhang, N. (2011). Uncovering intrinsic connectional architecture of functional networks in awake rat brain. *J. Neurosci.* 31, 3776–3783. doi: 10.1523/JNEUROSCI.4557-10.2011

Liu, X., Yanagawa, T., Leopold, D. A., Fujii, N., and Duyn, J. H. (2015). Robust long-range coordination of spontaneous neural activity in waking, sleep and anesthesia. *Cereb. Cortex* 25, 2929–2938. doi: 10.1093/cercor/bhu089

Logothetis, N. K., Pauls, J., Augath, M., Trinath, T., and Oeltermann, A. (2001). Neurophysiological investigation of the basis of the fMRI signal. *Nature* 412, 150–157. doi: 10.1038/35084005

Lowe, M., Rutecki, P., Woodard, A., Turski, P., and Sorenson, J. (1997). Auditory cortex fMRI noise correlations in callosal agenesis. *Hum. Brain Mapp.* 5, S194.

Lu, H., and Stein, E. A. (2013). Resting state functional connectivity: its physiological basis and application in neuropharmacology. *Neuropharmacology* 84, 79–89. doi: 10.1016/j.neuropharm.2013.08.023

Lu, H., Wang, L., Rea, W. W., Brynildsen, J. K., Jaime, S., Zuo, Y., et al. (2014). Low- but not high-frequency LFP correlates with spontaneous BOLD fluctuations in rat whisker barrel cortex. *Cereb. Cortex* 26, 683–694. doi: 10.1093/cercor/bhu248

Lu, H., Zou, Q., Gu, H., Raichle, M. E., Stein, E. A., and Yang, Y. (2012). Rat brains also have a default mode network. *Proc. Natl. Acad. Sci. U.S.A.* 109, 3979–3984. doi: 10.1073/pnas.1200506109

Lu, H., Zuo, Y., Gu, H., Waltz, J. A., Zhan, W., Scholl, C. A., et al. (2007). Synchronized delta oscillations correlate with the resting-state functional MRI signal. *Proc. Natl. Acad. Sci. U.S.A.* 104, 18265–18269. doi: 10.1073/pnas.0705791104

Ma, Y., Shaik, M. A., Kozberg, M. G., Kim, S. H., Portes, J. P., Timerman, D., et al. (2016). Resting-state hemodynamics are spatiotemporally coupled to synchronized and symmetric neural activity in excitatory neurons. *Proc. Natl. Acad. Sci. U.S.A.* 113, E8463–E8471. doi: 10.1073/pnas.1525369113

Magnuson, M. E., Thompson, G. J., Pan, W. J., and Keilholz, S. D. (2014). Effects of severing the corpus callosum on electrical and BOLD functional connectivity and spontaneous dynamic activity in the rat brain. *Brain Connect.* 4, 15–29. doi: 10.1089/brain.2013.0167

Mantini, D., Perrucci, M. G., Del Gratta, C., Romani, G. L., and Corbetta, M. (2007). Electrophysiological signatures of resting state networks in the human brain. *Proc. Natl. Acad. Sci. U.S.A.* 104, 13170–13175. doi: 10.1073/pnas.0700668104

Mateo, C., Knutsen, P. M., Tsai, P. S., Shih, A. Y., and Kleinfeld, D. (2017). Entrainment of arteriole vasomotor fluctuations by neural activity is a basis of blood-oxygenation-level-dependent "resting-state" connectivity. *Neuron* 96, 936.e3–948.e3. doi: 10.1016/j.neuron.2017.10.012

Matsui, T., Tamura, K., Koyano, K. W., Takeuchi, D., Adachi, Y., Osada, T., et al. (2011). Direct comparison of spontaneous functional connectivity and effective connectivity measured by intracortical microstimulation: an fMRI study in macaque monkeys. *Cereb. Cortex* 21, 2348–2356. doi: 10.1093/cercor/bhr019

Mishra, A. (2017). Binaural blood flow control by astrocytes: listening to synapses and the vasculature. *J. Physiol.* 595, 1885–1902. doi: 10.1113/JP270979

Mohajerani, M. H., McVea, D. A., Fingas, M., and Murphy, T. H. (2010). Mirrored bilateral slow-wave cortical activity within local circuits revealed by fast bihemispheric voltage-sensitive dye imaging in anesthetized and awake mice. *J. Neurosci.* 30, 3745–3751. doi: 10.1523/JNEUROSCI.6437-09.2010

Moore, C. I., and Cao, R. (2008). The hemo-neural hypothesis: on the role of blood flow in information processing. *J. Neurophysiol.* 99, 2035–2047. doi: 10.1152/jn.01366.2006

Mulligan, S. J., and MacVicar, B. A. (2004). Calcium transients in astrocyte endfeet cause cerebrovascular constrictions. *Nature* 431, 195–199. doi: 10.1038/nature02827

O'Connor, D. H., Clack, N. G., Huber, D., Komiyama, T., Myers, E. W., and Svoboda, K. (2010). Vibrissa-based object localization in head-fixed mice. *J. Neurosci.* 30, 1947–1967. doi: 10.1523/JNEUROSCI.3762-09.2010

Otsu, Y., Couchman, K., Lyons, D. G., Collot, M., Agarwal, A., Mallet, J. M., et al. (2015). Calcium dynamics in astrocyte processes during neurovascular coupling. *Nat. Neurosci.* 18, 210–218. doi: 10.1038/nn.3906

Pan, W., Thompson, G., Magnuson, M., Majeed, W., Jaeger, D., and Keilholz, S. (2010). Simultaneous FMRI and electrophysiology in the rodent brain. *J. Vis. Exp.* 42:1901.

Pan, W. J., Thompson, G., Magnuson, M., Majeed, W., Jaeger, D., and Keilholz, S. (2011). Broadband local field potentials correlate with spontaneous fluctuations in functional magnetic resonance imaging signals in the rat somatosensory cortex under isoflurane anesthesia. *Brain Connect.* 1, 119–131. doi: 10.1089/brain.2011.0014

Pawela, C. P., Biswal, B. B., Cho, Y. R., Kao, D. S., Li, R., Jones, S. R., et al. (2008). Resting-state functional connectivity of the rat brain. *Magn. Reson. Med.* 59, 1021–1029. doi: 10.1002/mrm.21524

Poskanzer, K. E., and Yuste, R. (2016). Astrocytes regulate cortical state switching in vivo. *Proc. Natl. Acad. Sci. U.S.A.* 113, E2675–E2684. doi: 10.1073/pnas.1520759113

Quigley, M., Cordes, D., Turski, P., Moritz, C., Haughton, V., Seth, R., et al. (2003). Role of the corpus callosum in functional connectivity. *Am. J. Neuroradiol.* 24, 208–212.

Raichle, M., MacLeod, A., Snyder, A., Powers, W., Gusnard, D., and Shulman, G. (2001). A default mode of brain function. *Proc. Natl. Acad. Sci. U.S.A.* 98, 676–682.

Raichle, M. E. (2009). A paradigm shift in functional brain imaging. *J. Neurosci.* 29, 12729–12734. doi: 10.1523/jneurosci.4366-09.2009

Raichle, M. E. (2011). The restless brain. *Brain Connect.* 1, 3–12. doi: 10.1089/brain.2011.0019

Rosenegger, D. G., Tran, C. H., Wamsteeker Cusulin, I. J., and Gordon, G. R. (2015). Tonic local brain blood flow control by astrocytes independent of phasic neurovascular coupling. *J. Neurosci.* 35, 13463–13474. doi: 10.1523/JNEUROSCI.1780-15.2015

Scemes, E., and Giaume, C. (2006). Astrocyte calcium waves: what they are and what they do. *Glia* 54, 716–725. doi: 10.1002/glia.20374

Schölvinck, M. L., Maier, A., Ye, F. Q., Duyn, J. H., and Leopold, D. A. (2010). Neural basis of global resting-state fMRI activity. *Proc. Natl. Acad. Sci. U.S.A.* 107, 10238–10243. doi: 10.1073/pnas.0913110107

Schulz, K., Sydekum, E., Krueppel, R., Engelbrecht, C. J., Schlegel, F., Schröter, A., et al. (2012). Simultaneous BOLD fMRI and fiber-optic calcium recording in rat neocortex. *Nat. Methods* 9, 597–602. doi: 10.1038/nmeth.2013

Seeley, W. W., Menon, V., Schatzberg, A. F., Keller, J., Glover, G. H., Kenna, H., et al. (2007). Dissociable intrinsic connectivity networks for salience processing and executive control. *J. Neurosci.* 27, 2349–2356. doi: 10.1523/jneurosci.5587-06.2007

Shi, Z., Wilkes, D. M., Yang, P. F., Wang, F., Wu, R., Wu, T. L., et al. (2019). On the relationship between MRI and local field potential measurements of spatial and temporal variations in functional connectivity. *Sci. Rep.* 9:8871. doi: 10.1038/s41598-019-45404-8

Shih, Y. Y., Chen, C. C., Shyu, B. C., Lin, Z. J., Chiang, Y. C., Jaw, F. S., et al. (2009). A new scenario for negative functional magnetic resonance imaging signals: endogenous neurotransmission. *J. Neurosci.* 29, 3036–3044. doi: 10.1523/JNEUROSCI.3447-08.2009

Shih, Y. Y., Chiang, Y. C., Shyu, B. C., Jaw, F. S., Duong, T. Q., and Chang, C. (2012). Endogenous opioid-dopamine neurotransmission underlie negative CBV fMRI signals. *Exp. Neurol.* 234, 382–388. doi: 10.1016/j.expneurol.2011.12.042

Shmuel, A., and Leopold, D. A. (2008). Neuronal correlates of spontaneous fluctuations in fMRI signals in monkey visual cortex: implications for functional connectivity at rest. *Hum. Brain Mapp.* 29, 751–761. doi: 10.1002/hbm.20580

Sofroniew, N. J., and Svoboda, K. (2015). Whisking. *Curr. Biol.* 25, R137–R140. doi: 10.1016/j.cub.2015.01.008

Sofroniew, N. J., Vlasov, Y. A., Hires, S. A., Freeman, J., and Svoboda, K. (2015). Neural coding in barrel cortex during whisker-guided locomotion. *eLife* 4:e12559. doi: 10.7554/eLife.12559

Steinmetz, N. A., Buetfering, C., Lecoq, J., Lee, C. R., Peters, A. J., Jacobs, E. A. K., et al. (2017). Aberrant cortical activity in multiple gcamp6-expressing transgenic mouse lines. *eNeuro* 4:ENEURO.0207-17.2017. doi: 10.1523/ENEURO.0207-17.2017

Sumiyoshi, A., Keeley, R. J., and Lu, H. (2019). Physiological considerations of functional magnetic resonance imaging in animal models. *Biol. Psychiatry Cogn. Neurosci. Neuroimaging* 4, 522–532. doi: 10.1016/j.bpsc.2018.08.002

Takata, N., Sugiura, Y., Yoshida, K., Koizumi, M., Hiroshi, N., Honda, K., et al. (2018). Optogenetic astrocyte activation evokes BOLD fMRI response with oxygen consumption without neuronal activity modulation. *Glia* 66, 2013–2023. doi: 10.1002/glia.23454

Verkhratsky, A., and Nedergaard, M. (2018). Physiology of astroglia. *Physiol. Rev.* 98, 239–389. doi: 10.1152/physrev.00042.2016

Voorn, P., Vanderschuren, L. J., Groenewegen, H. J., Robbins, T. W., and Pennartz, C. M. (2004). Putting a spin on the dorsal-ventral divide of the striatum. *Trends Neurosci.* 27, 468–474. doi: 10.1016/j.tins.2004.06.006

Wang, L., Saalmann, Y. B., Pinsk, M. A., Arcaro, M. J., and Kastner, S. (2012). Electrophysiological low-frequency coherence and cross-frequency coupling contribute to BOLD connectivity. *Neuron* 76, 1010–1020. doi: 10.1016/j.neuron.2012.09.033

Winder, A. T., Echagarruga, C., Zhang, Q., and Drew, P. J. (2017). Weak correlations between hemodynamic signals and ongoing neural activity during the resting state. *Nat. Neurosci.* 20, 1761–1769. doi: 10.1038/s41593-017-0007-y

Zhao, F., Zhao, T., Zhou, L., Wu, Q., and Hu, X. (2008). BOLD study of stimulation-induced neural activity and resting-state connectivity in medetomidine-sedated rat. *Neuroimage* 39, 248–260. doi: 10.1016/j.neuroimage.2007.07.063

Zonta, M., Angulo, M. C., Gobbo, S., Rosengarten, B., Hossmann, K. A., Pozzan, T., et al. (2003). Neuron-to-astrocyte signaling is central to the dynamic control of brain microcirculation. *Nat. Neurosci.* 6, 43–50. doi: 10.1038/nn980

Conflict of Interest: The authors declare that the research was conducted in the absence of any commercial or financial relationships that could be construed as a potential conflict of interest.

frontiers in Neuroscience

ORIGINAL RESEARCH
published: 25 October 2019
doi: 10.3389/fnins.2019.01126

The Relationship Between Local Field Potentials and the Blood-Oxygenation-Level Dependent MRI Signal Can Be Non-linear

*Xiaodi Zhang, Wen-Ju Pan and Shella Keilholz**

The Wallace H. Coulter Department of Biomedical Engineering, Georgia Institute of Technology, Emory University, Atlanta, GA, United States

Functional magnetic resonance imaging (fMRI) is currently one of the most important neuroimaging methods in neuroscience. The image contrast in fMRI relies on the blood-oxygenation-level dependent (BOLD) signal, which indirectly reflects neural activity through neurovascular coupling. Because the mechanism that links the BOLD signal to neural activities involves multiple complicated processes, where neural activity, regional metabolism, hemodynamics, and the BOLD signal are all inter-connected, understanding the quantitative relationship between the BOLD signal and the underlying neural activities is crucial for interpreting fMRI data. Simultaneous local field potential (LFP) and fMRI recordings provide a method to study neurovascular coupling. There were a few studies that have shown non-linearities in stimulus related responses, but whether there is any non-linearity in LFP—BOLD relationship at rest has not been specifically quantified. In this study, we analyzed the simultaneous LFP and resting state-fMRI data acquired from rodents, and found that the relationship between LFP and BOLD is non-linear under isoflurane (ISO) anesthesia, but linear under dexmedetomidine (DMED) anesthesia. Subsequent analysis suggests that such non-linearity may come from the non-Gaussian distribution of LFP power and switching from LFP power to LFP amplitude can alleviate the problem to a degree. We also confirmed that, despite the non-linearity in the mean LFP—BOLD curve, the Pearson correlation between the two signals is relatively unaffected.

Keywords: local field potentials, BOLD, electrophysiology, fMRI, non-linearity, neurovascular coupling, correlation

OPEN ACCESS

Edited by:
Jorge J. Riera, Florida International University, United States

Reviewed by:
Ying Zheng, University of Reading, United Kingdom
Basavaraju G. Sanganahalli, Yale University, United States

****Correspondence:***
Shella Keilholz
shella.keilholz@bme.gatech.edu

Specialty section:
This article was submitted to Brain Imaging Methods, a section of the journal Frontiers in Neuroscience

Received: *03 June 2019*
Accepted: *04 October 2019*
Published: *25 October 2019*

Citation:
Zhang X, Pan W-J and Keilholz S (2019) The Relationship Between Local Field Potentials and the Blood-Oxygenation-Level Dependent MRI Signal Can Be Non-linear. Front. Neurosci. 13:1126. doi: 10.3389/fnins.2019.01126

INTRODUCTION

After its inception in the early 1990s (Ogawa et al., 1990, 1992; Belliveau et al., 1991), functional magnetic resonance imaging (fMRI) quickly became the dominant method to study brain activity. Later on, Biswal et al. (1995) found that the fMRI acquired without a task reveals synchronous fluctuations in different brain regions, which reflects the functional connectivity. Whether the fMRI is performed with task-rest block design, or is performed at rest without any explicit task, ultimately all fMRI studies rely on a contrast mechanism called blood oxygenation level-dependent (BOLD), in order to non-invasively detect the relative neural activity. The image contrast in BOLD fMRI comes from the fact that deoxyhemoglobin is strongly paramagnetic, whereas oxyhemoglobin is diamagnetic. The presence of paramagnetic deoxyhemoglobin distorts the local magnetic fields,

and such distortion results in intravoxel dephasing of MRI signal ($T2^*$ weighting), which reduces the signal intensity in that region (Thulborn et al., 1982; Silvennoinen et al., 2003). Since the brain does not store oxygen, an increase of neural activity will demand more oxygen, and through a process called neurovascular coupling, the regional cerebral blood flow (CBF) will increase to fulfill the demand (Fox and Raichle, 1986). This brings more oxygenated blood to this region and lowers the relative concentration of deoxygenated hemoglobin, increasing the BOLD signal. It can be seen that the coupling between neural activity and BOLD signal changes involves multiple processes, and that neural activity, regional metabolism, hemodynamics, and the BOLD signal are all inter-connected via signaling pathways that are not completely understood. The fact that the BOLD signal is only an indirect measurement of neural activity makes the interpretation of fMRI studies difficult (Bandettini and Ungerleider, 2001; Arthurs and Boniface, 2002; Heeger and Ress, 2002; Logothetis, 2008).

To better understand the relationship between BOLD and neural activity, it is necessary to utilize modalities that can directly measure neural activity simultaneously with fMRI. Logothetis et al. (2001) pioneered the development of simultaneous acquisition of local field potentials (LFP) and fMRI data in primates. Their study showed that both LFPs and multi-unit activity (MUA) are correlated with the BOLD response, LFPs showed higher correlation than MUA. This outstanding work not only provided invaluable insights into the relationship between neural activity and the BOLD signal, but also established a feasible method for recording fMRI signal and neural activity simultaneously (Bandettini and Ungerleider, 2001; Arthurs and Boniface, 2002; Heeger and Ress, 2002). As a result, an increasing number of studies have employed simultaneous LFP and fMRI data acquisition (Shmuel et al., 2006; Huttunen et al., 2008; Shmuel and Leopold, 2008; Murayama et al., 2010; Mishra et al., 2011; Pan et al., 2011, 2013; Devonshire et al., 2012; Magri et al., 2012), improving our understanding of the underlying mechanisms that link the BOLD signal to neural activity.

Most studies that analyze the LFP-BOLD relationship, either implicitly (Shmuel et al., 2006; Huttunen et al., 2008; Murayama et al., 2010; Pan et al., 2011, 2013) or explicitly (Logothetis et al., 2001), assume a linear relationship between LFP and BOLD. For example, the Pearson correlation coefficient, the most widely used metric, implicitly assumes a linear dependency. However, the linear model may sometimes be overly simplified, and its applicability remains a topic of debate (Liu et al., 2010).

Logothetis et al. (2001) found that the root mean square value of LFP gamma vs. BOLD relationship is roughly linear. But when the LFP or BOLD is compared to the stimulus, the relationship is non-linear (Heeger and Ress, 2002). Huttunen et al. (2008) also found that the LFP/BOLD response, as a function of stimulus frequencies, is non-linear, but the LFP vs. BOLD relationship is quite linear. Devonshire et al. (2012) found that a non-linearity exists in sub-cortical regions but not in the cortex. Sanganahalli et al. (2009) found that both LFP and MUA show a linear relationship with hyperemic component [BOLD, cerebral blood volume (CBV), CBF] from the cortex in rats during forepaw stimulation with low frequency stimulation (1.5–3 Hz). The same group also showed that the relationship among LFP, MUA, and BOLD might be different in the cortex and sub-cortical regions in a recent study (Sanganahalli et al., 2016), but did not specifically quantify whether the relationship is linear. Magri et al. (2012) proposed to use mutual information to study the relationship between LFP band limited power and BOLD, which takes any non-linearity into account, however, they did not specifically measure how much non-linearity was present in the LFP-BOLD relationship.

To the best of our knowledge, there has not been a study specifically focusing on non-linearity in the relationship between spontaneous LFPs and BOLD in the cortex. So far, any non-linearities discovered in cortex seem to refer to the LFP vs. input stimulus, or BOLD vs. input stimulus relationship, but not the LFP and BOLD relationship. However, there have been some studies revealing the non-linearity between the BOLD signal and neural activity measured by methods other than LFP recordings (Devor et al., 2003; Jones et al., 2004; Sheth et al., 2004; Hewson-Stoate et al., 2005; Hoffmeyer et al., 2007; de Zwart et al., 2009; Liu et al., 2010). Since these studies suggests that there might be a non-linearity between BOLD and neural activity, it is worth trying to quantify if there is any non-linearity in the LFP-BOLD relationship. Please note that the linear relationship discussed in this paper refers to the simple $y = kx + b$ relationship, and the aim of this paper is to discuss whether this holds true for LFP-BOLD relationship, and if not, how the Pearson correlation is affected.

In our study, we took advantage of the previously acquired data with simultaneous LFP and fMRI acquisition in rodents. Using data-driven approaches, we found a non-linear relationship existing between LFP power and BOLD under isoflurane (ISO) anesthesia but not under dexmedetomidine (DMED) anesthesia. This non-linearity seems to come from the non-Gaussian distribution of LFP power under ISO anesthesia. Subsequent studies show that ultimately, the non-linearity may come from the intrinsic properties in LFP power, and LFP amplitude might be more desirable if the non-linearity is a concern. Despite the existence of non-linearity, we also found that it is not usually substantial enough to influence traditional Pearson correlation-based analysis.

MATERIALS AND METHODS

Simultaneous fMRI Imaging and LFP Recording

All animal experiments were performed in compliance with NIH guidelines and were approved by the Emory University Institutional Animal Care and Use Committee. Previously acquired data from 36 Sprague–Dawley rats (male, 200–300 g, Charles River) were used in this study. For each rat, first the surgery was performed to implant the glass electrodes in bilateral S1FL (primary somatosensory of forelimb) areas under 2% isoflurane (ISO) anesthesia (**Figure 1** shows the EPI image of a typical subject with the locations of the electrodes, as well as the LFP vs. BOLD cross-correlation map). Then, simultaneous resting state-fMRI scans and LFP recordings were acquired,

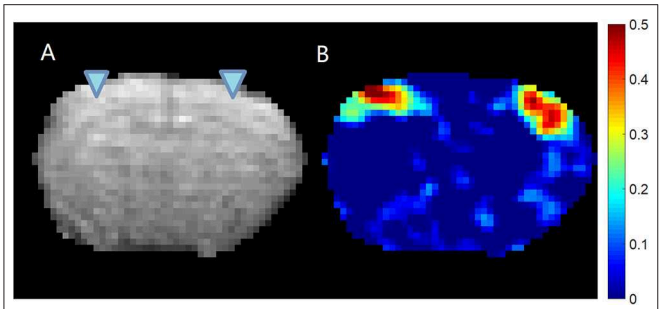

FIGURE 1 | EPI image **(A)** and cross-correlation **(B)** between the LFP recorded from left S1 area and the BOLD signal. The location of the electrodes was indicated by the triangles overlaid on the EPI image. It can be seen that for this subject, the LFP recorded from left S1 area shows significant localized correlation with the BOLD signal near the electrodes on both hemispheres. The colormap for the correlation is shown on the right.

first under a variety of ISO concentrations ranging from 1.2 to 2% (ISO, 96 sessions), and later under dexmedetomidine (DMED, 219 sessions). For DMED studies, a bolus of 0.025 mg/kg dexmedetomidine was injected subcutaneously. Isoflurane was disconnected 10 min afterwards, and a continuous subcutaneous infusion of dexmedetomidine (0.05 mg/kg/h) began. The dose was increased by a factor of three (0.15 mg/kg/h) after ∼1.5 h, following the protocol for prolonged sedation described in Pawela et al. (2009). The DMED scans were conducted >3 h after switching from ISO to avoid any residual ISO effects (Magnuson et al., 2014). Each session is 500 s long. A full description of the methods is given in previous publications (Pan et al., 2010, 2011). All physiological parameters were monitored and maintained within normal ranges, including rectal temperature, respiration rate, oxygen saturation and cardiac rate. The animals were euthanized at the end of the experiment.

Single slice gradient echo EPI scans were obtained on a 9.4T small animal MRI system (Bruker, Billerica, MA) with scan parameters: TR/TE = 500/15 ms, voxel size = 0.3 × 0.3 × 2 mm, matrix size = 64 × 64, FOV = 1.92 × 1.92 cm, number of repetitions = 1,000, number of dummy scans = 20. To improve the homogeneity of the magnetic field, the volume of interest (6 mm^3) was shimmed using FASTMAP (Gruetter, 1993). Manual shimming adjustment was then applied when necessary to improve the field homogeneity of the selected slice. The imaging slice was set to the coronal plane that covers bilateral S1FL areas, where the glass recording electrode tips were implanted.

Because the whole dataset was acquired over a period of several years, there were two different sets of LFP recording parameters: (1) ×500 amplified, 0–100 Hz bandpass-filtered, 60 Hz notch-filtered, 12 kHz sampling rate, and ∼10 min acquisition length (Pan et al., 2011), and (2) ×1,000 amplified, 0.1 Hz−5 kHz bandpass-filtered, 60 Hz notch-filtered, and 12 kHz sampling rate, and ∼14 min acquisition length (Pan et al., 2013). However, these differences in the recording parameters are eliminated in the LFP pre-processing, where the LFP was band-pass filtered to 1–100 Hz, the amplitude was normalized so that the LFP broadband power (1–100 Hz) in each scan session has zero mean and unit variance, and the excessive LFP segments were truncated to match the length of fMRI data.

LFP Data Pre-processing

The gradient switching that occurs during EPI acquisition induces voltage changes in the recorded LFP due to Faraday's law of induction. Such gradient-induced artifacts were removed following established methods, The denoised LFP signal was then low pass filtered to 100 Hz using to remove any residual artifacts, and down-sampled from 12 KHz to 500 Hz to reduce file size and computation cost. A 10 TR-long segment of raw LFP trace and the denoised LFP trace of a typical subject (same as the one shown in **Figure 1**) were shown in **Figures S1A,B**.

To obtain the LFP power time course, first a 1 s long sliding window was applied, then within the window, the power spectral density (PSD) function was estimated using Welch's method (four segments, 50% overlap). The PSD was integrated over a range of frequency bands (delta 1–4 Hz, theta 4–8 Hz, alpha 8–12 Hz, low frequency beta 12–25 Hz, high frequency beta 25–40 Hz, and gamma 40–100 Hz) to produce the LFP band-limited power (BLP) time courses. The sliding window has an overlap of 50%, meaning it moves 0.5 s at each step to match with the fMRI temporal resolution. The LFP BLP time courses were then band-pass filtered (0.01–0.1 Hz for ISO and 0.01–0.25 Hz for DMED). We chose these cut-off frequencies because a previous study (Pan et al., 2013) has demonstrated that frequencies below 0.1 Hz in ISO data or below 0.25 Hz in DMED data exhibited higher BOLD/BLP coherences, when compared to higher frequencies. Finally, the BLP time courses from the same scan were normalized by a common scaling factor, such that the standard deviation of the broadband power is equal to 1, which makes the datasets with various amplitudes comparable with each other.

FMRI Data Pre-processing

First the fMRI data was corrected for motion using SPM 12. The motion-corrected image series were then spatially smoothed using a Gaussian kernel with a FWHM of 2.8 voxel (2.8 × 0.3 = 0.84 mm). Finally, global signal and linear drift regression, as well as band-pass filtering (0.01–0.1 Hz for ISO and 0.01–0.25 Hz for DMED) were performed voxel-wisely. All data processing was performed on Matlab 2018b (The MathWorks, Natick, MA). The data will be available upon request.

ROI Selecting and Quality Assurance

As a quality assurance step, the cross-correlation map of LFP bandlimited power vs. BOLD is calculated at the lag when the correlation is expected to reach the maximum (4 s for ISO and 2.5 s for DMED). If there were high cross-correlations near the electrodes, the dataset was selected as high-quality dataset. Please note that the initial data pool (315 scan sessions) includes all saved data, including those with substantial noises, motions, and/or unstable physiological conditions. Most of them were not suitable for further study and were excluded. We have used several metrics to assess the quality of the data, including the noise in LFP and BOLD, the residue motion, image distortion, and function connectivity in bilateral S1 areas. All of the metrics

were manually inspected and labeled as "good," "fair" or poor (the guideline of how the metrics were labeled can be found in **Table 1**). Any scan must have at most one "fair" metric, in order to be selected as usable data. By these criteria, 82 scans under ISO and 160 scans under DMED were selected out of the initial 315-scan data pool. The correlation between LFP power and BOLD were inspected, and if a scan session has a LFP-BOLD correlation higher than 0.2 and the correlation map is well-localized to sites surrounding electrodes, it is selected as high-quality data for further analysis. By this criterion, 22 scans under DMED were selected out of 219 scans, and 32 scans under ISO selected out of 96 scans. A 3 × 3 ROI was manually chosen from the cross-correlation map, and centered at the electrodes, where the correlations are the highest. Finally, the BOLD signal averaged over the ROI was normalized so that the BOLD time course in each scan session has zero mean and unit variance, thus, the BOLD signal is comparable with other fMRI scans. The LFP broadband power time course and the BOLD signal within the ROI of a typical subject (same as the one shown in **Figure 1**) were shown in **Figure S1C**.

RESULTS

LFP Power vs. BOLD Relationship Shows Non-linearity Under ISO

Figure 2 shows the relationship between LFP power and BOLD using a scatter plot. The x-axis shows the BOLD value measured in units of standard deviation of BOLD and the y-axis shows the LFP band limited power (BLP) values measured in units of standard deviation of LFP broadband power, at a lead of 4 s under ISO and a lead of 2.5 s under DMED.

Besides the scatter plot, there is also a line plot showing the mean LFP power vs. spontaneous BOLD relationship. It is obtained by evenly dividing the data into 10 groups based on the BOLD values, and then calculating the average LFP power within each BOLD group. Since this curve is based on the actual bivariate relationship, we call it "experimental LFP vs. spontaneous BOLD relationship." It is evident that the LFP vs. spontaneous BOLD relationship is non-linear under ISO (panel A), whereas under DMED it is almost linear (panel B). In addition, while the scale of each plot is different (because the energy in each frequency band is different), the degree of non-linearity under ISO appears very consistent, suggesting that an underlying mechanism independent of the frequency bands induces the non-linearity. The degree of linearity under DMED also appears very consistent, except in high frequency bands, especially in gamma band. The correlation between gamma band under DMED and BOLD is only 0.0450, suggesting that they are only very weakly correlated. The reason why the correlation between high frequency band and BOLD under DMED is so small compared to the other frequency bands, is because the "signal-to-noise ratios" in these bands are small (The "signal" is the change in BOLD that is caused by LFP power changes, whereas the "noise" is the change in BOLD attributed to random fluctuations), which makes the LFP vs. spontaneous BOLD curve so flat. Under DMED anesthesia, there is little energy in these

TABLE 1 | Guidelines of data quality metrics.

	Good	Fair	Poor
LFP			
Number of gradient induced artifact	=1,020[a]		≠ 1,020
Residual noise in LFP	No large spike in de-noised LFP		More than one large spike in de-noised LFP
BOLD			
Trajectory of center of mass[b]	abs(Δx) ≤ 0.05 pixel and abs(Δy) ≤ 0.05 pixel	abs(Δx) ≤ 0.1 pixel and abs(Δy) ≤ 0.1 pixel and either abs(Δx) ≥ 0.05 pixel or abs(Δy) ≥ 0.05 pixel	abs(Δx) ≥ 0.1 pixel or abs(Δy) ≥ 0.1 pixel
DVARS[c]	DVARS ≤ 0.5%	0.5% ≤ DVARS ≤ 1% and the number of small spikes is fewer than 5	Either DVARS ≥ 1% (large spikes) or the number of small spikes is more than 5
Image distortion	No noticeable image distortion or signal loss		Noticeable image distortion or signal loss
Function connectivity (correlation between bilateral S1 areas)	Correlation ≥ 0.3 and the correlation map is localized[d] to somatosensory network	Correlation ≥ 0.15 and either correlation ≤ 0.3 or the correlation map is not completely localized	Correlation ≤ 0.15 or unlocalized correlation
LFP-BOLD correlation	Correlation ≥ 0.2 for both S1 areas and the correlation map is well-localized to sites surrounding electrodes	Correlation ≥ 0.1 and either correlation ≤ 0.2 or the correlation map is not completely localized	Correlation ≤ 0.1 or unlocalized correlation

[a] *Since there are 1,000 TRs and 20 dummy scans, the number of gradient artifacts identified should equal 1,020. If not, it usually indicates high noise level or missing segments. Also the correct identification of gradient artifacts is crucial to register the timing.*

[b] *Center of mass shows if there is any shifting in x-y plane.*

[c] *DVARS is calculated based on Power et al. (2012). It is also an indicator of motion.*

[d] *The reason why localized high correlation is needed as a metric is because some scan session exhibit high correlation over a huge area of the brain, which is not normal and may be attributed to motion. The threshold for the correlation is not a "hard" threshold, but rather it is roughly the range of correlation we observed in the scan sessions that show localized correlation map. It is intended to provide a general idea of the correlation in such dataset. So if the correlation between bilateral S1 areas ≥ 0.3, the correlation map is not necessarily localized. But on the other hand, if the correlation map is localized, most of the time the correlation in S1 areas we observed is roughly in the range that is larger than 0.3.*

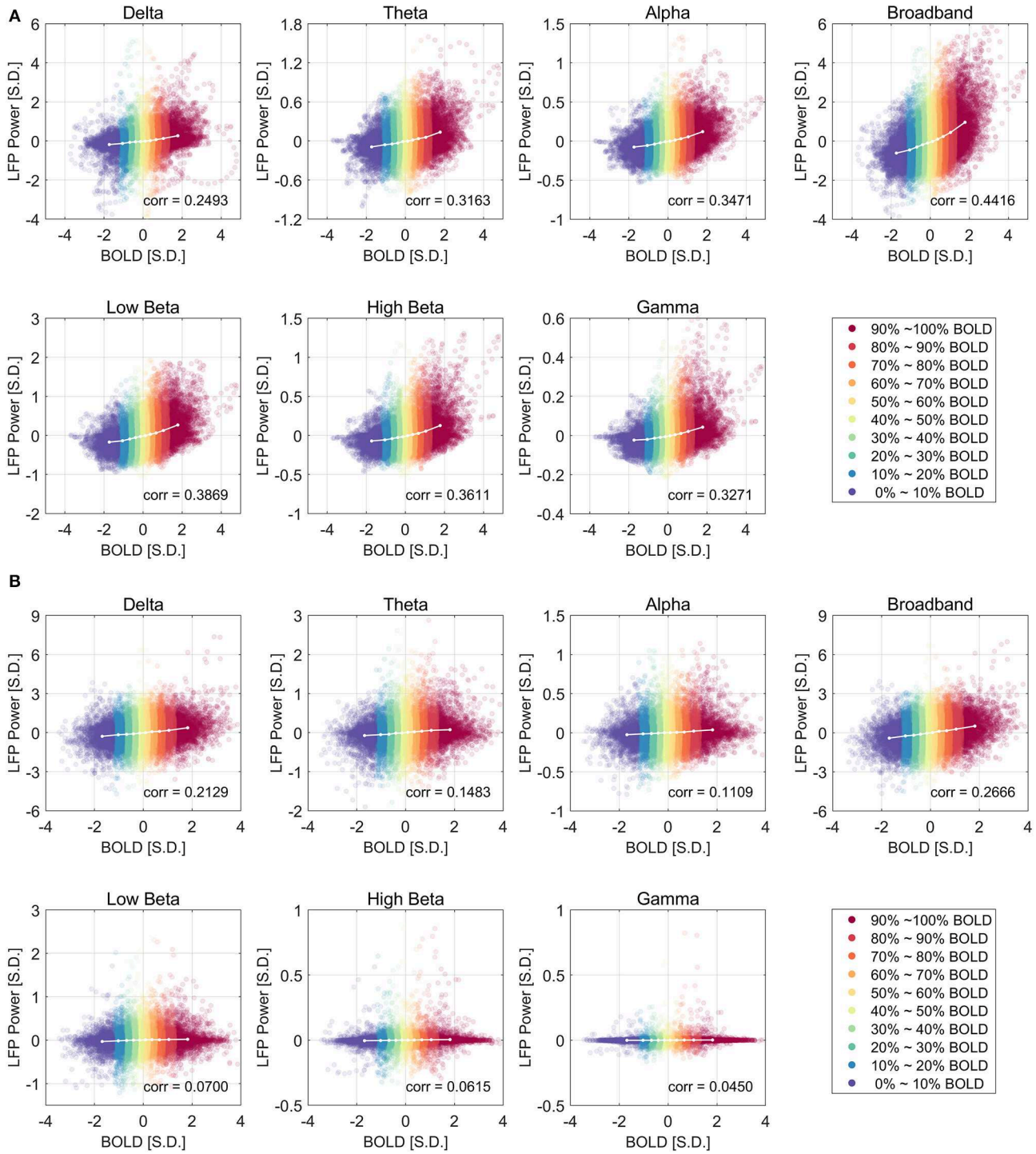

FIGURE 2 | Scatter plot of LFP power vs. BOLD and the centroids of each category under ISO **(A)** and DMED **(B)**. The 10 BOLD categories are color-coded (Red for high BOLD value and Blue for low BOLD value). Each dot in the figure represents a time point with its BOLD value and LFP power value. In total there are 32,000 points under ISO, and 22,000 points under DMED, since each scan session has exact 1,000 time points. The cross-correlation between LFP power and BOLD is shown for each LFP band. The BOLD value and the LFP power value were expressed in units of standard deviation [S.D.]. Both BOLD and LFP power were normalized so that the standard deviation of BOLD is 1, and the standard deviation of LFP broadband power is also 1. For the individual LFP frequency bands, the summation of the power in the six bands at any given time points equals to the LFP broadband power (so any individual band will have a standard deviation lower than 1 standard deviation of LFP broadband power. Note that the display scale of different frequency bands may be different.

high frequency bands, whereas under ISO anesthesia, the energy in these bands is considerably higher. We have included the energy distribution of LFP power in the **Figure S2**.

We also found that this non-linearity can be well-modeled by a simple second order polynomial function, shown in **Figure 3**. Let x_i and $y_{i,j}$ be the averaged BOLD and LFP power of the i-th percentile group ($i = 1, 2, \ldots 10$) in the j-th frequency band ($j = 1, 2, \ldots 6, 7$, representing delta, theta, alpha, low-frequency beta, high-frequency beta, gamma, and broadband, respectively). The collection of $[x_i, y_{i,j}]$ corresponds to the line plot in **Figure 2**. It appears that the non-linear relationship can be modeled as a quadratic function. To test that, we can predict the BOLD value $\hat{y}^1_{i,j}$ using the polynomials of the LFP power x_i:

$$\hat{y}^1_{i,j} = f(x_i) = a_j {x_i}^2 + b_j x_i + c_j = \beta_j^T X_i, \tag{1}$$

where $\beta_j = \left[a_j, b_j, c_j\right]^T$ and $X_i = \left[{x_i}^2, x_i, 1\right]^T$. We included a superscript in $\hat{y}^1_{i,j}$ because, in next section, we will introduce another model to predict the BOLD value. For each frequency band j, an optimal parameter set β_j can be found using the least squares method, such that the sum of squared error between the predicted BOLD and the actual BOLD is minimized:

$$\begin{aligned}\beta_j &= \underset{\beta_j}{\operatorname{argmin}} \sum_{i=1}^{10} \left(\hat{y}^1_{i,j} - y_{i,j}\right)^2 \\ &= \underset{\beta_j}{\operatorname{argmin}} \sum_{i=1}^{10} \left(a_j {x_i}^2 + b_j x_i + c_j - y_{i,j}\right)^2 \end{aligned} \tag{2}$$

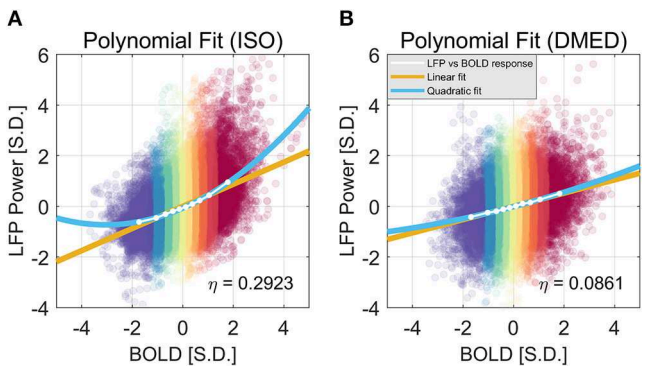

FIGURE 3 | Quadratic Fitting of LFP power vs. BOLD response under ISO **(A)** and DMED **(B)**. The quadratic fitting captures the shape of the LFP power vs. BOLD response well. Under ISO the LFP power-BOLD relationship is much more non-linear than under DMED. Under ISO, the fitted coefficients a, b, c, are 0.0713, 0.4344, −0.0696, respectively. The p-values are 2.06e-05, 2.13e-10, 0.00029, respectively. The 95% confidence intervals are [0.0546, 0.0881], [0.4151, 0.4536], [−0.0944, −0.0449], respectively. Under DMED, the fitted coefficients a, b, c, are 0.0124, 0.2606, −0.0130, respectively. The p-values are 0.0122, 8.06e-11, 0.0465, respectively. The 95% confidence intervals are [0.0036, 0.0211], [0.2505, 0.2706], [−0.0258, −0.0003], respectively. Both ISO and DMED have a second order coefficient still significantly different from zero ($p = 2.06\text{e-}05 < 0.05$ under ISO, $p = 0.0122 < 0.05$ under DMED), however under ISO the magnitude of the coefficient is much larger, which is why we can visually see a curvature. The non-linearity, measured by the ratio between the second order term and the first order term, is also shown in the figure.

The estimated parameters for the broadband power, their p-values, and 95% confidence interval can be found in the caption of **Figure 3**. The goodness of the fit can be measured by the root-mean-square-error (RMSE), and R^2. Under ISO, the RMSE and R^2 of the linear model are 0.0927 and 0.9639; the RMSE and R^2 of the quadratic model are 0.0252 and 0.9977. It is evident that the quadratic model has a smaller RMSE and higher R^2. Given that the second order coefficient also has a 95% confidence interval not overlapping with zero (0.0546, 0.0881), and the p-value is very small (2.06e-05), it can be concluded that there is substantial non-linearity in the LFP-BOLD relationship under ISO, and the quadratic model is more precise than the linear model. To quantitatively measure the non-linearity, naturally we would use the second order term, but the value of the second order term is also determined by the overall scale of the function. To normalize this effect, we propose to use the ratio of the second order term to the first order term as a measurement of how non-linear the function is. Recall Equation (1):

$$\hat{y}^1_j = f(x) = a_j x^2 + b_j x + c_j \tag{3}$$

To measure the non-linearity, we picked two points: the furthest point along the positive x-axis (denoted by $\left[x_1, y_1\right]$), and the origin (denoted by $\left[x_0, y_0\right]$). Taking the Taylor expansion at the origin, we have

$$f(x) = f(x_0) + f'(x_0)(x - x_0) + \frac{f''(x_0)}{2}(x - x_0)^2 \tag{4}$$

The change along y-axis $\Delta y = y_1 - y_0$ is determined by the change along x-axis $\Delta x = x_1 - x_0$ (note that $x_0 = 0$):

$$\begin{aligned}\Delta y &= f(x_1) - f(x_0) \\ &= f'(x_0)(x_1 - x_0) + \frac{f''(x_0)}{2}(x_1 - x_0)^2 \\ &= \left(2a_j x_0 + b_j\right)\Delta x + \frac{2a_j}{2}\Delta x^2 = a_j \Delta x^2 + b_j \Delta x, \end{aligned} \tag{5}$$

which consists of the first order term and the second order term. Since the BOLD distribution is approximately Gaussian, if we assess the non-linearity using the furthest point along the positive x-axis, which is the group mean of 90–100% BOLD, then Δx would be 1.819. The non-linearity in the LFP—BOLD relationship in the j-th frequency band, denoted as η_j, can be calculated using the following equation:

$$\eta_j = \frac{2nd\ order\ term}{1st\ order\ term} = \frac{a_j \Delta x^2}{b_j \Delta x} \tag{6}$$

Using this formula, the non-linearity in LFP broadband power vs. BOLD relationship is 0.2923 and 0.0862 under ISO and DMED, respectively.

The Non-linearity Might Be Induced by the Non-gaussian Distribution of LFP Power

It is also worth noting that in **Figure 2**, the scatter plot reaches further along the positive y-axis, especially for the 90–100% BOLD group, which makes the LFP vs. spontaneous BOLD

relationship appear as a curve. Therefore, the asymmetry along y-axis, or in another word, the skewed distribution of LFP power, might be the reason why the LFP—BOLD relationship is non-linear. **Figure 4** shows the distributions of LFP power and BOLD, where it can be seen that the LFP power under ISO is right tailed. This can be quantitatively confirmed by the skewness (a skewness >1 is often considered as highly skewed). Together with a kurtosis of 5.3575, which is much higher than 3 (Gaussian distributions always have a kurtosis of 3), it can be concluded that the LFP power under ISO is substantially non-Gaussian.

The skewness and kurtosis were calculated using the following equations:

$$Skew[X] = E\left[\left(\frac{X-\mu}{\sigma}\right)^3\right], \quad (7)$$

$$Kurt[X] = E\left[\left(\frac{X-\mu}{\sigma}\right)^4\right], \quad (8)$$

where X is the random variable, μ is the mean value of X, σ is the standard deviation. The skewness and kurtosis of the distributions were shown in **Table 2**.

The LFP power under DMED also has a kurtosis larger than 3, but it is relatively Gaussian when compared to LFP power under ISO. The BOLD signal, on the other hand, is approximately Gaussian-distributed, regardless of the anesthetizing agent, because the skewness is near 0 and the kurtosis is near 3.

It is apparent from the histogram, as well as from the skewness and kurtosis that the LFP power under ISO is the most non-Gaussian signal. Given the fact that the LFP power vs. spontaneous BOLD relationship under ISO is also the one showing substantial non-linearity, we hypothesized that these two findings are linked together, and the non-linearity may come from the non-Gaussian distribution of LFP power.

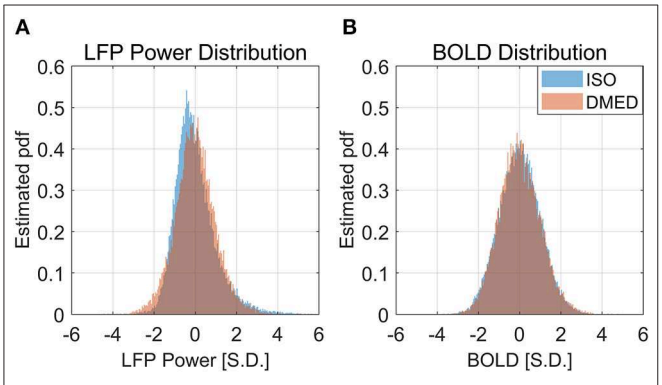

FIGURE 4 | Histogram of LFP broadband power, BOLD under ISO **(A)** and DMED **(B)**. It can be seen that the LFP power under ISO is non-Gaussian distributed.

TABLE 2 | Skewness and kurtosis of LFP power and BOLD under ISO and DMED anesthesia.

	LFP ISO	LFP DMED	BOLD ISO	BOLD DMED
Skewness	**1.0473**	0.2235	0.1191	0.1802
Kurtosis	**5.3575**	**4.1773**	3.0987	3.1723

The skewness or kurtosis that deviates from a Gaussian distribution were highlighted in bold.

Least Square Fitting of LFP vs. Spontaneous BOLD Relationship

To validate this hypothesis, we propose to obtain a theoretical LFP power vs. spontaneous BOLD relationship by making some assumptions, and then determine if the experimental curve matches the theoretical one.

A natural assumption would be that a positive spontaneous BOLD event is evoked by higher than average LFP power, and negative spontaneous BOLD event is evoked by lower than average LFP power. If there was a purely deterministic relationship between the two, we would see 90% percentile BOLD corresponds to 90% percentile LFP power. The relationship is stochastic, so the final observation is contaminated by random noise. But the mean value of BOLD within a certain percentile range should still correspond to the mean value of LFP power within the same percentile range even in the presence of noise. For example, the mean effect of LFP power with 90–100% percentile value should, on average, evoke a spontaneous BOLD event with 90–100% percentile value. The assumption made here is weaker than the assumption of linearity. In a special case where both LFP and BOLD follow Gaussian distributions, it is equivalent to the linear assumption; but in general, if any of the distributions are non-Gaussian, such an assumption should still faithfully reflect the averaged relationship between LFP and BOLD.

Figure 5 illustrates how the theoretical LFP vs. spontaneous BOLD relationship was obtained. First, the distributions of both LFP and BOLD were evenly divided into 10 groups, which is shown in the color-coded histograms. Next, the mean LFP power in a percentile group (y-axis value) was mapped to the mean BOLD in the corresponding percentile group (x-axis value). It is worth noting that the theoretical curve solely depends on the overall distributions of LFP power and BOLD, whereas the experimental curve was obtained from the one-to-one relationship in the data points.

Since the LFP-BOLD relationship seems consistent across all frequency bands, for the sake of robustness, we used the LFP broadband power to derive a single theoretical LFP vs. spontaneous BOLD curve. A least square fitting was then performed to find the optimal scaling factor for each frequency band, which minimizes the summed squared difference between the scaled theoretical curve and the experimental curve. Let $\tilde{x}_i$ and $\tilde{y}_{i,j}$ be the BOLD and LFP broadband power of the i-th point in the j-th frequency band in the theoretical curve (**Figure 5**), respectively. Since it is hypothesized that the non-linearity comes from the non-Gaussian distributions, which have been taken into account in the theoretical curve, the predicted LFP-BOLD relationship $[\hat{x}_i,\ \hat{y}^2_{i,j}]$ in each frequency band is then a scaled version of the theoretical curve in the LFP broadband power:

$$[\hat{x}_i,\ \hat{y}^2_{i,j}] = [\tilde{x}_i,\ \theta_j \tilde{y}_{i,7}], \quad (9)$$

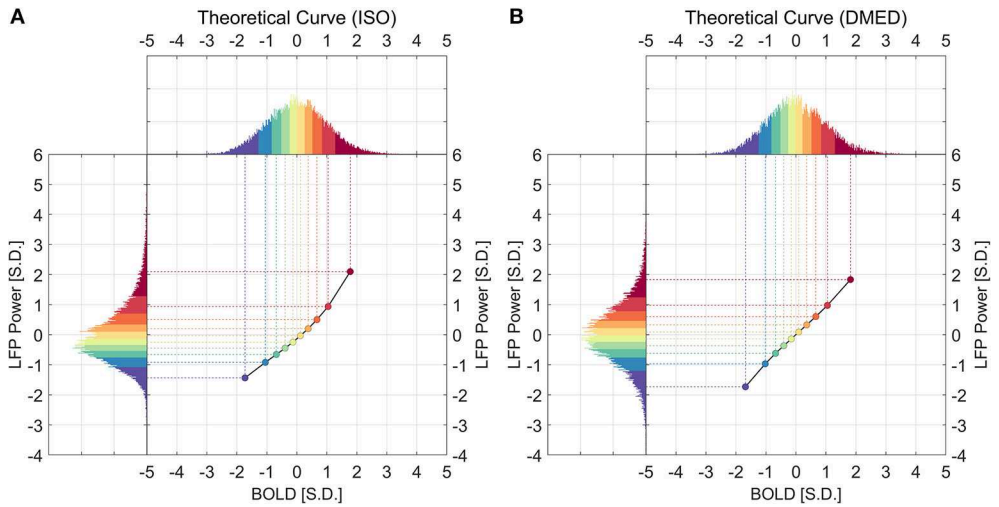

FIGURE 5 | Histograms of LFP, BOLD, and the derived theoretical LFP vs. BOLD response under ISO **(A)** and DMED **(B)**. For any given point in the LFP vs. BOLD response, the x-axis shows the averaged BOLD value of the BOLD group, while the y-axis shows the averaged LFP broadband power value of the corresponding LFP group.

where θ_j is the scaling factor for *jth* frequency band. Note that $x_i = \tilde{x}_i = \hat{x}_i$ (because they all represent the averaged BOLD within the $[10 \times (i-1)\,\%, 10 \times i\%]$ percentile group). The optimal scaling factor θ_j was found such that the sum of squared error between the predicted curve and the experimental curve is minimized:

$$\begin{aligned}\theta_j &= \underset{\theta_j}{\operatorname{argmin}} \sum_{i=1}^{10} \left(\hat{y}^2_{i,j} - y_{i,j} \right)^2 \\ &= \underset{\theta_j}{\operatorname{argmin}} \sum_{i=1}^{10} \left(\theta_j \tilde{y}_{i,7} - y_{i,j} \right)^2 \end{aligned} \tag{10}$$

It can be seen from **Figure 6** that the derived theoretical LFP vs. spontaneous BOLD curve match fairly well with the experimental ones, suggesting that the non-linearity may come from the non-Gaussian distribution of LFP power, although the experimental curves do deviate from the theoretical ones in low frequency beta, high frequency beta, and gamma bands under DMED. The reason again is the "Signal-to-noise" ratios mentioned earlier are very small in these bands, making them very sensitive to random noise, or fluctuations in BOLD that is not caused by LFP changes. We also increased the number of groups from 10 to 40 to get the fitting in finer grid. The fitting results (**Figure S3**) were consistent with the one obtained using 10 groups.

The Ultimate Source of Non-linearity

We have shown that the LFP power vs. BOLD relationship is non-linear, and that such non-linearity may come from the non-Gaussian distribution of LFP power. But there are still a few questions remaining. (1) What exactly makes LFP power under ISO non-Gaussian? (2) Why can the linearity be modeled by a simple second order polynomial fit? (3) And why does this non-linearity seem to exist only under ISO anesthesia?

We hypothesized that the ultimate reason for the non-linearity is that taking the power of LFP induces a second order non-linearity. So alternatively, we can look at the LFP amplitude—BOLD relationship. [The "amplitude" we use here is simply the square root of the LFP power. For a narrow band like alpha band, gamma band, this is closer to the amplitude of the signal, whereas for the broadband signal (1–100 Hz), it is more like a root-mean-square (r.m.s.) values in a 1 s time window]. The reasoning for the hypothesis is the following.

Suppose LFP amplitude follows a Gaussian distribution, so the LFP amplitude—BOLD relationship is linear. The LFP power is the square of LFP amplitude, which transforms the original Gaussian distribution into a non-Gaussian one and, as a consequence, makes the LFP power—BOLD relationship become a quadratic curve. Since the LFP amplitude–BOLD relationship is assumed to be linear, any non-linearity observed in LFP power—BOLD relationship is equivalent to the non-linearity in LFP power–LFP amplitude relationship. For a fixed curve, like $y = x^2$ in the LFP amplitude—LFP power relationship, the non-linearity depends on the baseline (mean value) of the signal. In the case where the LFP amplitude has a very high baseline, like the one under DMED anesthesia, the non-linearity η, which is the ratio of the second order change to the first order change, become relatively small, while in the case where the LFP amplitude has a very low baseline, like the one under ISO anesthesia, the non-linearity η becomes relatively large. To illustrate this effect, we applied low pass filtering (0.1 Hz under ISO and 0.25 Hz under DMED) instead of band pass filtering, so that the direct current (DC) component, or the mean value of the signal can be preserved. Each scan sessions were again normalized using the same scaling factor from the band pass filtered signal, so that the alternating current (AC) component (0.01–0.1 Hz under ISO and 0.01–0.25 Hz under DMED) of the broadband signal (1–100 Hz) has a standard deviation of 1. **Figure 7** shows the distribution of the low pass filtered LFP broadband (1–100 Hz) amplitude

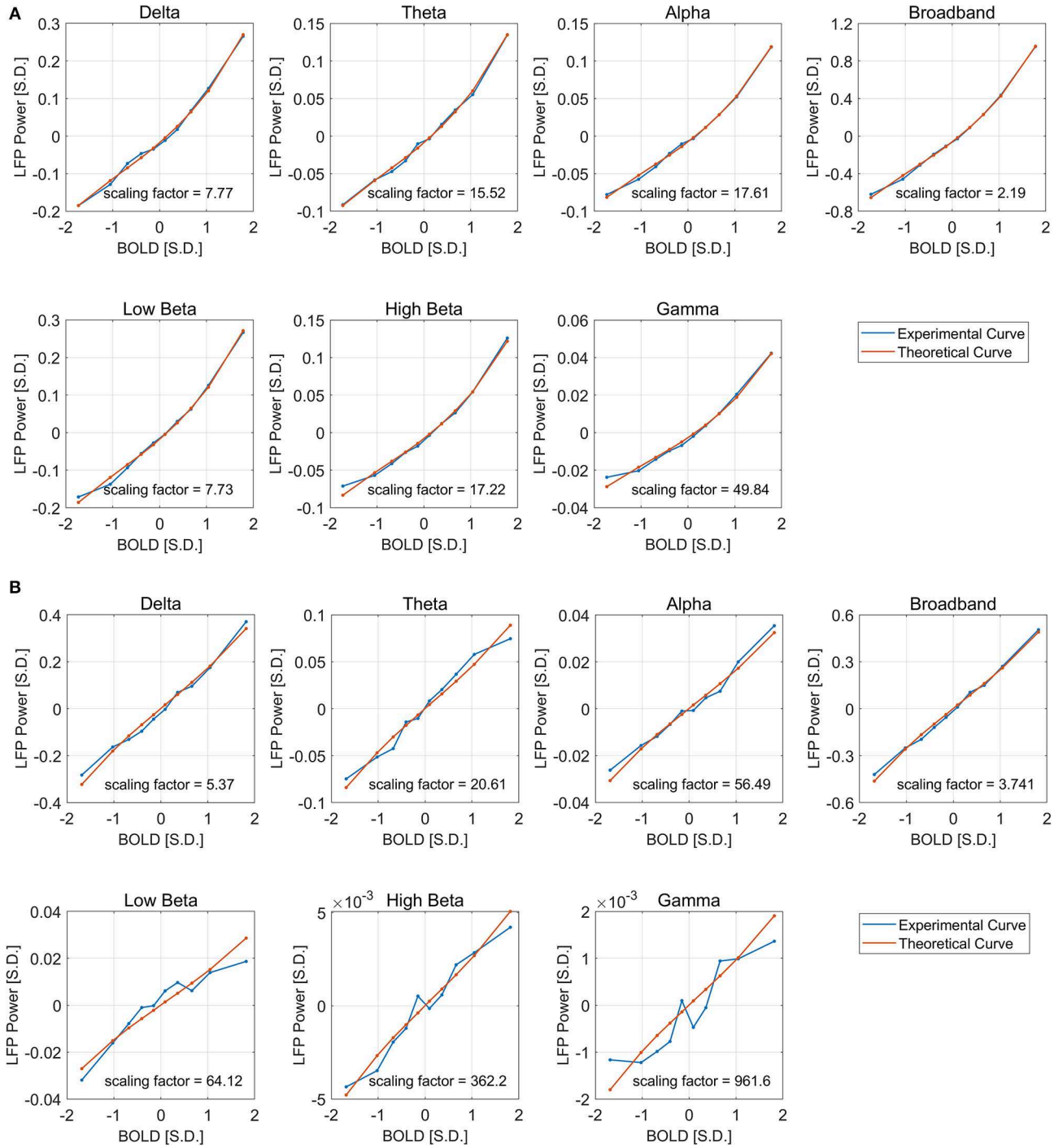

FIGURE 6 | Least square fitting of experimental and theoretical LFP vs. BOLD responses under ISO **(A)** and DMED **(B)**. The fitting is good across all frequency bands and both anesthesia conditions. The scaling factor shows the amount of amplification needed by the experimental response to match with the theoretical one.

time courses (with panel A shows five randomly selected scan sessions under ISO, and panel B shows the overall distributions under ISO and DMED). It is evident that the LFP amplitude has a significantly higher baseline under DMED when compared to under ISO. **Figure 8** shows the Monte Carlo simulation of how hypothetically four Gaussian distributions with different mean values (representing the LFP amplitude with different baseline) will transform into non-Gaussian ones by taking the power of two. The range of the mean values were selected to cover the distributions of LFP amplitude. It can be seen that

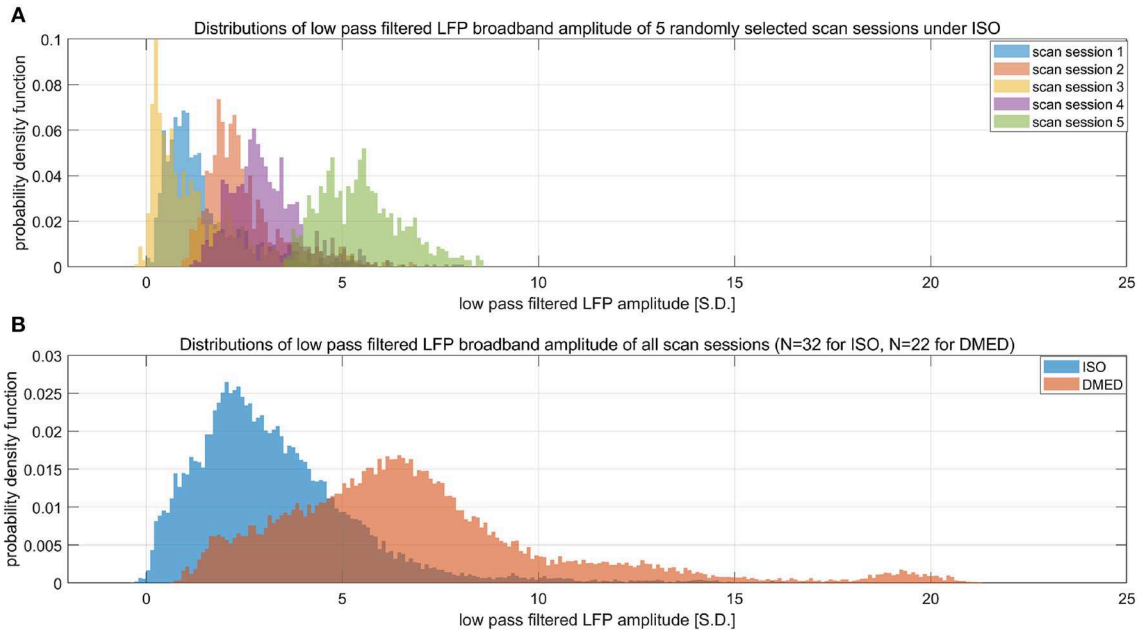

FIGURE 7 | Histograms of low pass filtered LFP broadband amplitude. **(A)** Shows five randomly selected scan sessions under ISO to illustrate the variety in their mean value. **(B)** Shows the overall distribution of low pass filtered (under 0.1 Hz under ISO and under 0.25 HZ under DMED) LFP broadband amplitude obtained from the entire dataset ($N = 32$ for ISO, $N = 22$ for DMED). Since low pass filtering preserves the direct current component, it can be seen that the LFP amplitude under ISO actually has a much lower baseline (mean value) when compared to under DMED. The unit in the figure is 1 standard deviation (S.D.) of the band pass filtered (0.01–0.1 Hz under ISO and 0.01–0.25 Hz under DMED) LFP broadband amplitude. So the scale of the signal is the same as the ones shown in previous figures, with the only difference being the superposition of the direct current component preserved by switching band pass filtering to low pass filtering.

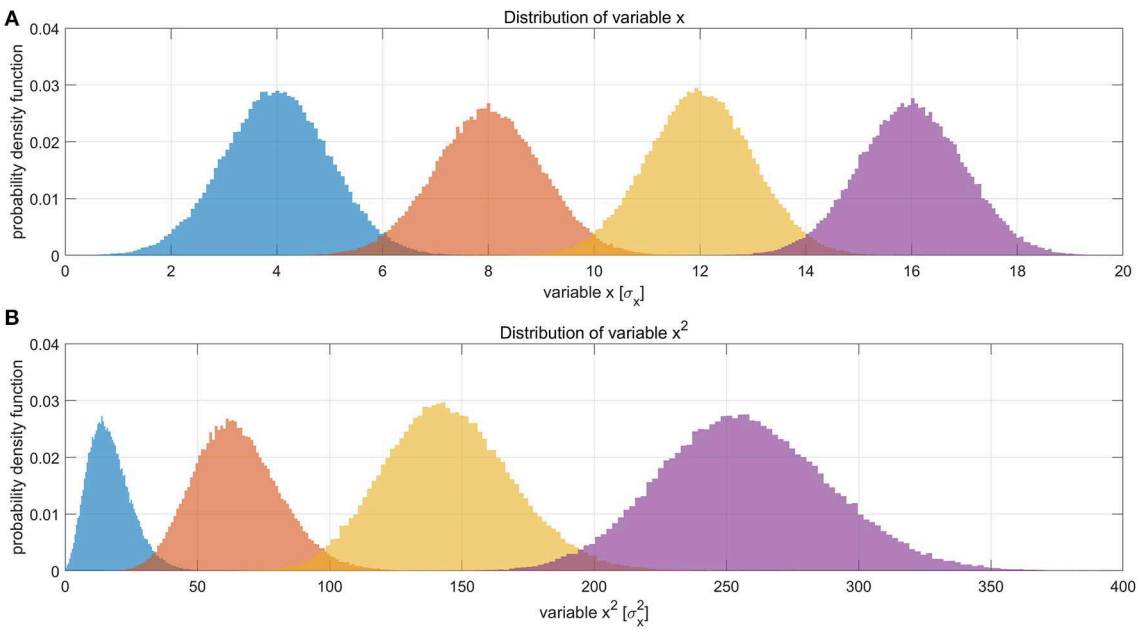

FIGURE 8 | Illustration of how Gaussian distributions can transform to non-Gaussian ones by taking the power of two, and the degree of non-linearity is influenced by the mean value (baseline) of the original distribution. **(A)** Shows four different distributions of a hypothetical variable x, representing the LFP amplitude. The histograms were obtained by Monte Carlo simulation of 100,000 points for each distribution. The four distributions have the same standard deviation ($\sigma = 1\sigma_x$) but different mean values ($\mu = 4\sigma_x,\ 8\sigma_x,\ 12\sigma_x,\ 16\sigma_x$, respectively). **(B)** Shows the distributions of variable x^2. The unit in panel B is σ_x^2. It can be clearly seen that the one with the lowest mean value (blue), become much more non-Gaussian after taking the power of two, whereas the one with the highest mean value (purple) still remains approximately Gaussian. This suggests that the non-Gaussian distribution of LFP power under ISO (shown in **Figure 4**) may partly come from taking the power of two.

for the one with the lowest mean value (blue), the transformed distribution clearly became non-Gaussian (to be more specific, positively skewed or right-tailed, just like the distribution of LFP power under ISO), whereas the one with the highest mean value (purple) still remains approximately Gaussian after taking the power of two. These suggest that the non-Gaussian distribution may come from taking the power of two, and since under ISO the baseline is lower, the non-linearity becomes greatly amplified. The hypothesis that the non-linearity comes from the nature of power might answer all of the questions at the same time, so it is very worthwhile to test whether this hypothesis is true or not.

Figure 9 shows the LFP amplitude vs. BOLD scatter plot. The settings are identical to **Figure 3**, except the LFP amplitude is substituted for LFP power. The histogram of LFP amplitude and BOLD are shown in **Figure 10**. While it appears that the LFP amplitude-BOLD relationship is still non-linear and the LFP amplitude is non-Gaussian, the non-linearity, measured by the ratio of second order term to first order term, does show a decrease when switched from LFP power to LFP amplitude (from 0.2923 to 0.2314). **Table 3** also shows that, the skewness of LFP amplitude is closer to 0 compared to LFP power. The kurtosis also became smaller, thereby the LFP amplitude is more Gaussian than LFP power. Using LFP amplitude does make the LFP–BOLD relationship a little bit more linear, although there are still other unknown factors that account for the remaining non-linearity.

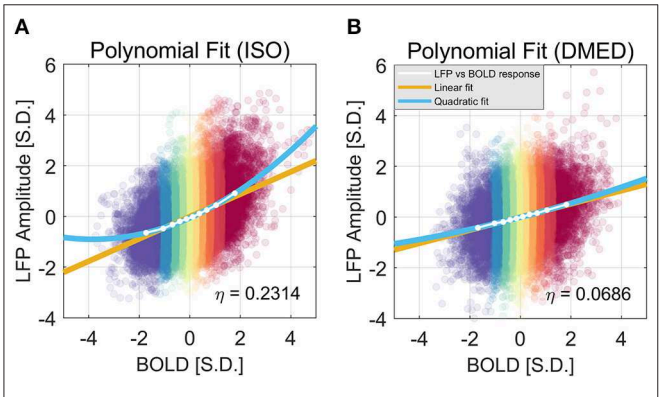

FIGURE 9 | Quadratic Fitting of LFP amplitude vs. BOLD response under ISO **(A)** and DMED **(B)**. It can be seen that, under ISO, the non-linearity in LFP amplitude–BOLD relationship is smaller than the one in LFP power—BOLD relationship, although the remaining non-linearity is still considerably larger than the one under DMED. Under ISO, the fitted coefficients a, b, c, are, 0.0570, 0.4386, −0.0606, respectively. The *p*-values are, 7.24e-6, 1.39e-11, 6.35e-5, respectively. The 95% confidence intervals are [0.0456, 0.0685], [0.4255, 0.4518], [−0.0775, −0.0437], respectively. Under DMED, the fitted coefficients a, b, c, are 0.0098, 0.2584, −0.0099, respectively. The *p*-values are 0.0321, 8.09e-11, 0.1085, respectively. The 95% confidence intervals are [0.0011, 0.0184], [0.2484, 0.2684], [−0.0226, 0.0028], respectively.

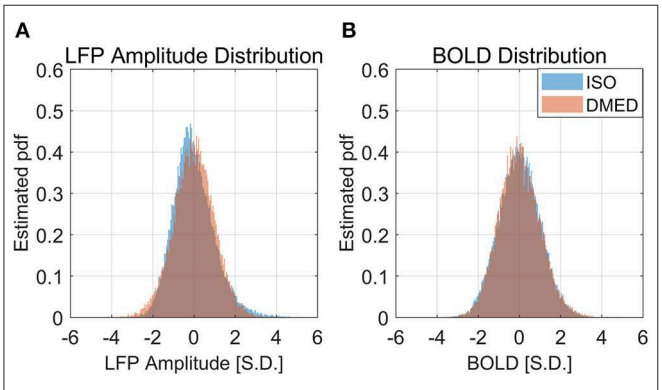

FIGURE 10 | Histogram of LFP broadband amplitude, BOLD under ISO **(A)** and DMED **(B)**. It can be seen that the LFP amplitude under ISO is less skewed than LFP power, but is still non-Gaussian distributed.

The Non-linearity Does Not Greatly Influence Pearson Correlation

We have shown that the LFP power–BOLD relationship is non-linear, and such non-linearity may come from the non-Gaussian distribution of LFP power. A further question is how this non-linearity will influence the data analysis, namely the correlation between LFP and BOLD. Theoretically, Pearson correlation coefficient only measures linear dependency. In the case that the relationship is extremely non-linear, more generalized analysis methods that do not assume linear relationship (e.g., mutual information) are desirable. We corrected the non-linearity of the LFP power—BOLD data by mapping the LFP-power distribution back to a Gaussian distribution using the inverse of the theoretical LFP-BOLD curve. From **Figure 11**, we can see that the non-linearity is reduced, judging by the non-linearity metric defined by Equation (6). However, the Pearson correlation is not significantly changed [the mean value of the Pearson correlation before and after correction were 0.4416 and 0.4411, respectively. The 95% confidence intervals of the Pearson correlation before and after correction were (0.4327, 0.4505), (0.4321, 0.4500), respectively].

DISCUSSIONS

LFP—BOLD Relationship Can Be Non-linear

Simultaneous LFP and fMRI data acquisition is an essential tool for understanding the connection between neural activity and the BOLD signal contrast. So far there is not a lot of detailed discussion about the non-linearity between LFP and BOLD recorded in the cortex. Logothetis et al. (2001) first described the relationship between LFP amplitude (more precisely, the root-mean-square value of gamma band LFP

TABLE 3 | Skewness and kurtosis of LFP amplitude and BOLD under ISO and DMED anesthesia.

	LFP ISO	LFP DMED	BOLD ISO	BOLD DMED
Skewness	**0.5870**	0.0170	0.0920	0.1753
Kurtosis	**3.8742**	3.4888	3.0895	3.0853

The skewness or kurtosis that deviates from a Gaussian distribution were highlighted in bold.

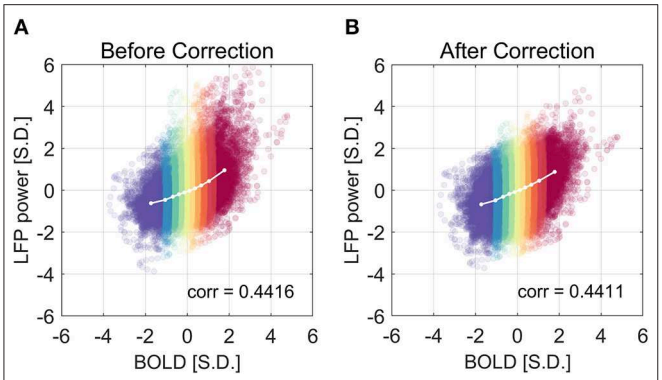

FIGURE 11 | The correlation coefficient is not improved after the non-linear correction. The correlation coefficient before and after non-linearity correction was shown in **(A)** and **(B)**, respectively. The experimental LFP power vs. BOLD relationship is more linear after the non-linear correction, but there is little change in the correlation coefficient.

time course) and BOLD as roughly linear. However, later in a review paper (Heeger and Ress, 2002), it was stated that their relationship is monotonic but non-linear, because a 12% stimulus contrast evoked about half the maximum fMRI response, but much less than half the maximum LFP and MUA (this does not actually contradict what Logothetis et al. found, because the non-linearity here is in the LFP/BOLD as a response to the stimulus, whereas the LFP directly plotted against BOLD is still roughly linear). Huttunen et al. (2008) performed a simultaneous LFP and BOLD recording under controlled fore paw stimulus with different frequencies. It is worth mentioning that, although many papers cited (Huttunen et al., 2008) as one revealing non-linearity in neural–hemodynamic coupling, the non-linearity was in the BOLD/LFP response as a function of stimulus frequencies. In terms of the LFP-BOLD relationship, which is the main focus of our paper, they discovered a strikingly high Pearson correlation between LFP and BOLD ($r = 0.97$ under urethane and $r = 0.89$ under alpha-chloralose). This correlation-based analysis suggests that the relationship between LFP and BOLD is actually quite linear under these anesthesia conditions. (Magri et al., 2012) proposed to use mutual information to study the relationship between LFP band limited power and BOLD in resting-state. Mutual information is the most general measure of the statistical dependency, and thus takes into account any non-linearity, which is superior to Pearson correlation in the presence of considerable non-linearity. However, they did not specifically measure how much non-linearity is present in the LFP-BOLD relationship. Devonshire et al. (2012) have found a non-linear relationship between the LFP responses and the BOLD responses (summed in a 40 s time window after stimulus) in sub-cortical regions, which manifests itself in a power law curve. In the meantime, they also found that the LFP-BOLD relationship was linear in S1 region. In our work, we proposed a method to quantify the non-linearity that is tailored for extremely noisy data like LFP and BOLD. The correlation between LFP and BOLD is 0.441 $\pm$ 0.124 under ISO, $n = 32$, and 0.267 $\pm$ 0.115 under DMED, $n = 22$. Given this range of correlation, it is not possible to provide a deterministic prediction for one variable if the other is known. By dividing the data into several subgroups based on BOLD values, and then averaging the LFP power within each BOLD subgroup, we obtained a LFP—BOLD relationship in which a non-linearity can be visually observed under ISO anesthesia. The group average is more robust to the randomness in the data, which enables the quantification of non-linearity.

From the 32 scan sessions under ISO, we observed a substantial non-linearity independent of the frequency band, in the form of second order polynomial fit. The consistency here suggests that the curved shape response is not a coincidence, but an actual phenomenon that is hiding under the noisy LFP—BOLD data. In contrast, the relationship is found to be linear in the 22 scan sessions under DMED, which suggests that such non-linearity is subject to the type of anesthesia. Isoflurane is commonly used to induce anesthesia, perform surgical procedures, and maintain a deep level of unconsciousness in rodents during setup for fMRI. At high isoflurane doses (>1.8%), widespread cortical neural burst suppression (Rehberg et al., 1996) results in reduced cortical excitation and reduced spatial sensitivity of functional connectivity, therefore, anesthesia is typically switched to an agent that is less suppressive of neural activity for during fMRI acquisition. However, at lower dosages (<1.5%), functional activity and connectivity remain fairly intact so there have been some studies using isoflurane during imaging as well (Guilfoyle et al., 2013; Kalthoff et al., 2013; Liu et al., 2013). In addition to the burst-suppression, isoflurane is also a vasodilator, which affects the cerebral blood flow (CBF), and thus will affect the BOLD signal. On the other hand, dexmedetomidine is less suppressive to neural activity, and induces a neural state very similar to natural sleep, while simultaneously causing muscular relaxation (Nelson et al., 2003). Dexmedetomidine is therefore more preferable in functional MRI in terms of the alterations of neural activity. However, dexmedetomidine is a vasoconstrictor, which also affects the CBF. We believe that comparing the data obtained under ISO and DMED can provide results that are more generalizable than using only one anesthetic agent. Thus, far, many studies performed with different anesthetic agents seem to conclude different frequency bands in LFP that best correlate with BOLD. From the ISO and DMED data presented here, it is possible that the apparent discrepancy is caused by the energy distribution under the specific anesthetic state. For example, the delta band might best correlate with BOLD if the anesthesia shifts the energy toward lower frequency bands. Further studies need to be performed on other anesthetic agents to support this hypothesis.

Non-linearity in LFP vs. BOLD Under ISO Anesthesia May Reflect the Non-gaussian Distribution of LFP Power

We proposed that the non-linearity may come from the highly skewed, non-Gaussian distribution of LFP power. We derived a theoretical LFP—BOLD curve solely from the overall distributions of LFP power and BOLD, without knowing any LFP-BOLD dynamics for any specific data points. The goodness

of the fit over all the frequency bands under both ISO and DMED suggests that the non-linearity in the LFP vs. BOLD relationship could come from the non-Gaussian distribution of LFP power.

Ultimately, the non-linearity may come from the LFP power itself, which has an intrinsic non-linear property when compared to the LFP amplitude. It is still questionable whether the LFP amplitude itself is linear vs. BOLD, and the observed non-linearity in LFP power may not come solely from taking the square. Nevertheless, the skewness, kurtosis, and the non-linearity measured by the second order/first order ratio are all smaller in LFP amplitude than in LFP power, suggesting the former one is relatively more linear. In addition, such hypothesis theoretically answered the three questions at the same time, making it quite reasonable, although it is still not fully confirmed. It appears that the non-linearity depends on the type of anesthesia, given the fact that in most studies the LFP—BOLD relationship is considered to be linear with the use of many different anesthetic agents, the non-linearity observed here might originated from something specific under ISO. One possible explanation is the burst-suppression, because the constant switching from "on" and "off" states, combined with a smoothing effect from the low pass filtering, does seem quite non-linear, and it is worth investigating in the future.

Implication for Future Studies

First, this study confirms that under some specific conditions, the LFP—BOLD relationship during spontaneous activity can be non-linear. Therefore, caution should be taken whenever analyzing simultaneous LFP and fMRI data, because apparently, depending on the animal model and the anesthetic agent used, there might be unexpected non-linearity present in the data. Mathematically, it is not accurate to use the Pearson correlation coefficient to describe the dependency between two variables when one variable is Gaussian distributed and the other is not Gaussian distributed (or the dependence is non-linear). The extent to which the accuracy is compromised depends on how much the distribution deviates from Gaussian distribution.

Secondly, we have evidence supporting the idea that the intrinsic properties of LFP power might contribute to some of the non-linearity between LFP power and BOLD. It is worth noting that, the LFP power is widely used because most studies involve the band limited LFP power in some specific frequency bands. Since the integration over a frequency band yield the LFP power in that band, naturally the LFP power would become the first option. If the LFP power does induce non-linearity, it might be worthwhile to think twice about whether to use LFP power or LFP amplitude, or at least to check the linearity when using LFP power. Currently, the most common ways to get LFP amplitude are wavelet transform or Fourier transform, Hilbert transformation, and direct band pass filtering. Other than the one obtained from Fourier transform, the different LFP amplitude components in different frequency bands are not orthogonal, and it is somewhat difficult to get back to the original form of signal.

Despite the fact that the LFP power—BOLD relationship is substantially non-linear, the correction of non-linearity between the two only slightly changes the correlation coefficient (from 0.4416 to 0.4411, not statistically significant). This leads to the conclusion that, in the presence of substantial non-linearity in this specific situation under ISO, the Pearson correlation coefficient is still a valid measurement of the dependency between LFP and BOLD, and in other cases where non-linearity is usually not detectable, Pearson correlation is a reasonable metric.

Technical Limitations

It is worth mentioning that the dataset for LFP—BOLD relationship analysis was deliberately chosen to have high cross-correlation between LFP power and BOLD around S1FL areas. While this ensures the overall quality of data, it may induce some bias as well. Only a very small portion of the dataset is usable for the analysis (32 scans out of 96 scans under ISO, and 22 scans out of 219 scans under DMED). Right now, the reason why the correlation coefficient can vary drastically in adjacent scans in the same rat, even with almost identical physiological conditions, is still unknown. Further studies are needed to understand the underlying mechanism to improve the utilization of the datasets, as well as to avoid the bias introduced by deliberately choosing datasets.

We would like to point out that there could be other ways to define non-linearity metrics, and the method we proposed here is not necessarily superior to any of these. For example, Emancipator and Kroll (1993) proposed a generic way to measure non-linearity by using the integral of the deviation (L2 norm) of the function from an ideal straight line. However, in this special case (quadratic model), the non-linearity measured using Equation (6) is relatively simple and intuitive. We would also like to mention that it is difficult to calculate statistical significance for the non-linearity term (defined as the ratio of the second order term to the first order term). It is relatively easy to test for differences between the first order coefficients or the second order coefficients alone, but much harder for the ratio, which has a non-Gaussian distribution. Although this is a drawback in our method, defining non-linearity in other ways e.g., using the method Emancipator and Kroll (1993), does not necessarily solve this problem.

CONCLUSION

We examined the simultaneous LFP and BOLD recording data and found that the relationship between LFP and BOLD can be non-linear, depending on the type of anesthesia. Under ISO, there is clear evidence not only showing the relationship is non-linear, but also suggesting such non-linearity may come from the non-Gaussian distribution of LFP power. The effect of taking the square to obtain power does not explain all of the non-linearity observed under ISO. Considering the "burst-suppression" phenomenon, which is unique in ISO anesthesia,

the switching from "on" and "off" state may induce some non-linearity through a mechanism that is not yet fully understood. This implies that in the future, more generalized methods that do not assume linear dependency might be more desirable than Pearson correlation-based analysis, although, in this particular situation under ISO, the non-linearity has little impact on the Pearson correlation coefficient.

DATA AVAILABILITY STATEMENT

The datasets analyzed in this manuscript are not publicly available. Requests to access the datasets should be directed to SK, shella.keilholz@bme.gatech.edu.

ETHICS STATEMENT

The animal study was reviewed and approved by The Institutional Animal Care and Use Committee.

AUTHOR CONTRIBUTIONS

XZ performed data analysis, developed the theory, and wrote the article. W-JP collected the data. SK supervised the work.

FUNDING

This work was supported by NIH 1 R01NS078095-01, BRAIN initiative R01 MH 111416, and NSF INSPIRE. The authors would like to thank Chinese Scholarship Council (CSC) for financial support and Center for Systems Imaging Core.

SUPPLEMENTARY MATERIAL

The Supplementary Material for this article can be found online at: https://www.frontiersin.org/articles/10.3389/fnins.2019.01126/full#supplementary-material

REFERENCES

Arthurs, O. J., and Boniface, S. (2002). How well do we understand the neural origins of the fMRI BOLD signal? *Trends Neurosci.* 25, 27–31. doi: 10.1016/S0166-2236(00)01995-0

Bandettini, P. A., and Ungerleider, L. G. (2001). From neuron to BOLD: new connections. *Nat. Neurosci.* 4:864. doi: 10.1038/nn0901-864

Belliveau, J. W., Kennedy, D. N., McKinstry, R. C., Buchbinder, B. R., Weisskoff, R., Cohen, M. S., et al. (1991). Functional mapping of the human visual cortex by magnetic resonance imaging. *Science* 254, 716–719. doi: 10.1126/science.1948051

Biswal, B., Zerrin Yetkin, F., Haughton, V. M., and Hyde, J. S. (1995). Functional connectivity in the motor cortex of resting human brain using echo-planar MRI. *Magn. Reson. Med.* 34, 537–541. doi: 10.1002/mrm.1910340409

de Zwart, J. A., van Gelderen, P., Jansma, J. M., Fukunaga, M., Bianciardi, M., and Duyn, J. H. (2009). Hemodynamic nonlinearities affect BOLD fMRI response timing and amplitude. *Neuroimage* 47, 1649–1658. doi: 10.1016/j.neuroimage.2009.06.001

Devonshire, I. M., Papadakis, N. G., Port, M., Berwick, J., Kennerley, A. J., Mayhew, J. E., et al. (2012). Neurovascular coupling is brain region-dependent. *Neuroimage* 59, 1997–2006. doi: 10.1016/j.neuroimage.2011.09.050

Devor, A., Dunn, A. K., Andermann, M. L., Ulbert, I., Boas, D. A., and Dale, A. M. (2003). Coupling of total hemoglobin concentration, oxygenation, and neural activity in rat somatosensory cortex. *Neuron* 39, 353–359. doi: 10.1016/S0896-6273(03)00403-3

Emancipator, K., and Kroll, M. H. (1993). A quantitative measure of nonlinearity. *Clin. Chem.* 39, 766–772.

Fox, P. T., and Raichle, M. E. (1986). Focal physiological uncoupling of cerebral blood flow and oxidative metabolism during somatosensory stimulation in human subjects. *Proc. Natl Acad. Sci. U.S.A.* 83, 1140–1144. doi: 10.1073/pnas.83.4.1140

Gruetter, R. (1993). Automatic, localized *in vivo* adjustment of all first-and second-order shim coils. *Magn. Reson. Med.* 29, 804–811. doi: 10.1002/mrm.1910290613

Guilfoyle, D. N., Gerum, S. V., Sanchez, J. L., Balla, A., Sershen, H., Javitt, D. C., et al. (2013). Functional connectivity fMRI in mouse brain at 7 T using isoflurane. *J. Neurosci. Methods* 214, 144–148. doi: 10.1016/j.jneumeth.2013.01.019

Heeger, D. J., and Ress, D. (2002). What does fMRI, and tell us about neuronal activity? *Nat. Rev. Neurosci.* 3:142. doi: 10.1038/nrn730

Hewson-Stoate, N., Jones, M., Martindale, J., Berwick, J., and Mayhew, J. (2005). Further nonlinearities in neurovascular coupling in rodent barrel cortex. *Neuroimage* 24, 565–574. doi: 10.1016/j.neuroimage.2004.08.040

Hoffmeyer, H. W., Enager, P., Thomsen, K. J., and Lauritzen, M. J. (2007). Nonlinear neurovascular coupling in rat sensory cortex by activation of transcallosal fibers. *J. Cereb. Blood Flow Metab.* 27, 575–587. doi: 10.1038/sj.jcbfm.9600372

Huttunen, J. K., Gröhn, O., and Penttonen, M. (2008). Coupling between simultaneously recorded BOLD response and neuronal activity in the rat somatosensory cortex. *Neuroimage* 39, 775–785. doi: 10.1016/j.neuroimage.2007.06.042

Jones, M., Hewson-Stoate, N., Martindale, J., Redgrave, P., and Mayhew, J. (2004). Nonlinear coupling of neural activity and CBF in rodent barrel cortex. *Neuroimage* 22, 956–965. doi: 10.1016/j.neuroimage.2004.02.007

Kalthoff, D., Po, C., Wiedermann, D., and Hoehn, M. (2013). Reliability and spatial specificity of rat brain sensorimotor functional connectivity networks are superior under sedation compared with general anesthesia. *NMR Biomed.* 26, 638–650. doi: 10.1002/nbm.2908

Liu, X., Zhu, X. H., Zhang, Y., and Chen, W. (2013). The change of functional connectivity specificity in rats under various anesthesia levels and its neural origin. *Brain Topogr.* 26, 363–377. doi: 10.1007/s10548-012-0267-5

Liu, Z., Rios, C., Zhang, N., Yang, L., Chen, W., and He, B. (2010). Linear and nonlinear relationships between visual stimuli, EEG and BOLD fMRI signals. *Neuroimage* 50, 1054–1066. doi: 10.1016/j.neuroimage.2010.01.017

Logothetis, N. K. (2008). What we can do and what we cannot do with fMRI. *Nature* 453, 869–878. doi: 10.1038/nature06976

Logothetis, N. K., Pauls, J., Augath, M., Trinath, T., and Oeltermann, A. (2001). Neurophysiological investigation of the basis of the fMRI signal. *Nature* 412, 150–157. doi: 10.1038/35084005

Magnuson, M. E., Thompson, G. J., Pan, W. J., and Keilholz, S. D. (2014). Time-dependent effects of isoflurane and dexmedetomidine on functional connectivity, spectral characteristics, and spatial distribution of spontaneous BOLD fluctuations. *NMR Biomed.* 27, 291–303. doi: 10.1002/nbm.3062

Magri, C., Schridde, U., Murayama, Y., Panzeri, S., and Logothetis, N. K. (2012). The amplitude and timing of the BOLD signal reflects the relationship between local field potential power at different frequencies. *J. Neurosci.* 32, 1395–1407. doi: 10.1523/JNEUROSCI.3985-11.2012

Mishra, A. M., Ellens, D. J., Schridde, U., Motelow, J. E., Purcaro, M. J., DeSalvo, M. N., et al. (2011). Where fMRI and electrophysiology agree to disagree: corticothalamic and striatal activity patterns in the WAG/Rij rat. *J. Neurosci.* 31, 15053–15064. doi: 10.1523/JNEUROSCI.0101-11.2011

Murayama, Y., Bießmann, F., Meinecke, F. C., Müller, K. R., Augath, M., Oeltermann, A., et al. (2010). Relationship between neural and hemodynamic signals during spontaneous activity studied with temporal kernel CCA. *Magn. Reson. Imag.* 28, 1095–1103. doi: 10.1016/j.mri.2009.12.016

Nelson, L. E., Lu, J., Guo, T., Saper, C. B., Franks, N. P., and Maze, M. (2003). The α2-adrenoceptor agonist dexmedetomidine converges on an endogenous sleep-promoting pathway to exert its sedative effects. *Anesthesiology* 98, 428–436. doi: 10.1097/00000542-200302000-00024

Ogawa, S., Lee, T. M., Kay, A. R., and Tank, D. W. (1990). Brain magnetic resonance imaging with contrast dependent on blood oxygenation. *Proc. Natl. Acad. Sci. U.S.A.* 87, 9868–9872. doi: 10.1073/pnas.87.24.9868

Ogawa, S., Tank, D. W., Menon, R., Ellermann, J. M., Kim, S. G., Merkle, H., et al. (1992). Intrinsic signal changes accompanying sensory stimulation: functional brain mapping with magnetic resonance imaging. *Proc. Natl. Acad. Sci. U.S.A.* 89, 5951–5955. doi: 10.1073/pnas.89.13.5951

Pan, W. J., Thompson, G., Magnuson, M., Majeed, W., Jaeger, D., and Keilholz, S. (2010). Simultaneous FMRI and electrophysiology in the rodent brain. *JoVE* 19:e1901. doi: 10.3791/1901

Pan, W. J., Thompson, G., Magnuson, M., Majeed, W., Jaeger, D., and Keilholz, S. (2011). Broadband local field potentials correlate with spontaneous fluctuations in functional magnetic resonance imaging signals in the rat somatosensory cortex under isoflurane anesthesia. *Brain Connect.* 1, 119–31. doi: 10.1089/brain.2011.0014

Pan, W. J., Thompson, G. J., Magnuson, M. E., Jaeger, D., and Keilholz, S. (2013). Infraslow LFP correlates to resting-state fMRI BOLD signals. *Neuroimage* 74, 288–297. doi: 10.1016/j.neuroimage.2013.02.035

Pawela, C. P., Biswal, B. B., Hudetz, A. G., Schulte, M. L., Li, R., Jones, S. R., et al. (2009). A protocol for use of medetomidine anesthesia in rats for extended studies using task-induced BOLD contrast and resting-state functional connectivity. *Neuroimage* 46, 1137–1147. doi: 10.1016/j.neuroimage.2009.03.004

Power, J. D., Barnes, K. A., Snyder, A. Z., Schlaggar, B. L., and Petersen, S. E. (2012). Spurious but systematic correlations in functional connectivity MRI networks arise from subject motion. *Neuroimage* 59, 2142–2154. doi: 10.1016/j.neuroimage.2011.10.018

Rehberg, B., Xiao, Y. H., and Duch, D. S. (1996). Central nervous system sodium channels are significantly suppressed at clinical concentrations of volatile anesthetics. *Anesthesiology* 84, 1223–1233. doi: 10.1097/00000542-199605000-00025

Sanganahalli, B. G., Herman, P., Blumenfeld, H., and Hyder, F. (2009). Oxidative neuroenergetics in event-related paradigms. *J. Neurosci.* 29, 1707–1718. doi: 10.1523/JNEUROSCI.5549-08.2009

Sanganahalli, B. G., Herman, P., Rothman, D. L., Blumenfeld, H., and Hyder, F. (2016). Metabolic demands of neural-hemodynamic associated and disassociated areas in brain. *J. Cereb. Blood Flow Metab.* 36, 1695–1707. doi: 10.1177/0271678X16664531

Sheth, S. A., Nemoto, M., Guiou, M., Walker, M., Pouratian, N., and Toga, A. W. (2004). Linear and nonlinear relationships between neuronal activity, oxygen metabolism, and hemodynamic responses. *Neuron* 42, 347–355. doi: 10.1016/S0896-6273(04)00221-1

Shmuel, A., Augath, M., Oeltermann, A., and Logothetis, N. K. (2006). Negative functional MRI response correlates with decreases in neuronal activity in monkey visual area V1. *Nat. Neurosci.* 9:569. doi: 10.1038/nn1675

Shmuel, A., and Leopold, D. A. (2008). Neuronal correlates of spontaneous fluctuations in fMRI signals in monkey visual cortex: implications for functional connectivity at rest. *Hum. Brain Mapp.* 29, 751–761. doi: 10.1002/hbm.20580

Silvennoinen, M. J., Clingman, C. S., Golay, X., Kauppinen, R. A., and Van Zijl, P. C. (2003). Comparison of the dependence of blood R2 and R on oxygen saturation at 1.5 and 4.7 Tesla. *Magnetic Resonance in Medicine: An Official Journal of the International Society for Magnetic Resonance in Medicine* 49, 47–60. doi: 10.1002/mrm.10355

Thulborn, K. R., Waterton, J. C., Matthews, P. M., and Radda, G. K. (1982). Oxygenation dependence of the transverse relaxation time of water protons in whole blood at high field. *Biochim. Biophys. Acta* 714, 265–270. doi: 10.1016/0304-4165(82)90333-6

Conflict of Interest: The authors declare that the research was conducted in the absence of any commercial or financial relationships that could be construed as a potential conflict of interest.

frontiers in Neuroscience

REVIEW
published: 23 April 2020
doi: 10.3389/fnins.2020.00321

Vigilance Effects in Resting-State fMRI

Thomas T. Liu[1,2]* *and Maryam Falahpour*[1]

[1] *Center for Functional MRI, University of California, San Diego, La Jolla, CA, United States,* [2] *Departments of Radiology, Psychiatry, and Bioengineering, University of California, San Diego, La Jolla, CA, United States*

Measures of resting-state functional magnetic resonance imaging (rsfMRI) activity have been shown to be sensitive to cognitive function and disease state. However, there is growing evidence that variations in vigilance can lead to pronounced and spatially widespread differences in resting-state brain activity. Unless properly accounted for, differences in vigilance can give rise to changes in resting-state activity that can be misinterpreted as primary cognitive or disease-related effects. In this paper, we examine in detail the link between vigilance and rsfMRI measures, such as signal variance and functional connectivity. We consider how state changes due to factors such as caffeine and sleep deprivation affect both vigilance and rsfMRI measures and review emerging approaches and methodological challenges for the estimation and interpretation of vigilance effects.

Keywords: vigilance, arousal, wakefulness, fMRI, EEG, functional connectivity

OPEN ACCESS

Edited by:
Shella Keilholz,
Emory University, United States

Reviewed by:
Michael W. L. Chee,
National University of Singapore, Singapore
Enzo Tagliazucchi,
Goethe University Frankfurt, Germany

***Correspondence:**
Thomas T. Liu
ttliu@ucsd.edu

Specialty section:
This article was submitted to Brain Imaging Methods, a section of the journal Frontiers in Neuroscience

Received: *08 November 2019*
Accepted: *18 March 2020*
Published: *23 April 2020*

Citation:
Liu TT and Falahpour M (2020) Vigilance Effects in Resting-State fMRI. Front. Neurosci. 14:321. doi: 10.3389/fnins.2020.00321

1. INTRODUCTION

Resting-state fMRI (rsfMRI) is a widely used method to characterize the functional organization of the brain at rest. A commonly used rsfMRI measure is the correlation coefficient between the blood oxygenation level dependent (BOLD) time series observed in different brain regions. This measure of functional connectivity (FC) has been shown to be sensitive to cognitive function and disease state (Greicius, 2008; Hampson et al., 2010). Other rsfMRI measures may also have diagnostic potential, such as the use of the variance of the rsfMRI global brain signal (defined as the mean of all BOLD signals in the brain) to distinguish schizophrenic patients from healthy controls (Yang et al., 2014). Because they do not require the subject to perform a task, rsfMRI measures are attractive for both research and clinical applications.

Despite the widespread use of rsfMRI-based methods, the origins of the underlying signals are still not well understood. However, there is growing evidence that fluctuations in vigilance can have a profound effect on the rsfMRI signal and derived metrics. In contrast to task-based fMRI studies in which there is an explicit task, rsfMRI studies are especially prone to vigilance effects due to the absence of an engaging task. Subjects often report difficulty in maintaining a constant level of vigilance or wakefulness during resting state scans. In a study that used data from over 1,100 subjects scanned by research groups across the world, Tagliazucchi and Laufs (2014) reported that about a third of participants lost wakefulness within the first 3 min of a resting-state scan and that half of the participants lost wakefulness after 10 min. In addition to vigilance fluctuations within a scan, there can be pronounced differences in the mean vigilance levels between subjects and scans, due to factors such as medication use, disease state, and anxiety levels. Unless properly accounted for, differences in vigilance can give rise to changes in resting-state activity that can be misinterpreted as primary disease-related effects. Most rsfMRI studies currently make the implicit

assumption that all participants are in similar states of wakefulness or vigilance, but the validity of this assumption is rarely evaluated. A better understanding of potential vigilance effects is critical to the correct interpretation of both past and future rsfMRI studies.

Our goal in this paper is to critically review the relevant findings regarding the link between vigilance and the rsfMRI signal. We will examine the evidence relating variations in vigilance to the amplitude of the rsfMRI signal and derived metrics such as measures of both static and dynamic functional connectivity. We will also consider how state changes due to factors such as caffeine and sleep deprivation affects both vigilance and rsfMRI measures. Finally, we will review emerging methods for the estimation of vigilance effects and conclude with a consideration of methodological concerns, potential mechanisms, and future avenues of research.

2. VIGILANCE METRICS

In this work, we will primarily use the term *vigilance* but will also use related terms such as *arousal* and *wakefulness*. The term vigilance has been employed in a number of prior studies (Matejcek, 1982; Jobert et al., 1994; Oken et al., 2006; Olbrich et al., 2009). Additional related terms in the literature include *cortical arousal*, *sustained attention*, and *tonic alertness* (Oken et al., 2006; Sadaghiani et al., 2010; Olbrich et al., 2011).

In considering vigilance effects in rsfMRI studies, we will find it useful to consider independent measures of vigilance that are applicable to the resting-state. Most metrics of resting-state vigilance are based on EEG measures that have emerged from a wide range of scientific studies over the past century (Oken et al., 2006; Olbrich et al., 2009; Knaut et al., 2019). Other measures include pupilometry and percent eyelid closure. However, these metrics are only applicable to studies in which the subjects are instructed to keep their eyes open.

2.1. EEG-Based Metrics

For differentiating wakefulness from sleep and characterizing different sleep stages, EEG-based metrics have been standardized by the American Academy of Sleep Medicine (AASM, 2009), with a sleep stage score assigned to each 30 s epoch. In contrast, there is not currently a standard metric for characterizing the temporal fluctuations in arousal and vigilance that occur between wakefulness (W) and the first stage (N1) of non-REM sleep. **Table 1** summarizes various EEG-based metrics that have been proposed over the past several decades. Although they differ in specific details, the metrics are generally related to the ratio of the power in middle frequency bands (e.g., α and β bands) associated with increased wakefulness to the power in lower frequency bands (e.g., δ and θ) associated with decreased wakefulness (Klimesch, 1999; Oken et al., 2006). In contrast to the 30 s epochs used for the standard sleep stage scores, these metrics have been used with temporal intervals as short as 1.8 s. In Jobert et al. (1994), Larson-Prior et al. (2009), and Wong et al. (2013), the proposed metrics have the form of either the ratio of the power in the alpha band to the power in the delta and theta bands or the square root of this ratio. Horovitz et al. (2008) used the inverse of the square root of the ratio as an inverse index of wakefulness. Olbrich et al. (2009) used the ratio of the power in the alpha band to the power in the delta, theta, and alpha bands. More recently, Knaut et al. (2019) proposed an EEG wakefulness index that is a ratio of powers that depends on both the EEG frequency band and topography. **Table 1** also includes two related metrics recently utilized by Chang et al. (2016) for non-human primate studies.

2.2. Other Metrics

In rsfMRI studies where subjects are instructed to keep their eyes open, measures of pupil or eyelid closure can be used to assess vigilance and arousal levels. For example a number of studies have used measures of eye closure to assess drowsiness and the presence of microsleeps (Poudel et al., 2014; Chang et al., 2016; Wang et al., 2016). Similarly, pupil diameter has been used to assess vigilance states during resting-state scans (Yellin et al., 2015; Schneider et al., 2016; Breeden et al., 2017).

3. RESTING-STATE BOLD SIGNAL AMPLITUDE AND VIGILANCE

In considering the relationship between BOLD signal amplitude and vigilance, investigators have considered (1) the mean amplitude of the BOLD signal in different brain regions of interest and (2) the amplitude of the global mean signal, defined as the average of the BOLD signals in either the entire brain or gray matter regions. Note that for rsfMRI signals the amplitude was defined in early studies as the standard deviation of the time course of interest (Fukunaga et al., 2006; Horovitz et al., 2008), a definition that has been adopted by a number of subsequent studies (Wong et al., 2012, 2013; Cordani et al., 2018). This is in contrast to the definition used in task-based fMRI for which the term amplitude typically refers to the difference between the BOLD signals measured in baseline and activation states. In addition to the use of the standard deviation, other metrics that are related to the amplitude have been used, including the variance of the rsfMRI signal (Jao et al., 2013; Yang et al., 2014) and the spectral power of the rsfMRI signal in a specified frequency band (Kiviniemi et al., 2005; Larson-Prior et al., 2009; Cordani et al., 2018). On the other hand, some studies have regressed the rsfMRI signal onto measures of vigilance state and examined the amplitudes of the regression fit coefficients as a function of state (Olbrich et al., 2009; Poudel et al., 2018). For these studies, the amplitudes can be interpreted as in a task-based fMRI study, with the fit coefficients providing information about the difference in BOLD signals between vigilance states.

3.1. Wakefulness to Light Sleep

The use of long duration (e.g., 30 min) resting-state scans has facilitated the study of the rsfMRI signal as subjects fluctuate between wakefulness and light sleep. In general, these studies have found that the amplitude of the BOLD signal increases with decreases in wakefulness. Fukunaga et al. (2006) reported that the mean BOLD signal amplitude in the visual cortex increased during early sleep stages, with amplitudes that were comparable to those observed with visual stimulation. In a follow-up

TABLE 1 | Vigilance metrics.

Name	Description	Electrodes	Period	References
Inverse index of wakefulness	$\sqrt{\frac{P_{\delta,\theta}:[2-7\ Hz]}{P_{\alpha}:[8-12\ Hz]}}$	C3,4; P3,4	120 s	Horovitz et al., 2008
Alpha slow wave index (1)	$\frac{P_{\alpha}:[8-11.5\ Hz]}{P_{\delta,\theta}:[2-8\ Hz]}$	Cz	30 s	Jobert et al., 1994
Alpha slow wave index (2)	$\frac{P_{\alpha}:[8-12\ Hz]}{P_{\delta,\theta}:[1-8\ Hz]}$	C3	30 s	Larson-Prior et al., 2009
EEG vigilance (1)	$\frac{P_{\alpha}:[8-12\ Hz]}{P_{\delta,\theta,\alpha}:[2-12\ Hz]}$	F3,4; O1,2	3 s	Olbrich et al., 2009
EEG vigilance (2)	$\sqrt{\frac{P_{\alpha}:[7-13\ Hz]}{P_{\delta,\theta}:[1-7\ Hz]}}$	All	1.8 s	Wong et al., 2013
EEG wakefulness index	$\frac{P_{\theta_f,\alpha_O,\alpha_O,\beta_f}:[4-30\ Hz]}{P_{\delta_f,\theta_O,\alpha_f,\alpha_C,\beta_f}:[0.5-30\ Hz]}$	F3,4; O1,2; C3,4	2 s	Knaut et al., 2019
LFP arousal index	$\sqrt{\frac{P_{\beta}:[15-25\ Hz]}{P_{\theta}:[3-7\ Hz]}}$	Intracranial: V1,V2, F, P	2.6 s	Chang et al., 2016
Pupillometry	Pupil diameter	NA	> 20 ms	Schwalm and Rosales Jubal, 2017
Behavioral arousal index	% Eyelid opening	NA	2.6s	Chang et al., 2016

The notation $P_{\delta,\theta}:[f_1-f_2\ Hz]$ indicates the power in the indicated EEG frequency bands (e.g., δ and θ bands), as well as the minimum f_1 and maximum f_2 frequencies covered by the collection of indicated bands.

EEG electrode locations are specified with the standard notation of F, O, C, and P for frontal, occipital, central, and parietal regions, respectively. For metrics where the band powers in the definition are limited to certain regions, these constraints are indicated as subscripts, with the subscripts f, o, and c referring to frontal, occipital, and central regions, respectively. For example θ_f indicates θ band power from the frontal region. With the exception of the Inverse Index of Wakefulness, all of the metrics are designed to increase with vigilance. For the vigilance metric proposed by Olbrich et al. (2009) the expression provided in the table is used to define two major stages of vigilance, each of which has three sub-stages as defined in the cited paper. In the work of Wong et al. (2013), variants of the EEG vigilance metric defined using regional subsets of electrodes were also used. For the metrics in Chang et al. (2016) the electrode locations refer to the placement of intracranial electrodes.

study using simultaneous EEG-fMRI, Horovitz et al. (2008) confirmed the prior findings of Fukunaga et al. (2006) and further demonstrated a significant correlation between the BOLD signal amplitude and an Inverse Index of Wakefulness (see **Table 1**) in multiple brain regions, including the visual cortex, auditory cortex, and precuneus. Larson-Prior et al. (2009) found that the global signal spectral power significantly increased during light sleep as compared with awake states, with a general trend toward significance in individual regions of interest. Using a measure of vigilance stages, Olbrich et al. (2009) found that decreases in vigilance were associated with an increase in the BOLD signal amplitude in the occipital cortex, the anterior cingulate, the frontal cortex, the parietal cortices, and the temporal cortices and a decrease in BOLD signal amplitude in the thalamus and frontal regions. McAvoy et al. (2018) demonstrated that the amplitude of the global mean signal increased with sleep depth. They concluded that the increase in global signal amplitude reflected a proportionally greater decrease in oxygen consumption with sleep as compared to the sleep-related decrease in blood flow.

3.2. Variations Across Subject Scans and States

The relation between BOLD signal amplitude and vigilance can also be examined by considering variations in the two quantities across scans and experimental conditions. Wong et al. (2013) looked at the amplitude of the resting-state global signal and EEG vigilance measures across scans and found a strong and significant negative correlation between the two quantities when subjects were studied in the eyes-closed condition, with a weaker and nearly significant correlation observed in the eyes-open condition. Thus, scans for which the subjects exhibited relatively higher vigilance levels had lower global signal amplitudes, while scans with relatively lower vigilance levels were associated with higher global signal amplitudes.

Wong et al. (2013) also considered the effects of caffeine on vigilance and global signal amplitude and found that increases in vigilance due to caffeine were significantly correlated with decreases in the amplitude of the resting-state global signal. In contrast, in a study using the sedative midazolam, Kiviniemi et al. (2005) found an increase in the spectral power of low frequency BOLD fluctuations. Similarly, Esposito et al. (2010) found that the depressant alcohol increased spontaneous BOLD fluctuations in the visual cortex. These pharmacological studies further support the notion of an inverse relation between vigilance and the amplitude of resting-state BOLD fluctuations.

A number of studies have examined differences in resting-state fMRI activity between the eyes-closed (EC) and eyes-open (EO) conditions (Yang et al., 2007; McAvoy et al., 2008, 2012; Bianciardi et al., 2009; Yan et al., 2009; Zou et al., 2009; Jao et al., 2013; Patriat et al., 2013; Xu et al., 2014; Yuan et al., 2014). In general, these studies have found that the amplitude of the resting-state BOLD signal is decreased in the eyes-open condition as compared to the eyes-closed condition. For example, Jao et al. (2013) found that the average variance of the BOLD signal was significantly lower in the eyes-open condition. There is some diversity in the findings, with regional resting-state activity sometimes found to be higher in the EO condition, with the differences most likely reflecting variations in processing approaches, such as the use of global signal regression and physiological noise reduction in some studies and not others.

Using simultaneous EEG fMRI, Wong et al. (2015) demonstrated an overall increase in EEG vigilance in the EO state as compared to the EC state and found that these increases in vigilance were negatively correlated with the differences in global signal amplitude between the two states. Interestingly, the slope between the changes in vigilance and differences in global signal amplitude was similar to the slope found in Wong et al. (2013) relating the caffeine-induced changes in vigilance and

global signal amplitude. The similarity between the relationships observed for the EO-EC changes and the caffeine-related changes suggest that the basic mechanisms underlying the vigilance and global signal amplitude relationship may to some extent be independent of the experimental manipulation.

Cordani et al. (2018) found that the resting-state BOLD signal amplitude in the sensory cortices decreases at times corresponding to dawn and dusk, possibly reflecting an anticipatory mechanism in which spontaneous activity is reduced in order to improve visual perception during times associated with low light levels. Yeo et al. (2015) reported that the amplitude of the global signal increased with sleep deprivation. Similarly, Poudel et al. (2018) observed spatially widespread increases in the BOLD signal associated with microsleeps after both normal rest and sleep deprivation conditions.

4. TEMPORAL FLUCTUATIONS IN VIGILANCE DURING A SCAN

The various studies reviewed in the prior section largely support the overall conclusion that the amplitude of the resting-state BOLD signal over a given time period is inversely proportional to the average vigilance level of the subject during that period. Over the course of scan, there are also moment to moment variations in arousal and vigilance. Their effect on rsfMRI data can be assessed by looking at the correlation between the rsfMRI signal and a vigilance-associated time course. Using simultaneous EEG fMRI, a number of studies have established that EEG alpha power is negatively correlated with fMRI signals in widespread regions of the brain, including the visual and fronto-parietal cortices (Goldman et al., 2002; Laufs et al., 2003a,b; Moosmann et al., 2003). Positive correlations have been reported for the thalamus, insula, and anterior cingulate (Goldman et al., 2002; Moosmann et al., 2003; Feige et al., 2005; Difrancesco et al., 2008; Sadaghiani et al., 2010). Using the metric of EEG vigilance from Wong et al. (2013), Falahpour et al. (2018a) found similar spatial patterns of correlation, which is expected given the close link between the vigilance metric and alpha power.

It has also been shown that there is a significant negative correlation between the rsfMRI global signal and EEG vigilance time courses (Falahpour et al., 2016, 2018a). **Figure 1** shows an example of this negative correlation, where the plot in the middle row shows the vigilance time series in blue and the global signal (inverted for display) in red. The top row shows the rsfMRI images obtained by averaging over time points corresponding to the top 10% of vigilance values. Consistent with prior observations, these show positive signal values in the thalamus and negative values in sensory areas. In the bottom row, images obtained by averaging over time points with the lowest 10% of vigilance values shows the opposite pattern, with negative signal values in the thalamus and positive values in sensory areas.

Han et al. (2019) have recently put forth the hypothesis that the observed correlations between the EEG and rsfMRI signals are due to stereotypical electrophysiological events, first observed in the global signal of large-scale electrocorticography (ECoG) recordings from monkeys by Liu et al. (2015). These sequential spectral transition (SST) events were found to last for 10–20 s and consisted of a decrease in mid-band (alpha and beta; 8–30 Hz) activity followed by an increase in low frequency (delta and theta; < 30 Hz) activity and a burst of high-frequency broadband gamma activity (>30 Hz). The SST events were later shown to be coupled with peaks in the rsfMRI global signal (Liu et al., 2018), roughly consistent with the aforementioned findings of a significant negative correlation between the rsfMRI global signal and EEG vigilance time series. As further evidence for the role of transient activity in EEG-BOLD correlations, Poudel et al. (2014) observed transient changes in BOLD activity associated with microsleeps. Furthermore, in subjects who exhibited a higher occurrence of microsleeps, the authors found that post-central EEG theta power was positively correlated with the BOLD signal in the thalamus, basal forebrain, visual, posterior parietal, and prefrontal cortices.

Using pupilometry, Schneider et al. (2016) found that spontaneous pupil dilations were associated with increased BOLD activity in the salience network, thalamus, and frontoparietal regions, whereas spontaneous pupil constrictions were associated with increased BOLD activity in the visual and sensoriomotor areas. Similarly, several studies have reported a positive correlation between pupil size and the rsfMRI BOLD signal in regions comprising cingulo-opercular, default mode, and fronto-parietal networks and a negative correlation in the visual and sensorimotor regions (Yellin et al., 2015; Breeden et al., 2017; DiNuzzo et al., 2019). To first order, the spatial pattern of correlations observed with pupilometry are roughly consistent with those reported using simultaneous EEG fMRI studies. In addition, a positive correlation has been demonstrated between pupil size and BOLD activity in the locus coeruleus (Murphy et al., 2014; DiNuzzo et al., 2019), a nucleus in the brainstem that contains norepinephrine neurons that are thought to modulate pupil size (Joshi et al., 2016).

5. FUNCTIONAL CONNECTIVITY AND VIGILANCE

Complementing the work relating vigilance to BOLD amplitude, the connection between vigilance and rsfMRI FC has also been explored by a number of investigators. The main investigative approaches include examining (1) differences in FC across sleep stages, (2) temporal variations in FC as a function of alpha power or a related time-varying measure of vigilance, and (3) FC changes associated with induced changes in state. A recent extensive review of the relation between FC and sleep has been provided by Tagliazucchi and Van Someren (2017). The effects of sleep deprivation have been recently reviewed by Chee and Zhou (2019).

5.1. Functional Connectivity and Sleep Stages

Both Larson-Prior et al. (2011) and Sämann et al. (2011) reported decreases in the extent of anti-correlations between the default mode network (DMN) and the task positive network (TPN) during the transition to light sleep. Tagliazucchi et al. (2012a) demonstrated that FC measures and nonlinear support vector machines could be used to classify sleep stages and later used

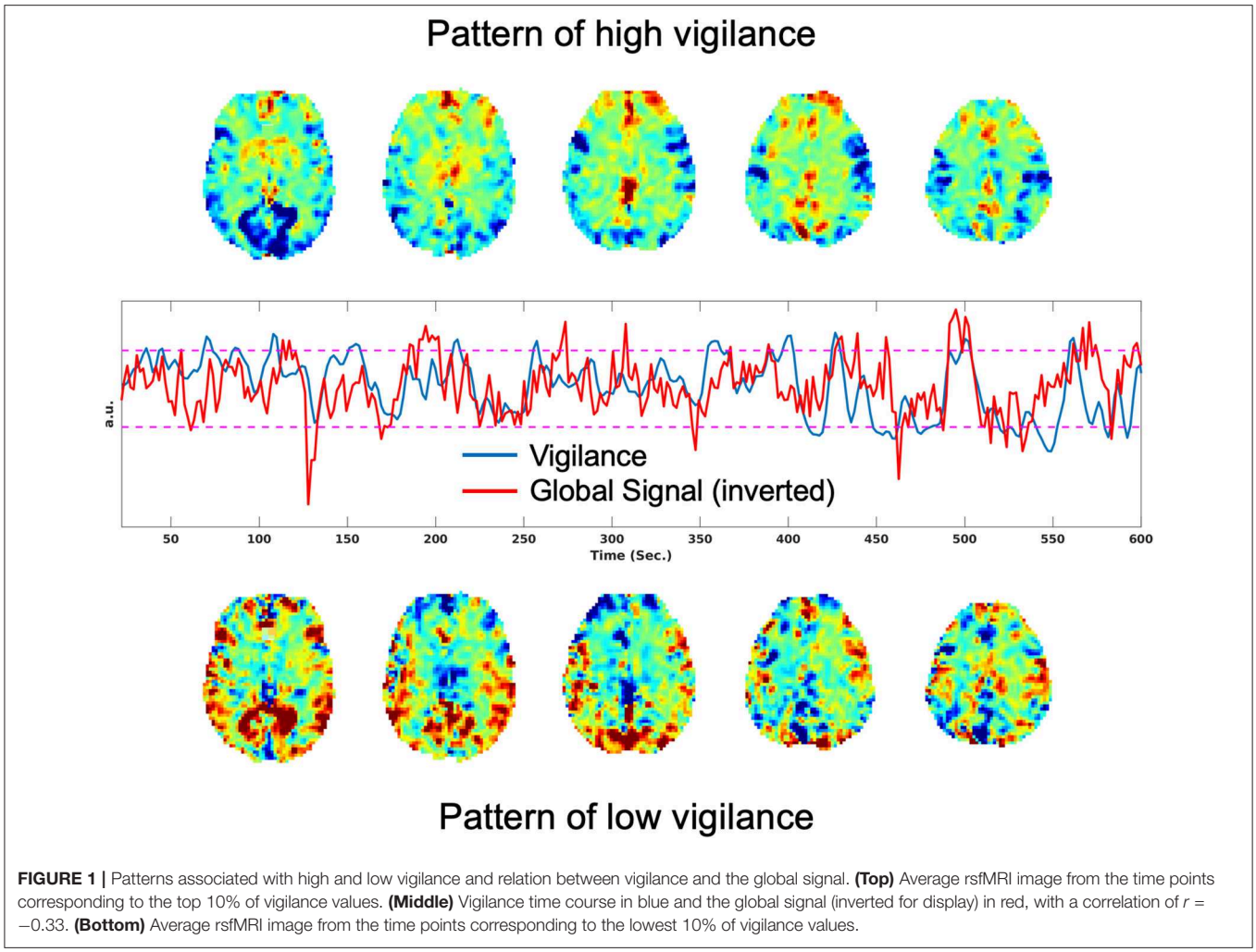

FIGURE 1 | Patterns associated with high and low vigilance and relation between vigilance and the global signal. **(Top)** Average rsfMRI image from the time points corresponding to the top 10% of vigilance values. **(Middle)** Vigilance time course in blue and the global signal (inverted for display) in red, with a correlation of $r = -0.33$. **(Bottom)** Average rsfMRI image from the time points corresponding to the lowest 10% of vigilance values.

this relation to characterize wakefulness levels across a large collection of rsfMRI studies (Tagliazucchi and Laufs, 2014). Subsequently, Altmann et al. (2016) found that linear support vector machines could also be used to predict sleep stages from FC measures.

Haimovici et al. (2017) found that dynamic functional connectivity states obtained through clustering algorithms were similar to the average FC state found in each sleep stage, suggesting that variations in dynamic functional connectivity states are associated with fluctuations in wakefulness. Zou et al. (2019) later reported similar findings. Using a Hidden Markov model (HMM) approach, Stevner et al. (2019) identified multiple FC states associated with each sleep stage and characterized the transition between states within and between stages. Laumann et al. (2017) showed that a multivariate measure of kurtosis was significantly correlated with an index of sleep and argued that this was evidence for a sleep-related increase in the temporal variability of FC measures.

5.2. Alpha Power and FC

In examining dynamic fluctuations in FC across the duration of a scan, Tagliazucchi et al. (2012b) found that time-varying increases in alpha power were correlated with decreases in functional connectivity as measured in awake subjects. As increased alpha power is proportional to vigilance (see EEG metrics), this finding suggests that time-varying FC decreases with increased vigilance in a manner that is largely consistent with the reductions in FC observed across an entire scan when mean vigilance increases (e.g., with caffeine). Similarly, Scheeringa et al. (2012) reported that increases in alpha power were associated with a decrease of FC within the visual system and also a diminishing of the negative relation between the visual cortex and thalamus. In related work, Chang et al. (2013) observed that the time-varying strength of connectivity between the DMN and default attention network (DAN) was inversely proportional to the alpha power measured within the same time window (40 s window length).

Allen et al. (2018) noted that certain dynamic FC (DFC) states were found more frequently in the EO condition while other DFC states were found predominantly in the EC condition. They identified a DFC state related to increased drowsiness (lower alpha and higher delta and theta power) in which there were high levels of FC in the sensorimotor and visual regions and the increased presence of anti-correlations between the thalamus and these regions.

5.3. Induced State Changes

Caffeine has been shown to lead to spatially widespread decreases in rsfMRI FC measures (Wong et al., 2012). Using the same sample of subjects, Tal et al. (2013) employed source-localized magnetoencephalography (MEG) to demonstrate similar decreases in MEG-based measures of resting-state connectivity. In a follow-up study, Wong et al. (2013) reported that caffeine-induced increases in EEG vigilance were significantly correlated with increases in the anti-correlation between nodes of the DMN and TPN. Taking into account the observation that caffeine also reduces the amplitude of the global signal, the authors concluded that the increased presence of anti-correlations could be largely attributed to the reduction in global rsfMRI activity (Wong et al., 2012, 2013). In addition, the caffeine-induced increases in anti-correlation were consistent with the aforementioned decreases in anti-correlations observed in the transition to light sleep (Larson-Prior et al., 2011; Sämann et al., 2011).

In studies with the sedative midazolam, Kiviniemi et al. (2005) found increased FC within the sensory-motor network, consistent with the observed increase in the amplitude of BOLD signal fluctuations. Further evidence for this increase was presented by Greicius et al. (2008), who observed a midazolam-related increase in FC in the sensory-motor network, but reported a decrease in FC in the DMN. In a study using the sedative zolpidem, Licata et al. (2013) reported a drug-related increase in FC in a number of sensory, motor, and limbic networks.

As discussed in section 3.2, vigilance is higher and the global signal amplitude is lower in the EO versus the EC state. It has also been found that functional connectivity is generally lower in the EO state as compared to the EC state (McAvoy et al., 2008; Bianciardi et al., 2009; Zou et al., 2009; Xu et al., 2014). This decreased connectivity is consistent with the decreased global activity and increased vigilance in the EO state. Furthermore, these decreases in global signal amplitude and increases in vigilance may account for the increased reliability of connectivity measures obtained in the EO condition as compared to the EC state (Patriat et al., 2013).

In reviewing prior studies that have observed state-based changes in functional connectivity, it is important to note that there can be some variability in the reporting of connectivity changes, especially when there are both positive and negative correlation values. As an example, for the studies reporting reduced connectivity in the EO state as compared to the EC state, the findings can be divided into three groups: (1) both EO and EC correlation values are positive, and the EO values are less positive (i.e., smaller numerical value) (McAvoy et al., 2008; Bianciardi et al., 2009), (2) the EO and EC correlation values are either both positive or both negative, and the EO values are either less positive or less negative, respectively (i.e., absolute magnitude of the EO correlation values are smaller independent of the sign) (Zou et al., 2009), or (3) EC values are positive, and EO values are either less positive or negative (i.e., the EC values are greater than the EO values, with the possibility that a negative EO value could have a larger magnitude than a positive EC value) (Xu et al., 2014). Paying attention to the sign of the correlation values is especially important when examining studies that use global signal regression, since this preprocessing step has been shown to introduce negative correlation values (Murphy et al., 2009).

5.4. Sleep Deprivation

De Havas et al. (2012) found that sleep deprivation led to reductions in both DMN functional connectivity and the degree of anticorrelation between the DMN and other regions. These findings were supported by a follow-up study by Yeo et al. (2015), who reported that subjects who exhibited less vigilance declines after sleep deprivation showed stronger anti-correlations among several networks. These results were obtained with global signal regression. When GSR was not applied, Yeo et al. (2015) observed a spatially widespread increase in functional connectivity with sleep deprivation. Wirsich et al. (2018) also reported widespread increases in FC with sleep deprivation. Zhang et al. (2019) found that sleep deprivation lead to decreases in FC between the cerebellum and a number of brain regions and an increase in FC between the cerebellum and bilateral caudate.

Ong et al. (2015) examined spontaneous eye closures in sleep deprived subjects and reported additional reductions in the FC in the DMN and DAN beyond what had been previously observed for sleep deprivation. In a related study, Wang et al. (2016) went on to identify a *low arousal* DFC state associated with spontaneous eye closures and another *high arousal* state associated with periods of the eyes remaining wide open. Patanaik et al. (2018) found that subjects with a greater fraction of *high arousal* states showed higher levels of vigilance, working memory, and processing speed after sleep restriction.

Kaufmann et al. (2016) reported that sleep deprivation led to significant alterations in several resting-state FC networks, including the dorsal attention, default mode, and hippocampal networks, with an overall increase in FC values with sleep deprivation. Furthermore, they found differences in FC between morning and evening measures with a return to morning FC patterns after a night of sleep. They used partial correlation instead of global signal regression. Tüshaus et al. (2017) observed that sleep pressure led to significant changes in the FC between resting-state networks as determined using independent components analysis. Yang et al. (2018) reported that sleep deprivation led to decreases in FC density (FCD) in brain regions including the posterior cingulate cortex and precuneus and increases in sensory integration and arousal regulating areas, such as thalamus.

6. fMRI-BASED VIGILANCE ESTIMATES

As discussed above, EEG and measures of eye closure or pupil size can be used to assess vigilance during rsfMRI studies. However, the additional acquisition and analysis efforts associated with these measures have precluded their widespread use in rsfMRI studies. Simultaneous EEG-fMRI scans are technically challenging and require specialized equipment and substantial set-up time (with current technologies). Pupilometry poses less of a logistical challenge, but the equipment costs, set-up time, and analysis requirements can still complicate its adoption

for many studies. Video-based measures of eye closure are more readily implemented and demand relatively little setup-time, but still require additional effort to analyze the images. Nevertheless, more rsfMRI studies should probably consider regular video monitoring of eye state given the relative ease of use and the potential benefit of the information.

Vigilance estimates based on the fMRI data alone can serve as a useful alternative to external measures, especially in studies where there is limited time available for additional set-up procedures. As noted in prior sections, Tagliazucchi et al. (2012a) and Altmann et al. (2016) used windowed rsfMRI connectivity estimates to estimate sleep stages in 30 s epochs. To provide estimates on a finer time scale, Chang et al. (2016) introduced an fMRI template-based approach to estimate arousal fluctuations in awake monkeys sitting in complete darkness. In this approach, a spatial template was first formed, where the value of each voxel in the template reflected the strength of the correlation between the fMRI data and an eye-based metric of arousal. Correlation of this spatial template with each volume of an independent fMRI dataset was then used to form an estimate of arousal for each timepoint in the test dataset.

Falahpour et al. (2018a) subsequently applied the template-based approach to simultaneous EEG-fMRI data acquired in humans and demonstrated the ability to predict EEG-based measures of vigilance fluctuations, supporting the generalizability of the approach from macaques to humans. They also demonstrated that the performance of the method was related to the overall amount of variability in a subject's vigilance state and that the approach could be used to estimate the variability across scans in the amplitude of the vigilance fluctuations. In a recent preprint, Gu et al. (2019) used a global co-activation map (Liu et al., 2018) as a template and found that the resulting estimates were similar to those derived using the template in Falahpour et al. (2018a). A graphical summary of the template-based approach is provided in **Figure 2**.

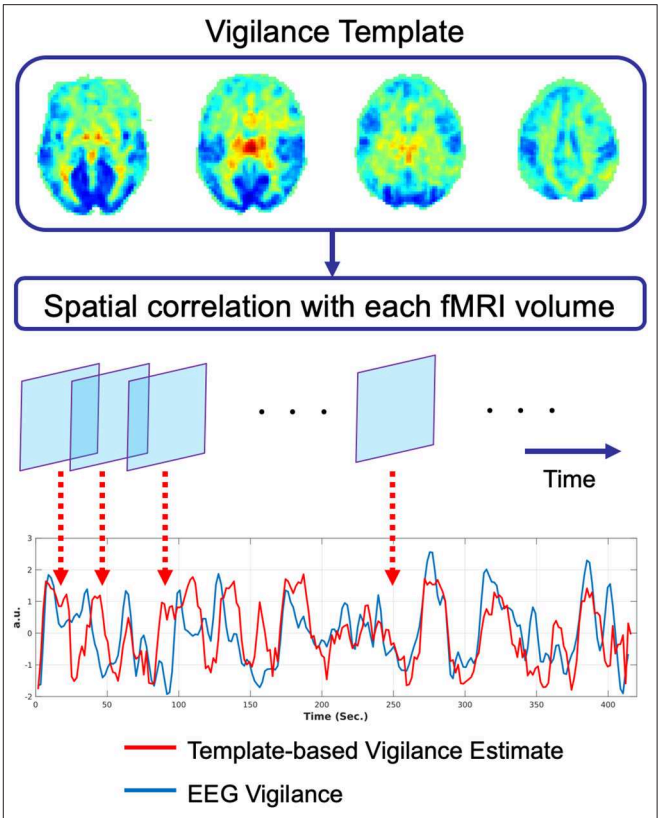

FIGURE 2 | Graphical summary of the template-based approach for prediction of vigilance fluctuations as described in Chang et al. (2016). The vigilance template is obtained by correlating the fMRI data with an estimate of EEG vigilance measure as described in Falahpour et al. (2018a), using data originally acquired for a prior study (Wong et al., 2013). This vigilance template was then applied to an independent simultaneous EEG-fMRI dataset. For each timepoint in the fMRI data, the spatial correlation between the template and the fMRI volume is computed to form an estimate of vigilance (red line). This estimate is highly correlated (r = 0.51) with the EEG-based measure of vigilance (blue line).

7. METHODOLOGICAL CONSIDERATIONS

One of the challenges in understanding vigilance effects in rsfMRI stems from the presence of noise components (both BOLD and non-BOLD weighted) such as system-related instabilities, subject motion, and physiological fluctuations. While there have been considerable efforts to characterize and mitigate the effects of these components in BOLD fMRI time series (Birn, 2012; Greve et al., 2013; Murphy et al., 2013; Power et al., 2015), the choice of methods varies widely between rsfMRI studies. This lack of uniformity makes it difficult to compare results across studies. For studies of vigilance, the problem is further complicated by the connection between vigilance and several of the primary noise confounds, such as the global signal, motion, and respiratory activity (Yuan et al., 2013; Liu et al., 2017; Patanaik et al., 2018). For example, Yuan et al. (2013) reported that the correlation between EEG alpha power and rsfMRI signal was reduced after respiratory and cardiac nuisance regressors were projected out of the rsfMRI data. Similarly, Patanaik et al. (2018) found that the relation between vigilance and the global signal was reduced when motion was used as a covariate.

In the case of the global signal, there is still an ongoing debate as to whether the global signal should be regressed out prior to the analysis of rsfMRI data (Liu et al., 2017). Due to the relation between the global signal and vigilance, the use of global signal regression (GSR) can have a significant effect on findings regarding the connection between vigilance and the rsfMRI signal. As an example, Falahpour et al. (2018b) noted that prior studies that did not use GSR generally found a negative correlation between EEG alpha power (or vigilance) and the BOLD signal in widespread regions of the brain, including the lingual gyrus, posterior cingulate, cuneus, and precuneus (Goldman et al., 2002; Laufs et al., 2003b; Falahpour et al., 2018a). In contrast, a study that used GSR found positive correlations in additional areas not reported in prior studies, including the dorsal anterior cingulate cortex, the anterior insula, and the anterior prefrontal cortex (Sadaghiani et al., 2010). Falahpour

et al. (2018b) went on to demonstrate that GSR induced a positive shift in the correlation between EEG vigilance and the rsfMRI signal, roughly consistent with the discrepancy in the prior findings.

To address the methodological challenges, the support and use of open multimodal neuroimaging databases and standardized processing approaches (Poldrack et al., 2017; Babayan et al., 2019) will become increasingly important. These resources will facilitate the comparison of various methods and studies and enable researchers to better understand the relation between rsfMRI and vigilance measures.

8. VIGILANCE AND DISEASE

There is growing evidence that disregulation of arousal is associated with a variety of mental disorders such as depression, autism, and schizophrenia (Boutros et al., 2008; Razavi et al., 2013; Sander et al., 2016; Jawinski et al., 2019). In a genome-wise association study, Jawinski et al. (2019) found an association between resting-state vigilance levels (as assessed with EEG) and genetic markers for major depressive disorder, autism spectrum disorder, and Alzheimer's disease. In parallel, there has been widespread use of rsfMRI to study disease-related alterations in resting-state brain activity and connectivity. For example, rsfMRI studies of schizophrenia have reported disease-related differences in functional connectivity and signal variance (Calhoun et al., 2011; Yang et al., 2014; Wang et al., 2015). Given the link between rsfMRI measures and vigilance and prior findings indicating a decrease in EEG vigilance with schizophrenia (Boutros et al., 2008; Razavi et al., 2013), it is likely that disease-related vigilance effects contributed to the observed differences. Yang et al. (2014) reported that the variance of the global signal was significantly higher in patients with schizophrenia as compared to normal controls and concluded that the differences reflected an increase in neural coupling. However, the authors acknowledged that the potential confound of vigilance differences between groups would need to be carefully considered in follow-up work.

9. POTENTIAL MECHANISMS

Although the mechanisms underlying the relationship between vigilance fluctuations and the rsfMRI signal are not well understood, the evidence from prior observational studies (see section 4) suggests a link with activity in brain regions related to arousal, such as the basal forebrain and the locus coeruleus. Recent studies involving invasive neuromodulation in animal models support this view. Turchi et al. (2018) observed reduced global signal fluctuations in macaques with inactivation of the nucleus basalis of Meynert, a group of neurons in the basal forebrain with widespread arousal-related modulatory projections to the cortex. Using chemogenetic activation of the locus coeruleus in a mouse model, Zerbi et al. (2019) found an increase in functional connectivity in several networks, including the salience network, consistent with the relation between increased rsfMRI activity and pupil size discussed in section 4.

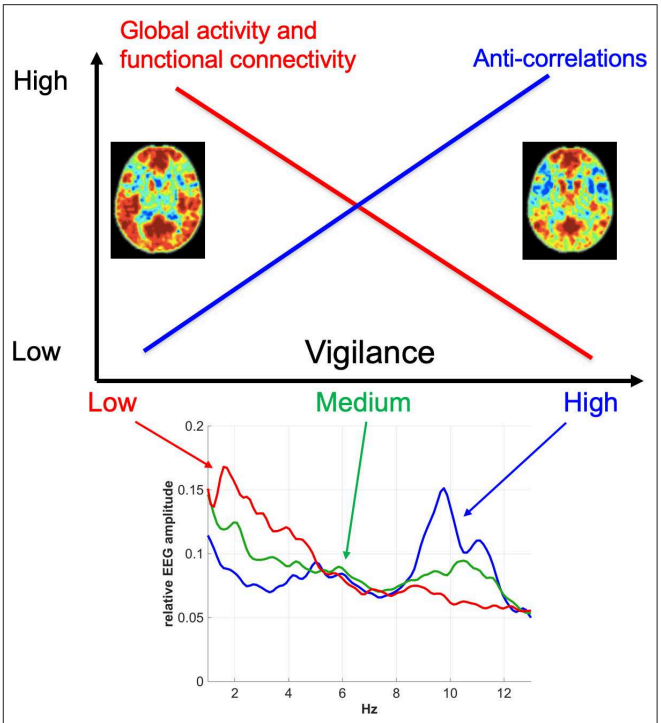

FIGURE 3 | Overview of the relationship between vigilance and rsfMRI signal amplitude and functional connectivity. In general, vigilance is negatively correlated with rsfMRI signal amplitude, with higher vigilance levels corresponding to global reductions in fMRI activity and functional connectivity. These reductions are associated with a greater presence of anti-correlations in functional connectivity maps at higher vigilance levels. The functional connectivity maps were obtained using a seed signal from the posterior cingulate cortex and acquired before (left) and after (right) the administration of caffeine (Wong et al., 2012). The bottom plot shows representative EEG spectra for low, medium, and high vigilance levels (Wong et al., 2013).

As the rsfMRI signal is a complex reflection of neural, metabolic, and vascular factors (Liu, 2013), a better understanding of the link between vigilance and the rsfMRI signal requires deeper insight into the relative contribution of these factors. Using data from all-night EEG-fMRI sleep studies, Özbay et al. (2019) demonstrated a tight relationship between the occurrence of K-complexes, episodic drops in finger skin vascular tone, and widespread decreases in the rsfMRI signal. The authors argued that the findings were consistent with a picture in which increased sympathetic activity associated with K-complexes resulted in vasoconstriction of the cerebral vasculature and a concomitant decrease in the rsfMRI signal. As this study focused on activity during NREM Stage 2 sleep, additional studies will be needed to further elucidate the role of arousal-related sympathetic activity in rsfMRI studies during which the subjects are largely awake.

10. CONCLUSION

There is now substantial evidence indicating that vigilance effects play a significant role in resting-state fMRI studies. The first

order effects are summarized in **Figure 3**. In general, there is a negative correlation between vigilance and global rsfMRI activity, with higher vigilance levels leading to global reductions in signal variance and functional connectivity and an increase in the presence of anti-correlations in functional connectivity maps. However, the details of the observed effects vary between studies and conditions. While part of this variation may reflect differences in processing and analysis approaches, it is likely that a significant part of the remaining variation reflects different underlying causes for the vigilance changes and variability. A better understanding of the mechanisms linking vigilance and resting-state brain activity will be helpful for understanding these variations and their impact on the interpretation of rsfMRI studies. Toward that end, invasive studies in animal models (Turchi et al., 2018; Zerbi et al., 2019) can provide insights not readily attainable in human studies. Finally, differences in vigilance can give rise to changes in resting-state activity that can be misinterpreted as primary disease-related effects. The further development of approaches to better estimate and account for vigilance effects will play a critical role in the improved interpretation of rsfMRI data in both clinical and research settings.

AUTHOR CONTRIBUTIONS

All authors listed have made a substantial, direct and intellectual contribution to the work, and approved it for publication.

FUNDING

This work was supported in part by NIH grant R21MH112155.

REFERENCES

AASM (2009). *The AASM Manual for the Scoring of Sleep and Associated Events: Rules, Terminology and Technical Specification.*

Allen, E. A., Damaraju, E., Eichele, T., Wu, L., and Calhoun, V. D. (2018). EEG signatures of dynamic functional network connectivity states. *Brain Topogr.* 31, 101–116. doi: 10.1007/s10548-017-0546-2

Altmann, A., Schröter, M. S., Spoormaker, V. I., Kiem, S. A., Jordan, D., Ilg, R., et al. (2016). Validation of non-REM sleep stage decoding from resting state fMRI using linear support vector machines. *Neuroimage* 125, 544–555. doi: 10.1016/j.neuroimage.2015.09.072

Babayan, A., Erbey, M., Kumral, D., Reinelt, J. D., Reiter, A. M. F., Röbbig, J., et al. (2019). A mind-brain-body dataset of MRI, EEG, cognition, emotion, and peripheral physiology in young and old adults. *Sci. Data* 6:180308. doi: 10.1038/sdata.2018.308

Bianciardi, M., Fukunaga, M., van Gelderen, P., Horovitz, S., de Zwart, J., and Duyn, J. (2009). Modulation of spontaneous fMRI activity in human visual cortex by behavioral state. *Neuroimage* 45, 160–168. doi: 10.1016/j.neuroimage.2008.10.034

Birn, R. M. (2012). The role of physiological noise in resting-state functional connectivity. *NeuroImage* 62, 864–870. doi: 10.1016/j.neuroimage.2012.01.016

Boutros, N. N., Arfken, C., Galderisi, S., Warrick, J., Pratt, G., and Iacono, W. (2008). The status of spectral EEG abnormality as a diagnostic test for schizophrenia. *Schizophr. Res.* 99, 225–237. doi: 10.1016/j.schres.2007.11.020

Breeden, A. L., Siegle, G. J., Norr, M. E., Gordon, E. M., and Vaidya, C. J. (2017). Coupling between spontaneous pupillary fluctuations and brain activity relates to inattentiveness. *Eur. J. Neurosci.* 45, 260–266. doi: 10.1111/ejn.13424

Calhoun, V. D., Sui, J., Kiehl, K., Turner, J., Allen, E., and Pearlson, G. (2011). Exploring the psychosis functional connectome: aberrant intrinsic networks in schizophrenia and bipolar disorder. *Front. Psychiatry* 2:75. doi: 10.3389/fpsyt.2011.00075

Chang, C., Leopold, D. A., Schölvinck, M. L., Mandelkow, H., Picchioni, D., Liu, X., et al. (2016). Tracking brain arousal fluctuations with fMRI. *Proc. Natl. Acad. Sci. U.S.A.* 113, 4518–4523. doi: 10.1073/pnas.1520613113

Chang, C., Liu, Z., Chen, M. C., Liu, X., and Duyn, J. H. (2013). EEG correlates of time-varying BOLD functional connectivity. *NeuroImage* 72, 227–236. doi: 10.1016/j.neuroimage.2013.01.049

Chee, M. W. L., and Zhou, J. (2019). Functional connectivity and the sleep-deprived brain. *Prog. Brain Res.* 246, 159–176. doi: 10.1016/bs.pbr.2019.02.009

Cordani, L., Tagliazucchi, E., Vetter, C., Hassemer, C., Roenneberg, T., Stehle, J. H., et al. (2018). Endogenous modulation of human visual cortex activity improves perception at twilight. *Nat. Commun.* 9:1274. doi: 10.1038/s41467-018-03660-8

De Havas, J. A., Parimal, S., Soon, C. S., and Chee, M. W. L. (2012). Sleep deprivation reduces default mode network connectivity and anti-correlation during rest and task performance. *NeuroImage* 59, 1745–1751. doi: 10.1016/j.neuroimage.2011.08.026

Difrancesco, M. W., Holland, S. K., and Szaflarski, J. P. (2008). Simultaneous EEG/functional magnetic resonance imaging at 4 Tesla: correlates of brain activity to spontaneous alpha rhythm during relaxation. *J. Clin. Neurophysiol.* 25, 255–264. doi: 10.1097/WNP.0b013e3181879d56

DiNuzzo, M., Mascali, D., Moraschi, M., Bussu, G., Maugeri, L., Mangini, F., et al. (2019). Brain networks underlying eye's pupil dynamics. *Front. Neurosci.* 13:965. doi: 10.3389/fnins.2019.00965

Esposito, F., Pignataro, G., Renzo, G. D., Spinali, A., Paccone, A., Tedeschi, G., et al. (2010). Alcohol increases spontaneous BOLD signal fluctuations in the visual network. *NeuroImage* 53, 534–543. doi: 10.1016/j.neuroimage.2010.06.061

Falahpour, M., Chang, C., Wong, C. W., and Liu, T. T. (2018a). Template-based prediction of vigilance fluctuations in resting-state fMRI. *NeuroImage* 174, 317–327. doi: 10.1016/j.neuroimage.2018.03.012

Falahpour, M., Nalci, A., and Liu, T. T. (2018b). The effects of global signal regression on estimates of resting-state blood oxygen-level-dependent functional magnetic resonance imaging and electroencephalogram vigilance correlations. *Brain Connect.* 8, 618–627. doi: 10.1089/brain.2018.0645

Falahpour, M., Wong, C. W., and Liu, T. T. (2016). "The resting state fMRI global signal is negatively correlated with time-varying EEG vigilance," in *Proceedings of the 24th Annual Meeting of the ISMRM* (Singapore), 641.

Feige, B., Scheffler, K., Esposito, F., Di Salle, F., Hennig, J., and Seifritz, E. (2005). Cortical and subcortical correlates of electroencephalographic alpha rhythm modulation. *J. Neurophysiol.* 93, 2864–2872. doi: 10.1152/jn.00721.2004

Fukunaga, M., Horovitz, S. G., Van Gelderen, P., De Zwart, J. A., Jansma, J. M., Ikonomidou, V. N., et al. (2006). Large-amplitude, spatially correlated fluctuations in BOLD fMRI signals during extended rest and early sleep stages. *Magn. Reson. Imaging* 24, 979–992. doi: 10.1016/j.mri.2006.04.018

Goldman, R. I., Stern, J. M., Engel, J., and Cohen, M. S. (2002). Simultaneous EEG and fMRI of the alpha rhythm. *Neuroreport* 13, 2487–2492. doi: 10.1097/00001756-200212200-00022

Greicius, M. (2008). Resting-state functional connectivity in neuropsychiatric disorders. *Curr. Opin. Neurol.* 21, 424–430. doi: 10.1097/WCO.0b013e328306f2c5

Greicius, M. D., Kiviniemi, V., Tervonen, O., Vainionpää, V., Alahuhta, S., Reiss, A. L., et al. (2008). Persistent default-mode network connectivity during light sedation. *Hum. Brain Mapp.* 29, 839–847. doi: 10.1002/hbm.20537

Greve, D. N., Brown, G. G., Mueller, B. A., Glover, G., and Liu, T. T. (2013). A survey of the sources of noise in fMRI. *Psychometrika* 78, 396–416. doi: 10.1007/s11336-012-9294-0

Gu, Y., Han, F., Sainburg, L. E., and Liu, X. (2019). Transient arousal modulations are responsible for resting-state functional connectivity changes associated with head motion. *bioRxiv*. doi: 10.1101/444463

Haimovici, A., Tagliazucchi, E., Balenzuela, P., and Laufs, H. (2017). On wakefulness fluctuations as a source of BOLD functional connectivity dynamics. *Sci. Rep.* 7:5908. doi: 10.1038/s41598-017-06389-4

Hampson, M., Driesen, N., Roth, J. K., Gore, J. C., and Constable, R. T. (2010). Functional connectivity between task-positive and task-negative brain areas and its relation to working memory performance.

Magn. Reson. Imaging 28, 1051–1057. doi: 10.1016/j.mri.2010.03.021

Han, F., Gu, Y., and Liu, X. (2019). A neurophysiological event of arousal modulation may underlie fMRI-EEG correlations. *Front. Neurosci.* 13:823. doi: 10.3389/fnins.2019.00823

Horovitz, S. G., Fukunaga, M., De Zwart, J. A., Van Gelderen, P., Fulton, S. C., Balkin, T. J., et al. (2008). Low Frequency BOLD fluctuations during resting wakefulness and light sleep: a simultaneous EEG-fMRI study. *Hum. Brain Mapp.* 29, 671–682. doi: 10.1002/hbm.20428

Jao, T., Vértes, P. E., Alexander-Bloch, A. F., Tang, I.-N., Yu, Y.-C., Chen, J.-H., et al. (2013). Volitional eyes opening perturbs brain dynamics and functional connectivity regardless of light input. *NeuroImage* 69, 21–34. doi: 10.1016/j.neuroimage.2012.12.007

Jawinski, P., Kirsten, H., Sander, C., Spada, J., Ulke, C., Huang, J., et al. (2019). Human brain arousal in the resting state: a genome-wide association study. *Mol. Psychiatry* 24, 1599–1609. doi: 10.1038/s41380-018-0052-2

Jobert, M., Schulz, H., Jahnig, P., Tismer, C., Bes, F., and Escola, H. (1994). A computerized method for detecting episodes of wakefulness during sleep based on the alpha slow-wave index. *Sleep* 17, 37–46.

Joshi, S., Li, Y., Kalwani, R. M., and Gold, J. I. (2016). Relationships between pupil diameter and neuronal activity in the locus coeruleus, colliculi, and cingulate cortex. *Neuron* 89, 221–234. doi: 10.1016/j.neuron.2015.11.028

Kaufmann, T., Elvsåshagen, T., Alnæs, D., Zak, N., Pedersen, P. Ø., Norbom, L. B., et al. (2016). The brain functional connectome is robustly altered by lack of sleep. *NeuroImage* 127, 324–332. doi: 10.1016/j.neuroimage.2015.12.028

Kiviniemi, V. J., Haanpää, H., Kantola, J.-H., Jauhiainen, J., Vainionpää, V., Alahuhta, S., et al. (2005). Midazolam sedation increases fluctuation and synchrony of the resting brain BOLD signal. *Magn. Reson. Imaging* 23, 531–537. doi: 10.1016/j.mri.2005.02.009

Klimesch, W. (1999). EEG alpha and theta oscillations reflect cognitive and memory performance: a review and analysis. *Brain Res. Brain Res. Rev.* 29, 169–195. doi: 10.1016/S0165-0173(98)00056-3

Knaut, P., von Wegner, F., Morzelewski, A., and Laufs, H. (2019). EEG-correlated fMRI of human alpha (de-)synchronization. *Clin. Neurophysiol.* 130, 1375–1386. doi: 10.1016/j.clinph.2019.04.715

Larson-Prior, L. J., Power, J. D., Vincent, J. L., Nolan, T. S., Coalson, R. S., Zempel, J., et al. (2011). Modulation of the brain's functional network architecture in the transition from wake to sleep. *Prog. Brain Res.* 193, 277–294. doi: 10.1016/B978-0-444-53839-0.00018-1

Larson-Prior, L. J., Zempel, J. M., Nolan, T. S., Prior, F. W., Snyder, A. Z., and Raichle, M. E. (2009). Cortical network functional connectivity in the descent to sleep. *Proc. Natl. Acad. Sci. U.S.A.* 106, 4489–4494. doi: 10.1073/pnas.0900924106

Laufs, H., Kleinschmidt, A., Beyerle, A., Eger, E., Salek-Haddadi, A., Preibisch, C., et al. (2003a). EEG-correlated fMRI of human alpha activity. *NeuroImage* 19, 1463–1476. doi: 10.1016/S1053-8119(03)00286-6

Laufs, H., Krakow, K., Sterzer, P., Eger, E., Beyerle, A., Salek-Haddadi, A., et al. (2003b). Electroencephalographic signatures of attentional and cognitive default modes in spontaneous brain activity fluctuations at rest. *Proc. Natl. Acad. Sci. U.S.A.* 100, 1053–1058. doi: 10.1073/pnas.1831638100

Laumann, T. O., Snyder, A. Z., Mitra, A., Gordon, E. M., Gratton, C., Adeyemo, B., et al. (2017). On the stability of BOLD fMRI correlations. *Cereb. Cortex* 27, 4719–4732. doi: 10.1093/cercor/bhw265

Licata, S. C., Nickerson, L. D., Lowen, S. B., Trksak, G. H., MacLean, R. R., and Lukas, S. E. (2013). The hypnotic zolpidem increases the synchrony of BOLD signal fluctuations in widespread brain networks during a resting paradigm. *NeuroImage* 70, 211–222. doi: 10.1016/j.neuroimage.2012.12.055

Liu, T. T. (2013). Neurovascular factors in resting-state functional MRI. *NeuroImage* 80, 339–348. doi: 10.1016/j.neuroimage.2013.04.071

Liu, T. T., Nalci, A., and Falahpour, M. (2017). The global signal in fMRI: nuisance or information? *NeuroImage* 150, 213–229. doi: 10.1016/j.neuroimage.2017.02.036

Liu, X., De Zwart, J. A., Schölvinck, M. L., Chang, C., Ye, F. Q., Leopold, D. A., et al. (2018). Subcortical evidence for a contribution of arousal to fMRI studies of brain activity. *Nat. Commun.* 9:395. doi: 10.1038/s41467-017-02815-3

Liu, X., Yanagawa, T., Leopold, D., Chang, C., Ishida, H., Fuji, I. N., et al. (2015). Arousal transitions in sleep, wakefulness, and anesthesia are characterized by an orderly sequence of cortical events. *NeuroImage* 116, 222–231. doi: 10.1016/j.neuroimage.2015.04.003

Matejcek, M. (1982). "Vigilance and the EEG," in *Electroencephalography in Drug Research*, ed W. Herrmann (Stuttgart: Gustav Fischer), 405–441.

McAvoy, M., Larson-Prior, L., Ludwikow, M., Zhang, D., Snyder, A. Z., Gusnard, D. L., et al. (2012). Dissociated mean and functional connectivity BOLD signals in visual cortex during eyes closed and fixation. *J. Neurophysiol.* 108, 2363–2372. doi: 10.1152/jn.00900.2011

McAvoy, M., Larson-Prior, L., Nolan, T., Vaishnavi, S., Raichle, M., and d'Avossa, G. (2008). Resting states affect spontaneous bold oscillations in sensory and paralimbic cortex. *J. Neurophysiol.* 100, 922–931. doi: 10.1152/jn.90426.2008

McAvoy, M. P., Tagliazucchi, E., Laufs, H., and Raichle, M. E. (2018). Human non-REM sleep and the mean global BOLD signal. *J. Cereb. Blood Flow Metab.* 19, 2210–2222. doi: 10.1177/0271678X1879107

Moosmann, M., Ritter, P., Krastel, I., Brink, A., Thees, S., Blankenburg, F., et al. (2003). Correlates of alpha rhythm in functional magnetic resonance imaging and near infrared spectroscopy. *NeuroImage* 20, 145–158. doi: 10.1016/S1053-8119(03)00344-6

Murphy, K., Birn, R. M., and Bandettini, P. A. (2013). Resting-state fMRI confounds and cleanup. *NeuroImage* 80, 349–359. doi: 10.1016/j.neuroimage.2013.04.001

Murphy, K., Birn, R. M., Handwerker, D. A., Jones, T. B., and Bandettini, P. A. (2009). The impact of global signal regression on resting state correlations: are anti-correlated networks introduced? *NeuroImage* 44, 893–905. doi: 10.1016/j.neuroimage.2008.09.036

Murphy, P. R., O'Connell, R. G., O'Sullivan, M., Robertson, I. H., and Balsters, J. H. (2014). Pupil diameter covaries with BOLD activity in human locus coeruleus. *Hum. Brain Mapp.* 35, 4140–4154. doi: 10.1002/hbm.22466

Oken, B., Salinsky, M., and Elsas, S. (2006). Vigilance, alertness, or sustained attention: physiological basis and measurement. *Clin. Neurophysiol.* 117, 1885–1901. doi: 10.1016/j.clinph.2006.01.017

Olbrich, S., Mulert, C., Karch, S., Trenner, M., Leicht, G., Pogarell, O., et al. (2009). EEG-vigilance and BOLD effect during simultaneous EEG/fMRI measurement. *NeuroImage* 45, 319–332. doi: 10.1016/j.neuroimage.2008.11.014

Olbrich, S., Sander, C., Matschinger, H., Mergl, R., Trenner, M., Schönknecht, P., et al. (2011). Brain and body. *J. Psychophysiol.* 25, 190–200. doi: 10.1027/0269-8803/a000061

Ong, J. L., Kong, D., Chia, T. T. Y., Tandi, J., Thomas Yeo, B. T., and Chee, M. W. L. (2015). Co-activated yet disconnected-Neural correlates of eye closures when trying to stay awake. *NeuroImage* 118, 553–562. doi: 10.1016/j.neuroimage.2015.03.085

Özbay, P. S., Chang, C., Picchioni, D., Mandelkow, H., Chappel-Farley, M. G., Gelderen, P. V., et al. (2019). Sympathetic activity contributes to the fMRI signal. *Commun. Biol.* 2:421. doi: 10.1038/s42003-019-0659-0

Patanaik, A., Tandi, J., Ong, J. L., Wang, C., Zhou, J., and Chee, M. W. L. (2018). Dynamic functional connectivity and its behavioral correlates beyond vigilance. *NeuroImage* 177, 1–10. doi: 10.1016/j.neuroimage.2018.04.049

Patriat, R., Molloy, E., Meier, T., Kirk, G., Nair, V., Meyerand, M., et al. (2013). The effect of resting condition on resting-state fMRI reliability and consistency: a comparison between resting with eyes open, closed, and fixated. *Neuroimage* 78, 463–473. doi: 10.1016/j.neuroimage.2013.04.013

Poldrack, R. A., Baker, C. I., Durnez, J., Gorgolewski, K. J., Matthews, P. M., Munafò, M. R., et al. (2017). Scanning the horizon: towards transparent and reproducible neuroimaging research. *Nat. Rev. Neurosci.* 18, 115–126. doi: 10.1038/nrn.2016.167

Poudel, G. R., Innes, C. R. H., Bones, P. J., Watts, R., and Jones, R. D. (2014). Losing the struggle to stay awake: divergent thalamic and cortical activity during microsleeps. *Hum. Brain Mapp.* 35, 257–269. doi: 10.1002/hbm.22178

Poudel, G. R., Innes, C. R. H., and Jones, R. D. (2018). Temporal evolution of neural activity and connectivity during microsleeps when rested and following sleep restriction. *NeuroImage* 174, 263–273. doi: 10.1016/j.neuroimage.2018.03.031

Power, J. D., Schlaggar, B. L., and Petersen, S. E. (2015). Recent progress and outstanding issues in motion correction in resting state fMRI. *NeuroImage* 105, 536–551. doi: 10.1016/j.neuroimage.2014.10.044

Razavi, N., Jann, K., Koenig, T., Kottlow, M., Hauf, M., Strik, W., et al. (2013). Shifted coupling of EEG driving frequencies and fMRI resting state networks in schizophrenia spectrum disorders. *PLoS ONE* 8:e76604. doi: 10.1371/journal.pone.0076604

Sadaghiani, S., Scheeringa, R., Lehongre, K., Morillon, B., Giraud, A.-L., and Kleinschmidt, A. (2010). Intrinsic connectivity networks, alpha oscillations, and tonic alertness: a simultaneous electroencephalography/functional magnetic resonance imaging study. *J. Neurosci.* 30, 10243–10250. doi: 10.1523/JNEUROSCI.1004-10.2010

Sämann, P. G., Wehrle, R., Hoehn, D., Spoormaker, V. I., Peters, H., Tully, C., et al. (2011). Development of the brain's default mode network from wakefulness to slow wave sleep. *Cereb. Cortex* 21, 2082–2093. doi: 10.1093/cercor/bhq295

Sander, C., Hensch, T., Wittekind, D. A., Böttger, D., and Hegerl, U. (2016). Assessment of wakefulness and brain arousal regulation in psychiatric research. *Neuropsychobiology* 72, 195–205. doi: 10.1159/000439384

Scheeringa, R., Petersson, K. M., Kleinschmidt, A., Jensen, O., and Bastiaansen, M. C. M. (2012). EEG alpha power modulation of fMRI resting-state connectivity. *Brain Connect.* 2, 254–264. doi: 10.1089/brain.2012.0088

Schneider, M., Hathway, P., Leuchs, L., Sämann, P. G., Czisch, M., and Spoormaker, V. I. (2016). Spontaneous pupil dilations during the resting state are associated with activation of the salience network. *NeuroImage*. 139, 189–201. doi: 10.1016/j.neuroimage.2016.06.011

Schwalm, M., and Rosales Jubal, E. (2017). Back to pupillometry: how cortical network state fluctuations tracked by pupil dynamics could explain neural signal variability in human cognitive neuroscience. *eNeuro* 4:ENEURO.0293–16.2017. doi: 10.1523/ENEURO.0293-16.2017

Stevner, A. B. A., Vidaurre, D., Cabral, J., Rapuano, K., Nielsen, S. F. V., Tagliazucchi, E., et al. (2019). Discovery of key whole-brain transitions and dynamics during human wakefulness and non-REM sleep. *Nat. Commun.* 10:1035. doi: 10.1038/s41467-019-08934-3

Tagliazucchi, E., and Laufs, H. (2014). Decoding wakefulness levels from typical fMRI resting-state data reveals reliable drifts between wakefulness and sleep. *Neuron* 82, 695–708. doi: 10.1016/j.neuron.2014.03.020

Tagliazucchi, E., and Van Someren, E. J. W. (2017). The large-scale functional connectivity correlates of consciousness and arousal during the healthy and pathological human sleep cycle. *NeuroImage* 160, 55–72. doi: 10.1016/j.neuroimage.2017.06.026

Tagliazucchi, E., von Wegner, F., Morzelewski, A., Borisov, S., Jahnke, K., and Laufs, H. (2012a). Automatic sleep staging using fMRI functional connectivity data. *NeuroImage* 63, 63–72. doi: 10.1016/j.neuroimage.2012.06.036

Tagliazucchi, E., von Wegner, F., Morzelewski, A., Brodbeck, V., and Laufs, H. (2012b). Dynamic BOLD functional connectivity in humans and its electrophysiological correlates. *Front. Hum. Neurosci.* 6:339. doi: 10.3389/fnhum.2012.00339

Tal, O., Diwakar, M., Wong, C. W., Olafsson, V., Lee, R., Huang, M.-X., et al. (2013). Caffeine-induced global reductions in resting-state BOLD connectivity reflect widespread decreases in MEG connectivity. *Front. Hum. Neurosci.* 7:63. doi: 10.3389/fnhum.2013.00063

Turchi, J., Chang, C., Ye, F. Q., Russ, B. E., Yu, D. K., Cortes, C. R., et al. (2018). The basal forebrain regulates global resting-state fMRI fluctuations. *Neuron* 97, 940–952.e4. doi: 10.1016/j.neuron.2018.01.032

Tüshaus, L., Balsters, J. H., Schläpfer, A., Brandeis, D., O'Gorman Tuura, R., and Achermann, P. (2017). Resisting sleep pressure: impact on resting state functional network connectivity. *Brain Topogr.* 30, 757–773. doi: 10.1007/s10548-017-0575-x

Wang, C., Ong, J. L., Patanaik, A., Zhou, J., and Chee, M. W. L. (2016). Spontaneous eyelid closures link vigilance fluctuation with fMRI dynamic connectivity states. *Proc. Natl. Acad. Sci. U.S.A.* 113, 9653–9658. doi: 10.1073/pnas.1523980113

Wang, H.-L. S., Rau, C.-L., Li, Y.-M., Chen, Y.-P., and Yu, R. (2015). Disrupted thalamic resting-state functional networks in schizophrenia. *Front. Behav. Neurosci.* 9:45. doi: 10.3389/fnbeh.2015.00045

Wirsich, J., Rey, M., Guye, M., Bénar, C., Lanteaume, L., Ridley, B., et al. (2018). Brain networks are independently modulated by donepezil, sleep, and sleep deprivation. *Brain Topogr.* 31, 380–391. doi: 10.1007/s10548-017-0608-5

Wong, C. W., DeYoung, P. N., and Liu, T. T. (2015). Differences in the resting-state fMRI global signal amplitude between the eyes open and eyes closed states are related to changes in EEG vigilance. *NeuroImage* 124(Pt A), 24–31. doi: 10.1016/j.neuroimage.2015.08.053

Wong, C. W., Olafsson, V., Tal, O., and Liu, T. T. (2012). Anti-correlated networks, global signal regression, and the effects of caffeine in resting-state functional MRI. *NeuroImage* 63, 356–364. doi: 10.1016/j.neuroimage.2012.06.035

Wong, C. W., Olafsson, V., Tal, O., and Liu, T. T. (2013). The amplitude of the resting-state fMRI global signal is related to EEG vigilance measures. *NeuroImage* 83, 983–990. doi: 10.1016/j.neuroimage.2013.07.057

Xu, P., Huang, R., Wang, J., Van Dam, N. T., Xie, T., Dong, Z., et al. (2014). Different topological organization of human brain functional networks with eyes open versus eyes closed. *NeuroImage* 90, 246–255. doi: 10.1016/j.neuroimage.2013.12.060

Yan, C., Liu, D., He, Y., Zou, Q., Zhu, C., Zuo, X., et al. (2009). Spontaneous brain activity in the default mode network is sensitive to different resting-state conditions with limited cognitive load. *PLoS ONE* 4:e5743. doi: 10.1371/journal.pone.0005743

Yang, G. J., Murray, J. D., Repovs, G., Cole, M. W., Savic, A., Glasser, M. F., et al. (2014). Altered global brain signal in schizophrenia. *Proc. Natl. Acad. Sci. U.S.A.* 111, 7438–7443. doi: 10.1073/pnas.1405289111

Yang, H., Long, X.-Y., Yang, Y., Yan, H., Zhu, C.-Z., Zhou, X.-P., et al. (2007). Amplitude of low frequency fluctuation within visual areas revealed by resting-state functional MRI. *NeuroImage* 36, 144–152. doi: 10.1016/j.neuroimage.2007.01.054

Yang, L., Lei, Y., Wang, L., Chen, P., Cheng, S., Chen, S., et al. (2018). Abnormal functional connectivity density in sleep-deprived subjects. *Brain Imaging Behav.* 12, 1650–1657. doi: 10.1007/s11682-018-9829-9

Yellin, D., Berkovich-Ohana, A., and Malach, R. (2015). Coupling between pupil fluctuations and resting-state fMRI uncovers a slow build-up of antagonistic responses in the human cortex. *NeuroImage* 106, 414–427. doi: 10.1016/j.neuroimage.2014.11.034

Yeo, B. T. T., Tandi, J., and Chee, M. W. L. (2015). Functional connectivity during rested wakefulness predicts vulnerability to sleep deprivation. *NeuroImage* 111, 147–158. doi: 10.1016/j.neuroimage.2015.02.018

Yuan, B.-K., Wang, J., Zang, Y.-F., and Liu, D.-Q. (2014). Amplitude differences in high-frequency fMRI signals between eyes open and eyes closed resting states. *Front. Hum. Neurosci.* 8:503. doi: 10.3389/fnhum.2014.00503

Yuan, H., Zotev, V., Phillips, R., and Bodurka, J. (2013). Correlated slow fluctuations in respiration, EEG, and BOLD fMRI. *NeuroImage* 79, 81–93. doi: 10.1016/j.neuroimage.2013.04.068

Zerbi, V., Floriou-Servou, A., Markicevic, M., Vermeiren, Y., Sturman, O., Privitera, M., et al. (2019). Rapid reconfiguration of the functional connectome after chemogenetic locus coeruleus activation. *Neuron* 103, 702–718.e5. doi: 10.1016/j.neuron.2019.05.034

Zhang, Y., Yang, Y., Yang, Y., Li, J., Xin, W., Huang, Y., et al. (2019). Alterations in cerebellar functional connectivity are correlated with decreased psychomotor vigilance following total sleep deprivation. *Front. Neurosci.* 13:134. doi: 10.3389/fnins.2019.00134

Zou, G., Xu, J., Zhou, S., Liu, J., Su, Z. H., Zou, Q., et al. (2019). Functional MRI of arousals in non-rapid eye movement sleep. *Sleep* 43:zsz218. doi: 10.1093/sleep/zsz218

Zou, Q., Long, X., Zuo, X., Yan, C., Zhu, C., Yang, Y., et al. (2009). Functional connectivity between the thalamus and visual cortex under eyes closed and eyes open conditions: a resting-state fMRI study. *Hum. Brain Mapp.* 30, 3066–3078. doi: 10.1002/hbm.20728

Conflict of Interest: The authors declare that the research was conducted in the absence of any commercial or financial relationships that could be construed as a potential conflict of interest.

frontiers in Neuroscience

ORIGINAL RESEARCH
published: 29 October 2020
doi: 10.3389/fnins.2020.00832

Dexmedetomidine – Commonly Used in Functional Imaging Studies – Increases Susceptibility to Seizures in Rats But Not in Wild Type Mice

Aleksandra Bortel[1,2], Roland Pilgram[1,2], Ze Shan Yao[1,3] and Amir Shmuel[1,2,3]**

[1] *Montreal Neurological Institute, McConnell Brain Imaging Centre, McGill University, Montreal, QC, Canada,* [2] *Department of Neurology and Neurosurgery, McGill University, Montreal, QC, Canada,* [3] *Department of Biomedical Engineering, McGill University, Montreal, QC, Canada*

OPEN ACCESS

Edited by:
Shella Keilholz,
Emory University, United States

Reviewed by:
Joanes Grandjean,
Radboud University Nijmegen Medical Centre, Netherlands
Basavaraju G. Sanganahalli,
School of Medicine, Yale University, United States

***Correspondence:**
Aleksandra Bortel
aleksandra.bortel@mcgill.ca
Amir Shmuel
amir.shmuel@mcgill.ca

Specialty section:
This article was submitted to Brain Imaging Methods, a section of the journal Frontiers in Neuroscience

Received: *13 November 2019*
Accepted: *16 July 2020*
Published: *29 October 2020*

Citation:
Bortel A, Pilgram R, Yao ZS and Shmuel A (2020) Dexmedetomidine – Commonly Used in Functional Imaging Studies – Increases Susceptibility to Seizures in Rats But Not in Wild Type Mice. Front. Neurosci. 14:832. doi: 10.3389/fnins.2020.00832

Functional MRI (fMRI) utilizes changes in metabolic and hemodynamic signals to indirectly infer the underlying local changes in neuronal activity. To investigate the mechanisms of fMRI responses, spontaneous fluctuations, and functional connectivity in the resting-state, it is important to pursue fMRI in animal models. Animal studies commonly use dexmedetomidine sedation. It has been demonstrated that potent sensory stimuli administered under dexmedetomidine are prone to inducing seizures in Sprague-Dawley (SD) rats. Here we combined optical imaging of intrinsic signals and cerebral blood flow with neurophysiological recordings to measure responses in rat area S1FL to electrical forepaw stimulation administered at 8 Hz. We show that the increased susceptibility to seizures starts no later than 1 h and ends no sooner than 3 h after initiating a continuous administration of dexmedetomidine. By administering different combinations of anesthetic and sedative agents, we demonstrate that dexmedetomidine is the sole agent necessary for the increased susceptibility to seizures. The increased susceptibility to seizures prevails under a combination of 0.3–0.5% isoflurane and dexmedetomidine anesthesia. The blood-oxygenation and cerebral blood flow responses to seizures induced by forepaw stimulation have a higher amplitude and a larger spatial extent relative to physiological responses to the same stimuli. The epileptic activity and the associated blood oxygenation and cerebral blood flow responses stretched beyond the stimulation period. We observed seizures in response to forepaw stimulation with 1–2 mA pulses administered at 8 Hz. In contrast, responses to stimuli administered at 4 Hz were seizure-free. We demonstrate that such seizures are generated not only in SD rats but also in Long-Evans rats, but not in C57BL6 mice stimulated with similar potent stimuli under dexmedetomidine sedation. We conclude that high-amplitude hemodynamic functional imaging responses evoked by peripheral stimulation in rats sedated with dexmedetomidine are possibly due to the induction of

epileptic activity. Therefore, caution should be practiced in experiments that combine the administration of potent stimuli with dexmedetomidine sedation. We propose stimulation paradigms that elicit seizure-free, well detectable neurophysiological and hemodynamic responses in rats. We further conclude that the increased susceptibility to seizures under dexmedetomidine sedation is species dependent.

Keywords: dexmedetomidine, medetomidine, seizures, hemodynamic response, neurovascular coupling, cerebral blood flow, blood oxygenation level-dependent functional MRI, forepaw electrical stimulation

INTRODUCTION

Functional connectivity (FC) refers to the temporal correlation between spatially remote neurophysiological events (Friston et al., 1993). FC analysis based on functional magnetic resonance imaging (fMRI) makes it possible to obtain an approximation of the pattern of thalamocortical and cortico-cortical connections non-invasively; thus, it is readily usable on human subjects. FC analysis can be pursued using data obtained during subject stimulation, task performance, or in the resting-state. In addition to shedding light on the pattern of connections, FC carries information that can be used to detecting a malfunction of the brain in disease (Fox and Greicius, 2010).

fMRI of the resting-state utilizes spontaneous fluctuations in metabolic and hemodynamic signals to infer the underlying local changes in neuronal activity (Shmuel and Leopold, 2008). Thus, the fMRI signal is an indirect measure of changes in neuronal activity. Therefore, for correct interpretation of spontaneous fluctuations and FC in the resting-state, it is important to characterize the neuronal mechanisms of these phenomena by combining fMRI and neurophysiology in animal models.

Animal studies of the resting-state and neurovascular coupling in general commonly use dexmedetomidine. Dexmedetomidine has been the sedative of choice for long functional imaging and neurophysiology studies in rats (Pawela et al., 2008; Zhao et al., 2008; Sotero et al., 2010; Nasrallah et al., 2012; Fukuda et al., 2013) and mice (Adamczak et al., 2010; Bukhari et al., 2017). It was previously reported that medetomidine sedation does not affect seizure vulnerability, nor does it affect LFP and BOLD responses during seizures evoked by systemic administration of kainic acid in rats (Airaksinen et al., 2010, 2012). In contrast, Fukuda et al. (2013) demonstrated that sedation induced by intravenous administration of dexmedetomidine for more than 2 h changes seizure susceptibility in rats. Forelimb stimulation elicited seizure- like responses accompanied by changes in cerebral blood flow (CBF) in Sprague-Dawley (SD) rats (Fukuda et al., 2013). These results have been corroborated by Bortel et al. (2019) who showed that seizures can be elicited not only with forelimb stimulation but also with the less-potent digit stimulation and that they propagated from the onset zone to adjacent cortical areas. Bortel et al. (2019) observed high-amplitude, high-frequency oscillations prior to and during the seizures, and demonstrated that the seizures are not induced by damage caused by inserting the electrodes into the cortex. To elicit the seizure, Fukuda et al. (2013) and Bortel et al. (2019) stimulated the forelimb or digit over 10 s long blocks. In contrast, short (e.g., 1 s) stimulation blocks of SD rats under dexmedetomidine sedation are not sufficient for inducing epileptiform activity (Sotero et al., 2015). Therefore, electrical stimuli administered at 8 Hz over a long duration under dexmedetomidine sedation elicit seizures.

Such potent forepaw stimulation – in the range of 9–12 Hz – are commonly used for imaging under medetomidine, isoflurane, or urethane anesthesia as these frequencies elicit the strongest BOLD response (Masamoto et al., 2007; Huttunen et al., 2008; Zhao et al., 2008; Kim et al., 2010; Krautwald and Angenstein, 2012; Paasonen et al., 2017; Albers et al., 2018; Nunes et al., 2019; Lambers et al., 2020). Therefore, it is important to test whether these stimuli induce seizures that could influence the hemodynamic responses. Moreover, mice sedated with dexmedetomidine are commonly used for studying the mechanisms underlying neurovascular coupling and resting-state fMRI. However, whether dexmedetomidine increases the susceptibility to seizures in mice remains unknown.

Here we demonstrate that the seizures induced by forepaws stimulation in SD rats are accompanied by spatially extended cerebral blood flow and blood oxygenation responses. We show that the increased susceptibility to seizures starts no later than 1 h after initiating the dexmedetomidine administration and lasts for at least 2 h. We demonstrate that the seizure susceptibility depends on the stimulation parameters and anesthesia regime. We propose reliable anesthesia regimes along with forepaw stimulation parameters that do not induce seizures but do generate well detectable hemodynamic responses. We further show that dexmedetomidine sedation increases the susceptibility to seizures not only in SD rats but also in Long-Evans (LE) rats. In contrast, C57BL6 (C57) wild type mice do not show susceptibility to seizures under the same anesthesia regime and stimulation protocol. We conclude that dexmedetomidine sedation increases the susceptibility to seizures accompanied by extended hemodynamic responses in SD and LE rats but not in wild type mice.

MATERIALS AND METHODS

Animals, Surgical Procedures, and Anesthesia

All procedures were approved by the animal care committees of the Montreal Neurological Institute and McGill University and were carried out in accordance with the guidelines of the Canadian Council on Animal Care. Here we report on experiments performed on 19 adult (100– 107 days old) male

SD rats weighing 440–560 g, 5 adult (100–109 days old) male LE rats weighing 475–495 g, and 5 age-matched adult C57 mice weighing 30–37 g. In **Table 1** which summarizes the conditions under which we observed seizures – we include results obtained from 6 additional 100–107 days old male SD rats, on which we reported in detail in Bortel et al. (2019). All 25 SD rats, 5 LE rats, and 5 C57 mice were stimulated with electrical forepaw stimulation. The rats and mice were housed under the same controlled environmental conditions at 22 ±·2°C with a 12 h light/12 h dark cycle (lights on from 7:00 a.m. to 7:00 p.m.) and received food and water *ad libitum*. A brief description of the surgical procedures is included below. All procedures carried out for experiments in SD rats are described in detail in Bortel et al. (2019). The procedures applied for experiments in LE rats were identical to those used for experiments in SD rats.

The rats were first injected with the anti-inflammatory drug carprofen (5 mg/kg SC; Zoetis, Canada) and anesthetized with a solution of xylazine (10 mg/kg IP; Bayer Inc., Canada) and ketamine (50 mg/kg IP; Wyeth, Canada). They were then intubated and placed in a stereotaxic frame. The surgical procedure was performed under ventilation with 100% oxygen and anesthesia with isoflurane (0.6–2%; Benson Medical Industries Inc., Canada). The scalp was incised to expose the skull covering the primary somatosensory cortex (S1) of the left hemisphere. One stainless steel screw (2.4 mm in length) – used as a ground and reference – was fixed to the skull above the visual cortex of the right hemisphere. The part of the skull overlying S1 was thinned until soft and transparent. We then performed an approximate 4 mm wide square-shaped craniotomy, centered on the forelimb representation in area S1FL based on a stereotaxic atlas (AP 0.00 mm, ML ± 4.50 mm, DV –2.5 mm; Paxinos and Watson, 2005). The dura mater within the craniotomy was resected. At the end of the surgical procedure, a silicon chamber was created around the craniotomy and filled with Hank's Balanced Salt Solution (Invitrogen, Canada).

Following the surgery, prior to starting the recordings, we changed the ventilation of the animal to a mixture of 20% oxygen and 80% medical air. At the same time, we injected a single dose of buprenorphine (0.04 mg/kg, SC; Schering-Plough, United Kingdom) and started administering dexmedetomidine that we kept running continuously throughout the recordings (0.075 mg/kg/h, SC; Pfizer Inc., Canada). The isoflurane administration was stopped following the administration of dexmedetomidine and buprenorphine. To examine the effect of anesthesia on the epileptic activity, we performed three additional experiments on SD rats without using ketamine before the intubation. To further examine the effect of anesthesia, we performed seven additional experiments on SD rats anesthetized with a combination of dexmedetomidine (0.075 mg/kg/h, SC) and simultaneous administration of isoflurane (0.3–0.5%), without administering buprenorphine.

The forepaw representation of area S1FL was delineated by optical imaging of the cerebral blood volume (CBV) response to forepaw stimulation. Then, a linear multi-contact probe was inserted into the forepaw region, in an approximately orthogonal orientation relative to the local surface. To determine the effect of dexmedetomidine on seizure susceptibility in a different animal species, we performed similar procedures and the same type of forepaw stimulation in five age-matched mice.

Before the surgery, the mice were injected with the anti-inflammatory drug carprofen (4 mg/kg SC; Zoetis, Canada). The surgical procedure was performed under anesthesia with a solution of ketamine (100 mg/kg IP; Wyeth, Canada) and xylazine (10 mg/kg IP; Bayer Inc., Canada) injected before the surgery, with the addition of isoflurane (0.6–1%; Benson Medical Industries Inc., Canada). The core temperature and heart rate were monitored. The primary somatosensory cortex (S1) of the left hemisphere was exposed, by performing a craniotomy, centered on the forelimb representation in area S1 (S1FL) based on a mouse stereotaxic atlas (AP −0.30 mm, ML ± 2.20 mm, DV –1.3 mm; Franklin and Paxinos, 2007). Following the surgery, prior to starting the recordings, the mice were injected with a single dose of buprenorphine (0.1 mg/kg, SC; Schering-Plough, United Kingdom). We then started a continuous administration of dexmedetomidine (0.05 mg/kg/h, SC; Pfizer Inc., Canada). Following the administration of dexmedetomidine and buprenorphine, we stopped administering isoflurane.

Then, a linear multi-contact probe was inserted into area S1FL. To maintain the sedation throughout the experiment, we infused dexmedetomidine continuously at a rate of 0.05 mg/kg/h SC. We assessed the depth of sedation by continuously monitoring the vital signs of the animal and by monitoring whether the animal stayed still or performed any movement. In case this monitoring showed that additional sedation was required, we increased the rate of the dexmedetomidine infusion to 0.1 mg/kg/h SC.

Electrical Stimulation of the Forepaw

Electrical stimuli were generated using a stimulator/isolator (A365, WPI, Sarasota, FL, United States) and delivered through two needle electrodes inserted into the web spaces of digits 2/3 and 4/5 of the rat or mouse forepaw. With rats and mice, we began our experiments with optical imaging of area S1FL, in order to guide the insertion of the neurophysiology probe to the forepaw representation. Runs for eliciting CBV-based optical imaging responses consisted of ten 4 s long stimulation blocks of 1 ms long, 1 mA electrical current pulses delivered at a frequency of 8 Hz. Following the insertion of the probe, we obtained data for the main experiment, including LFP, HbO, and CBF responses to electrical stimuli delivered to the forepaw. In rats, 8 runs were performed, each consisting of ten 35 s long stimulation trials, separated by ten 55 s long trials in which no stimulus was delivered (see time course in **Figure 1A**). Each stimulation trial started with 5 s recordings of baseline activity, followed by 10 s of stimulation and 20 s of baseline activity. In thirteen SD rats and five LE rats, each 10 s stimulation block consisted of a train of 1 ms long, 2 mA electrical pulses delivered at a frequency of 8 Hz. In three SD rats, 8 runs were performed with two different stimulus frequencies (4 and 8 Hz) and two different currents (1 and 2 mA). In runs 1–2, 3–4, 5–6, and 7–8 we administered 1 mA at 4 Hz, 2 mA at 4 Hz,

TABLE 1 | Average number of rats and mice with seizures and average number of seizures per run according to anesthesia regime and stimulation parameters.

Species and Stimulation Type	Anesthesia Regime	Stimulation parameters											
		4 Hz						6 Hz		8 Hz			
		1 mA		1.5 mA		2 mA		2 mA		1 mA		2 mA	
		Animals with seizures	No. of seizures per run	Animals with seizures	No. of seizures per run	Animals with seizures	No. of seizures per run	Animals with seizures	No. of seizures per run	Animals with seizures	No. of seizures per run	Animals with seizures	No. of seizures per run
SD Rats Forepaw stim	Dex and Bup	0/3	–			0/3	–			3/3	1.50 ± 0.81	7/9	2.14 ± 0.40
	Dex and Bup measured with ECoG											5/6	3.04 ± 0.42
	Dex and Bup without Ketamine											3/3	2.37 ± 0.35
	Dex and Iso without Bup			0/3	–							2/4	1.88 ± 0.44
LE Rats Forepaw stim	Dex and Bup											5/5	3.73 ± 0.50
C57 Mice Forepaw stim	Dex and Bup					0/5	–	0/5	–			0/5	–

The first column presents the species and strain (SD rats, LE rats or C57 mice) and the type of stimulation, i.e., forepaw stimulation. The second column presents the anesthesia regime, i.e., dexmedetomidine with buprenorphine sedation (Dex and Bup), dexmedetomidine with buprenorphine sedation without ketamine (Dex and Bup without Ketamine), and dexmedetomidine with isoflurane without buprenorphine (Dex and Iso without Bup). All neurophysiology data were recorded using a linear probe, except for the data presented in the second row labeled 'Dex and Bup measured with ECoG' which were recorded using electrocorticography arrays. The experiments in this row, whose anesthesia regime is labeled in red font were presented in detail in Bortel et al. (2019). The 3rd, 5th, 7th, 9th, 11th, and 13th columns present the number of rats/mice with seizures and the 4th, 6th, 8th, 10th, 12th, and 14th columns present the average number of seizures per run (including all runs in rats and mice that had or did not have seizures). Results are expressed as a mean ± SEM.

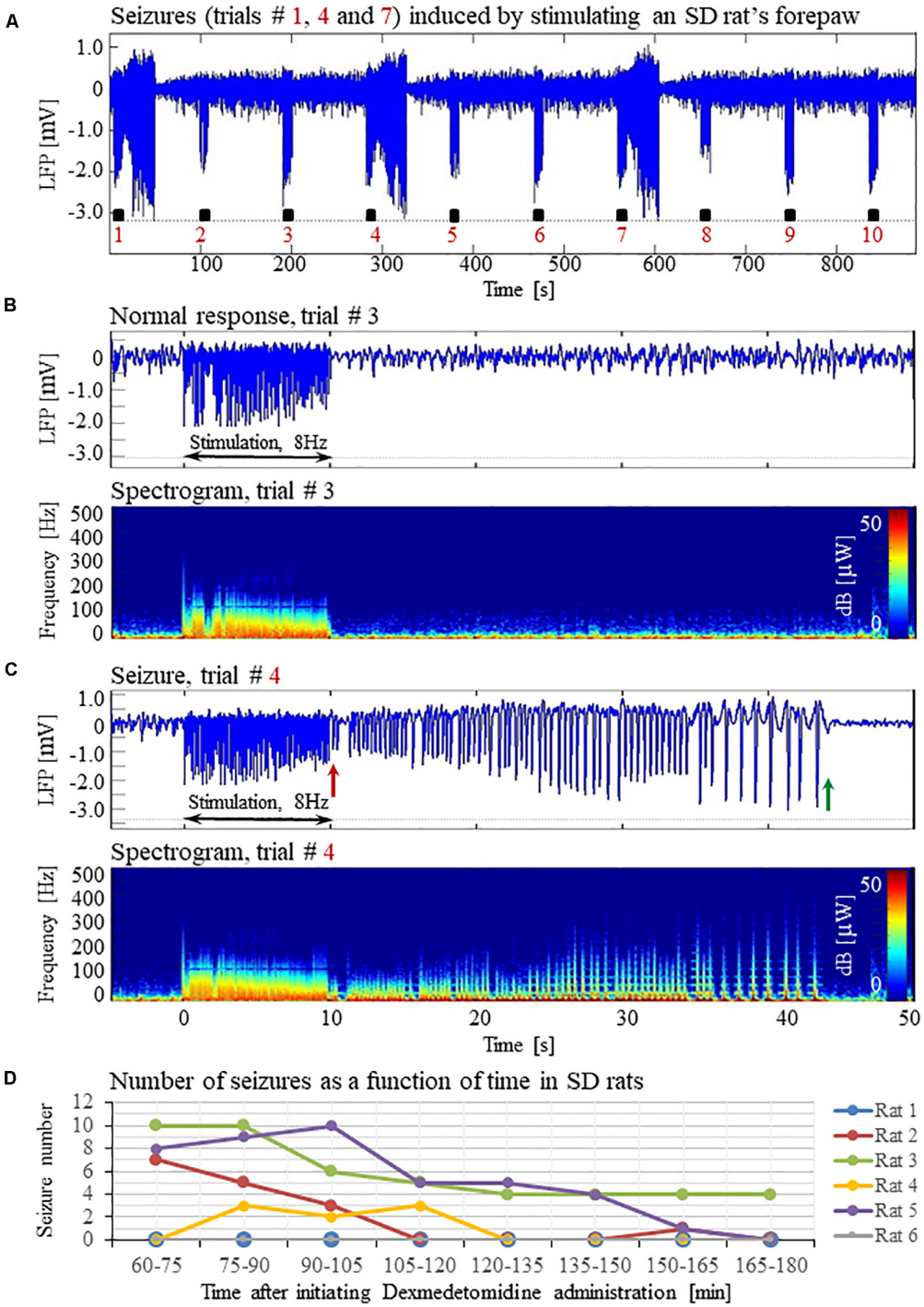

FIGURE 1 | Forepaw stimulation induces epileptic activity in rat area S1FL. **(A)** LFP recordings of ten trials, each with 10 s-long stimulation. The stimulation periods are marked by black rectangles. Each 10 s stimulus consisted of a train of electrical pulses delivered at 8 Hz to the forepaw. Note that during the first, fourth, and seventh trials, the stimulation evoked a seizure. **(B)** Top: The LFP (mean averaged over electrode contacts spanning the cortical depth) demonstrates a normal-evoked response in trial #3. Bottom: The corresponding spectrogram (power as a function of frequency and time) computed for the same trial. **(C)** Top: LFP (mean averaged over electrode contacts spanning the cortical depth) showing a seizure pattern in trial #4. The red and green arrows indicate the onset and termination, respectively, of a seizure induced by forepaw stimulation. Bottom: The corresponding spectrogram, computed for the same seizure. **(D)** The number of evoked seizures per rat as a function of time shows that seizures were induced already during the first or the second run, only one hour after initiating the dexmedetomidine administration.

1 mA at 8 Hz, and 2 mA at 8 Hz, respectively. In mice, 9 similar runs were performed, except that three different stimulus frequencies (4, 6, and 8 Hz) were applied. The recordings were performed in runs with increasing (3 mice) or decreasing (2 mice) stimulation frequency. The duration and intensity of all electrical pulses delivered to mice were 1 ms and 2 mA, respectively. In all experiments in rats and mice, the polarity of stimulation was switched in each pulse relative to the polarity of the preceding pulse.

Optical Imaging of Intrinsic Signals

All procedures applied for optical imaging of intrinsic signals (OIS) (Grinvald et al., 1999) are described in detail by Bortel et al. (2019). The ROI we imaged was centered on the atlas coordinates of area S1FL in the left hemisphere in rats (AP 0.00 mm, ML ± 4.50 mm, DV –2.5 mm; Paxinos and Watson, 2005) and mice (AP −0.30 mm, ML ± 2.20 mm, DV –1.3 mm; Franklin and Paxinos, 2007). We imaged the hemodynamic responses to forepaw stimulation at a frame rate of 30 Hz under the illumination of a green and orange LED light with a center wavelength of 530 nm (isosbestic point) and 617 nm, respectively. We computed percent change maps for oxyhemoglobin (HbO) using the modified Beer–Lambert law (Dunn et al., 2003). We applied a correction to adjust for the differential path length through the gray matter at different wavelengths.

Laser Speckle Flowmetry

One laser Speckle diode (Sharp LTO25MD = 798 nm, 30 mW; Thorlabs, Newton, NJ, United States) was coupled into a 600-μm diameter silica optical fiber (Thorlabs FT600-EMT) with a collimating lens (f = 8 mm, C240-TM; Thorlabs) connected to the distal end of the fiber. The lens was placed approximately 10 cm above the cortical ROI. It was adjusted to provide even illumination over an area with 8 mm diameter on the exposed cortical surface. The coherence length of the laser was approximately 1 cm. The speckle pattern was imaged using a CCD camera (Teledyne Dalsa, Waterloo, ON, Canada), which made it possible to obtain 2D maps of CBF at high spatial and temporal resolution. To this end, we quantified the spatial blurring of the speckle pattern that results from blood flow (Boas and Dunn, 2010). Conversion of the raw speckle images to blood flow maps was done using custom-written software that computed the speckle contrast and correlation time values at each pixel (Dunn et al., 2001).

Electrophysiological Data Pre-processing and Seizure Analysis

The methods used for the pre-processing of electrophysiological data and seizure analysis are specified in detail in Bortel et al. (2019).

Statistical Evaluation

We used the Levene's test to examine whether the variances of two or more compared groups were equal. In the cases where equal variances were verified, a Student's t-test was performed to test a difference between the means of two groups. If there was evidence to support non-equal variances, a Mann–Whitney or *post hoc* Tamhane's test was applied to evaluate statistical differences between two or more groups, respectively. A non-parametric Wilcoxon test was applied to groups of paired data variables. Results are presented as a mean ± SEM. Differences with $p < 0.05$ were considered statistically significant (IBM SPSS Statistics).

RESULTS

Characterization of Normal Evoked Responses and Epileptic Responses

Typical LFP patterns recorded during normal evoked responses in area S1FL of an SD rat are presented in **Figure 1A** (trials 2, 3, 5, 6, 8, 9, and 10) and **Figure 1B**. The normal evoked responses were confined within the 10 s period of stimulation. As illustrated in **Figure 1B**, the LFP amplitudes in response to electrical stimulation pulses were higher than the spontaneous LFP amplitudes. In four of six rats, we detected seizures induced by somatosensory stimulation of the forepaw. **Figure 1A** (trials 1, 4, and 7) and 1C present seizures induced by the forepaw stimulation. As can be observed in **Figure 1C**, the onset of the seizure (marked by a red arrow) consisted of high-frequency negative or positive-going deflections of the mean extracellular field potential.

The seizures typically extended for several seconds longer than the stimulation period. Before they terminated, the seizures consisted of low-frequency, high amplitude deflections of the field potential, extending above or below the baseline (**Figure 1C**; the seizure end is marked by a green arrow). The LFP and the corresponding spectrograms were used to estimate the seizure onset and termination times, relative to the first stimulation pulse. All seizures evoked in our rats were brief, lasting less than 1 min. The average duration of seizures was 31.50 ± 1.83 s. The seizures were followed by another seizure (55 cases out of 113 seizures), or a refractory period (40 refractory periods out of 113 seizures) or a normal response (14 normal responses out of 113 seizures).

The first recording run was performed 15 min after the isoflurane administration was stopped, thus 30 min following the administration of dexmedetomidine and buprenorphine. In the first 10-min run, we stimulated the forepaw for eliciting CBV-based optical imaging responses (4 s stimulation blocks, administering 1 mA pulses at 8 Hz). We did not observe any epileptic activity during this first stimulation run. Approximately 40 min following the administration of dexmedetomidine and buprenorphine, prior to the stimulation runs, we acquired two 10 min long runs of spontaneous activity. We did not observe any epileptic activity during these runs. These findings indicate that dexmedetomidine alone does not induce seizures: for generating seizures, potent stimuli are required too.

Seizures were observed already after 1 h of dexmedetomidine administration, during the first or the second run in which we applied the potent stimulation: 10 s stimulation blocks of 2 mA pulses at 8 Hz (**Figure 1D**). In SD rats, the average number of

observed seizures during the period of 60–120 min following the initiation of dexmedetomidine administration (14.3 ± 5.9, median equal 11.5) was larger than the corresponding number observed during the period of 120–180 min following this initiation (4.5 ± 2.8, median equal 0.5, $n = 6$ rats; $p = 0.07$, Wilcoxon test; non- significant trend).

The seizures induced in rats by electrical forepaw stimulation were exclusively electrographic seizures. We did not observe any epileptic behavior.

Seizures Induced by Forepaw Stimulation Under Dexmedetomidine Sedation Are Associated With Extended Cerebral Blood Oxygenation and Flow Responses

To test how the seizures induced by forepaw stimulation under dexmedetomidine sedation influence hemodynamic responses, we analyzed the spatial extent of the hemodynamic responses elicited during normal evoked responses and seizures. **Figures 2A,B**, **3A,B** present the spatial HbO and CBF responses, respectively, 1 s before the stimulus onset (1), 10 s after the stimulus onset (2), and 10 s after the cessation of the stimulus (3), for normal evoked response and seizure recorded in a single trial in one animal.

The spatial extent of the cerebrovascular hemodynamic responses 10 s following the onset of stimulation was slightly larger during a seizure (**Figures 2B**, **3B**, panel 2) than during a normal response (**Figures 2A**, **3A**, panel 2). The spatial extent of the responding region 10 s following the cessation of the stimulus was substantially larger during a seizure (**Figures 2B**, **3B**, panel 3) than during a normal response (**Figures 2A**, **3A**, panel 3). The time-courses of the HbO and CBF changes during a normal evoked response and an induced seizure response are presented on the right panels of **Figures 2A,B**, **3A,B**, respectively. The two different colored lines correspond to the two brain regions marked in **Figure 2C**. At any time-point following the onset of the stimulus, the HbO and CBF amplitudes during the seizure (**Figures 2B**, **3B**) were higher than the corresponding amplitudes during the normal evoked response (**Figures 2A**, **3A**). The bar plot in **Figure 3C** presents the spatial extent of the CBF responses averaged over six animals, during normal responses, seizures, and refractory periods, respectively. During the period of 5–10 s relative to the onset of the stimulus, the spatial extent of the cerebrovascular hemodynamic responses during seizures was larger than during normal refractory periods (**Figure 3C**; $^{**}p < 0.001$, Tamhane's test). For each of the periods of 10–15 s, and 15–20 s relative to the onset of the stimulus, the spatial extent of the cerebrovascular hemodynamic responses during seizures was larger than during normal evoked responses and refractory periods (**Figure 3C**; $^{*}p < 0.05$, $^{**}p < 0.001$, Tamhane's test). Note that these two periods – namely 10–15 s and 15–20 s relative to the onset of the stimulus – are part of the post-stimulation period in which the seizures persist with no sensory stimulation. Interestingly, not only the average spatial extent of the seizures was larger than that of normal responses obtained during the same period following the cessation of the stimulus, also the seizure's spatial extent *post-stimulation* was larger than that observed in normal responses *during stimulation* (**Figures 3C**; $p < 0.001$, Tamhane's test). Thus, the hemodynamic responses elicited by the seizures propagated beyond the spatial extent of the normal responses to forepaw stimulation.

The Increased Susceptibility to Seizures Does Not Depend on Using Ketamine, Buprenorphine, or Combining Isoflurane With Dexmedetomidine

To evaluate the dependence of seizure generation on the anesthesia regime, we first performed three experiments under dexmedetomidine and buprenorphine sedation but without using the anesthetic ketamine before the intubation and surgery. All three rats had seizures in response to forepaw stimulation of 8 Hz and 2 mA (**Figures 4A–D**).

Previous studies reported that isoflurane protects against seizures and that combining dexmedetomidine with isoflurane anesthesia prevents seizures in response to forepaw stimulation. To test these assertions, we performed four additional experiments using SD rats anesthetized with a combination of dexmedetomidine and 0.3–0.5% isoflurane, without administering buprenorphine. In response to forepaw stimuli of 2 mA administered at 8 Hz, we observed seizures in 50% of these rats (2 out of 4; **Figures 5A–D**). We concluded that ketamine and buprenorphine are not necessary for the effect of increasing susceptibility to seizures. We also concluded that combining isoflurane with dexmedetomidine does not eliminate the effect of increased susceptibility to seizures.

The Susceptibility to Seizures Depends on the Stimulation Paradigm: Seizures-Free Stimulation Parameters

Our results show that under dexmedetomidine sedation, forepaw stimulation with pulses of 2 mA administered at 8 Hz generates seizures. To test the dependence of the seizure generation on the electrical stimulation parameters, we administered forepaw stimuli with different currents (1 and 2 mA) and frequencies (4 and 8 Hz) in 3 SD rats under dexmedetomidine and buprenorphine sedation. Forepaw stimuli of 1 and 2 mA administered at 4 Hz did not generate seizures (**Figures 6A,B**). In contrast, administering electrical pulses of 1 and 2 mA at 8 Hz induced seizures in 2 out of 3 and all 3 rats, respectively (**Figures 7A–C**). Decreasing the stimulation current and frequency made it possible to obtain seizure-free response to forepaw stimulation under dexmedetomidine and buprenorphine sedation (**Figure 6**). This indicates that similar decreases may result in seizure-free forepaw responses under dexmedetomidine and isoflurane too. We, therefore, aimed to find a seizure-free forepaw stimulation paradigm under dexmedetomidine and isoflurane sedation. To this end, we performed experiments in 3 additional SD rats whose forepaw was stimulated with 1.5 mA electrical pulses administered

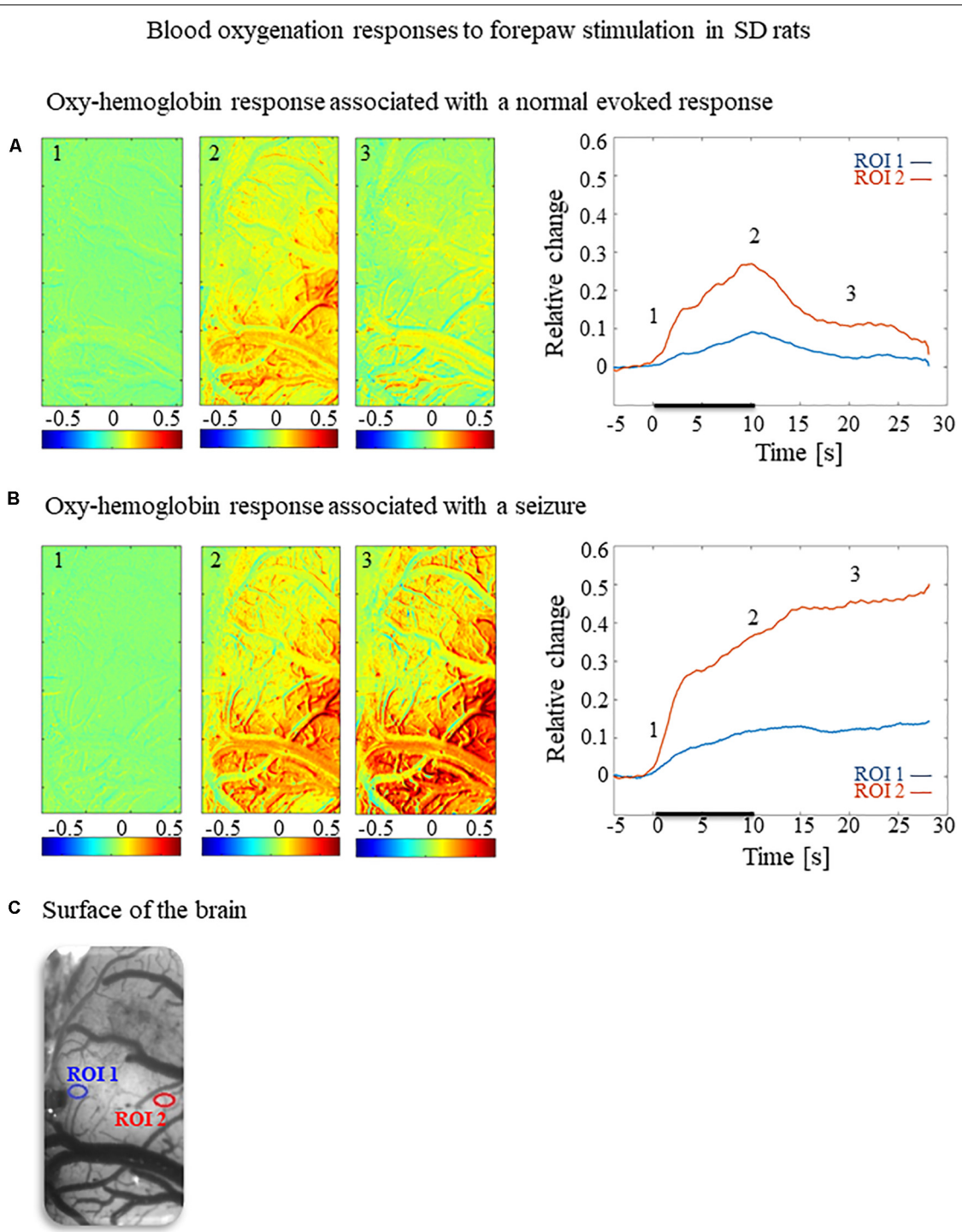

FIGURE 2 | Cerebral blood oxygenation responses evoked by forepaw stimulation. **(A)** Cerebral blood oxygenation response evoked by stimulation of the contralateral forepaw. To the left, the spatial responses before (the 1 s before stimulus onset), during (9–10 s following stimulus onset), and after (9–10 s following the cessation of the stimulus) the 10 s-long forepaw stimulation period. The reference for obtaining these responses was imaged between 3 and 1 seconds before stimulus onset. Note that positive responses are indicated in indexed yellow and red colors, representing increases in blood oxygenation. To the right are two time-courses presenting the corresponding temporal responses from two regions (blue and red ROIs in panel C) within the activated area. The stimulation period between 0 and 10 seconds is marked by a dark bar. **(B)** Maps of the blood oxygenation changes during a response that evoked a seizure, from before, during, and after the 10 s-long forepaw stimulation period (exact time periods are as in A). To the right are two time-courses presenting the corresponding temporal responses from two regions (blue and red ROIs in panel C) within the activated area. **(C)** The imaged cortical surface with the two ROIs used for sampling the time-courses presented in A and B.

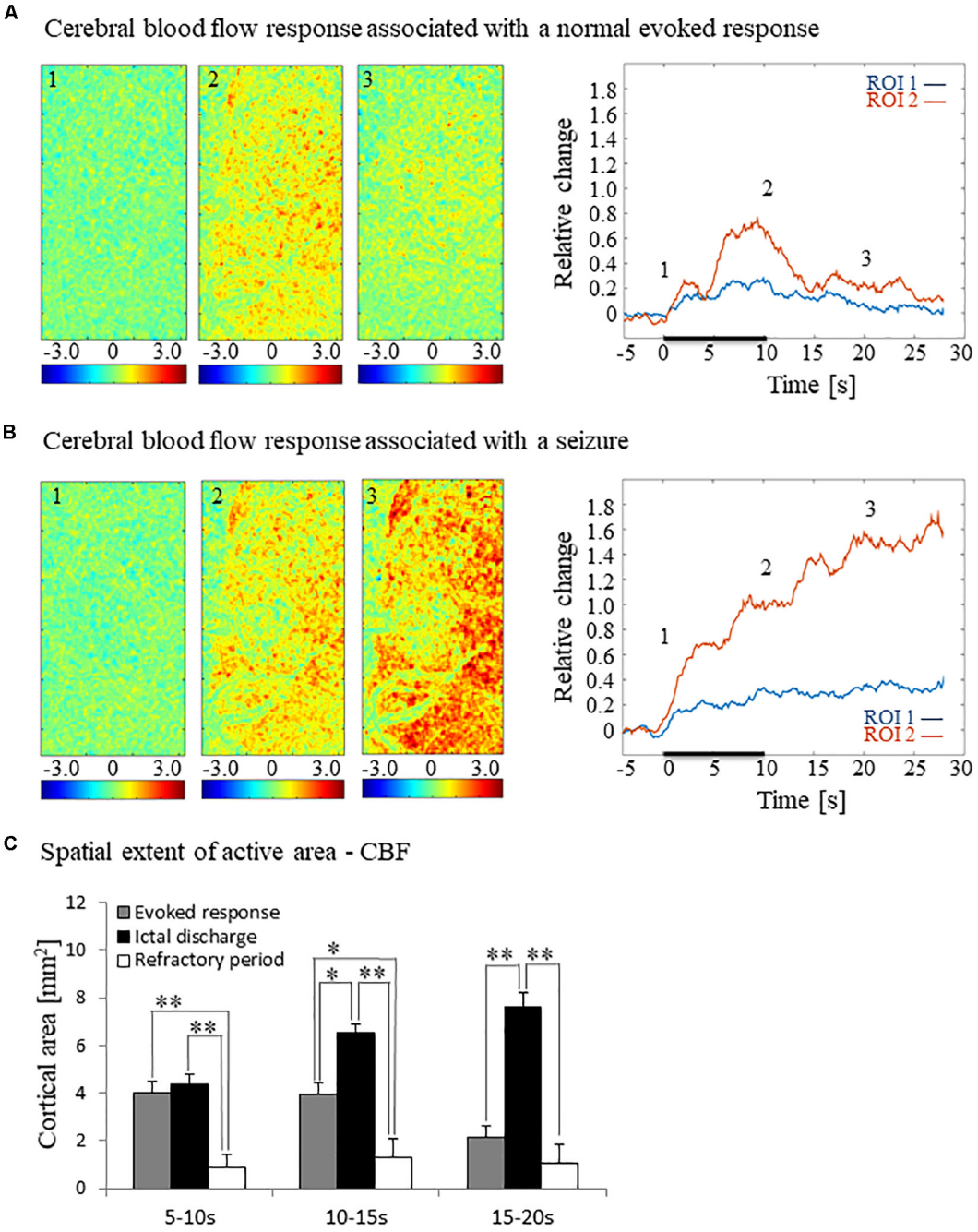

FIGURE 3 | Cerebral blood flow responses evoked by forepaw stimulation. **(A)** Cerebral blood flow response evoked by stimulation of the contralateral forepaw. To the left, the spatial responses before (the 1 s before stimulus onset), during (9–10 s following stimulus onset), and after (9–10 s following the cessation of the stimulus) the 10 s-long forepaw stimulation period. The reference for obtaining these responses was imaged between 3 and 1 seconds before stimulus onset. Note that positive responses indicated in indexed yellow and red colors represent increases in blood flow. To the right are two time-courses presenting the corresponding temporal responses from two regions (blue and red ROIs in **Figure 2C**) within the activated area. The stimulation period between 0 and 10 seconds is marked by a dark bar. **(B)** Maps of the blood flow changes during a response that evoked a seizure, from before, during, and after the 10 s-long forepaw stimulation period (exact time periods are as in A). To the right are two time-courses presenting the corresponding temporal responses from the same ROIs as described in **(A)**. **(C)** A bar graph showing the spatial extent of the CBF response calculated for the epochs of 5–10 s, 10–15 s, and 15–20 s relative to the onset of the stimulus during normal evoked responses ($n = 21$), seizure responses ($n = 20$) and refractory periods ($n = 14$; $^{*}p < 0.05$, $^{**}p < 0.001$; Tamhane's test).

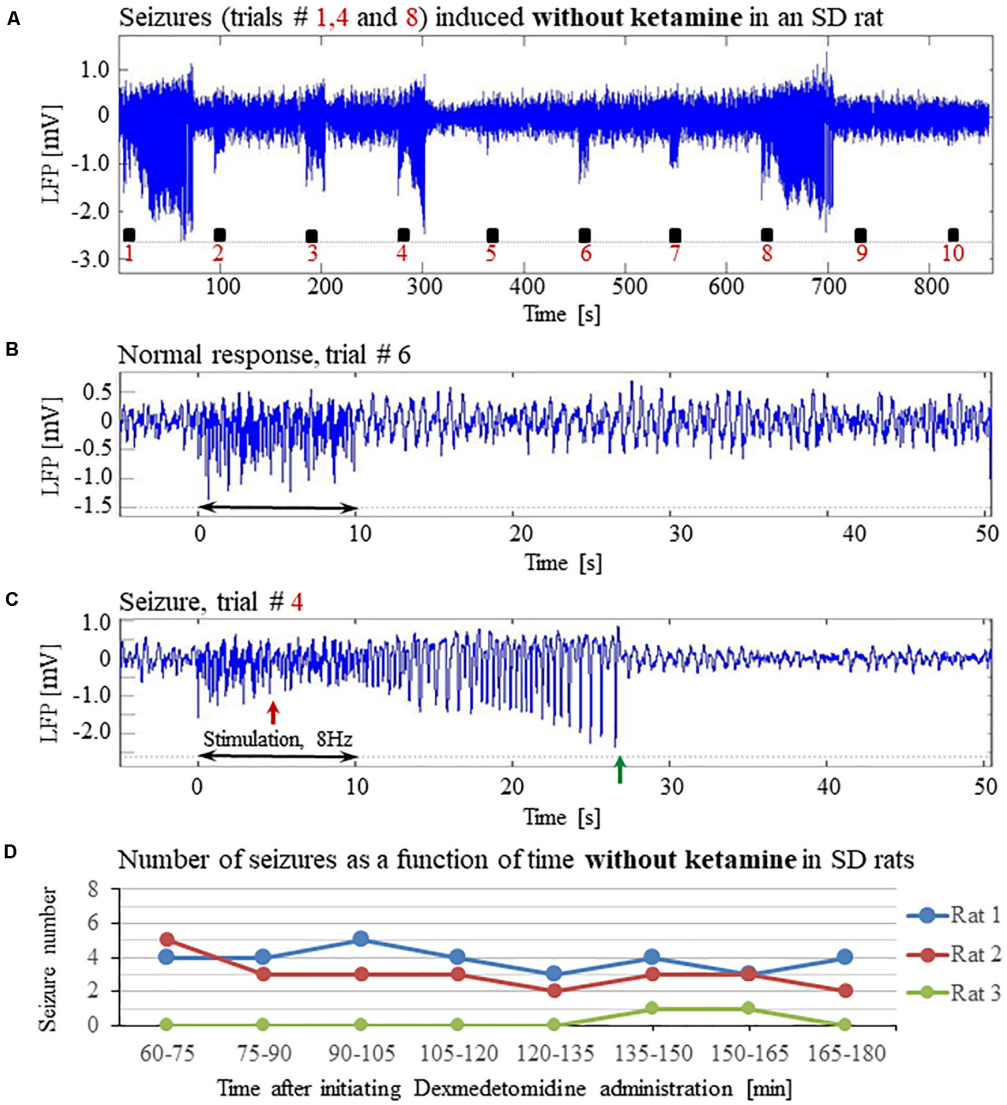

FIGURE 4 | The increased susceptibility to seizures in SD rats under dexmedetomidine and buprenorphine does not depend on ketamine. The data presented in this figure were obtained from 3 rats under dexmedetomidine and buprenorphine sedation with no administration of ketamine. The format of the presentation is similar to that used in **Figure 1**. **(A)** A time-course of LFP (averaged over electrode contacts spanning the cortical depth) recorded during ten trials, each with 10 s-long stimulation. The stimulation periods are marked by black rectangles. Note the seizures induced by the stimulus in the first, fourth, and eighth trials. **(B)** A normal-evoked LFP response recorded in trial #6. **(C)** A seizure pattern recorded in trial #4. The red and green arrows indicate the onset and termination of the seizure, respectively. **(D)** The number of seizures recorded in each of the 3 rats as a function of time after the initiation of the dexmedetomidine administration.

at 4 Hz. Under this condition, we did not observe any seizure (**Figure 8**).

Hemodynamic Responses Associated With the Seizure-Free Forepaw Stimulation Paradigms

To compare and evaluate the detectability of the hemodynamic responses associated with the three seizure-free paradigms we have demonstrated (**Figures 6A,B**, **8**), we first analyzed the CBV responses obtained in single-trials under these paradigms. **Figures 9A,B** compare the spatial extent and time courses obtained under dexmedetomidine and buprenorphine in response to stimulation at 4 Hz with 1 mA and 2 mA pulses, respectively. **Figure 9C** presents the spatial extent and time courses obtained under dexmedetomidine and isoflurane in response to 1.5 mA pulses administered at 4 Hz. All three paradigms generated single-trial hemodynamic responses that were well detectable.

The CBV responses obtained under dexmedetomidine and buprenorphine were higher in response to 2 mA pulses than to 1 mA pulses ($p < 0.001$, Tamhane's test; **Figure 10**). They were also higher than the responses to 1.5 mA pulses obtained under dexmedetomidine and isoflurane sedation ($p < 0.001$; **Figure 10**).

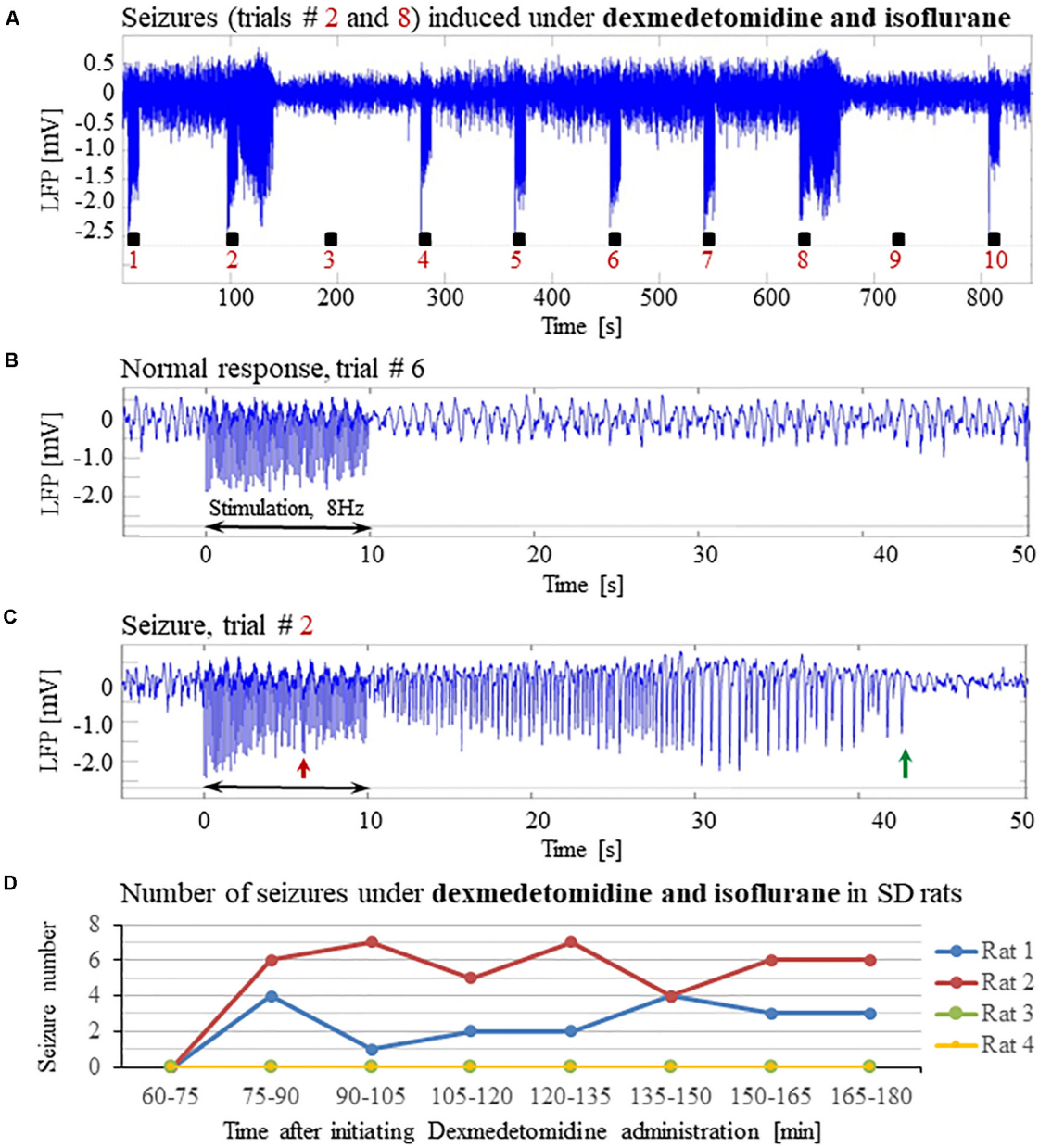

FIGURE 5 | Potent forepaw stimulation induces seizures in SD rats under dexmedetomidine and isoflurane anesthesia. The data presented in this figure were obtained from 4 rats under dexmedetomidine and isoflurane anesthesia. **(A)** LFP recordings of ten trials, each with 10 s-long stimulation. Note the seizures induced by the stimulus in the second and eighth trials. **(B)** A normal-evoked LFP response recorded in trial #6. **(C)** A seizure pattern recorded in trial #2. **(D)** The number of seizures recorded in each of the 4 rats as a function of time after the initiation of the dexmedetomidine administration. Seizures were induced already during the second run, less than 90 min after initiating the dexmedetomidine administration.

Long Evans Rats Under Dexmedetomidine Sedation Are Susceptible to Seizures; Wild Type Mice Are Not

The susceptibility of the brain to seizure generation is known to depend on animal species (Schauwecker, 2002). In addition to SD rats, Long-Evans (LE) rats and mice of different strains are commonly used for studying the resting-state and neurovascular coupling. To test the susceptibility of these strains to seizure generation under dexmedetomidine sedation, we pursued similar experiments using LE rats and C57BL6 wild type mice.

Forepaw stimulation with current of 2 mA administered at 8 Hz elicited seizures in all 5 LE rats we tested under dexmedetomidine and buprenorphine sedation. The LFP characteristics of seizures evoked in LE rats were similar to those

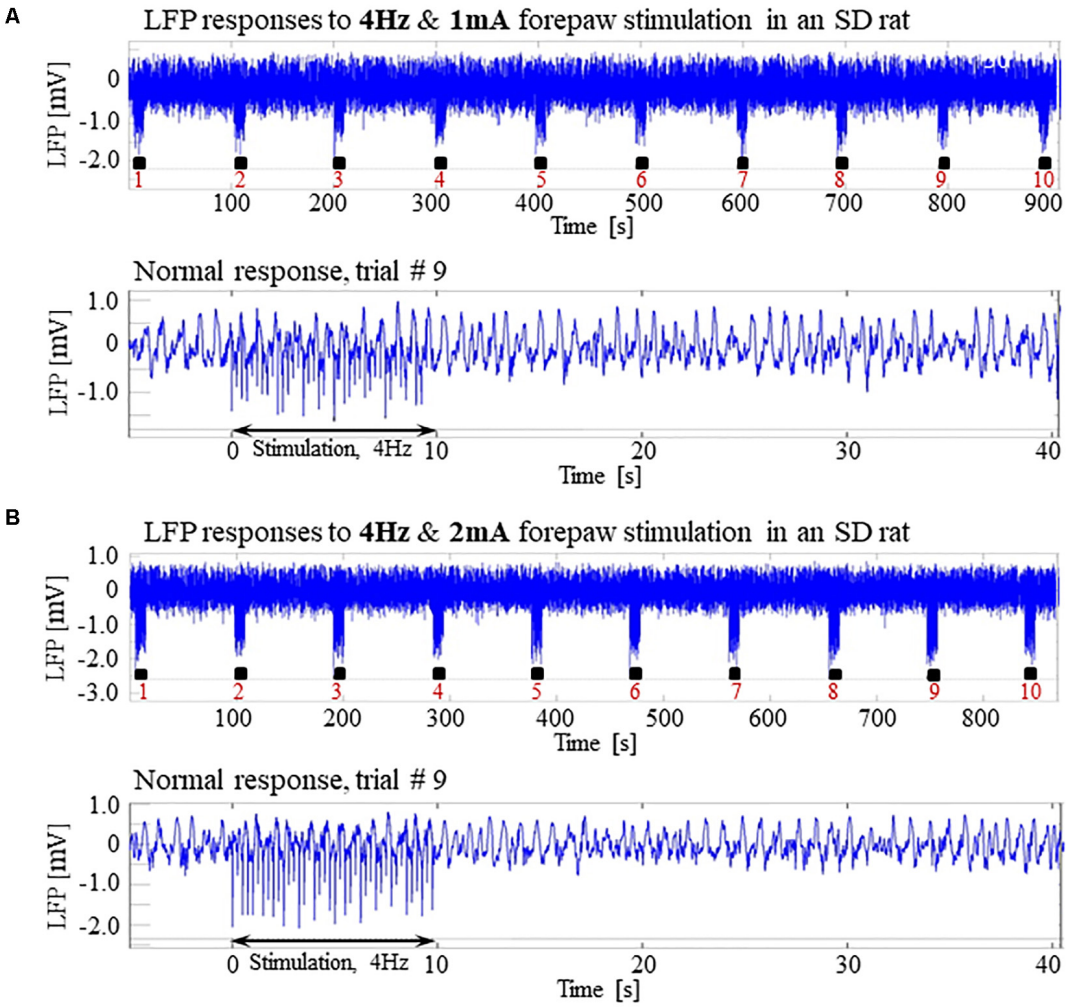

FIGURE 6 | Normal LFP responses to forepaw stimulation administered at 4 Hz in SD rats under dexmedetomidine and buprenorphine. The data presented in this figure were obtained from 3 rats under dexmedetomidine and buprenorphine sedation. **(A)** Top: Normal LFP responses obtained from area S1FL, in response to 4 Hz & 1 mA forepaw stimulation. The panel shows ten trials, each with 10 s-long stimulation. Bottom: A magnification of the normal evoked response from the ninth trial. **(B)** Top: Normal LFP responses to 4 Hz & 2 mA forepaw stimulation. Bottom: A magnification of the normal evoked response from the ninth trial.

evoked in SD rats (**Figures 11A–D**). Seizures induced in LE rats were observed as soon as 1 h after the dexmedetomidine administration, during the first or second stimulation run (**Figure 11D**). The average number of seizures during the period of 60- 120 min following the initiation of dexmedetomidine administration (15.8 ± 5.6, median equal 17) was not statistically different than the corresponding number observed during the period of 120–180 min following this initiation (14.0 ± 5.2, median equal 20; p = 0.34 Wilcoxon test). The seizures were followed by another seizure (72 cases out of 149 seizures), or a normal response (60 normal responses out of 149 seizures), or a refractory period (16 refractory periods out of 149 seizures; **Figures 11A–C**). Lastly, 100% of LE rats had seizures, in comparison to 67% of the SD rats from which we obtained data from 8 runs. We observed a non-statistically significant trend of a higher number of seizures in LE rats (29.8 ± 10.7 per animal) than the corresponding number observed in SD rats (18.8 ± 8.5 per animal; p = 0.43, Mann–Whitney's test).

In pilot experiments in two mice, we did not observe seizures and not even high-amplitude LFP responses to stimuli of 2 mA administered at 8 Hz, identical to those that elicited high-amplitude responses in SD and LE rats. We hypothesized that the reason for the lack of high-amplitude responses was that the inhibition elicited by the response in mice remains effective for a longer duration than it does in rats. In addition, lower frequency 6 Hz, 3 s corneal stimulation previously produced 'psychomotor' seizures in mice (Barton et al., 2001; Esneault et al., 2017). Based on these observations, we decided to administer forepaw stimuli to five age-matched mice using three different frequencies of stimulation: 4, 6, and 8 Hz. **Figures 12A,B** present normal responses obtained with 4 and 6 Hz stimulation, respectively. Note that the normal

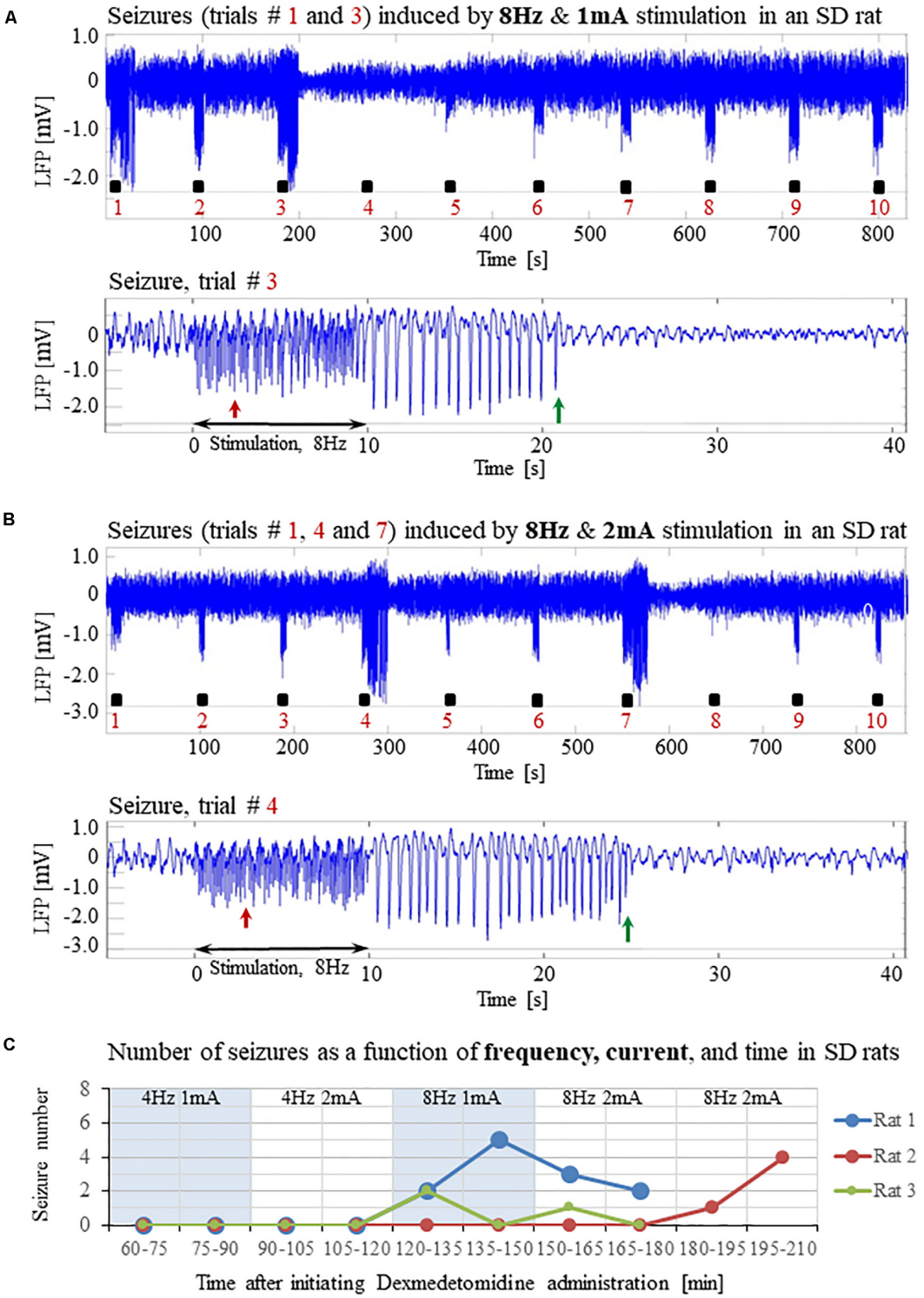

FIGURE 7 | Forepaw stimulation administered at 8Hz induces epileptic activity in SD rats under dexmedetomidine and buprenorphine. The data presented in this figure were obtained from the same 3 rats whose responses to forepaw stimulation with different parameters are presented in **Figure 6**. **(A)** Top: LFP responses to 8 Hz & 1 mA forepaw stimulation. Note the seizures induced by the stimulus in the first and third trials. Bottom: A magnified view of the seizure recorded in the third trial. **(B)** Top: LFP responses to 8 Hz & 2 mA forepaw stimulation. Note the seizures induced by the stimulus in the first, fourth, and seventh trials. Bottom: A magnified view of the seizure recorded in the fourth trial. **(C)** The number of seizures recorded in each of the 3 rats whose responses to forepaw stimulation are presented in **Figures 6** and **7**. The number of seizures is presented as a function of time after the initiation of the dexmedetomidine administration. The stimulation parameters used for each pair of consecutive blocks are presented at the upper part of the panel.

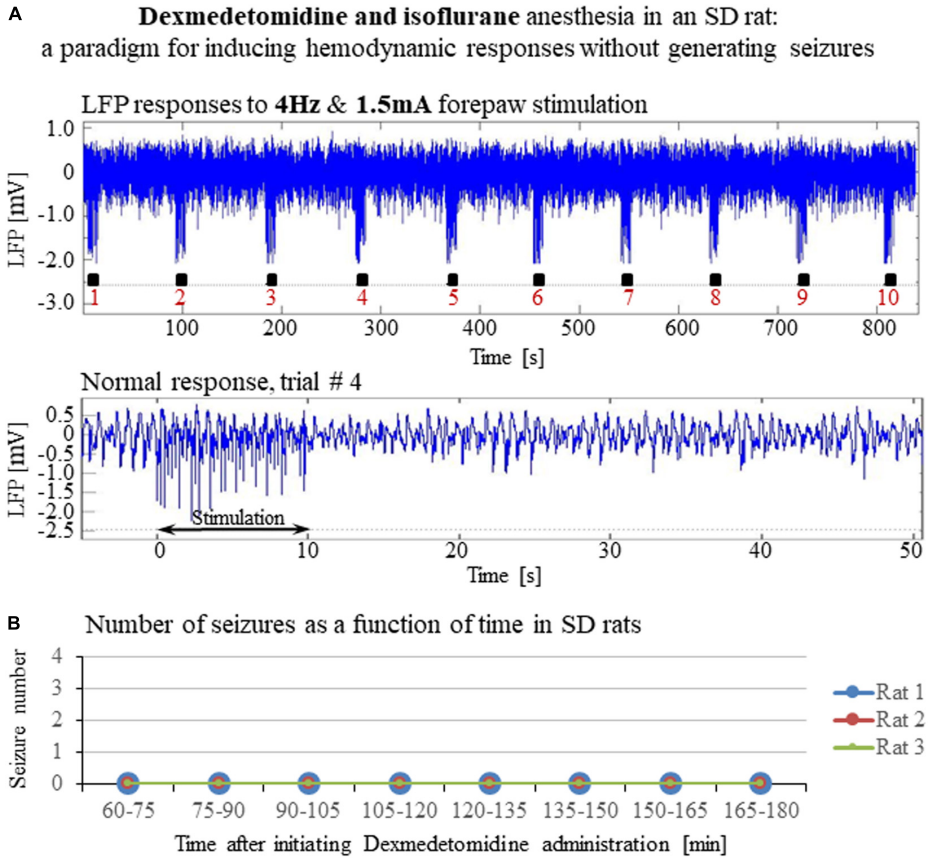

FIGURE 8 | A paradigm for seizure-free forepaw stimulation under dexmedetomidine and isoflurane. The data presented in this figure were obtained from 3 rats under dexmedetomidine and isoflurane anesthesia. Forepaw stimuli of 1.5 mA were administered at a rate of 4 Hz. **(A)** Top: Normal LFP responses to 10 s-long stimulation blocks obtained from area S1FL. Bottom: A magnification of the normal evoked response from the fourth trial. **(B)** The number of seizures (none) recorded in each of the 3 rats as a function of time shows that forepaw stimuli of 1.5 mA administered at 4 Hz do not induce seizures in SD rats under dexmedetomidine and isoflurane anesthesia.

responses to stimuli are noticeable with the 4 Hz – the lowest stimulation frequency – and are substantially weaker with 6 Hz stimulation. The LFP responses to forepaw stimuli administered at 8 Hz were virtually undetectable (**Figure 12C**). As illustrated in **Figures 12A–C**, we did not evoke any seizure with any of the stimulation frequencies we administered to any of the mice under dexmedetomidine and buprenorphine. In conclusion, seizures were observed in SD and LE rats, but not in C57 mice.

DISCUSSION

Dexmedetomidine Sedation Increases Susceptibility to Seizures

We have demonstrated that under sedation or anesthesia that involve dexmedetomidine, long (10 s), potent (1 or 2 mA), repetitive and frequent (8 Hz) peripheral electrical stimuli evoke seizures (**Figures 1–5**, **7A–C**). Epileptic activity induced in our rats consisted of brief and focal electrographic seizures; the animals did not show any epileptic behavior.

To identify the compound that causes the increased susceptibility to seizures, we managed several sedation and anesthetic regimes by administering different combinations of the following compounds: ketamine, xylazine, carprofen, dexmedetomidine, buprenorphine, isoflurane, and urethane (we used the latter in Bortel et al., 2019).

To test whether ketamine could be the compound that increases the susceptibility to seizures, we performed three experiments under dexmedetomidine and buprenorphine but without administering ketamine before the surgery. Our main stimulation paradigm (2 mA pulses administered at 8 Hz) induced seizures in all three SD rats (**Figure 4**), confirming that ketamine is not necessary for increasing the susceptibility to seizures.

We then used a combination of dexmedetomidine and isoflurane without buprenorphine, and we observed seizures response to our main stimulation paradigm in 2 out of 4 rats (**Figure 5**). This makes it possible to exclude buprenorphine as an agent necessary for increasing the observed susceptibility to seizures.

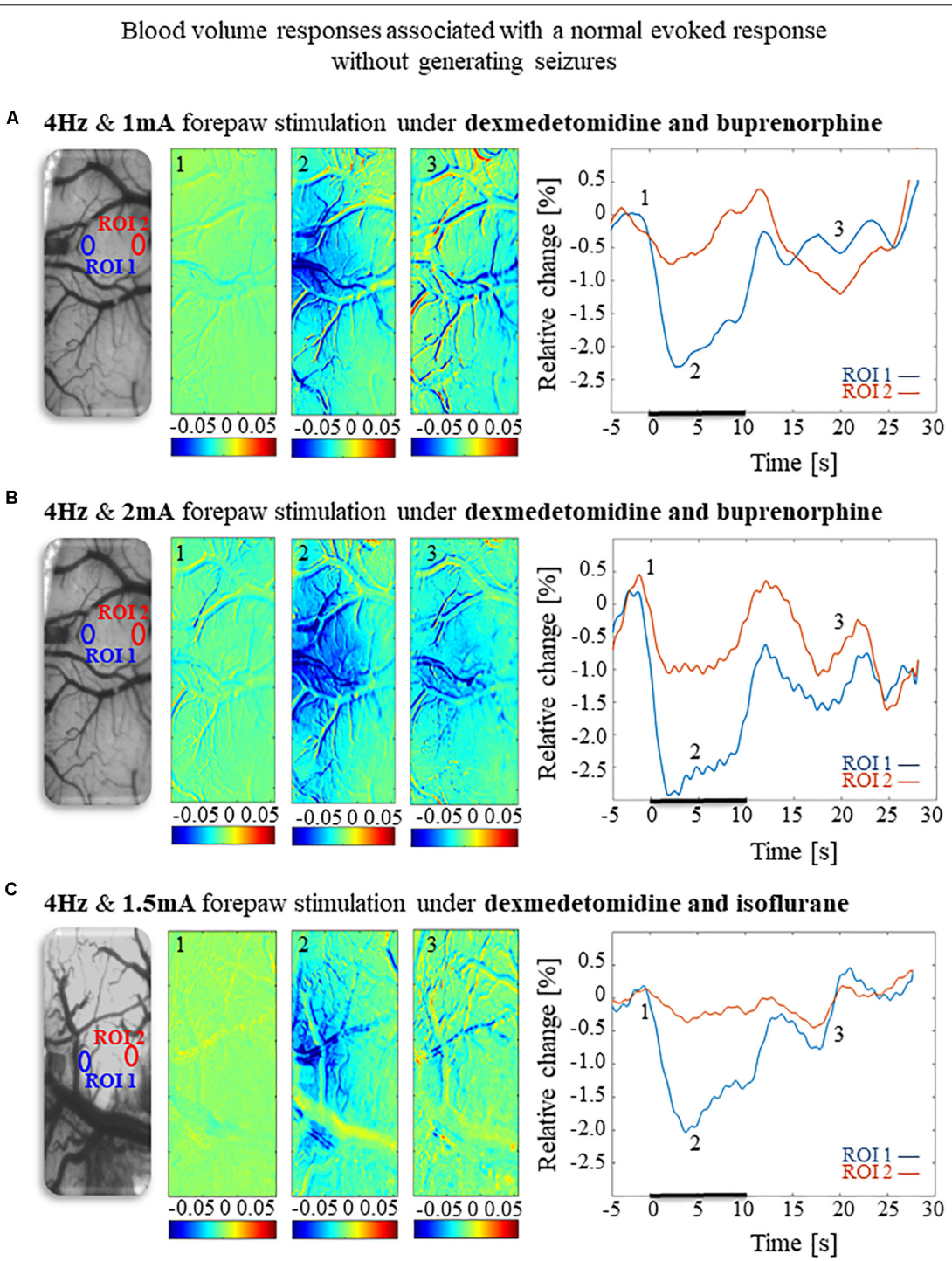

FIGURE 9 | Cerebral blood volume responses associated with seizure-free responses to 4 Hz forepaw stimulation under different anesthesia regimes. **(A)** A cerebral blood volume response to a 10 s-long block of forepaw stimuli of 1 mA administered at 4 Hz under dexmedetomidine and buprenorphine sedation. To the left, the imaged cortical surface. The 3 maps presented in color show the spatial responses before (the 1 s before stimulus onset), during (4–5 s following stimulus onset), and after (9–10 s following the cessation of the stimulus) the 10 s-long forepaw stimulation period. The reference for obtaining these responses was imaged between 3 and 1 seconds before stimulus onset. Note that negative responses indicated in indexed blue colors represent increases in blood volume. To the right are two time-courses presenting the corresponding temporal responses from two regions (blue and red ROIs in the left panel) within the activated area. The stimulation period between 0 and 10 seconds is marked by a dark bar. **(B)** Cerebral blood volume response evoked by 4 Hz and 2 mA forepaw stimulation under dexmedetomidine and buprenorphine sedation. The format of the presentation is identical to that used in panel A. **(C)** Cerebral blood volume response evoked by 4 Hz and 1.5 A forepaw stimulation under dexmedetomidine and isoflurane anesthesia. The format of the presentation is identical to that used in panel A.

Isoflurane has anticonvulsant properties: it suppresses drug-induced convulsions (Kofke et al., 1987) and terminates status epilepticus in patients when administered at concentrations of 0.5%- 3.0% (Kofke et al., 1985; Ropper et al., 1986). This makes it unlikely that isoflurane increases the susceptibility to seizures. In addition, we obtained seizures in rats under dexmedetomidine and buprenorphine sedation, without administrating isoflurane, showing that isoflurane is not necessary for the seizure generation.

In Bortel et al. (2019) we applied a similar stimulation paradigm – although we stimulated a single digit, not the entire forepaw. Under dexmedetomidine and buprenorphine sedation, we observed seizures in response to digit stimulation in 6/10 rats. Under urethane anesthesia, with no administration of buprenorphine, we did not observe any seizures.

The only other compounds which we administered in all experiments – those with seizures and those without seizures – are xylazine, which we injected just before the intubation, and carprofen, which we injected approximately at the same time, before the surgical procedures. Similar to dexmedetomidine, xylazine belongs to the α2-adrenoceptor agonists that exert sedation and have additional muscle-relaxant and analgesic properties. A single standard dose of xylazine produces sedation of 30–40 min duration, and its elimination half-life is 30 min (Pawson, 2008). With such elimination half-life, it is very unlikely that xylazine is the compound that increases the susceptibility to seizures in our experiments, because we observed seizures during the time frame of 1–3 h following the initiation of the dexmedetomidine, which is equivalent to $1^1/_2$ to $3^1/_2$ hours after injecting xylazine. Carprofen is a non-steroidal anti-inflammatory drug (NSAID) that has non-narcotic analgesic and antipyretic activity. The mechanism of action of carprofen, like that of other NSAIDs, involves inhibition of cyclooxygenase (COX-2) activity (Rubio et al., 1980). COX-2 is known to play an important role in the early inflammatory response to an insult and in post-seizure inflammation and hyper-excitability of the brain. It was shown that pretreatment of animals with a selective COX-2 inhibitor before applying a convulsant stimulus weakens seizure intensity (Rojas et al., 2014). Therefore, it is unlikely that carprofen increases the susceptibility to seizures in our experiments; in fact, we expect that it decreases this susceptibility. Lastly, we did administer xylazine and carprofen before the surgeries of the experiments we ran with urethane, in which we did not observe any seizures (Bortel et al., 2019). This means that neither xylazine nor carprofen can be the agent causing the seizures.

The results summarized above leave dexmedetomidine as the sole agent that could increase the susceptibility to seizures.

Adding Isoflurane to Dexmedetomidine Does Not Prevent the Increased Susceptibility to Seizures

It is widely accepted that anesthetics modify the balance between excitation and inhibition toward increased relative inhibition, and consequently, they modulate evoked neuronal responses (Franceschini et al., 2010). Isoflurane is a general anesthetic that affects many neurotransmitter systems; it acts on GABA, NMDA, and glycine receptors (Grasshoff and Antkowiak, 2006). Although isoflurane reduces neuronal excitation and cerebral metabolism, it is commonly used in electrophysiology studies. However, at higher doses (≥1.6%) isoflurane increases the baseline cerebral blood flow (CBF) (Eger, 1984; Franceschini et al., 2010) and for this reason, it is no longer the anesthetics of choice for hemodynamics-based functional studies.

However, fMRI studies often use a combination of dexmedetomidine and low-percentage of isoflurane in rats (Fukuda et al., 2013; Paasonen et al., 2018) and mouse models (Grandjean et al., 2014; Bukhari et al., 2017). Combining dexmedetomidine with isoflurane constitutes an attractive anesthesia regime for fMRI studies because both cortical and striatal functional connectivity can be reliably detected with no adverse side effects. Moreover, with dexmedetomidine alone, the sedation effect lasts 60–90 min even if the administration is continuous, thus forcing short imaging sessions (Pawela et al., 2009). When adding low- percentage isoflurane to dexmedetomidine, the anesthesia effects of isoflurane make it possible to run longer experiments. Importantly, dexmedetomidine and isoflurane provide a synergistic effect as they exert opposing effects on the cerebrovascular system. Whereas isoflurane acts as a vasodilator (Eger, 1984; Franceschini

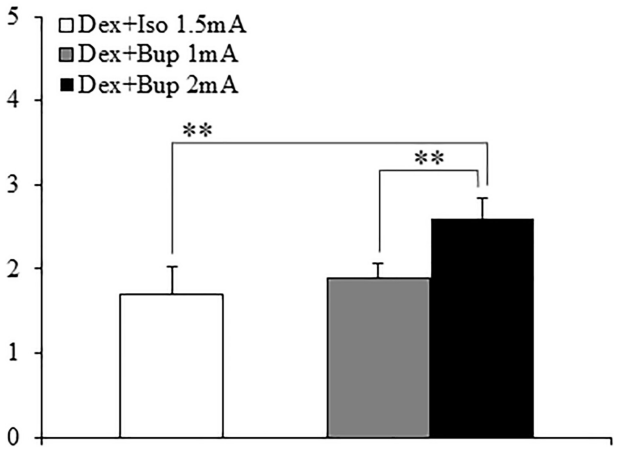

FIGURE 10 | The amplitudes of cerebral blood volume responses associated with seizure-free responses to 4 Hz forepaw stimulation under different anesthesia regimes. A bar graph showing the peak amplitude of CBV normal responses sampled from the gray matter region that showed the highest response. The white bar to the left shows the amplitude of response to stimuli of 1.5 mA administered at 4 Hz under dexmedetomidine and isoflurane anesthesia (Dex + Iso; mean ± SEM, n = 60 trials from 3 SD rats). The gray and black bars show the amplitudes of responses to stimuli of 1.0 mA and 2.0 mA, respectively, administered at 4 Hz under dexmedetomidine and buprenorphine sedation (Dex + Bup; n = 60 trials from the same 3 SD rats). $^{**}p < 0.001$; Tamhane's test.

et al., 2010), dexmedetomidine induces cerebral vasoconstriction (Jonckers et al., 2015).

As described in the previous section, isoflurane has anticonvulsant properties (Kofke et al., 1985, 1987; Ropper et al., 1986). Therefore, isoflurane could be expected to suppress seizure generation when combined with dexmedetomidine. Under dexmedetomidine combined with 0.3–0.5% isoflurane anesthesia, Fukuda et al. (2013) obtained seizure-free responses to 10 s-long blocks of 1 ms long pulses of 1.5 mA administered at 8 Hz. In contrast, we observed seizures in response to our main stimulation paradigm (2 mA pulses administered at 8 Hz) in 2 out of 4 rats anesthetized with dexmedetomidine combined with 0.3–0.5% isoflurane. We, therefore, conclude that adding low-percentage isoflurane to dexmedetomidine does not prevent the increased susceptibility to seizures caused by dexmedetomidine. In the next section, we propose stimulation parameters for obtaining seizure-free responses under three anesthesia regimes, including the combination of dexmedetomidine and low-percentage isoflurane.

Blood-Oxygenation and Cerebral Blood Flow Responses to Seizures

The blood-oxygenation and cerebral blood flow responses to seizures induced by forepaw stimulation have a higher amplitude and a larger spatial extent relative to physiological responses to the same stimuli (**Figures 2**, **3**). It is generally accepted that epileptic events consist of synchronous, rhythmic firing of a population of pathologically interconnected neurons capable of generating high-frequency oscillations (Bragin et al., 2002; Shariff et al., 2006). Each physiological increase in neuronal activity increases the cerebral metabolic rate of oxygen consumption, leading to an increase in CBF and CBV as the brain attempts to perfuse sufficiently the active neurons with oxygenated hemoglobin (Schwartz and Bonhoeffer, 2001; Shariff et al., 2006; Zhao et al., 2008). The signaling molecules such as adenosine and nitric oxide are released by the firing neurons, causing nearby pial arterioles to dilate (Haglund and Hochman, 2007). Consequently, seizures elicit a large focal increase in metabolism and utilization of oxygen and glucose, resulting in an enormous increase in blood volume and flow to the ictal focus to provide adequate oxygenation (Engel et al., 1982; Patel et al., 2013; Harris et al., 2018). It was demonstrated that during pilocarpine-induced status epilepticus a compensation phase lasting up to 30 min is observed with an acute increase in CBF, followed by a decompensation phase with CBF decrease (Lothman, 1990; Choy et al., 2010; Reddy and Kuruba, 2013). There is a preferential distribution of blood flow to certain regions of the brain during seizures. The degree of perfusion change in the cortex is greater than in the thalamus, and the hippocampus is hypo-perfused when compared to the cortex (Choy et al., 2010). In the present experiment, an increase in cerebral hemodynamics is observed during seizures simultaneously with an increase in neuronal activity, extending beyond the period and spatial extent of normal responses to sensory stimulation.

The findings reported here are in agreement with previous studies that characterized the cerebral hemodynamics during seizures: partial seizures have widespread effects on cortical function and cerebral perfusion (Zhao et al., 2007; Harris et al., 2014).

Seizure-Free Stimulation Paradigms and Anesthesia Regimes for Functional Imaging in Rats

Dexmedetomidine alone and dexmedetomidine combined with low-percentage isoflurane are two commonly used anesthesia regimes for functional imaging. However, our results show that these anesthesia regimes increase the susceptibility to seizures in rats. We observed seizures when applying forepaw stimulation of 10 s blocks with 1 ms long pulses of 1.0–2.0 mA administered at 8 Hz (**Figures 1–5**).

Similar potent peripheral stimulation paradigms in the range of 8–12 Hz and 1–2 mA are commonly used to elicit BOLD responses in dexmedetomidine sedated rats (Kim et al., 2010; Huttunen et al., 2011; Schulz et al., 2012; Paasonen et al., 2017; Nunes et al., 2019). These studies likely induced seizures and interpreted fMRI responses to seizures as normal responses.

We, therefore, conducted experiments to determine the stimulation parameters for seizure-free experiments under these anesthesia regimes. Our results show that when using relatively long stimulations blocks of 10 s – that are required for fMRI block paradigms – forepaw stimulation with 1 ms long pulses of 1.5–2.0 mA at 4 Hz elicits seizure-free responses (**Figures 6**, **9**). Importantly, these stimulation parameters elicit hemodynamic responses that can be clearly detected in single trials (**Figures 9**, **10**). Therefore, we propose these paradigms for safe stimulation that does not induce seizures but still generates well detectable hemodynamic responses.

Another possibility is to use urethane anesthesia, in studies that do not require recovery of the animal following the neurophysiology and/or functional imaging experiment. Urethane has modest effects on both the inhibitory and excitatory systems and does not affect the noradrenergic system (Hara and Harris, 2002). The changes it exerts on multiple neurotransmitter-gated ion channels are much smaller than those seen with anesthetics more selective for one neurotransmitter system, such as ketamine. Therefore, urethane is suitable for maintaining anesthesia during electrophysiological recording and functional imaging (Hara and Harris, 2002). As we demonstrated previously (Bortel et al., 2019), under urethane anesthesia, 10 s blocks of digit stimulation with 1 ms long pulses of 2 mA administered at 8 Hz elicited seizure-free, well detectable neurophysiological and hemodynamic responses.

Mechanisms of Stimulation-Induced Seizures Under Dexmedetomidine Sedation

Both sedation and general anesthesia suppress the central nervous system, but only general anesthesia results in unconsciousness and lack of sensation (Turner and Knapp, 1995; Young-McCaughan and Miaskowski, 2001; Miller, 2010). Under general anesthesia, the activity of the thalamic and midbrain reticular formation nuclei is suppressed. The suppression of

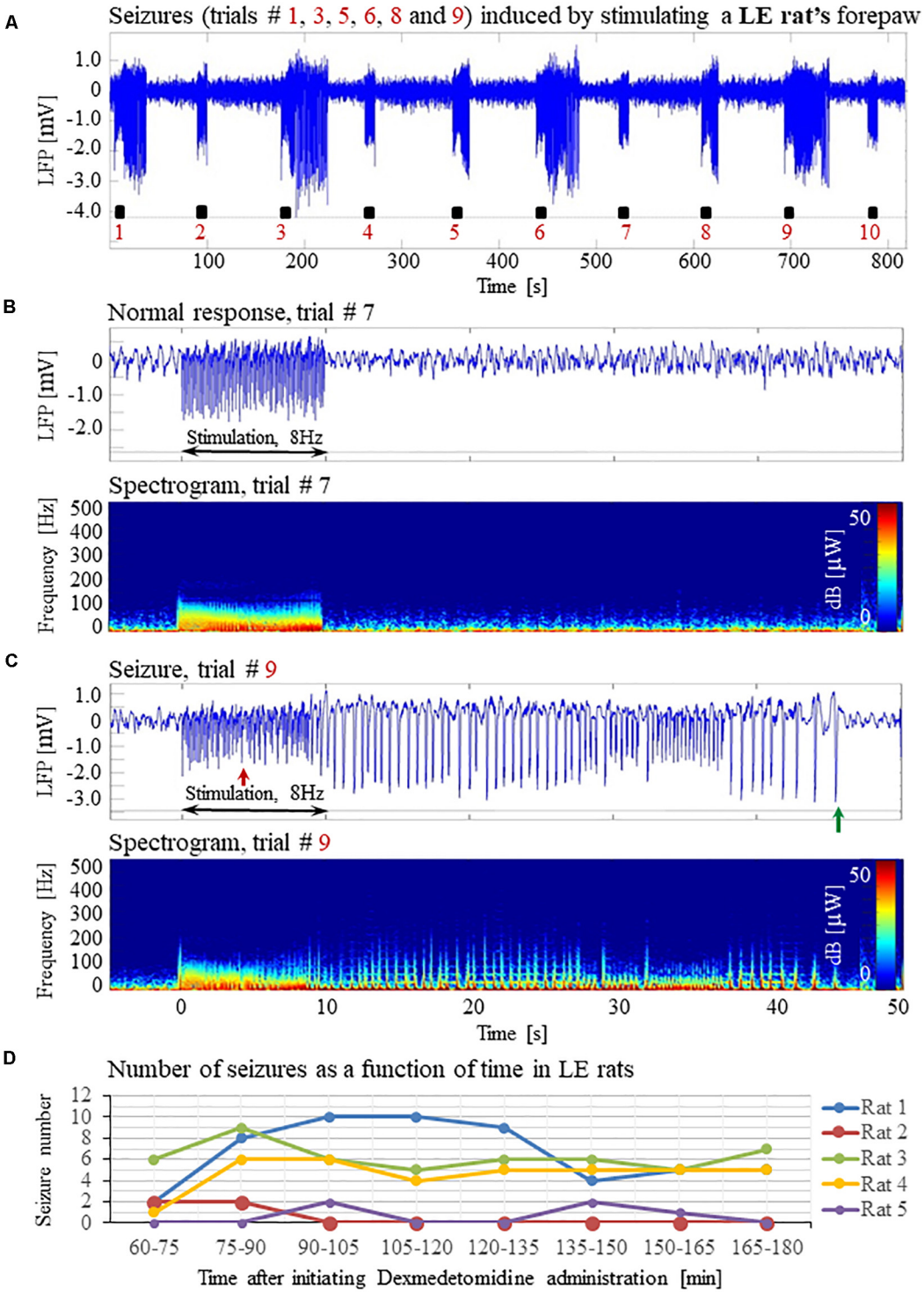

FIGURE 11 | Forepaw stimulation induces epileptic activity in LE rat. **(A)** LFP recordings of ten trials, each with 10 s-long stimulation. The stimulation periods are marked by black rectangles. Note that during the first, third, fifth, sixth, eighth, and ninth trials, the stimulation induced a seizure. **(B)** Top: The LFP (mean averaged over electrode contacts spanning the cortical depth) demonstrates a normal-evoked response in trial #7. Bottom: The corresponding spectrogram (power as a function of frequency and time) computed for the same trial. **(C)** Top: LFP (mean averaged over electrode contacts spanning the cortical depth) showing a seizure pattern in trial #9. The red and green arrows indicate the onset and termination, respectively, of a seizure induced by forepaw stimulation. Bottom: The corresponding spectrogram, computed for the same seizure. **(D)** The number of evoked seizures per rat as a function of time shows that seizures are induced already during the first or the third run, only one hour after initiating the dexmedetomidine administration.

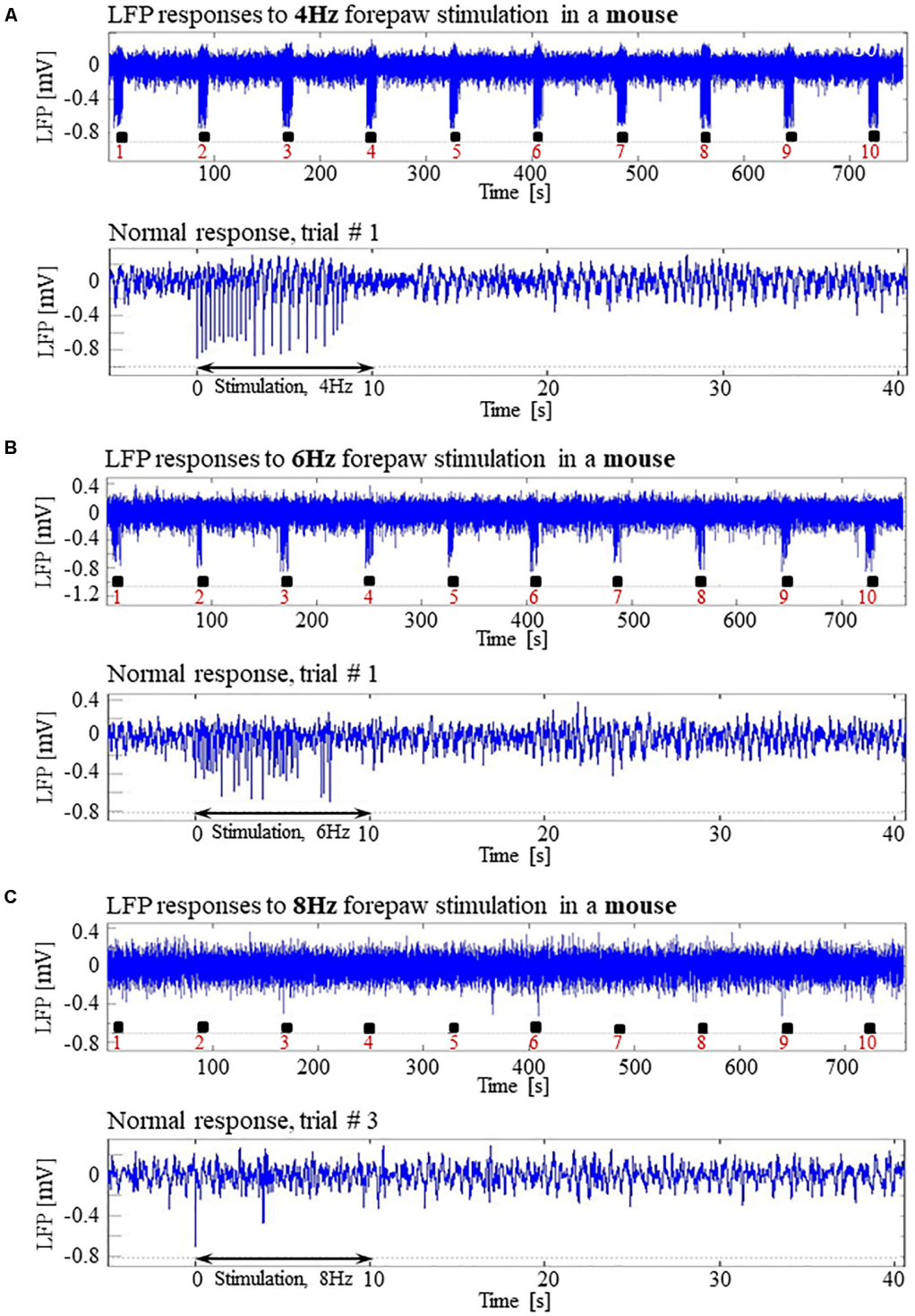

FIGURE 12 | Absence of seizures in the C57BL6 mouse strain. **(A)** Top: Normal LFP responses obtained from area S1FL, in response to 4 Hz forepaw stimulation. The panel shows ten trials, each with 10 s-long stimulation. The stimulation blocks are marked by black rectangles. Bottom: A magnification of the normal evoked response from the first trial. **(B)** Top: Normal LFP responses to 6 Hz forepaw stimulation. Bottom: A magnification of the normal evoked response from the first trial. **(C)** Top: A typical activity pattern of evoked responses to 8 Hz forepaw stimulation. Bottom: A magnification of the normal evoked response from the third trial.

the thalamic information transfer disrupts the somatosensory input from reaching higher cortical areas (Miller, 2010). Dexmedetomidine has sedative properties, and buprenorphine is an opioid with analgesic properties. It is possible that the combination of dexmedetomidine and buprenorphine modifies the anesthesia regime from sedation (with dexmedetomidine alone) closer to anesthesia (with dexmedetomidine and buprenorphine). However, since this is unclear, here we use the term 'sedation' when describing the effect of dexmedetomidine and buprenorphine. In contrast, given that isoflurane is a general anesthetic, we use the term 'anesthesia' when referring to the effect of combining dexmedetomidine and isoflurane.

Dexmedetomidine is an α2-adrenergic agonist with sedative properties, predominantly acting on presynaptic receptors in the locus coeruleus. It regulates the central adrenergic function and in consequence induces cerebral vasoconstriction mediated by direct agonist binding to receptors on the cerebral vessels, resulting in a reduced baseline of CBF and CBV (Weber et al., 2006; Pawela et al., 2009; Adamczak et al., 2010; Jonckers et al., 2015; Paasonen et al., 2018). The degree of vasoconstriction depends on the dose and delivery method (topical vs. systemic) (Jonckers et al., 2015). Dexmedetomidine decreases noradrenaline release (Gertler et al., 2001), which in turn decreases seizure threshold (Oishi and Suenaga, 1982).

There have been several conflicting reports on the influence of dexmedetomidine on seizure generation. It was shown that the seizure frequency and onset time evoked by kainic acid (Airaksinen et al., 2010, 2012) or pilocarpine (Choy et al., 2010) are similar in the awake and medetomidine-sedated rats. Halonen et al. (1995) demonstrated that rat convulsions induced by kainic acid are prevented by the administration of medetomidine. Similarly, it was shown that rat seizures induced by the administration of cocaine were suppressed by medetomidine sedation (Whittington et al., 2002). Furthermore, high doses (100 μg/kg or higher) of dexmedetomidine effectively decreases the number and cumulative time of repeated seizures evoked by prolonged intracranial electrical stimulation of the amygdala (Kan et al., 2013). In contrast, it was shown that dexmedetomidine increases the epileptiform activity in epileptic patients (Chaitanya et al., 2015). In addition, dexmedetomidine exerts a significant proconvulsant action in the pentylenetetrazol seizure animal model. The proconvulsant effect is dose-dependent and stereospecific. It can be blocked by the selective α2-adrenergic antagonist atipamezole (Mirski et al., 1994). Likewise, Fukuda et al. (2013) demonstrated that epileptic activity could be induced in rats by electrical stimulation of the forelimb after 2 h-long continuous IV infusion of dexmedetomidine (Fukuda et al., 2013).

In line with the findings by Whittington et al. (2002) and Airaksinen et al. (2012) we did not observe any seizure-like responses to short and weak forelimb stimuli (1 s-long, 0.6–0.8 mA current pulses delivered at 8 Hz) under dexmedetomidine sedation (Sotero et al., 2015). Here, we did not observe seizures with 10 s-long stimulation with either 1 or 2 mA pulses delivered at 4 Hz (**Figures 6A,B**), as was also shown by Fukuda et al. (2013). Nevertheless, under the same sedation regime, long (10 s), potent (1 or 2 mA), repetitive and frequent (8 Hz) peripheral electrical stimuli evoke seizures (**Figures 1–5**, **7A–C**), as was also demonstrated by Bortel et al. (2019). Therefore, dexmedetomidine increases the susceptibility to seizures. However, potent stimuli are necessary, too, for inducing seizures by peripheral stimulation under such increased susceptibility.

We did not perform systematic experiments to test the effect of dexmedetomidine dose on the susceptibility to seizure. Therefore, we cannot rule out the possibility that the susceptibility to the generation of seizures depends on the dose of dexmedetomidine. However, we obtained data that indicate that the lack of seizures in C57 mice did not depend on the dose. To maintain proper sedation in three of the mouse experiments, we had to increase the rate of dexmedetomidine from 0.05 mg/kg/h to 0.1 mg/kg/h approximately 80 min after the infusion started. However, no seizures were observed in these mice or the other mice. These results are consistent with Fukuda et al. (2013) findings that increasing the dexmedetomidine IV infusion rate from 0.05 mg/kg/h to 0.15 mg/kg/h in SD rats does not change the susceptibility to seizure generation.

The trigger to the epileptic activity in our animals is repetitive electrical somatosensory stimulation. Therefore, these seizures are reflex seizures. Reflex seizures are defined as seizures triggered by repetitive, 5–20 s long sensory stimulations (Kanemoto et al., 2001; Panayiotopoulos(ed.), 2005; Striano et al., 2012; Sala-Padro et al., 2015; Wolf, 2015). Epileptic activity induced in our rats consisted of brief and focal electrographic seizures; the animals did not show any epileptic behavior. Similar to our observation in rats, touch induced seizures in humans manifest as focal, brief seizures that may have only an electrographic display without any overt clinical manifestations (Panayiotopoulos(ed.), 2005).

Dexmedetomidine Sedation Increases Susceptibility to Seizures in Rats but Not in Wild-Type Mice

We have shown that dexmedetomidine increases susceptibility to seizures in SD and LE rats, but not in C57 mice. Previous works have demonstrated that the rat and mouse strains show diverse susceptibility to seizure-induction (Ferraro et al., 1995; Golden et al., 1995; McKhann et al., 2003). Wistar-Furth rats are more sensitive to the convulsant effects of kainic acid (KA) than Sprague- Dawley and Long-Evans Hooded rats (Golden et al., 1991, 1995). It was shown that the C57BL6 mouse strain has lower seizure sensitivity than several strains reported as sensitive to seizures, including the SWR/J, FVB/NJ, CBA/J, DBA/1, and DBA/2 strains (Frankel et al., 2001). Indeed, DBA/2J mice exhibit a higher susceptibility to maximal electroshock and KA-induced seizures relative to C57BL/6J mice (Ferraro et al., 1995, 2002). Similarly, McKhann et al. (2003) showed that C57BL/6J and C3HeB/FeJ mice are more resistant to seizures than 129/SvEms mice. Our results support the assertion that C57 mice have low susceptibility to seizures. More in general, our findings support the concept that seizure susceptibility depends on the animal's species and strain.

Our findings demonstrate the lack of significant, sustained LFP responses to 8 Hz — and only reduced LFP responses to 6 Hz — relative to responses to 4 Hz forepaw stimulation in mice (**Figures 12A–C**). The maintenance of the proper balance between excitation and inhibition is critical for the normal function of cortical circuits (Turrigiano, 2011). This continuum of changes in response amplitude suggests that changes in the balance between excitation and inhibition take place as a function of the stimulation frequency. We propose that the inhibitory tone is overall enhanced at higher stimulation frequencies, possibly because the inhibitory response following a stimulus is still in effect when the next stimulus is administered in a train of stimulation at 8 Hz but not at 4 Hz. Indeed, one of the explanations proposed by Wang et al. (2013) is that the effect of inhibition remains longer than that of the excitation, and therefore the subsequent excitation in a train overlaps the inhibition. It was also shown that a decrease in the firing of neurons to high-frequency stimuli is a consequence of an altered balance in excitatory and inhibitory cortical activity (Li et al., 2009; House et al., 2011).

Our findings in mice experiments differ from Fukuda et al. (2013) findings and our findings (**Figures 6**, **7**) in SD rat experiments. Fukuda et al. (2013) reported that under dexmedetomidine sedation (with the addition of pancuronium bromide) the evoked LFP responses to forepaw stimulation were larger at a frequency of 8–10 Hz than those elicited by 4, 6, and 12 Hz stimulation. The difference in the stimulus frequency dependence of the LFP responses between mice and SD rats suggests that the effect of stimulus frequency on the balance between excitation and inhibition is different for these two species.

CONCLUSION

Our findings demonstrate that hemodynamic responses to potent stimuli in rats sedated with dexmedetomidine or anesthetized with dexmedetomidine and isoflurane are possibly due to induced seizures. We ruled out the possibility that the increased susceptibility to seizures in our experiments was caused by any agent other than dexmedetomidine. The induction of seizures in experiments that use dexmedetomidine depends on stimulation strength. To obtain physiological yet detectable neuronal and hemodynamic responses, we propose stimulation parameters that ensure seizure-free responses under dexmedetomidine sedation or dexmedetomidine and isoflurane anesthesia. By definition, obtaining spontaneous activity for the study of the resting-state condition does not involve administering stimuli. Indeed, we did not observe any seizures during spontaneous activity (data not shown).

Our results reveal that dexmedetomidine increases susceptibility to seizures in the 2 rat strains we tested, SD and LE rats, but not in wild type C57 mice. More in general, our findings support the concept that seizure susceptibility depends on the animal's species.

DATA AVAILABILITY STATEMENT

The complete optical imaging and neurophysiology data generated for this article will be made available upon request sent by email to the corresponding author. See https://www.mcgill.ca/neuro/amir-shmuel-phd.

AUTHOR CONTRIBUTIONS

AB acquired the data, analyzed the data, interpreted the results, and wrote the manuscript. RP wrote the pipeline for analyzing the neurophysiology data and interpreted the results. ZY set up the optical imaging experiments and wrote the pipeline for analyzing the optical imaging data. AS oversaw the data acquisition and the data analysis, interpreted the results and wrote the manuscript. All the authors contributed to the article and approved the submitted version.

FUNDING

This study was supported by the Canadian Institute of Health Research (Grant MOP-102599), and the Natural Sciences and Engineering Research Council of Canada (RGPIN 375457-09 and RGPIN 2015-05103) awarded to AS.

ACKNOWLEDGMENTS

We thank Jean Gotman, Massimo Avoli, Victor Mocanu, and Pascal Kropf for their helpful technical advice and discussions.

REFERENCES

Adamczak, J. M., Farr, T. D., Seehafer, J. U., Kalthoff, D., and Hoehn, M. (2010). High field BOLD response to forepaw stimulation in the mouse. *Neuroimage* 51, 704–712. doi: 10.1016/j.neuroimage.2010.02.083

Airaksinen, A. M., Hekmatyar, S. K., Jerome, N., Niskanen, J. P., Huttunen, J. K., Pitkanen, A., et al. (2012). Simultaneous BOLD fMRI and local field potential measurements during kainic acid-induced seizures. *Epilepsia* 53, 1245–1253. doi: 10.1111/j.1528-1167.2012.03539.x

Airaksinen, A. M., Niskanen, J. P., Chamberlain, R., Huttunen, J. K., Nissinen, J., Garwood, M., et al. (2010). Simultaneous fMRI and local field potential measurements during epileptic seizures in medetomidine-sedated rats using raser pulse sequence. *Magn. Reson. Med.* 64, 1191–1199. doi: 10.1002/mrm.22508

Albers, F., Schmid, F., Wachsmuth, L., and Faber, C. (2018). Line scanning fMRI reveals earlier onset of optogenetically evoked BOLD response in rat somatosensory cortex as compared to sensory stimulation. *Neuroimage* 164, 144–154. doi: 10.1016/j.neuroimage.2016.12.059

Barton, M. E., Klein, B. D., Wolf, H. H., and White, H. S. (2001). Pharmacological characterization of the 6 Hz psychomotor seizure model of partial epilepsy. *Epilepsy Res.* 47, 217–227. doi: 10.1016/s0920-1211(01)00302-3

Boas, D. A., and Dunn, A. K. (2010). Laser speckle contrast imaging in biomedical optics. *J. Biomed. Opt.* 15:011109. doi: 10.1117/1.3285504

Bortel, A., Yao, Z. S., and Shmuel, A. (2019). A rat model of somatosensory-evoked reflex seizures induced by peripheral stimulation. *Epilepsy Res.* 157:106209. doi: 10.1016/j.eplepsyres.2019.106209

Bragin, A., Mody, I., Wilson, C. L., and Engel, J. (2002). Local generation of fast ripples in epileptic brain. *J. Neurosci.* 22, 2012–2021. doi: 10.1523/jneurosci.22-05-02012.2002

Bukhari, Q., Schroeter, A., Cole, D. M., and Rudin, M. (2017). Resting state fMRI in mice reveals anesthesia specific signatures of brain functional networks and their interactions. *Front. Neural Circ.* 11:5. doi: 10.3389/fncir.2017.00005

Chaitanya, G., Arivazhagan, A., Sinha, S., Reddy, K. R., Thennarasu, K., Bharath, R. D., et al. (2015). Dexmedetomidine anesthesia enhances spike generation during intra-operative electrocorticography: a promising adjunct for epilepsy surgery. *Epilepsy Res.* 109, 65–71. doi: 10.1016/j.eplepsyres.2014.10.006

Choy, M., Wells, J. A., Thomas, D. L., Gadian, D. G., Scott, R. C., and Lythgoe, M. F. (2010). Cerebral blood flow changes during pilocarpine-induced status epilepticus activity in the rat hippocampus. *Exp. Neurol.* 225, 196–201. doi: 10.1016/j.expneurol.2010.06.015

Dunn, A. K., Bolay, H., Moskowitz, M. A., and Boas, D. A. (2001). Dynamic imaging of cerebral blood flow using laser speckle. *J. Cereb. Blood Flow Metab.* 21, 195–201. doi: 10.1097/00004647-200103000-00002

Dunn, A. K., Devor, A., Bolay, H., Andermann, M. L., Moskowitz, M. A., and Boas, D. A. (2003). Simultaneous imaging of total cerebral hemoglobin concentration, oxygenation, and blood flow during functional activation. *Opt. Lett.* 28, 28–30.

Eger, E. I. (1984). The pharmacology of isoflurane. *Br. J. Anaesth.* 56(Suppl. 1), 71s–99s.

Engel, J., Kuhl, D. E., and Phelps, M. E. (1982). Patterns of human local cerebral glucose metabolism during epileptic seizures. *Science* 218, 64–66. doi: 10.1126/science.6981843

Esneault, E., Peyon, G., and Castagne, V. (2017). Efficacy of anticonvulsant substances in the 6Hz seizure test: comparison of two rodent species. *Epilepsy Res.* 134, 9–15. doi: 10.1016/j.eplepsyres.2017.05.002

Ferraro, T. N., Golden, G. T., Smith, G. G., and Berrettini, W. H. (1995). Differential susceptibility to seizures induced by systemic kainic acid treatment in mature DBA/2J and C57BL/6J mice. *Epilepsia* 36, 301–307. doi: 10.1111/j.1528-1157.1995.tb00999.x

Ferraro, T. N., Golden, G. T., Smith, G. G., DeMuth, D., Buono, R. J., and Berrettini, W. H. (2002). Mouse strain variation in maximal electroshock seizure threshold. *Brain Res.* 936, 82–86. doi: 10.1016/s0006-8993(02)02565-9

Fox, M. D., and Greicius, M. (2010). Clinical applications of resting state functional connectivity. *Front. Syst. Neurosci.* 4:19. doi: 10.3389/fnsys.2010.00019

Franceschini, M. A., Radhakrishnan, H., Thakur, K., Wu, W., Ruvinskaya, S., Carp, S., et al. (2010). The effect of different anesthetics on neurovascular coupling. *Neuroimage* 51, 1367–1377. doi: 10.1016/j.neuroimage.2010.03.060

Frankel, W. N., Taylor, L., Beyer, B., Tempel, B. L., and White, H. S. (2001). Electroconvulsive thresholds of inbred mouse strains. *Genomics* 74, 306–312. doi: 10.1006/geno.2001.6564

Franklin, K., and Paxinos, G. (2007). *The Mouse Brain in Stereotaxic Coordinates*, 3rd Edn. New York, NY: Elsevier Academic Press.

Friston, K. J., Frith, C. D., Liddle, P. F., and Frackowiak, R. S. (1993). Functional connectivity: the principal-component analysis of large (PET) data sets. *J. Cereb. Blood Flow Metab.* 13, 5–14. doi: 10.1038/jcbfm.1993.4

Fukuda, M., Vazquez, A. L., Zong, X., and Kim, S. G. (2013). Effects of the alpha(2)-adrenergic receptor agonist dexmedetomidine on neural, vascular and BOLD fMRI responses in the somatosensory cortex. *Eur. J. Neurosci.* 37, 80–95. doi: 10.1111/ejn.12024

Gertler, R., Brown, H. C., Mitchell, D. H., and Silvius, E. N. (2001). Dexmedetomidine: a novel sedative- analgesic agent. *Proc (Bayl Univ Med Cent)* 14, 13–21. doi: 10.1080/08998280.2001.11927725

Golden, G. T., Smith, G. G., Ferraro, T. N., and Reyes, P. F. (1995). Rat strain and age differences in kainic acid induced seizures. *Epilepsy Res.* 20, 151–159. doi: 10.1016/0920-1211(94)00079-c

Golden, G. T., Smith, G. G., Ferraro, T. N., Reyes, P. F., Kulp, J. K., and Fariello, R. G. (1991). Strain differences in convulsive response to the excitotoxin kainic acid. *Neuroreport* 2, 141–144. doi: 10.1097/00001756-199103000-00008

Grandjean, J., Schroeter, A., Batata, I., and Rudin, M. (2014). Optimization of anesthesia protocol for resting-state fMRI in mice based on differential effects of anesthetics on functional connectivity patterns. *Neuroimage* 102(Pt 2), 838–847. doi: 10.1016/j.neuroimage.2014.08.043

Grasshoff, C., and Antkowiak, B. (2006). Effects of isoflurane and enflurane on GABAA and glycine receptors contribute equally to depressant actions on spinal ventral horn neurones in rats. *Br. J. Anaesth.* 97, 687–694. doi: 10.1093/bja/ael239

Grinvald, A., Shoham, D., Shmuel, A., Glaser, D. E., Vanzetta, I., Shtoyerman, E., et al. (1999). "*In-vivo* optical imaging of cortical architecture and dynamics," in *Modern Techniques in Neuroscience Research*, eds U. Windhorst and H. Johansson (Berlin; Heidelberg: Springer), 893–969.

Haglund, M. M., and Hochman, D. W. (2007). Imaging of intrinsic optical signals in primate cortex during epileptiform activity. *Epilepsia* 48(Suppl. 4), 65–74. doi: 10.1111/j.1528-1167.2007.01243.x

Halonen, T., Kotti, T., Tuunanen, J., Toppinen, A., Miettinen, R., and Riekkinen, P. J. (1995). Alpha 2- adrenoceptor agonist, dexmedetomidine, protects against kainic acid-induced convulsions and neuronal damage. *Brain Res.* 693, 217–224. doi: 10.1016/0006-8993(95)00744-b

Hara, K., and Harris, R. A. (2002). The anesthetic mechanism of urethane: the effects on neurotransmitter-gated ion channels. *Anesth. Analg.* 94, 313–318. doi: 10.1213/00000539-200202000-00015

Harris, S., Boorman, L., Bruyns-Haylett, M., Kennerley, A., Ma, H., Zhao, M., et al. (2014). Contralateral dissociation between neural activity and cerebral blood volume during recurrent acute focal neocortical seizures. *Epilepsia* 55, 1423–1430. doi: 10.1111/epi.12726

Harris, S. S., Boorman, L. W., Kennerley, A. J., Sharp, P. S., Martin, C., Redgrave, P., et al. (2018). Seizure epicenter depth and translaminar field potential synchrony underlie complex variations in tissue oxygenation during ictal initiation. *Neuroimage* 171, 165–175. doi: 10.1016/j.neuroimage.2017.12.088

House, D. R., Elstrott, J., Koh, E., Chung, J., and Feldman, D. E. (2011). Parallel regulation of feedforward inhibition and excitation during whisker map plasticity. *Neuron* 72, 819–831. doi: 10.1016/j.neuron.2011.09.008

Huttunen, J. K., Grohn, O., and Penttonen, M. (2008). Coupling between simultaneously recorded BOLD response and neuronal activity in the rat somatosensory cortex. *Neuroimage* 39, 775–785. doi: 10.1016/j.neuroimage.2007.06.042

Huttunen, J. K., Niskanen, J. P., Lehto, L. J., Airaksinen, A. M., Niskanen, E. I., Penttonen, M., et al. (2011). Evoked local field potentials can explain temporal variation in blood oxygenation level-dependent responses in rat somatosensory cortex. *NMR Biomed.* 24, 209–215. doi: 10.1002/nbm.1575

Jonckers, E., Shah, D., Hamaide, J., Verhoye, M., and Van der Linden, A. (2015). The power of using functional fMRI on small rodents to study brain pharmacology and disease. *Front. Pharmacol.* 6:231. doi: 10.3389/fphar.2015.00231

Kan, M. C., Wang, W. P., Yao, G. D., Li, J. T., Xie, T., and Ma, W. Q. (2013). Anticonvulsant effect of dexmedetomidine in a rat model of self-sustaining status epilepticus with prolonged amygdala stimulation. *Neurosci. Lett.* 543, 17–21. doi: 10.1016/j.neulet.2013.03.036

Kanemoto, K., Watanabe, Y., Tsuji, T., Fukami, M., and Kawasaki, J. (2001). Rub epilepsy: a somatosensory evoked reflex epilepsy induced by prolonged cutaneous stimulation. *J. Neurol. Neurosurg. Psychiatry* 70, 541–543. doi: 10.1136/jnnp.70.4.541

Kim, T., Masamoto, K., Fukuda, M., Vazquez, A., and Kim, S. G. (2010). Frequency-dependent neural activity, CBF, and BOLD fMRI to somatosensory stimuli in isoflurane-anesthetized rats. *Neuroimage* 52, 224–233. doi: 10.1016/j.neuroimage.2010.03.064

Kofke, W. A., Snider, M. T., O'Connell, B. K., and Wang, W. (1987). Isoflurane stops refractory seizures. *Anesthesiol. Rev.* 15, 58–59.

Kofke, W. A., Snider, M. T., Young, R. S. K., and Ramer, J. C. (1985). Prolonged low flow isoflurane anesthesia for status epilepticus. *Anesthesiology* 62, 653–656. doi: 10.1097/00000542-198505000-00023

Krautwald, K., and Angenstein, F. (2012). Low frequency stimulation of the perforant pathway generates anesthesia-specific variations in neural activity and BOLD responses in the rat dentate gyrus. *J. Cereb. Blood Flow Metab.* 32, 291–305. doi: 10.1038/jcbfm.2011.126

Lambers, H., Segeroth, M., Albers, F., Wachsmuth, L., van Alst, T. M., and Faber, C. (2020). A cortical rat hemodynamic response function for improved detection of BOLD activation under common experimental conditions. *Neuroimage* 208:116446. doi: 10.1016/j.neuroimage.2019.116446

Li, P., Rudolph, U., and Huntsman, M. M. (2009). Long-term sensory deprivation selectively rearranges functional inhibitory circuits in mouse barrel cortex. *Proc. Natl. Acad. Sci. U.S.A.* 106, 12156–12161. doi: 10.1073/pnas.0900922106

Lothman, E. (1990). The biochemical basis and pathophysiology of status epilepticus. *Neurology* 40, 13–23.

Masamoto, K., Kim, T., Fukuda, M., Wang, P., and Kim, S. G. (2007). Relationship between neural, vascular, and BOLD signals in isoflurane-anesthetized rat somatosensory cortex. *Cereb. Cortex* 17, 942–950. doi: 10.1093/cercor/bhl005

McKhann, G. M., Wenzel, H. J., Robbins, C. A., Sosunov, A. A., and Schwartzkroin, P. A. (2003). Mouse strain differences in kainic acid sensitivity, seizure behavior, mortality, and hippocampal pathology. *Neuroscience* 122, 551–561. doi: 10.1016/s0306-4522(03)00562-1

Miller, R. D. (2010). *Miller's Anesthesia*, 7th Edn. London: Elsevier.

Mirski, M. A., Rossell, L. A., McPherson, R. W., and Traystman, R. J. (1994). Dexmedetomidine decreases seizure threshold in a rat model of experimental generalized epilepsy. *Anesthesiology* 81, 1422–1428. doi: 10.1097/00000542-199412000-00017

Nasrallah, F. A., Tan, J., and Chuang, K. H. (2012). Pharmacological modulation of functional connectivity: alpha2-adrenergic receptor agonist alters synchrony but not neural activation. *Neuroimage* 60, 436–446. doi: 10.1016/j.neuroimage.2011.12.026

Nunes, D., Ianus, A., and Shemesh, N. (2019). Layer-specific connectivity revealed by diffusion- weighted functional MRI in the rat thalamocortical pathway. *Neuroimage* 184, 646–657. doi: 10.1016/j.neuroimage.2018.09.050

Oishi, R., and Suenaga, N. (1982). The role of the locus coeruleus in regulation of seizure susceptibility in rats. *Jpn J. Pharmacol.* 32, 1075–1081. doi: 10.1254/jjp.32.1075

Paasonen, J., Salo, R. A., Huttunen, J. K., and Grohn, O. (2017). Resting-state functional MRI as a tool for evaluating brain hemodynamic responsiveness to external stimuli in rats. *Magn. Reson. Med.* 78, 1136–1146. doi: 10.1002/mrm.26496

Paasonen, J., Stenroos, P., Salo, R. A., Kiviniemi, V., and Grohn, O. (2018). Functional connectivity under six anesthesia protocols and the awake condition in rat brain. *Neuroimage* 172, 9–20. doi: 10.1016/j.neuroimage.2018.01.014

Panayiotopoulos, C. P. (ed.) (2005). "Reflex seizures and reflex epilepsies," in *The Epilepsies: Seizures, Syndromes and Management* (Oxfordshire: Bladon Medical Publishing).

Patel, K. S., Zhao, M., Ma, H., and Schwartz, T. H. (2013). Imaging preictal hemodynamic changes in neocortical epilepsy. *Neurosurg. Focus* 34:E10.

Pawela, C. P., Biswal, B. B., Cho, Y. R., Kao, D. S., Li, R., Jones, S. R., et al. (2008). Resting-state functional connectivity of the rat brain. *Magn. Reson. Med.* 59, 1021–1029.

Pawela, C. P., Biswal, B. B., Hudetz, A. G., Schulte, M. L., Li, R., Jones, S. R., et al. (2009). A protocol for use of medetomidine anesthesia in rats for extended studies using task-induced BOLD contrast and resting-state functional connectivity. *Neuroimage* 46, 1137–1147. doi: 10.1016/j.neuroimage.2009.03.004

Pawson, P. (2008). "Chapter 6 - Sedatives," in *Small Animal Clinical Pharmacology*, 2nd Edn, eds J. E. Maddison, S. W. Page, and D. B. Church (Edinburgh: W.B. Saunders), 113–125.

Paxinos, G., and Watson, C. (2005). *The Rat Brain in Stereotaxic Coordinates*, 5th Edn. Boston: Elsevier Academic Press.

Reddy, D. S., and Kuruba, R. (2013). Experimental models of status epilepticus and neuronal injury for evaluation of therapeutic interventions. *Int. J. Mol. Sci.* 14, 18284–18318. doi: 10.3390/ijms140918284

Rojas, A., Jiang, J., Ganesh, T., Yang, M. S., Lelutiu, N., Gueorguieva, P., et al. (2014). Cyclooxygenase-2 in epilepsy. *Epilepsia* 55, 17–25. doi: 10.1111/epi.12461

Ropper, A. H., Kofke, W. A., Bromfield, E. B., and Kennedy, S. K. (1986). Comparison of isoflurane, halothane, and nitrous oxide in status epilepticus [Letter]. *Ann. Neurol.* 19, 98–99. doi: 10.1002/ana.410190124

Rubio, F., Seawall, S., Pocelinko, R., DeBarbieri, B., Benz, W., Berger, L., et al. (1980). Metabolism of carprofen, a nonsteroidal anti-inflammatory agent, in rats, dogs, and humans. *J. Pharm. Sci.* 69, 1245–1253. doi: 10.1002/jps.2600691104

Sala-Padro, J., Toledo, M., Sarria, S., Santamarina, E., Gonzalez-Cuevas, M., Sueiras-Gil, M., et al. (2015). Reflex seizures triggered by cutaneous stimuli. *Seizure* 33, 72–75. doi: 10.1016/j.seizure.2015.10.013

Schauwecker, P. E. (2002). Complications associated with genetic background effects in models of experimental epilepsy. *Prog. Brain Res.* 135, 139–148. doi: 10.1016/s0079-6123(02)35014-3

Schulz, K., Sydekum, E., Krueppel, R., Engelbrecht, C. J., Schlegel, F., Schroter, A., et al. (2012). Simultaneous BOLD fMRI and fiber-optic calcium recording in rat neocortex. *Nat. Methods* 9, 597–602. doi: 10.1038/nmeth.2013

Schwartz, T. H., and Bonhoeffer, T. (2001). In vivo optical mapping of epileptic foci and surround inhibition in ferret cerebral cortex. *Nat. Med.* 7, 1063–1067. doi: 10.1038/nm0901-1063

Shariff, S., Suh, M., Zhao, M., Ma, H., and Schwartz, T. H. (2006). Recent developments in oximetry and perfusion-based mapping techniques and their role in the surgical treatment of neocortical epilepsy. *Epilepsy Behav.* 8, 363–375. doi: 10.1016/j.yebeh.2005.11.006

Shmuel, A., and Leopold, D. A. (2008). Neuronal correlates of spontaneous fluctuations in fMRI signals in monkey visual cortex: implications for functional connectivity at rest. *Hum. Brain Mapp.* 29, 751–761. doi: 10.1002/hbm.20580

Sotero, R. C., Bortel, A., Martínez-Cancino, R., Neupane, S., O'Connor, P., Carbonell, F., et al. (2010). Anatomically-constrained effective connectivity among layers in a cortical column modeled and estimated from local field potentials. *J. Integ. Neurosci.* 9, 355–379. doi: 10.1142/s0219635210002548

Sotero, R. C., Bortel, A., Naaman, S., Mocanu, V. M., Kropf, P., Villeneuve, M. Y., et al. (2015). Laminar distribution of phase-amplitude coupling of spontaneous current sources and sinks. *Front. Neurosci.* 9:454. doi: 10.3389/fnins.2015.00454

Striano, S., Coppola, A., del Gaudio, L., and Striano, P. (2012). Reflex seizures and reflex epilepsies: old models for understanding mechanisms of epileptogenesis. *Epilepsy Res.* 100, 1–11. doi: 10.1016/j.eplepsyres.2012.01.013

Turner, B. H., and Knapp, M. E. (1995). Consciousness: a neurobiological approach. *Integr. Physiol. Behav. Sci.* 30, 151–156.

Turrigiano, G. (2011). Too many cooks? Intrinsic and synaptic homeostatic mechanisms in cortical circuit refinement. *Annu. Rev. Neurosci.* 34, 89–103. doi: 10.1146/annurev-neuro-060909-153238

Wang, Z., Qi, H. X., Kaas, J. H., Roe, A. W., and Chen, L. M. (2013). Functional signature of recovering cortex: dissociation of local field potentials and spiking activity in somatosensory cortices of spinal cord injured monkeys. *Exp. Neurol.* 249, 132–143. doi: 10.1016/j.expneurol.2013.08.013

Weber, R., Ramos-Cabrer, P., Wiedermann, D., van Camp, N., and Hoehn, M. (2006). A fully noninvasive and robust experimental protocol for longitudinal fMRI studies in the rat. *Neuroimage* 29, 1303–1310. doi: 10.1016/j.neuroimage.2005.08.028

Whittington, R. A., Virag, L., Vulliemoz, Y., Cooper, T. B., and Morishima, H. O. (2002). Dexmedetomidine increases the cocaine seizure threshold in rats. *Anesthesiology* 97, 693–700. doi: 10.1097/00000542-200209000-00024

Wolf, P. (2015). Reflex epileptic mechanisms in humans: lessons about natural ictogenesis. *Epilepsy Behav.* 71(Pt B), 118–123. doi: 10.1016/j.yebeh.2015.01.009

Young-McCaughan, S., and Miaskowski, C. (2001). Definition of and mechanism for opioid-induced sedation. *Pain. Manag. Nurs.* 2, 84–97. doi: 10.1053/jpmn.2001.25012

Zhao, F., Zhao, T., Zhou, L., Wu, Q., and Hu, X. (2008). BOLD study of stimulation-induced neural activity and resting-state connectivity in medetomidine-sedated rat. *Neuroimage* 39, 248–260. doi: 10.1016/j.neuroimage.2007.07.063

Zhao, M., Suh, M., Ma, H., Perry, C., Geneslaw, A., and Schwartz, T. H. (2007). Focal increases in perfusion and decreases in hemoglobin oxygenation precede seizure onset in spontaneous human epilepsy. *Epilepsia* 48, 2059–2067. doi: 10.1111/j.1528-1167.2007.01229.x

Conflict of Interest: The authors declare that the research was conducted in the absence of any commercial or financial relationships that could be construed as a potential conflict of interest.

Advantages of publishing in Frontiers

OPEN ACCESS
Articles are free to read for greatest visibility and readership

FAST PUBLICATION
Around 90 days from submission to decision

HIGH QUALITY PEER-REVIEW
Rigorous, collaborative, and constructive peer-review

TRANSPARENT PEER-REVIEW
Editors and reviewers acknowledged by name on published articles

Frontiers
Avenue du Tribunal-Fédéral 34
1005 Lausanne | Switzerland

Visit us: www.frontiersin.org
Contact us: info@frontiersin.org | +41 21 510 17 00

REPRODUCIBILITY OF RESEARCH
Support open data and methods to enhance research reproducibility

DIGITAL PUBLISHING
Articles designed for optimal readership across devices

FOLLOW US
@frontiersin

IMPACT METRICS
Advanced article metrics track visibility across digital media

EXTENSIVE PROMOTION
Marketing and promotion of impactful research

LOOP RESEARCH NETWORK
Our network increases your article's readership